# Study of Electrical, Optical and Magnetic properties in doped $CeO_2$

## A Thesis

**Submitted for the award of Ph.D. degree**

**In Physics**

**(Faculty of Science)**

**To the**

**University of Kota**


**By**

**SWATI SONI**




**Under the Supervision of**

**Dr. SAURABH DALELA**

**(Associate Professor)**

**DEPARTMENT OF PURE & APPLIED PHYSICS**

**UNIVERSITY OF KOTA**

**KOTA (RAJASTHAN)**


**JANUARY 2019**

**Department of Pure & Applied Physics**
**University of Kota, Kota**
**M.B.S. Marg, Kabir Circle, Kota**

**TELEFAX: +91-744-2471-038**
**E-mail: sdalela@uok.ac.in**
**Website: www.uok.ac.in**

**Dr. Saurabh Dalela**
**Ph.D. (Material Science)**
**Associate Professor**

# CERTIFICATE

*I feel great pleasure in certifying that the thesis entitled "**Study of Electrical, Optical and Magnetic properties in doped $CeO_2$**" by **Ms Swati Soni** under my guidance. She has completed the following requirements as per Ph.D regulations of the University.*

*(a) Course work as per the university rules.*

*(b) Residential requirements of the university (200 days)*

*(c) Regularly submitted annual progress report.*

*(d) Presented his work in the departmental committee.*

*(e) Published/accepted minimum of one research paper in a referred research journal,*

*I recommend the submission of thesis.*

***Date:***

***Dr. Saurabh Dalela***
***Associate Professor***
***Department of Pure & Applied Physics***
***University of Kota, Kota***

# ANTI-PLAGIARISM CERTIFICATE

It is certified that PhD Thesis Titled, **"Study of Electrical, Optical and Magnetic properties in doped $CeO_2$"** by **Ms Swati Soni** has been examined by us with the following anti-plagiarism tools. We undertake the follows:

a. Thesis has significant new work/knowledge as compared already published or are under consideration to be published elsewhere. No sentence, equation, diagram, table, paragraph or section has been copied verbatim from previous work unless it is placed under quotation mark and duly referenced.

b. The work presented is original and own work of the author (i.e. there is no plagiarism). No ideas, processes, results or words of the others have been presented as author's own work.

c. There is no fabrication of data or results which has been compiled and analyzed.

d. There is no falsification by manipulating research materials, equipment or processes, or changing or omitting data or results such that the research is not accurately represented in the research record.

e. The thesis has been checked using 'URKUND' Software and found within limits as per HEC plagiarism Policy and instructions issued from time to time.

| | |
|---|---|
| **Ms Swati Soni** | **Dr. Saurabh Dalela** |
| (Name & Signature of Research Scholar) | (Name & Signature and seal of Research Supervisor) |
| Place: Kota | Place: Kota |
| Date: | Date: |

# ABSTRACT

Nanoscience and Nanotechnology is not only dealt with the fundamental understanding of physical property and phenomenon of nanomaterials and nanostructures but also it is the most important and exciting frontier area of research in almost all field of science and technology. The nanotechnology provides the path of many breakthrough changes in different areas of advanced technological applications. The nano-structured materials with variable dimensions exhibit unique characteristics and having similar chemical composition but behave differently from their bulk solid and molecular structures. Among various nanostructured materials, semiconductor nanostructures have gained considerable interest of research in the field of various technological applications that are already commercialized like solar cells, electroluminescent devices, optical gain devices etc.

One of the important characteristics of nanostructured semiconductors is Quantum confinement effect that plays an important role to explore many properties which are probably used for practical application. Mainly, quantum confinement effect dominates in the low dimensional structures with large surface to volume ratio that result in enhancing the band gap along with discrete energy levels. Generally, the doped semiconductor nanocrystals form a new class of materials, which is having wide range of application in devices i.e. LASER, light emitting diodes and sensors.

The dilute magnetic semiconductor (DMS) is a new class of materials having ferromagnetic properties compatible with the existing semiconductor technology. DMS are developed by incorporating a fractional quantity of transition metal/Rare earth atoms into a traditional semiconductor. These materials can exhibit ferromagnetism at/above room temperature make them a promising material for spintronics, optoelectronics or other electronics devices by using both charge and spin degrees of freedom of electrons. Generally, II-VI and III-VI group of DMS nanomaterials have received much attention in the past few years due to their interesting physical properties and potential applications in spintronics and magneto-optical devices. The study of their new physical properties based on certain

applications of nanomaterials is possible only when these materials are made available with desired size, morphology, crystal structure and chemical composition. Among all DMS based nanomaterials, Cerium Oxide ($CeO_2$) is one of the important DMS materials with high mechanical strength, thermal stability, excellent optical properties, good oxygen ion conductivity and oxygen storage capacity. $CeO_2$ has variety of applications such as catalysts for three-way automatic exhaust system, mechanical polishing of microelectronic devices, in sunscreen for UV-absorbent, oxygen gas sensors and blocking material in UV shielding etc. Furthermore, doping of TM/RE metals in $CeO_2$ can also enhance the catalytic and electrical properties of $CeO_2$ that depends on some factors such as particle size, morphology and structural characteristics etc. RE-doped $CeO_2$ solid solution has been widely used as promising electrolytes for intermediate temperature solid oxide fuel cells (SOFC's). In the recent years, a large efforts have been made to investigate the doped $CeO_2$ based DMS compounds due to their potential application in spintronic devices. For this practical application, $CeO_2$ based DMS material require both Curie temperature at/above room temperature and ferromagnetic properties.

The most important field of research is to develop such nanocrystalline structures that induce the ferromagnetism at room temperature which should be intrinsic in nature. So, one of the important aims of the present work is to investigate pure and doped $CeO_2$ nanocrystalline structures possessing intrinsic ferromagnetism at room temperature. Extensive investigations have been carried out on the structural, optical, electronic structure, magnetic and electrical properties of pure $CeO_2$, TM (Fe) and RE (Sm, Gd) doped $CeO_2$ nanocrystalline samples with different concentration of dopants at room temperature. The origin of room temperature ferromagnetism (RTFM) has been mainly ascribed to the presence of oxygen vacancies and defects on the surface of the pure and doped $CeO_2$ nanoparticles (NPs). Based on the experimental data, correlation between the structural, optical, electronic structure, magnetic and electrical properties of these samples have also been developed. Based on the dependence of formation of oxygen vacancies and defects, F-centre exchange mechanism (FCE) and Bound Magnetic polaron model (BMP) have been proposed for the observed room temperature ferromagnetism

(RTFM) in pure and doped $CeO_2$ nanocrystalline samples. So that, these nanocrystalline prospects of potential applications in the development of efficient spintronics devices working at room temperature shall be explored.

The present thesis consists of six chapters. The significance of spintronics, DMS materials, different magnetic materials, nanomaterials and their applications in different area of science and technology are briefly introduced in the **first chapter**. Moreover, some theoretical models such as FCE, BMP, Double exchange model and carrier mediated exchange (RKKY Model) are discussed for explaining the origin of ferromagnetism in the pure and doped $CeO_2$ samples. The general introduction of cerium oxide and a brief review on the different properties of pure and doped $CeO_2$ is also initiated in this chapter, represents the major parts of the research have been carried out on these samples.

The **second chapter** describes the various experimental techniques including XRD, TEM, HRTEM, SAED and EDX for structural characterization, UV-Vis-NIR and SERS for optical characterization, XPS for electronic structure studies, MPMS-3 SQUID-VSM for magnetic studies and Keithley source-meter for electrical studies of the synthesized samples for this work. These experimental techniques are discussed in the line of the introduction of instrumentation, data acquisition, data analysis and information we can infer from the analysis.

In the **third chapter**, the pure $CeO_2$ and RE (Sm)-doped $CeO_2$ NPs with different dopant concentrations are synthesized by co-precipitation method. The structural, optical and electrical properties of these samples have been investigated in details using XRD, TEM, HRTEM, SAED, UV-Vis-NIR, SERS and Keithley source-meter. The formation of oxygen vacancies, changes in the oxidation state of Ce cation with the concentration of dopant have been used to explain the band gap, semiconducting and electrical conductivity of Sm-doped $CeO_2$ NPs.

The **fourth chapter** includes the synthesis and characterization of pure $CeO_2$ and RE (Gd)-doped $CeO_2$ NPs with different dopant concentrations prepared by co-precipitation method. The structural, optical, electronic structure and magnetic

properties of these samples have been investigated in detail. The visible light photocatalytic activity of all the samples has been demonstrated experimentally and gradual enhancement in hydrogen production with fluency of Gd-content in $CeO_2$ is also observed. Furthermore, presence of oxygen vacancies and chemical state of Ce and Fe-ions has been discussed in core level O 1s, Ce 3d and Gd 4d XPS spectra for pure $CeO_2$ and Gd-doped $CeO_2$ nanocrystalline samples to explain the magnetic properties of the samples. A theoretical FCE mechanism has been proposed for explaining the observed RTFM in pure $CeO_2$ and paramagnetic dominated weak ferromagnetism in Gd-doped $CeO_2$ nanocrystalline samples.

The **fifth chapter** gives the detailed investigations on the structural, optical, electronic structure and magnetic properties of pure $CeO_2$ and TM (Fe)-doped $CeO_2$ nanocrystalline samples synthesized using co-precipitation method. The structural and morphological analysis of all samples had been done using XRD, TEM, HRTEM and SAED measurements. The optical band gap and formation of oxygen vacancy defects has been confirmed by UV-Vis-NIR and Raman spectra. However, the formation of oxygen vacancies and chemical state of all samples has been also confirmed by Ce 3d, O 1s and Fe 3d XPS core level spectra. The magnetic measurements has been confirmed the RTFM for pure $CeO_2$ whereas Fe-ions implantation shows the paramagnetic dominated weak ferromagnetism for Fe-doped $CeO_2$ samples that has been explained in the line of change in the oxidation state of Ce-ions due to formation of oxygen vacancies and may be correlated with F-centre exchange mechanism. The observed signature of ferromagnetism in pure $CeO_2$ nanocrystalline sample shows significant in the development of spintronics devices at room temperature.

The **sixth chapter** summarizes the summary and conclusion of the total work performed in the thesis. Finally, the scopes for the further investigation are also highlighted in this chapter to explain the justification of the remaining work to be performed in the coming time.

# CANDIDATE'S DECLARATION

*I, hereby, certify that the work, which is being presented in the thesis, entitled,* ***"Study of Electrical, Optical and Magnetic properties in doped $CeO_2$"*** *in partial fulfilment of the requirement for the award of the Degree of Doctor of Philosophy, carried under the supervision of* ***Dr. Saurabh Dalela****, Associate Professor and submitted to the Department of Pure & Applied Physics, University of Kota, Kota, represents my ideas in my own words and where others ideas or words have been included. I have adequately cited and referenced the original sources. The work presented in this thesis has not been submitted elsewhere for the award of any other degree or diploma from any Institutions. I also declare that I have adhered to all principles of academic honesty and integrity and have not misrepresented or fabricated or falsified any idea/data/fact/source in my submission. I understand that any violation of the above will cause for disciplinary action by the University and can also evoke penal action from the sources which have thus not been properly cited or from whom proper permission has not been taken when needed.*

**Date:** **(*Swati Soni*)**

*This is to certify that the above statement made by* ***Swati Soni*** *(Registration No.* ***RS/2063/13,*** *dated* ***14/08/2013*** *and Enrolment No.* ***2013/000117****) is correct to the best of my knowledge.*

**Date:**

***Dr. Saurabh Dalela***
***(Research Supervisor)***
***Associate Professor***
***Department of Pure & Applied Physics***
***University of Kota, Kota***

# ACKNOWLEDGEMENT

The journey of my doctoral research work has been completed with the encouragement, motivation, inspiration and support of many people, which I have been received from different sources. Without their support, it would be impossible for me to complete my research work. Sometimes, it is impossible to acknowledge all sources individually; therefore, I take this opportunity to express my gratefulness to many people including my well-wishers, my friends and colleagues from various institutions whose contribution is obvious for completion of this thesis work.

**"A true teacher or Guru would never tell you what to do. But he would give you the knowledge with which you could decide what would be best for you to do. A Guru desires nothing from you except your well-being and progress on the path".**

These words are not enough for expressing my sincere gratitude and respect to my supervisor. At the moment of accomplishment, first of all I take this opportunity and privilege to express my sincere, deep sense of gratitude and regards to my supervisor **Dr. Saurabh Dalela**, Associate Professor, Department of Pure & Applied Physics, University of Kota, for his most knowledgeable guidance with constant encouragement throughout the entire period of my research work. It has been a great experience to work with him and learn advancement in the field of nanotechnology under his guidance. His deep knowledge, intellectuality and innovative ideas in pure and applied Physics have inspired me a lot and I feel privileged to gain many skills under his guidance during my research tenure. He has established many research facilities in our department which are very helpful to conduct research work in stipulated tenure. Without his support, motivation and limitless kindness, I could not accomplish my research work successfully. He has always given me enough freedom to express my views regarding the problem, which I have faced during the work and supported me to overcome the problems. I will always remember his calm and joyous attitude.

I am also grateful to **Prof. Neelima Singh**, Vice Chancellor, **Prof. P. K. Dashora**, former Vice-Chancellor, **Dr. O. P. Rishi**, Director of Research and all the Faculty & staff members of University of Kota, Kota for supporting and facilitating me to carry out my research work.

I would like to express my special thanks to all the faculty member of the Department of Pure & Applied Physics, University of Kota. I express my sincere and courteous gratitude to **Prof. K. P. Maheshwari Sir**, **B. L. Suthar Sir** and **Prof. N. K. Jaiman Sir** for their valuable suggestions and cooperation during my research work. I want to thank **Dr. Ghanshyam Sharma**, Associate Professor, for his kind guidance during my Ph.D. tenure. I also express my courteous gratitude to **Dr. Namrata Sengar** and **Dr. N. L. Heda**, Assistance Professor for their moral support, motivation, helpful suggestions, encouragement and blessings during this period.

I am deeply grateful to our Research Collaborator and faculty members at various research institutes and universities for facilitating necessary instrumentation for the proper completion of my research work. I express my sincere gratitude to **Dr. P. A. Alvi**, Associate Professor, **Dr. Saral Gupta**, Associate Professor and Head, Department of Physics, **Banasthali Vidhyapith**, Newai, for providing XRD, Raman and EDX facilities to analyze my samples and their constant encouragement for completion of my work.

I am thankful to **Dr. R. S. Meena**, **Dr. Govind Gupta** and **Dr. Monu Mishra**, Scientist in **National Physical Laboratories** (**NPL**), New Delhi for extending the XPS facility for analyzing my samples. I am extremely grateful to **Dr. Budhika Mendis** from Department of Physics, **Durham University, Durham, United Kingdom (UK)**, for helping me to carry out the surface morphology of my samples using TEM facility.

I express this opportunity to acknowledge Micro and Nano Characterization Facility (MNCF), Centre for Nano Science & Engineering (CeNSE), **Indian Institute of Science, Bengaluru**, for the magnetic analysis of my samples

using MPMS-3 SQUID. I owe a great deal of appreciation and gratitude to **Dr. Vikram S. Raghavan** from optics and microfluidics (OMI) Lab, Department of Instrumentation and Applied Physics, **Indian Institute of Science (IISc), Bengaluru**, for helping me to carry out the magnetic measurement and data analysis. I will be grateful for his constant endeavour to encourage me during path of completion of my research work.

I expand my sincere thanks to **Dr. Shyam Sunder Sharma**, Assistance Professor, **Govt. Women Engineering College, Ajmer**, for extending Keithley source-meter instrument facility for electrical measurements of my samples. I am deeply indebted to the Staff members of **Elettra Synchrotron Trieste and CNR, Italy,** for providing the beam-time at the BACH beam line for XAS and XMCD measurements. I cordially express my gratitude to the entire staff of **Central Library, University of Kota,** for their cooperation and support in accessing the library facility of the University of Kota.

I express my sincere thanks to the non-teaching staff of our department for providing me with the necessary help and cooperation during different phases of my research work. I find myself short of words for the inexhaustible perseverance of my senior **Dr. Kuntal Kabra** and research mates **Ms Maya Kaur, Ms Shweta Arora** and **Ms Mridula Dave**, for their meticulous assistance, sustained encouragement, immaculate suggestions and unflagging moral support throughout my research tenure. I also would like to thank my lab mates, **Mr. K. K. Soni**, **Ms Shalu Jain** and **Ms Jyoti Sahu**, for their sincere cooperation and suggestions during this work. I would like to thank every staff at my university, who helped me directly and indirectly during this period.

I am grateful to my family members, who encouraged and helped me at every stage of my life and desired to see this achievement come true. My parents deserve special appreciation for their inseparable support and prayers for my success. First and foremost my father, **Mr. J. C. Soni** who has been ignited the spirit and encouraged me to undertake research career. My mother, **Ms Uma Soni**, who is the real architect of my life, I am indebted to her for supporting me during many

occasions and caring with the warmth of love. I also express my thanks to my younger brother **Mr. Ankit Soni** and my bhabhi **Ms Rakhi Soni** for their continuous encouragement, support, love, care and prayers for my success. Once again, I would like to thank my entire family member for their unconditional love, support and great care that are fathomless during my research tenure.

I am indebted to **Department of Science and Technology (DST), Ministry of Science and Technology, Government of India, New Delhi**, for their financial support to undertake this research work entitled, **"Study of Electrical, Optical and Magnetic properties in doped $CeO_2$"**, under DST WOS-A project scheme (**DST Ref. No.:SR/WOS-A/PM-1021/2015, Dated 11.07.2016**) as a **Women Scientist** and **Principal Investigator** of this project under the mentorship of **Dr. Saurabh Dalela**, Associate Professor, Department of Pure & Applied Physics, University of Kota, Kota.

I thank the **Almighty God** for showering blessing in every stage of my life and I bow to my **Spiritual Guru** with reverence for giving me the knowledge, strength and patience to complete this research work through all these years.

Last but not least I would like to thank all the people I did not mention namely or at all, I certainly did not forget you and blame the lack of space for your absence in my acknowledgement.

**Swati Soni**

# TABLE OF CONTENTS

# LIST OF TABLES

# LIST OF FIGURES

# LIST OF ACRONYMS

| | |
|---|---|
| BMP | Bound Magnetic Polaron |
| CCD | Charge Coupled Device |
| $CeO_2$ | Cerium Oxide |
| DMS | Dilute Magnetic Semiconductor |
| EXAFS | Extended X-ray Absorption Fine Structure |
| *fcc* | Face Centered Cubic |
| FCE | F-centre Exchange |
| GMR | Giant Magneto Resistance |
| MBE | Molecular Beam Epitaxial |
| NPs | Nanoparticles |
| PMT | Photomultiplier Tube |
| RE | Rare Earth |
| RIXS | Resonant Inelastic X-ray Scattering |
| RKKY | Ruderman-Kittel-Kasuya-Yosida |
| RTFM | Room Temperature Ferromagnetism |
| SAED | Selected Area Electron Diffraction |
| SOFC's | Solid Oxide Fuel Cells |
| TEM | Transmission Electron Microscopy |
| $TiO_2$ | Titanium Oxide |
| TM | Transition Metals |
| TMR | Tunnelling Magneto Resistance |
| XANES | X-ray Absorption Near-Edge Structure |
| XAS | X-ray Absorption Spectroscopy |
| XES | X-ray Emission Spectroscopy |
| XPS | X-ray Photoelectron Spectroscopy |
| XRD | X-ray Diffraction |
| ZnO | Zinc Oxide |

# Chapter 1

# Introduction

# CHAPTER 1

# INTRODUCTION

## 1.1 Spintronics

**Spintronics** is the phenomena of spin transport in metals and semiconductor, also known as “spin transport electronics” [1]. Spintronics explain the intrinsic spin of an electron, magnetic moment and fundamental electronic charge in solid-state devices, so sometimes it is also termed as “magneto-electronics”. After the electron charge, the electron spin corresponds to an additional degree of freedom that could be used for information storage and processing. Spintronics involves the study of active control and manipulation of spin degree of freedom in solid-state systems. The electrical properties of electrons are characterized by electrical conductivity, charge carrier mobility, voltage and electric current, whereas, spin properties are characterized by magnetization, magnetic resonance and spin relaxation rates [2]. It is well known that for information processing and communication, integrated circuits and high-frequency devices have been successfully used through controlling the charge of electron in semiconductors but mass storage information technology is carried out by magnetic recording using only electron spin in the ferromagnetic materials. Therefore, it is quite natural, both the spin and the charge of an electron can be used at the same time to enhance the performance of a device. This is the main idea of spintronics for future microelectronic device to downsize current even in nanometres. The main goal of spintronics is to understand the interaction between the particle spin and its solid-state environment and to make useful devices using the acquired knowledge. The most useful applications are the giant magnetoresistance (GMR) and tunnelling magnetoresistance (TMR) in devices, built of ferromagnetic metals [3]. Now possibility of making a material that shows both ferromagnetic and semiconductor properties at operating temperature is magnetic semiconductor. Thus, the functional spintronics devices require a compatible semiconducting material with ferromagnetic ordering at operating temperature.

## 1.2 Spintronics materials

On the basis of magnetic materials there are three types of semiconductor spintronics materials as shown in Figure 1.1.

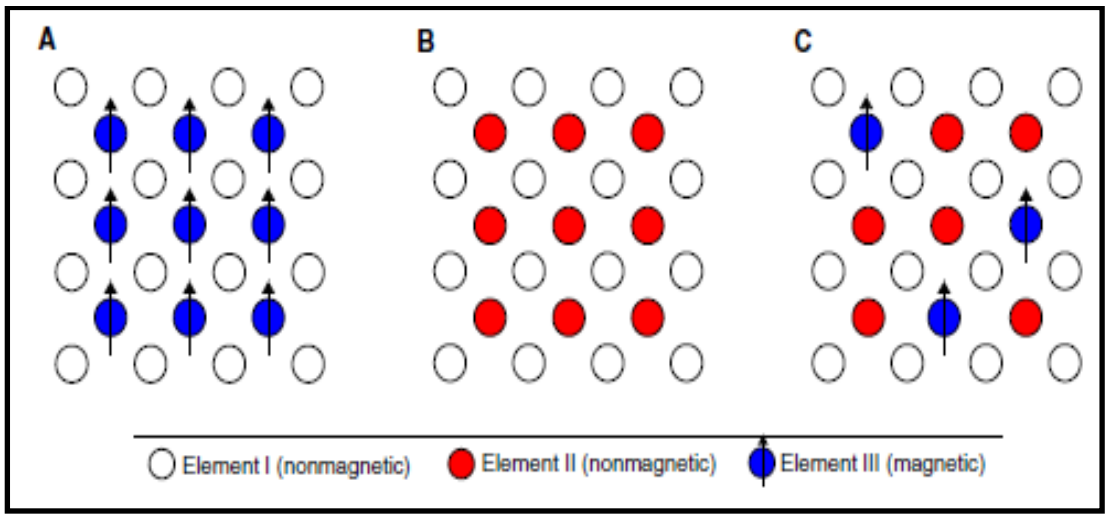


**Figure 1.1: Schematic presentation of (A) Magnetic Semiconductor, (B) Non-Magnetic Semiconductor and (C) Dilute Magnetic Semiconductor [4].**

In Figure 1.1 (A) magnetic semiconductor are shown, in which one of the two elements have local magnetic moment. Magnetic semiconductors are the magnetite, chromium and europium chalcogenides etc., which have a periodic array of magnetically ordered spins in their crystal structure [5]. These magnetic semiconductors are difficult to grow, show incompatibility with semiconductor materials such as Si or GaAs, and also have low Curie temperature i.e. below 100K [4]. Figure 1.1 (B) shows the non-magnetic semiconductors like GaAs or ZnO, which are composed of two non-magnetic elements (white and red). Now, Figure 1.1 (C) shows the DMS, in which few atoms of non-magnetic semiconductors are replaced by atom (transition metal/ rare earth elements) possessing local magnetic moments.

There are two major criteria to select the most promising material for semiconductor spintronics:

a) First, the ferromagnetism should be retained by the material at operating temperature i.e. room temperature.

b) Second, manipulation of electron spin in semiconducting devices should be undertaken so that it can improve the conventional semiconductor technology.

Hence, being a ferromagnetic semiconductor material, DMS is a promising material for this need. Dilute magnetic semiconductors are non-magnetic semiconductors doped with few percentages of magnetic elements such as transition metals (TM), which is expected to integrate with the existing semiconductors technology with high spin-polarization. The most common DMS are II-VI compounds such as CdS, CdSe, ZnSe, ZnS, CuO, ZnO etc., substituted for the parent cation with TM ions (Cr, Mn, Fe or Co) and rare earth (Sm, Gd, Eu) ions. The III-V compounds display ferromagnetism due to incorporation of Mn in the low temperature region, such as Mn-doped InAs and GaAs showed 35 K and 60 K Curie temperature ($T_C$), respectively [6, 7]. The optimization of the preparation as well as fabrication method is difficult for II-VI compounds for achieving high temperature ferromagnetism in these compounds. On the other hand, IV-VI compounds such as $TiO_2$, $ZrO_2$, $HfO_2$ and $SnO_2$ mainly depends on the carrier concentration and presence of lattice defects. The carrier concentration in IV-VI compounds is controlled by dopant ions that influence the magnetic behaviour of the host lattice. The TM and rare earth (RE) metals used as magnetic atoms in DMS have partially filled d and f states, respectively, containing unpaired electrons. These unpaired electrons interact with the host semiconductor by exchange mechanism that responsible for magnetic behaviour in DMS [6, 8]. In case of TM-doped DMS, TM ions occupy the substituted sites of host semiconductor via sp-d exchange interaction and enhance the spin dependent transportation that increases both the magnetization and $T_C$ of the semiconductor system [9]. It is generally accepted that few percent of doping concentration of TM or RE with partially filled d or f shell, respectively, is sufficient to involve ferromagnetism in DMS. Many DMS compounds such as, TM-doped ZnO, $TiO_2$, $HfO_2$, $SnO_2$ and $CeO_2$ have shown room temperature ferromagnetism (RTFM) due to some defects, but intrinsic origin of RTFM is still under debate [10-14]. The ferromagnetism in metal oxide $CeO_2$, $Al_2O_3$, ZnO, $In_2O_3$ and $SnO_2$ NPs has been reported due to the exchange interaction between localized

electron spin moments originating from the surface of the NPs [15]. Since, the insulating materials has no free charge carriers, therefore, high temperature ferromagnetism is reported to be attributed due to the oxygen vacancies. The high $T_C$ ferromagnetism in TM-doped insulating oxide is proposed by the mechanism of oxygen vacancy mediated ferromagnetism or called F-centre exchange (FCE) coupling instead of the carrier induced ferromagnetism [16]. In FCE mechanism an electron is trapped in the oxygen vacancy which acts as a coupling centre from which doped magnetic ions align in the ferromagnetic order. However, the solubility of magnetic ions is very low in the host matrix of doped magnetic semiconductors so that the origin of ferromagnetism in these compounds has been attributed to the magnetic impurities [17]. Therefore, there is a requirement of the host matrix that has highly soluble magnetic ions to form stable magnetic semiconductor.

## 1.3 Type of Magnetism

The first naturally occurring magnetic mineral on earth is called magnetite ($Fe_3O_4$). The different types of magnetism are associated with three main categories of material, such as diamagnetic, paramagnetic and ferromagnetic. In addition to that, antiferromagnetism and ferrimagnetisms consider as the sub-classified materials of ferromagnetism. The behaviour of magnetic materials totally depends on the response of an electron and magnetic dipoles to an externally applied magnetic field. As we are going to use this terminology of magnetic materials throughout the thesis, we would like to discuss various magnetic properties in short in the following sections.

### 1.3.1 Diamagnetism

The weakest magnetic form in magnetic materials is diamagnetism, which is induced by the orbital motion of an electron due to the applied magnetic field. The magnitude of the induced magnetic moment is very small that is induced in the opposite direction of the applied magnetic field. That's why, diamagnetic materials shows a negative and very small magnetic susceptibility ($\chi \sim 10^{-5}$) and relative permeability ($\mu_r$) less than unity or zero for perfectly diamagnetic material. A schematic magnetic dipole configuration for diamagnetic material in the presence and absence of applied magnetic field is shown in the Figure 1.2.

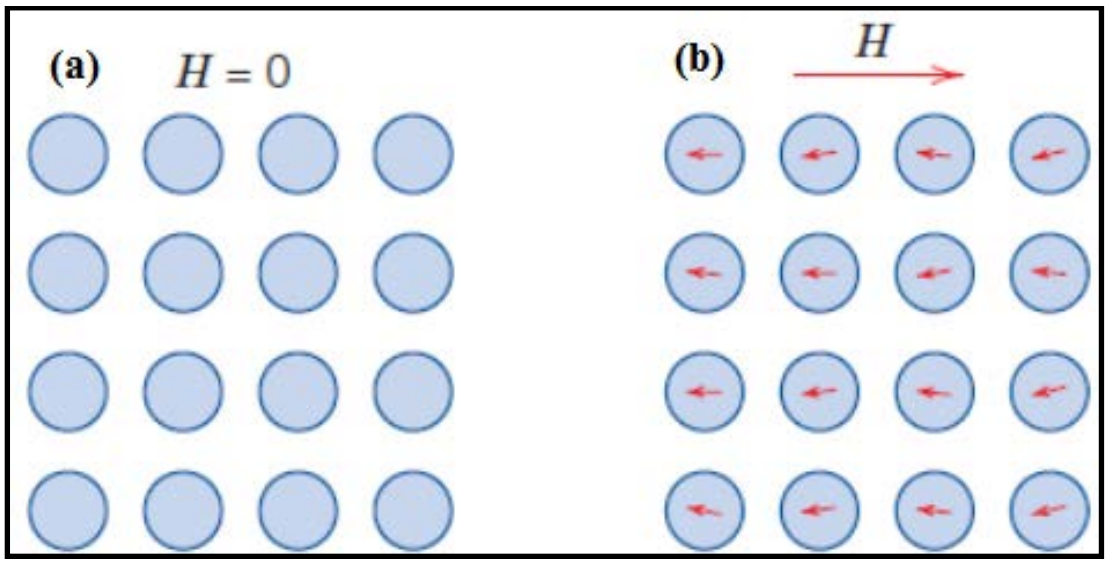


**Figure 1.2: The magnetic dipole configuration for diamagnetic material (a) without and (b) with applied magnetic field (dipoles are aligned in the opposite direction of magnetic field)**

### 1.3.2 Paramagnetism

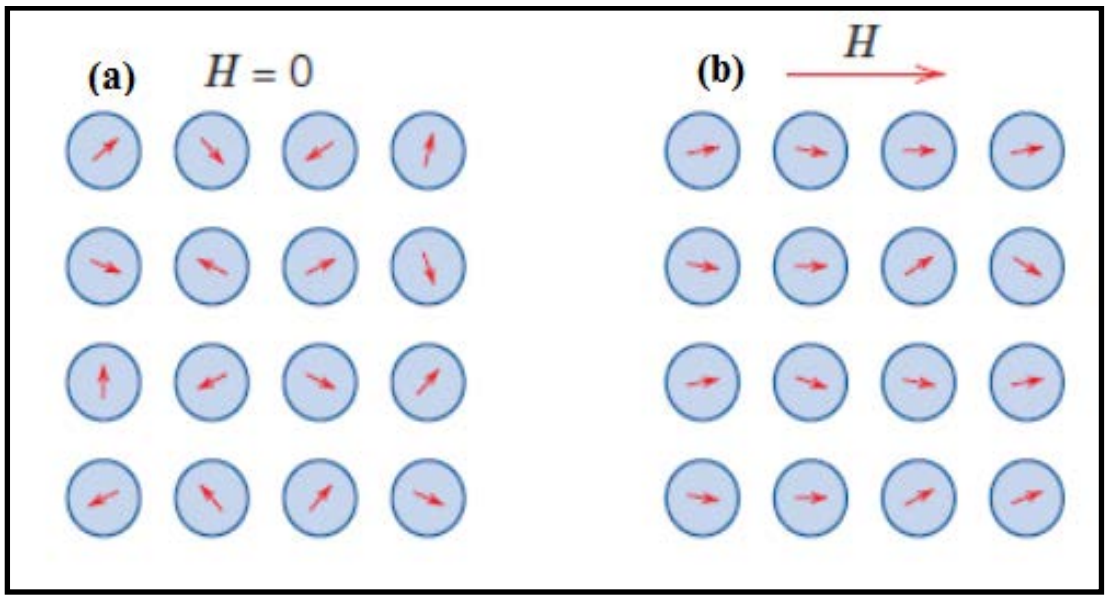


**Figure 1.3: The magnetic dipole configuration for paramagnetic material (a) without and (b) with applied magnetic field.**

Paramagnetism is the form of magnetism, in which material is weakly attracted by an externally applied magnetic field and internally magnetic field is induced in the direction of applied magnetic field. It occurs in those materials which

have atoms or molecules with permanent dipole moment. In absence of external magnetic field, these atomic dipoles are randomly oriented, means no magnetization. The magnetic susceptibility of paramagnetic material is small and positive with the order of $10^{-3}$ to $10^{-5}$. The paramagnetism is found in lithium (Li), molybdenum (Mo), magnesium (Mg) etc., which has the unpaired electrons to have a stable sufficient magnetic moment upon magnetic field application.

### 1.3.3 Ferromagnetism

Ferromagnetism is the phenomenon exhibited by some naturally available TM elements as Fe, Ni and Co, and some of the rare earth like Gd and Dy. These elements have spontaneous very large and permanent magnetization even in the absence of the external magnetic field. Ferromagnetic materials exhibits a long rang ordering phenomenon which causes the unpaired electron spins to line up parallel with each other in a region called domain. The coupling interaction causes the net spin moment of the nearby atoms to align to one another, even in the absence of an external magnetic field also. Figure 1.4 represents the spin alignment in ferromagnetic material. The magnetic susceptibility of ferromagnetic materials is positive and vey high with the order of $10^{6}$.

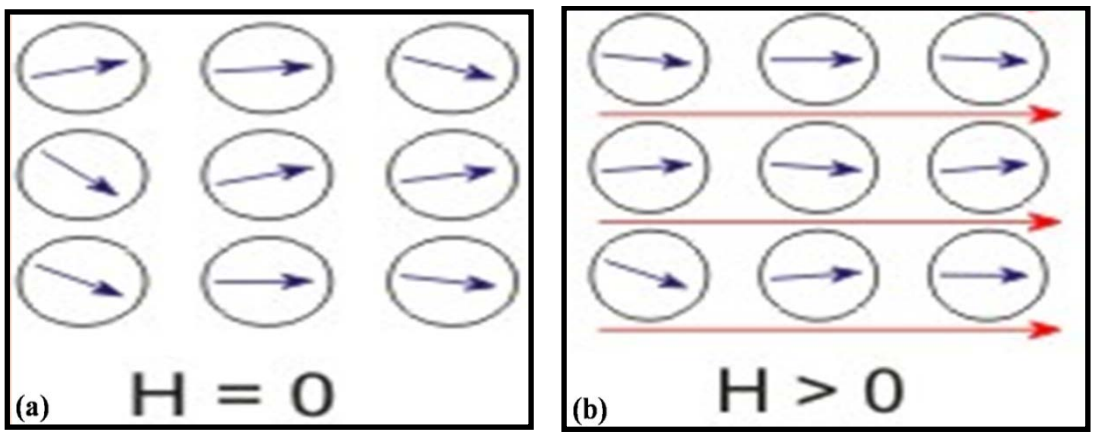


**Figure 1.4: The spin alignment for ferromagnetic material (a) without and (b) with externally applied magnetic field.**

The magnetic susceptibility varies with temperature and above a certain temperature called $T_C$, the spontaneous magnetization is vanished and material behaves like a paramagnetic material.

Therefore, in ferromagnetic material at temperature below $T_C$ have small domains that are automatically magnetized and separated by domain wall from which the spin change gradually, as shown in Figure 1.5. The domain size could vary from $10^{-6}$ cm to the volume of the crystal.

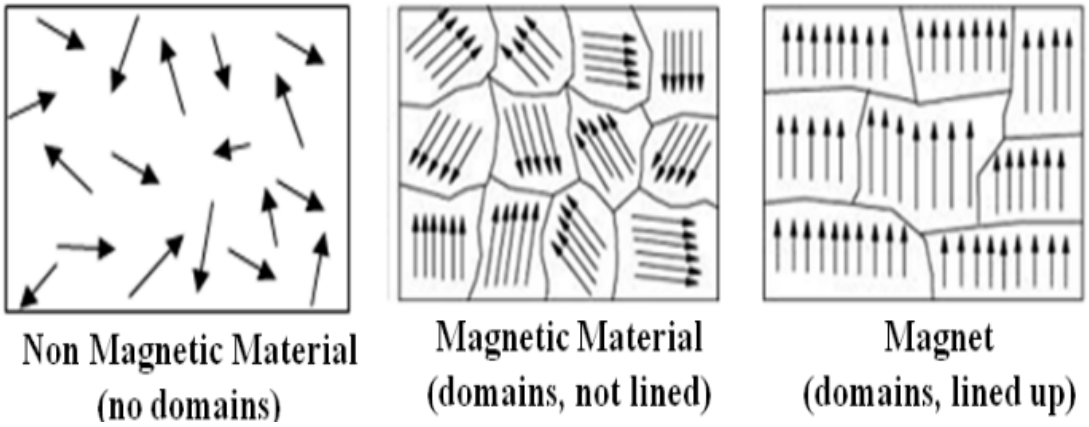


**Figure 1.5: Schematic variation of domains in a material and arrows represent atomic magnetic moment [18]**

When an external magnetic field is applied to the ferromagnetic material, it get magnetized and as the applied magnetic field is removed it will try to demagnetise but not take similar path for demagnetisation as the path followed for magnetisation and hence these materials exhibit a hysteresis loop between magnetization and the applied magnetic field as shown in Figure 1.6.

Now, according to the domain theory, initially the moments of domains are randomly oriented that gives zero net magnetization (as shown in Figure 1.7). As the external magnetic field is applied, domains are oriented in the direction of the applied field grow at the expense of those domains which are not favourably oriented (point B to D in Figure 1.7). This process continues with increasing magnetic field until the macroscopic sample becomes a single domain (point E). The state of saturation is achieved when domains rotation become oriented with the field (point F). When the magnetic field exceeds a particular value then it diminishes the domain walls that cannot fully reversed back to their original position, which results in remanent magnetization.

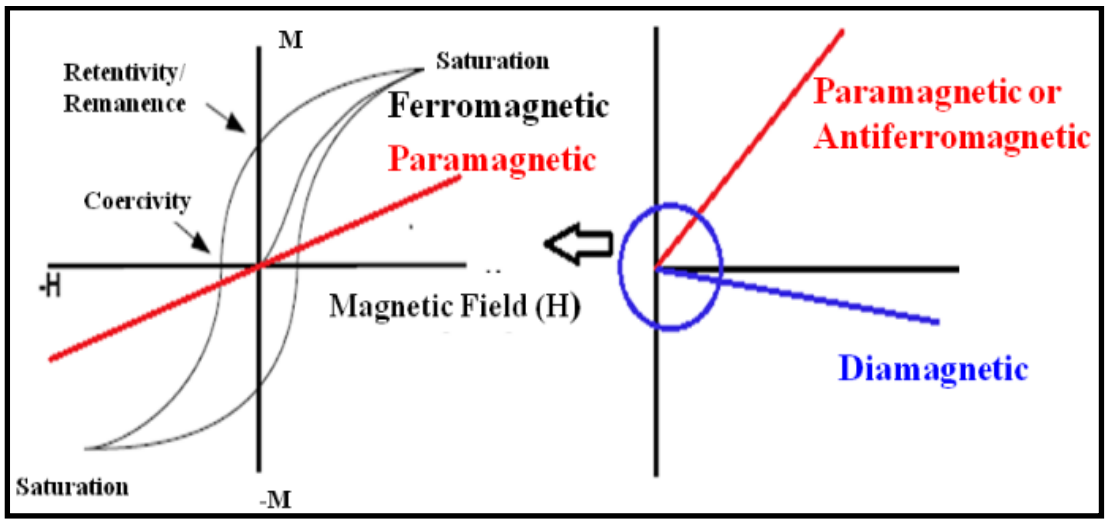


**Figure 1.6: A schematic hysteresis loop expected for ferromagnetic, paramagnetic and diamagnetic materials.**

As shown in Figure 1.6, if the applied field (H) is reduced in the reverse direction, magnetization does not retrace its original path and at zero fields there exist a residual magnetization called as remanence. When field is applied in the opposite direction then magnetization within the sample vanishes, this phenomenon is called coercivity and the field is known as coercive field ($H_c$). The slop of the magnetisation and demagnetisation curve for diamagnetic material is small and negative while for a paramagnetic substance it is small but positive.

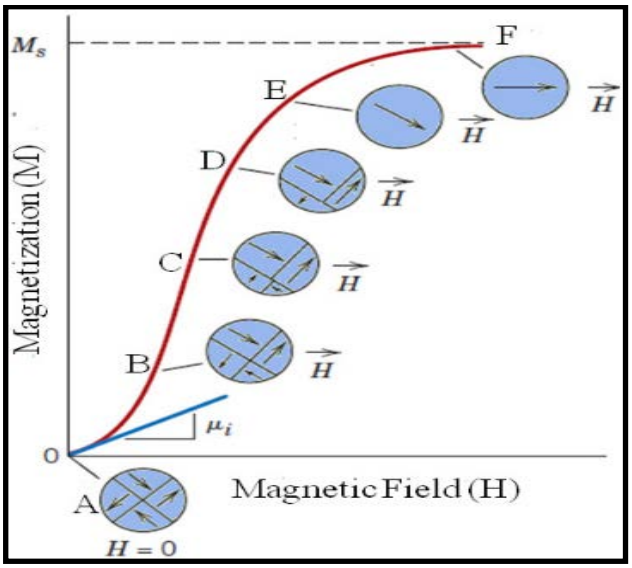


**Figure 1.7: M-H curve for ferromagnetic material represents domain configuration with several state of magnetization [19]**

## 1.4 Theoretical Models for explaining origin of ferromagnetism in DMS

This section describes the models that are commonly used to describe the magnetic interaction in DMS. Some of them promote ferromagnetism in the system such as double exchange interaction, while other can result in either ferromagnetism or antiferromagnetism that depends on physical factors such as chemical bonding, defect structure and carrier concentration.

### 1.4.1 Direct and Super-exchange interaction in insulators

Direct exchange interaction couples the spins ($s_i$) of the localized electron in insulators, which can be described by the Heisenberg Hamiltonian as [20]:

$$H_{ex} = -\sum_{ij} J_{ij} s_i \cdot s_j \qquad (1.1)$$

If the two electronic states of a free atom coupled by the exchange integral then $J_{ij}$ tends to positive and spins are aligned parallel, as reflected in Hund's rule. Besides of that if the interaction takes place between localized electrons of different neighbouring atoms, $J_{ij}$ tends to negative. For most of the solids with unpaired electrons, $J_{ij}$ may be either positive or negative, but typically the negative value dominates that leads to anti-ferromagnetic alignment of the neighbouring spins.

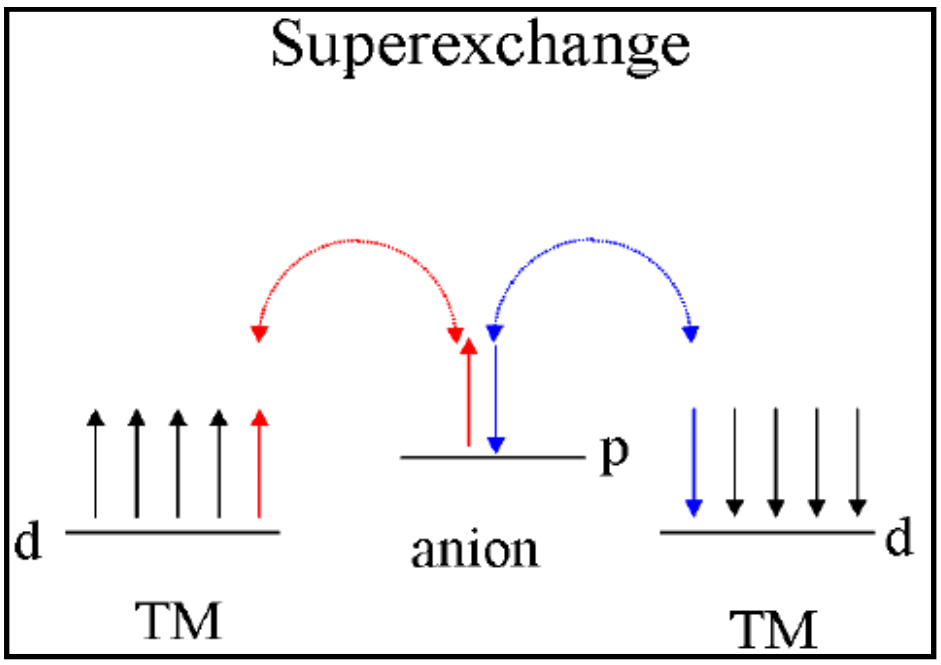


**Figure 1.8: A schematic representation of superexchange interation [21].**

Since, direct exchange interaction cannot explain the antiferromagnetism of the TM compounds due to localized d-orbital and direct hopping between the d-orbitals of different atoms. Besides that the concept of direct exchange can be extended to these cases by hopping via the intermediate p-orbital, the mechanism is called super-exchange. Therefore, in TM oxides, the superexchange interaction is the magnetic interactions between the TM metal ions (d-orbital) and in oxygen anions (p-orbital). Superexchange can also be described by the Heisenberg Hamiltonian, in which $J_{ij}$ is determined by the metal-oxygen-metal bond angle and by the d-electron configuration on TM ions [4].

### 1.4.2 Carrier mediated exchange (RKKY Model)

The Ruderman-Kittel-Kasuya-Yosida (RKKY) model has been known for 50 years as the basic interaction in the metallic ferromagnetic materials [22]. This interaction permits the coupling of magnetic moment through Coulomb exchange via band electrons over relatively large distance. This theory has been generated to explain the ferromagnetism in metals and efficiently explained the mechanism when high concentration of delocalized free charge carriers is present in the host material. This model explains the magnetic interaction between the magnetic ion having a single localized inner d or f-shell electron and delocalized conduction band electrons. It is also showed that the spin polarization of the conduction electron oscillates as a function of distance from the localized moments through this model. These conduction electrons near to the magnetic ion get magnetized and act as an effective field to influence the polarization of the neighbouring magnetic ions. The oscillatory polarization decreases with the distance from the magnetic ion, which cause indirect super exchange interaction RKKY between two magnetic ions or nearest magnetic neighbours. This coupling may be in a parallel (ferromagnetic) or anti-parallel (antiferromagnetic) arrangement, which is depending on the separation of the interacting atom. The ferromagnetic interaction for 4f localized electrons is explained by this mechanism, in which there is an indirect exchange interaction between the outer most 5d electrons. These 5d electrons have partially overlapped the 4f shells.

### 1.4.3 Double Exchange model

This exchange interaction involves the coupling of magnetic ions in different charge state, due to it electron hopping takes place between ions through interaction between the p-orbital. Spin cannot be flipped in this model. This mechanism is favourable when both ions have similar magnetic structure. The magnetism in spinel magnetite, manganites and Mn-perovskites can be explained by this model.

### 1.4.4 Bound Magnetic Polaron Model

The ferromagnetic exchange coupling between the TM ions in n-type oxide DMS can be explained successfully from bound magnetic polaron (BMP) model. *Coey et al*., has proposed this model for n-type DMS material, which is based on exchange interaction between the impurity band and the atomic spin moment on dopant ions [23]. Generally, oxides contains significant amount of oxygen vacancy defects during synthesis process, which introduces electrons in the system. These electron are associated with the defect such as oxygen vacancy, which is confined in a hydrogenic orbital of radius $r_h = \varepsilon\ (m/m^*)\ a_o$, here $\varepsilon$ is the dielectric constant, $m$ is the mass of an electron, $m^*$ is the effective mass of the donor electron and $a_o$ is the Bohr radius. Now, these hydrogenic donor electrons form a BMP by coupling with 3d TM ions within their orbits [24]. This interaction is responsible to the parallel or anti-parallel alignment of the magnetic impurity, depending on the system. The net energy distribution differs in parallel and anti-parallel alignment, which results in a non-zero spin flip energy and that is the main characteristic of BMP. In parallel alignment of ions, net energy of the system can be lowered as they all interact with carriers in the same way. The s-d exchange energy exceeds by $k_BT$ at low temperature, so that the mutual alignment of the ions and charge carriers results in ferromagnetic ordering. The temperature up to which a BMP can make possible magnetic ordering depends on the nature of the interaction between atomic spins and the carriers. However, the area of these polaron increases as the temperature decreases.

Figure 1.9 shows the schematic interaction in oxides, where oxygen vacancies defects act as electron source. These electrons interact with all magnetic ions, lying within the orbit. Inside the orbit, if enough number of magnetic spins is present then electron is completely spin polarized. So, these atomic magnetic moments have an indirect exchange interaction coupled by carriers that results into the ferromagnetic ordering in the sample.

The main issue is to understand the origin of oxygen vacancies in the ferromagnetic doped DMS compounds. The exchange mechanism that establishes the ferromagnetism can be considered using both the RKKY interaction and the BMP theory; in which former require a metallic system while the latter can be observed in semiconductor or an insulating material. Another classification of the BMP theory is termed as FCE mechanism. This mechanism can also apply to explain the RTFM in magnetic insulators [25, 26]. The FCE mechanism deals with the ferromagnetism arising due to presence of oxygen vacancies. The charge state of an oxygen vacancy can be categorized in three possible forms, such as (a) $F^{2+}$ centre with no trapped electrons, (b) $F^{+}$ centre with one trapped electron and (c) $F^{0}$ centre with two trapped electrons. The $F^{0}$ centre charge state is in a single state (S=0) and form a shallow donor level or lie above the conduction band. This can only mediate weak antiferromagnetism (AFM) exchange between the magnetic dopants. For some other cases, the impurity band is formed due to the $F^{0}$ centre charge states when it is overlapped with the conduction band of the host oxide (i.e. 4s band), this favours the ferromagnetism in the system but its strength is quite weak. In comparison of this, singly occupied vacancies i.e. $F^{+}$ centre lie deep in the gap and favour a strong ferromagnetism in ground state [25].

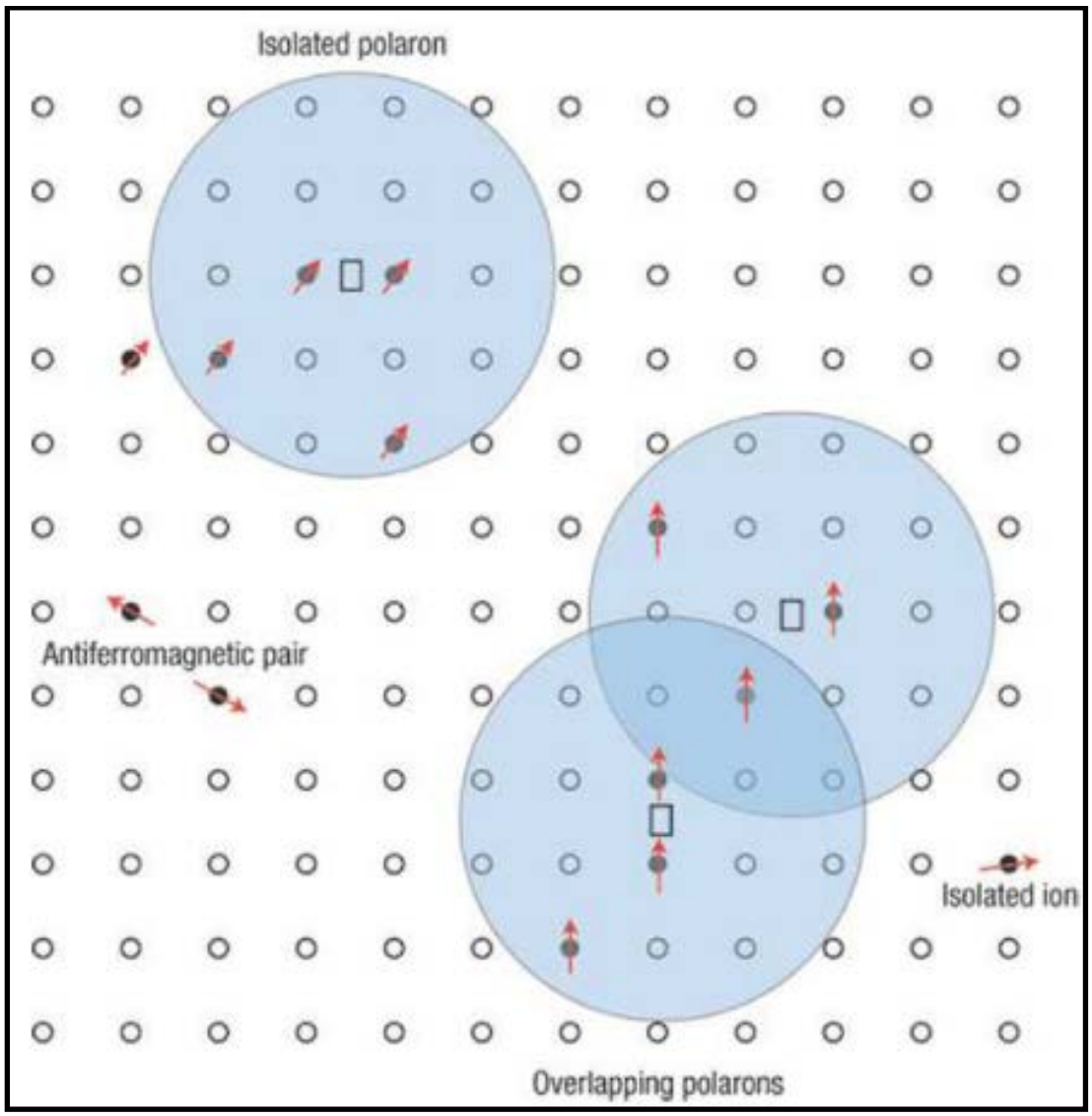


**Figure 1.9: A schematic representation of magnetic polarons in DMS [27, 28].**

## 1.5 Nano-Materials: An Introduction

Nanotechnology refers to the branch of science which deals with the different aspects of a material in nano-regime, which is about 1 to 100 nm. The concept and idea of nanoscience and nanotechnology was presented by Richard P. Feynman during his famous lecture ***"There's Plenty of Room at the Bottom"*** [29]. Nanotechnology has the potential significant impact on society that has been already used by information and communication sectors. It is also used in textiles, coatings, in cosmetics, sunscreens, some food and energy technologies, as well as in medical products and medicines. Nanotechnology produced different types of materials at

nanoscale level. There are two types of nanocrystals that have huge interest; first is semiconductor and second is metallic [30, 31]. The semiconductors nanocrystals have extent of separation between the valance band and conduction band that define the property of the system and also depends on the size of the nanocrystals. So that, with the variation in the size of the nanocrystal, different properties can be achieved in the same nanocrystal. On the other side, metal nanocrystal doesn't have the autonomy of varying band gap with the variation in the size. Usually, nanoparticles (NPs) have wide class of materials which include substance having range less than 100 nm and according to the shape of the material it can be 0D, 1D, 2D or 3D [32]. NPs are not a simple molecules but it is composed of three layers; first is the surface layer that may be functionalized with the variety of small molecules, metal ions and surfactants. Second is the shell layer that is chemically different material from the core material and the last third is the core, which is central portion of the NPs and usually refers as the NPs itself [33, 34]. NPs have unique physical and chemical properties, such as the electronic, optical and chemical properties of NPs could be different from the bulk samples. The behaviour of material at nanoscale is quite different as compare to large scale (bulk), therefore it's become very difficult to predict the physical and chemical properties of particles on a very small size. The main parameters of NPs are their shape, size, surface characteristics and inner structure. The composition of the NPs can be very complex that is depending on the interacting chemical or particles as well as on its lifetime. NPs has different way of interacting with each other, either they can remain free or group together, which is depending on the attractive or repulsive interaction force between them. At nanoscale, the particle-particle interaction can be dominated by weak Van der Waals forces, strong polar and electrostatic interaction or covalent interaction. These interaction forces are either attractive or repulsive; crucially determine the fate of the individual and collective NPs. Such interaction between NPs is resulting in aggregation and/or agglomeration, which may influence on their behaviour [35]. NPs can be formed through either breaking down of large particles or by controlled assembly process. There are two methods for manufacturing of NPs.

- First is "top-down" method, which involves the breaking down of large pieces of material to generate the required nanostructured form. This approach is particularly suitable for making integrated structures such as in electronic circuits.
- Second is "bottom-up" method, in which single atoms and molecules are assembled to form nanostructure. This is a powerful approach of creating identical structures with atomic precision.

Detection of NPs is difficult in both gases and liquids. Actually, NPs are so small that they cannot be detected by optical microscope. Electron microscope is the method to analyze the particle size, shape and structure of NPs below 10 nm. When these instruments are equipped with a specific spectrometer then chemical composition can also be determined at least for large NPs.

## 1.6 Cerium Oxide ($CeO_2$): A Dilute Magnetic Semiconductor

The RTFM in most of the DMS materials discovered so far has non-cubic crystal symmetry. Besides of that, RTFM in the cubic crystal systems will facilitate the integration of spintronics devices with advances silicon (Si) based microelectronic devices. Among all DMS materials that having cubic symmetry, cerium oxide ($CeO_2$) NPs is an interesting material due to its potential for various application such as: three way catalysis, in solid oxide fuel cell (SOFC's), ceramic materials, UV absorber, Photocatalyst, oxygen sensors and for advanced spintronics devices.

Cerium (IV) oxide is one of the important rare earth oxides, also known as ceric oxide, ceria or cerium dioxide. It is an insulating material with high dielectric constant ($\varepsilon = 26$) i.e. transparent over the visible and infrared electromagnetic (EM) radiation. $CeO_2$ is a pale yellow-white powder within Ce has electronic configuration [Xe] $4f^1 5d^1 6s^2$. The atomic weight of Ce is 140.116 g $mol^{-1}$. Ce has been found in two oxidation states $Ce^{3+}$ and $Ce^{4+}$. Ce also forms cerium (III) oxide ($Ce_2O_3$) but $CeO_2$ is the most stable phase at room temperature ($25^oC$) and atmospheric pressure (100 kPa). Ce has 30 isotopes with atomic weight ranging from 123 to 152 g/mol. There are three stable isotopes $^{136}Ce$, $^{138}Ce$ and $^{140}Ce$. The

most abundant isotope is $^{140}$Ce at 88.5% nature occurrence. Cerium resembles to iron in colour and lustre, but it is soft, malleable and ductile. $CeO_2$ is used in various application such as solid electrolyte in SOFC's due to its high oxygen ion conductivity at temperature 500$^o$-800$^o$C [36], three way catalysts for automobile exhaust systems [37], oxygen gas sensors, having wide band gap energy of 3.2 eV used as sunscreen for UV absorbent [38], blocking material in UV-shielding [39], and $CeO_2$ thin films can also be used as protective coating of SOFC's interconnector [40]. Doping with rare earth metals such as Yttrium (Y), Gadolinium (Gd) and Samarium (Sm) in $CeO_2$ increases the oxygen ion conductivity which is more useful as an electrolyte in SOFC's [41-43]. $CeO_2$ is a good n-type semiconductor with wide band gap of 3.2 eV, which indicates that $CeO_2$ can only respond to ultraviolet light [44, 45].

### 1.6.1 Structure of $CeO_2$

$CeO_2$ crystallizes in the fluorite structure with a face centered cubic (*fcc*) unit cell within the space group *Fm*-3*m*. In this *fcc* structure, eight nearest neighbour oxygen anions are coordinated around each Ce cation at the corners of the cube and each anion is coordinated by four cation forming a tetrahedron [46]. Experimentally it has been determined that the bulk $CeO_2$ has lattice constant 0.5411 nm at 300 K with cubic fluorite structure [47]. The high oxygen ion conductivity as well as high catalysis activity can be attributed to the inherent ability of $CeO_2$ that to be reduced from $Ce^{4+}$ to $Ce^{3+}$ through creation of an oxygen vacancy. Non-stoichiometric $CeO_{2-\delta}$ ($0 \leq \delta \leq 0.5$) can also be formed by release and reduction of $Ce^{4+}$ to $Ce^{3+}$ with the formation of oxygen vacancies in the crystal structure. This can be expressed by the following reaction, using Kroger-Vink notation as [46]:

$$2Ce_{Ce} + O_o \rightarrow V_o^{\bullet\bullet} + 2Ce'_{Ce} + \frac{1}{2}O_2 \qquad (1.2)$$

Where, $O_o$ is a neutral oxygen on oxygen lattice site, $Ce_{Ce}$ is a neutral cerium on neutral cerium site, $V_o^{\bullet\bullet}$ is +2 oxygen vacancy and $Ce'_{Ce}$ is $Ce^{3+}$ atom on a $Ce^{4+}$ site. However, at low oxygen pressure and temperature above 685$^o$C, $CeO_2$ is reduced and forming an oxygen deficient non-stoichiometric oxide that is called α-phase with composition in the range of $0 < \delta < 0.286$ for $CeO_{2-\delta}$. This α-phase has a disordered non-stoichiometric fluorite structure [48].

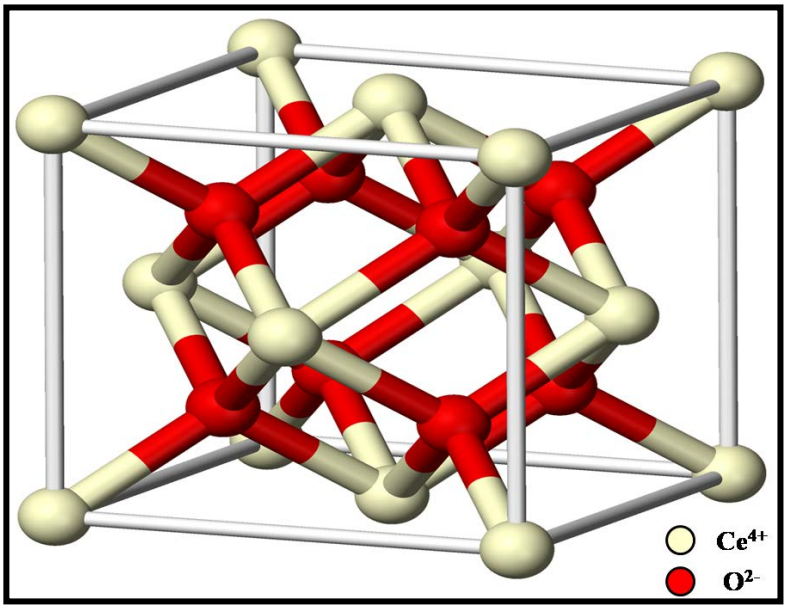


**Figure 1.10: A Schematic crystal structure of $CeO_2$**

Now, according to the partial pressure of oxygen and temperature, at bulk and nanoscale $CeO_2$ has many point defects such as oxygen vacancies ($V_o$), cerium anti-sites ($Ce_o$), cerium interstitials ($Ce_i$), impurities on lattice side ($D_{o,Ce}$), interstitial impurities ($D_i$) [49].

## 1.7 Review of literature

### 1.7.1 Structural and Surface morphological Properties of doped $CeO_2$

***S. Kumar et al.*** [50] have reported the structural and magnetic properties on Fe-doped $CeO_2$ NPs, prepared by co-precipitation method. X-ray diffraction (XRD) and selected area electron diffraction (SAED) pattern for $Ce_{1-x}Fe_xO_2$ ($x$ = 0.01, 0.05 and 0.07) samples showed the single phase nature with fluorite cubic structure. From Transmission electron microscopy (TEM) and SAED pattern, they have shown the particle size distribution histogram of $Ce_{1-x}Fe_xO_2$ NPs. TEM pattern shows that Fe-doped $CeO_2$ NPs have spherical shape and particle size increases with increasing doping concentration from 1 to 7% in $CeO_2$ NPs. ***Qi. Y. Wen et al.*** [51] have reported the $Ce_{1-x}Fe_xO_{2-\delta}$ ($x$ = 0-0.08) polycrystalline sample fabricated by solid state reaction method. The XRD pattern for $Ce_{1-x}Fe_xO_{2-\delta}$ affirm that the diffraction peaks are corresponding to $CeO_2$ fluorite structure which has not been altered with Fe-content as high as 7.6%. The surface topography SEM images shows that 0.9% Fe-doped $CeO_2$ exhibits a dense and compact structure, while the pure

$CeO_2$ has a porous and loosen structure that results the small dielectric constant. ***J. Wang et al.*** [52] have reported high specific surface area, pore volumes and pore size for as-synthesized $CeO_2$ and Co-doped $CeO_2$ nanopowder that can be used for many potential applications. ***K. R. Hailstone et al.*** [53] have reported in a study of lattice expansion in $CeO_2$ NPs by TEM that the particles are highly crystalline with predominantly (111) surfaces. SAED image indicates that the fluorite lattice structure persists for particle size as small as 1 nm. Oxygen storage capacity (OSC) indicates that $Ce^{4+}$ ion are present at 1 nm size consistent with a fluorite lattice. ***S. Yuna-Qiang et al.*** [54] have reported that Co-doped $CeO_2$ thin film with composition of $Ce_{0.97}Co_{0.03}O_{2-\delta}$ (CCO) are deposited on Si (111) and glass substrates. The XRD shows that CCO film with (111) preferential orientation is grown on Si, while the film on glass is polycrystalline with NPs. ***M. C. Dimri et al.*** [55] have reported fluorite crystal structure from XRD and Raman spectra for rare earth (RE = Nd, Sm, Gd, Tb, Er and Dy) doped $CeO_2$ samples. ***E. Swatsitang et al.*** [56] have reported single face-centered cubic structure phase for $Ce_{1-x}Sm_xO_2$ ($x$ = 0, 0.05, 0.10, 0.15 and 0.20) indicating that $Sm^{3+}$ ions actually substituting the $Ce^{4+}$ sites. The particle size (10-20 nm) calculated from TEM images are compared with XRD line broadening and particles agglomeration. ***A. A. Aboud et al.*** [57] have reported for pure and Gd-doped $CeO_2$ nano-powder synthesized by co-precipitation method and confirmed the single phase *fcc* structure of samples and crystallite size calculated from Scherrer's equation showed reduction in particle size from 29 nm to 20 nm as a result of doping through their XRD and Raman spectra. ***P. Z. Li et al.*** [58] have reported defect cluster with ordered structures in Gd-doped $CeO_2$, verified by transmission electron microscopy with the dumb-bell structure formation with 6-oxygen vacancies in $CeO_2$ matrix that has been identified for defect cluster growth.

### 1.7.2 Optical properties of doped $CeO_2$

For Ni-doped $CeO_2$ NPs, ***F. Abbas et al.*** [59] reported that the band gap energy ($E_g$) for pure $CeO_2$ is found to be 3.19 eV which shows a systematic decrease up to 2.72 eV for 7% Ni-doped $CeO_2$ NPs. This reduction in $E_g$ value of $CeO_2$ NPs with Ni doping is correlated with formation of impurity energy levels and micro-

structural variations. The micro-structural properties are also analyzed using Raman spectroscopy and a peak shifting is reported towards lower wave number side (as compared to bulk $CeO_2$) for $F_{2g}$ Raman active mode that has been attributed to the formation of oxygen vacancies in the system. Increasing Ni concentration again shows suppression of $F_{2g}$ mode which may be associated with more oxygen vacancies. ***S. Debnath et al***. [60] have reported the optical study of $CeO_2$ film in the wavelength range $200 < \lambda < 850$ nm. It has also been shown a lower reflectance in the UV-region whereas a very high absorbance in this region. The optical band gap has been found to increase with increase in thickness. The value of absorption coefficient increases up to a certain value of wavelength in UV-region and it decrease exponentially and becomes constant towards the visible region, the absorption coefficient decreases with the increase in film thickness. The calculated optical band gap for $CeO_2$ thin film has been found to decreases with increase in film thickness such as 4.11 eV, 3.81 eV and 3.6 eV. XRD pattern shows that the film is crystalline structure with (111) orientation and small crystalline size. ***T. V. Semikina et al.*** [61] have reported the optical properties of dielectric layers with $CeO_2$ along with amorphous film $WO_3$, amorphous complex film $WO_3$+$CeO_2$ and $CeO_2$+$Dy_2O_3$. From their XRD results, it is observed that $CeO_2$ film has sharp peaks in the crystalline phase and complex film $WO_3$+$CeO_2$ possesses the amorphous structure. The Raman spectroscopy of $CeO_2$ has shown the presence of peaks at the wavelength 466 $cm^{-1}$ for $CeO_2$ and obtained that the energy exciting radiation at wavelength 647.1 nm is not enough to excite vibration and hence $CeO_2$ has wide band gap (2.3 to 3.37 eV) which are required for new gate dielectrics applications. The refraction coefficient (n = 1.85-2.85) for $CeO_2$ film and complex film is not more than 2.37. For their Mn-doped $CeO_2$ NPs, ***F. Abbas et al.*** [62] have reported the value of $E_g$ for pure $CeO_2$ NPs is 3.19 eV, which decreases to 2.83 eV with Mn-doping, may be due to the formation of defects especially oxygen vacancies and impurities caused by Mn-doping. These defects are further verified by the Raman spectroscopy as there is a great Raman peak shifting of 22 $cm^{-1}$ compared to that of bulk $CeO_2$. This shifting is linked with the presence of $Ce^{3+}$ ions too in the system. Moreover, further reduction in the peak intensity is also reported with Mn-doping, which again explains the enhancement of lattice defects and oxygen

vacancies. For Fe-doped $CeO_2$ NPs, ***F. Abbas et al.*** [63] have reported the band gap energy for pure $CeO_2$ NPs is 4.16 eV and it is reduced to 4.06 eV (for 7% Fe doping) in a zig-zag manner. The decreasing value of $E_g$ up to 3% Fe doping may be related with the fact that incorporation of Fe ions resulted in defects and in the formation of impurity level below conduction band, which in turn resulted in the reduction of $E_g$ value. After certain limit of doping, at higher concentration of Fe, it is reported that band filling effect may arise to enhance the $E_g$ value. From Raman spectra they have reported red shift, symmetric peak broadening and decrease in the peak intensity of $F_{2g}$ mode peak with Fe-doping and explained due to defects like interstitial defects and oxygen vacancies. This decrement also shows the decrease in the crystalline quality of NPs, which is confirmed by XRD. ***Y. Wu et al.*** [64] have also reported two other low intense peaks at high and low energy sides of $F_{2g}$ peak in their Raman spectra. One more peak is also reported in the Co-doped samples at 978 $cm^{-1}$ which is absent in the pure one and reported due to the formation of additional oxygen vacancies.

### 1.7.3 Electronic structure properties of doped $CeO_2$

***Phokha et al.*** [65] have reported weak RTFM in Fe-doped $CeO_2$ NPs, induced by oxygen vacancy or defects which are generated by $Ce^{3+}$ and $Fe^{3+}$ spin electrons confirmed from their XANES measurements. ***W. C. Wang et al.*** [66] have reported experimental investigations on electronic structure of pure $CeO_2$ and Fe-doped $CeO_2$ by X-ray absorption (XAS) and X-ray emission spectroscopy (XES). The effect of dopant ion concentration on the ferromagnetism has been discussed and they suggested at low concentration of Fe-doping, the oxygen vacancies are formed and the magnetism is found to increase but at high doping concentration the ferromagnetism is found to decrease in the samples. ***Chen et al.*** [67] have reported dopant-induced structural differences and defects in Sm-doped $CeO_2$ NPs with doping concentration of 3, 5, 7, 9, and 11%. Their results based on XAS, EXAFS, Raman and STEM-EELS measurements have observed that below and above 7% distribution of defects strongly depend on the concentration of $Sm^{3+}$ ions in $CeO_2$ NPs. ***Smid et al.*** [68] have reported XPS measurement for Cu-doped $CeO_2$ NPs and in their results they have observed that after preparation and calcination, the main

state of Ce ion is $Ce^{4+}$ in Ce 3d spectra while after reaction the main state is reduced to $Ce^{3+}$. On the other hand the existence of binary phase on the edge of $Cu/CeO_2$ helps the reduction of $CeO_2$ because the Cu-Ce bond also competes with Ce-O bond. For this reason oxidation starts at much lower temperature on $Cu/CeO_2$ powder than $CeO_2$. ***J. Fang et al.*** [69] have reported that $TiO_2$ and $CeO_2$ are in anatase phase and cubic fluorite phase in $CeO_2$-$TiO_2$ mixed oxide respectively prepared by the sol-gel method. From their XPS analysis they have reported that Ce atoms nucleate as cubic like ($CeO_8$) polyhedron with the formation of a Ce-O-Ti interface with cubic fluorite $CeO_2$. From their EXAFS study they have shown that $CeO_2$ in mixed oxide exhibit local structure different from pure $CeO_2$ and have a much lower absorption capacity of methyl orange than pure $CeO_2$. ***J. F. Lee et al.*** [70] have reported the local structure around Ce atom in nanocrystalline $CeO_2$ using Ce K-edge EXAFS. The value for calculated debye-waller factor ($\boldsymbol{\sigma}^2$) for the first three coordinate shells have been reported that the degree of disorder increases with the reduction of particle size. The value of $\boldsymbol{\sigma}^2$ for the second shell Ce-Ce has been found to be smaller than for the value for the first shell Ce-O in the same sample. The larger particle size shows a monotonous increase in the coordination number of second shell Ce-Ce, observed from the radial distribution function. ***M. Baron et al.*** [71] have reported a comparative study of gold supported $CeO_2$ (111) thin film and $CeO_x$ NPs using STM, XPS and IRAS. $CeO_2$ NPs grown on crystalline thin silica films possess Ce in both the 3+ and 4+ oxidation states. From their XPS and IRAS data they have reported that partially charged $Au^{\delta+}$ species are formed by deposition at low temperature (~100K) and low coverage on both $CeO_2$ supports. On $CeO_2$ (111) film these species transform into metallic Au particle upon heating up to 300K. ***M. S. P. Francisco et al.*** [72] have reported XPS, XAS and XRD characterization of $CuO$-$TiO_2$-$CeO_2$ catalyst system. From XRD analysis it can be shown that the amount of observed phase depends on composition and is independent of copper content. From their XPS, XAS analysis they have reported that CuO is in small crystallized grain and there are no CuO bulk phases, even for high copper contents. XPS analysis has indicated that Cu dispersion on the mixed support suffered no influence of cerium concentration, but it is independent of the cerium species. ***A. Bouaine et al.*** [73] have reported ferromagnetism in Co-doped $CeO_2$ NPs,

prepared by solid-state reaction method. The electronic structure of as-prepared Co-doped $CeO_2$ has been investigated by using XAS and XPS spectroscopy. From the analysis it is found that there is no metallic Co cluster and Co atoms reside entirely at substitutional/ interstitial sites within the host lattice. Co L-edge resonant inelastic X-ray scattering (RIXS) spectra indicate the direct Co-Co bond is formed due to the precipitation of Co atom in $CeO_2$ with the presence of metallic cluster of Co. This metallic cluster is also supported by temperature dependent measurement of magnetization. ***J. P. Rueff et al.*** [74] have reported on the 4f electron properties at $\gamma - \alpha$ transition in Ce by RIXS. From Ce 2p3d – RIXS spectra they have found that the electronic structure changes result from band formation of 4f electrons which reduced electron correlation and increased Kondo screening at high pressure. ***C. H. Hu et al.*** [75] have reported that the XRD spectra of as-synthesized Mn-doped $CeO_2$ growing at 200 $^oC$ for 72 hours have all the peaks, which indicate the cubic phase with lattice constant $a$ = 0.5411 nm for $CeO_2$. From their XPS spectra they have indicated that the manganese exists as $Mn^{4+}$ state in $CeO_2$ sample.

### 1.7.4 Magnetic Properties of doped $CeO_2$

***S. Kumar et al.*** [50] have reported the coercivity ($H_c$) of Fe-doped $CeO_2$ NPs decreases from 66.7 to 28.6 Oe, whereas remnant magnetization ($M_r$) and saturation magnetization ($M_s$) are increased from $4.2\times10^{-3}$ to $5.2\times10^{-3}$ emu/g and $5.5\times10^{-3}$ to $14\times10^{-3}$ emu/g respectively with increase in the Fe-content in $CeO_2$. This shows that the Fe-doped $CeO_2$ exhibit RTFM. ***S. Kumar et al.*** [76] have reported RTFM for Co-doped $CeO_2$ NPs and their results indicate that saturation magnetization decreases with increase in Co-doping beyond 3%. ***A. Thurber et al***. [77] have reported that the saturation magnetization increases with Ni-doped $CeO_2$ up to 4% and decreases with further increase in the Ni doping. ***A. Sundaresan et al.*** [15] have reported that the RT-magnetization field of $CeO_2$ at 500 $^oC$ (for 15 nm particle size) shows ferromagnetic behaviour with coercivity ~100 Oe and at 1000 $^oC$ (for 500 nm particle size) $CeO_2$ exhibits a linear M-H behaviour with low magnetic moment which is close to diamagnetism for $CeO_2$. It shows that $CeO_2$ exhibit RTFM but their corresponding bulk oxide exhibit diamagnetism and assumed that the origin of ferromagnetism may be arise due to the exchange interaction between unpaired

electron spins arising from oxygen vacancies at the surface of NPs. ***P. K. Slusser et al.*** [49] have reported that $Ce_{1-x}Cu_xO_{2-\delta}$ thin film for $x$=0.03, exhibited RTFM with saturated magnetization of ~1.0 $\mu_B$/Cu atom. XPS measurement also shows that Cu ions are in 2+ states. When an additional Cu ions are introduced within the $Ce_{1-x}Cu_xO_{2-\delta}$ system ($x$=0.15) super paramagnetic behaviour has been observed, but when majority of Cu ions were in 1+ state, ferromagnetic behaviour has been observed. It shows that ferromagnetism is an intrinsic property of $CeO_2$. ***M. C. Dimri et al.*** [55] have reported that magnetic properties of rare earth (RE= Nd, Sm, Gd, Tb, Er and Dy) doped $CeO_2$ samples. They have found RTFM for Nd and Sm-doped $CeO_2$ samples, whereas for other RE dopants i.e. Gd, Tb, Er and Dy paramagnetic behaviour is observed. The cause of magnetism in these samples may be due to oxygen vacancies created by RE dopants in $CeO_2$, which has been confirmed from the Raman spectra. Raman spectra also confirmed the formation of fluorite crystal structure of RE-doped $CeO_2$ samples. The magnetization has been found to be lower for RE-doped $CeO_2$ samples as compare to the transition metal (TM) doped $CeO_2$.

### 1.7.5 Electrical Properties of doped $CeO_2$

***A. Arabac et al.*** [78] have reported that 10% Gd-doped $CeO_2$ sample prepared by pechini method shows significantly high ion conductivity of $3.4\times10^{-2}$ S/cm at 500$^o$C in air. ***T. Li. et al.*** [79] have reported the highest ion conductivity at 800$^o$C is about $5.6 \times 10^{-2-}$ S/cm and activation energy is 0.83 eV for $Ce_{0.65}Sm_{0.2}Bi_{0.15}O_{1.825}$ sample, which is due to the increasing Bi-content (for $x \leq 0.15$) and attribute to the rise of oxygen vacancies as well as unit cell volume. These results promote this sample as a promising electrolyte for the intermediate temperature SOFC's application. ***R. V. Mangalaraja et al.*** [80] have reported nanocrystalline $Ce_{0.9}Sm_{0.1}O_{1.95}$ prepares by citrate gel combustion technique. The electrical conductivity for the Sm-doped $CeO_2$ sample has been found to be the order of $10^{-2}$ S/cm at 600 $^o$C and activation energy is about 0.84 eV in the temperature range of 100-650 $^o$C. ***M. Pilar lobera et al.*** [81] have reported that RE-doped $CeO_2$ catalysts for ODHE reaction in a catalytic modified MIEC membrane based on the system $Ce_{1-x}Ln_xO_{2-\delta}$ ($x$ = 0.1 or 0.2, Ln = Tb, Pr, Er, Gd and Tb+Er) including the effect of cobalt in $Ce_{0.8}Tb_{0.2}O_{2-\delta}$. Ln-doped $CeO_2$

materials ($Ce_{1-x}Ln_xO_{2-\delta}$) have combination of high oxygen ion mobility, redox catalytic properties and stability in reducing, wet and $CO_2$ rich atmosphere at high temperature. XRD pattern of $Ce_{1-x}Ln_xO_{2-\delta}$ sintered at 1573K has shown that all powder samples have single cubic fluorite structure. The pattern indicates that the lanthanides has been incorporated in the lattice of $CeO_2$ and $Ce_{0.8}Tb_{0.2}O_{2-\delta} + CO_2\%$ shows the sharper and more intense diffraction peaks, which indicate greater grain size. The modification of the MIEC membrane allowed to increase the oxygen permeation flux when using both Argon and methane as sweep gas in the permeate side. ***B. C. H. Steele et al.*** [82] have reported the comparative study of the ionic conductivity of $CGO_{10}$, $CGO_{20}$, $Ce_{0.9}Sm_{0.1}O_{2-\delta}$ and $Ce_{0.9}Y_{0.1}O_{2-\delta}$ at three different temperatures 500°C, 600°C and 700°C and they have observed that at 500°C $CGO_{10}$ yields the highest ionic conductivity and at 600°C and 700°C temperature, $Ce_{0.9}Y_{0.1}O_{2-\delta}$ samples shows higher conductivity.

## 1.8. Motivation of the proposed work

In above mentioned reports of various researchers we can observe that the $CeO_2$ lattice is reported to show diamagnetic behaviour when it is in bulk polycrystalline state. However, when this lattice is doped with TM (3d cation) or rare earth impurities it is observed with room temperature ferromagnetic properties due to creation of defects and oxygen vacancies induced in the lattice of $CeO_2$. The confirmation of these defects and oxygen vacancies has been discussed by many researchers on the basis of their Raman spectra, electronic structure studies and many other methods. One more point to report is that with few elements doping up to a certain percentage of doping the magnetic properties is attributed towards ferromagnetism but with certain doping it is showing super paramagnetism or other magnetic properties. Hence, we can conclude that the room temperature ferromagnetic properties in the $CeO_2$ lattice appeared to be intrinsic and to establish this fact a lot of research work on the doped $CeO_2$ is required. Still a lot of work is lacking to have a correlation between structural, optical, electrical and magnetic properties of these samples and hence we decided to undertake this work in the present thesis with TM and RE impurities in the $CeO_2$ lattice to study all properties along with its use for various applications.

# Chapter 2

# Experimental Techniques

# CHAPTER 2

# EXPERIMENTAL TECHNIQUES

## 2.1. Introduction

Various methods are available for the preparation of the nanomaterials. Every method has its own advantage and disadvantage; therefore few methods are adopted for the synthesis of the nanomaterials, which are perfect in nature. Therefore, it is essentially required a proper caring and tuning of the parameters to get high quality materials, which possesses strong potential for diverse applications. Suitable characterization techniques are helpful to identify the properties and the nature of the material perfectly. Among all the characterization techniques, some of them are qualitative, which provide the image of the surface of the nanomaterials and some of others are quantitative that gives enhanced insight into the relative concentration of all the atoms that comprise the nanomaterials. At last, appropriate characterization technique is very essential to understand the complete picture of the nanomaterials, which helps the researcher to find out the exact field of its application. The characterization of a nanomaterial is totally depended on the physical conditions or environment, method of preparation and pre-treatment conditions. One can tune the chemical, mechanical and electrical properties of the nanomaterials for any particular application, but for making a correlation between the properties of the material and its application, appropriate characterization techniques are necessarily required. Several techniques are available for the characterization of the nanomaterials with the specific properties and applications but main aim of these techniques are to determine the crystal structure, identification the defects in the structure, phase, crystalline or grain size, shape and composition etc. Generally, the spectroscopy is widely used for the better understanding of the molecular structure, composition and vibrational frequencies of the nanomaterials, which is also used for the qualitative and quantitative determination of the impurity in the system. The electronic structure spectroscopy and optical microscopy are the widely used characterization techniques, which are available for the analysis of the solid nanomaterials and provide essential information about the nanomaterials. This chapter includes the preparation technique used for synthesizing the pure and doped

$CeO_2$ NPs and analysis techniques, which has been used to gather the information from the prepared NPs.

## 2.2. Preparation Techniques

As mentioned in the chapter 1 about the synthesis process for NPs that has been divided into two categories i.e. “Top-Down” and “Bottom-Up”.

Top-down method is usually started from patterns generated at large scale i.e. from bulk pieces of material and then step-by-step they are reduced to nanoscale. This method is based on the miniaturization technique such as machining, templating or lithographic technique. The top-down method includes some preparation techniques such as ion beam technique, laser ablation method, inert gas condensation method, lithography and sputtering method. The main disadvantage of this method are included the low surface area, the highly poly-disperse size distribution and partially amorphous state of the as-prepared nanopowder sample. Besides of that, the bottom-up method includes the miniaturization of material (up to atomic level) with further self assembly process leading to the formation of the nanostructures. This method uses the chemical or physical forces, which are operating at the nanoscale to assemble the basic units into the large structure. The main advantage of this method is that, it displays a wide variety of preparation methods such as hydrothermal method, solvothermal method, ionothermal method, combustion method, co-precipitation method, microwave assisted technique, sol-gel method and chemical vapour deposition (CVD) method etc. [83]. These methods are allowed a good control onto scale dimension even at atomic or molecular level and they are not as expensive as top-down methods. However, co-precipitation method is very simple, facile and rapid synthesizing method under inert/ambient conditions, which can easily, controlled the particle size, composition of the nanomaterials, modify the particle state and maintain the homogeneity of the solution. This method is briefly outlined in the following section.

### 2.2.1. Co-precipitation Method

Co-precipitation method involves the formation of a precipitate when a solid is formed during the chemical reaction or diffusion process. It requires the metal

cation of various salts such as hydroxides, carbonates, citrates and oxalates, which are co-precipitated under a fine controlled environment of pH by using NaOH or $NH_4OH$ solutions, and then subsequently calcined at appropriate temperature to yield the final oxide NPs in powder form. This method can control the various parameters such as pH of the solution, concentration of the solution, temperature and stirring speed of the mixture, which are in order to obtain the final product with required properties. The particle size of the oxide nanoparticles is strongly depended on the pH of the precipitate and molarity of the starting precursors. The various steps are involved in the co-precipitation method, which are represented as a flow chart shown in Figure 2.1.

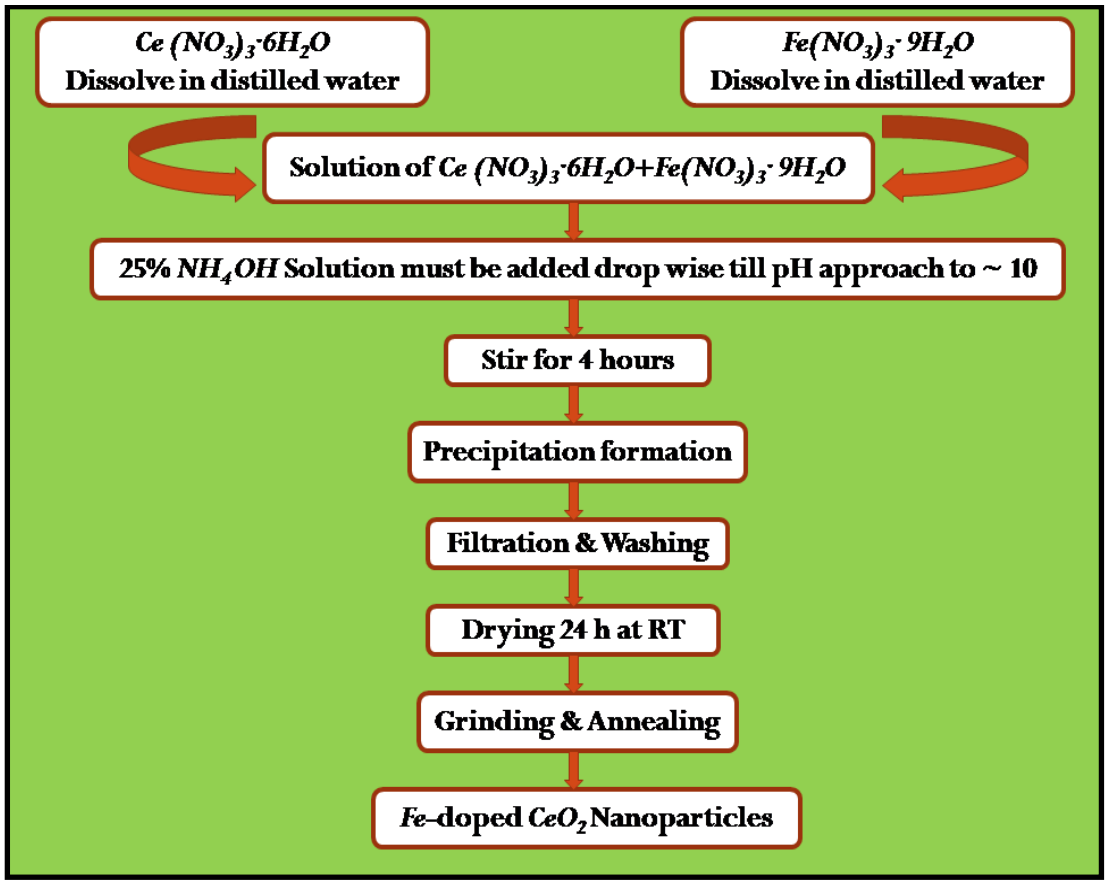


**Figure 2.1: Flow chart describing the various steps involved in the co-precipitation method.**

In this process, the high purity chemicals such as $Ce(NO_3)_3 \cdot 6H_2O$ (99.99%) and $Fe(NO_3)_3 \cdot 9H_2O$ (99.9%) powder from Alpha Aesar has been used as starting precursor, for synthesizing Fe-doped $CeO_2$ NPs. Firstly, these chemicals

carefully weighs according to their stichometery ratio by using Percisa XB 220A balance with 0.0001 gm accuracy, as shown in Figure 2.2. After weighing the chemicals, an appropriate amount of $Ce(NO_3)_3 \cdot 6H_2O$ and $Fe(NO_3)_3 \cdot 9H_2O$ chemicals were dissolved in 100 mL of distilled water under stirring at room temperature for 1 hour and both solutions were prepared separately.


**Figure 2.2: Weighing Machine**

Then these solutions were mixed during continuously stirring, an aqueous solution of 25% $NH_4OH$ was added drop wise into this mixture under constant stirring until the pH of the solution reached to 10. During adding of $NH_4OH$ sloution, precipitation was start. Then, the final solution was stirred for 4 hours at room temperature, so that homogeneity can be maintained. After that, the synthesized precipitate were filltered and wased with distilled water several times. The filtered precipitate were dried at room temperature and then obtained samples grined to make fine powder using agate mortar and pestle. In order to carry out heat treatment (annealing) high themperature Microprocessor controlled Muffle Furnace

has been used as shown in Figure 2.3. this furnace has maximum range upto 1500$^{o}$C. So that all samples is annealied at 500$^{o}$C for 8 hours in the furnace.


**Figure 2.3: Microprocessor Controlled Muffle Furnace**

The pellets of the annealed powder has been made using hydraullic press unit (Athena technology Model ATHP-15), as shown in Figure 2.4.


**Figure 2.4: Hydraulic Press Unit**

The pellets has dimoension of 12 mm diaeter and thickness 1 mm. The hydraulic press unit has maximum pressure of 15 tonn that has been used for uniaxial pressing of annealied powder. These pellets has been used during charaterization of the samples for detection the electronic structure and electrical properties by using XPS and I-V characteristics, respectively.

The synthiszation process for Sm and Gd-doped $CeO_2$ NPs samples will be discussed in the chapter 3 and 4, respectively. Now, the next section includes the brief description of the theory and various characterization techniques that has been used in this study.

## 2.3. Characterization Techniques

This part of the chapter deals with the description of the various experimental techniques used in the course of the study. These techniques include X-ray Diffraction (XRD), Transmission Electron Microscopy (TEM), High-Resolution Transmission Electron Microscopy (HRTEM), Selected Area (Electron) Diffraction (SAED), Energy Dispersive X-ray Spectroscopy (EDX), Ultraviolet-Visible-Near Infrared (UV-Vis-NIR) Spectroscopy, Surface-Enhanced Raman Spectroscopy (SERS), X-ray Photoelectron Spectroscopy (XPS), Superconducting Quantum Interference Device-Vibrating Sample Magnetometer (SQUID-VSM) and Keithley 2400 Electrometer. The XRD, TEM, HRTEM, SAED and EDX analysis are the common methods used to interpret the structure and the morphology of the nanomaterials. XPS measurements have been carried out for the advance study of electronic structure of the nanomaterials. The magnetic and electrical properties of the prepared nanomaterials samples have been studied using MPMS-3 SQUID-VSM magnetometer and Keithley 2400 electrometer, respectively.

## 2.4. X-ray Diffraction (XRD)

XRD is a powerful technique for determining the structure of the crystal, as well as it provides the idea regarding the crystallinity, crystalline or grain size, lattice parameter, lattice spacing, phase composition and lattice defects. This method is classified into two main techniques such as spectroscopic and photographic. The spectroscopic technique is the most widely used diffraction method, which is also

known as X-ray powder diffractometer. Besides of that, the photographic technique is not so common technique, it is used to determine the unknown crystal structure [84]. In XRD, the monochromatic X-ray beam is applied onto the crystalline nanomaterials that interact with the structural planes of the lattice and produce diffraction in which lattice points of each plane act as a slit. The diffraction phenomenon occurs when the X-ray beam is interacted with a regular structure, whose repeated distance is about same as the wavelength of X-ray. Since, the wavelength of the X-rays is comparable to the size of the atoms; therefore they are suitable for probing the structural arrangement of atoms and molecules in the nanomaterials.

Basically, XRD is a non-destructive technique, which is used to determine the arrangement of atoms within a crystal structure. X-ray beam strikes a crystal and diffract into many specific directions, which strikes to an electron and produces secondary spherical waves emanating from an electron. These regular array of electrons can be produced a regular array of spherical waver. These waves are added in few directions through constructive interference and cancel out each other in other directions through destructive interference. When the path difference between two diffracted rays differs by an integral number of used wavelengths then constructive interference takes place between the scattered rays. This condition is to be satisfied by Bragg's equation, called as "Bragg's law", which is given as:

$$\boldsymbol{2d\ \sin\theta = n\lambda} \qquad (\mathbf{2.1})$$

Where, λ is the wavelength of the X-ray, n is the integer, d is the interplanar distance, θ is the angle between incident beam and lattice planes. The diffraction peak is observed only due to constructive interference of X-rays scattered from the atomic plane of the given crystal. According to Bragg's law, for a given set of parallel plane of a crystal, the diffraction will be maxima only in the direction for which the angle will satisfy the Bragg's law. The diffraction patterns provide the information about the phase purity, crystallinity and cell parameters [85]. When X-ray beam, having a wavelength λ that is similar to the order of the inter-atomic distance d incident on a crystalline material with an angle θ, the incident X-ray interacts with the periodic atomic structure, causing elastic scattering of the X-ray.

The scattered X-ray beam is reflected from the atomic planes and constructive interference produces the diffraction patterns on detector (as shown in Figure 2.5 and 2.6).

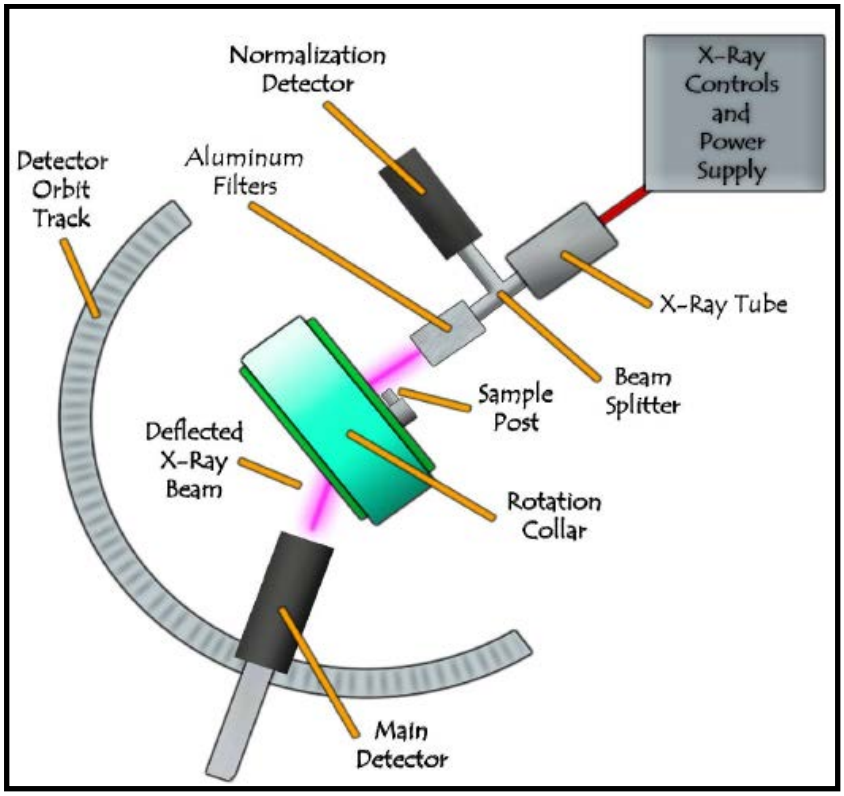


**Figure 2.5: A schematic representation of X-ray diffractometer [86]**

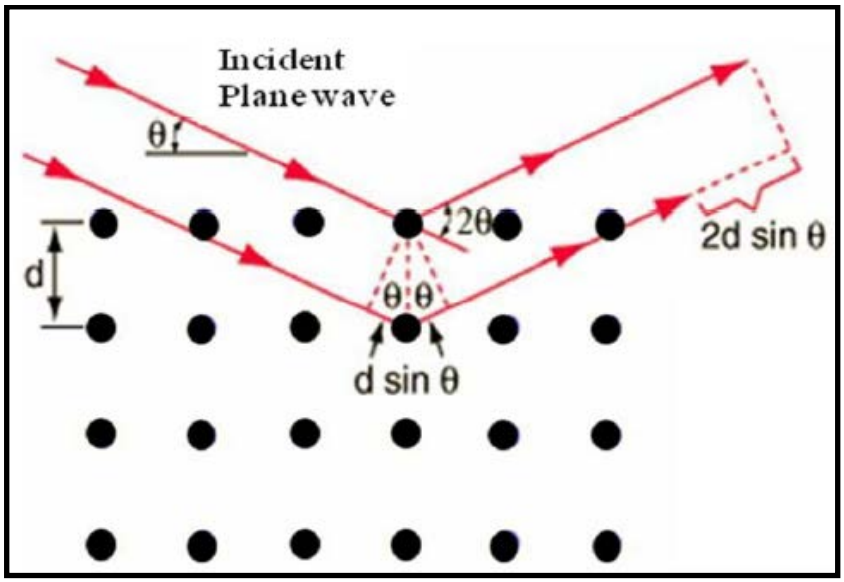


**Figure 2.6: A schematic representation of diffraction of X-ray by crystallographic plane (Bragg's Law) [86]**

In the present work, XRD patterns of all NPs samples were collected with the Brucker D8 Advance X-ray diffractometer using monochromatic Cu $K_\alpha$ radiation ($\lambda$ = 1.5406 Å) (as shown in Figure 2.7 and 2.8). To perform an XRD measurments, the powder sample kept onto a sample holder. After that, the sample holder was placed in the measurning chamber of the X-ray diffractormeter. The source of X-ray was fixed, the sample holder rotate aboout its own axis and the dectector moved with the sample holder. The XRD patterns of all the samples were recorded at room temperature in the 2$\theta$ range from $10^o$ to $90^o$ with scanning speed $0.05^o$ $min^{-1}$ and the counting time of 5 sec/step.


**Figure 2.7: Photograph of Brucker D8 Advance X-ray diffractometer**

XRD is also used to determine the crystallite size according to the Debye Scherre's equation, which is shown as [87]

$$\boldsymbol{D = \frac{k\lambda}{\beta \cos\theta}} \qquad (\mathbf{2.2})$$

Where, $k$ is the particle shape factor (0.9), $\lambda$ is the X-ray wavelength of Cu $K_\alpha$ radiation (1.5406 Å), $\beta$ is the full width at half maxima (FWHM) of the diffraction peaks. This is calculated by $\beta = \sqrt{(\beta_m{}^2 - \beta_i{}^2)}$, here $\beta_m$ and $\beta_i$ are the measured and instrumental broadening (in radian), respectively and $\theta$ is the Bragg's diffraction angle of the peak in degree. The lattice parameter of all the samples is calculated by the following formula [88]:

$$\boldsymbol{a = d\,(h^2 + k^2 + l^2)^{1/2}} \qquad (\mathbf{2.3})$$

Where '$a$' refers to the lattice parameter, $d$ is the crystalline lattice spacing ($\boldsymbol{d = \lambda/2Sin\theta}$) and $h$, $k$, $l$, are the miller indices of crystal. The phase of the corresponding plane can be identified by comparing it with the reference spectra from JCPDS card number.

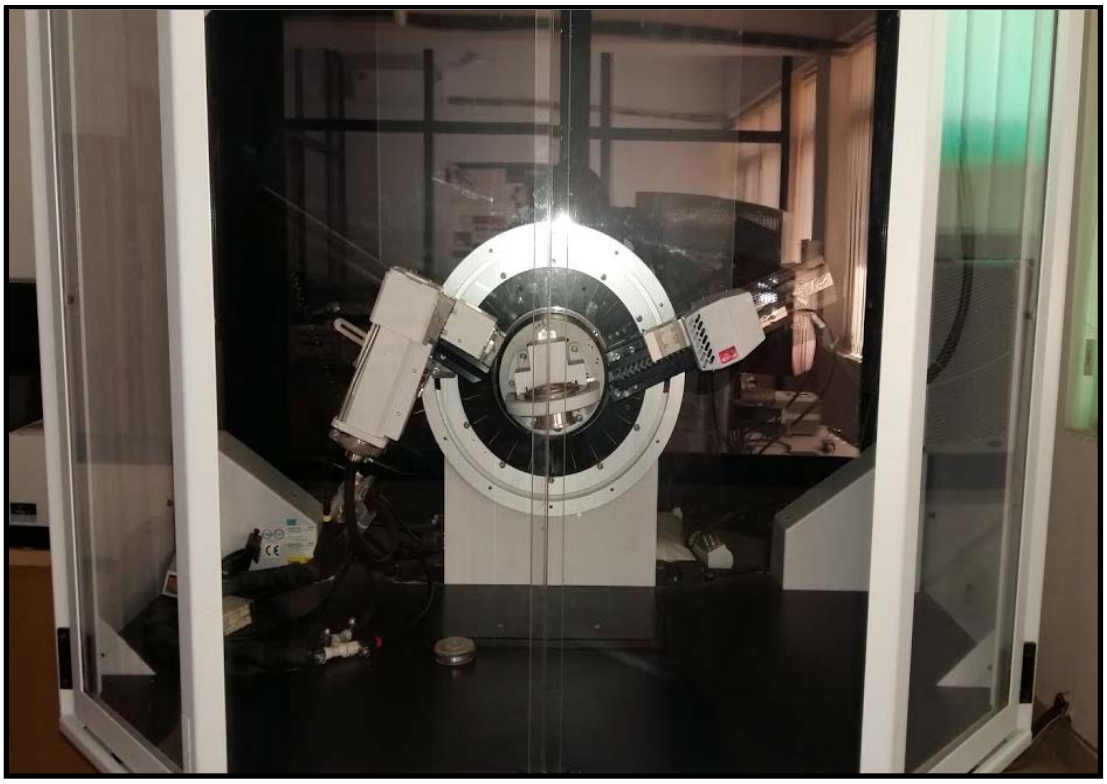

**Figure 2.8: Photograph of the measurning chamber of the X-ray diffractormeter**

The collected data were also analyzed using *FullProf* suite software based Rietveld refinement, which is described in the next section.

### 2.4.1. Rietveld Refinement analysis

H. Rietveld developed a technique for characterization of crystalline solid materials, known as Rietveld Refinement [89]. It is an extremely powerful method for analyzing all types of crystalline materials. This method is used least square approach to refine a theoretical line profile until it matches the measured profile. This method has a significant step in the diffraction analysis of the powder samples. The six factors affecting the intensities of the diffraction lines on a powder patterns, such as, polarization factor, structure factor, multiplicity factor, Lorentz factor, absorption factor and last is temperature factor. This technique makes use of the fact that the peak shape i.e. variations of their FWHM of the Bragg reflections can be described analytically with the scattering angle 2θ.

The parameters in the Rietveld refinement method is mainly classified into three types; peak shape function, profile parameters and structural or atomic parameters. The peak shapes function is observed both the sample (i.e. domain size, stress/strain, defects) and the instrument (i.e. radiation source, geometry, slit size), as well as they vary as a function of 2θ. The profile parameter includes the lattice parameters as well as shapes and width of the Bragg's peaks (i.e. change in the FWHM, peak asymmetry as a function of 2θ, unit cell parameters and 2θ correction). Usually, peak widths are smooth functions of scattering angle 2θ and it uses only five parameters, called as u, v, w, x and y that describe the shape of all peaks in the powder patterns. The structural parameter describes the underlying atomic model that includes the position, types and occupancies of the atoms in the structural model and isotropic or anisotropic thermal parameters. The changes in the positional parameters causes change in the structure factor magnitude and therefore in the relative peak intensities, while atomic displacement parameters have the effect of emphasizing the high angle region or de-emphasizing it. The scale of occupancy parameters and the thermal parameters are extremely correlated with one another and they are more sensitive to the background correction then the positional parameters [90].

After getting the structure and suitable starting model, the Rietveld method is allowed the least-squares refinement (i.e. chi-square $\chi^2$ minimization) of an atomic model (i.e. crystal structure parameters) combined with an appropriate peak shape function. With the complete structural model and suitable starting values of the background contribution (i.e. unit cell parameters and the profile parameters), the Rietveld refinement of structural parameters can be began. The refinement of structure with average complexity can require hundred cycles, whereas, the structure with high complexity may be easily required several hundred cycles. One can easily see the progress of refinement from the resultant profile fit and the value of the reliability factor or R-value. All the structural and profile parameters should be refined simultaneously for obtaining correct estimated standard deviation, that can be given numerically in terms of R-value [91].

The weighted R value, $R_{wp}$ is defined as [92]:

$$\boldsymbol{R_{wp} = 100\left[\frac{\sum_{i=1,n} w_i \left|y_i - y_{c,i}\right|^2}{\sum_{i=1,n} w_i y_i^2}\right]^{1/2}} \qquad (\mathbf{2.4})$$

Ideally, the final $R_{wp}$ value should approach the statistically expected R value i.e. $R_{exp}$,

$$\boldsymbol{R_{exp} = 100\left[\frac{n-p}{\sum_{i=1,n} w_i y_i^2}\right]^{1/2}} \qquad (\mathbf{2.5})$$

Where, n is the difference value of the total number of points in the pattern and the total number of excluded points, p is the number of refined parameters. N = n-p is called, the number of degree of freedom or number of observations. Thus, the ratio between the two (goodness of fit) is given as,

$$\boldsymbol{\chi_v^2 = \left[\frac{R_{wp}}{R_{exp}}\right]^2 = s^2} \qquad (\mathbf{2.6})$$

R-value is observed and calculated structure factors ($F_{hkl}$) that can also be calculated by distributing the intensities of the overlapping reflections according to the structural model, which is given as,

$$\boldsymbol{R_F = 100\frac{\sum_h \left|'F_{obs,k}' - F_{calc,h}\right|}{\sum_h \left|'F_{obs,h}'\right|}} \qquad (\mathbf{2.7})$$

Similarly, the Bragg's intensity R-value is given as,

$$R_B = 100 \frac{\sum_h \left| 'I_{obs,h}' - I_{calc,h} \right|}{\sum_h \left| 'I_{obs,h}' \right|} \qquad (2.8)$$

Since, R-values are useful for the evaluation of Rietveld refinement, basically in the case of small improvements of the model, but they should not be over interpreted. The most important criteria of fitting quality on the experimental data of Rietveld refinement is confirmed by following parameters [90, 91, 93].

(a) The goodness of fit ($\chi^2$) should be 1 or less than 1.3

(b) The Durbin-Watson statistics (d) must be 2.00 or very close to 2.00 in the early stage if refinement

(c) The Weighted-profile R value and $R_{wp}$, for the XRD data should be ~10%

Two input files are essentially required for performing the calculations using Rietveld refinement method. The first file is DAT file that contains the collected experimental XRD data of the corresponding samples. The second file is PCR file that contains the crystal data i.e. space groups, unit cell parameters, atomic positions, occupation numbers, overall scale parameters, etc., and also the experimental data such as wavelength, half-width parameters, preferred orientation parameters, minimum and maximum angles of collection, profile function, etc.

Finally, Rietveld refinement is an adjustment process of the parameters until the residual get minimize in some sense and the best fit of the all calculated pattern to the entire observed patterns is obtained.

### 2.4.2. Information from XRD

XRD is a non-destructive technique, which is used for determining the atomic and molecular structure of a crystal. It can identify the crystalline phase and orientation of the nanocrystalline sample. This technique provides the information about the lattice parameters, strain, grain/particle size, expitaxy, dislocation density and phase composition.

## 2.5. Transmission Electron Microscopy (TEM)

TEM is a technique used for high-resolution imaging of thin film of solid samples for structural and compositional analysis. It is very useful tool for the characterization of the nano-sized particles. Since, XRD can provide information about particle size of the crystallites from the peak broadening information while TEM is useful for the visualization of the nano-sized particle and morphology. Furthermore, TEM studies provide significant information about the particle size distribution.

According to the working principle of TEM, the beam of electrons emitted from the electron gun is focused to get the fine energetic beam by the use of the condenser lens. This lens is restricted by the condenser aperture to eliminate the high angle electrons. Basically, the group of electromagnetic lenses are used to focus the beam and resolve the images. These electromagnetic lenses produce the intense magnetic film, which acts as a thin convex lens for the electron beam. The electron beam is transmitted when it strikes the surface of the sample. This transmission is totally depending on the thickness and the electron transparency of the sample. Now, the transmitted electrons are focused by the objective lens create an image on charger coupled device (CCD). When, the sample is very thin then the transmitted electrons through the sample are detected and the internal structure image of the crystal is formed (as shown in Figure 2.9). The image can be studied directly by the photographed with a camera [94].

The topographic information obtained by TEM images can also be utilized for structural characterization and identification of various forms of nanomaterials, such as hexagonal, cubic crystal structure etc. The limitation of TEM is that, the forward electron scattering information on TEM originates from the three dimensional image which is then projected on a two dimensional detector. So that, the structural information along with the electron beam direction is superimposed at the image plane [95].

A very important advantage of TEM is that, it has an excellent horizontal resolution. The resolution of TEM depends on the wavelength of the radiation employed. If the wavelength of the radiation is smaller than the resolution is greater. In TEM, the wavelength of the incident radiation (i.e. a beam of electrons) is given as [96]:

$$\boldsymbol{\lambda\,(nm)} = \sqrt{\frac{\mathbf{1.5}}{\boldsymbol{V}}} \qquad (\mathbf{2.9})$$

Here, V (in volts) is the voltage applied to accelerate the electrons. The interaction occurs between the incident beam of electrons and the sample is not only on the surface but also in a certain volume of the sample. This volume is also depending on the accelerating potential and average atomic number of the sample. The volume of sample is greater at greater acceleration potentials but it is smaller at the larger average atomic number of the sample.

HRTEM is also refers to imaging, in which lattice fringes (i.e. crystallographic planes) are observed and atomic resolution can be achieved. In HRTEM, the indirect heating and field emission methods are used instead of thermal emission that is generally used in the conventional TEM, because they gives a greater intensity. HRTEM images are formed from a number of diffracted beams, which are also known as phase contrast imaging and useful to construct an image of crystal lattice. However, the contrast images are arising from the interference in the image plane of the electron wave with itself and the phase of an electron wave that carries the information about the sample. This makes compulsory of preparing thin sample, so that the amplitude variation slightly affect the image.

Form the analysis of HRTEM images; one can obtain information about the crystalline and structural defects, interfaces at atomic scale, useful information on grain sizes, orientation of crystal structure and size of nanostructures. [97].

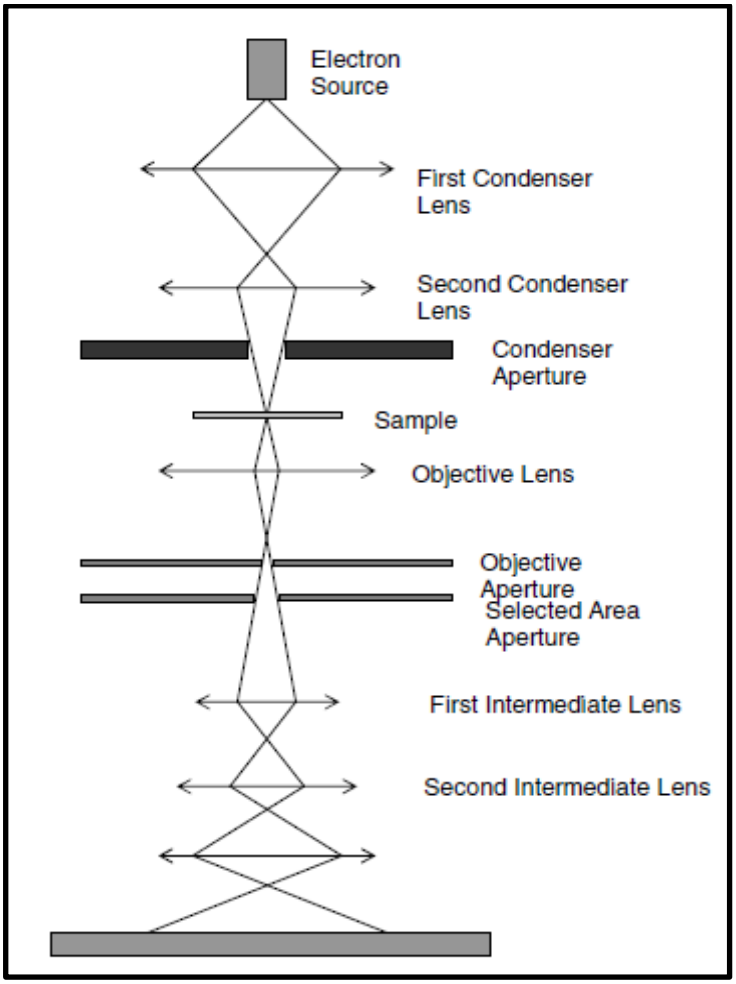


**Figure 2.9: A schematic diagram of TEM**

SAED is another experimental technique that is also performed using TEM. Electron diffraction of the sample in a selected area is recorded by inserting an aperture into the incident electron beam path. Selected area aperture is a thin strip of metal, which can block the beam. It contains different sized holes to allow passage of electron beams. The selected area aperture is moved in a manner to select a particular area in the sample, that's why it is called as 'selected area', and only this portion interact with the electrons. However, the wavelength of the incident high energy electron beam (about few thousand nanometers) is about 100 times smaller than the spacing between the atoms in the solid, so that the atoms act as a diffraction grating to the electrons and diffracted it to a particular angle. The obtained SAED pattern is just similar to the XRD; only difference is that it's unique in a particular area of the sample and used to analyze the phase purity, structure of nanostructures etc.

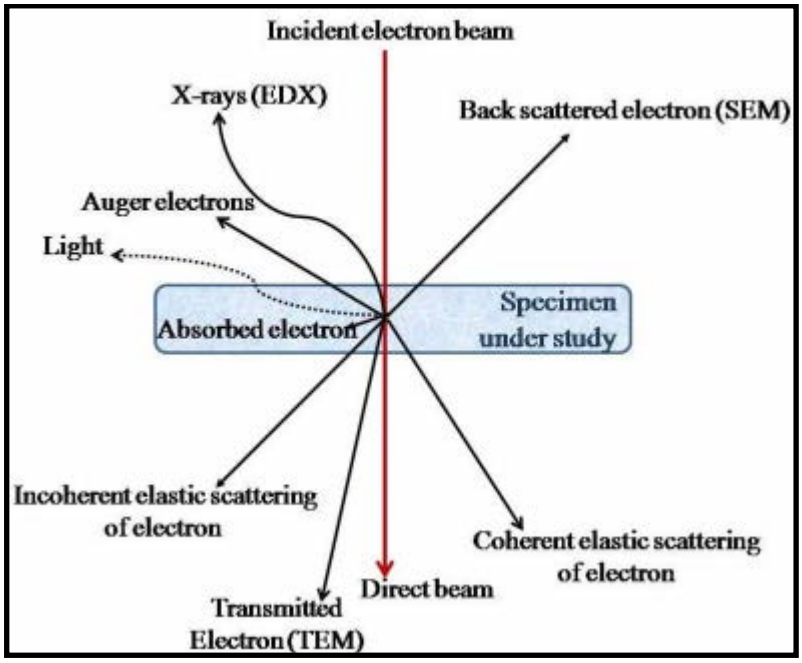


**Figure 2.10: A schematics representation of various processes associated with the interaction between the electrons and the sample, which forms a basis for different analysis methods**

For single crystal samples, SAED pattern consists of dots, whereas in case of polycrystalline or amorphous solids, it consist series of solid rings. SAED patterns can also be used to analyze the information about the space group of a single crystal [98].

In the present work, the particle size, surface morphology, diffraction rings and patterns, and the crystallinity of the pure $CeO_2$ and doped (Fe, Sm and Gd) $CeO_2$ NPs samples have been examined using TEM with TECNAI $G^2$ 20 S-TWIN (FEI Netherlands) instrument operated at an accelerating voltage of 200 kV, having a point resolution of 0.24 nm and a lattice or line resolution of 0.14 nm (as shown in Figure 2.11). Samples for the TEM investigation were prepared by dispersing the nanopowder in ethanol using an ultrasonicator to produce a dilute suspension. A standard holey carbon film supported on Cu grid was immersed in the suspension to produce the TEM sample. The particle size distribution was measured for a total 150 particles using image-j software of TEM images.


**Figure 2.11: Photograph of TECNAI $G^2$ 20 S-TWIN (FEI Neitherlands) TEM instrument from IIT Roorkee**

### 2.5.1. Information from TEM

TEM is a powerful technique used to provide the crystallographic information about the crystal structure, dislocations, compositional information, defects, grain boundaries and growth of layers in the semiconducting materials. The high resolution can be used to analyze the quality, shape, size and arrangement of particles on scale of atomic diameters. SAED patterns can obtain the structural information of the sample, such as, crystalline symmetry, unit cell parameters and space group.

## 2.6. Energy-Dispersive X-ray Spectroscopy (EDX)

EDX is an analytical technique used for compositional analysis and for the quantitative analysis of various elements present in the sample. The set up of EDX consist of four main components, these are (1) beam source, (2) X-ray detector, (3) pulse processor and (4) analyzer.

When a beam of high-energy electrons are allowed to fall on the sample, the atoms within the sample gets this high energy, due to it the electrons in the inner shell of the atom may get excited and could be ejected from the shell. Thus, electron-hole pairs are formed in the inner shell of the atom, which is filled by the electron from the outer hole. The energy difference between the higher energy shell and low energy shell is transmitted in the form of X-ray. As this emitted energy is the characteristic of the atomic structure of the element, so that these X-rays are used for identifying the elements. Moreover, the quantitative estimation of various elements present in the sample is calculated by measuring the total number of emitted X-rays of that particular element. The number and energy of the emitted X-rays are measured by the EDX detector. This detector is used to convert the X-ray into voltage signal according to the energy and pass it to the analyzer for analysis that produces the elemental image. Generally, EDX system is equipped with SEM or FESEM and sometimes with TEM.


**Figure 2.12: Photograph of TESCAN MIRA 3 FESEM instrument equipped with EDX**

In the present work, the elemental analysis of pure $CeO_2$ and Sm-doped $CeO_2$ NPs were probed using TESCAN MIRA 3 FESEM instrument equipped with EDX system at Banasthali Vidhyapith, Newai, Jaipur, India (as shown in Figure 2.12).

### 2.6.1. Information from EDX

EDX is a non-destructive characterization technique that can be used for identifying the chemical composition and quantifying the elemental composition in a very small sample of material.

## 2.7. Ultraviolet-Visible-Near Infrared (UV-Vis-NIR) Spectroscopy

UV-Vis-NIR spectroscopy is an important experimental technique, which is involving the measurements of the absorption of the UV and visible light by a sample. The instrument used in the measurements of absorption of UV-Vis-NIR spectroscopy is called as UV-Vis-NIR spectrophotometer. This spectrophotometer provides a way for analyzing the liquids, gases and solids through the use of radiant energy in the far and near ultraviolet, visible and near infrared regions of an electromagnetic spectrum. According to the electromagnetic radiation, the wavelengths for ultraviolet (UV), visible (Vis), and near infrared (NIR) radiations are in the range of 300 to 400 nm, 400 to 765 nm, and 765 to 3200 nm, respectively.

The UV-Vis-NIR instrument operates by passing a beam of light through a sample and measure wavelength of light reaching the detector. The measured wavelength of the sample gives the valuable information about the chemical structure and intensity that is related to the number of the molecules and concentration. The analytical information of a sample can be given in terms of transmittance, absorbance or reflectance of the energy in the wavelength range 160 to 3500 mill microns [99]. The ultraviolet and visible spectrum originates from the electronic excitations. It is well known that light is quantized into tiny packets called photons, the energy of which can be transferred to an electron upon collision. However, the transfer of energy occurs only when the energy level of the photon equals the energy required for an electron to get promoted onto the next energy state i.e. from ground state to the first excitation state. This is the basis process for absorption spectroscopy. Normally, light of a certain wavelength and energy is

illuminated on the sample that absorbs a certain amount of energy from the incident light. The amount of energy of the light transmitted from the sample is measured by using a photo detector, which collects the absorbance of the sample. The absorption of UV and visible light by the molecules of the sample leads to the transition among the electronic energy levels of the molecules. The amount of light absorbed or transmitted from the matter as a function of wavelength is graphically represented as a form of spectrum. The absorbance is calculated by using Beer-Lambert's law. This law is the relation between absorbance and concentration of an absorbing material, which is given as:

$$\boldsymbol{A = a(\lambda)\, c\, l} \qquad (\mathbf{2.10})$$

Where, A is the measured absorbance, $a(\lambda)$ is a wavelength-dependent absorptive coefficient, $l$ is the path length through the cuvette in cm, and c is the molar concentration (mol/L).

When concentration unit is in molarity, then the Beer-Lambert law given as:

$$\boldsymbol{A = \varepsilon\, c\, l} \qquad (\mathbf{2.11})$$

Where**,** ε is the wavelength-dependent molar absorptive coefficient **(**$M^{-1}cm^{-1}$**).** When a light with intensity $I_o$ is directed at a material and light with intensity I is transmitted, then the value $I/I_o$ is called transmittance (T) and the value $(I/I_o)*100$ is called transmission rate (T%). The value log (1/T) = log ($I_o$/I) is called absorbance (A). Now, Beer-Lambert's law can be written as:

$$\boldsymbol{A = \log\frac{1}{T} = \log\frac{I_o}{I} = -\varepsilon\, c\, l} \qquad (\mathbf{2.12})$$

Figure 2.13 shows a schematic representation of UV-Vis-NIR spectrophotometer, which consist of a number of fundamental components, such as light source (UV and Vis), monochromator (wavelength selector), sample holder, detector, signal processor. The light radiation source used is a tungsten filament, a deuterium arc lamp which is continuous over the ultraviolet region, and light emitting diodes (LED) and xenon arc lamps for the visible wavelengths. The detector is a photodiode or a CCD. Photodiodes are used with monochromator that filters the light of a single wavelength reaches the detector. During the measurements of absorbance at UV spectrum, the other lamp has to be switched off, that same goes on when measuring visible light absorbance. As shows in

Figure 2.13, from monochromator light source, the light splits into two equal intensity beams by a half mirrored device before it reaches the sample. One beam (i.e. sample beam) passes through a small container (cuvette) containing the sample, either in a transparent solvent or mixed with the standard powder chemical. The other beam (i.e. reference beam) passes through an identical cuvette containing only either solvent or standard powder chemical. The container for the sample and the reference solution must be transparent to the radiation which will be passed through them. The quartz cuvettes are essentially required for UV-Vis-NIR region. The light sensitive detector follows the sample chamber and measure the intensity of light that is transmitted from the cuvettes and passes the information to a meter, which records and displays the values to the operator on LCD screen. The intensity of the reference beam is defined as $I_o$ and the intensity of the sample beam is defined as I. The intensities of these beams are to be measured by electronic detectors and compared [100].

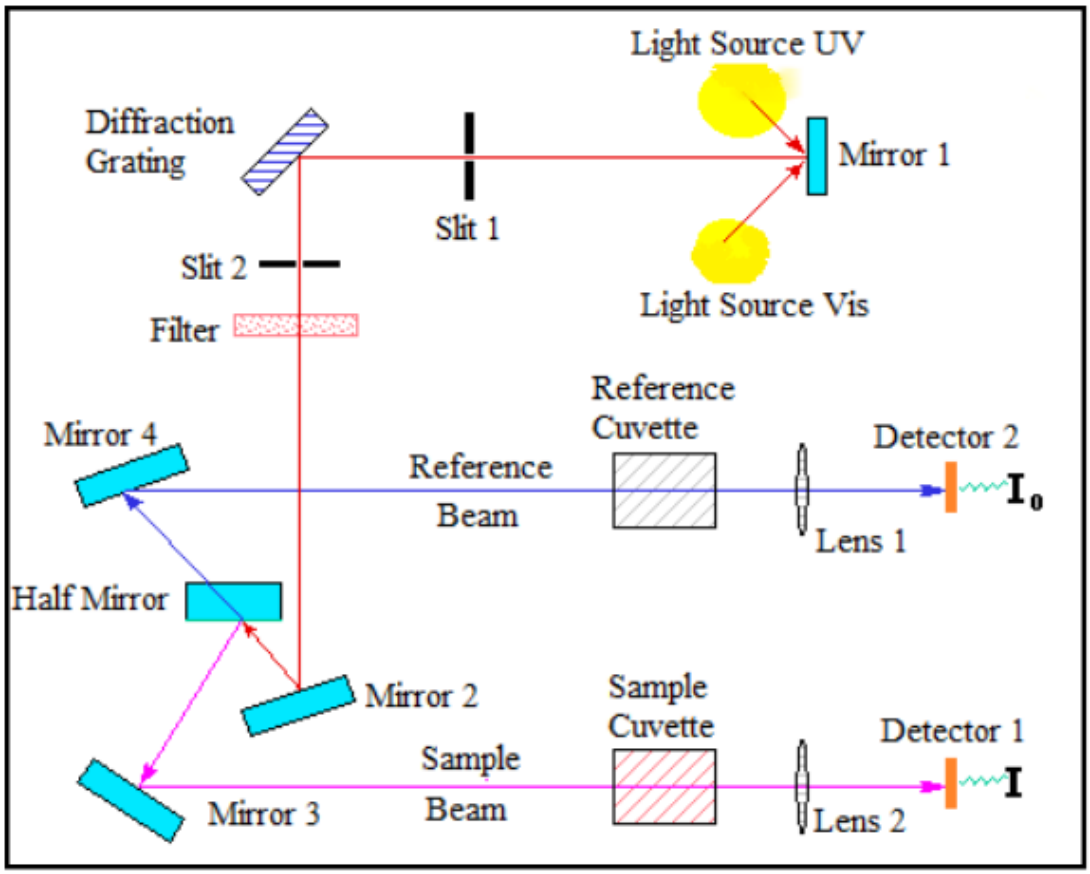


**Figure 2.13: A schematic representation of UV-Vis-NIR spectrophotometer**

In the present work, the optical absorption spectra of pure $CeO_2$ and doped (Fe, Sm and Gd) $CeO_2$ NPs samples were recorded at room temperature using Shimadzu UV-3600 Plus UV-Vis-NIR spectrophotometer with an integrating sphere (as cuvette). The photograph of Shimadzu UV-3600 Plus spectrophotometer is shown in Figure 2.14. The spectrometer operates in the wavelength range of 185 nm to 3300 nm with a slit width variation of 0.1 to 30 nm and the maximum resolution of 0.1 nm. The spectrophotometer consist three detectors; Photomultiplier Tube (PMT) for UV and visible regions, and InGaAs and PbS detectors for the near-infrared region. The source incorporates a tungsten halogen lamp for wavelengths greater than 375 nm and a deuterium discharge lamp for values below that and a solenoid operated mirror that automatically deflects light from either one as the machine scans through the wavelengths. The optical absorption spectra were recorded for the pure and doped (Fe, Sm and Gd) $CeO_2$ NPs samples in the wavelength region 200 to 1000 nm with $BaSO_4$ as an internal standard. The peak position of the spectrum was obtained using peak-pick facility provided in the spectrophotometer. The uncertainty in the measurement was about ±1 nm.


**Figure 2.14: Photograph of Shimadzu UV-3600 Plus spectrophotometer**

### 2.7.1. Information from UV-Vis-NIR Spectroscopy

UV-Vis-NIR spectroscopy is an important technique for studying the optical properties of the nanomaterials. It provides the information about the absorbance, transmittance, reflectance, band gape energy, refractive index and nature of the materials.

## 2.8. Surface-Enhanced Raman Spectroscopy (SERS)

One of the straightforward and non-destructive techniques, which requires no sample preparation and can be used to identify the wide range of substance like solid, liquid and gas, is known as Raman spectroscopy. This technique involves a process, in which sample is illuminating with monochromatic light by using a spectrometer, to examine the light scattered by the sample.

Raman spectroscopy is a vibrational spectroscopic technique based on an inelastic scattering of the monochromatic light that usually comes from a laser source. In inelastic scattering of monochromatic light, the frequency of the photons changes upon interaction with the sample. These photons comes from laser light are absorbed by the sample and then reemitted. Now, frequency of the reemitted photons is shifted up or down in comparison with the original monochromatic frequency that is called Raman effects. This frequency shift provides the information about the vibrational, rotational and other low frequency transitions in molecules [101]. Generally, scattering process involves instantaneous absorption of an incident photon and subsequent emission of photon or scattered photon by phonon. On the basis of that, three types of scattering are possible (as shown in Figure 2.15).

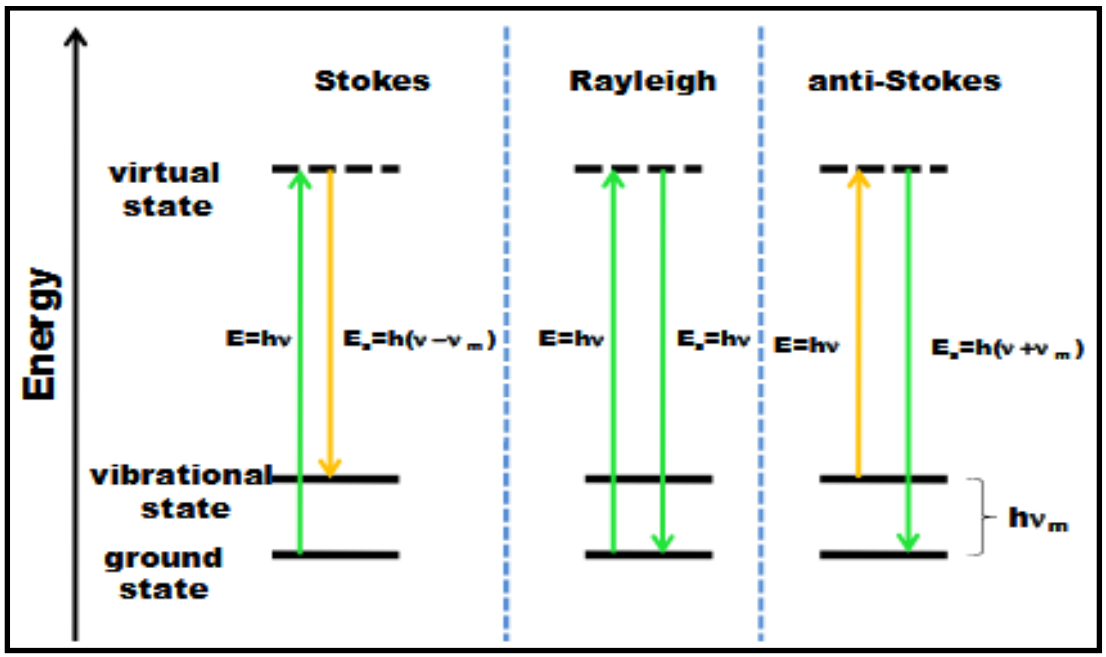


**Figure 2.15: Systematic representation of Stokes, Rayleigh and anti-Stokes process in Raman scattering**

When the emitted photon is elastically scattered with the same frequency as the absorbed photon then this process is called as Rayleigh scattering [102]. In contrast, Raman scattering involves inelastic scattering of an emitted photon is a consequence of the interaction of the optical and vibrational oscillations and its probability is small but finite. When the molecules moves to more vibrational excited state from the ground electronic states, the photons are emitted with energy lesser by the amount equal to the vibrational transition and are called as Stokes scattered photons. Whereas, the molecules makes a transition to a less vibrational excited state then the emitted photons are called as anti-Stokes scattered photons. The anti-Stokes scattering occurs at higher energy in compare to Rayleigh scattering, and Stokes scattering has less energy than Rayleigh scattering, whereas, both Stokes and anti-Stokes are equally displaced from the Rayleigh line in the spectra. Generally, Stokes lines are followed in Raman spectroscopy and anti-Stokes scattering is less intense. Since, the vibrational spectrum is unique for each molecule, so that the Raman spectra are referred as a chemical fingerprint of the scattered molecules. Mathematically, Raman scattering process can be expressed as:

$$\boldsymbol{h\nu + E = h\nu' + E'} \qquad (\mathbf{2.13})$$

$$\boldsymbol{\Delta E = h(\nu - \nu')} \qquad (\mathbf{2.14})$$

Where, $\nu$ and $\nu'$ are the incident and scattered frequency, respectively. According to the definition, the elastic and inelastic scattering can be given classified as,

i) For Rayleigh scattering, when $\nu = \nu'$, then $\Delta E = 0$

ii) For Stokes line of Raman scattering, when $\nu > \nu'$ (i.e. $\Delta\nu$ is positive), then $\Delta E < 0$

iii) For anti-Stokes line of Raman scattering, when $\nu < \nu'$ (i.e. $\Delta\nu$ is negative), then $\Delta E > 0$

In Raman experiment, the Raman shift ($\boldsymbol{\Delta\lambda}$) is a wave number and it is given as:

$$\boldsymbol{\Delta\lambda\ (cm^{-1}) = \left(\frac{1}{\lambda_o} - \frac{1}{\lambda_1}\right) \times \frac{10^7}{cm}} \qquad (\mathbf{2.15})$$

Where, $\lambda_o$ and $\lambda_1$ is the excitation wavelength and Raman scattered wavelength in nm, respectively. When the emitted photon has less energy than the absorbed photon, this energy difference is known as Stokes shift. If the emitted photon has more energy than the absorbed photon, this energy difference is called as anti-Stokes shift. Actually, this extra energy comes from dissipation of thermal phonons in a crystal lattice [103]. The Raman shift does not depend upon the frequency of the incident light but it is a characteristic of the substance causing Raman scattering.

Although, Raman spectra provide a vibrational fingerprint of a scattered molecule and have enough potential applications in different sectors such as physics, chemistry and biology. Instead of that its practical applications are limited, because it has very low scattering cross section about $10^{-29}$ $cm^2$ $sr^{-1}$. Even if the molecule is in Raman active, the intensity of the Raman spectra may not be within the measurable count. Hence, in order to explore the benefit of Raman spectroscopy, a new method is required to enhance the Raman scattering cross section. SERS is a well-known method based on Raman spectroscopy and nanotechnology. SERS is surface-sensitive techniques that enhance the Raman scattering by molecules adsorbed on the rough metal surface. It has been widely applied for obtaining Raman spectra of compounds at low concentration as well as it offers many advantages over other spectroscopic techniques such as Fourier transform infrared (FTIR) spectroscopy, UV-Vis-NIR spectroscopy, nuclear magnetic resonance, and mass spectrometry etc. Some other advantage of SERS includes, it can directly extract a significant amount of information from complex environments such as living tissues, biological fluids and cells without any need of prior sample preparation, and simultaneously it provides molecular fingerprint specificity with potential single-molecule sensitivity. SERS also provides the possibility to overcome the small scattering cross-section limitation as well as to examine weak Raman scattering even at low concentrations. The high sensitivity and enhancement mechanism in SERS shows its strong dependence on the size, structure and proximity of the nanostructures [104]. Generally, surface enhanced Raman effect is explained as the combination of a dominant electromagnetic (EM) enhancement that results from Localized Surface Plasmon Resonance (LSPR) and a chemical enhancement related to charge transfer between the substrate and surface associated

molecules [105]. The main goal of this method is to enhance the weak signal of Raman spectra. The enhancement factor can be $10^{10}$ to $10^{11}$, which means that the technique may be detected single molecules. The experimental set up of Raman spectrometer consists of four major components:

1) Excitation source (Laser)
2) Sample illumination system and light collection optics
3) Wavelength selector (Filter or Spectrometer)
4) Detector (Photodiode array, CCD or PMT)

Figure 2.16 shows the schematic experimental set up of Raman spectrometer. In Raman spectrometer, a powder sample is illuminated with the laser beam. The light, which is coming from the illuminated spot is collected with a lens and send through interference filter or spectrometer for obtaining the Raman spectra of the set sample. Due to the elastic Rayleigh scattering the wavelengths close to the laser line are filtered out, while the rest of the collected light is discrete onto a detector. By changing the laser light one can confirm that the peak is a true Raman peak and it's not a peak associated with the wavelength of the laser light that has been used in the experiment. Generally, the spontaneous Raman scattering signal is very weak because most of the incident photons undergo elastic Rayleigh scattering. Therefore, instruments such as notch filter, tuneable filters, laser stop apertures, double and triple spectrometric systems are used for reducing the Rayleigh scattering and obtain high quality Raman spectra. Before taking every measurement the scattered light would have to be aligned in the spectrometer so that maximum signal would hit the detector. This can be achieved by moving the sample to different positions by using lens and mirror system. The Raman scattered light is detected by either Photo Diode Arrays (PDA) or Charger Coupled Devices (CCD). In between of these detectors, CCD has enormously helped for taking data quickly and more preciously. CCD has an array of detectors, which can look at a range of wavelength at one time and reducing the collection time. Raman shift is related to the vibrational frequencies of the molecules in the sample and when it is plotted against their intensities gives the spectrum known as Raman spectrum.

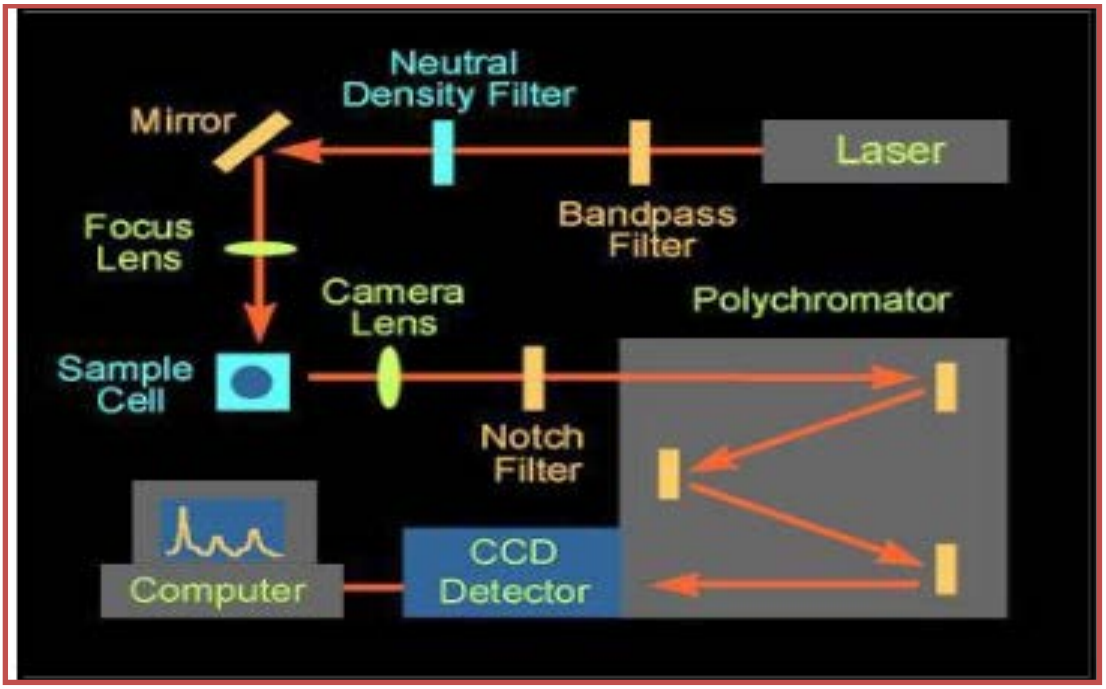


**Figure 2.16: A schematic representation of Raman Spectrometer**

**Figure 2.17: Photograph of Thermo Scientific DXRxi Raman spectrometer**

In the present work, the Raman spectra for pure $CeO_2$ and doped (Fe, Sm and Gd) $CeO_2$ NPs samples were recorded at room temperature on Thermo Scientific DXRxi Raman Imaging Microscope with Charge Injection device (CID) detector using Green Laser (532 nm) for excitating light source with the power of 10 mW. The laser spot on the sample was 1 μm in diameter and 100X objective was used to focuse the incident laser light. Integration time was taken 10 sec for the samples.

The Raman scattering spectra for all samples were measured from 50 to 3300 $cm^{-1}$ wavenumber. The photograph of Thermo Scientific DXRxi Raman Imaging Microscope is shown in Figure 2.17.

### 2.8.1. Information from SERS

SERS is a surface sensitive technique that enhances Raman scattering by molecules absorbed by nanostructures. It provides information about chemical structure and phase of material, intrinsic stress/strain, contamination and impurity in the nanomaterials samples.

## 2.9. X-ray Photoelectron Spectroscopy (XPS)

XPS is surface-sensitive quantitative spectroscopic technique that measures the elemental composition, chemical structure, valence state and electronic state of the elements present in the samples. XPS is based on the photoelectric effect, in which when a material is irradiated with a beam of high energy photon i.e. X-rays, the element present in the material get ionized and emits the electrons i.e. photoelectrons. If the energy of the X-ray photon ($E_{hv}$) is higher than the binding energy of electron ($E_{BE}$) then the remaining energy will be utilized as the kinetic energy ($E_{KE}$) of the ejected photoelectrons, which is given as:

$$\boldsymbol{E_{KE} + \phi_o = E_{hv} - E_{BE}} \qquad (\mathbf{2.16})$$

Where, $\phi_o$ is the work function. The XPS spectra consist of a plot between kinetic energy and number of electron. These numbers of electron with certain kinetic energy is directly proportional to the amount of that particular element and by measuring the kinetic energy of an electron from XPS spectra; its binding energy can be calculated. The binding energy of the ejected photoelectron is characteristic of the orbital from which the electrons originates and depends upon the final state configuration after photoemission. The initial and final state configuration is shown in Figure 2.18. Thus, XPS measurements can be used for quantitative estimation of the chemical composition of various elements in the sample. The electrons detected by XPS spectra are originated from the depth of the surface of the material i.e. 10-12 nm, which are escaped to vacuum in the instrument. XPS measurements require ultra-high vacuum (UHV) conditions. It is mainly a surface technique and useful for the analysis of the surface chemistry of the material.

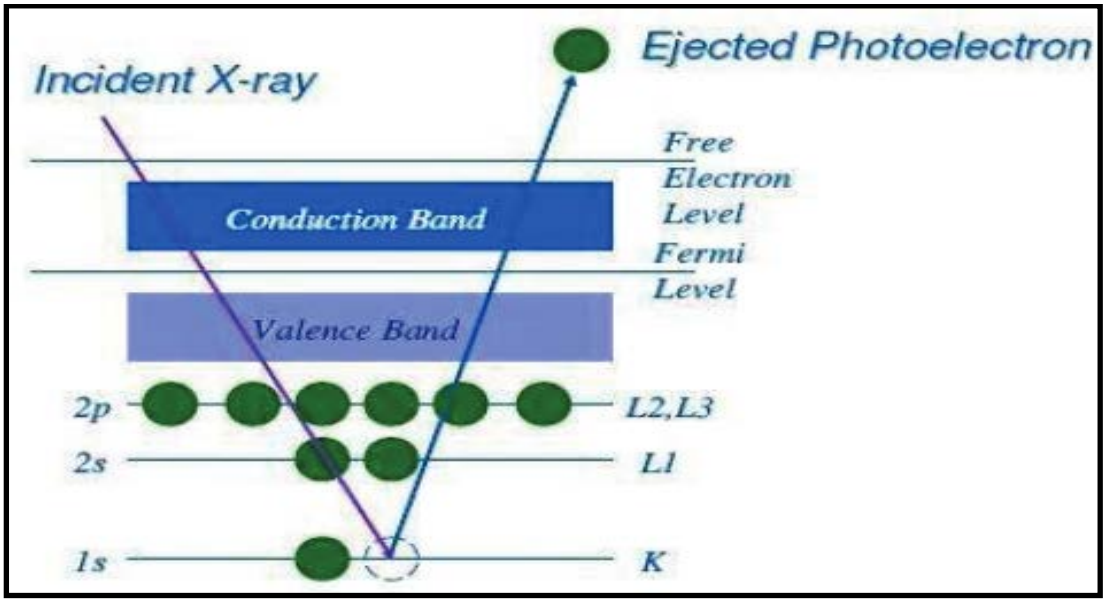


**Figure 2.18: A schematic diagram of XPS process**

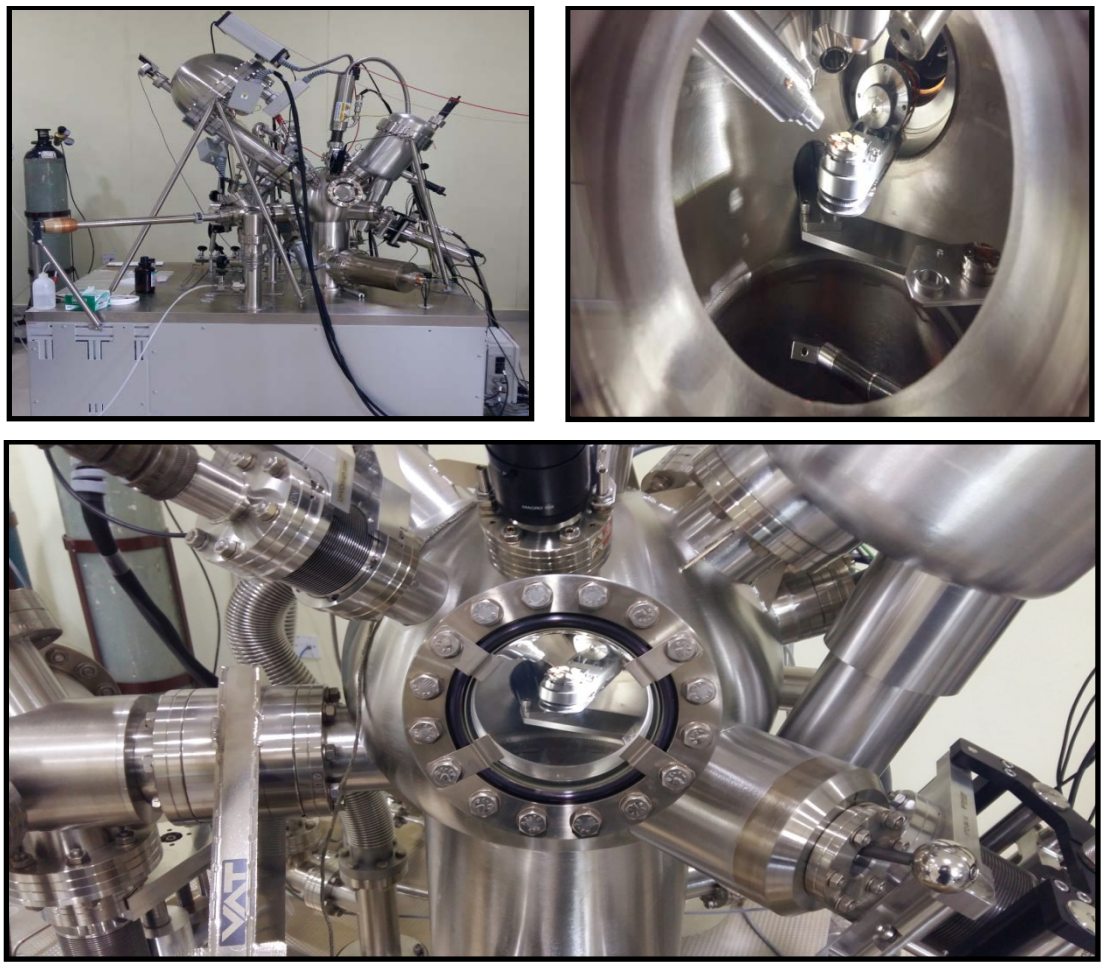

**Figure 2.19: Photograph of ESCA+ Omicron nanotechnology (Oxford Instrument, Germany) XPS instrument at MNIT, Jaipur**

The binding energy of an emitted photoelectron is not only depending upon the energy level of emission but also on the oxidation state of the particular atom and surrounding of that atom. The environmental dependent shift in the binding energy for that atom in the spectrum is usually referred as chemical shift or core level shift. For example, the binding energy of Cu 2p peaks in CuO is totally different from the binding energy of Cu 2p peaks of pure Copper. This is because; Cu is surrounded by oxygen atoms in CuO, whereas copper is surrounded by only copper atoms in pure Copper. Thus, the binding energy of Cu 2p is different in CuO rather than pure Copper. An atom of a higher positive oxidation state exhibits a higher binding energy due to extra coulombic interaction between the emitted photoelectron and the core level ion. The similar shift of the peak to the higher binding energy side is observed with the presence of an electronegative atom around of that atom. Thus, XPS has an ability to discriminate between different oxidation states and chemical environments of an atom.

In the present work, the XPS spectra were recorded on ESCA+ Omicron nanotechnology (Oxford Instrument, Germany) instrument equipped with a base pressure in the analysis chamber of $10^{-8}$ Torr. The X-ray source was monochromatized Al $K\alpha$ ($h\nu$ =1486.7 eV) radiation and the binding energy scale was calibrated using the C 1s line ($h\nu$ = 284.6 eV) of the adsorbed hydrocarbon on the sample surface. The operating voltage and current of the instrument was kept on 15 kV and 20 mA, respectively. The short scan pass energy was 20 eV and in case of survey scan it was 50 eV. Sample were taken in pellet form and deposited on Cu tape and degased for overnight in XPS FEL chamber to minimize the air contaminatior at sample surfaceas as well as degasing in the main sample chamber. To overcome the charging problem, a charge neutralizer of 2 keV was applied to the sample. The electron takeoff angle i.e. angle between the analyzer to source is $90^{o}$ and the resolution was confirmed by FWHM anout 0.60 eV in the measurments. The produced X-ray were allowed to fall on the sample mounted on the sample stage (as shown in Figure 2.19). electron collection lens, electron detector system and electron energy analyzer were used to analyse the kinetic energy of the ejected electrons and

to count the electrons with particular kinetic energy. In order to avoide the loss of electron energy by interacting with the residual gaeous molecule, this analysis is performed under ultra-high vacuum condition.

### 2.9.1. Information from XPS

XPS provides the useful information about the oxidation state of an atom in the sample. Apart of the chemical shift, secondary effects like multiple splitting, spin-orbit splitting and shake-up structure can also give useful information about the bonding and electronic structure of the material.

## 2.10. Superconducting Quantum Interference Device-Vibrating Sample Magnetometer (SQUID-VSM)

MPMS-3 SQUID-VSM is the most powerful SQUID magnetometer that based on the 2ω detection technique, which makes both SQUID and VSM techniques in combined form. It is a very sensitive device, which is able to measure very low field (order of $10^{-8}$ emu) and widely used instrument for magnetic characterization of nanomaterials [106]. VSM measures the voltage induced in the pickup coils by Faraday's law of induction, as the sample is vibrated in its surrounding area. VSM is relatively faster albeit with poorer sensitivity in comparison to a relatively-slow SQUID magnetometer. SQUID-VSM instrument is a unique combination of best features of both SQUID and VSM i.e. sensitivity of SQUID and speed of VSM.

Basically, SQUID is very sensitive detector of magnetic flux which combines the physical phenomenon of flux quantization and Josephson tunnelling and can operate at temperature as low as few Kelvin. This Josephson junction is consisting of two superconducting ring that is broken by one (RF SQUID) or two (DC SQUID) and separates by a thin insulating film called as weak link (as shown in Figure 2.20). The tunnelling of electrons can be taken place through that junction [107].

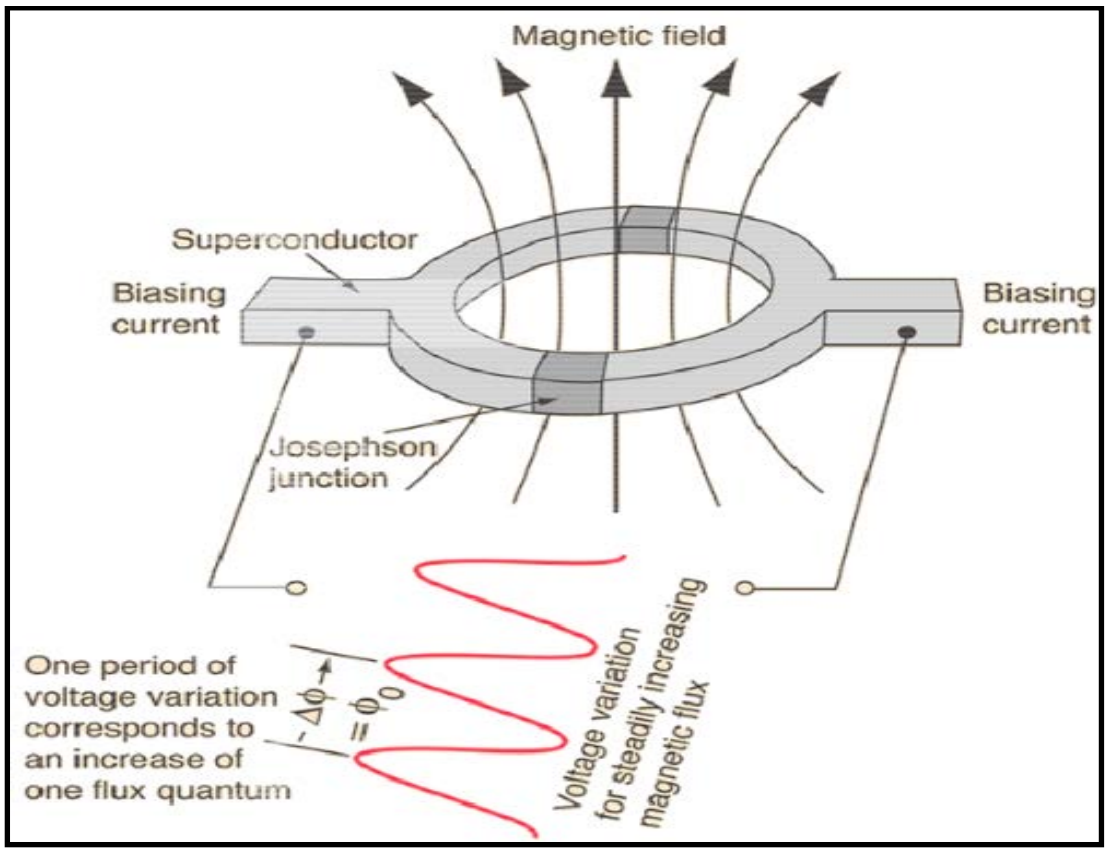


**Figure 2.20: A systematic representation of SQUID Josephson device**

The flow of super-current through the coil is very less about $10^{-5}$ A, which can be limited by the thin insulating layer. Its pickup system and sensors are sensitive to change in the magnetic flux and magnetization of magnetic material as a function of temperature, magnetic field and time. As the area of the junction is increased, the sensitivity of Josephson junction to applied magnetic field is also increased, which justifies making the device large so that the control current can be reduced to a minimum. However, the switching speed of junction is decreased with increase in the area of the junction. Recently in some devices, the conflicting demands of speed and sensitivity are met by replacing a single junction with two or more junctions connected by a continuous superconducting loop. This multi-junction device is called as Josephson interferometer or SQUID. SQUID has one or more than one Josephson junctions as its active element. In most of the systems, SQUID is located inside a small cylindrical, superconducting magnetic shield in the middle of a liquid helium Dewar. The pickup coils are configured as a second-order gradiometer that detects the difference in one component of the field between two

points, which are located at the bottom of the Dewar and placed underneath of the magnetometer. The remaining hardware is designed to eliminate RF interference, minimize helium boil off, and avoid noise or any external distortion A.C. fields. During the measurements, if a constant biasing current is maintained in the SQUID device, the measured voltage oscillates according to the change in the phase at the two junctions that depends on the change in the magnetic flux. The change in flux can be evaluated by counting the oscillations. Since, the sensitivity of SQUID is $10^{-14}$ Tesla that is very large to measure any magnetic signal obtained from the sample. Systematic diagram of signal detection method of SQUID magnetometer is shown in Figure 2.21.

During the measurements, sample is placed within the superconducting pickup coils, which are situated at the centre of the superconducting magnets. Due to induction, the magnetized sample induces an electric current in the pickup coils, so that a superconducting loop is formed by the detection coils and an input coil of SQUID. Any change in the magnetic flux in the coil can produce a proportional current in the loop. It is well known that SQUID works as current-to-voltage converter in the linear manner, so any change in the current in the detection coil produces a change in the SQUID output voltage, which is proportional to the change in the magnetic moment of the corresponding sample.

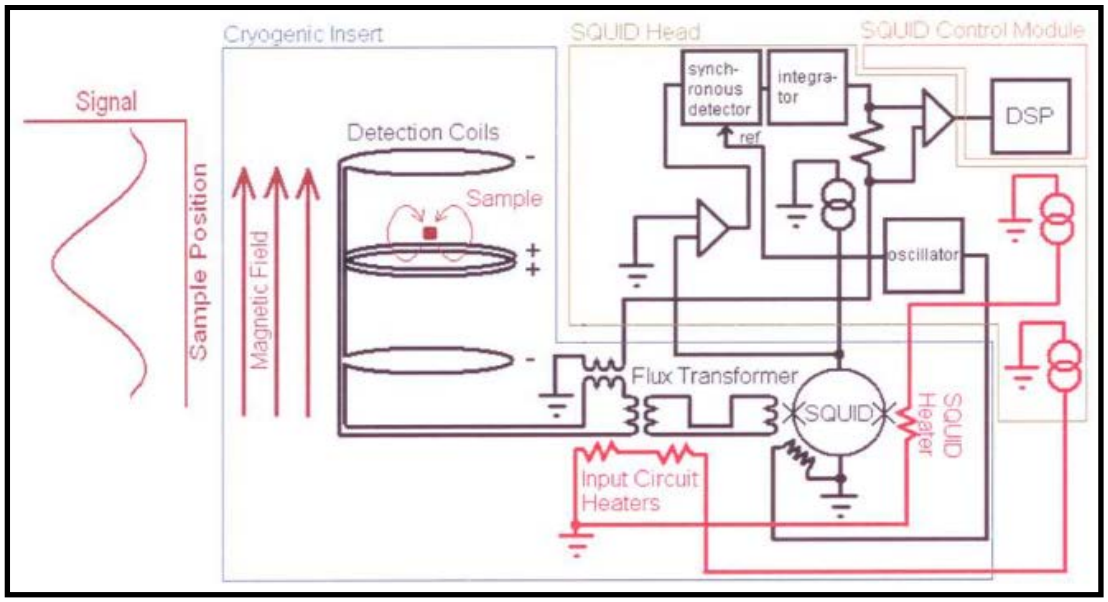


**Figure 2.21: A systematic diagram of SQUID detection system**

Now, a fully calibrated system at the end stage of the system directly converts this output voltage to the magnetic moment that is produced from the SQUID. For doing calibration, a small piece of a material of known mass and magnetic susceptibility is used. A MPMS-3 SQUID-VSM contains all parts similar to a SQUID magnetometer, along with a VSM motor component. This VSM motor-head is used for vibrating the sample in-between the detection coil and motion of the sample is controlled by an electric motor current module. The sample position is controlled by the DC signals, while the frequency and the amplitude of the vibration are controlled by the AC signals.

In the present work, the magnetic measurements of the pure $CeO_2$ and doped (Fe and Gd) $CeO_2$ NPs samples were recorded at room temperature on Quantum Design MPMS-3 SQUID-VSM magnetometer available at Micro and Nano characterization Facility (MNCF), Centre for Nano Science and Engineering (CeNSE), Indian Institute of Science (IISc), Bengaluru. The magnetic measurements were conducted by varying the applied field from -7 T to +7 T at room temperature. The photograph of the Quantum Design MPMS-3 SQUID-VSM system is shown in Figure 2.22.

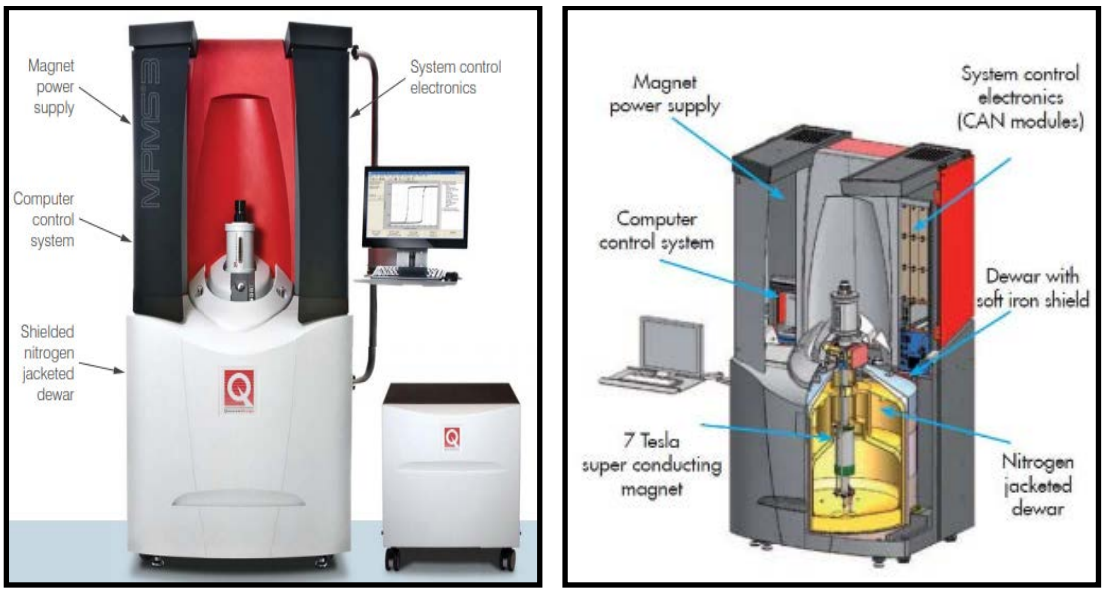


**Figure 2.22: Photograph and cross-section view of MPMS-3 SQUID-VSM**

### 2.10.1 Information from SQUID-VSM

Quantum design MPMS-3 SQUID is a very sensitive magnetometer due to utilization of liquid helium cooled SQUID system for measuring the change in the magnetic flux that converts and measured as current, as the sample moves through the superconducting detection coil. We can measure M-H and M-T curve with the help of this instrument, which provides the information about magnetic moment, saturation magnetization, magnetic susceptibility, coercivity, retentivity and magnetic behaviour of the samples.

## 2.11. Keithley Electrometer

Keithley source-meter unit is the most common measuring instrument for current-voltage (I-V) characterization in laboratories. Source-measurement unit (SMU) is an electronic instrument that has capability of both sourcing and measuring at the same time. This capability adds an extra degree of versatility for many measurement applications and eliminates the requirement for using separate instruments for such applications. This instrument can operate in two modes where it can functions as a current or a voltage source.

i) In the first mode (source V measure I), the instrument function as a voltage source and simultaneously measure the current give across the circuit. This instrument is capable of sourcing voltage from ±100 nV to ±200 V. When instrument programmed to source voltage, current measuring meter is connected in series with source V and output (as shown in Figure 2.23 a).

ii) In the second mode (source I measure V), the instrument functions as a current source and measure the potential drop across the given circuit. This instrument is capable of sourcing ±10 fA to ±10 A. When instrument programmed to source current, voltage measuring meter is connected in parallel with the current source and the output (as shown in Figure 2.23 b).

The high current measurement sensitivity (as low as 10 fA) and high input resistance (~100 TΩ) makes source-meter suitable for low level measurements. Source-meter has another important property that is sweeping capability. In which, it can programmed to sweep in a given voltage or current interval with a given number of steps. The source-meter is basically designed for the high speed production test

applications and it is very useful instrument for research applications such as semiconductor device characterization.

This instrument operates in two modes namely DC mode and Sweep mode. The source-meter unit operations that consists both DC and sweep modes also have source delay measure (SDM) cycles. During each SDM cycles, source-meter unit follows some steps such as; setting the source output level, perform the delay and finally make the measurements. Each measurement is stored in sweep buffer.

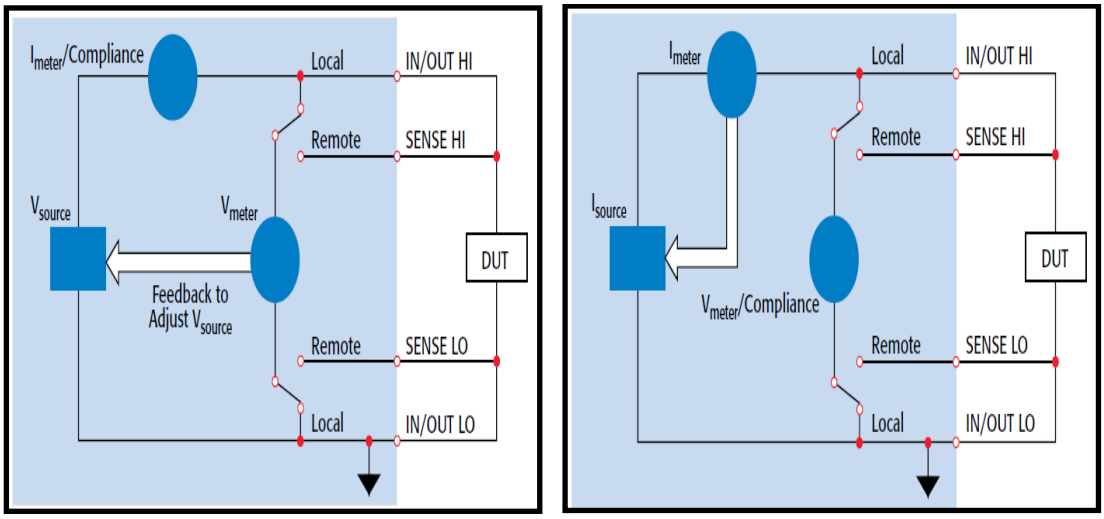


**(a)** **(b)**

**Figure 2.23: Schematic circuit diagram of conductivity meter (a) Source V Measure I, (b) Source I Measure V mode**

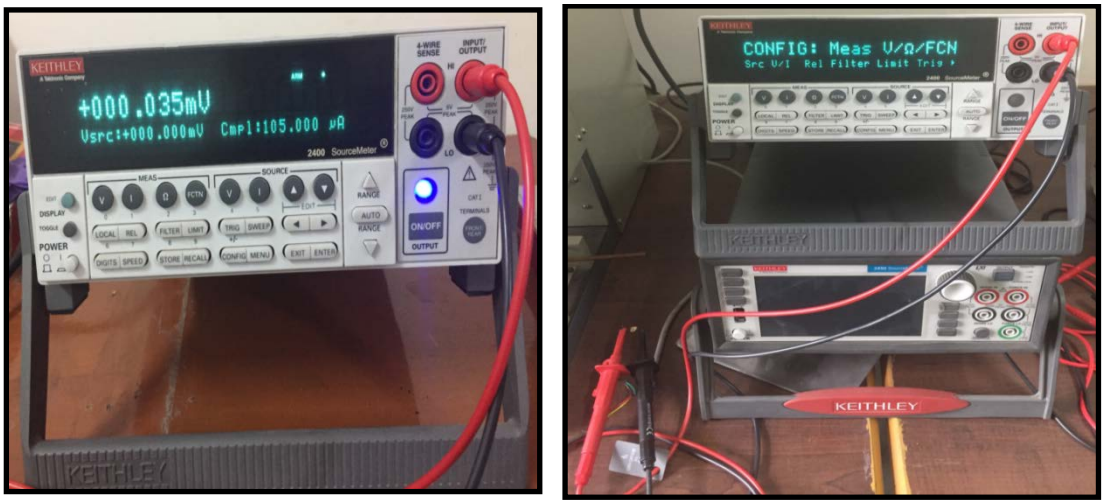


**Figure 2.24: Photograph of Keithley 2400 source-meter instrument (Tektronix Company)**

In the present work, the electrical properties of pure $CeO_2$ and Sm-doped $CeO_2$ NPs samples was performed by measuring current with increasing voltage at room temperature on Keithley 2400 source-meter instrument (make of Tektronix Company). I-V characteristic was determined using two probe technique. Samples used for this technique were symmetric in shape. During the measurement, the independent electrical terminals of copper wires were joining with the help of silver paint onto the samples. One terminal was connected to source meter to apply constant current to the sample and other one terminal measure the resulting potential drop across a defined portion of the sample through nanovoltmeter. The electrical contacts of wires on the samples were made by conducting silver paint. The samples were subjected to increasing voltage from 0 V to ±1 V. This instrument has a current handling capability ranging from ±1 pA to ±1.05 A and voltage capability of ±100 nV to ±210 V at a maximum power of 22 W. Resistance value can be measured by the device is as low as 0.2 Ω to 200 MΩ. This Keithley 2400 source-meter was attached with a computer and controlled by the help of software LabTracer 2.0 [108]. The photograph of Keithley 2400 source-meter instrument (Tektronix Company) is shown in Figure 2.24.

### 2.11.1. Information from Keithley Electrometer

Keithley electrometer is an instrument used for studying the electrical properties of samples. We can measure current and voltage of the sample and I-V characteristics measure the conductivity and resistivity of the samples.

# Chapter 3

# Study of Structural, Optical and Electrical Properties of RE ($Sm^{3+}$)-doped $CeO_2$ Nanoparticles

# CHAPTER 3

# STUDY OF STRUCTURAL, OPTICAL AND ELECTRICAL PROPERTIES OF RE ($Sm^{3+}$)-DOPED $CeO_2$ NANOPARTICLES


## ABSTRACT

In this study, the correlation between the concentration of dopant ions and oxygen vacancy defect of Sm-doped $CeO_2$ NPs were investigated systematically by XRD, UV-Vis-NIR and SERS. The nanocrystalline pure $CeO_2$ and $Ce_{1-x}Sm_xO_2$ ($x$ = 0.02, 0.04, 0.06, 0.08 and 0.10) samples were synthesized using co-precipitation chemical route. The XRD measurements revealed that $Sm^{3+}$ ions are successfully incorporated at the $Ce^{4+}$ ion sites in the face centered cubic (*fcc*) lattice of $CeO_2$ NPs. The HRTEM and SAED patterns were analyzed to study the surface morphology, crystallinity, atomic structure of the samples. The average particle size calculated with TEM images was obtained in the range of 5-8 nm for pure $CeO_2$ and $Ce_{1-x}Sm_xO_2$ samples for all the doping concentrations. The UV-Vis-NIR spectroscopy and SERS were analyzed to investigate the optical properties and defect structure in these NPs. The UV-Vis-NIR spectroscopy measurements revealed that due to aggregation of particles the optical band gap energy was varied with fluencies of $Sm^{3+}$ ions as well as due to particle size variations of NPs. Peak asymmetry and broadening of Raman active mode further ascribed the presence of oxygen vacancy (whether extrinsic or intrinsic), which were varied with the fluencies of $Sm^{3+}$ ions in $CeO_2$ NPs. This chapter presented a systematic study on the fluencies of Sm-doping in $CeO_2$ NPs lattice to understand the role of vacancies, intrinsic and extrinsic oxygen vacancies and their effect on tailoring the structural, electrical and optical properties of doped $CeO_2$ NPs for various applications like luminescent materials, oxygen transportation, catalysts, ultraviolet fuel cells, corrosion prevention etc.


## 3.1. Introduction

In recent years, DMS have been extensively studies due to their enormous spintronic properties for various spintronic applications. Among them, $CeO_2$ is

considered as a promising candidate, which has evoked a great deal of interest among the researchers for its wide range of applications such as solid electrolyte in solid oxide fuel cells (SOFC's) [36], three way catalysts for automobile exhaust systems [37], oxygen gas sensors, having wide band gap energy of 3.2 eV used as sunscreen for UV absorbent [38], blocking material in UV shielding [39], and $CeO_2$ films can also be used as protective coating of SOFC's interconnector [40]. Most of the chemical, mechanical and magnetic properties of $CeO_2$ directly depend on the presence of related point defects, such as oxygen vacancies, which are believed to be generated due to reduction of $Ce^{4+}$ to $Ce^{3+}$ oxidation states of cerium ions and further change in material properties may be attributed due its particle size change from micro to nano-scale. It is also reported by researchers that $CeO_2$ NPs have a tendency to liberate more oxygen ions and create more oxygen vacancies than bulk $CeO_2$, due to increased surface-to-volume ratio [109], which may result into increase in oxygen storage capacity as well as oxygen ion conductivity in these materials [110, 111]. Further, it is also reported that the type of dopant also alters the ion conductivity of $CeO_2$ NPs i.e. rare earth (RE) ions as dopant significantly increases the oxygen vacancies, which is responsible for enhancement in the oxygen ion conductivity and in mechanical properties in RE-doped $CeO_2$ nanomaterials [112-114]. *V. V. Ursaki et al*., reported that substitution of $Ce^{4+}$ ions by $Sm^{3+}$ ions form the oxygen vacancies which are responsible for enhancement of the ionic conductivity of Sm-doped $CeO_2$ film synthesized by using electrochemical deposition method [115]. The room temperature ferromagnetic properties are also reported to be enhanced due to RE-doping into $CeO_2$ nanomaterials [116] i.e. recently enhanced room temperature ferromagnetic properties were reported by *K. Kaviyaras et al.* for Gd-doped $CeO_2$ nanocrystal prepared using hydrothermal method, attributed to the formation of the oxygen vacancies due to Gd-ion incorporation and increased annealing temperature [117]. *Chen et al.* for their Sm-doped $CeO_2$ NPs (for 3, 5, 7, 9, 11 and 15% doping concentrations) prepared using co-precipitation method, have observed that the concentration of dopant ions also affect the localized environment of the $CeO_2$ NPs [67]. *E. Swatsitang et al*., have observed the stable room temperature ferromagnetism induced by oxygen vacancies in accordance with BMP model, for pure and Sm-doped $CeO_2$ (5, 10, 15

and 20%) NPs synthesized by polymer pyrolysis method [56]. However, a correlation between the dopant and oxygen vacancies also affects the conductivity and ferromagnetism in doped $CeO_2$, which is not only depend on the size of the dopant but also on the doping concentration [116, 118]. Recently, the electronic structure of the pure $CeO_2$ and Fe-doped $CeO_2$ polycrystalline samples have been investigated by XPS and it is revealed that the $Ce^{4+}$ states are reduced to $Ce^{3+}$ states for Fe-doped $CeO_2$ samples, which may be explained by the formation of the oxygen vacancies in the samples [119]. Further, *Lee et al*., [120] reported that the trapping effect of the oxygen vacancies between dopant and cerium ions can be varied with small and large size RE-dopant ions in $CeO_2$, which finally affects the local structure in the lattice by generating strain due to the dopant ion radius. Although, there are few experimental reports that have studied the oxygen vacancy defect variation with small doping concentrations in Sm-doped $CeO_2$ NPs. The origin of ferromagnetism in these compounds is still controversial; there are doubts whether the ferromagnetism is intrinsic or extrinsic in these compounds. Generally, it is acceptable that the Sm-ions are substituting the Ce-site in the lattice and hence the ferromagnetism in these compounds is intrinsic in nature. Hence, the main motive behind this study is to explore the formation of defects and oxygen vacancies, which arises due to the small doping concentration of $Sm^{3+}$ ions in $CeO_2$ NPs.

It is requisite that the microstructure of the $Sm^{3+}$ ions doped $CeO_2$ NPs have to be studied using some appropriate method and hence in the present work, pure and Sm-doped $CeO_2$ NPs with different doping concentration (2, 4, 6, 8 and 10%) are synthesized by co-precipitation method. In order to identify the information on direct defects and oxygen vacancies in these samples, SERS is used as the other techniques like XRD and electron microscopies are not suitable for probing the atomic scale defect structures in the lattice. The effect of Sm-doping on the structural, surface morphological and optical properties of Sm-doped $CeO_2$ NPs with different doping concentration (2, 4, 6, 8 and 10%) has been investigated using various techniques such as XRD, TEM, EDX, UV-Vis-NIR spectroscopy and SERS. The electrical property of all the samples has been analyzed by measuring current with increase in voltage at room temperature on Keithley 2400 source-meter.

Specifically, we have also discussed the relationship between doping concentration and oxygen vacancies defects with a view to explain the microstructure of Sm-doped $CeO_2$ NPs.

## 3.2. Experimental Details

### 3.2.1. Materials

Cerium (III) Choride heptahydrate ($CeCl_3.7H_2O$) (Alpha Aesar 99.9%), Samarium (III) Choride hexahydrate ($SmCl_3.6H_2O$) (Alpha Aesar 99.9%) and Ammonium hydroxide ($NH_4OH$) 30% solution.

### 3.2.2. Material preparation

Nanocrystalline pure $CeO_2$ and $Ce_{1-x}Sm_xO_2$ ($x$ = 0.02, 0.04, 0.06, 0.08, and 0.10) samples were synthesized by using co-precipitation method. The appropriate stoichiometric amount of $CeCl_3.7H_2O$ and $SmCl_3.6H_2O$ were used for synthesizing $Ce_{1-x}Sm_xO_2$ NPs. Initially, $CeCl_3.7H_2O$ and $SmCl_3.6H_2O$ precursor solution was prepared in distilled water with magnetic stirring at the rate of 600 rpm. Then 30% $NH_4OH$ solution was added drop wise to this solution until the pH level was reached about 10. This solution was stirred for about 4 hours with the stirring rate of 1600 rpm at room temperature. After that, the synthesized pale-yellow precipitate was collected and washed with distilled water. The samples were dried at room temperature and annealed in the furnace for about 500 $^oC$ for 8 hours. A set of samples, i.e. pure $CeO_2$, and $Ce_{1-x}Sm_xO_2$ ($x$ = 0.02, 0.04, 0.06, 0.08 and 0.10) NPs were formed. The chemical reaction occurring during the experimental process can be written as follows:

$$\boldsymbol{CeCl_3 \cdot 7H_2O_{(aq)} + 3NH_4OH_{(aq)} \rightarrow Ce(OH)_{3(s)} + 3NH_4Cl_{(aq)} + 7H_2O_{(aq)}} \quad (3.1)$$

$$\boldsymbol{2Ce(OH)_{3(s)} \xrightarrow{500℃} 2CeO_{2(s)} + 2H_2O_{(g)} + H_{2(g)} \uparrow} \quad (3.2)$$

Assumed chemical reactions for the growth on various ratios ($x$ = 0.02, 0.04, 0.06, 0.08 and 0.10) of dopant Sm-ion in $CeO_2$ NPs can be occurred as follows:

$$\boldsymbol{(1-x)[CeCl_3 \cdot 7H_2O] + x[SmCl_3 \cdot 6H_2O] + 3NH_4OH \rightarrow Ce_{1-x}Sm_xO_2 + \text{Molecular gases} \uparrow} \quad (3.3)$$

### 3.2.3. Nanomaterials Characterization

The structural properties of the samples were studied using XRD method on Brucker D8 Advance diffractometer utilizing Cu $K_\alpha$ radiation ($\lambda$= 1.5406 Å). The diffraction patterns were recorded at room temperature in the $2\theta$ range from $10^o$ to $90^o$ with $0.05^o$ $min^{-1}$ scanning speed and the counting time of 5 sec per step. The surface morphology, particle size and crystalline nature of the samples were studied using TEM with Technai G2 20 S-TWIN (FEI Netherlands) instrument operated at an accelerating voltage of 200 kV. Samples for the TEM investigation were prepared by dispersing the nanopowder in ethanol using an ultrasonicator to produce a dilute suspension for correct particle size measurements. A standard carbon film mesh supported on Cu grid was immersed in the suspension to produce the sample for TEM measurements. The particle size distribution was measured for a total 150 particles using the Image-j software. EDX spectra were recorded from TESCAN MIRA 3 FESEM equipped with EDX (OXFORD detector with AZtec software) operating at an accelerating voltage of 15 kV. EDX analysis was used to confirm the presence of the elements. The optical and defect characterizations were carried out by SERS on a Thermo Scientific DXRxi Raman Imaging Microscope with Charge Injection device (CID) detector having a green laser with 532 nm excitation light source with its power was kept at 10mW. The UV-Vis-NIR spectroscopy was performed for the optical absorbance spectra of the samples in the range of 200-1000 nm with $BaSO_4$ as an internal standard, were recorded employing a Shimadzu UV-3600 Plus spectrophotometer with an integrating sphere. Finally, the electrical property was performed for current-voltage (I-V) characteristic of all samples at room temperature on Keithley 2400 source-meter instrument (make of Tektronix Company). For measuring the dc electrical conductivity, the electrical contacts of copper wires were made by applying conducting sliver paste on both sides of the pallet. The conducting properties of all samples were measured by dc two-point probe method with the increasing voltage from 0 V to ±1 V and measured current at room temperature.

### 3.2.4. Theoretical background

Generally, four-point probe arrangement is very convenient and commonly used for measuring resistivity of a semiconductor. However, this arrangement may give inaccurate results for several reasons, such as charge carrier injection by the current probes and surface leakage. Therefore, two-point probe arrangement has

been used in order to overcome the drawbacks of the four-point probe arrangement for a bar-shaped sample [121, 122].

Figure 3.1 shows the schematic diagram of the two-point probe arrangement on a rectangular bar-shaped sample, and the sample resistivity is given as:

$$\boldsymbol{\rho = \left(\frac{V}{I}\right)\left(\frac{ah}{S}\right)} \qquad (\mathbf{3.4})$$

Where, $\rho$ is the sample resistivity, $I$ is the uniform current being passed through the sample, $V$ is the applied potential difference measured between the two voltage probes, '$a$' is the sample width and $h$ is the sample height and $S$ is the separation between the two-probes.

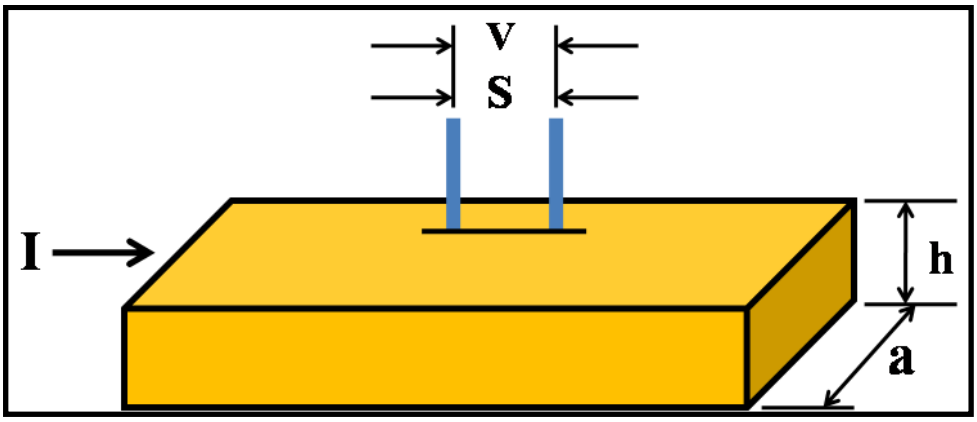


**Figure 3.1: Two-point probe arrangement on rectangular bar-shaped sample**

## 3.3. Results and discussion

### 3.3.1. Structural Properties

#### 3.3.1.1. XRD Analysis

Figure 3.2 displays the indexed powder XRD patterns for pure $CeO_2$ and $Ce_{1-x}Sm_xO_2$ ($x$ = 0.02, 0.04, 0.06, 0.08, and 0.10) NPs. All major Bragg peaks (111), (200), (220), (311), (222), (400), (331), (420) and (422) corresponding to the crystallographic plane having face-centered cubic fluorite (*fcc*) structure with the space group *Fm-3m* in which Ce is located at *4a* position and surrounded by eight oxygen located at *8b* position [123] are marked on the XRD pattern. Further, in order to rule out the presence of any peak corresponding to secondary impurity phase such as $Sm_2O_3$ the XRD patterns are plotted on Log scale (see Figure 3.3). Figure 3.3 depicts only the allowed Bragg reflections and no impurity peak can be detected in the XRD patterns of all the samples. These observations clearly indicate

well incorporation of $Sm^{3+}$ ions on $CeO_2$ lattice site and indeed confirming the single phase formation of doped $Ce_{1-x}Sm_xO_2$ samples.

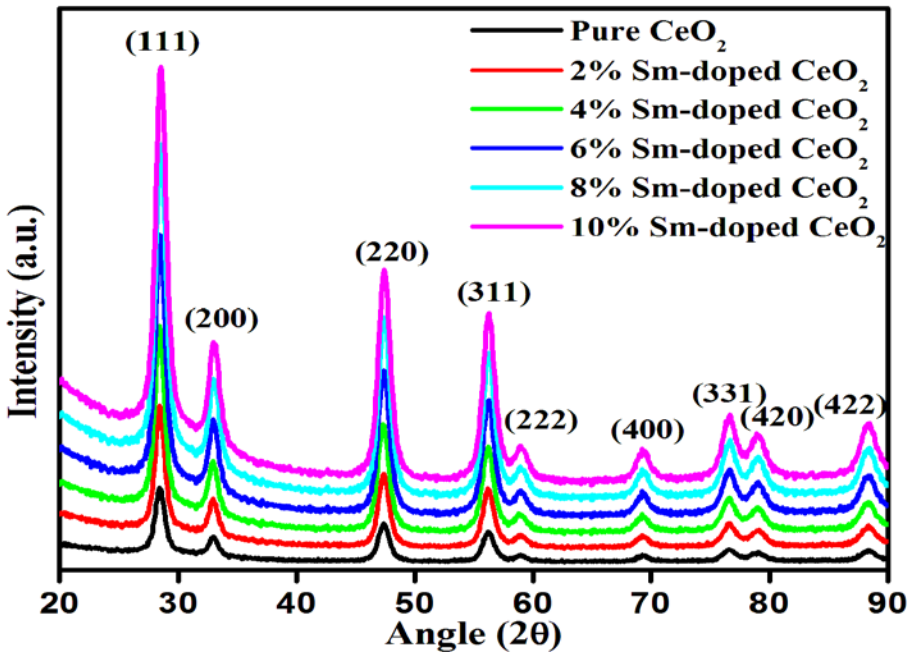


**Figure 3.2: XRD patterns of pure $CeO_2$ and $Ce_{1-x}Sm_xO_2$ (for $x$ = 0.02, 0.04, 0.06, 0.08, and 0.10) NPs**

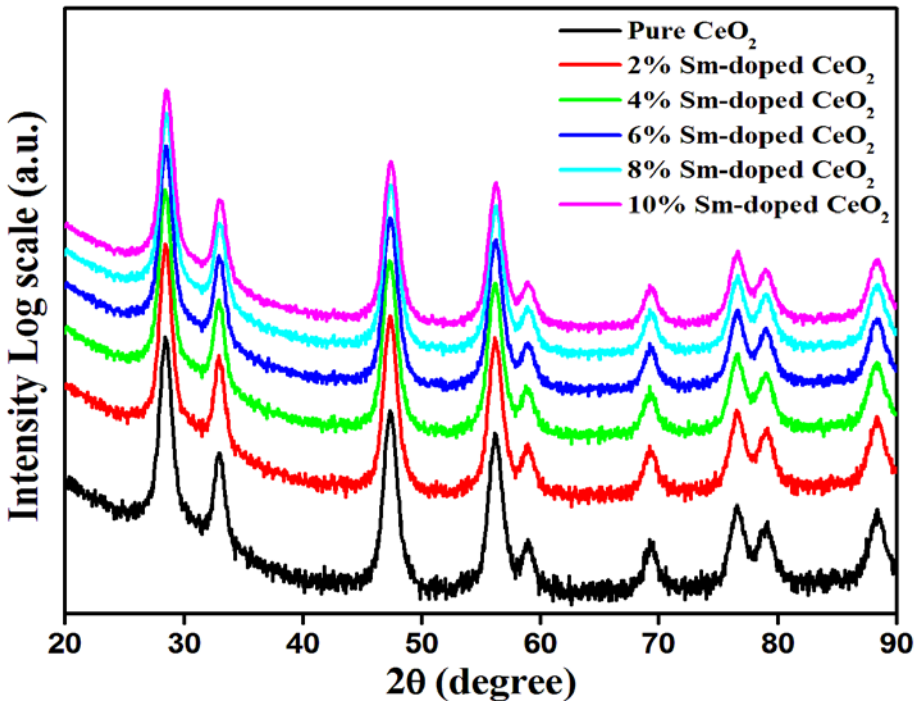


**Figure 3.3: XRD patterns of pure $CeO_2$ and $Ce_{1-x}Sm_xO_2$ (for $x$ = 0.02, 0.04, 0.06, 0.08, and 0.10) NPs plotted on Log scale**

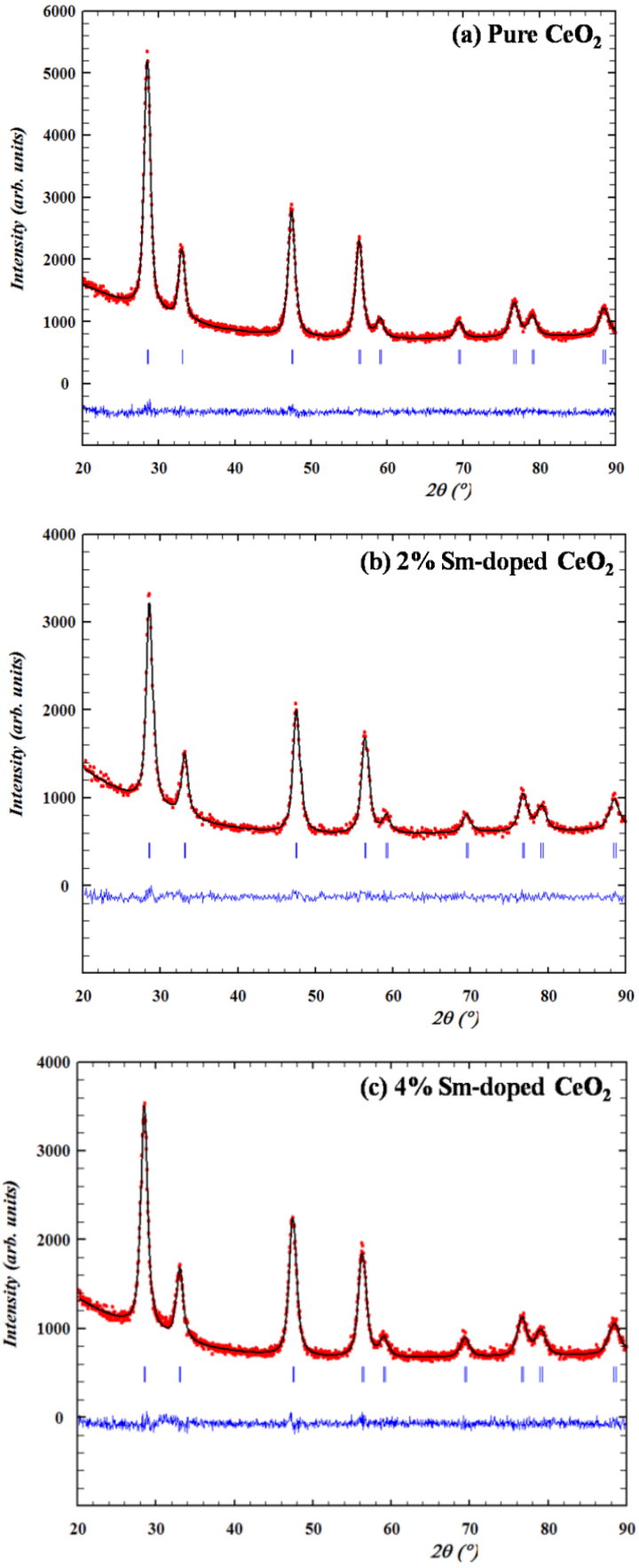
(a) Pure CeO2
(b) 2% Sm-doped CeO2
(c) 4% Sm-doped CeO2
Intensity (arb. units)
2θ (°)

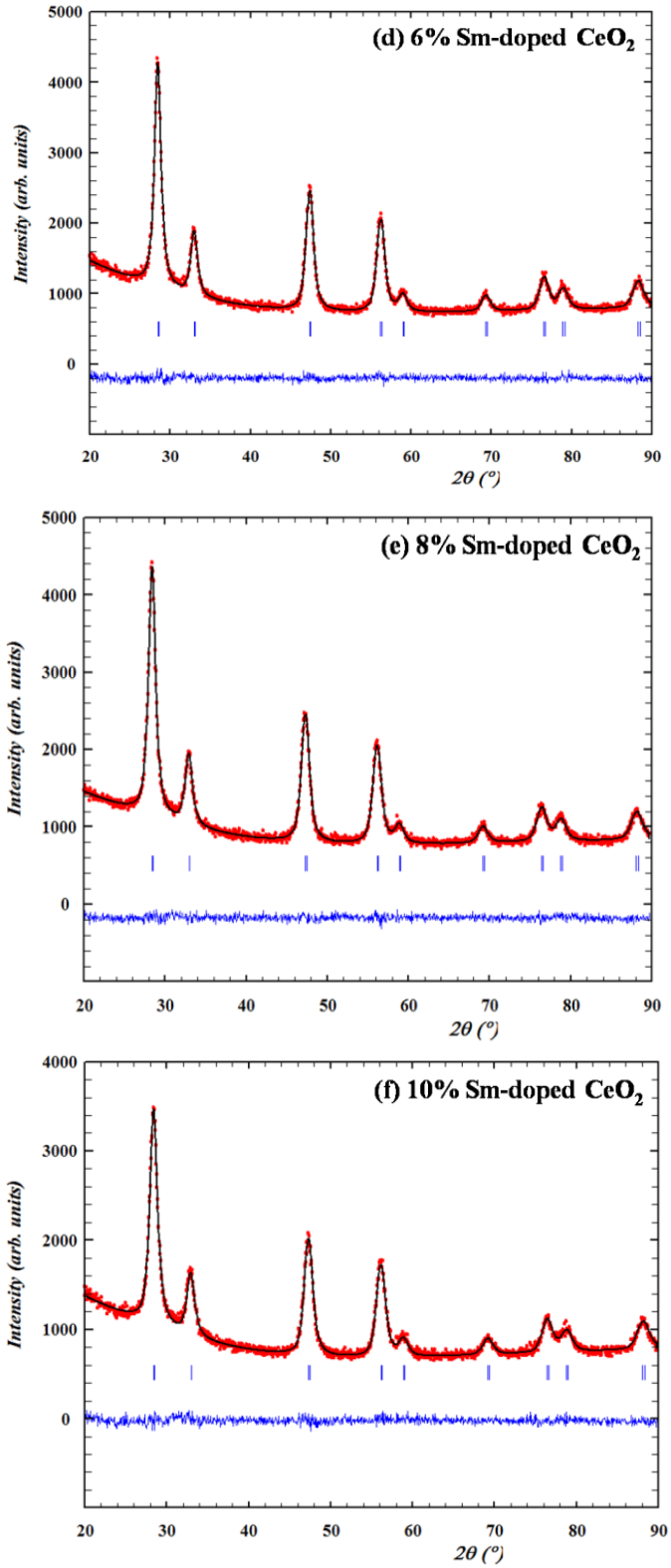


**Figure 3.4 (a-f): Rietveld refined and fitted XRD patterns of pure $CeO_2$ and $Ce_{1-x}Sm_xO_2$ ($x$ = 0.02, 0.04, 0.06, 0.08 and 0.10) samples at 300 K. Observed (calculated) profiles are shown by dotted (solid) lines. The short vertical marks represent Bragg reflections. The lower curve is the difference plot.**

Figure 3.4 (a-f) shows the Rietveld refined and fitted XRD spectra for all the pure $CeO_2$ and $Ce_{1-x}Sm_xO_2$ samples, which has been carried out on a series of $x$ = 0.02, 0.04, 0.06, 0.08 and 0.10 doping concentration at room temperature and the results of the Rietveld refinement are tabulated in Table 3.1. It indicates that all peaks are in good agreement with the standard data for $CeO_2$ (with peak intensity according to JCPDS Card No. 43-1002) [124].

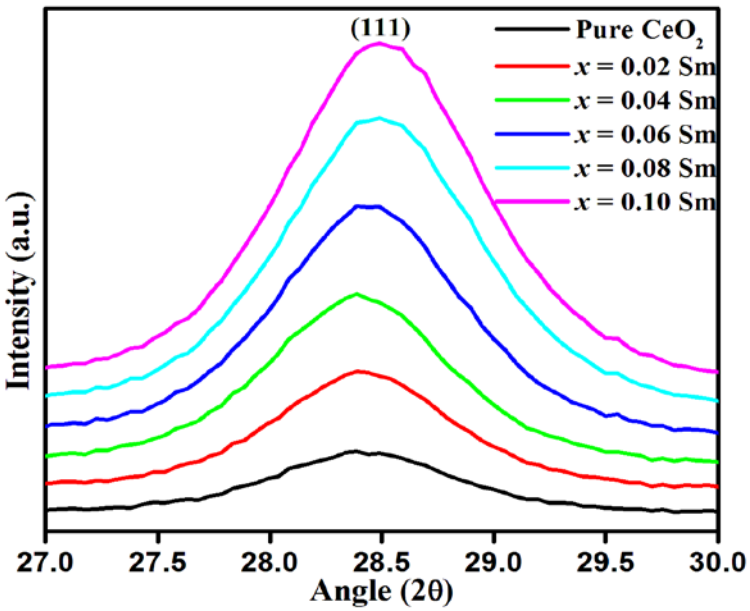


**Figure 3.5: Limited range XRD diffraction pattern plotted in the vicinity of the (111) Bragg peak for pure $CeO_2$ and $Ce_{1-x}Sm_xO_2$ ($x$ = 0.02, 0.04, 0.06, 0.08 and 0.10) NPs**

As shown in Figure 3.5, the intensity of most intense Bragg diffraction peak (111) is not changed much with the incorporation of $Sm^{3+}$ ions for $x$ = 0.02 and 0.04 fluencies, but with further increase in concentration of Sm (for $x$ = 0.06, 0.08 and 0.10) the peak intensity is changed drastically. It is reported that the increasing intensity in the diffraction peak signifies an improvement in the crystalline nature while decreasing intensity signifies low crystalline nature of the $CeO_2$ NPs [125]. Simultaneously, Figure 3.5 indicates that incorporation of $Sm^{3+}$ ions for $x$ = 0.02 and 0.04 the diffraction peak (111) is shifted towards lower angle side and for $x$ = 0.06, 0.08 and 0.10 concentration the peak is shifted towards higher angle side. It is also reported that the shifting of (111) peak to the lower and higher angle side is attributed to the lattice expansion and contraction, respectively, with the doping of $Sm^{3+}$ ions in $CeO_2$ NPs [126].

**Table 3.1: Obtained values of lattice parameter (*a*), unit cell volume (V) and other fine details from Rietveld refinement analysis of the XRD data.**

| **Samples** $Ce_{1-x}Sm_xO_2$ | ***x* = 0.00** | ***x* = 0.02** | ***x* = 0.04** | ***x* = 0.06** | ***x* = 0.08** | ***x* = 0.10** |
|---|---|---|---|---|---|---|
| **a (Å)** | 5.4146(2) | 5.4105(25) | 5.4167(18) | 5.4195(18) | 5.4209(30) | 5.4294(22) |
| **V (Å$^3$)** | 158.74(8) | 158.38(13) | 158.93(9) | 159.41(9) | 160.01(9) | 160.05(12) |
| **$R_p$** | 2.50 | 2.83 | 2.71 | 2.56 | 2.44 | 2.70 |
| **$R_{wp}$** | 3.17 | 3.57 | 3.47 | 3.26 | 3.10 | 3.39 |
| **$R_{exp}$** | 3.01 | 3.39 | 3.25 | 3.08 | 3.01 | 3.19 |
| $\chi^2$ | 1.11 | 1.11 | 1.14 | 1.12 | 1.06 | 1.13 |
| **$R_{Bragg}$** | 1.28 | 1.30 | 1.76 | 1.96 | 1.42 | 2.84 |

As clearly seen in Figure 3.2, the XRD diffraction peaks become broader after doping and broadness of peaks are changed with the fluency of $Sm^{3+}$ ions in $CeO_2$ NPs, indicating that crystal size and crystalline nature of the samples are affected due to change in the concentration of dopant ions in $CeO_2$ NPs. The average particle size (D) of pure $CeO_2$ and $Ce_{1-x}Sm_xO_2$ samples is calculated by the Debye Scherrer's formula [87, 88]:

$$\boldsymbol{D = \frac{k\,\lambda}{\beta\,cos\theta}} \qquad (\mathbf{3.5})$$

Where, $k$ is the particle shape factor (0.9), $\lambda$ is the X-ray wavelength, $\beta$ is the full width at half maxima (FWHM) of XRD (111) diffraction peak, which was calculated by $\beta = ({\beta_m}^2 - {\beta_i}^2)^{1/2}$, here $\beta_m$ and $\beta_i$ are the measured and instrumental broadening (in radian), respectively and $\theta$ is the Bragg's diffraction angle of the peak in degree. Table 3.1 incorporates the calculated lattice parameter of pure $CeO_2$ and $Ce_{1-x}Sm_xO_2$ samples. The increase in the lattice parameter corresponding to pure $CeO_2$ indicates that the volume of the $CeO_2$ cell has been increased with Sm-doping, which is related with the effective ionic radius of the dopant ion [127], as the ionic radius of $Sm^{3+}$ (0.1079 nm) is larger than the ionic radius of $Ce^{4+}$ (0.097 nm) ions [128]. This incorporation of $Sm^{3+}$ ions in $CeO_2$ sample possibly will create the larger radius of $Ce^{3+}$ ions (0.114 nm) rather than smaller radii $Ce^{4+}$ ions. Furthermore, in order to maintain charge equilibrium, $Sm^{3+}$ and $Ce^{3+}$ ions are collectively creating oxygen vacancies in the $CeO_2$ lattice, which is also reported for further lattice expansion [126]. This variation in lattice parameter clearly indicates the effect of $Sm^{3+}$ ions doping concentration in $CeO_2$ NPs. It has been reported that the lattice parameter and particle size are related to each other as particle size increases this causes a decrease in the lattice parameter [129]. This can also be explained by the increased rigidity, which may be caused by increasing lattice strain results from the substitution of $Ce^{4+}$ ions by $Sm^{3+}$ ions. Now, lattice strain (ε) is calculated using formula [130, 131]:

$$\boldsymbol{\varepsilon = \frac{\beta\ \cos\theta}{4}} \qquad (\mathbf{3.6})$$

As tabulated in Table 3.2, all positive values of strain are related to the tensile strain in $Ce_{1-x}Sm_xO_2$ samples. The results revealed that due to incorporation of $Sm^{3+}$ ions, strain is decreased for initial doping concentration $x$ = 0.02, which increases for $x$ = 0.04 concentration, decreases for $x$ = 0.06 and increase can be seen for further doping concentrations. This indicates that due to incorporation of larger radii $Sm^{3+}$ (0.1079 nm) ion, lattice is relaxed for $x$ = 0.02 and 0.06 concentrations, while strain expands the lattice for other doping concentrations (as shown in Table 3.2). It is also reported in **s**ome theoretical investigation that the tensile strain promotes the formation of oxygen vacancies more than the compressive strain [132]. Hence, the increment in tensile strain in our samples can be directly related to the endorsement of oxygen vacancies, which is related to the bonding length and the strength between the surface oxygen and Ce atom [133]. Since, for tensile strain, the bandwidth of the O 2p orbital decreases and overlapping between O 2p and Ce 5d as well as Ce 4f orbital also decreases, which leads a weaker Ce-O bond and responsible for the formation of oxygen vacancies [132].

Furthermore, the dislocation density is another crystallographic defect, or irregularity, which is also found within a crystal structure. The dislocation density (δ) is defined as the total length of dislocation lines per unit volume, which is calculated using formula [134]:

$$\boldsymbol{\delta = \frac{1}{D^2}} \qquad (\mathbf{3.7})$$

Here, D is average particle size measured from TEM images.

**Table 3.2: Calculated values of lattice spacing (*d*) for (111) plane, average crystalline size (D) measured from TEM, XRD and Raman line broadening, dislocation density (δ), lattice strain (ε), absorbance wavelength (λ), optical band gap energy ($E_g$) and refractive index (*n*) are summarized in the table.**

| Sample | *d* (nm) | D (nm) | | | δ ($nm^{-2}$) | ε×$10^{-2}$ | λ (nm) | $E_g$ (eV) | *n* |
|---|---|---|---|---|---|---|---|---|---|
| | | TEM | XRD | Raman spectra | | | | | |
| **Pure $CeO_2$** | 0.317 | 7.24 | 9.16 | 8.07 | 0.019 | 3.88 | 313 | 2.87 | 2.43 |
| $Ce_{0.98}Sm_{0.02}O_2$ | 0.308 | 5.94 | 9.49 | 9.28 | 0.028 | 3.75 | 329 | 2.69 | 2.48 |
| $Ce_{0.96}Sm_{0.04}O_2$ | 0.317 | 6.45 | 9.12 | 8.04 | 0.024 | 3.83 | 320 | 2.86 | 2.43 |
| $Ce_{0.94}Sm_{0.06}O_2$ | 0.316 | 8.13 | 9.62 | 7.40 | 0.015 | 3.78 | 324 | 2.83 | 2.44 |
| $Ce_{0.92}Sm_{0.08}O_2$ | 0.317 | 6.62 | 7.72 | 6.34 | 0.022 | 4.68 | 323 | 2.87 | 2.43 |
| $Ce_{0.90}Sm_{0.10}O_2$ | 0.322 | 6.76 | 6.91 | 5.03 | 0.021 | 6.98 | 316 | 2.64 | 2.50 |

The dislocation density is found to increase after incorporation of $Sm^{3+}$ ions for all the doping concentrations of Sm in $CeO_2$ NPs (except for $x = 0.06$), δ found to be decreased (as shown in Table 3.2). This increase in the dislocation density corresponds to the promotion of disorder for Sm-doped $CeO_2$ samples [125].

### 3.3.1.2. Surface Morphology

The average crystallite particle size of all the samples was further confirmed by TEM, which is used to get the information about the shape, size and the presence of any secondary phase in doped $Ce_{1-x}Sm_xO_2$ NPs samples. The particle size and morphology of pure $CeO_2$ and $Ce_{1-x}Sm_xO_2$ samples analyzed by TEM are shown in Figure 3.6. It can be clearly seen from the TEM images that the particles are crystallized nanoparticles and agglomerated with spherical geometry. The particle size distribution (histogram is shown in the inset of Figure 3.6) shows that the distribution is quite narrow in the size range of 5-8 nm for all pure $CeO_2$ and $Ce_{1-x}Sm_xO_2$ NPs samples, which are in good agreement with the results obtained from XRD data (listed in Table 3.2).

This agglomeration of particles with smaller particle size (< 8 nm) indicates that the obtained particles are nanocrystallites. The particle size measured directly from TEM images promotes crystal growth with the doping concentration of $Sm^{3+}$ ions. However, the morphology of all the samples is not changing but the agglomeration of particles is increased with increasing doping concentration of $Sm^{3+}$ ions (as shown in Figure 3.6). Since, agglomeration of nanoparticles is more stable configuration according to the energy point of view, which allows nanoparticles for crystallite growth [128]. Furthermore, HRTEM and SAED are also used to get the information about the nanocrystallinity and the impurity phase present in the pure $CeO_2$ and $Ce_{1-x}Sm_xO_2$ samples.

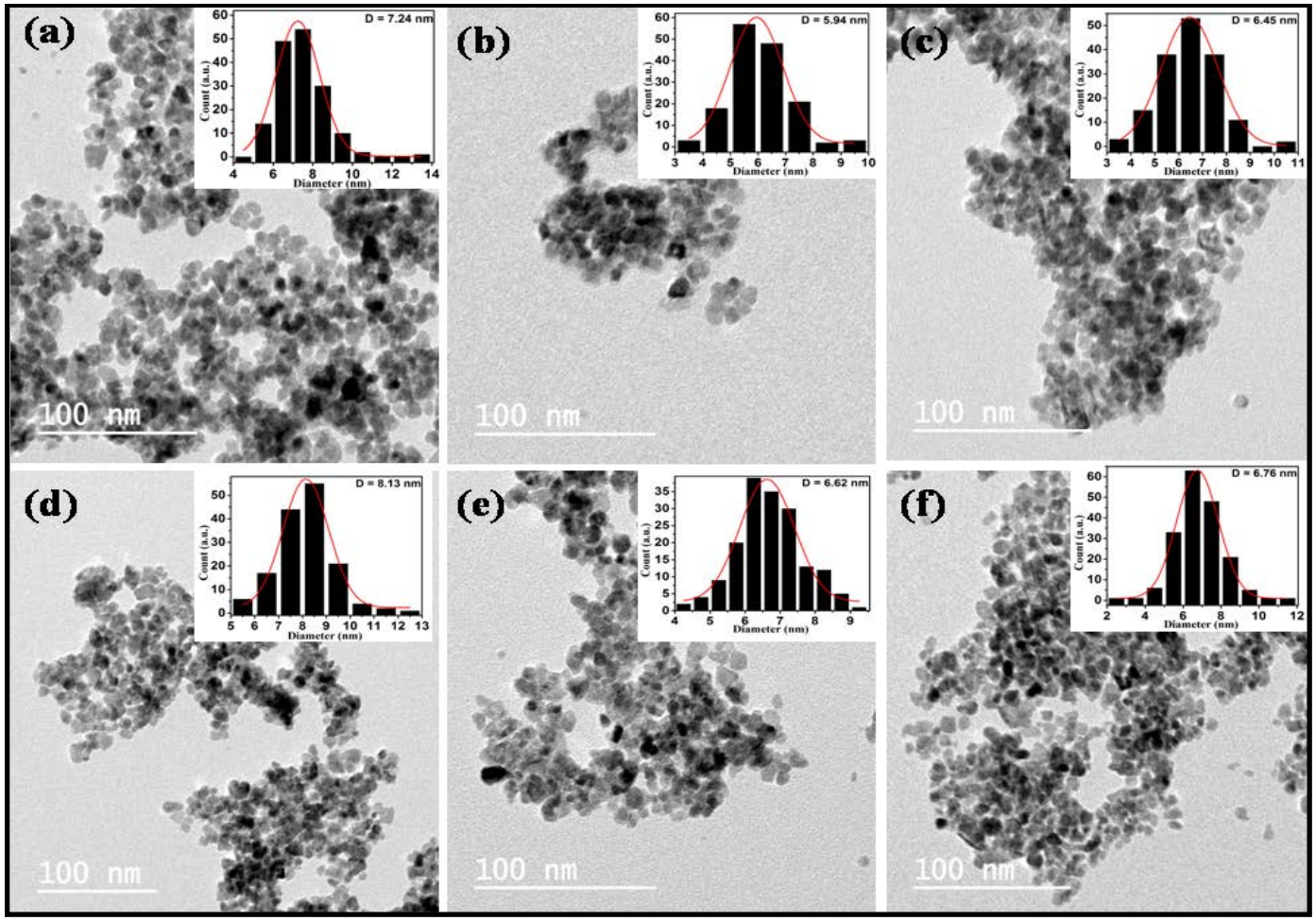


**Figure 3.6: TEM image for (a) Pure $CeO_2$, (b) 2% Sm-doped $CeO_2$, (c) 4% Sm-doped $CeO_2$, (d) 6% Sm-doped $CeO_2$, (e) 8% Sm-doped $CeO_2$, (f) 10% Sm-doped $CeO_2$ and inset histogram show the particle-size distribution of the corresponding samples.**

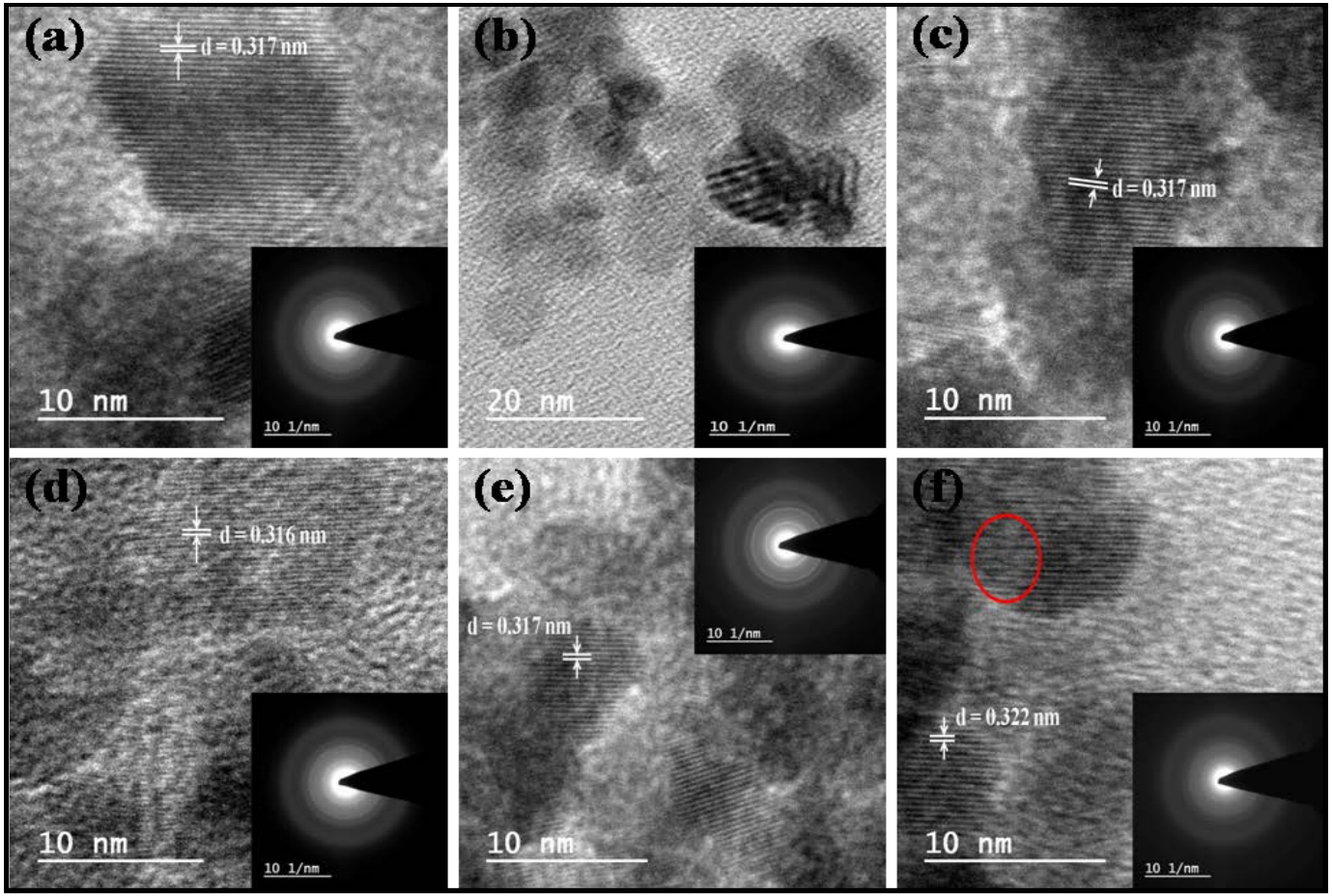


**Figure 3.7: HRTEM images with *d*-spacing corresponding to (111) plane for (a) Pure $CeO_2$ (b) 2% Sm-doped $CeO_2$ (c) 4% Sm-doped $CeO_2$ (d) 6% Sm-doped $CeO_2$ (e) 8% Sm-doped $CeO_2$ (f) 10% Sm-doped $CeO_2$ and inset shows the SAED pattern of corresponding samples**

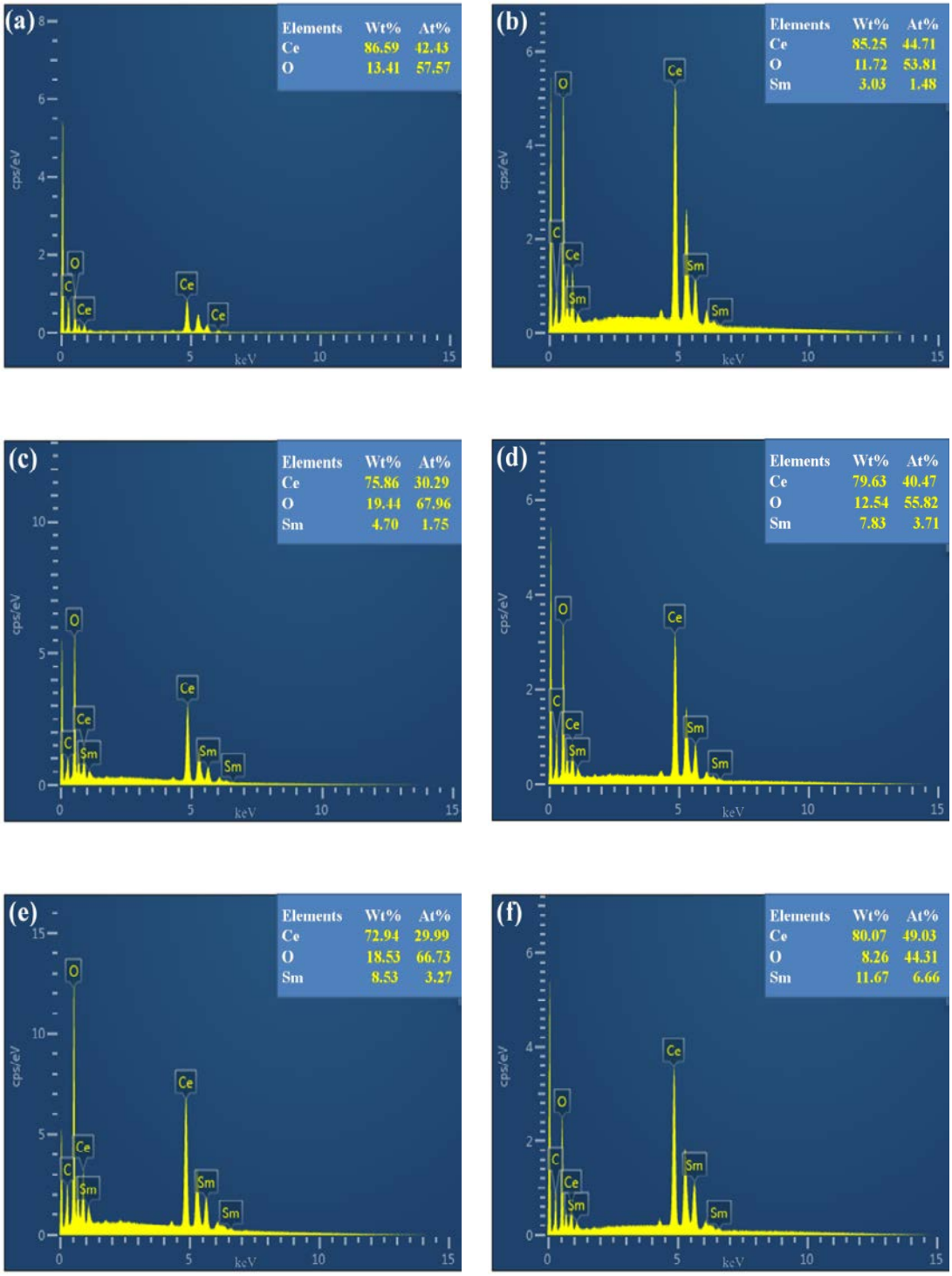


**Figure 3.8: EDX spectrum for (a) pure $CeO_2$, (b) 2% Sm-doped $CeO_2$, (c) 4% Sm-doped $CeO_2$, (d) 6% Sm-doped $CeO_2$, (e) 8% Sm-doped $CeO_2$, and (f) 10% Sm-doped $CeO_2$ NPs**

HRTEM images (as shown in Figure 3.7) indicate that the lattice fringes are well developed and randomly oriented with respect to each other. Most of the lattice fringes of pure $CeO_2$ and $Ce_{1-x}Sm_xO_2$ samples are about at a distance of 0.31 nm (values are tabulated in Table 3.2) that corresponding to the (111) lattice plane of the fluorite like cubic structure. However, interplanar distance (*d*) has been changed with $Sm^{3+}$ ions doping in $CeO_2$ NPs. As shown in Table 3.2, no significant change has been observed in the interplanar distance (*d*) for pure $CeO_2$, 4%, 6% and 8% Sm-doped $CeO_2$ samples but for 2% and 10% Sm-doped $CeO_2$ samples, the interplanar distance $d$ = 0.308 and 0.322 nm for (111) plane, respectively, has been changed. The increased value of interplanar distance (*d*) indicates the crystal growth and the low crystallinity. Some defects, such as dislocations (shown in Figure 3.7(f) marked with a red ring) are also observed in the HRTEM micrograph of 10% Sm-doped $CeO_2$ NPs. Moreover, SAED patterns are also taken (shown in the insets of Figure 3.7) for all the pure $CeO_2$ and $Ce_{1-x}Sm_xO_2$ NPs samples. The SAED pattern exhibits four broad rings, which could be attributed to (111), (200), (220) and (311) planes. These rings indicate that the particles are crystallized and diffraction rings are very well agreeing with the XRD pattern of all the samples. The broadening of diffraction rings indicates the sizes of the particles are small and crystalline nature of all the samples getting low with increasing doping concentration of $Sm^{3+}$ ions.

Figure 3.8(a-f) gives the EDX spectra for the pure $CeO_2$ and $Ce_{1-x}Sm_xO_2$ ($x$ = 0.02, 0.04, 0.06, 0.08, and 0.10) NPs. It is observed that the cerium (Ce), samarium (Sm) and oxygen (O) elements are present in the spectra nearly in the stoichiometric ratio. No other elements were found in the spectra reflecting the high purity of the synthesized samples. Note that the Carbon signals were from the carbon conducting adhesive double side tape on which the powder sample were loaded for measurements. The EDX data on the oxygen is not reliable to have an estimation of oxygen in these samples; it also reflects the surface oxygen contamination.

### 3.3.2. Optical Properties

#### 3.3.2.1. UV-Vis-NIR analysis

Figure 3.9(a) shows the UV-visible absorption optical spectra for all the pure $CeO_2$ and $Ce_{1-x}Sm_xO_2$ ($x$ = 0.02, 0.04, 0.06, 0.08, and 0.10) NPs samples. It can be seen that these samples exhibit strong absorption below 400 nm with an absorption

peak in UV-range corresponding to the different doping concentration of $Sm^{3+}$ ions in $CeO_2$ NPs, which are tabulated in the Table 3.2. These peaks are originated due to charge transfer from $O^{2-}$ (2p) valance band to $Ce^{4+}$ (4f) conduction band, which is a direct recombination of the electrons in $Ce^{4+}$ (4f) conduction band with the holes in the $O^{2-}$ (2p) valance band. As shown in the Figure 3.9(a), due to formation of the smaller size nanocrystals with the incorporation of $Sm^{3+}$ ions in $CeO_2$ NPs lattice, the wavelength is shifted towards longer wavelength (red shift) side i.e. 329 nm (for $x$ = 0.02). Whereas, aggregation of NPs is expected to increase with increasing doping concentration of $Sm^{3+}$ ions (for $x$ = 0.04) in $CeO_2$ NPs, due to this reason wavelength is shifted towards lower wavelength side (i.e. blue shift). Again, it increases towards the higher wavelength side for $x$ = 0.06 and 0.08 doping concentrations and for $x$ = 0.10, the wavelength is again decreased which shows a decrement in the aggregation of NPs.

From all the absorption data, the optical band gap energies ($E_g$) of pure $CeO_2$ and $Ce_{1-x}Sm_xO_2$ samples were calculated using Tauc's equation:

$$\boldsymbol{\alpha h\nu = A\,(h\nu - E_g)^n} \qquad (\mathbf{3.8})$$

Where, $\alpha$ is the absorption coefficient, $h\nu$ is the photon energy, $A$ is a constant related to the material, $E_g$ is the optical band gap energy and $n$ is a constant which depends on the probability of direct or indirect transition of electron from the valance band to conduction band. Figure 3.9(b) shows the graphical variation of $(\alpha h\nu)^2$ vs. Energy ($h\nu$) curve shown as per the direct transition $n$ = 1/2 in the equation 3.8 as per the reference [135]. The calculated values of band gap energies are tabulated in Table 3.2 (generally reported band gap energy of bulk $CeO_2$ is 3.2 eV [136]). Since, NPs show much different UV-absorption behaviour than their corresponding bulk structure, the direct band gap energy of pure $CeO_2$ NPs were found to be 2.87 eV, which is attributed to owe this position due to increase in the concentration of $Ce^{3+}$ level on grain boundaries, confirms the increase in concentration of $Ce^{3+}$ ions in pure $CeO_2$ lattice.

While incorporation of $Sm^{3+}$ ion in $CeO_2$ sample, further reduction in the band gap energy can be seen as ~2.69 eV for 2% Sm-doping, this may be attributed to the creation of oxygen defect or local bond distortions in the $CeO_2$ lattice. The incorporation of $Sm^{3+}$ ions may increase the concentration of $Ce^{3+}$ ions in $CeO_2$ sample due to the creation of oxygen defects or vacancies in the $CeO_2$ lattice. These

oxygen defects create impurity levels, which are present in between O 2p and Ce 4f states and capture the excited electrons to decrease the band gap energy of Sm-doped $CeO_2$ samples [137].

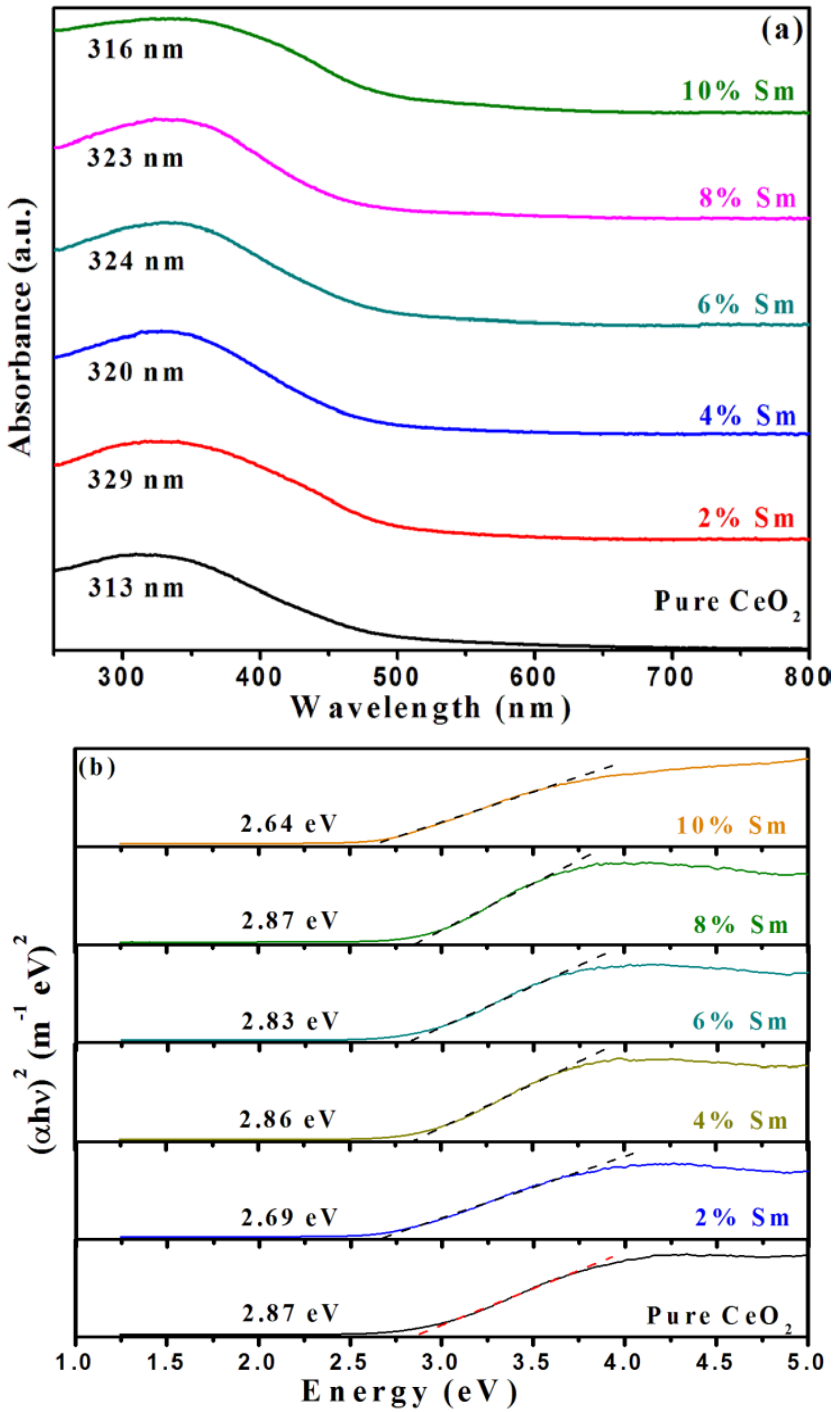


**Figure 3.9: (a) Room temperature optical absorbance spectra of pure $CeO_2$ and $Ce_{1-x}Sm_xO_2$ ($x$ = 0.02, 0.04, 0.06, 0.08 and 0.10) samples taken in the UV-visible range, (b) Tauc's plot of $(\alpha h\upsilon)^2$ versus Energy for pure $CeO_2$ and $Ce_{1-x}Sm_xO_2$ samples.**

This red shifting implies successful incorporation of $Sm^{3+}$ ions in $CeO_2$ lattice [138]. For other doping of $Sm^{3+}$ ions in $CeO_2$ NPs, band gap energy is found to increase and decrease irregularly from 4% to 10% Sm-doping concentrations (as shown in Table 3.2). These irregularities in the band gap values with increasing $Sm^{3+}$ ions may be related to the formation of new impurity energy levels in-between the band gap of the doped samples [139]. However, the UV-absorption ability of $Ce_{1-x}Sm_xO_2$ samples also depends on its particle size. The variation of the band gap energy with particle size, measured from TEM images, has been shown in the Figure 3.10. The decrease in the particle size at 4% Sm-doping may be attributed to the confinement of the carriers and because of this the band gap energy increases for this concentration in compared to 2% Sm-doped $CeO_2$ NPs. Again the band gap energy is decreased for 6% Sm concentration, which can be explained with Burstein-Moss (BM) effect [137].

$$\Delta E_g^{BM} = \frac{h^2}{2m_{vc}^*} (3\pi^2 n_e)^{2/3} \qquad (3.9)$$

Here, $m_{vc}^*$ is an effective mass of electrons, $n_e$ is the electron concentration and $h$ is the Planck's constant. BM effect suggested that, above the Mott critical density, the increased number of free electron concentration lead to fill 4f level partially, which in turn blocks the lowest states and led to increase the band gap. Here, we can say that the 6% Sm-doping is not sufficiently enough to cross the Mott critical density concentration for BM effect, which leads to a decrement in band gap energy. The increment in band gap energy at 8% and then decrement for 10% Sm-doping can be attributed to the fact that the ground and excited f-energy states are created in the mid-band gap of $CeO_2$. At 8%, these energy states of Sm take up few excited electrons coming from O 2p level, but at 10% many of excited electrons already have taken up these energy states and hence could not occupy the states, which finally lead to increase and decrease the band gap energy for 8% and 10% Sm-doping concentrations, respectively.

The refractive indices of pure $CeO_2$ and $Ce_{1-x}Sm_xO_2$ samples have also been calculated by using the following formula [140]:

$$\frac{n^2 - 1}{n^2 + 2} = 1 - \sqrt{\frac{E_g}{20}} \qquad (3.10)$$

Where, $n$ is the refractive index of the material and $E_g$ is the optical band gap energy. Table 3.2 shows the calculated value of refractive index of pure and $Ce_{1-x}Sm_xO_2$ samples as a function of the doping concentration of Sm-ions. Compare to pure $CeO_2$, value of $n$ is increased with incorporation of $Sm^{3+}$ ions for $x$ = 0.02 in $CeO_2$ NPs lattice, whereas for $x$ = 0.04, 0.06 and 0.08 concentrations a minute variation can be seen and finally at $x$ = 0.10, the value of $n$ is found to increase. These results show that the refractive index is depending on the concentration of $Sm^{3+}$ ions in $CeO_2$ NPs.

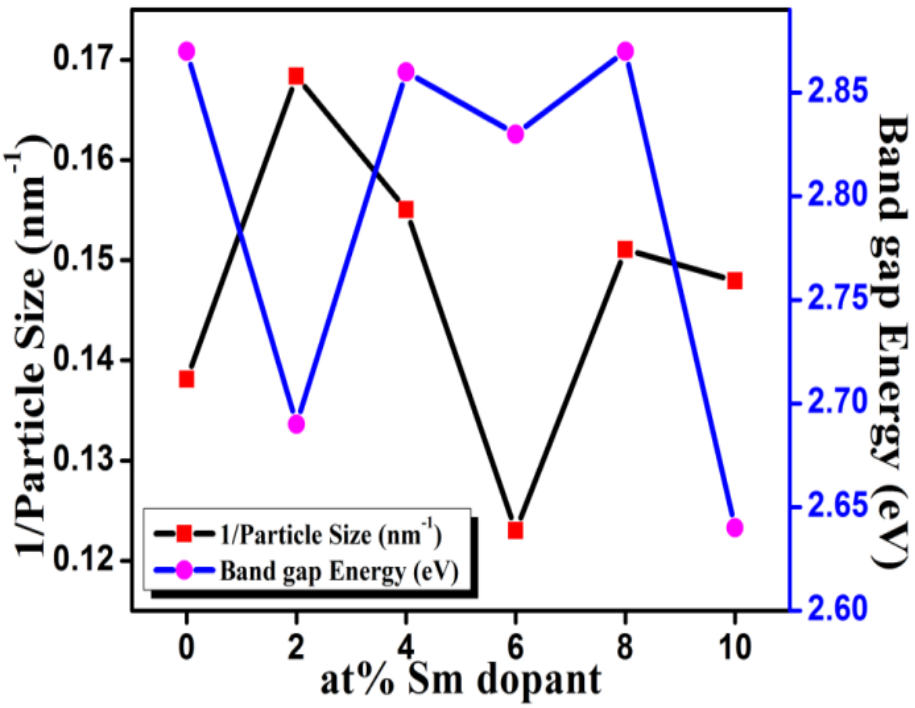


**Figure 3.10: Variation of particle size and band gap energy with Sm-doping concentration (0%, 2%, 4%, 6%, 8% and 10%) in Sm-doped $CeO_2$ samples.**

### 3.3.2.2. Raman Analysis

SERS is an important characterization technique for investigating the structural symmetry and defects in nanocrystalline samples due to doping of few percentages of dopant ions. Figure 3.11 shows the Raman spectra of pure $CeO_2$ and $Ce_{1-x}Sm_xO_2$ NPs sample with various doping concentrations ($x$ = 0.02, 0.04, 0.06, 0.08 and 0.10) of Sm-ions. As shown in Figure 3.11, pure $CeO_2$ NPs exhibit a Raman peak at 462.50 $cm^{-1}$, which can be associated to the triply degenerate $F_{2g}$ mode of the cubic fluorite crystal structure of $CeO_2$.

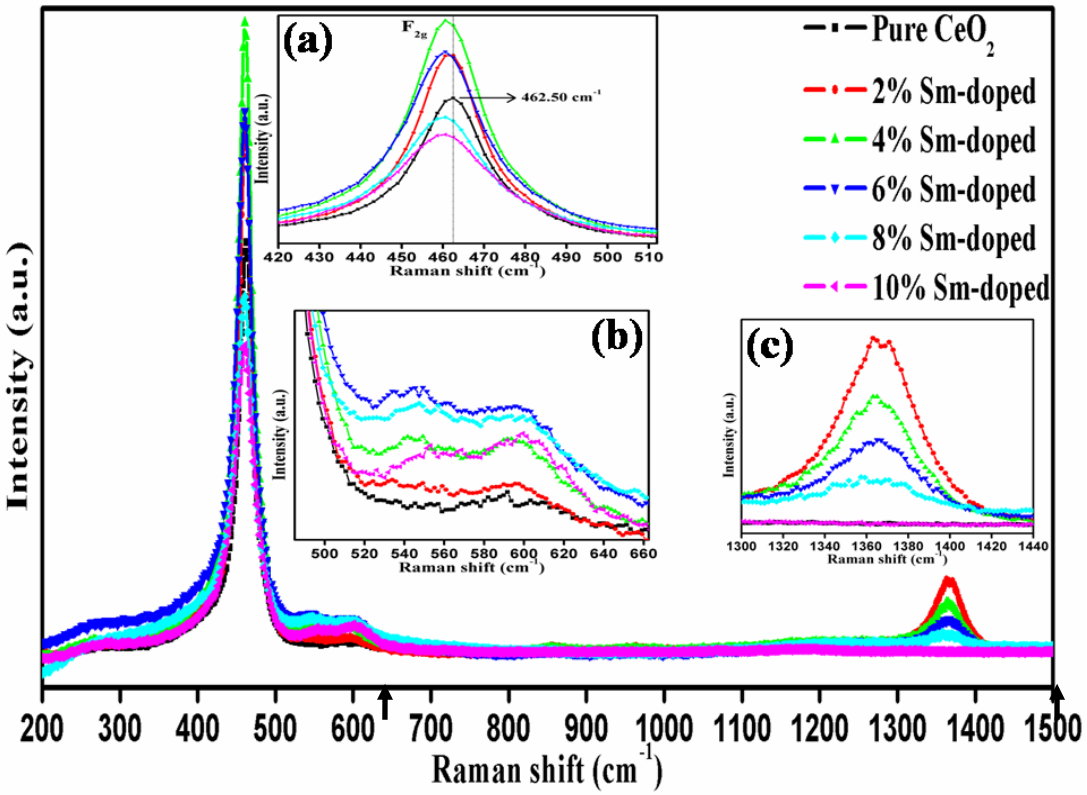


**Figure 3.11: Raman spectra of pure $CeO_2$ and Sm-doped $CeO_2$ nanoparticles. Inset (a), (b) and (c) of the figure contains the enlarged views of their corresponding Raman spectra in the 420-510 cm$^{-1}$ energy range related to $F_{2g}$ mode, 500-660 cm$^{-1}$ range related to oxygen defects and 1300-1440 cm$^{-1}$ range related to 3LO, respectively.**

This mode can be considered as the symmetrical stretching mode of eight oxygen atoms around $Ce^{4+}$ ions (O-Ce-O) and the molecule maintain its tetrahedral symmetry throughout [141]. This vibrational mode is nearly independent of the cation mass due to the movement of oxygen atoms, therefore, this peak is very sensitive to any disorder in the oxygen sub-lattice resulting from thermal, doping or grain size induced non-stoichiometric disorders [142]. Besides of $F_{2g}$ mode, some other weak intensity Raman peaks are also observed in the Raman spectra of pure $CeO_2$ samples (as shown in the inset of Figure 3.11(b-c)). The peak located at 598.5 cm$^{-1}$ (in Figure 3.11(b)) for pure $CeO_2$ is attributed to the second order Raman spectrum, with phonon mode ωTO(X) + LA(X), ascribed its presence due to $Ce^{3+}$ ions and oxygen vacancies [143, 144]. In the $CeO_2$ lattice, oxygen vacancies are reported to be formed when the average particle size decreased down to dimensions of the order of nano-size [145]. In our results, we can see that the particle size measured from TEM images (as shown in Table 3.2) are decreased down to nano-size.

**Table 3.3: The Position of Raman active modes ($cm^{-1}$) from Raman spectra and relative peak area ratio**

| Sample | Position of Raman active mode ($cm^{-1}$) and Vibrational Mode# | | | | | | $A_{O_v}/A_{F_{2g}}$ | $\frac{(A_{(O_v)_1} + A_{(O_v)_2})}{A_{F_{2g}}}$ |
|---|---|---|---|---|---|---|---|---|
| | First-order Scattering | Second-order Scattering [147,142] | | | | Third-order Scattering | | |
| | $F_{2g}$ | $A_{1g}$ $(O_v)$ | $A_{1g} + F_{2g}$ $(O_v)_1$ | $A_{1g} + E_g + F_{2g}$ $(O_v)_2$ | $2LO$ | $3LO$ | | |
| **Pure $CeO_2$** | 462.5 | 598.5 | - | - | 1175.8 | - | 0.044 | - |
| $Ce_{0.98}Sm_{0.02}O_2$ | 461.1 | - | 537.1 | 591.3 | - | 1364.6 | - | 0.062 |
| $Ce_{0.96}Sm_{0.04}O_2$ | 460.5 | - | 548.6 | 593.5 | - | 1361.5 | - | 0.091 |
| $Ce_{0.94}Sm_{0.06}O_2$ | 459.6 | - | 546.5 | 589.5 | - | 1360.2 | - | 0.185 |
| $Ce_{0.92}Sm_{0.08}O_2$ | 459.1 | - | 546.9 | 590.7 | - | 1349.9 | - | 0.271 |
| $Ce_{0.90}Sm_{0.10}O_2$ | 459.5 | - | 558.5 | 600.1 | 1175.2 | - | - | 0.123 |

**# Vibrational modes corresponding to Second-order Scattering are given as per the Ref. [147, 142].**

According to this, there can be three possible defect induction mechanisms for generation of oxygen vacancy in the pure $CeO_2$ lattice, which can be given as [146]:

$$Ce_{Ce} + 2O_O \rightarrow V^{''''} + 2V_O^{..} + CeO_2 \quad (3.11)$$

$$Ce_{Ce} \rightarrow V_{Ce}^{''''} + Ce_i^{....} \quad (3.12)$$

$$O_O \rightarrow V_O^{..} + O_i^{''} \quad (3.13)$$

In the SERS spectra, another second-order Raman peak can be seen at 1175.8 $cm^{-1}$ for pure $CeO_2$, which is associated with 2LO (second overtone band of longitudinal optical mode) Raman mode. The Raman active mode ($F_{2g}$) for $Ce_{1-x}Sm_xO_2$ samples (for $x$ = 0.02, 0.04, 0.06, 0.08 and 0.10) is also obtained in the range of ~461-459 $cm^{-1}$ (as shown in Table 3.3). We can see from the SERS spectra that with increasing doping fluency of $Sm^{3+}$ ions, $F_{2g}$ mode is shifted towards the lower wave-number side with the asymmetrical broadening of the mode. This may be attributed due to the cell expansion, inhomogeneous strain, phonon confinement and variation in phonon relaxation with the substitution of $Sm^{3+}$ ions in the $CeO_2$ lattice [148, 149]. In Figure 3.11 the characteristic band for $Sm_2O_3$ i.e. 345 $cm^{-1}$ is absent in the Raman spectra [150, 151], clearly indicates the successful incorporation of $Sm^{3+}$ ions into the $CeO_2$ lattice, which is in agreement with the XRD results. As incorporation of $Sm^{3+}$ ions in $CeO_2$ (for $x$ = 0.02), three second-order Raman modes are detected at 537.1, 591.3 and 1364.6 $cm^{-1}$, where first two are assigned to the presence of oxygen vacancies generated into $CeO_2$ lattice due to incorporation of $Sm^{3+}$ ions and third mode is 3LO (third overtone band of longitudinal optic mode) mode.

Moreover, with increasing fluencies of $Sm^{3+}$ ions (for $x$ = 0.04, 0.06, 0.08 and 0.10 doping concentrations) into $CeO_2$ lattice, the second-order Raman features near the value of ~548-558 $cm^{-1}$, associated with extrinsic oxygen vacancies induced by replacing $Ce^{4+}$ ions by $Sm^{3+}$ ions in order to maintain charge neutrality into $CeO_2$

NPs [152, 153]. The possible disorder mechanism for extrinsic oxygen vacancies in Sm-doped $CeO_2$ NPs can be given as:

$$\boldsymbol{Sm_2O_3 + 2Ce_{Ce}^{x} + O_O^{x} \rightarrow 2Sm_{Ce}^{'} + V_O^{\cdot\cdot} + 2CeO_2} \qquad (\mathbf{3.14})$$

Where, symbols has the following meaning as; $Ce_{ce}^{x}$ and $Sm_{Ce}^{'}$ are $Ce^{4+}$ and $Sm^{3+}$ ions on the $CeO_2$ lattice site, respectively, $O_O^{x}$ is $O^{-2}$ ions on an oxygen lattice site, and $V_O^{\cdot\cdot}$ is neutral oxygen vacancy site.

Another oxygen vacancy peak can also be seen in the range of ~593-600 $cm^{-1}$, which is attributed to the defect space including intrinsic oxygen vacancies due to the presence of $Ce^{3+}$ ions as reported [154, 155]. The possible disorder mechanism for the creation of intrinsic oxygen vacancies in the sample can be given as per the reaction [156]:

$$\boldsymbol{2Ce_{Ce}^{x} + O_O^{x} \rightarrow 2Ce_{Ce}^{'} + V_O^{\cdot\cdot} + 1/2\, O_2(g)} \qquad (\mathbf{3.15})$$

Where, symbols has the following meaning as; $Ce_{ce}^{x}$ and $Ce_{Ce}^{'}$ are $Ce^{4+}$ and $Ce^{3+}$ ions on the Ce lattice site, respectively, $O_O^{x}$ is $O^{-2}$ ions on an oxygen lattice site, and $V_O^{\cdot\cdot}$ is neutral oxygen vacancy site [141]. Moreover, a band ~1364-1349$cm^{-1}$ is assigned to 3LO Raman mode, which is activated due to multiphonon relaxation by resonance Raman Effect [157]. The intensity of 3LO Raman mode is decreasing with fluencies of $Sm^{3+}$ ions in $CeO_2$ NPs from $x$ = 0.02 to 0.08 and its peak is shifted near at ~1175 $cm^{-1}$ for $x$ = 0.10 doping concentration, which is assigned for 2LO mode. The intensity of Raman peaks near ~548-558 $cm^{-1}$ and ~593-600 $cm^{-1}$ is increasing with $Sm^{3+}$ ions concentration from $x$ = 0.02 to 0.06, which indicates that both extrinsic and intrinsic oxygen vacancies are increased with fluency of $Sm^{3+}$ ions, while for further doping fluencies ($x$ = 0.08 and 0.10) the intensity of these peaks is decreased (shown in Figure 3.11(b)). This behaviour can be explained as, due to the incorporation of $Sm^{3+}$ ions the $Ce^{4+}$ ions are substituted by the $Ce^{3+}$ ions which release the oxygen ions into the $CeO_2$ lattice for maintaining the electroneutrality.

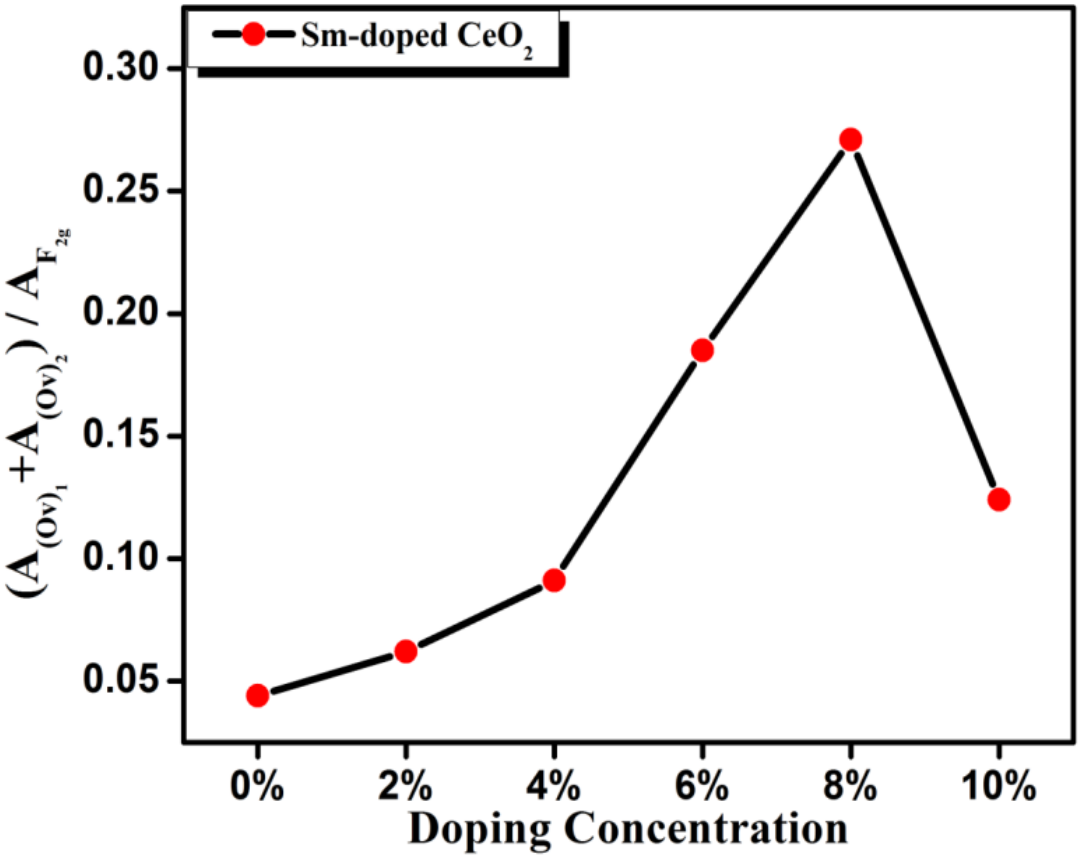


**Figure 3.12: Relative peak area ratio for bands of oxygen vacancies and $F_{2g}$ mode for $Ce_{1-x}Sm_xO_2$ ($x$ = 0.00, 0.02, 0.04, 0.06, 0.08 and 0.10) samples.**

The particle size of pure $CeO_2$ and $Ce_{1-x}Sm_xO_2$ NPs samples can also be calculated from Raman spectra using following equation:

$$\Gamma\ (cm^{-1}) = 10 + \left(\frac{124.7}{D}\right) nm \qquad (3.16)$$

Where, Γ ($cm^{-1}$) is FWHM of Raman active ($F_{2g}$) mode and D is particle size of pure $CeO_2$ and $Ce_{1-x}Sm_xO_2$ NPs samples measured from TEM images [158, 159]. The calculated particle size from Raman spectra is in good agreement with the particle size calculated by XRD spectra and TEM images (as shown in Table 3.2). The quantitative estimation of the overall concentration of oxygen vacancies (intrinsic and extrinsic) is also calculated by the peak area of the oxygen vacancies $A_{O_v}$, $A_{(O_v)_1}$, $A_{(O_v)_2}$ and $A_{F_{2g}}$ bands, which are corresponding to 598.5 $cm^{-1}$, ~548-558 $cm^{-1}$, ~593-600 $cm^{-1}$ and for the $F_{2g}$ band, respectively. The calculated values of

relative peak area ratios for pure $CeO_2$ and $Ce_{1-x}Sm_xO_2$ NPs samples are tabulated in Table 3.3 and shown in Figure 3.12. The relative peak area ratios are calculated by fitting the Lorentzian function for the corresponding oxygen vacancies mode and $F_{2g}$ mode [$A_{O_v}/A_{F_{2g}}$ and $(A_{(Ov)_1} + A_{(Ov)_2})/A_{F_{2g}}$ for pure $CeO_2$ and $Ce_{1-x}Sm_xO_2$ NPs samples for all doping ($x$ = 0.02, 0.04, 0.06, 0.08 and 0.10), respectively], which reflect the relative oxygen vacancy concentration. It can be seen from Table 3.3, the relative peak area ratio is increased for $Ce_{1-x}Sm_xO_2$ samples from $x$ = 0.00 to 0.08 and then decrease at $x$ = 0.10 doping concentration. Hence, we can conclude that with increasing $Sm^{3+}$ ions fluency in the $CeO_2$, oxygen vacancies are gradually increased but at higher fluency ($x$ = 0.10) they are found to decrease.

### 3.3.3. Electrical Properties

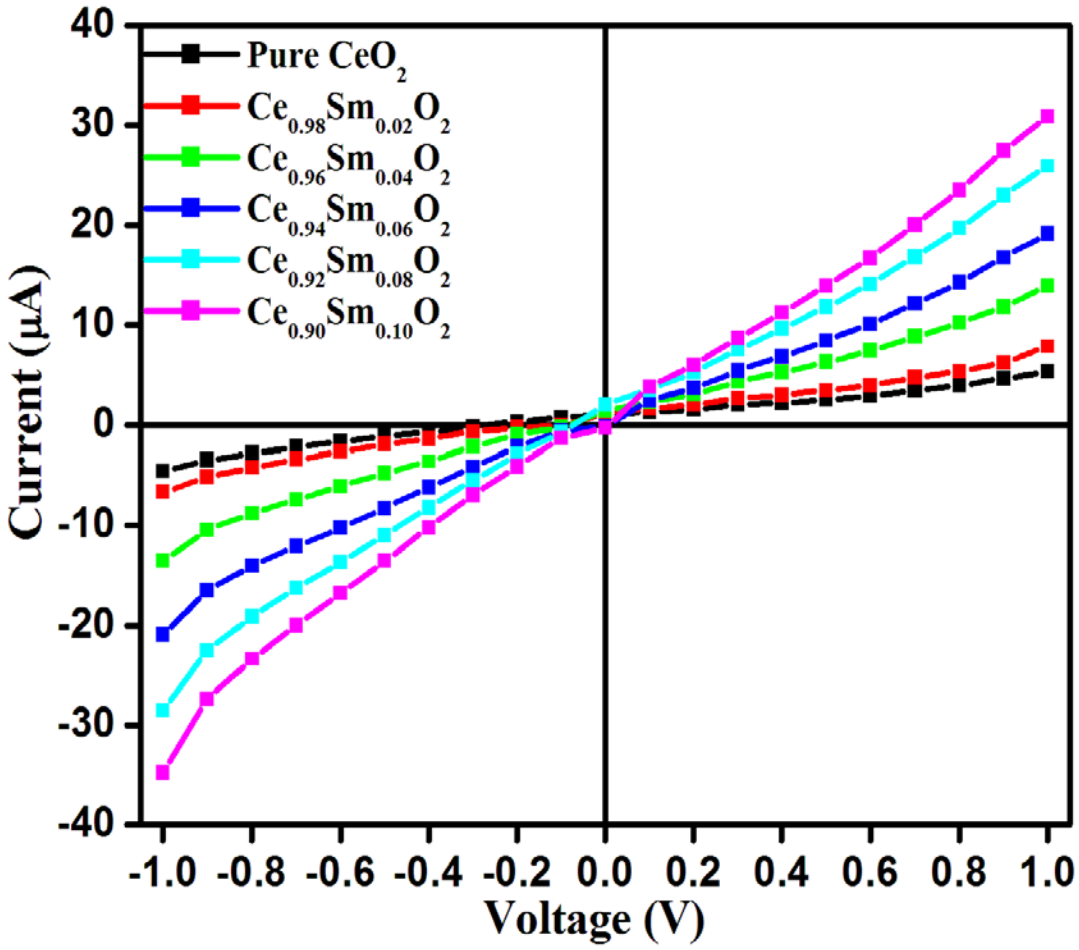


**Figure 3.13: I-V characteristic of pure $CeO_2$ and $Ce_{1-x}Sm_xO_2$ ($x$ = 0.02, 0.04, 0.06, 0.08 and 0.10) NPs samples at room temperature**

In order to investigate the electrical properties of pure $CeO_2$ and $Ce_{1-x}Sm_xO_2$ ($x$ = 0.02, 0.04, 0.06, 0.08 and 0.10) NPs samples, I-V characteristics are carried out using Keithley electrometer 2400 with two-point probe setup. Figure 3.13 shows the I-V characteristics of pure $CeO_2$ NPs with different concentration of Sm-ions. The applied potential ranges from -1 V to +1 V and the corresponding current is measured at room temperature, which indicates an exponential increasing and decreasing curve in the positive and negative direction of applied voltage, respectively. The electrical conductivity of the prepared samples are calculated by the following relation,

$$\boldsymbol{\rho = \frac{RA}{l} = \left(\frac{V}{I}\right) \times \left(\frac{A}{l}\right)} \qquad (\mathbf{3.17})$$

$$\boldsymbol{\sigma = \frac{1}{\rho}} \qquad (\mathbf{3.18})$$

From equation (3.17) and (3.18),

$$\boldsymbol{\sigma = \left(\frac{I}{V}\right)\left(\frac{l}{A}\right) S/cm} \qquad (\mathbf{3.19})$$

Where, $\rho$ is the resistivity, $\sigma$ is the conductivity, $R$ is the resistance, $I$ is the current (μA), $V$ is the applied voltage (Volt), $l$ is the thickness and $A$ is the cross-sectional area of the samples [160].

**Table 3.4: Electrical resistivity and conductivity with crystalline size, band gap energy and oxygen vacancy of all samples at room temperature**

| Sample | Crystallite Size (nm) | Band gap energy (eV) | Oxygen vacancy concentration from Raman spectra | Resistivity ($\rho$) (Ω cm) × $10^2$ | Conductivity ($\sigma$) (S/cm) × $10^{-2}$ |
|---|---|---|---|---|---|
| **Pure $CeO_2$** | 7.24 | 2.87 | 0.044 | 1.28 | 0.78 |
| **$Ce_{0.98}Sm_{0.02}O_2$** | 5.94 | 2.69 | 0.062 | 1.22 | 0.81 |
| **$Ce_{0.96}Sm_{0.04}O_2$** | 6.45 | 2.86 | 0.091 | 0.38 | 2.64 |
| **$Ce_{0.94}Sm_{0.06}O_2$** | 8.13 | 2.83 | 0.185 | 0.33 | 2.96 |
| **$Ce_{0.92}Sm_{0.08}O_2$** | 6.62 | 2.87 | 0.271 | 0.31 | 3.20 |
| **$Ce_{0.90}Sm_{0.10}O_2$** | 6.76 | 2.64 | 0.123 | 0.26 | 3.84 |

Table 3.4 shows the DC electrical resistivity ($\rho$) and conductivity ($\sigma$) values at room temperature, which is calculated from equation (3.17) and (3.18). The resistivity ($\rho$) is found to be in the range $0.26 \times 10^2$ and $1.28 \times 10^2$ Ω cm and conductivity ($\sigma$) is found in the range $0.78 \times 10^{-2}$ and $3.84 \times 10^{-2}$ S/cm. It can be seen clearly that conductivity of the pure $CeO_2$ improves after incorporation of $Sm^{3+}$ ions, which may be due to increase in the crystallinity and decrease in the crystallite size of $CeO_2$ after incorporation of $Sm^{3+}$ ions. The decrease in the crystallite size results in increase in the conductivity of Sm-doped $CeO_2$ samples, which may be attributed to increase in both carrier density and mobility because of larger change in surface to volume ratio. These results are also evident from our XRD and TEM analysis. For maintaining the electrical neutrality, oxygen vacancy defects are formed and number of oxygen vacancies increases with the fluency of $Sm^{3+}$ ions on Ce sites, which has been evidenced from our Raman spectra. The defect equation can be shown as:

$$2Sm^{3+} \xrightarrow{Ce^{4+}} 2Sm'_{Ce} + V_O \qquad (3.20)$$

Doping of $Sm^{3+}$ ions into the cubic fluorite phase of $CeO_2$ leads to two different effects in the physical property. First, the electrical conductivity of our samples is found to increase continuously but slightly, which is obvious behaviour for doped semiconductor. This behaviour of conductivity and resistivity may be ascribed due to generation of oxygen vacancies according to the defect equation 3.20, which may create trap levels to support this increase up to an optimal doping (6% Sm) [79]. However, for 10% Sm-doped sample the oxygen vacancies are found to decrease (as shown in Table 3.4), but looking to the optical results the band gap value for this doping is found to decrease. So, enhancement in the conductivity of 10% Sm-doped sample may be ascribed due to smaller direct band gap value. Second, according to the XRD analysis, $Sm^{3+}$ doping leads to increase in the unit cell volume (as shown in Table 3.1), which favours the migration of oxygen vacancies and therefore improves the conductivity of Sm-doped samples. Furthermore, the variation in the particle size of these nanomaterials can also give rise to the band gap behaviour of the Sm-doped samples, along with the oxygen vacancies represents the systematic increase in the conductivity of the samples.

These results indicate that the $Sm^{3+}$ doping content increases the conductivity of the doped $CeO_2$ NPs at room temperature.

## 3.4. Conclusion

$CeO_2$ nanocrystalline samples of size 5-8 nm with different doping concentration $x$ = 0.00, 0.02, 0.04, 0.06, 0.08 and 0.10 of $Sm^{3+}$ ions are successfully synthesized by co-precipitation route of chemical synthesis, having *fcc* structure without having any impurity phases present in the lattice as confirmed by XRD results. The crystallinity of $Ce_{1-x}Sm_xO_2$ samples is found to be increased after incorporation of $Sm^{3+}$ ions in the lattice up to a certain doping level after that it is found to be decreased. Further, it is also observed that the value of tensile strain is increasing, which is related to the promotion of oxygen vacancies due to incorporation of larger ionic radii $Sm^{3+}$ ions, which leads to increase in the lattice parameter and expansion of the $CeO_2$ lattice, which also promoted the $Ce^{3+}$ ions as well as oxygen vacancies with lattice expansion. We have also calculated the dislocation density, which also reveal the disordering in the $CeO_2$ lattice system after doping of $Sm^{3+}$ ions. As per our analysis of TEM images of $Ce_{1-x}Sm_xO_2$ samples the spherical size crystalline NPs in the range of 5-8 nm are obtained, it is also confirmed that NPs get agglomerated as the concentration of $Sm^{3+}$ ions is increased in $CeO_2$ NPs and finally leads to the crystal growth in $Ce_{1-x}Sm_xO_2$ samples. HRTEM images are also revealed that there is no significance change in the interplanar distance ($d$) for (111) plane of $x$ = 0.00, 0.04, 0.06 and 0.08 doping concentrations while for $x$ = 0.02 and 0.10 it is changed and some dislocation can also be seen for $x$ = 0.10 Sm-doped $CeO_2$ sample. SAED patterns indicated that nano-sized particles are formed with low crystallinity, which is confirmed by the broadness of diffraction rings. EDX spectra have confirmed the presence of Ce, Sm and O elements nearly in stoichiometric ratio for pure and Sm-doped $CeO_2$ samples. Further, from our UV-Vis-NIR spectrum, mainly originated from defect state existing extensively between the Ce 4f band and O 2p band, we can say that with the Sm-doping in the $CeO_2$ NPs lattice, above the Mott critical density, the increased number of free electron concentration lead to fill Ce 4f level partially, which in turn blocks the lowest states available for occupancy and led to increase the band gap.

Hence up to the Mott critical density, the band gap is found to decrease and above this, it starts to increase. Raman spectra are also shown the formation of cubic fluorite structure of pure $CeO_2$ and Sm-doped $CeO_2$ samples without any impurity phases. Raman results are also further clarifying the presence of oxygen vacancies for pure $CeO_2$ NPs, which is found to increase with increasing doping of $Sm^{3+}$ ions (both intrinsic and extrinsic oxygen vacancies) but for further higher doping concentrations, it is found to decrease. The I-V characteristics show the semiconducting nature of all the samples and the conductivity measurements shows that the conductivity of the $CeO_2$ increases with increasing of Sm-content. Finally, in this chapter we are able to show controlled band gap, size, grain morphology, higher conductivity, controlled extrinsic and intrinsic oxygen vacancies with the RE cation Sm-doping in the $CeO_2$ lattice. The size and Sm-doping controlled morphologies, microstructure, optical and electrical properties of $CeO_2$ NPs can make these NPs suitable alternatives for various applications like luminescent materials, oxygen transportation, catalysts, ultraviolet fuel cells, corrosion prevention etc. Further control on the density and nature of the oxygen vacancies can be used to provide a means to tailor the reactivity of $CeO_2$ catalyst.

# Chapter 4

# Study of Structural, Optical, Electronic Structure and Magnetic Properties of RE ($Gd^{3+}$)-doped $CeO_2$ Nanoparticles

# CHAPTER 4

# STUDY OF STRUCTURAL, OPTICAL, ELECTRONIC STRUCTURE AND MAGNETIC PROPERTIES OF RE ($Gd^{3+}$)-DOPED $CeO_2$ NANOPARTICLES


## ABSTRACT

Enhanced visible light photocatalytic activity of pure $CeO_2$ and Gd-doped $CeO_2$ NPs has been experimentally demonstrated, whereas there are very few reports on this mechanism with RE-doping. All pure $CeO_2$ and Gd-doped $CeO_2$ NPs are synthesized using co-precipitation method and characterized using XRD, TEM, UV-Vis-NIR spectroscopy, SERS, X-ray Photoelectron Spectroscopy (XPS), MPMS-3 SQUID magnetometer. Effect of Gd-doping on properties of $CeO_2$ is discussed along with defects and oxygen vacancies generation. The XRD confirms the incorporation of $Gd^{3+}$ at the $Ce^{3+}$/ $Ce^{4+}$ site by keeping the crystal structure same. The average particle size from TEM images are in the range of 5-7 nm for the samples. The XPS spectra of Ce 3d, O 1s and Gd 4d are discussed to report the formation of oxygen vacancies to maintain the charge neutrality when $Ce^{4+}$ changes to $Ce^{3+}$. The gradual increase in hydrogen production is observed with increasing Gd concentration. The observed results are found in good correlation with the characterisation results and proposed mechanism of water splitting is reported on the basis of analyses. The absorption spectra reveal optical band gap 2.5-2.7eV of samples, showing band gap narrowing leads to desired optical absorbance and photo-activity of NPs.


## 4.1. Introduction

RE oxide $CeO_2$ has attracted great interest of research due to their unique properties, including high oxygen storage capacity and ability to uptake and release oxygen ($O^{2-}$) ions via conversion of oxidation state of cerium ion from $Ce^{4+}$ to $Ce^{3+}$, due to formation of defect space such as oxygen vacancies in the lattice of $CeO_2$ [141]. On account of this uniqueness, $CeO_2$ has been widely used as three-way catalysts (TWC) for eliminating vehicle exhaust gases [46], UV blocker materials in sunscreens, UV-shielding in cotton fabrics [161], functionalize silk fiber for

antibacterial activity [162], oxygen sensors [163] and oxygen ion conductors in solid oxide fuel cells (SOFCs) [164]. Generally, it has been reported that type of dopant strongly influenced the electrical properties of $CeO_2$ and high conductivity at low temperature is an essential requirement for SOFCs, therefore, RE-doped $CeO_2$, $Ce_{1-x}RE_xO_{2-\delta}$ (RE= Sm, Gd, Dy, Er, Lu), are preferable dopants used as electrolytes for intermediate-temperature SOFC's [165, 166]. Alike $TiO_2$, bulk cerium dioxide ($CeO_2$) is a wide band gap (3.2 eV) cubic fluorite semiconductor [167], which possess the interesting properties such as a high dielectric constant ($\varepsilon$ = 26), good transparency in the visible range and capacity to exhibit the high photocatalytic activity under UV light irradiation. Therefore, $CeO_2$ seems to be a promising inorganic material that can be used for the UV filtration in sunscreen/cosmetic products [168]. Therefore, to enhance the workability of this compound in visible light some kind of structural engineering and doping of heavy metal might be done for reducing the band gap of $CeO_2$.

Among all RE-doped $CeO_2$, Sm and Gd-stabilized $CeO_2$ has been extensively studied for utilization as electrolyte and anode material [169, 170]. It has been reported that, addition of $Sm^{3+}$ and $Gd^{3+}$ cations in $CeO_2$ system produced highest conductivity with least distortion of parent lattice, which is attributed to the smallest association enthalpy between the dopant cation and oxygen vacancies in the $CeO_2$ lattice [171-173]. Besides of dopant type, theoretical and experimental observations have also suggested that the ionic conduction can be altered by the concentration of dopant [174-177]. Moreover, it is well known that material properties changes when particle size reduces to nano-scale, as reported by *I. Kosacki et al.* [178] in their nanocrystalline $CeO_2$ thin film, electrical conductivity has found to be enhanced due to reduced enthalpy of oxygen vacancy formation. *Li et al.* [179] have reported increase in catalytic activity as well as in optical and magnetic properties of porous $Gd^{3+}$-doped $CeO_2$ (10 at% Gd) nanostructure due to $Gd^{3+}$ ions or formation of oxygen vacancies. In most of these studies, the local ordering of oxygen vacancies on grain boundaries in heavily RE-doped $CeO_2$ samples has been reported [180-182]. *Chen et al.* [67] have reported dopant-induced structural differences and defects in Sm-doped $CeO_2$ NPs with doping concentration

of 3, 5, 7, 9, and 11%. On the basis of their results based on XAS, EXAFS, Raman and STEM-EELS measurements they have discussed that below and above 7% distribution of defects strongly depend on the concentration of $Sm^{3+}$ ions in $CeO_2$ NPs.

Metal oxide photocatalyst have attracted increasing attention due to their potential applications in the environmental protection and energy utilization, such as water splitting for hydrogen production. In the Zn-, Mg- and Ca-doped $CeO_2$ materials the impurities tends to shift the band position and can tune the band gap because of their effects on electronic transition [183]. Gd-doped $CeO_2$ is used for thermolysis of water that can produce 101.6 $H_2$ (μmol/g) hydrogen [184]. It has been demonstrated experimentally that the RE dopants and oxygen vacancies greatly influence the photocatalytic properties of $CeO_2$; however, the effect of interaction between the RE dopant and the oxygen vacancy defects on visible light photocatalytic activity of $CeO_2$ is still not investigated so far.

Since, there is a lack of literature available on the evidence of the distribution of defect study with small doping concentration of RE-doped $CeO_2$ NPs. Hence in this study, we systematically explore to develop the correlation between the RE dopants, its concentration and oxygen vacancy defects to enhance the photocatalytic activity of doped $CeO_2$. To undertake this study we have investigated the structural properties, dopant distribution and their association with the oxygen vacancies in Gd-doped $CeO_2$ NPs. The $CeO_2$ NPs have been doped with different concentrations of $Gd^{3+}$ ions (2, 4, 6, 8, and 10%) to discuss the presence of defect induced oxygen vacancies (either intrinsic or extrinsic) and their association with doped cation with SERS measurements. TEM have been used to observe changes in the surface morphology and particle size with increased fluencies of $Gd^{3+}$ ions in $CeO_2$ lattice. The optical absorption spectra have been measured using UV-Vis-NIR spectrometer to find out the band gap energy. Finally, we have attempted to investigate how doping concentration affect the oxygen vacancies and the cation ($Ce^{3+}$) defects, present in the pure $CeO_2$ and Gd-doped $CeO_2$ NPs. These results offer a physical understanding for the available experimental results to explain the enhanced

photocatalytic activities of Gd-doped $CeO_2$ NPs, which can be useful for designing and understanding the novel doped $CeO_2$ photocatalyst.

## 4.2. Experimental Details

### 4.2.1. Materials for synthesis of NPs

Ammonium cerium (IV) nitrate $(NH_4)_2Ce(NO_3)_6$ (Alpha Aesar 99.99%), Gadolinium (III) nitrate hexahydrate $Gd(NO_3)_3.6H_2O$ (Alpha Aesar 99.9%) and Sodium hydroxide NaOH.

### 4.2.2. Material Preparation

Nanocrystalline pure $CeO_2$ and $Ce_{1-x}Gd_xO_2$ (for $x$ = 0.02, 0.04, 0.06, 0.08 and 0.10) samples were synthesized using co-precipitation method. The appropriate stoichiometric amount of $(NH_4)_2Ce(NO_3)_6$ and $Gd(NO_3)_3.6H_2O$ were used for synthesizing $Ce_{1-x}Gd_xO_2$ NPs. Initially, $(NH_4)_2Ce(NO_3)_6$and $Gd(NO_3)_3.6H_2O$ precursor solutions were prepared in distilled water with magnetic stirring at the rate of 600 rpm. Then NaOH solution was added drop by drop to this solution until the pH level reached about 11. This solution was stirred about 4 hours and then the synthesized pale-yellow precipitate was collected. The precipitate was dried at room temperature and annealed in the furnace about 500$^o$C for 8 hours. A set of samples, i.e. pure $CeO_2$ and $Ce_{1-x}Gd_xO_2$ (for $x$ = 0.02, 0.04, 0.06, 0.08 and 0.10) NPs were prepared. The main chemical reactions during the experimental process are as follows:

$$\boldsymbol{6NaOH_{(S)} \rightarrow 6Na^{+}_{(aq)} + 6OH^{-}_{(aq)}} \quad (4.1)$$

$$\boldsymbol{(NH_4)_2Ce(NO_3)_6 \rightarrow Ce^{3+}_{(aq)} + 6NO^{-}_{3\,(aq)} + 2NH^{+}_{4\,(aq)}} \quad (4.2)$$

$$\boldsymbol{6Na^{+}_{(aq)} + 6NO^{-}_{3\,(aq)} \rightarrow 6NaNO_{3\,(aq)}} \quad (4.3)$$

$$\boldsymbol{2NH^{+}_{4\,(aq)} + 2OH^{-}_{(aq)} \rightarrow 2NH_{3\,(g)} \uparrow + 2H_2O_{(aq)}} \quad (4.4)$$

$$\boldsymbol{Ce^{3+}_{(aq)} + 4OH^{-}_{(aq)} + xH_2O_{(aq)} \rightarrow Ce(OH)_4 \cdot xH_2O_{(s)} \downarrow} \quad (4.5)$$

$$\boldsymbol{Ce(OH)_4 \cdot xH_2O_{(S)} \xrightarrow{at\ RT} Ce(OH)_{4(s)} + xH_2O_{(g)} \uparrow} \quad (4.6)$$

$$\boldsymbol{Ce(OH)_{4(s)} \xrightarrow{500℃} CeO_{2\,(s)} + 2H_2O_{(g)}} \quad (4.7)$$

The complete chemical reaction can be combined as:

$$(NH_4)_2Ce(NO_3)_6 + 6NaOH \rightarrow Ce(OH)_4 + 6NaNO_3 + 2NH_3 + 2H_2O \quad (4.8)$$

$$Ce(OH)_4 \rightarrow CeO_2 + 2H_2O \quad (4.9)$$

The final chemical reaction for the growth of various concentrations ($x$ = 0.02, 0.04, 0.06, 0.08 and 0.10) of dopant Gd-ions in $CeO_2$ lattice are as follows:

$$(1-x)[(NH_4)_2Ce(NO_3)_6] + x[Gd(NO_3)_3 \cdot 6H_2O] + 6NaOH \rightarrow Ce_{1-x}Gd_xO + \text{Molecular gases} \uparrow \quad (4.10)$$

### 4.2.3. Nanomaterials Characterization

The structural properties of all the samples were characterized using XRD measurements on a Brucker D8 Advance diffractometer with Cu $K_\alpha$ radiation (λ= 1.5406 Å). The diffraction patterns were recorded at room temperature in the $2\theta$ range from $10^o$ to $90^o$. The surface morphology, particle size and crystallinity of the samples were studied using TEM with Technai G2 20 S-TWIN (FEI Netherlands) instrument operating at an accelerating voltage of 200 kV. Samples for the TEM investigation were prepared by dispersing the nanopowder in ethanol using an ultrasonicator to produce a dilute suspension. Then a standard holey carbon film supported on Cu grid was immersed in the suspension to produce the TEM sample. The particle size distribution was calculated for a total 150 number of particles using image-j software for TEM images. The optical characterizations were carried out by using SERS. For collecting Raman spectra, SERS of make Thermo Scientific DXRxi Raman Imaging Microscope with Charge Injection device (CID) detector using green laser with 532 nm excitation light source with its power kept at 10mW were used. The UV-Vis-NIR absorbance spectra on the samples in the wavelength range of 200-1000 nm with $BaSO_4$ as standard were recorded employing a Shimadzu UV-3600 Plus spectrophotometer with an integrating sphere. XPS spectra were recorded on a ultrahigh vacuum based Omicron Multiprobe Surface analysis System (Germany, Gmbh) operating at a base pressure of $5\times10^{-11}$ Torr. Mg $K_\alpha$ radiation source (with energy of 1253.6 eV) was used for data acquisition. An OMICRON EA125 hemispherical analyser equipped with a 7 channeltron parallel

detection unit was used to collect the XPS spectra. The calibration of binding energy in photoemission spectra was done referring to standard Au $4f_{7/2}$ emission line with energy resolution of ~0.9 eV FWHM on Au $4f_{7/2}$ with pass energy of 20 eV during the measurement. The XPS core level data were analysed after necessary carbon corrections for the Fermi energy referencing. The magnetic properties of the samples were investigated at room temperature using a Quantum Design MPMS-3 SQUID system. The magnetization measurements were conducted by varying the applied field from -1.5 T to +1.5 T.

Photocatalytic cleavage of the water for hydrogen generation was carried out using the powder of photocatalytic molecular device (0.3 g powder of Pt/$CeO_2$ or Pt/$Ce_{1-x}Gd_xO_2$ or $CeO_2$ or $Ce_{1-x}Gd_xO_2$) that was suspended in 120 mL of aqueous hole-scavenger electrolyte (20% $CH_3OH$; pH=7.0) in a reaction cell, under the irradiation of 1 Sun (100 mW/cm$^2$, AM1.5 G) visible light. The powder of the photocatalyst (0.2 g with and without Pt loading) was suspended in 120 mL of aqueous electrolyte (20% $CH_3OH$ pH=7.0) in a double walled- Pyrex glass reaction cell (volume ~150 mL, with water jacket) that was sealed with a rubber septum and plastic wire lock [185, 186]. Prior to start the photochemical reaction, the suspension was continuously purged with Ar for 1 hour by maintaining the 1 atm pressure of the inner jacket solution for expelling the air content from the solution. Circulating water bath is used to maintain the temperature of the outer jacket at 25$^o$C. Afterwards, the suspension was irradiated with a 300 W Xe lamp (>420 nm, light intensity $1\times10^{22}$ photons per hour Xe lamp-HX1, Model PE300UV, ISS). All the experiments were carried out under ambient conditions. Photocatalytic responses were hourly monitored in terms of the amount of hydrogen generated at 1-4 hour time intervals. Hydrogen gas has very small density and not soluble in water. Therefore, the evolved hydrogen was collected into the inverted gas collection graduated bottle by displacement of water from a container. The collected gas was checked with the gas chromatograph (Shimazdu, Japan, thermal conductivity detector and molecular sieve with 5 A columns) throughout the course of the reaction.

## 4.3. Results and Discussion

### 4.3.1. Structural Properties

#### 4.3.1.1. XRD analysis

XRD measurements have been made on pure $CeO_2$ and $Ce_{1-x}Gd_xO_2$ ($x$ = 0.02, 0.04, 0.06, 0.08 and 0.10) NPs at room temperature are shown in Figure 4.1. Pure $CeO_2$ and $Ce_{1-x}Gd_xO_2$ ($x$ = 0.02, 0.04, 0.06, 0.08 and 0.10) NPs samples exhibits fundamental Bragg reflections corresponding to the fluorite type face centered cubic structure in the space group of *Fm-3m*, in which Ce and Gd atoms are located at 4a position, surrounded by eight O (located at 8b) positions [123]. Absence of any secondary phase corresponding to $Gd_2O_3$ or other impurity peaks indicates well incorporation of $Gd^{3+}$ ions on $CeO_2$ lattice site, which confirms the single phase formation of all the $Ce_{1-x}Gd_xO_2$ NPs. The intensity of XRD peaks are found to vary with incorporation of $Gd^{3+}$ ions in $CeO_2$ NPs (as shown in Figure 4.1).

The rising intensity signifies an improvement in the crystalline nature while falling intensity signifies low crystallinity of $Ce_{1-x}Gd_xO_2$ samples [125]. Moreover, with fluency of $Gd^{3+}$ ions, no peak shifting is observed for $x$ = 0.02 doping concentration, whereas with increasing concentration (for $x$ = 0.04 and 0.06) diffraction peak (111) is shifted towards higher angle side (as shown inset of Figure 4.1). For higher doping concentrations ($x$ = 0.08 and 0.10), peak is shifted towards lower angle side. This shifting of (111) peak towards lower and higher angle side is attributed to the lattice expansion and reduction, respectively, which is induced by incorporation of $Gd^{3+}$ ions in $CeO_2$ NPs [126].

Furthermore, it can be seen in Figure 4.1, diffraction peaks becomes broader after doping and broadness of peaks are also observed to change with fluency of $Gd^{3+}$ ions in $CeO_2$ NPs, indicating that particle size and crystallinity of the samples is affected with the fluencies of $Gd^{3+}$ ions. The average particle size (D) of pure $CeO_2$ and $Ce_{1-x}Gd_xO_2$ ($x$ = 0.02, 0.04, 0.06, 0.08 and 0.10) NPs samples have been calculated with XRD diffraction spectra using the Debye Scherrer's formula [87]:

$$\boldsymbol{D = \frac{k\,\lambda}{\beta\,cos\theta}} \qquad (\mathbf{4.11})$$

Where, all the parameters are as per the details given in the Ref. [173].

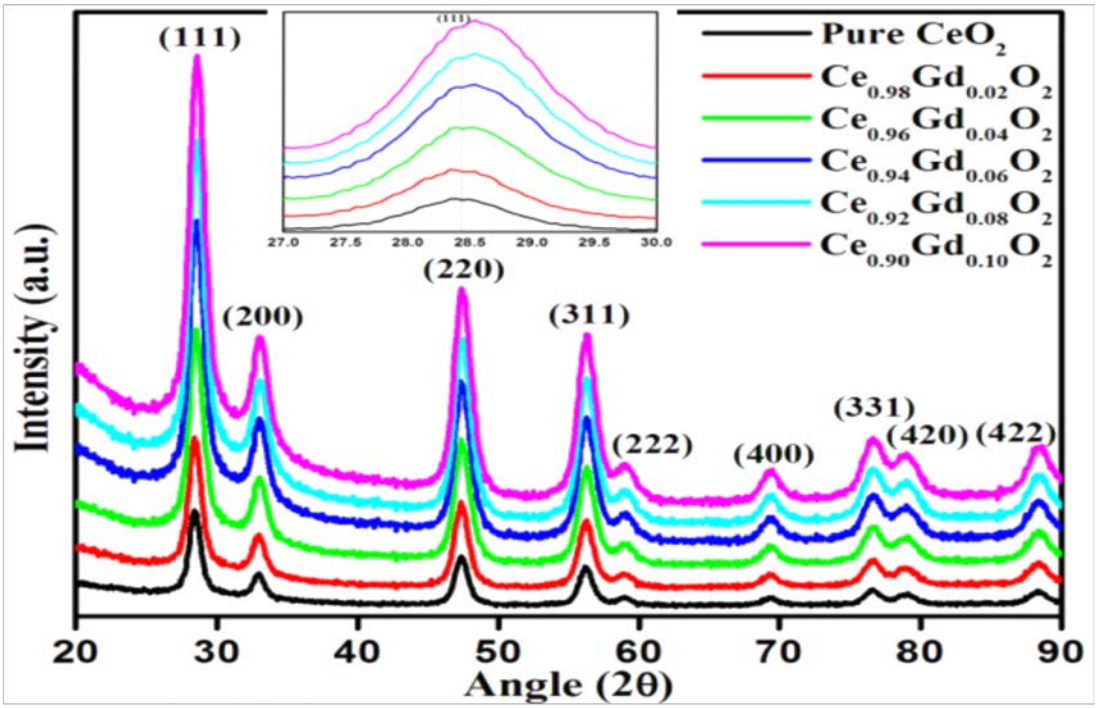


**Figure 4.1: XRD pattern of pure $CeO_2$ and $Ce_{1-x}Gd_xO_2$ (for $x$ = 0.02, 0.04, 0.06, 0.08, and 0.10) samples**

The lattice parameters of all the samples corresponding to (111) diffraction peak can also be calculated by the following formula [88]:

$$\boldsymbol{a = d\,(h^2 + k^2 + l^2)^{1/2}} \qquad (\mathbf{4.12})$$

Where, '*a*' refers to the lattice parameter, *d* is the crystalline lattice spacing and *h*, *k*, *l*, are the miller indices of crystal.

Rietveld profile refinements (shown in Figure 4.2) of all the samples are carried out and the results are listed in the Table 4.1. The Refinement results clearly indicate that Gd ions are well incorporated in the $CeO_2$ matrix and Gd-doping in $CeO_2$ leads to small enhancement in the unit-cell volume. Table 4.1 shows calculated values of lattice parameter with fluency of $Gd^{3+}$ ions in $CeO_2$ NPs, which indicates that the larger ionic radii Gd-dopant ions are affecting the lattice parameter. Since, the larger ionic radii $Gd^{3+}$ (0.1053 nm) ions are substituted for the smaller ionic radii $Ce^{4+}$ (0.097 nm) ions and created the larger radii $Ce^{3+}$ ions (0.114 nm) [128]. Furthermore, for maintaining charge neutrality in $CeO_2$ lattice, $Gd^{3+}$ and $Ce^{3+}$ ions are collectively created oxygen vacancies in the $CeO_2$ lattice, which causes further lattice expansion [126].

**Table 4.1: Calculated values of lattice parameter (*a*), lattice spacing (*d*) for (111) plane, average crystalline size (D) measured from TEM, XRD line broadening and Raman line broadening, dislocation density (δ), lattice strain (ε), absorbance wavelength (λ), optical band gap energy ($E_g$) and refractive index (*n*) are summarized in the table.**

| Sample | Parameters | | | | | | | | | |
|---|---|---|---|---|---|---|---|---|---|---|
| | *a* (Å) | *d* (nm) | D (nm) | | | $\delta=\frac{1}{D^2}$ ($nm^{-2}$) [134] | $\varepsilon=\frac{\beta \cos\theta}{4}\times10^{-2}$ [130,131] | λ (nm) | $E_g$ (eV) | *n* |
| | | | TEM | XRD | Raman spectra | | | | | |
| **Pure $CeO_2$** | 5.436 | 0.318 | 5.55 | 9.21 | 10.9 | 0.0324 | 3.88 | 367 | 2.60 | 2.51 |
| $Ce_{0.98}Gd_{0.02}O_2$ | 5.433 | 0.307 | 5.27 | 6.95 | 7.52 | 0.0360 | 8.60 | 363 | 2.66 | 2.49 |
| $Ce_{0.96}Gd_{0.04}O_2$ | 5.392 | 0.318 | 6.44 | 7.10 | 6.45 | 0.0241 | 8.89 | 359 | 2.71 | 2.48 |
| $Ce_{0.94}Gd_{0.06}O_2$ | 5.394 | 0.316 | 7.47 | 6.51 | 6.07 | 0.0179 | 7.82 | 365 | 2.67 | 2.49 |
| $Ce_{0.92}Gd_{0.08}O_2$ | 5.393 | 0.324 | 5.55 | 6.22 | 5.66 | 0.0324 | 14.18 | 368 | 2.64 | 2.50 |
| $Ce_{0.90}Gd_{0.10}O_2$ | 5.398 | 0.312 | 6.34 | 6.26 | 5.06 | 0.0248 | 9.11 | 371 | 2.52 | 2.54 |

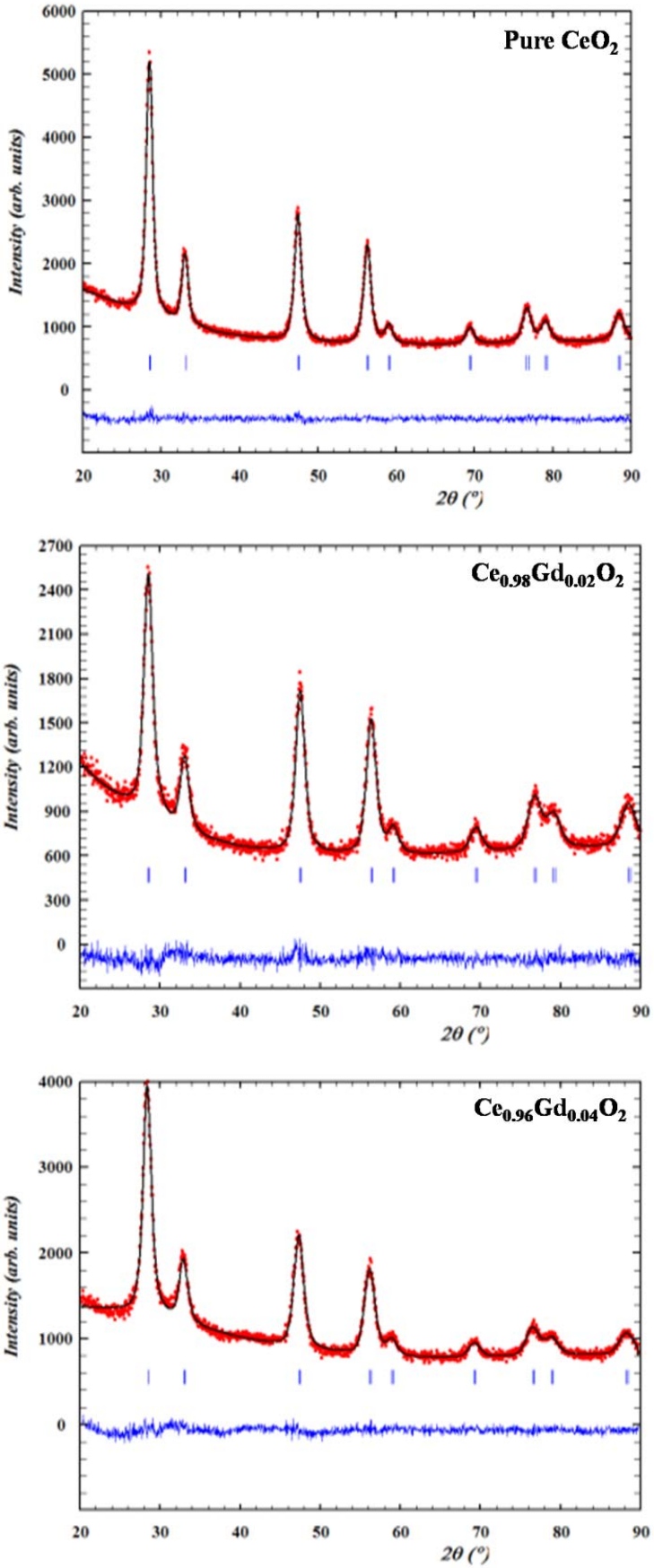
Pure $CeO_2$
$Ce_{0.98}Gd_{0.02}O_2$
$Ce_{0.96}Gd_{0.04}O_2$
Intensity (arb. units)
2θ (°)

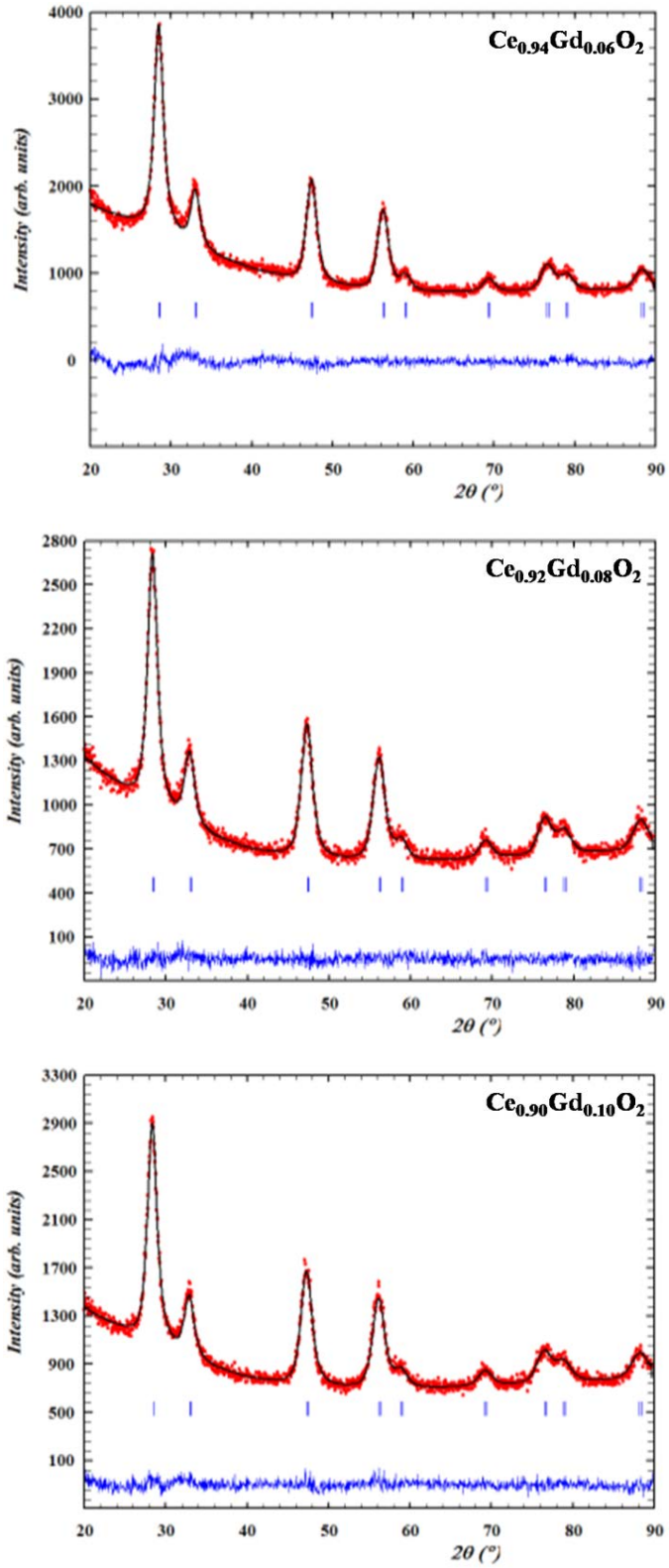


**Figure 4.2: Refined and fitted X-ray diffraction patterns of pure $CeO_2$ and $Ce_{1-x}Gd_xO_2$ ($x$ = 0.02, 0.04, 0.06, 0.08 and 0.10) at 300 K. Observed (calculated) profiles are shown by dotted (solid) lines. The short vertical marks represent Bragg reflections. The lower curve is the difference plot.**

It is clear from the Table 4.1, the dislocation density is found to increase for $x$ = 0.02 doping concentration but decreases for $x$ = 0.04 and 0.06, which is again increased for $x$ = 0.08 and decreased for $x$ = 0.10 doping concentrations of $Gd^{3+}$ cation. This variation in dislocation density is related to the promotion and reduction of disorder in the crystal structure [125].

Looking to the Table 4.1, the values of strain indicates tensile strain for Gd-doped $CeO_2$ NPs. Due to incorporation of $Gd^{3+}$ (0.1053 nm) ions in $CeO_2$ NPs, the maximum value of strain is for $x$ = 0.08 doping concentration. Some theoretical investigation revealed that tensile strain promotes the formation of oxygen vacancies rather than compressive strain [132]. Therefore, in Gd-doped $CeO_2$ samples, increased value of tensile strain could be directly related to the endorsement of oxygen vacancies in doped $CeO_2$ samples, which may be associated to the bonding length and the strength between the surface O and Ce atoms [133]. Since, for tensile strain, the bandwidth of the O 2p orbital decreases and overlapping between O 2p and Ce 5d as well as 4f orbital also decreases, which leads a weaker Ce-O bond and responsible for the formation of oxygen vacancies in doped $CeO_2$ system [132]. The crystallinity, morphology and particle size of pure $CeO_2$ and $Ce_{1-x}Gd_xO_2$ samples are discussed in the next segment by TEM, HRTEM and SAED images.

#### 4.3.1.2. Surface Morphology

The average crystallite particle size of all the samples is confirmed by electron microscopy investigations. TEM measurement is used to manifest the information about the shape, size and the presence of any secondary phase in pure $CeO_2$ and $Ce_{1-x}Gd_xO_2$ NPs. The particle size and morphology of pure $CeO_2$ and $Ce_{1-x}Gd_xO_2$ NPs are analyzed by TEM as shown in Figure 4.3. From TEM analysis, it is observed that the particles are crystallized nanoparticles and agglomerated with spherical morphology. The average particle size calculated from TEM images are ranging from 5-7 nm for pure $CeO_2$ and $Ce_{1-x}Gd_xO_2$ NPs, which are in good agreement with the results obtained from Debye Scherrer's formula (listed in Table 4.1). It can be observed from TEM images that crystal growth is promoted with doping concentration of Gd-ions. However, the morphology of all the samples are not changing but the agglomeration of particles is increased with the doping concentration of Gd-ions (as shown in Figure 4.3).

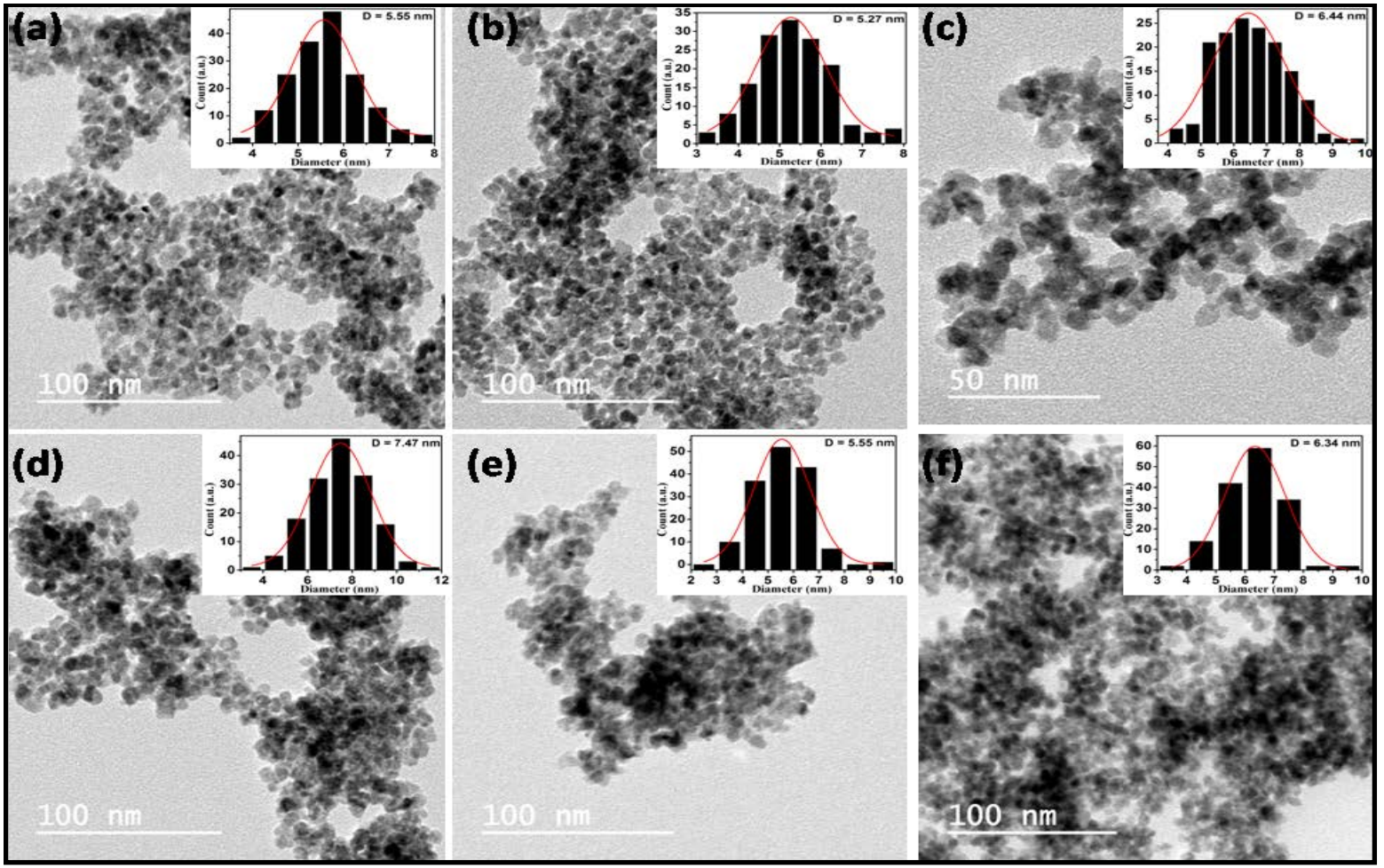


**Figure 4.3: TEM image for (a) Pure $CeO_2$, (b) 2% Gd-doped $CeO_2$, (c) 4% Gd-Doped $CeO_2$, (d) 6% Gd-doped $CeO_2$, (e) 8% Gd-doped $CeO_2$, (f) 10% Gd-doped $CeO_2$ and inset histogram graphs shows the particle size of the corresponding sample.**

The particle size distribution histogram (shown in the inset of Figure 4.3) shows that the distribution is quite narrow in the size range of 5-7 nm for pure $CeO_2$ and $Ce_{1-x}Gd_xO_2$ NPs. This agglomeration of particles with smaller particle-size (<7 nm) indicates that the obtained particles are nano-crystalline. Furthermore, HRTEM and SAED are also used to decipher the information about the nano-crystallinity and impurity phases, if any present in pure $CeO_2$ and $Ce_{1-x}Gd_xO_2$ NPs. HRTEM images (shown in Figure 4.4) indicate that the lattice fringes are well developed and randomly oriented with respect to each other. Most of the lattice fringes of pure $CeO_2$ and $Ce_{1-x}Gd_xO_2$ samples are about at a distance of 0.31 nm (values are tabulated in Table 4.1) that corresponding to the (111) lattice plane of the fluorite like cubic structure.

As shown in Table 4.1, no significant change is observed in the interplanar distance ($d$) for Gd-doped $CeO_2$ samples but for 8% Gd-doped $CeO_2$ sample, the interplanar distance ($d$ = 0.32 nm) is slightly increased, which again promotes the crystal growth and indicates the low crystallinity. Some defects, such as dislocations (shown in Figure 4.4(c) and 4.4(d), marked with a red ring) are also observed in the HRTEM micrograph of 4% and 6% Gd-doped $CeO_2$ samples. Moreover, SAED patterns are also taken (shown in the insets of Figure 4.4) for Gd-doped $CeO_2$ samples. SAED pattern exhibits four broad rings, which could be attributed to (111), (200), (220) and (311) planes. These rings indicate that the particles are crystallized and diffraction rings are very well matched with the XRD measurement results. The fluency of $Gd^{3+}$ ions in $CeO_2$ NPs also affect the optical band gap energy, which is further discussed in the next segment by UV-Vis-NIR spectroscopy.

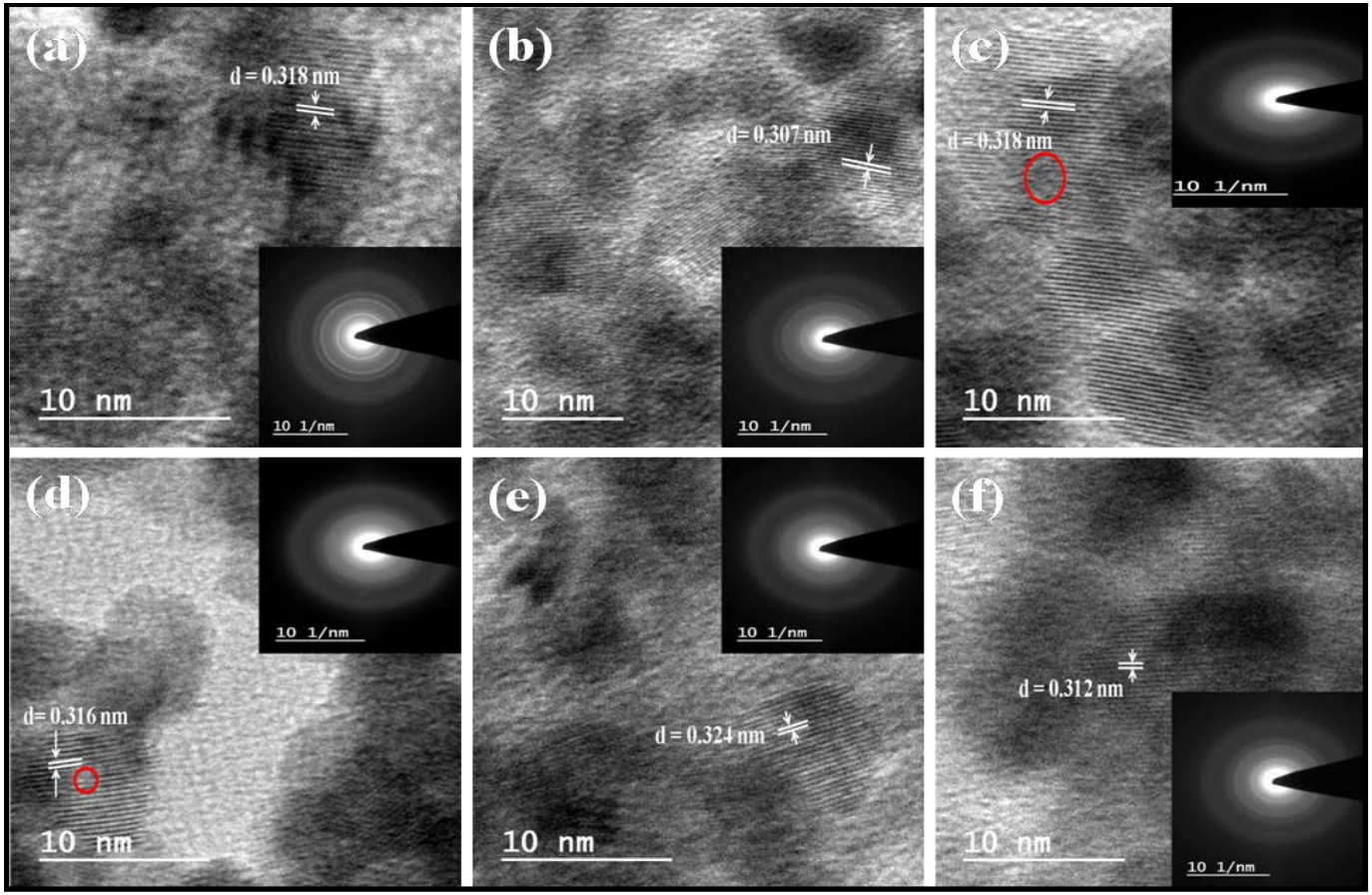


**Figure 4.4: HRTEM images with *d*-spacing corresponding to (111) plane for (a) Pure $CeO_2$ (b) 2% Gd-doped $CeO_2$ (c) 4% Gd-doped $CeO_2$ (d) 6% Gd-doped $CeO_2$ (e) 8% Gd-doped $CeO_2$ (f) 10% Gd-doped $CeO_2$ and inset shows the SAED pattern of corresponding sample.**

### 4.3.2. Optical Properties

#### 4.3.2.1. UV-Vis-NIR analysis

Figure 4.5(a) shows the UV-visible absorption spectra of pure $CeO_2$ and $Ce_{1-x}Gd_xO_2$ ($x$ = 0.02, 0.04, 0.06, 0.08, and 0.10) samples. These samples exhibit a strong absorption below 400 nm with an absorption peak in UV-range corresponding to the different doping concentration of $Gd^{3+}$ ions in $CeO_2$ NPs as tabulated in the Table 4.1. These peaks are originated due to direct charge transfer from 2p valance band of $O^{2-}$ to 4f conduction band of $Ce^{4+}$ ions [187]. It is well known that $CeO_2$ has wide band gap semiconductor with a forbidden gap of 5.5 eV [188]. The valance band consists of O 2p level with a width of 4 eV and conduction band consist of Ce 5d level. Ce 4f level is present in between these two states, just above the Fermi level, that lies about 3eV higher than the valance band (O 2p) [189].

Hence, there is direct recombination of the electrons in $Ce^{4+}$ (4f) conduction band with the holes in the $O^{2-}$ (2p) valance band. It can be seen from Figure 4.5(a), the absorbance peak is obtained at 367 nm for pure $CeO_2$ but after incorporation of $Gd^{3+}$ ions peak is shifted towards lower wavelength (blue-shift) up to optimal doping concentration $x$ = 0.04, while for further fluencies, $x$ = 0.06 to 0.10, peak is shifted towards higher wavelength (red-shift) side. It has been reported that when metal NPs are forming smaller size particles, the $\lambda_{max}$ shifts towards shorter wavelength (blue shift) side, whereas, when the smaller particles aggregate to form bigger/larger size particles, the $\lambda_{max}$ value shifts towards longer wavelength (red shift) side [190]. This may indicate that smaller sized particles has been formed up to doping concentration ($x$ = 0.04), while with increasing fluencies of Gd-ions (for $x$ = 0.06 to 0.10) in $CeO_2$ NPs, these smaller sized particles are agglomerated (as shown in Figure 4.3).

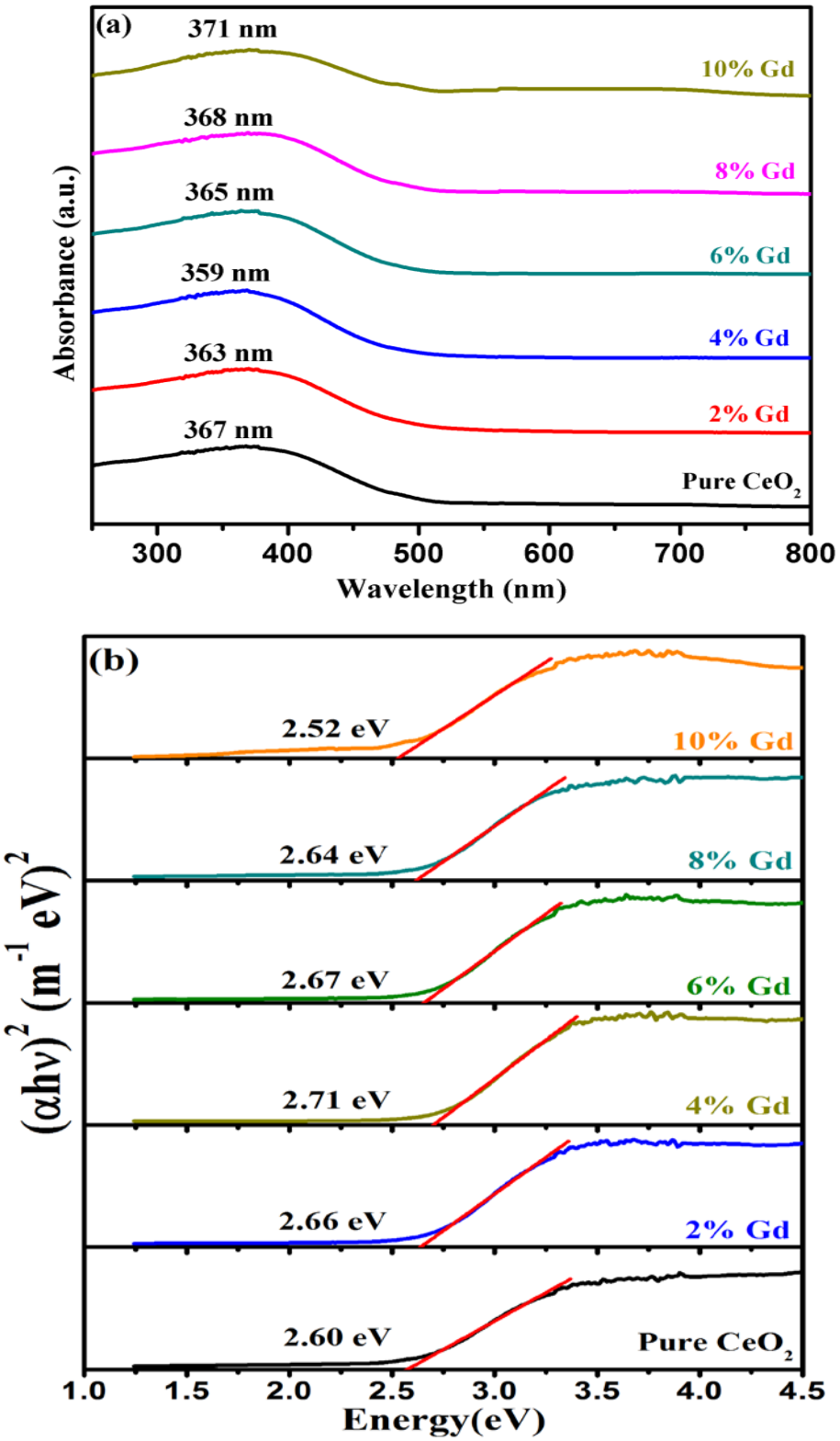


**Figure 4.5: (a) Room temperature optical absorbance spectra of pure $CeO_2$ and $Ce_{1-x}Gd_xO_2$ ($x$ = 0.02, 0.04, 0.06, 0.08 and 0.10) samples taken in the UV-visible range. (b) Tauc's plot of $(\alpha h\upsilon)^2$ versus Energy for the pure $CeO_2$ and Gd-doped $CeO_2$ samples.**

As, *C. Hu et al*., reported that the agglomeration of nanoparticles occurs because nanoparticles have a tendency to decrease the exposed surface in order to lower the surface energy, which results decreases in particle size with strong agglomeration [191]. Furthermore, blue shifting in the absorption spectra with the fluency of $Gd^{3+}$ ions in $CeO_2$ NPs can be due to change of $Ce^{4+}$ to $Ce^{3+}$ state, that increases the direct charge transfer transition gap between O 2p and Ce 4f bands and reduces the particle size [179, 192]. In addition of that the average particle size obtained from TEM images for Gd-doped $CeO_2$ NPs is in the range of 5-6 nm at lower doping concentration ($x$ = 0.02 and 0.04), which is smaller than the predictable Bohr exciton radius for $CeO_2$ (7-8 nm) [179, 136]. Therefore, the quantum confinement effect may also be taken place that contributes to the blue shift of the absorption spectra with small fluencies of Gd-ions in $CeO_2$ NPs. Generally, quantum confinement effect results when the Bohr radius of an exciton approaches the grain or particle size, spatially confining the electron-hole pair. When this happens, the energy of the lowest excited state increases and the increased band gap produces a blue shift in the absorption spectra. Now at the higher fluencies (for $x$ = 0.06 to 0.10) of $Gd^{3+}$ ions, the contribution of blue shifting from $Ce^{4+}$ to $Ce^{3+}$ valance state change will become small. Therefore, red shifting is occurred in the absorption spectra for $x$ = 0.06, 0.08 and 0.10 doping concentrations of $Ce_{1-x}Gd_xO_2$ sample. This red shifting may be the outcome of an interfacial polaron effect arising from electron-phonon coupling phenomenon [193, 194]. Form all above absorption data, the band gap energy ($E_g$) of pure $CeO_2$ and $Ce_{1-x}Gd_xO_2$ ($x$ = 0.02, 0.04, 0.06, 0.08, and 0.10) NPs have been calculated using Tauc's equation:

$$\boldsymbol{\alpha h\nu = A\,(h\nu - E_g)^n} \qquad (\mathbf{4.13})$$

Where, all the parameters have their usual meaning. For direct transition $n$ =1/2 and for $n$ =2 for indirect transition [135]. Figure 4.5(b) displays the measured values of $(\alpha h\nu)^2$ as a function of the incident photon energy ($h\nu$). Table 4.1 contains the calculated value of band gap energy ($E_g$) of all samples. Pure $CeO_2$ NPs shows band gap energy of 2.60 eV that is smaller than the band gap energy reported for bulk $CeO_2$ i.e. 3.15 eV [137]. This decrease in band gap energy may be attributed due to increase in the concentration of $Ce^{3+}$ states on grain boundaries. Moreover, the optical band gap energy is found to increase for low fluency of $Gd^{3+}$ ions (for

$x$ = 0.02 and 0.04) in $CeO_2$ NPs while it decreases subsequently with increasing fluencies of $Gd^{3+}$ ions (for $x$ = 0.06 to 0.10) in $CeO_2$ NPs (as shown in Table 4.1). This blue shift in the band gap energy at lower doping concentration (for $x$ = 0.02 and 0.04) of $Gd^{3+}$ ions may be correlated with the decrease of $Ce^{3+}$ concentration as well as oxygen vacancies during annealing process. This may eliminate some localized defect energy states within the band gap due to the corresponding decrease of vacancies content, which results increase in the band gap energy [195]. Another reason for explaining the increase in band gap energy may be correlated with the Burstein-Moss (BM) shift [137],

$$\Delta E_g^{BM} = \frac{h^2}{2m_{vc}^*} (3\pi^2 n_e)^{2/3} \qquad (4.16)$$

Here, $m_{vc}^*$ is effective mass of electrons, $n_e$ is the electron concentration and $h$ is the Planck's constant. Now, according to BM effect, above the Mott critical density, the increased number of free electron concentration is leading to fill 4f level partially, which in turn blocks the lowest states and led to band gap widening [137, 196]. With incorporation of $Gd^{3+}$ ions into $CeO_2$ sample, the crystalline size is reduced (as shown in Table 4.1). Therefore, the charge carriers are more confined in the small sized particles, which in turn increasing the band gap energy at lower doping concentration of $Ce_{1-x}Gd_xO_2$ NPs. This implies that, both particle size and BM effect results in the increase in band gap energy. Besides that, the red shift in band gap energy with higher fluencies of $Gd^{3+}$ ions ($x$ = 0.06, 0.08 and 0.10) is caused with the existence of $Ce^{3+}$ contents at the grain boundaries, which increases with decreasing particle size [197]. The refractive index of pure $CeO_2$ and $Ce_{1-x}Gd_xO_2$ ($x$ = 0.02, 0.04, 0.06, 0.08, and 0.10) NPs have been calculated by using the following formula [140]:

$$\frac{n^2 - 1}{n^2 + 2} = 1 - \sqrt{\frac{E_g}{20}} \qquad (4.17)$$

The obtained values for the refractive index of pure $CeO_2$ and $Ce_{1-x}Gd_xO_2$ ($x$ = 0.02, 0.04, 0.06, 0.08, and 0.10) NPs are tabulated in the Table 4.1. These values indicates that the refractive index is found to decrease with fluency of Gd-ions up to optimal doping concentration of $x$ = 0.04, whereas it is increased for further fluencies ($x$ = 0.06, 0.08 and 0.10) of $Gd^{3+}$ ions in $CeO_2$ NPs.

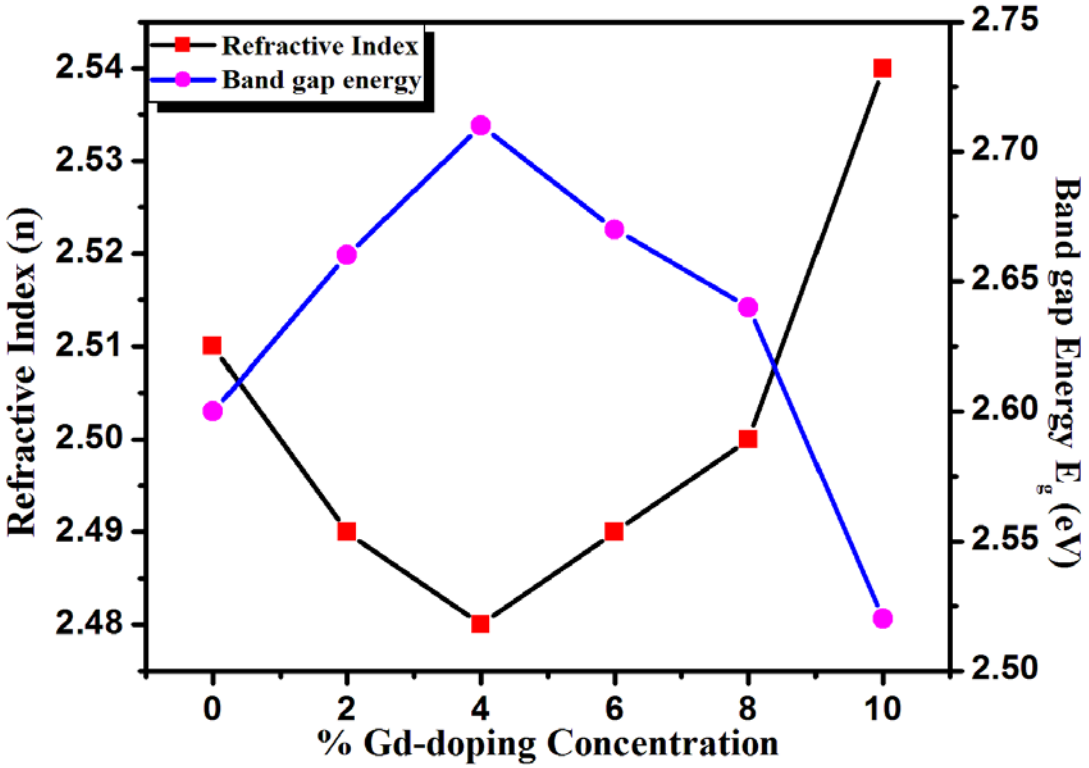


**Figure 4.6: Variation of refractive index and bang gap energy with Gd-doping concentration in pure $CeO_2$ sample.**

The variation in the refractive index and band gap energy has been shown in Figure 4.6 with different concentration of Gd-ions in $CeO_2$ NPs. Therefore, absorption of UV light at low concentration of Gd-ions ($x$ = 0.02 and 0.04) in $CeO_2$ NPs has been increased due to reduction of particle size as well as refractive index, whereas, due to increasing doping concentration the transparency and UV protection qualities are decreased [39].

#### 4.3.2.2. Raman Analysis

SERS is a powerful vibrational technique which allows for highly sensitivity structural detection of low concentration analyses through the amplification of electromagnetic fields generated by the excitation of localized surface plasmons [198]. SERS provides the same information as traditional Raman spectroscopy does, but with enhanced signals. It can easily detect additional modes that cannot be observed in the traditional Raman spectrum. Therefore, SERS has been used for getting information of different modes presented in pure $CeO_2$ and $Ce_{1-x}Gd_xO_2$ ($x$ = 0.02, 0.04, 0.06, 0.08, and 0.10) NPs samples.

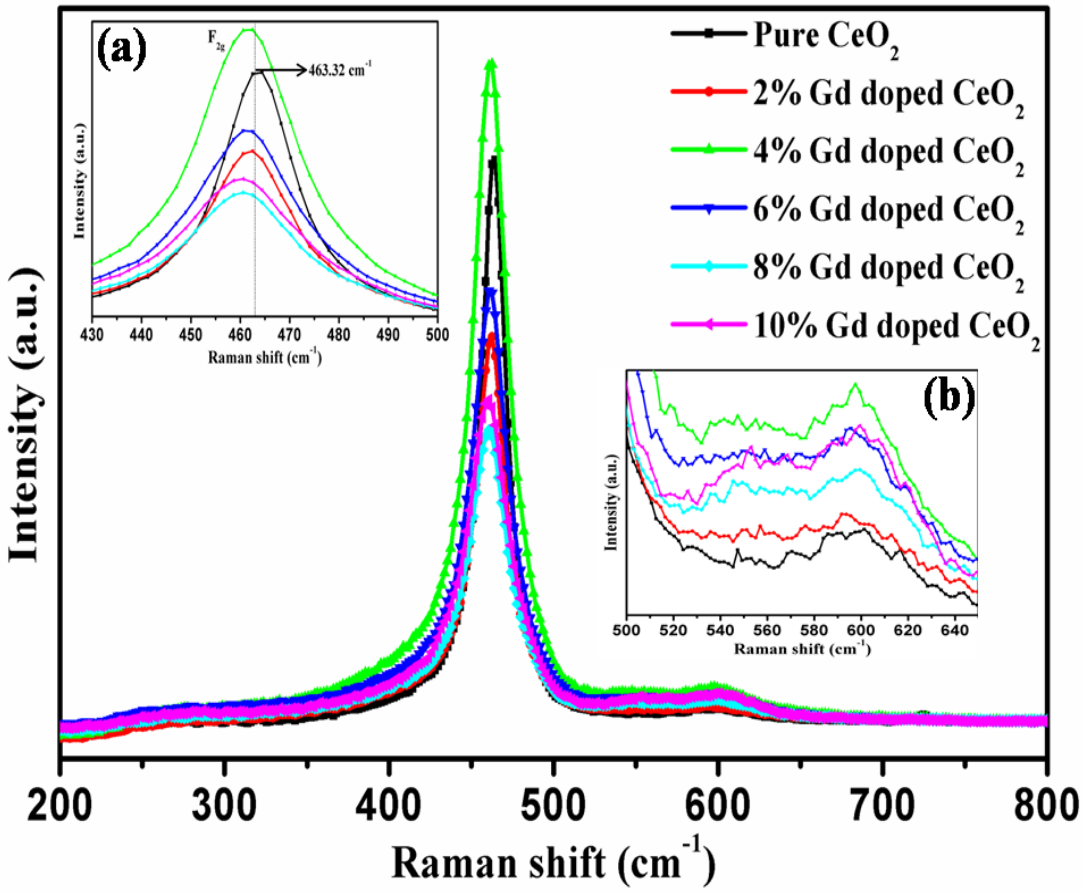


**Figure 4.7: Raman spectra of pure $CeO_2$ and Gd-doped $CeO_2$ NPs. Inset (a) and (b) of figure contains the enlarge views of their corresponding Raman spectra in the 430-500 cm$^{-1}$ energy range related to $F_{2g}$ mode and 500-650 cm$^{-1}$ range related to oxygen defects, respectively.**

Figure 4.7 shows Raman active ($F_{2g}$) mode for pure $CeO_2$ and $Ce_{1-x}Gd_xO_2$ ($x$ = 0.02, 0.04, 0.06, 0.08 and 0.10) samples, at 463.3 cm$^{-1}$ and in the range of 461.4-459.5 cm$^{-1}$, respectively, which is assigned for first-order scattering [199]. This Raman active mode is attributed to a symmetrical stretching mode of Ce-O8 vibration unit. Therefore, this mode is very sensitive for any disorder in the oxygen sub lattice results from non-stoichiometry of $CeO_2$ [200]. We can see from Figure 4.7, the absence of characteristic band for $Gd_2O_3$ (360 cm$^{-1}$) that confirms the absence of any impurity phase in the lattice, in agreement with XRD results [150, 151]. $F_{2g}$ mode corresponding to pure $CeO_2$ and $Ce_{1-x}Gd_xO_2$ is slightly shifted towards lower wavenumber side (or lower energy side) and broadening in its

FWHM can also be observed with doping fluencies of $Gd^{3+}$ ions in $CeO_2$ sample. These structural changes in Raman spectra with Gd-doping is attributed to the inhomogeneous strain and defects caused by substitution at the smaller radii $Ce^{4+}$ (0.097 nm) site by larger ionic radii $Gd^{3+}$ (0.1053 nm) ions [157]. In addition of $F_{2g}$ mode, weak intensity second-order Raman peaks are also obtained at 598.5 $cm^{-1}$ and 595.6 $cm^{-1}$ for pure $CeO_2$ and 2% Gd-doped $CeO_2$, respectively, generated due to non degenerated longitudinal optical (LO) mode [158]. These peaks are assigned to defect space that include intrinsic oxygen vacancies due to non-stoichiometry of $CeO_2$. The three possible defect induced mechanism for oxygen vacancies in pure $CeO_2$ sample can be given as [146]:

$$\boldsymbol{Ce_{Ce} + 2O_O \rightarrow V^{''''} + 2V_O^{\cdot\cdot} + CeO_2} \qquad (\mathbf{4.18})$$

$$\boldsymbol{Ce_{Ce} \rightarrow V_{Ce}^{''''} + Ce_i^{\cdot\cdot\cdot\cdot}} \qquad (\mathbf{4.19})$$

$$\boldsymbol{O_O \rightarrow V_O^{\cdot\cdot} + O_i^{''}} \qquad (\mathbf{4.20})$$

Since, these peaks are generated for maintaining the electrically neutrality in the system, therefore all Ce-ions not only shows $Ce^{4+}$ state but also $Ce^{3+}$ state. For doing so, oxygen ($O^{2-}$) ions are released from the structure and finally oxygen vacancies are formed in the system. The intensity of this peak is increased with incorporation of Gd-ions indicates the rise of oxygen vacancies in $CeO_2$ lattice. With increasing the fluency of Gd-ions, two weak second-order Raman modes in the range of 554.3-558 $cm^{-1}$ and 598-600.1 $cm^{-1}$ are also obtained (as shown in the inset (b) of Figure 4.7). The Raman mode in the range of 554.3-558 $cm^{-1}$ is related to the extrinsic oxygen vacancies, which are generated due to charge compensating defects due to substitution of $Ce^{4+}$ ions by $Gd^{3+}$ ions. The possible disorder mechanism for extrinsic oxygen vacancies in $Ce_{1-x}Gd_xO_2$ ($x$ = 0.02, 0.04, 0.06, 0.08, and 0.10) NPs can be given as [153]:

$$\boldsymbol{Gd_2O_3 + 2Ce_{Ce}^{x} + O_O^{x} \rightarrow 2Gd_{Ce}^{'} + V_O^{\cdot\cdot} + 2CeO_2} \qquad (\mathbf{4.21})$$

Where symbols have following meaning as; $Ce_{ce}^{x}$ and $Gd_{Ce}^{'}$ are $Ce^{4+}$ and $Gd^{3+}$ ions on the $CeO_2$ lattice site, respectively, $O_O^{x}$ is $O^{-2}$ ions on an oxygen lattice site, and $V_O^{\cdot\cdot}$ is neutral oxygen vacancy site. In addition, another vacancy peak can

also be observed in the range of 598-600.1 $cm^{-1}$, which is assigned to the defect space including intrinsic oxygen vacancies due to reduction of $Ce^{4+}$ to $Ce^{3+}$ i.e. non-stoichiometry of $CeO_2$ [146]. The possible disorder reaction for intrinsic oxygen vacancies in the sample can be given as [156]:

$$\boldsymbol{2Ce_{Ce}^{x} + O_{O}^{x} \rightarrow 2Ce_{Ce}^{'} + V_{O}^{\cdot\cdot} + 1/2\, O_2(g)} \qquad (\mathbf{4.22})$$

Where symbols have following meaning as; $Ce_{ce}^{x}$ and $Ce_{Ce}^{'}$ are $Ce^{4+}$ and $Ce^{3+}$ ions on the Ce lattice site, respectively, $O_O^x$ is $O^{-2}$ ions on an oxygen lattice site, and $V_O^{\cdot\cdot}$ is neutral oxygen vacancy site [141]. As shown in the inset (b) of Figure 4.7, the intensity of intrinsic and extrinsic oxygen vacancies mode increases with doping fluency up to $x$ = 0.04. With further increase in fluency, the intensity of this mode decreases and then again increases at $x$ = 0.10 concentration. The variation of intensity of vacancy mode is related to the concentration of oxygen vacancies. The quantitative estimation of oxygen vacancies of pure $CeO_2$ and $Ce_{1-x}Gd_xO_2$ samples are made from the relative peak area of vacancy modes (intrinsic and extrinsic) with area of $F_{2g}$ mode. For doing so, Lorentzian fitting is done for measuring the peak area of the respected peaks. All calculated values are tabulated in Table 4.2, which indicates an increment in the concentration of oxygen vacancies with fluency of Gd-ions up to $x$ = 0.08 (i.e. maximum in this range) and then slightly decreased at $x$ = 0.10 concentration. The increment in the concentration of oxygen vacancies can be explained by considering, with incorporation and rising fluency of large radii $Gd^{3+}$ ions (0.1053 nm), the dislocation density as well as strain has been increased up to $x$ = 0.08 doping concentration in $CeO_2$. Due to this reason every two $Gd^{3+}$ ions substituted the smaller radii $Ce^{4+}$ (0.097 nm) ions increases the probability of oxygen ion ($O^{2-}$) to leave the $CeO_2$ lattice to maintain electrical neutrality in the lattice and creates more oxygen vacancies (as shown in Figure 4.8) [154]. In addition to that, pure $CeO_2$ and Gd-doped $CeO_2$ samples also exhibit one more extra weak second-order Raman mode at 1064.9 $cm^{-1}$ and in the range of 1173.9-1175.3 $cm^{-1}$, (as shown in Table 4.2), which are assigned to 2LO mode that emanate from the second order scattering of the surface superoxide species ($O_2^-$), and has small

additional contribution from $F_{2g}$ symmetry (which is not mentioned in Figure 4.7) [199, 141].

The particle size of pure $CeO_2$ and $Ce_{1-x}Gd_xO_2$ samples has been being calculated from Raman spectra using the equation:

$$\boldsymbol{\Gamma\ (cm^{-1}) = 10 + \left(\frac{124.7}{D}\right)\ nm} \qquad (\mathbf{4.23})$$

Where, Γ ($cm^{-1}$) is FWHM of Raman active ($F_{2g}$) mode and D is particle size of pure $CeO_2$ and $Ce_{1-x}Gd_xO_2$ samples [158, 159]. The calculated particle size from Raman spectra is in good agreement with the particle size calculated from XRD and TEM images (as shown in Table 4.1). The quantitative estimation of the overall concentration of oxygen vacancies have been made by the peak area of the oxygen vacancies $A_{O_v}$ corresponding to 598.5 $cm^{-1}$ and 595.6 $cm^{-1}$ for pure $CeO_2$ and 2% Gd-doped $CeO_2$. The relative ratios of $A_{(O_v)_1}$, $A_{(O_v)_2}$ and $A_{F_{2g}}$ bands, which are corresponding to 554.3-558 $cm^{-1}$, 598-600.1 $cm^{-1}$ and for $F_{2g}$ band is also calculated to estimate the oxygen vacancies concentration for further doping concentrations of Gd for 4% onwards. The calculated values are shown in Figure 4.8.

**Table 4.2: The Position of Raman active modes ($cm^{-1}$) from Raman spectra and relative peak area ratio**

| Sample | Position of Raman active mode ($cm^{-1}$) and Vibrational Mode | | | | | | |
|---|---|---|---|---|---|---|---|
| | First-order Scattering | Second-order Scattering[142,147] | | | | | |
| | $F_{2g}$ | $A_{1g}$ $(O_v)$ | $A_{1g} + F_{2g}$ $(O_v)_1$ | $A_{1g} + E_g + F_{2g}$ $(O_v)_2$ | $2LO$ | $A_{O_v} / A_{F_{2g}}$ | $\frac{(A_{(O_v)_1} + A_{(O_v)_2})}{A_{F_{2g}}}$ |
| **Pure $CeO_2$** | 463.3 | 598.5 | - | - | 1064.9 | 0.036 | - |
| $Ce_{0.98}Gd_{0.02}O_2$ | 461.4 | 595.6 | - | - | 1173.9 | 0.076 | - |
| $Ce_{0.96}Gd_{0.04}O_2$ | 460.9 | - | 554.3 | 598 | 1175.6 | - | 0.084 |
| $Ce_{0.94}Gd_{0.06}O_2$ | 460.5 | - | 554.9 | 597 | 1176 | - | 0.114 |
| $Ce_{0.92}Gd_{0.08}O_2$ | 459.8 | - | 555.6 | 598.3 | 1175.7 | - | 0.121 |
| $Ce_{0.90}Gd_{0.10}O_2$ | 459.5 | - | 558 | 600.1 | 1175.3 | - | 0.119 |

**Note: Vibrational modes corresponding to Second-order Scattering were given based on the Ref. [142, 147].**

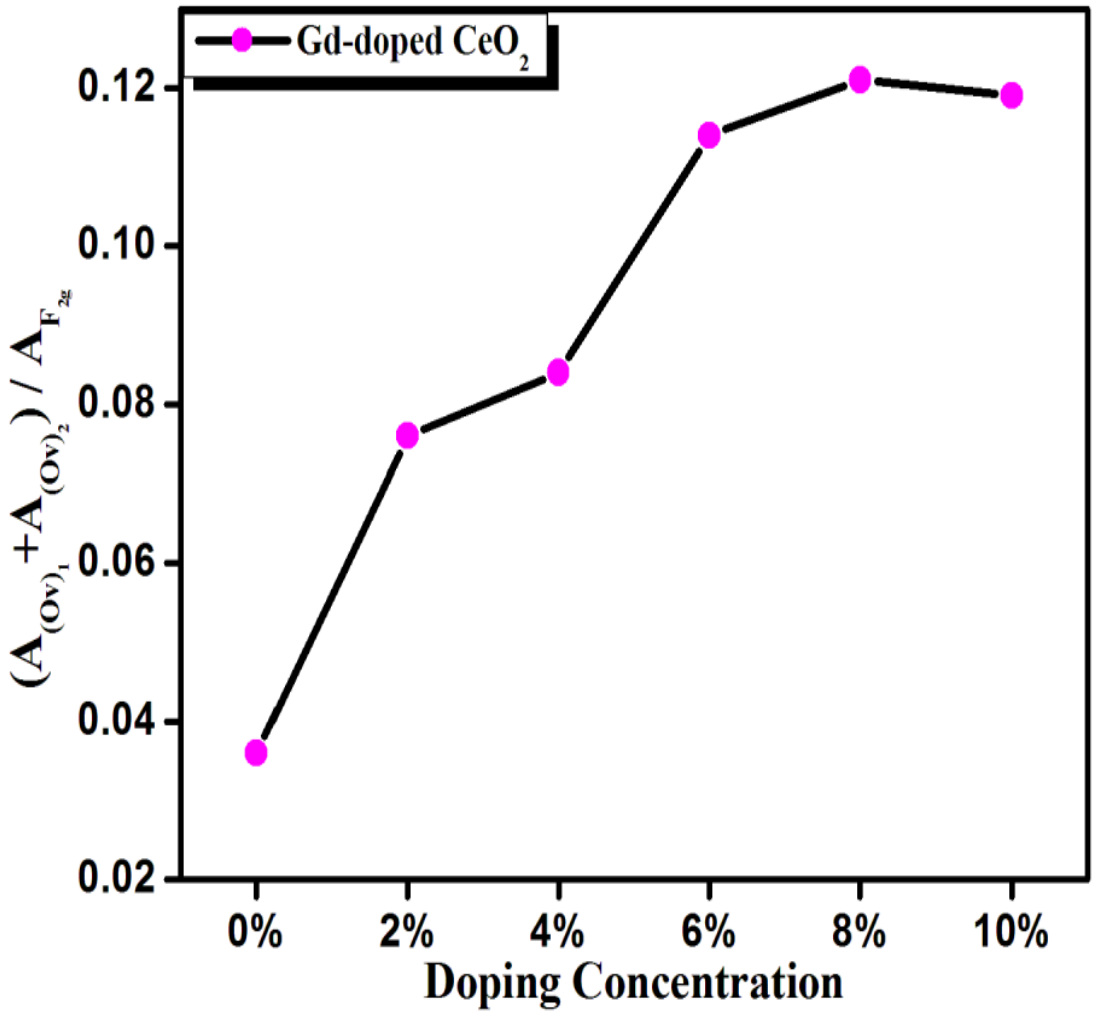


**Figure 4.8: Relative peak area ratio for bands of oxygen vacancies and $F_{2g}$ mode for pure $CeO_2$ and Gd-doped $CeO_2$ (for 2%, 4%, 6%, 8% and 10%) samples.**

This relative peak area ratio of oxygen vacancies and $F_{2g}$ mode is calculated by fitting the Lorentzian function for the corresponding modes. Ratio $A_{O_v}/A_{F_{2g}}$ for pure $CeO_2$ and 2% Gd-doped $CeO_2$, whereas, $(A_{(Ov)_1} + A_{(Ov)_2})/A_{F_{2g}}$ ratios are calculated for $Ce_{1-x}Gd_xO_2$ (for $x$ = 0.04, 0.06, 0.08 and 0.10) samples. From these calculated values one can infer that the relative oxygen vacancy concentration is found to gradually increase with fluencies of $Gd^{3+}$ ions in $CeO_2$ NPs.

### 4.3.3. Electronic Structure Properties

#### 4.3.3.1. XPS analysis

##### 4.3.3.1.1. Ce 3d XPS Spectra

The chemical composition and the valence state of the pure $CeO_2$ and $Ce_{1-x}Gd_xO_2$ ($x$ = 0.02, 0.04, 0.06, 0.08 and 0.10) NPs have been further characterized using XPS measurements of Ce 3d, Gd 4d, and O 1s core levels. Figure 4.9 illustrates the Ce 3d core level XP spectra of pure $CeO_2$ and $Ce_{1-x}Gd_xO_2$ ($x$ = 0.02, 0.04, 0.06, 0.08 and 0.10) samples. All binding energies have been corrected for the charge shift using the C 1s peak (binding energy = 284.6 eV) as reference [201]. The high-resolution Ce 3d core level spectra in the energy range of 880-930 eV has been deconvoluted by mean of Gaussian shape fitting as shown in Figure 4.9. These deconvoluted Ce 3d core-level spectra are generally characterized by distinct features which are related to the final-state occupation of Ce 4f level [202]. On Account of spin-orbit coupling, these deconvoluted Ce 3d core-level spectra are resolved into ten peaks, which includes six and four structures arise from $Ce^{4+}$ and $Ce^{3+}$ ions, respectively. These series of peaks are labelled as '*u*' and '*v*', which are due to $3d_{3/2}$ and $3d_{5/2}$ spin-orbit states, respectively [126]. The four peaks labelled with $v_o$, *v'*, $u_o$ and *u'* are characteristic peaks of $Ce^{3+}$, whereas, the peaks labelled with *v*, *v''*, *v'''*, *u*, *u''* and *u'''* are characteristic peaks of $Ce^{4+}$ (shown in Figure 4.9) [203]. The separation in binding energy between *v* and *u* spin-orbit doublets is found around ~18.4 eV for pure $CeO_2$, and for $Ce_{1-x}Gd_xO_2$ ($x$ = 0.02, 0.04, 0.06, 0.08 and 0.10) samples, which are in good agreement with the reported papers [204, 205]. We can see from the Ce 3d core level spectra that Ce ions are present in mixed valance state of both $Ce^{3+}$ and $Ce^{4+}$ for pure $CeO_2$ and $Ce_{1-x}Gd_xO_2$ samples. All peak positions for '*u*' and '*v*' of pure $CeO_2$ and $Ce_{1-x}Gd_xO_2$ NPs samples have been tabulated in Table 4.3.

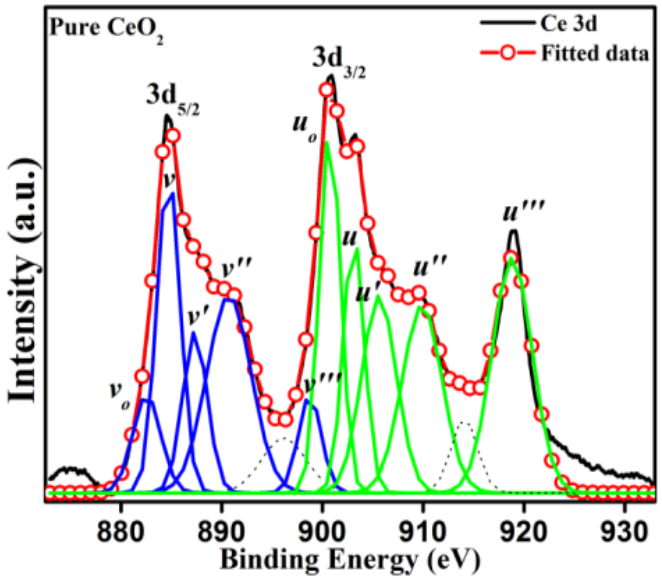
Pure CeO2
Ce 3d
Fitted data
3d5/2
3d3/2
v
vo
v'
v''
v'''
uo
u
u'
u''
u'''
Intensity (a.u.)
880
890
900
910
920
930
Binding Energy (eV)

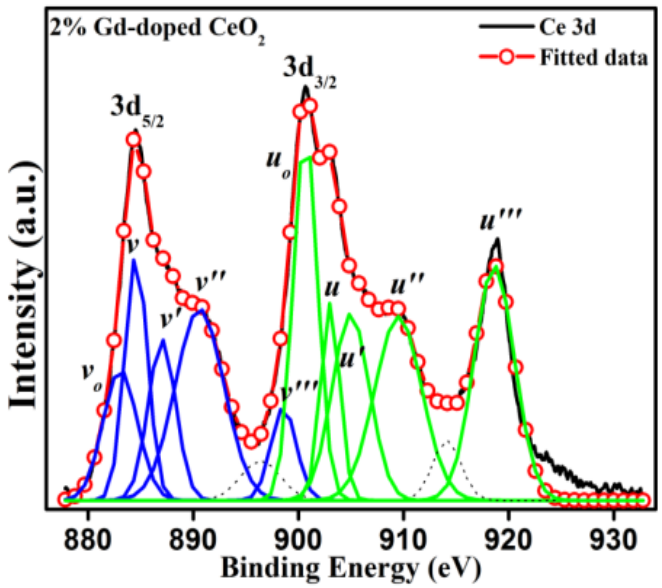
2% Gd-doped CeO2
Ce 3d
Fitted data
3d5/2
3d3/2
v
vo
v'
v''
v'''
uo
u
u'
u''
u'''
Intensity (a.u.)
880
890
900
910
920
930
Binding Energy (eV)

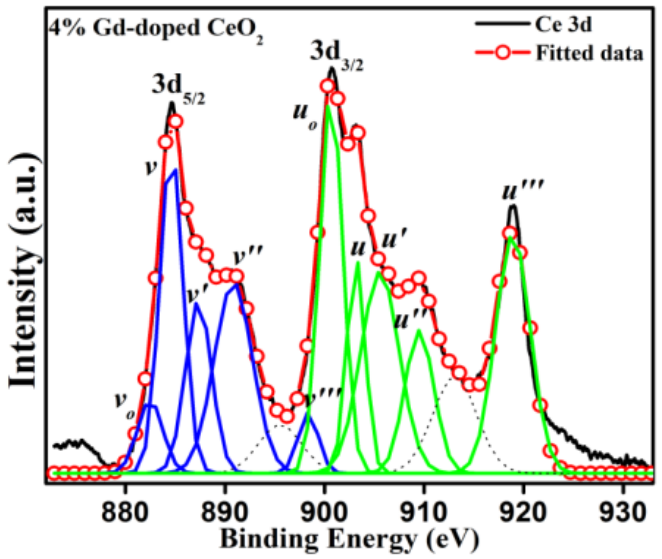
4% Gd-doped CeO2
Ce 3d
Fitted data
3d5/2
3d3/2
v
vo
v'
v''
v'''
uo
u
u'
u''
u'''
Intensity (a.u.)
880
890
900
910
920
930
Binding Energy (eV)

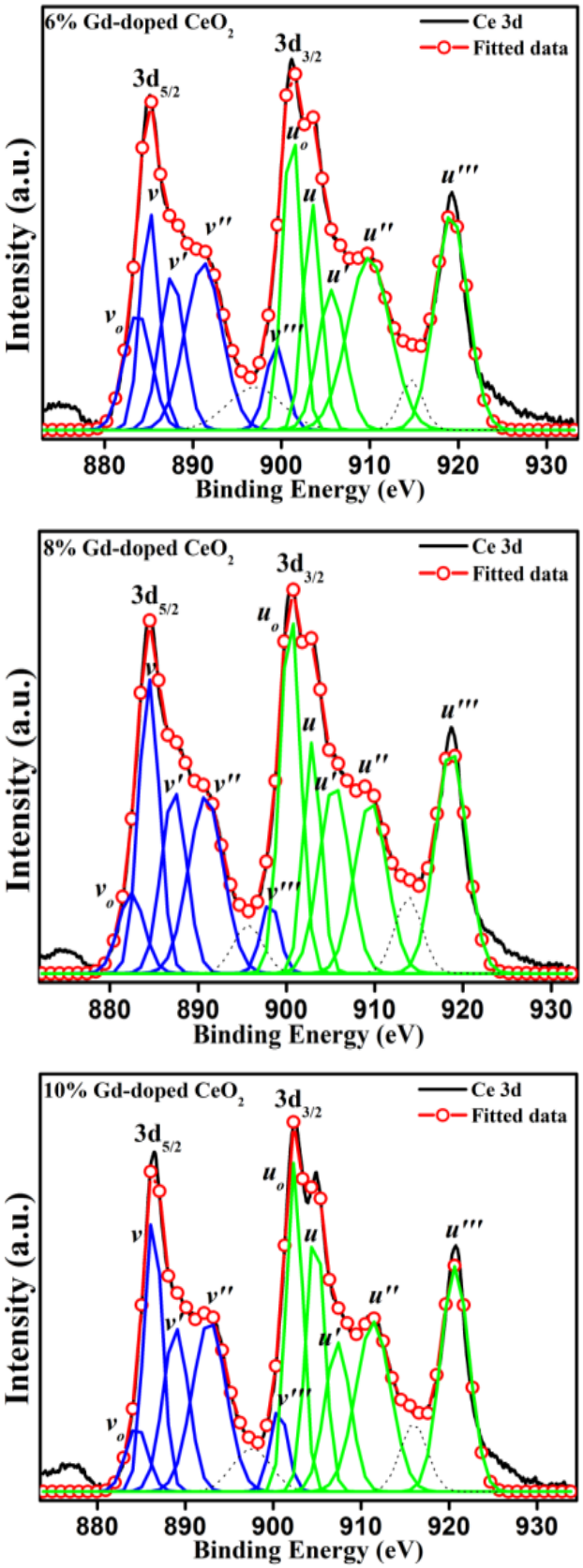


**Figure 4.9: Deconvoluted XPS spectra of Ce 3d profile of pure $CeO_2$ and $Ce_{1-x}Gd_xO_2$ ($x$ = 0.02, 0.04, 0.06, 0.08 and 0.10) samples**

The total concentration of $Ce^{3+}$ and $Ce^{4+}$ in the samples has been calculated using following formula [206],

$$\%\, \boldsymbol{Ce^{3+}} = \frac{\boldsymbol{A_{Ce^{3+}}}}{\boldsymbol{A_{Ce^{3+}} + A_{Ce^{4+}}}} \times \mathbf{100}\% \qquad (\mathbf{4.24})$$

$$\%\, \boldsymbol{Ce^{4+}} = \frac{\boldsymbol{A_{Ce^{4+}}}}{\boldsymbol{A_{Ce^{3+}} + A_{Ce^{4+}}}} \times \mathbf{100}\% \qquad (\mathbf{4.25})$$

Here, $A_{Ce^{3+}} = v_o + v' + u_o + u'$ and $A_{Ce^{4+}} = v + v'' + v''' + u + u'' + u'''$ are the sum of the integrated area of all characteristics peaks of $Ce^{3+}$ and $Ce^{4+}$, respectively. These calculated values are tabulated in Table 4.3. The quantitative ratio of $Ce^{3+}/Ce^{4+}$ shows that the concentration of $Ce^{3+}$ ions over $Ce^{4+}$ ions is gradually increasing for $Ce_{1-x}Gd_xO_2$ ($x$ = 0.00, 0.02 and 0.04) samples. While, at 6% Gd-doping concentration $Ce^{3+}/Ce^{4+}$ value is deceased, which is again increased and then decreased at 8% and 10% doping. This shows that due to incorporation of larger radii $Gd^{3+}$ ions (0.1053 nm) in $CeO_2$ NPs, replaces the smaller radii $Ce^{4+}$ ions (0.097 nm) and for maintaining the charge neutrality, the concentration of $Ce^{3+}$ ions (0.114 nm) are gradually increased for 2% and 4% doping concentrations.

**Table 4.3: Ce 3d XPS peak assignments for pure $CeO_2$ and $Ce_{1-x}Gd_xO_2$ ($x$ = 0.02, 0.04, 0.06, 0.08 and 0.10) samples**

| Sample | Peak assignment | $Ce\ 3d_{5/2}$ | | | | | $Ce\ 3d_{3/2}$ | | | | | $Ce^{3+}$ (%) | $Ce^{4+}$ (%) | $Ce^{3+}/Ce^{4+}$ |
|---|---|---|---|---|---|---|---|---|---|---|---|---|---|---|
| | | $v_o$ $Ce^{3+}$ | $v$ $Ce^{4+}$ | $v'$ $Ce^{3+}$ | $v''$ $Ce^{4+}$ | $v'''$ $Ce^{4+}$ | $u_o$ $Ce^{3+}$ | $u$ $Ce^{4+}$ | $u'$ $Ce^{3+}$ | $u''$ $Ce^{4+}$ | $u'''$ $Ce^{4+}$ | | | |
| **Pure $CeO_2$** | | 882.5 | 884.7 | 887.7 | 890.7 | 898.7 | 900.7 | 903.1 | 905.6 | 909.8 | 918.8 | 34.23 | 65.76 | 0.52 |
| $Ce_{0.98}Gd_{0.02}O_2$ | | 883 | 884.5 | 887 | 890.5 | 898.5 | 900.6 | 903 | 904.9 | 909.5 | 918.6 | 38.86 | 61.13 | 0.63 |
| $Ce_{0.96}Gd_{0.04}O_2$ | **Binding energy (eV)** | 882.4 | 884.6 | 887.3 | 890.8 | 898.3 | 900.6 | 903.1 | 905.5 | 909.5 | 918.9 | 41.36 | 58.63 | 0.70 |
| $Ce_{0.94}Gd_{0.06}O_2$ | | 883.7 | 885.1 | 887.6 | 891.2 | 899.3 | 901.1 | 903.4 | 905.6 | 909.9 | 919.2 | 35.04 | 64.95 | 0.54 |
| $Ce_{0.92}Gd_{0.08}O_2$ | | 882.4 | 884.4 | 887.2 | 890.8 | 898.1 | 900.4 | 902.9 | 905.4 | 909.5 | 918.6 | 39.50 | 60.49 | 0.65 |
| $Ce_{0.90}Gd_{0.10}O_2$ | | 884.4 | 886.3 | 888.9 | 892.7 | 900.6 | 902.4 | 904.7 | 907.3 | 911.3 | 920.6 | 33.61 | 66.38 | 0.51 |

The presence of $Ce^{3+}$ can be due to either due to the formation of $Ce_2O_3$ or creation of oxygen vacancies in $CeO_2$ lattice. This can be verified by calculating the stoichiometry ratios $x = [O]/[Ce]$ and $x' = [O_{1s}]/[Ce_{3d}]$, which can be estimated from their integrated peak area while considering their sensitivity factor. In order to calculate oxygen content in the samples, we assume that the total oxygen content is the sum of the required oxygen to fully oxidize $Ce^{3+}$ and $Ce^{4+}$ to form $Ce_2O_3$ and $CeO_2$. Then, considering the stoichiometry $x = [O]/[Ce]$, which is equal to 1.5 for $Ce_2O_3$ and 2 for $CeO_2$. Now, the stoichiometric ratio of the oxygen to the total Ce ions ($Ce^{3+}$+$Ce^{4+}$) can be determined using the concentration of [$Ce^{3+}$] and [$Ce^{4+}$] as given in Table 4.4 according to the following equation [197],

$$\boldsymbol{x = \frac{[O]}{[Ce]} = \frac{3}{2} \times [Ce^{3+}] + 2 \times [Ce^{4+}]} \qquad (\mathbf{4.26})$$

The stoichiometry calculated from equation (4.26) has been compared with the actual stoichiometry determined from the XPS integrated area $A_O$ and $A_{Ce}$ of the O 1s and Ce 3d peaks, respectively, which has been calculated according to the following equation [207]:

$$\boldsymbol{x' = \frac{O_{1s}}{Ce_{3d}} = \frac{A_O}{A_{Ce}} \times \frac{S_{Ce}}{S_O}} \qquad (\mathbf{4.27})$$

Where, $S_{Ce}$ = 7.399 and $S_O$ = 0.711 are the sensitivity factors of the Ce and O atoms, respectively [208]. Figure 4.10 shows the stoichiometry variation with the concentration of Gd-dopant determined by both methods, *x* and *x'*, which is provided the concentration of $Ce^{3+}$ and $Ce^{4+}$ ions in pure $CeO_2$ and $Ce_{1-x}Gd_xO_2$ (*x* = 0.02, 0.04, 0.06, 0.08 and 0.10) samples (as listed in Table 4.4).

**Table 4.4: Concentration of $Ce^{3+}$ and $Ce^{4+}$ ions and Stoichiometry $x = [O]/[Ce]$ and $x' = [O_{1s}]/[Ce_{3d}]$ of the pure $CeO_2$ and $Ce_{1-x}Gd_xO_2$ (x = 0.02, 0.04, 0.06, 0.08 and 0.10) samples.**

| Sample | $[Ce^{3+}]$ | $[Ce^{4+}]$ | $x = [O]/[Ce]^a$ | $x' = [O_{1s}]/[Ce_{3d}]^b$ |
|---|---|---|---|---|
| **Pure $CeO_2$** | 0.342 | 0.657 | 1.83 | 2.73 |
| $Ce_{0.98}Gd_{0.02}O_2$ | 0.388 | 0.611 | 1.80 | 1.84 |
| $Ce_{0.96}Gd_{0.04}O_2$ | 0.413 | 0.586 | 1.79 | 1.60 |
| $Ce_{0.94}Gd_{0.06}O_2$ | 0.350 | 0.649 | 1.82 | 1.71 |
| $Ce_{0.92}Gd_{0.08}O_2$ | 0.395 | 0.604 | 1.80 | 1.51 |
| $Ce_{0.90}Gd_{0.10}O_2$ | 0.336 | 0.663 | 1.83 | 1.61 |

**[a]Using Eq. (4.26) and [b]Using Eq. (4.27)**

Although, the calculated values of actual stoichiometry (*x'*) is higher than that (*x*) calculated by Eq. (4.26) for pure $CeO_2$ and $Ce_{0.98}Gd_{0.02}O_2$ sample, which exhibits low concentration of $Ce^{3+}$ ions for pure $CeO_2$ NPs in comparison with $Ce_{0.98}Gd_{0.02}O_2$ sample. This means that due to incorporation of $Gd^{3+}$ ions in $CeO_2$ NPs, $Gd^{3+}$ ions replaces the $Ce^{4+}$ ions with formation of oxygen vacancies in the $Ce_{0.98}Gd_{0.02}O_2$ sample. On the other hand, the value of (*x'*) is smaller than (*x*) for 4%, 6%, 8% and 10% doping concentrations, which suggested that the entire $Ce^{3+}$ ions are consumed in the formation of $Ce_2O_3$. Simultaneously, the oxygen deficiency with increasing $Ce^{3+}$ ions suggests that $Ce^{3+}$ ions are associated with $Ce_2O_3$ as well as oxygen vacancies in $CeO_2$ and both kinds may coexist in 4%, 6%, 8% and 10% Gd-doped $CeO_2$ samples. This means that core level Ce 3d spectra prove the existence of $Ce_2O_3$ in the Gd-doped $CeO_2$ samples, while from XRD analysis only $CeO_2$ is identified. This $Ce_2O_3$ phase has amorphous character indicates that this phase is located at the grain surface and at the grain boundaries. *Patsalas et al*. [197], has reported a dimensional analysis which determined that $Ce_2O_3$ and $CeO_2$ are located at grain surface and volume, respectively.

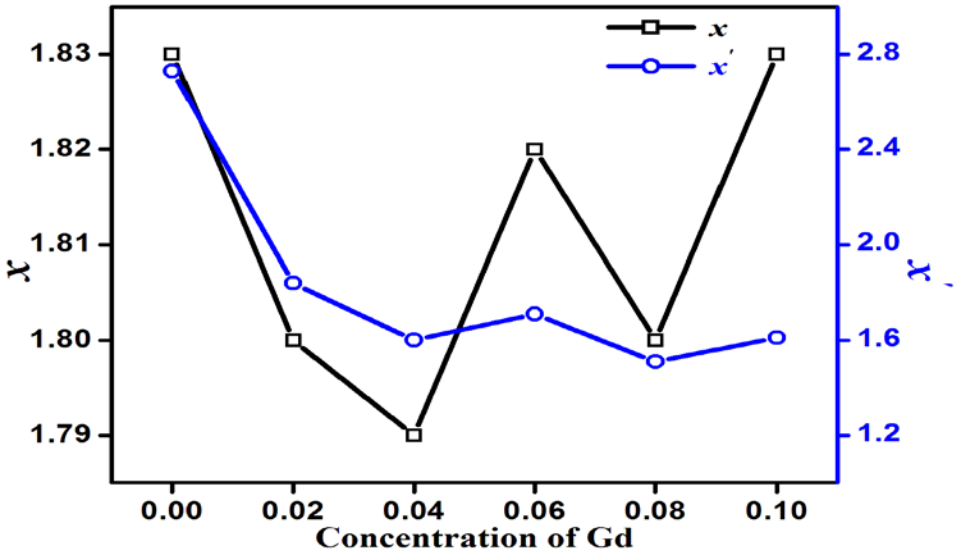


**Figure 4.10: The $CeO_x$ stoichiometry for pure $CeO_2$ and $Ce_{1-x}Gd_xO_2$ ($x$ = 0.02, 0.04, 0.06, 0.08 and 0.10) samples calculated from stoichiometry ratio $x = [O]/[Ce]$ and $x' = [O_{1s}]/[Ce_{3d}]$**

A linear correlation can be established between third power of $[Ce^{4+}]$ (grain volume distribution) as well as third power of D (which is proportional to the grain volume $V_g$) with square of $[Ce^{3+}]$ (surface distribution).

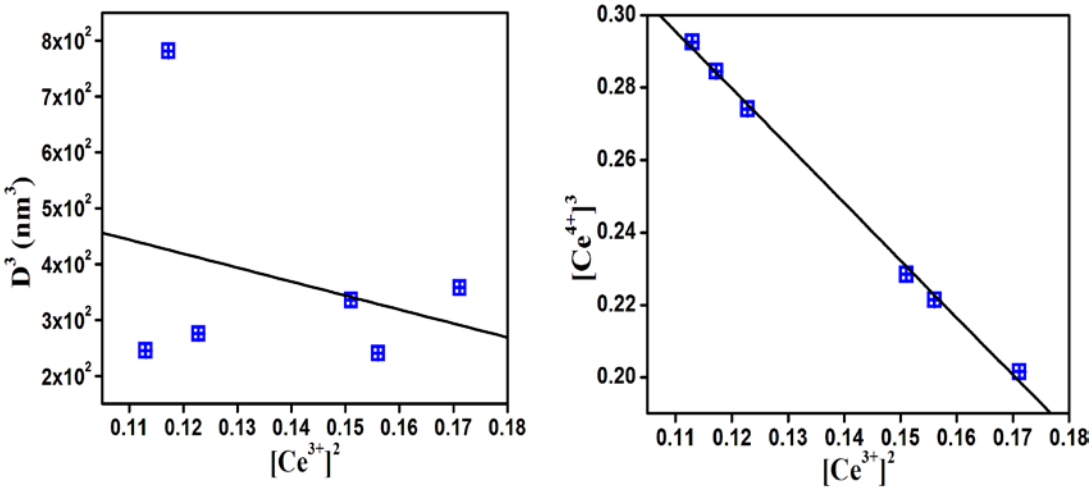


**Figure 4.11: The correlation of the $[Ce^{3+}]^2$ with $[Ce^{4+}]^3$ and grain volume ($V_g \propto D^3$), showing that $Ce^{3+}$ and $Ce^{4+}$ ions are located at the grain surface and volume, respectively.**

Figure 4.11 shows a linear relation between $[Ce^{3+}]^2$ and $[Ce^{4+}]^3$ that confirms the distribution of $Ce_2O_3$ and $CeO_2$ at the grain surface and volume. While, the experimental points of $D^3$ vs $[Ce^{3+}]^2$ are more scattered around straight line of the

dimensional analysis, which is attributed to the strain in the grain that affects the broadening of the XRD peaks with Gd-doping in $CeO_2$ samples. From Table 4.4, it can also be seen that the difference between *x* and *x'* increases and decreases with increase and decrease of $Ce^{3+}$ ions for $Ce_{1-x}Gd_xO_2$ (*x* = 0.04, 0.06, 0.08 and 0.10) samples, which shows an up and down in the formation of oxygen vacancies in these samples.

#### 4.3.3.1.2. O 1s XPS Spectra

The O 1s spectra for pure $CeO_2$ and $Ce_{1-x}Gd_xO_2$ (*x* = 0.02, 0.04, 0.06, 0.08 and 0.10) samples are shown in Figure 4.12. The asymmetrical O 1s core level spectra in the binding energy range ~526-540 eV are deconvoluted into four peaks to determine the surface concentration of oxygen ions for all samples. The deconvoluted binding energy peaks of O 1s core level spectra at ~528.6-529.9 eV can be assigned to the lattice oxygen $O^{2-}$ (denoted as $O_L$) in pure $CeO_2$ and $Ce_{1-x}Gd_xO_2$ (*x* = 0.02, 0.04, 0.06, 0.08 and 0.10) samples, while peak at higher binding energy side ~530.3-533.3 eV and ~533.5-536.4 eV are possibly assigned to oxygen vacancies (denoted as $O_V$) corresponds to $Ce^{3+}$ species originated from $Ce_2O_3$ [209] and formation of hydroxyl or absorbed $H_2O$ species [210] (denoted as $O_\alpha$ and $O_\beta$) on the surface of the samples, respectively (as shown in Table 4.5) [211, 212].

As shown in Figure 4.12, all the samples are showing the similar O 1s core level spectra, which is also used as another source of information about Ce oxidation state. Since, it is well known that the electro-negativity of Gd ion (1.21) is higher than Ce ion (1.12) on Pauling scale, therefore, O 1s peak from $Gd_2O_3$ should be at higher binding energy than that from metal oxide $CeO_2$ [213]. Thus, due to incorporation of $Gd^{3+}$ ions in the lattice of $CeO_2$, not only the intensity of the lattice oxygen peak ($O_L$) but also oxygen vacancies peak ($O_V$) is found to increase for 2% Gd-doped $CeO_2$ NPs. The quantitative estimation of $O_L$ and $O_V$ peaks show that due to incorporation of $Gd^{3+}$ ions the oxygen vacancies are formed on the surface of the Gd-doped $CeO_2$ samples. These vacancies are found to show variation with change in the concentration of Gd-ions in the $CeO_2$ NPs. Furthermore, as 1s electron of oxygen atom attached more tightly bound to $Ce^{3+}$ rather than $Ce^{4+}$ oxidation state. Thus, change in the oxidation state of Ce-ions (+4 to +3) due to incorporation of $Gd^{3+}$ ions in the $CeO_2$ NPs, may also be responsible for the change in the formation of oxygen vacancies.

**Table 4.5: XPS binding energies of individual peaks of O 1s spectra for pure $CeO_2$ and $Ce_{1-x}Gd_xO_2$ ($x$ = 0.02, 0.04, 0.06, 0.08 and 0.10) samples**

| Sample | O 1s Peak position | | | | | |
|---|---|---|---|---|---|---|
| | Lattice oxygen species ($O_L$) | | Oxygen vacancy species ($O_V$) | | $OH^-$ group species BE (eV) | |
| | BE (eV) | $\%O_L = \frac{A_{O_L}}{A_{O_L} + A_{O_V}} \times 100$ | BE (eV) | $\%O_V = \frac{A_{O_V}}{A_{O_L} + A_{O_V}} \times 100$ | ($O_\alpha$) | ($O_\beta$) |
| **Pure $CeO_2$** | 529.8 | 35.94 | 532.9 | 64.05 | 533.6 | 535.7 |
| $Ce_{0.98}Gd_{0.02}O_2$ | 528.6 | 28.16 | 530.3 | 71.84 | 533.5 | 535.5 |
| $Ce_{0.96}Gd_{0.04}O_2$ | 529.3 | 28.41 | 532.4 | 71.58 | 533.7 | 535.9 |
| $Ce_{0.94}Gd_{0.06}O_2$ | 529.8 | 35.79 | 532.6 | 64.20 | 533.9 | 536.1 |
| $Ce_{0.92}Gd_{0.08}O_2$ | 529.2 | 26.60 | 532.2 | 73.40 | 533.5 | 535.7 |
| $Ce_{0.90}Gd_{0.10}O_2$ | 529.9 | 33.32 | 533.3 | 66.70 | 534.1 | 536.3 |

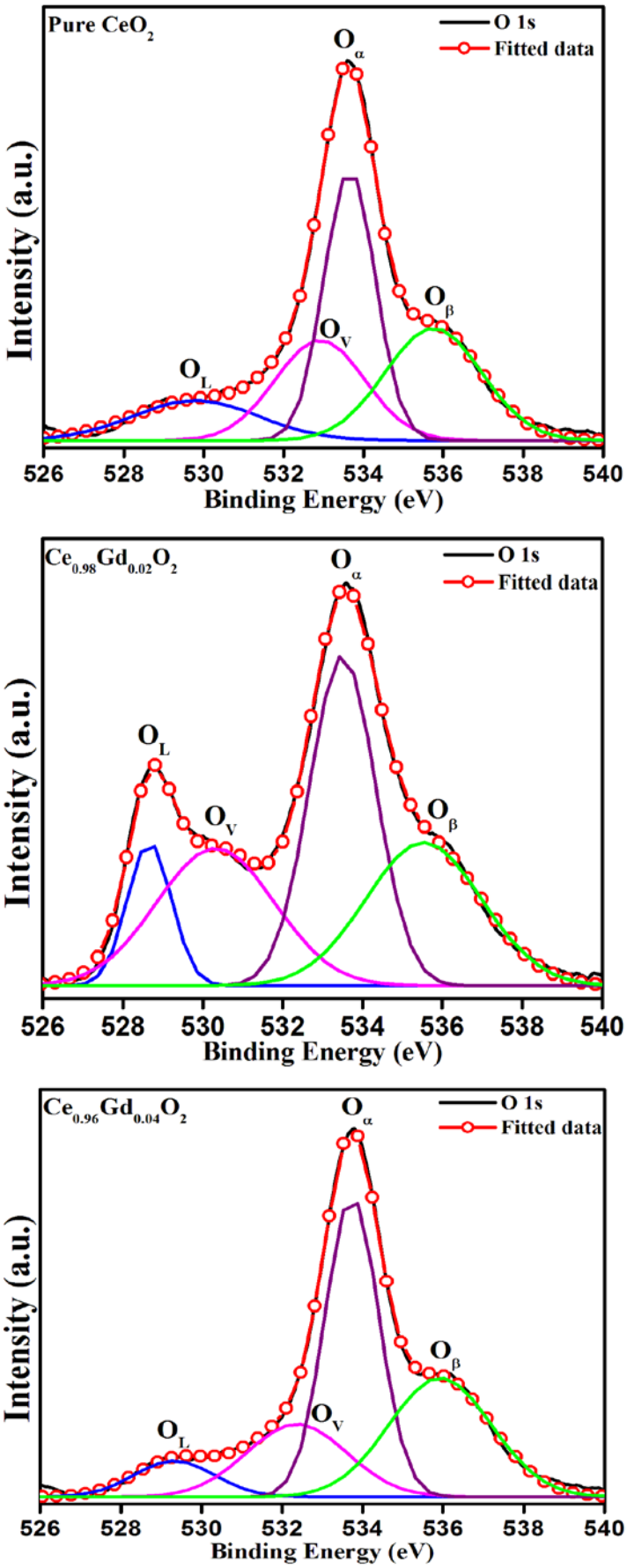
Pure CeO2
O 1s
Fitted data
Oα
Oβ
OV
OL
Intensity (a.u.)
526 528 530 532 534 536 538 540
Binding Energy (eV)
Ce0.98Gd0.02O2
O 1s
Fitted data
Oα
OL
OV
Oβ
Intensity (a.u.)
526 528 530 532 534 536 538 540
Binding Energy (eV)
Ce0.96Gd0.04O2
O 1s
Fitted data
Oα
Oβ
OV
OL
Intensity (a.u.)
526 528 530 532 534 536 538 540
Binding Energy (eV)

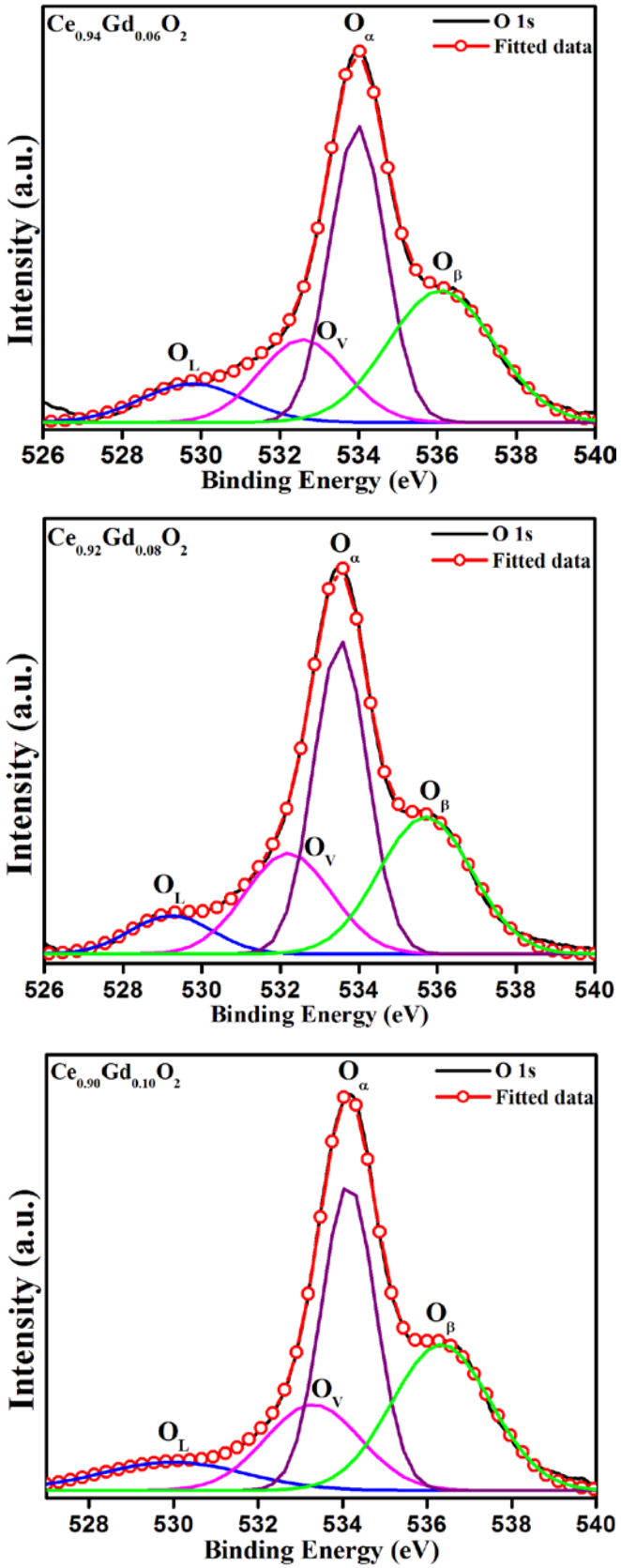


**Figure 4.12: Deconvoluted core level spectra of O 1s profile for pure $CeO_2$ and $Ce_{1-x}Gd_xO_2$ ($x$ = 0.02, 0.04, 0.06, 0.08 and 0.10) samples.**

The quantitative percentage of $Ce^{3+}$ oxidation state from core level spectra of Ce 3d for pure $CeO_2$ and $Ce_{1-x}Gd_xO_2$ ($x$ = 0.02, 0.04, 0.06, 0.08 and 0.10) samples, if compared with quantitative percentage of $O_V$ from O 1s core level spectra, one can infer that the increasing $Ce^{3+}$ concentration is also helpful in increasing the oxygen vacancies on the surface of samples (as shown in Table 4.3 and 4.5) along with the percentage increase in the concentration of the $Gd^{3+}$ ions.

#### 4.3.3.1.3. Gd 4d XPS Spectra

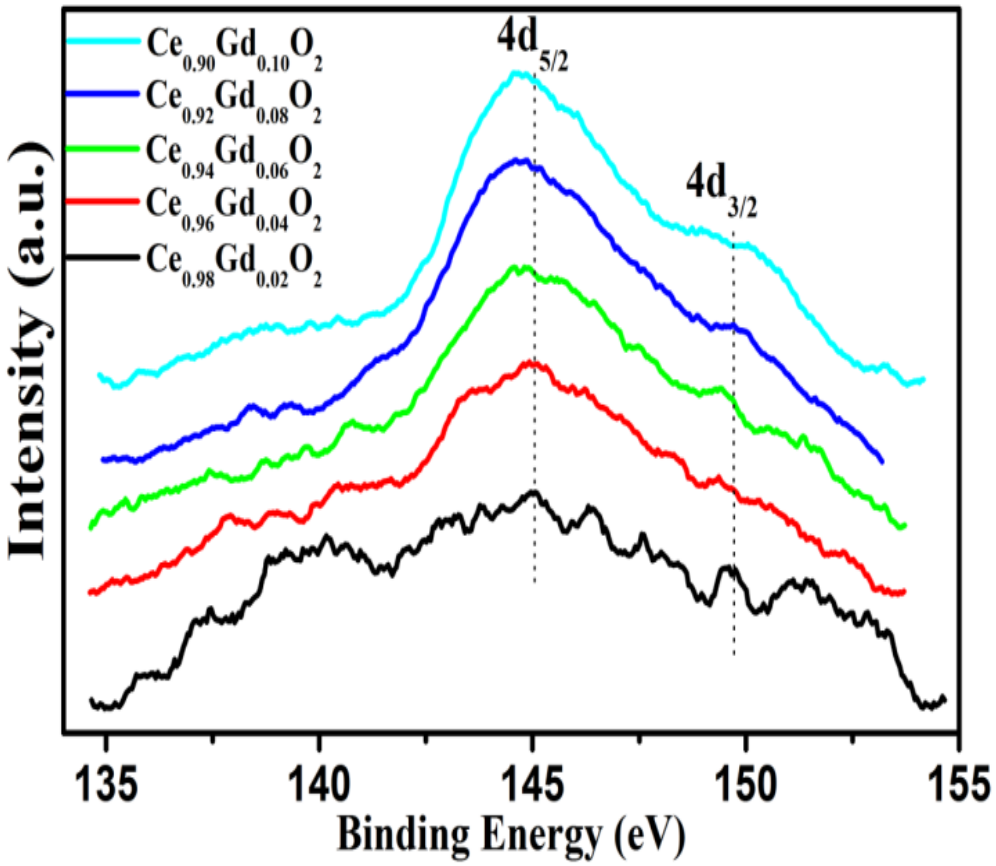


**Figure 4.13: Gd 4d core level XPS spectra of $Ce_{1-x}Gd_xO_2$ ($x$ = 0.02, 0.04, 0.06, 0.08 and 0.10) samples `**

The deconvoluted Gd 4d core level XPS spectra are split into doublet (Gd $4d_{5/2}$ and Gd $4d_{3/2}$) due to spin orbit coupling for $Ce_{1-x}Gd_xO_2$ ($x$ = 0.02, 0.04, 0.06, 0.08 and 0.10) samples, as shown in Figure 4.13. These two peaks existed in the range of ~143.7-145.8 eV and ~148.7-151.7 eV can be attributed to Gd $4d_{5/2}$ and Gd $4d_{3/2}$ states, respectively, which is indicating the presence of $Gd^{3+}$ ions in $Ce_{1-x}Gd_xO_2$ ($x$ = 0.02, 0.04, 0.06, 0.08 and 0.10) doped lattice [214-216].

### 4.3.4. Magnetic Properties

Figure 4.14 (a, b) shows the room temperature magnetization (M) vs. magnetic field (H) curves for pure $CeO_2$ and $Ce_{1-x}Gd_xO_2$ ($x$ = 0.02, 0.04, 0.06, 0.08 and 0.10) NPs. It is observed that pure $CeO_2$ nanoparticles are found to exhibit weak ferromagnetic (FM) behaviour at room temperature with saturation magnetization $M_s$ = 0.049 emu/g. Although, it has been reported that bulk $CeO_2$ exhibit diamagnetic behaviour where it is reported that at nano-regime the undoped $CeO_2$ NPs exhibit weak ferromagnetism with small value of saturation magnetization by few reports [217-223]. Since, a significant amount of coercivity $H_c$ = 77.95 Oe has been observed for pure $CeO_2$ NPs, which ensures the ferromagnetic nature in our pure $CeO_2$ sample. The weak ferromagnetic behaviour in pure $CeO_2$ NPs at room temperature is associated with oxygen vacancies that have been originated by the conversion of $Ce^{4+}$ to $Ce^{3+}$ oxidation state of cerium [224].

Although, after incorporation of $Gd^{3+}$ ions in $CeO_2$ NPs, $Ce_{0.98}Gd_{0.02}O_2$ sample still exhibit weak FM behaviour with increasing $M_s$ = 0.140 emu/g while $H_c$ has been decreased 22.48 Oe as compared to pure $CeO_2$ NPs. While, further increase in $Gd^{3+}$ ions concentration are not able to maintain this FM behaviour, that can be clearly seen from the hysteresis curves (in Figure 4.14(b)) for $Ce_{1-x}Gd_xO_2$ ($x$ = 0.04, 0.06, 0.08 and 0.10) samples. The magnetization of the Gd-doped $CeO_2$ samples is increased with increasing dopant concentration (as shown in Figure 4.14b and Table 4.6).

**Table 4.6: Summary of saturation magnetization ($M_s$), retentivity ($M_r$), and coercivity ($H_c$) for pure $CeO_2$ and $Ce_{1-x}Gd_xO_2$ ($x$ = 0.02, 0.04, 0.06, 0.08 and 0.10) NPs**

| Sample | $M_s$ (emu/g) | $M_r$ (emu/g) ($\times 10^{-4}$) | $H_c$ (Oe) |
|---|---|---|---|
| **Pure $CeO_2$** | 0.049 | 5.77 | 77.95 |
| **$Ce_{0.98}Gd_{0.02}O_2$** | 0.140 | 3.56 | 22.48 |
| **$Ce_{0.96}Gd_{0.04}O_2$** | 0.194 | 0.46 | 1.30 |
| **$Ce_{0.94}Gd_{0.06}O_2$** | 0.296 | 0.87 | 1.38 |
| **$Ce_{0.92}Gd_{0.08}O_2$** | 0.333 | 1.16 | 6.18 |
| **$Ce_{0.90}Gd_{0.10}O_2$** | 0.421 | 3.15 | 12.96 |

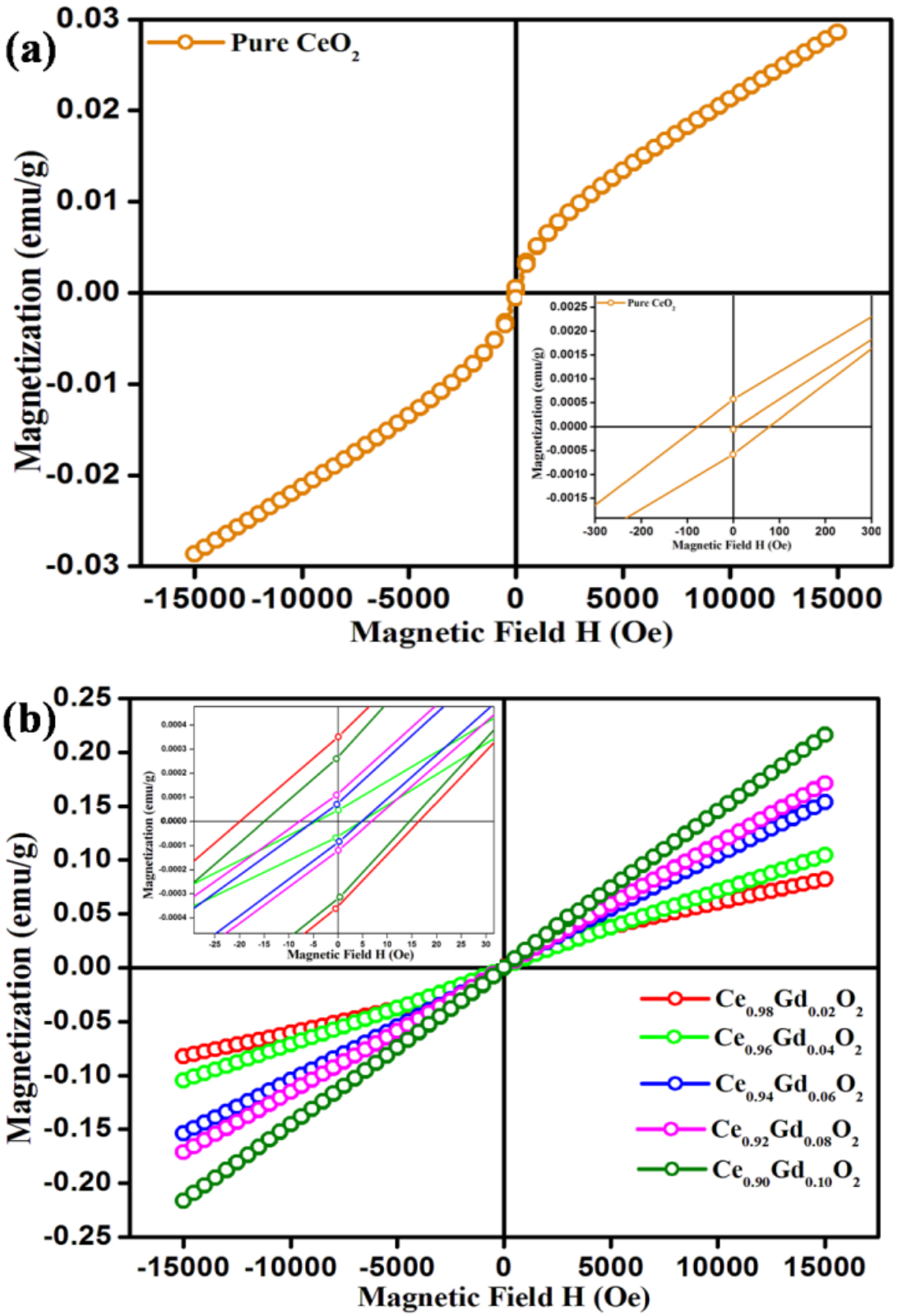


**Figure 4.14: Magnetization vs. magnetic field plot for (a) pure $CeO_2$ and (b) $Ce_{1-x}Gd_xO_2$ ($x$ = 0.02, 0.04, 0.06, 0.08 and 0.10) samples at room temperature (300K)**

Since, the electronic configuration of $Gd^{3+}$ is [Xe] $6s^2 5d^1 4f^7$ with 7 unpaired electrons in the 4f shell. These unpaired 4f electrons polarize the 6s and 5d valence electrons, results high effective magnetic moment $\mu_{eff}$ = 7.94 $\mu_B$ (calculated by the formula $\mu_{eff} = g_J\sqrt{J(J+1)}\,\mu_B$, where $g_J$ is the Lande g-factor and for $Gd^{3+}$ ion ground state $^8S_{7/2}$, S = 7/2, L = 0, J = 7/2, $g_J$ = 2) [225, 226]. With increasing dopant concentration, the interaction of these unpaired spins of 4f electrons with the outermost ligands or other $Gd^{3+}$ is anticipated to get weaker. These non-interacting and localized magnetic spins of $Gd^{3+}$ ions have induced the paramagnetism with increase in magnetization [227, 228]. The paramagnetic moment from the $Gd^{3+}$ ions incorporated into the $CeO_2$ lattice increase with increasing the dopant concentration which results in reduction of ferromagnetic ordering in Gd-doped samples. Therefore, 4%, 6%, 8%, and 10% Gd-doped samples have small ferromagnetic behaviour in addition to linear paramagnetic signals, which is gradually increasing with the fluency of $Gd^{3+}$ ions in $CeO_2$ NPs. Though, RAMAN and XPS analyses are showing an increase in the oxygen vacancies but this increase in oxygen vacancy concentration may not enhance the ferromagnetic ordering in Gd-doped samples [229]. *Nithyaa et al*., reported the ferromagnetic behaviour of pure $TiO_2$ NPs but incorporation of Gd-ions enhanced the paramagnetic nature which has been reported due to oxygen defects [230]. In other reports on Gd-doping in ZnO, the paramagnetism in these samples is reported due to high magnetic moment of Gd-ions ($\mu$ = 7.1 $\mu_B$) and due to presence of secondary phases of $Gd_2O_3$ [231-233].

Now, the main issue herein is to understand the possible origin of ferromagnetic dominated paramagnetic behaviour in pure $CeO_2$ and Gd-doped $CeO_2$ NPs, respectively. The origin of FM behaviour has been discussed in this manuscript accounting the F-centre exchange (FCE) mechanism, as a subcategory of bound magnetic polaron (BMP) model [25]. The conception of FCE coupling is based on BMP model that has been interpreted with the presence of oxygen vacancies ($V_O$). These oxygen vacancies and magnetic ions constitute a BMP that produces the ferromagnetism in these systems. In pure $CeO_2$ NPs, the origin of ferromagnetism is supposed to the reduction of the oxidation state of Ce ions i.e. $Ce^{4+}$ to $Ce^{3+}$. The formations of oxygen vacancies give rise to the reduction of $Ce^{4+}$ to $Ce^{3+}$ state. The

formation of oxygen vacancy left two electrons which may be transferred to a $Ce^{4+}$ ion converting $Ce^{4+}$ into $Ce^{3+}$. Due to this process, mixed $Ce^{3+}$ and $Ce^{4+}$ states yield in the pure $CeO_2$ NPs, which has already been confirmed by Ce 3d core level spectra analysis. The ferromagnetism in pure $CeO_2$ NPs may be arise from the nearest-neighbour interaction i.e. either double exchange ($Ce^{3+}$-$V_O$-$Ce^{4+}$) or super-exchange ($Ce^{3+}$-$V_O$-$Ce^{3+}$), which is mediated by oxygen ions [234]. The double exchange interaction forms an $F^+$ centre because the two electrons left by $V_O$ are trapped on $Ce^{4+}$ ion and $V_O$ (hydrogenic orbital), while super-exchange interaction forms an $F^{2+}$ centre due to the both electrons are trapped on $Ce^{4+}$ ions [235]. When Gd-ion is incorporated into $CeO_2$, it has suppressed the ferromagnetism of $CeO_2$ NPs (as shown in Figure 4.16(b)). Now, for $Ce_{0.98}Gd_{0.02}O_2$ sample, the $F^+$ centre may be coupled with the nearest $Ce^{3+}$ or Gd 4f orbital and form $Ce^{3+}$-$V_O$-$Gd^{3+}$ complex (BMP), which is dominated in this sample. When the size of this BMP is large enough to percolate through the lattice, long-range (weak) room temperature ferromagnetism can be realized with higher saturation magnetization. However, it is clearly observed that ferromagnetism has been suppressed with the increase in Gd-doping concentration up to 10%. Due to increase in Gd-ion doping concentration, the number of Gd-ions in the interior of $CeO_2$ lattice is less than that on its surface or on the grain boundaries. Only those Gd-ions are allowed to enter the lattice that is permitted by the host ions and rest is expelled. Due to higher doping concentration the separation among $Gd^{3+}$ ions is decreased. These largely separated $Gd^{3+}$ ions suppress the ferromagnetism and undergo super-exchange interaction with each other via $O^{2-}$ ions and results in anti-parallel alignment of the magnetic spins of Gd 4f shell present in the nearest neighbour ions that do not negotiate in ferromagnetic ordering. Thus higher doping concentration of $Gd^{3+}$ ions tends to destroy the observed ferromagnetism in Gd-doped $CeO_2$ NPs. Hence in our case the increase in paramagnetic signals may be attributed to increase in oxygen vacancy concentrations without enhancing the ferromagnetic ordering of the samples. This ferromagnetic ordering is further suppressed due to the increased concentrations of $Gd^{3+}$-cation as the separation between these $Gd^{3+}$-ions are decreased results in anti-parallel alignment of the spins of Gd 4f state due to super-exchange interaction.

### 4.3.5. Water Splitting Analysis

The amount of photocatalytic $H_2$ evolved from the samples has been hourly monitored (Table 4.7 and Figure 4.15(a)) and after four hours exposure to light the respective release of hydrogen is observed as: 1.47406, 1.4847, 1.4923, 1.4984, 1.51367 and 1.5243 mmol/h/g for pure Pt/$CeO_2$, Pt/$Ce_{0.98}Gd_{0.02}O_2$, Pt/$Ce_{0.96}Gd_{0.04}O_2$, Pt/$Ce_{0.94}Gd_{0.06}O_2$, Pt/$Ce_{0.92}Gd_{0.08}O_2$, Pt/$Ce_{0.90}Gd_{0.10}O_2$ samples, respectively (Figure 4.15(a)). According to the mechanism, when the surface of the molecular device Pt/$Ce_{1-x}Gd_xO_2$ exposed to the light, an electron of the valance band (VB) get energised after receiving that energy of light and jumped from VB to conduction band (CB), which generates a pair of photo-hole (at VB) and photoelectron (at CB) at $Ce_{1-x}Gd_xO_2$ samples surface. Nascent photoelectrons of CB are arrived at the junction of Pt/electrolyte interface by passing through the electron-pool of the metallic Pt (that can segregate the photoelectrons from photo-holes). These photoelectrons interact with $H^+$ ions [236] of the water at the interface and liberate the nascent H that combined with another nascent H atom to generate $H_2$ gas. Hole amassed at VB of the doped semiconductor is responsible for the breakdown of $CH_3OH$ in formaldehyde or formic acid or both as mentioned in the following equations (4.28-4.38) [237, 238], which can be used to depict the proposed electron transfer mechanism of the water splitting, as illustrated by the Figure 4.15(b).

$\mathrm{Gd-CeO_2} \xrightarrow{\text{light}} (\text{CV of } \mathrm{Gd-CeO_2})e^- + (\text{VB of } \mathrm{Gd-CeO_2})h^+$ (photocarriers generation) **(4.28)**

$(CV\ of\ \mathrm{Gd-CeO_2})\ e^- \rightarrow Pt\ e^-$ (transfer of photoelectron) **(4.29)**

$(\text{CV of } \mathrm{Gd-CeO_2})e^- + H_2O \rightarrow H^* + OH^-$ (generation of free radical H*) **(4.30)**

$H^* + H^* \rightarrow H_2$ (0.00 eV ) (generation of $H_2$) **(4.31)**

$H^* + h^+ \rightarrow H^+$ (generation of $H^+$) **(4.32)**

$H^+ + H^+ \rightarrow H_2$ (0.00 eV ) (generation of $H_2$) **(4.33)**

$(\text{VB of } \mathrm{Gd-CeO_2})\ h^+ + CH_3OH \rightarrow CH_2OH^* + H^+$(-0.1264eV) **(4.34)**

$h^+ + CH_2OH^* + OH^- \rightarrow HOCH_2OH^* \rightarrow HCHO + H_2O$ $(-3.848\ eV)$ (formation of HCHO) **(4.35)**

$CH_2OH^* + O \rightarrow OCH_2OH^* \rightarrow HCHO + OH^*$ $(-3.18\ eV)$ (formation of HCHO) **(4.36)**

$CH_2OH^* + O \rightarrow OCH_2OH^* \rightarrow HCOOH + H^*$ $(-4.125\ eV)$ (formation of HCOOH) **(4.37)**

$HCOOH + 2h^+ \rightarrow CO_2 + 2H^+$ $(-0.19\ eV)$ (formation of $CO_2$ from HCHO) **(4.38)**

There are many factors which can dominate the water splitting activity such as: particle size of photocatalyst, binding energy, dopant concentration and position (either $Gd^{3+}$ ion is taking position of $Ce^{3+}$ or $Ce^{4+}$ ion), oxygen vacancies, band gap and band positions, and many more. All of the above factors collectively responsible for increase in hydrogen generation activity on increasing the dopant concentration in $CeO_2$.

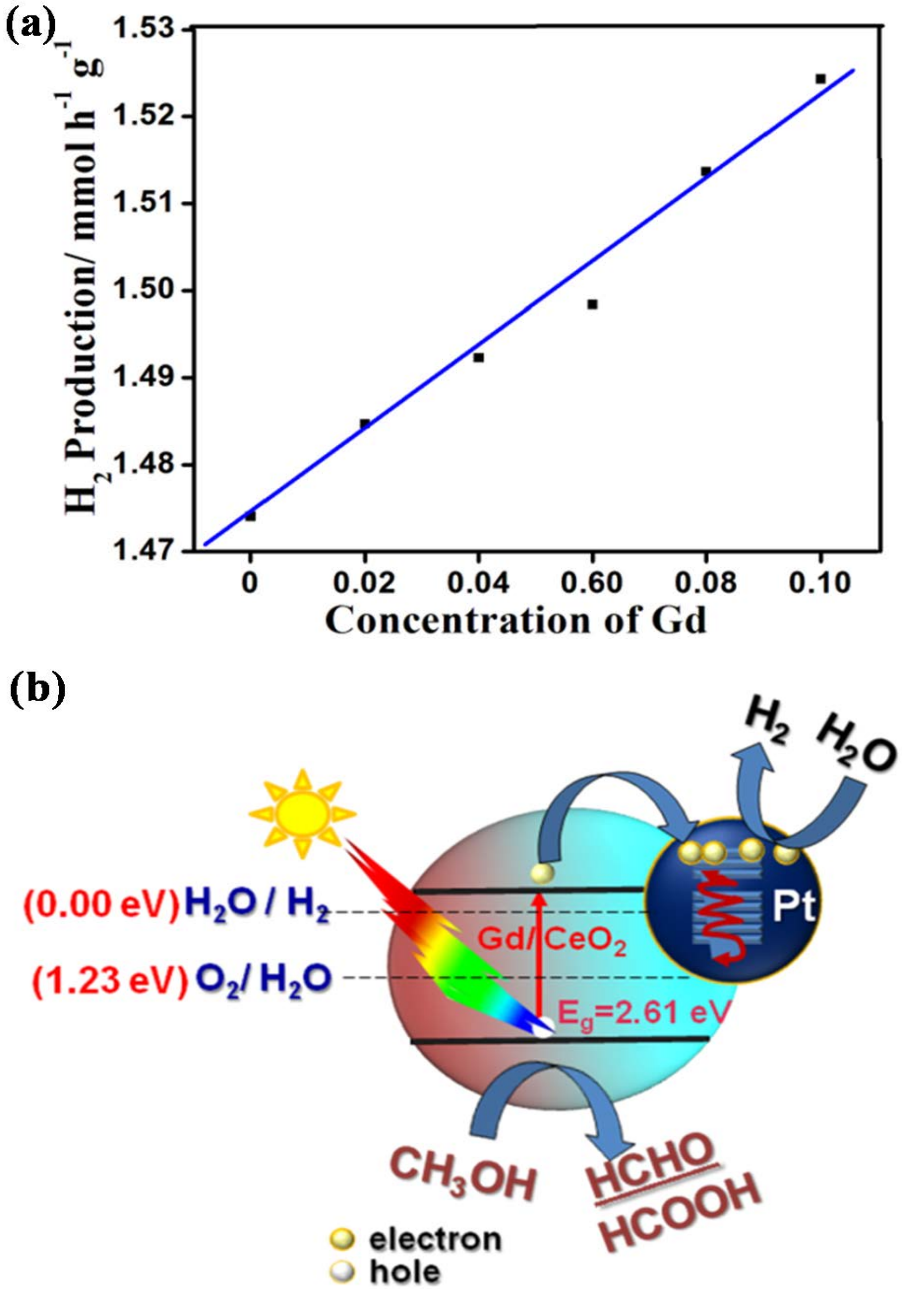


**Figure 4.15: (a) Hydrogen production rate for pure $CeO_2$ and $Ce_{1-x}Gd_xO_2$ ($x$ = 0.02, 0.04, 0.06, 0.08 and 0.10) samples in 10% $CH_3OH$ under visible light exposure of 300W Xe light source and (b) charge transfer reaction at oxidative and reductive sites**

Usually the steady decrease in particle size increases water splitting activity with increase in Gd proportion due to the large. Introduction of Gd-dopant into the $CeO_2$ lattice, also gradually increases the oxygen vacancy in the lattice arrangement of $CeO_2$ because $Gd^{3+}$ (radius of $Gd^{3+}$ = 0.1053 nm and charge density = 91) replaced the high charged but small $Ce^{4+}$ ion (radius of $Ce^{4+}$ = 0.097 nm and charge density = 148) in 2%, 4%, 8% doped samples but also replaced low charged but bigger sized $Ce^{3+}$ (radius of $Ce^{3+}$ cation = 0.114 nm and charge density = 75) in 6% and 10% Gd-doped $CeO_2$ samples. [184].

All of the above changes due to Gd-doping in $CeO_2$ lattice maintained the phase purity (checked with XRD) with minor but favourable changes in lattice parameters and suggested the lattice arrangement of atoms with expanded electron clouds between high charge M($Ce^{3+}$/$Ce^{4+}$) and low charge M($Gd^{3+}$) bonds through bridging O and O as shown in Figure 4.16(a). That results into creating active side to generate more carriers that bring about the enhanced photocatalytic activity of the doped $CeO_2$.

Local cluster framework of the tetrahedral coordinated groups of multivalent metal cations ($Ce^{3+}$/$Ce^{4+}$and $Gd^{3+}$) and anions ($O_2^{2-}$) generates a strong local electrostatic field inside the tetrahedra, as confirmed by the XRD, XPS and Raman results. Residual water molecules are captured by the strong local electrostatic field of the molecular device $Ce_{1-x}Gd_xO_2$ ($x$ = 0.02, 0.04, 0.06, 0.08 and 0.10). These water molecules attract the bridging oxygen through the protonic side and the metallic cation, i.e., Ce through the hydroxyl side (Figure 4.16(b)).

**Table 4.7: Comparative Band gaps with their CB and VB positions, Hydrogen production with and without Pt loading, with respect to the pure $CeO_2$ and $Ce_{1-x}Gd_xO_2$ ($x$ = 0.02, 0.04, 0.06, 0.08 and 0.10) samples.**

| Samples | Oxygen vacancy % | D (nm) | $Ce^{3+}/Ce^{4+}$ | Band gap (eV) | CB (eV) | VB (eV) | $H_2$ generation without Pt loading (mmol $g^{-1}$ $h^{-1}$) | $H_2$ generation with Pt loading (mmol $g^{-1}$ $h^{-1}$) |
|---|---|---|---|---|---|---|---|---|
| **Pure $CeO_2$** | 64.05 | 5.55 | 0.52 | 2.60 | -0.240 | 2.360 | 1.4695 | 1.47406 |
| $Ce_{0.98}Gd_{0.02}O_2$ | 71.84 | 5.27 | 0.63 | 2.66 | -0.270 | 2.390 | 1.4771 | 1.4847 |
| $Ce_{0.96}Gd_{0.04}O_2$ | 71.58 | 6.44 | 0.70 | 2.71 | -0.295 | 2.415 | 1.4832 | 1.4923 |
| $Ce_{0.94}Gd_{0.06}O_2$ | 64.20 | 7.47 | 0.54 | 2.67 | -0.275 | 2.395 | 1.4923 | 1.4984 |
| $Ce_{0.92}Gd_{0.08}O_2$ | 73.40 | 5.55 | 0.65 | 2.64 | -0.260 | 2.380 | 1.5030 | 1.51367 |
| $Ce_{0.90}Gd_{0.10}O_2$ | 66.70 | 6.34 | 0.51 | 2.52 | -0.200 | 2.320 | 1.5167 | 1.5243 |

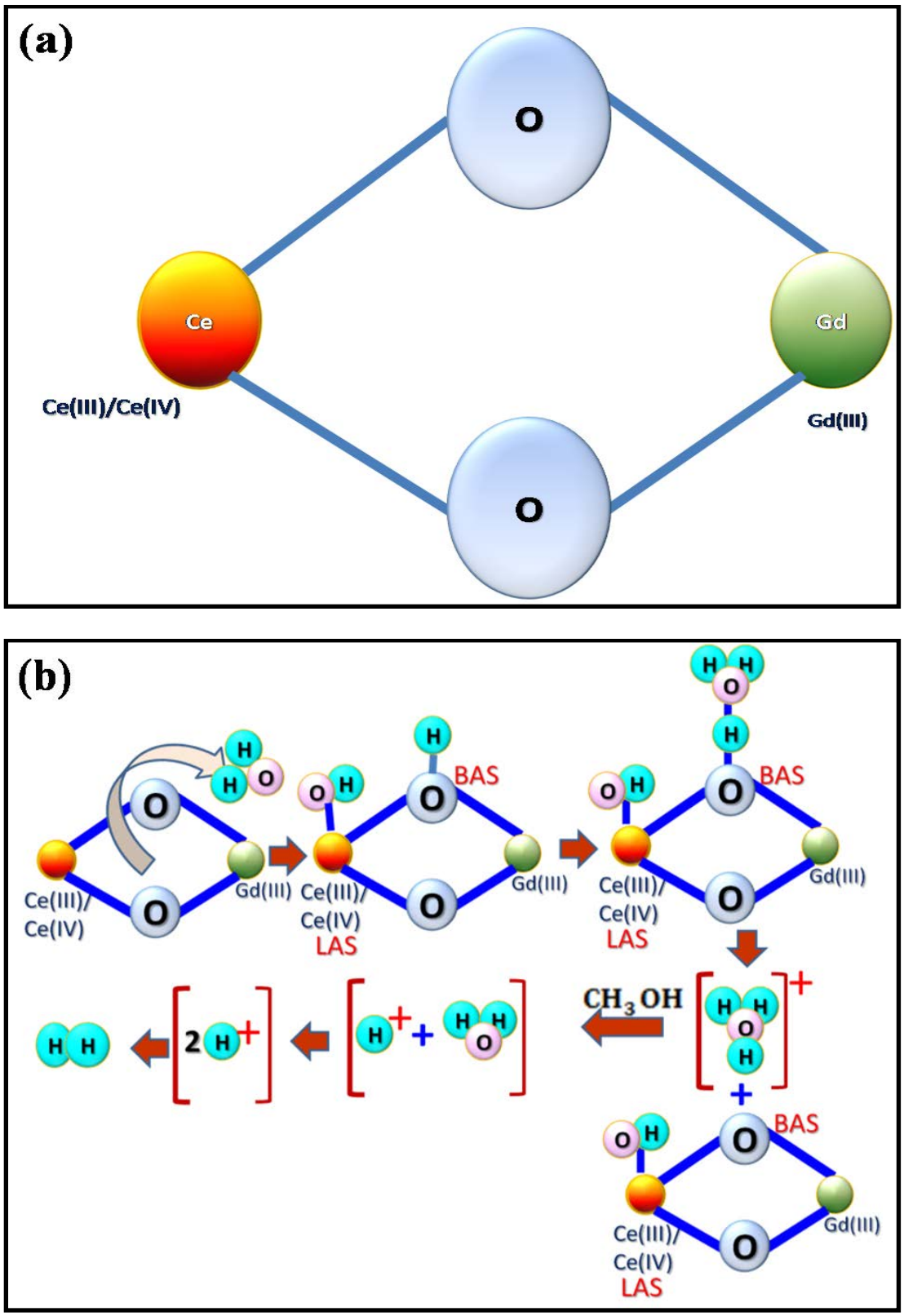


**Figure 4.16: (a) M-M bond through bridging O atoms and (b) water splitting phenomena at atomic lattice level through Lewis acid site (LAS) and BrÖnsted acid site (BAS)**

Finally, we get bridging oxygen impregnated with a hydroxyl proton and the Ce metallic side with a hydroxyl group that function as Lewis acid sites (LAS), which create strong electron withdrawing centres neighbouring bridging O-H groups [239] as shown by Figure 4.16(b). These withdrawing centres can act as super-acidic BrÖnsted acid sites (BAS) with a highly negative cluster framework. $H_3O^+$ that detached from BAS to release the tension of the bulky species and generate $H^+$. These $H^+$ reacts with the photoelectrons of the solid solutions and produce nascent H that couples with another H. Thus, hydrogen gas is generated.

## 4.4. Conclusions

In summary, pure $CeO_2$ and $Ce_{1-x}Gd_xO_2$ NPs have been successfully synthesized by the co-precipitation method. The structural and morphological studies have been made by XRD, TEM, HRTEM and SAED analysis. From the XRD analysis all the lattice parameters, volume, particle size of pure $CeO_2$ and $Ce_{1-x}Gd_xO_2$ NPs have been calculated, the particle size of these NPs is further verified with TEM and SERS analysis and observed approximately similar to the results obtained with XRD analysis. The particles are spherical in shape and getting agglomerated with fluencies of $Gd^{3+}$ ions in $CeO_2$ sample and the particle size is in the range of 5-7 nm, which is confirmed from the TEM images. From the TEM results and analysis we have observed the broadening of diffraction rings, which indicates that the particles are small in size and crystallinity becomes low with increasing doping concentration of $Gd^{3+}$ ions in $CeO_2$ NPs.

From the analysis of the UV-Vis-NIR absorption spectra, we have observed the variation in the refractive index and band gap energy with different concentration of Gd-ions in $CeO_2$ NPs. The reduction of refractive index with incorporation of $Gd^{3+}$ ions in $CeO_2$ NPs is beneficial to UV protection. Normally, UV protection ability is strongly depending on the particle size and at nano-regime UV absorption ability is stronger than that of micro-sized ones. From the SERS spectra on pure $CeO_2$ and $Ce_{1-x}Gd_xO_2$ NPs, the particle size, oxygen vacancy concentrations etc. have been made to understand the mechanism of other properties

of these samples. From the SERS spectra we can say that no other impurity phases are present in our samples and hence the nature of ferromagnetism in these NPs is intrinsic in nature and derived from the defects and intrinsic and extrinsic oxygen vacancy concentrations, which is found to gradually increase with fluencies of $Gd^{3+}$ ions in $CeO_2$ NPs.

Further for electronic structure of these NPs the core level Ce 3d, O1s and Gd 4d XPS spectra have been recorded and analyzed in details. From this analysis the change of oxidation state of $Ce^{+4}$ to $Ce^{+3}$ ions, incorporation of the $Gd^{+3}$ ions in the lattice and formation of oxygen vacancies is reported. From the core level Ce 3d spectra the presence of both $Ce^{3+}$ and $Ce^{4+}$ ions in all the samples and an increase in the $Ce^{3+}$ concentration can be seen with the fluencies of $Gd^{3+}$ dopant ions in $CeO_2$ NPs, due to the formation of defects or an amorphous phase of $Ce_2O_3$. From the O 1s core level spectra analysis we are able to demonstrate that doping of $Gd^{3+}$ ions in $CeO_2$ NPs can modify the rate of reduction of $Ce^{4+}$ to $Ce^{3+}$ oxidation state as well as affects the formation of oxygen vacancies in $Ce_{1-x}Gd_xO_2$ ($x$ = 0.02, 0.04, 0.06, 0.08 and 0.10) doped samples. However, the Gd 4d core level spectra cannot be recorded with good statistics due to very small concentrations but reports the presence of Gd-ion in our NPs. In our magnetic measurements we can see that all the samples pure and Gd-doped $CeO_2$ are showing the weak ferromagnetism dominated paramagnetic behaviour, which is assumed to be triggered due to change of oxidation state of $Ce^{+4}$ to $Ce^{+3}$ ions, incorporation of the $Gd^{+3}$ ions in the lattice and formation of oxygen vacancies. From Raman and XPS analyses, the presence of oxygen vacancy related defects is apparent. From Ce 3d XPS spectra one can reveal that a significant increase in $Ce^{3+}$ ions is not only able to increase the oxygen vacancies due to formation of $Ce_2O_3$ phase in Gd-doped samples, which is not traceable with the XRD analysis but also may be due to the substitution of $Ce^{4+}$ ions by $Gd^{3+}$ ions and this substitution actually creates the oxygen vacancies and owe the presence of ferromagnetic ordering in $Ce_{0.98}Gd_{0.02}O_2$ sample.

In the water splitting results, the amount of photocatalytic $H_2$ evolved from the samples is monitored, and the respective release of hydrogen is found to increase for pure Pt/$CeO_2$, Pt/$Ce_{1-x}Gd_xO_2$ NPs samples with the increased doping concentrations of the Gd-ion. The particle size of photocatalyst, binding energies, oxygen vacancy concentrations, band gap and many other factors are collectively responsible for increase in hydrogen generation activity with increasing dopant concentration in $CeO_2$. The observed release of hydrogen is found in good correlation with the characterisation results and the proposed mechanism of water splitting is reported on the basis of analyses.

# Chapter 5

# Study of Structural, Optical, Electronic Structure and Magnetic Properties of TM ($Fe^{3+}$)-doped $CeO_2$ Nanoparticles

# CHAPTER 5

# STUDY OF STRUCTURAL, OPTICAL, ELECTRONIC STRUCTURE AND MAGNETIC PROPERTIES OF TM ($Fe^{3+}$)-DOPED $CeO_2$ NANOPARTICLES


## ABSTRACT

In this chapter, pure $CeO_2$ and Fe-doped $CeO_2$ NPs synthesized using co-precipitation method are reported for establishing the correlation between oxygen vacancy defects, chemical and electronic state with the particle size, surface morphology and optical properties of NPs. The various properties of these NPs are characterised using XRD, TEM, SERS and XPS. From the XRD and Raman analysis the formation of cubic fluorite-type structure with incorporation of Fe-ions in $CeO_2$ lattice is confirmed. The defect structure, oxygen vacancies are also discussed with the detaile analysis of the Raman spectra. The surface morphology and particle size distribution of all the samples is discussed with TEM and the particle size are found in between 4 to 5 nm. From optical absorption measurements, the inhomogenous distribution of the dopant is significantly discussed in the light of optical band gap energy and surface information such as peak intensity and shape near at 460 and 577 $cm^{-1}$. The band gap is found to decrease with the increased doping of the Fe-ions, indicating that Fe-doping introduces the oxygen vacancies. The core level spectra of Ce 3d are discussed to explain the change in electronic state of $Ce^{4+}$ to $Ce^{3+}$, which are further supported with the Fe 2p and O 1s core level spectra. While, comparing the local electronic structure at Ce site around the Fe site, we could infer that the Fe-ion substituted the Ce site and creating the oxygen vacancies, which give rise to the RTFM properties of the samples. The results for weak RTFM in pure $CeO_2$ and Fe-doped $CeO_2$ samples is explained in the line of change of oxidation state of Ce-ions due to formation of oxygen vacancies, correlating with F-centre exchange (FCE) mechanism.


## 5.1. Introduction

A most reactive RE oxide, such as $CeO_2$ has attracted cosiderable interest due to its wide band gap ($E_g$ = 3.2 eV) and high dielectric costant (ε = 26) [240]. These properties are beneficial for the electronic and vibrational study of $CeO_2$ NPs,

which has been used in large number of application, such as three-way catalysts [241], solid oxide fuel cells [242], UV-absorbent [192] and magneto-optoelectronic devices [223]. For understanding the functional properties of $CeO_2$ based materials, it is vitally important to understand the fundamental understanding of the influence on the properties of these materials on particle size, dopant ion type and concentrations, morphology and defects states such as oxygen vacancies. Since, the microstructure and particle size influences the performance of $CeO_2$ NPs at the grain boundaries and depletion of carriers in anisotropic nanosystems that strongly modify the redox or transport properties of $CeO_2$. Generally, nanocrystalline $CeO_2$ become non-stoichiometric at lower partial oxygen pressure of the environment during the annealing process of these materials [243]. This non-stoichiometry of these materials become more pronounced at normal atmospheric condition in $CeO_{2-\delta}$ NPs due to the excessive increase of surface-to-volume ratio of the nanoparticles with decrease in the particle size [244]. This decrease in the particle size reduces the formation energy of oxygen vacancies near to the crystallite surface and accommodate large amount of oxygen vacancies without siginficantly affecting the cubic structure of $CeO_2$ NPs. As the oxygen vacancies develops in the lattice, the valence state of Ce-ions in $CeO_2$ NPs can be seen in two oxidation state i.e. $Ce^{3+}$ and $Ce^{4+}$, which is very important for applications of $CeO_2$ such as oxygen stroage capacity, catalytic and in spintronic devices. However, the oxygen vancancies are also responsible for the origin of RTFM in these $CeO_2$ NPs. The basic idea of doping TM in $CeO_2$ matrix is to enhance magnetization between the magnetic ions by manipulating the charge carries, that enables the changes in both the charge and spin degree of freedom of electrons [245]. It is reported in many studies that 3d TM element-doped $CeO_2$ exhibit RTFM [77, 246-248]. *Maensiri et al*. have reported sol-gel synthesized undoped $CeO_2$ showing diamagnetic behaviour, whereas, their Fe-doped $CeO_2$ NPs are showing intrinsic ferromagnetism above 673 K [249]. *Phokha et al*., have also reported weak RTFM in Fe-doped $CeO_2$ NPs, induced by oxygen vacancy or defects which are generated by $Ce^{3+}$ and $Fe^{3+}$ spin electrons and from their X-ray absorption near edge structure (XANES) measurments they confirm the formation of oxygen vacancies with $Ce^{3+}$ and $Fe^{3+}$ states [65]. *Wang et al*. have reported experimental investigations on electronic structure of pure $CeO_2$ and Fe-doped $CeO_2$ using X-ray absorption (XAS) and X-ray emission spectroscopy (XES) to show the effect of

dopant ion concentration on the ferromagnetism and their results suggested that at low cocentration of Fe-doping the oxygen vacancies are formed with increased magnetism but at high doping concentration the ferromagnetism is found to decrease [66]. The localized or delocalized 4f electronic state of Ce-ions affect the defects and vacancies of the pure $CeO_2$ and 3d element Fe-doped $CeO_2$ [245]. Therefore, for understanding the fundamental mechanism as well as the effect of different doping concentration on the electronic structure of Fe-doped $CeO_2$ NPs, it is essential to investigate the physical properties and their correlation with the electronic structure of these materials. XPS is a powerful tool to investigate electronic structure along with the defect concentration induced in the lattice due to variation in doping concentration in $CeO_2$ NPs [250].

In this present work, we would like to undertake this study to further verify the effect of doping concentration of $Fe^{3+}/Fe^{2+}$ cation on various properties of $CeO_2$ NPs. To understand the effect on physical properties of these nanomaterials, which are being altered due to the presence of Fe-cation and their effect on defect and oxygen vacancies using various techniques as XRD, TEM, SERS, UV-Vis-NIR spectroscopy and XPS have been studied. Further, the magnetic properties of the all samples are discussed using SQUID measurments at room temperature.

## 5.2. Experimental Details

### 5.2.1. Materials for synthesis of NPs

Cerium (III) nitrate hexahydrate ($Ce(NO_3)_3 \cdot 6H_2O$) (Alpha Aesar 99.99%), Iron(III) nitrate nonahydrate ($Fe(NO_3)_3 \cdot 9H_2O$) (Alpha Aesar 99.9%), and Ammonium hydroxide ($NH_4OH$) 25% solution.

### 5.2.2. Material Preparation

Nanocrystalline pure $CeO_2$ and $Ce_{1-x}Fe_xO_2$ (for $x$ = 0.02, 0.04, 0.06, 0.08, and 0.10) samples were synthesized using co-precipitation method. The appropriate stoichiometric amount of $Ce(NO_3)_3 \cdot 6H_2O$ and $Fe(NO_3)_3 \cdot 9H_2O$ were used for synthesizing $Ce_{1-x}Fe_xO_2$ NPs. Initially $Ce(NO_3)_3 \cdot 6H_2O$ and $Fe(NO_3)_3 \cdot 9H_2O$ precursor solution was prepared in distilled water along with magnetic stirring at the rate of 600 rpm. Then 25% $NH_4OH$ solution was added drop by drop in this solution until the pH level was reached about 11. This solution was further stirred about

4 hours with the stirring rate of 1600 rpm at room temperature. After that, the synthesized pale-yellow precipitate were collected and washed out with distilled water. The samples were dried at room temperature and annealed in the furnace for about 500 $^{o}$C for 8 hours. A set of samples, i.e. pure $CeO_2$ and $Ce_{1-x}Fe_xO_2$ (for $x$ = 0.02, 0.04, 0.06, 0.08 and 0.10) NPs were synthesized. The chemical reactions during the experimental process for pure $CeO_2$ NPs can be written as follows:

$$Ce(NO_3)_3 \cdot 6H_2O_{(aq)} + 3NH_4OH_{(aq)} \rightarrow Ce(OH)_{3(s)} + 3NH_4NO_{3(aq)} + 6H_2O_{(aq)} \quad (5.1)$$

$$2Ce(OH)_{3(s)} \xrightarrow{500^{\circ}C} 2CeO_{2(s)} + 2H_2O_{(g)} + H_{2(g)} \uparrow \quad (5.2)$$

Similarly, chemical reactions for the growth on various concentrations ($x$ = 0.02, 0.04, 0.06, 0.08, and 0.10) of Fe-dopant ions in $CeO_2$ NPs can be written as follows:

$$(1-x)[Ce(NO_3)_3 \cdot 6H_2O] + x[Fe(NO_3)_3 \cdot 9H_2O] + 3NH_4OH \rightarrow Ce_{1-x}Fe_xO_2 + 3NH_4NO_3 + yH_2O \quad (5.3)$$

### 5.2.3. Nanomaterials Characterization

The structural characterization of the samples were made using Brucker D8 Advance X-ray diffractometer with Cu $K_\alpha$ radiation ($\lambda$ = 1.5406 Å). The diffraction patterns were recorded at room temperature in the $2\theta$ range from 10$^{o}$ to 90$^{o}$ with 0.05$^{o}$ min$^{-1}$ scanning speed and the counting time of 5 sec per step. The surface morphology, particle size and crystallinity of the samples were studied using TEM of make Technai G2 20 S-TWIN (FEI Netherlands) instrument operating at an accelerating voltage of 200 kV. NPs samples were ultrasonicated in iso-propanol solvent and deposited on holey carbon grids for examination in a JEOL 2100F field emission gun (FEG) TEM operating at 200 kV. Images and diffraction patterns were recorded on a Gatan Orius CCD camera. The particle size distribution was taken for a total 150 particles using image-j software of TEM images. All the Raman spectra were collected on Thermo Scientific DXRxi Raman Imaging Microscope with Charge Injection device (CID) detector using green laser of 532 nm excitation light source with its power kept at 10 mW. The UV-Vis-NIR spectroscopy measurements were performed for absorbance spectra of the samples in the range of 200-1000 nm with $BaSO_4$ as an internal standard were recorded employing a Shimadzu UV-3600 Plus spectrophotometer with an integrating sphere. Chemical state of different elements were analyzed using XPS that was carried out on ESCA+ Omicron

nanotechnology (Oxford Instrument, Germany) instrument with a base pressure in the analysis chamber of $10^{-9}$ Torr. The X-ray source was monochromatized Al $K\alpha$ ($hv$ =1486.7 eV) radiation and the binding energy scale was calibrated using the C 1s line ($hv$ = 284.6 eV) of the adsorbed hydrocarbon on the sample surface. The operating voltage and current of the instrument was kept on 15 kV and 20 mA, respectively and short scan pass energy was kept at 20 eV. The magnetization measurments of all the samples were investigated at room temperature by varying the applied field from -7 T to +7 T using a Quantum Design MPMS-3 SQUID system. The zero field cooled (ZFC) and field cooled (FC) measurements were also recorded from 5 K to 300 K under different applied fields.

## 5.3. Results and Discussion

### 5.3.1. Structural Properties

#### 5.3.1.1. XRD analysis

Figure 5.1(a) shows the indexed XRD patterns of the pure $CeO_2$ and $Ce_{1-x}Fe_xO_2$ (for $x$ = 0.02, 0.04, 0.06, 0.08, and 0.10) samples. The XRD patterns for pure $CeO_2$ and $Ce_{1-x}Fe_xO_2$ samples shows the Bragg peaks (111), (200), (220) and (311) corresponding to the face centered cubic fluorite structure with *Fm-3m* space group [123]. The symmetry of the XRD patterns does not altered due to the incorporation of Fe-ions into the $CeO_2$ lattice. The diffraction patterns shows absence of any secondary or impurity phase of $Fe_2O_3$, $Fe_3O_4$ or FeO in $Ce_{1-x}Fe_xO_2$ samples confirms the single face formation [119]. The peak position of the (111) plane is slightly shifted to the lower angle side (Table 5.1). This indicates that $Fe^{3+}$ ions have been successfully incorporated into $CeO_2$ lattice without forming any crystalline impurity phases. However, this peak shifting is also attributed to the lattice expansion induced by the incorporation of $Fe^{3+}$ ions into the $CeO_2$ lattice. XRD patterns of pure $CeO_2$ and $Ce_{1-x}Fe_xO_2$ ($x$ = 0.02, 0.04, 0.06, 0.08 and 0.10) NPs along with the Rietveld refinements are shown in Figure 5.2. The horizontal lower curve has been shown at the bottom of each Rietveld profile represent the difference between observed and calculated diffraction profile. The parameters obtained by the Rietveld refinement are listed in the Table 5.2. Rietveld refinements shows all the observed peak positions corresponds to standard Bragg positions of cubic fluorite structure of $CeO_2$ with the space group *Fm-3m*, confirming the single phase of $Ce_{1-x}Fe_xO_2$

($x$ = 0.02, 0.04, 0.06, 0.08, 0.10) NPs. All the XRD peaks are indexed according to JCPDS card no. 81-0792 for pure $CeO_2$ [251].

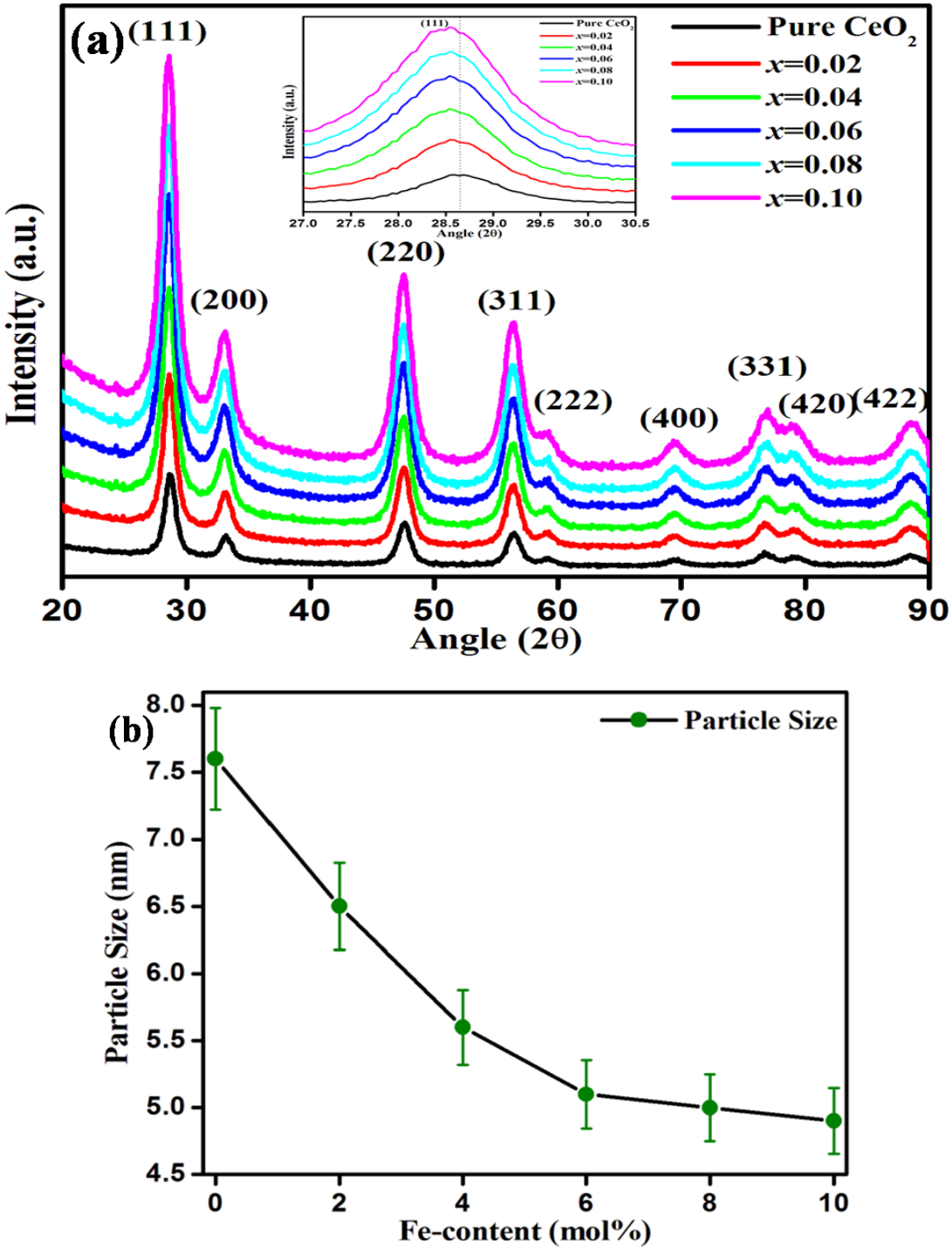


**Figure 5.1: (a) XRD pattern of pure $CeO_2$ and $Ce_{1-x}Fe_xO_2$ (for $x$ = 0.02, 0.04, 0.06, 0.08, and 0.10) samples (inset shows the [111] peak of all the samples) and (b) average crystalline size as a function of Fe-content obtained from TEM images.**

**Table 5.1: Calculated value of lattice spacing (*d*) for (111) plane, FWHM, Position of diffraction peak (2θ) for (111) plane, average crystalline size (D) measured from TEM, XRD line broadening corresponding to (111) diffraction peak and Raman line broadening, dislocation density (δ), lattice strain (ε), density ($\rho$) and specific surface area ($S_a$) are summarized in the table.**

| Samples | Parameters | | | | | | | | |
|---|---|---|---|---|---|---|---|---|---|
| | $d$ (nm) | FWHM | Position | D (nm) | | δ ($nm^{-2}$) | $\varepsilon \times 10^{-2}$ | $\rho$ ($g/cm^3$) | $S_a$ ($cm^2/g$) $\times 10^5$ |
| | | (111) | (2θ) | TEM | XRD | | | | |
| Pure $CeO_2$ | 0.312 | 0.840 | 28.64 | 5.87 | 7.6 | 1.71 | 4.54 | 7.19 | 14.20 |
| $Ce_{0.98}Fe_{0.02}O_2$ | 0.308 | 0.998 | 28.47 | 5.66 | 6.5 | 2.34 | 5.31 | 7.22 | 14.68 |
| $Ce_{0.96}Fe_{0.04}O_2$ | 0.307 | 1.155 | 28.35 | 5.07 | 5.6 | 3.17 | 6.17 | 7.24 | 16.34 |
| $Ce_{0.94}Fe_{0.06}O_2$ | 0.305 | 1.230 | 28.46 | 4.85 | 5.1 | 3.83 | 6.78 | 7.22 | 17.12 |
| $Ce_{0.92}Fe_{0.08}O_2$ | 0.304 | 1.253 | 28.47 | 4.59 | 5.0 | 3.88 | 6.83 | 7.23 | 18.08 |
| $Ce_{0.90}Fe_{0.10}O_2$ | 0.303 | 1.286 | 28.43 | 4.01 | 4.9 | 4.05 | 6.97 | 7.26 | 20.6 |

**Table 5.2: Calculated values of lattice parameter (*a*), unit cell volume (V) and other fine details from Rietveld refinement analysis of the X-ray Diffraction data.**

| Samples | *a* (Å) | V(Å$^3$) | $R_p$ | $R_{wp}$ | $R_{exp}$ | $\chi^2$ | $R_{Bragg}$ |
|---|---|---|---|---|---|---|---|
| Pure $CeO_2$ | 5.420 (17) | 158.86 (9) | 2.45 | 3.15 | 3.09 | 1.04 | 1.23 |
| $Ce_{0.98}Fe_{0.02}O_2$ | 5.4096(20) | 158.30 (10) | 2.43 | 3.07 | 3.00 | 1.05 | 1.41 |
| $Ce_{0.96}Fe_{0.04}O_2$ | 5.4033 (30) | 157.76 (15) | 2.70 | 3.42 | 3.03 | 1.27 | 3.18 |
| $Ce_{0.94}Fe_{0.06}O_2$ | 5.4084 (30) | 158.20 (15) | 2.42 | 3.03 | 2.86 | 1.14 | 1.53 |
| $Ce_{0.92}Fe_{0.08}O_2$ | 5.4053 (36) | 157.93 (18) | 2.80 | 3.52 | 3.19 | 1.22 | 2.50 |
| $Ce_{0.90}Fe_{0.10}O_2$ | 5.3986 (35) | 157.34 (18) | 2.47 | 3.09 | 2.93 | 1.11 | 1.47 |

The crystallite size (D) of pure $CeO_2$ and $Ce_{1-x}Fe_xO_2$ ($x$ = 0.02, 0.04, 0.06, 0.08, 0.10) NPs have been calculated for the most prominent (111) diffraction peak using Debye-Scherrer's equation [88]:

$$\boldsymbol{D = \frac{0.9\,\lambda}{\beta\,\cos\theta}} \qquad (\mathbf{5.4})$$

Where, λ is the wavelength of Cu $K_\alpha$ radiation (1.5406 Å) of X-ray used, β is the full width at half maxima (FWHM) of XRD peaks (express in radian), θ is the Bragg angle of the diffraction planes. The crystallite size based on the characteristic peak (111) has been found in the range of ~4-7 nm for all the samples (tabulated in Table 5.1). It has been apparent that the crystallite size is decreased with increase in the Fe-doping concentration, which exhibited the grain growth during the synthesis process [252]. On comparing the XRD diffraction peak (111) of pure $CeO_2$ and $Ce_{1-x}Fe_xO_2$ NPs, the FWHM values of the diffraction peak has been found to increase with the Fe-doping concentration, implying the reduction of the crystallite size of the particles. This may be due to replacement of the $Ce^{4+}$ (0.097 nm) ions by $Fe^{3+}$ (0.065 nm) ions in the crystal lattice, which has lower ionic radius as compared to $Ce^{4+}$ ion. The lattice parameter ($a$) of pure $CeO_2$ NPs is obtained from Rietveld refinement about 0.541 nm. After incorporation of $Fe^{3+}$ ions in the $CeO_2$ NPs, a continuous decrease has been found in the lattice parameter of $Ce_{1-x}Fe_xO_2$NPs (as shown in Table 5.2). This change in lattice parameter induces the lattice strain due to the incongruity in the ionic radii of $Fe^{3+}$ and $Ce^{4+}$ and introducing $Ce^{3+}$ ions as well as generate oxygen vacancies in the $CeO_2$ lattice to retain the charge balance. These oxygen vacancies on the lattice site induce the strain in the crystal lattice and in order to minimize the strain, the unit cell undergoes an expansion [252]. The lattice strain (ε) has been calculated using the following formula [131]:

$$\boldsymbol{\varepsilon = \frac{\beta\,\cos\theta}{4}} \qquad (\mathbf{5.5})$$

The calculated values of lattice strain are given in Table 5.1. All samples have positive lattice strain and it increases after $Fe^{3+}$ ion incorporation in the lattice, indicates tensile strain [253]. The lattice strain originated in the pure $CeO_2$ NPs is due to the oxygen vacancies and $Ce^{3+}$ ions present on the surface of the structure. With the incorporation of $Fe^{3+}$ ions in $CeO_2$, the value of lattice strain is increased due to formation of more oxygen vacancies in Fe-doped samples [158]. These

induced strains in pure and Fe-doped $CeO_2$ samples could be localized near the grain boundaries, which can be a reason for the reduction of the crystallite size on increasing the Fe-doping concentration in doped samples [254].

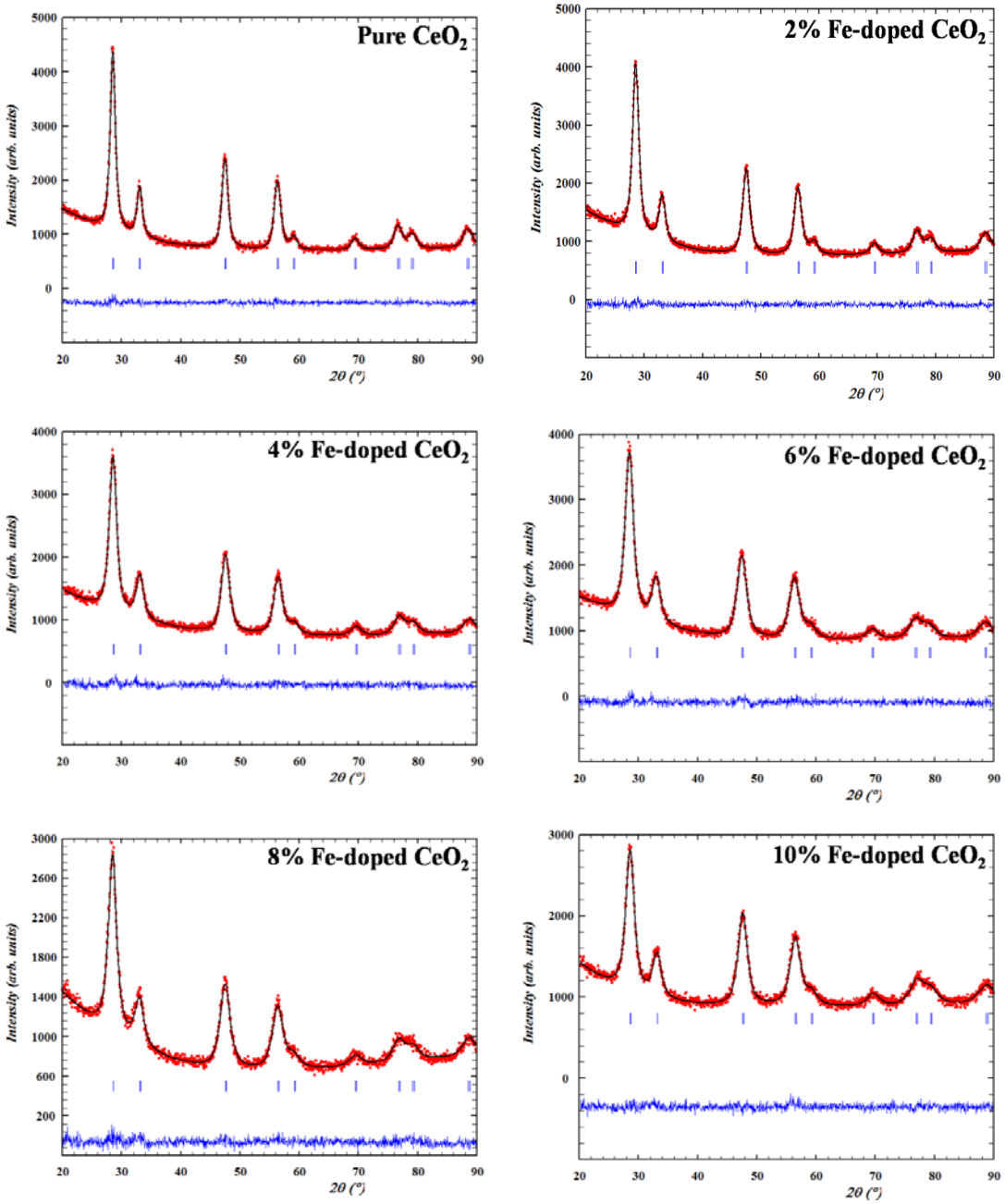


**Figure 5.2: Rietveld refinement profile of X-ray diffraction patterns of pure $CeO_2$ and Fe-doped $CeO_2$ (for 2%, 4%, 6%, 8% and 10%) NPs at 300 K. Observed (calculated) profiles are shown by dotted (solid) lines. The short vertical marks represent Bragg reflections. The lower curve is the difference plot.**

The length of dislocation per unit volume is defined as the dislocation density (δ), which has been calculated using the following relation [134, 255]:

$$\boldsymbol{\delta = \frac{1}{D^2}} \qquad (\mathbf{5.6})$$

Where, D is the average crystallite size. The dislocation density increases with the increase in Fe-doping concentration.

Now, the volume-mass density is another powerful parameter to characterize any material and its ability. It has ability to explore any changes in the crystal structure of the crystalline material [256]. It can be calculated theoretically from XRD and termed as X-ray density. For pure and Fe-doped $CeO_2$ samples the density can be calculated using the following equation [257]:

$$\boldsymbol{\rho = \frac{nM}{NV}} \qquad (\mathbf{5.7})$$

Where, M is the molecular weight of the sample, N is Avogadro number ($6.023\times 10^{23}$), V is the volume of the unit cell ($V = a^3$) and $n$ is the number of atom per unit cell ($n = 4$) for the prepared $CeO_2$ sample [258]. The X-ray density is found to increase with $Fe^{3+}$ doping concentration which is because of decrease in the volume of the unit cell. It has been reported that the lattice parameter is inversely proportional to the X-ray density; therefore it decreases as the X-ray density increase. [255, 259].

The specific surface area ($S_a$) is calculated using X-ray density ($\rho$) and average crystallite size (D) of the samples by the following formula [260]:

$$\boldsymbol{S_a = \frac{6}{D \times \rho}} \qquad (\mathbf{5.8})$$

It can be seen from Table 5.1 that the specific surface area increases with increasing $Fe^{3+}$ doping concentration. This may be due to decrease in the average crystalline size of the Fe-doped samples. It should be noted that total surface energy increases with increase in the total surface area. Therefore, an increase in specific surface area is attributed to the high value of surface energy and hence a higher number of active surface sites [261].

### 5.3.1.2. Surface Morphology

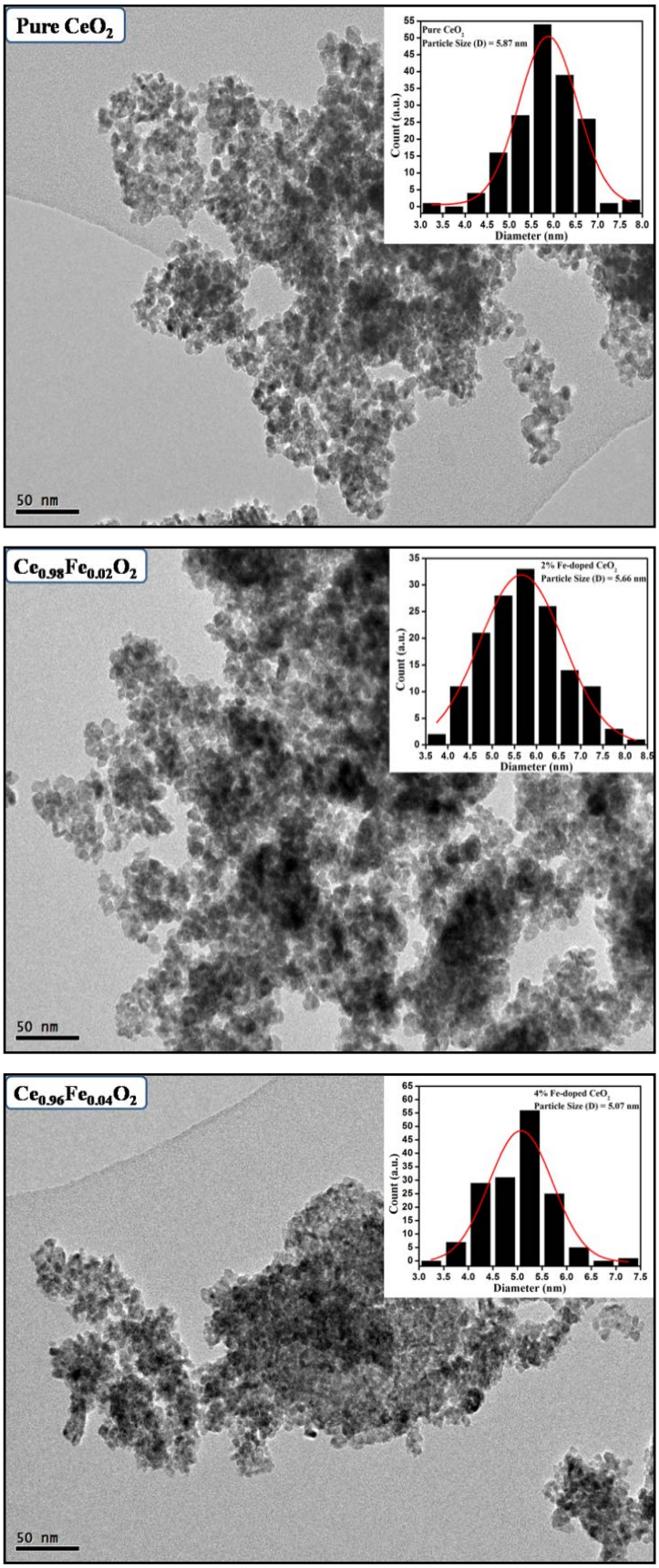

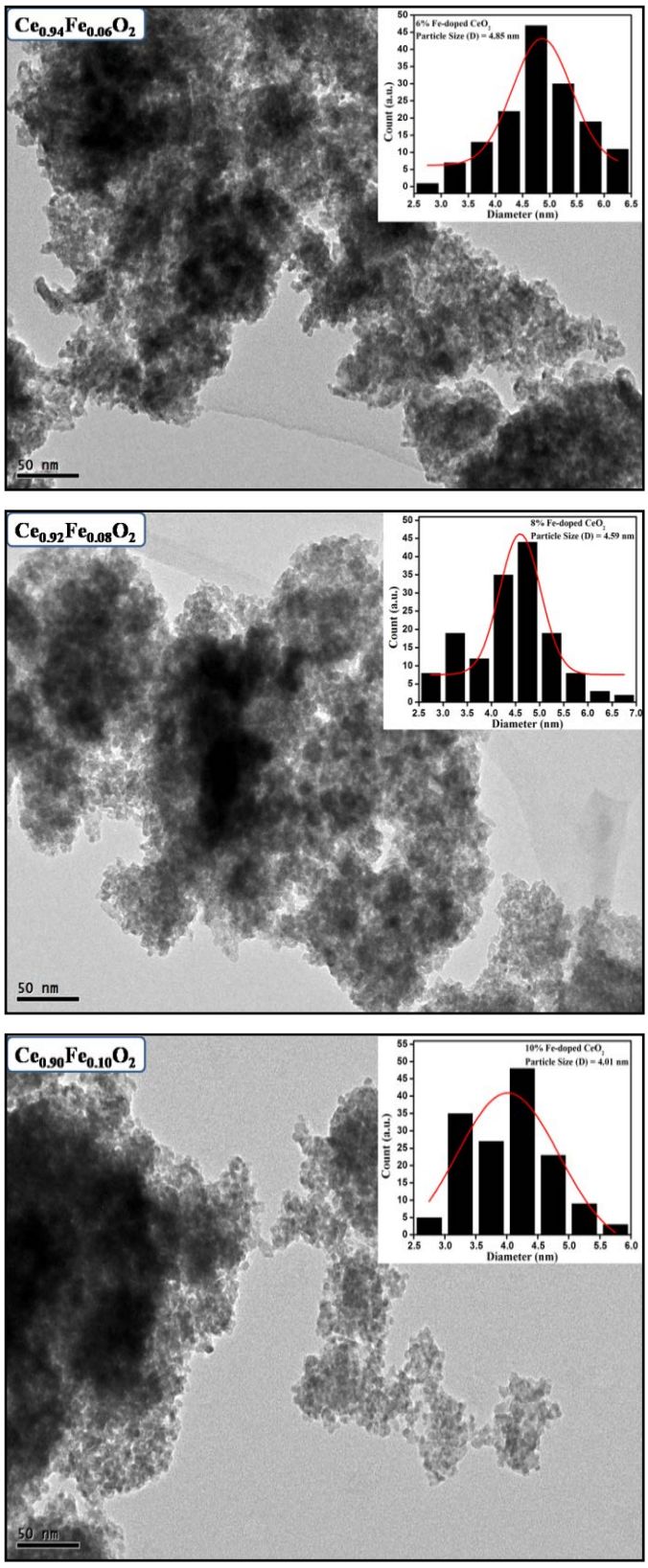


**Figure 5.3: TEM image for pure $CeO_2$ and $Ce_{1-x}Fe_xO_2$ (for $x$ = 0.02, 0.04, 0.06, 0.08, and 0.10) samples and inset histogram graphs shows the particle size of the corresponding sample.**

The surface morphology, size and structure of the pure $CeO_2$ and $Ce_{1-x}Fe_xO_2$ (for $x$ = 0.02, 0.04, 0.06, 0.08 and 0.10) NPs has been discussed using transmission electron spectroscopy. Figure 5.3 and 5.4 shows the TEM and HRTEM images for pure $CeO_2$ and $Ce_{1-x}Fe_xO_2$ (for $x$ = 0.02, 0.04, 0.06, 0.08 and 0.10) NPs, respectively. These images show the spherical shaped particles with aggregation and the morphology of the particles does not change with the incorporation of $Fe^{3+}$-ions in $CeO_2$ NPs. From the TEM images, the average crystallite size of the prepared samples has been calculated by the particle size distribution histogram (as shown in the inset of Figure 5.3).

The distribution has been found quite narrow in the range of ~4-5 nm, which are in good agreement with those obtained by XRD (as shown in Figure 5.1(b) and Table 5.1). The agglomeration of the particles indicates that the particles are nanocrystalline and promote the crystal growth with increase in the doping concentration of $Fe^{3+}$ ions. Figure 5.4 shows the HRTEM images of pure $CeO_2$ and $Ce_{1-x}Fe_xO_2$ NPs. These images indicate well developed, fine crystalline and clear fringes, which are randomly oriented to each other corresponding to (111) plane of pure $CeO_2$ and $Ce_{1-x}Fe_xO_2$ NPs. The lattice spacing ($d$) for pure $CeO_2$ is about 0.312 nm corresponding to (111) plane of the cubic fluorite structure. However, with the incoporation of $Fe^{3+}$ ions a gradual decrease has been found in the lattice spacing (as shown in Table 5.1). The decrease value of lattice spacing indicates the high crystallinity of all samples as well as the incorporation of small radie $Fe^{+3}$ cation in place of $Ce^{+3}$/$Ce^{+4}$ cation.

The inset of Figure 5.4 shows the SAED pattern of pure $CeO_2$ and $Ce_{1-x}Fe_xO_2$ samples. These SAED patterns made of concentric rings which are correspond to (111), (200), (220) and (311) planes for pure $CeO_2$ and $Ce_{1-x}Fe_xO_2$ samples, which confirms the cubic crystal structure of nanoparticles. These diffraction rings indicate that the particles are well crystallized with small particle size. The crystallinity of the samples has been found to increase with $Fe^{3+}$ doping concentration.

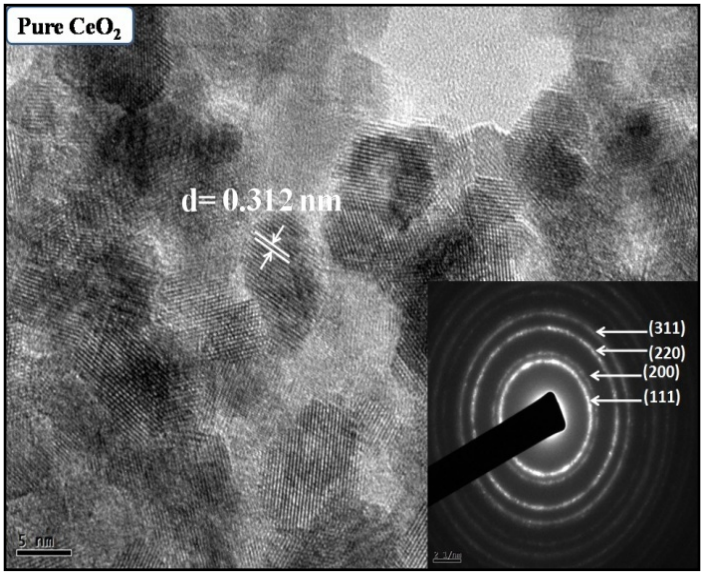
Pure $CeO_2$
d= 0.312 nm
(311)
(220)
(200)
(111)
5 nm

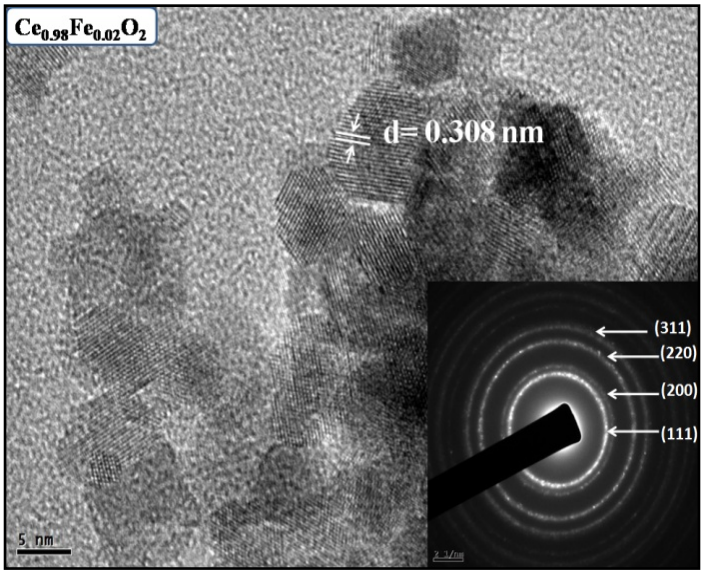
$Ce_{0.98}Fe_{0.02}O_2$
d= 0.308 nm
(311)
(220)
(200)
(111)
5 nm

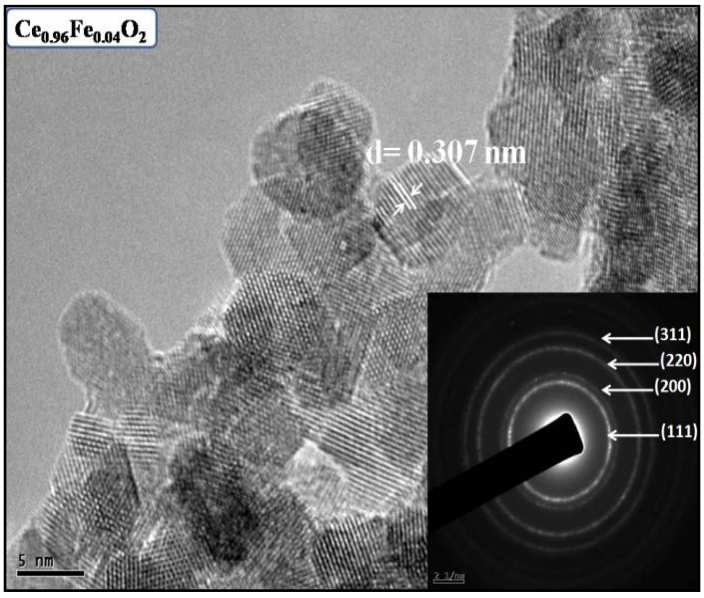
$Ce_{0.96}Fe_{0.04}O_2$
d= 0.307 nm
(311)
(220)
(200)
(111)
5 nm

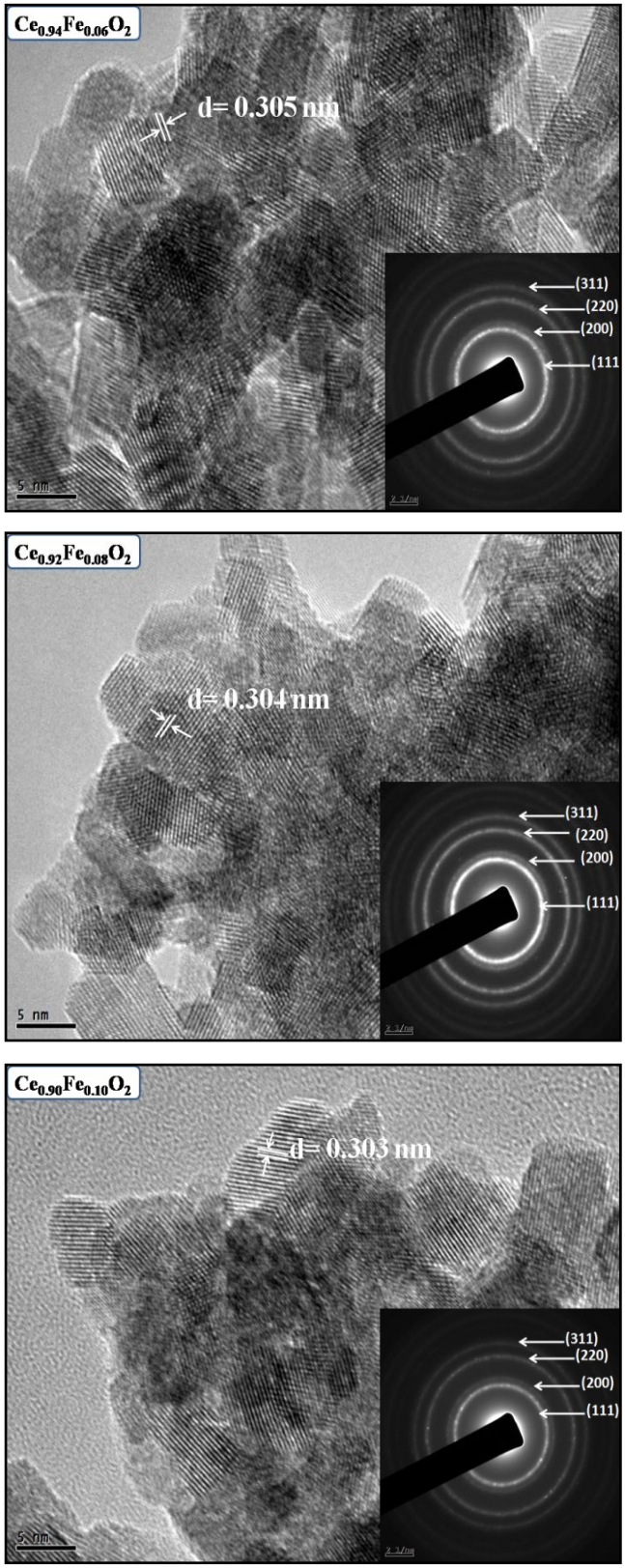


**Figure 5.4: HRTEM images of pure $CeO_2$ and $Ce_{1-x}Fe_xO_2$ (for $x$ = 0.02, 0.04, 0.06, 0.08, and 0.10) samples with *d*-spacing for (111) plane and inset show the SAED pattern of corresponding sample.**

### 5.3.2. Optical Properties

#### 5.3.2.1. UV-Vis-NIR analysis

The optical absorption spectra of pure $CeO_2$ and $Ce_{1-x}Fe_xO_2$ ($x$ = 0.02, 0.04, 0.06, 0.08 and 0.10) NPs are shown in the Figure 5.5(a). The absorption spectra have been measured in the range of 200-700 nm. The sharp absorbance peak of pure $CeO_2$ appears at about 308 nm. After incorporation of $Fe^{3+}$ ions, the maximum absorption peaks of $Ce_{1-x}Fe_xO_2$ ($x$ = 0.02, 0.04, 0.06, 0.08 and 0.10) NPs are found at 327.8, 328, 327.7, 330 and 338 nm, respectively. This shows a strong absorbance below 400 nm with the absorption peak in the UV-range. These peaks are generated due to charge transfer from 2p valance band of $O^{2-}$ to 4f conduction band of $Ce^{4+}$ states in $CeO_2$ NPs [179]. It can be clearly seen from absorption spectra, the optical properties are changed due to doping of $Fe^{3+}$ ions in $CeO_2$ NPs. The doping of $Fe^{+3}$ ion shift the absorption edges towards higher wavelength i.e. red shift and increases up to 338 nm. Since, the absorbance appear in the UV region that indicates that the band gap energy ($E_g$) of $Ce_{1-x}Fe_xO_2$ ($x$ = 0.02, 0.04, 0.06, 0.08 and 0.10) NPs is lower than that of pure $CeO_2$ NPs, which clearly show the doping effect in $CeO_2$ NPs. The red shift of the absorption edges of $Ce_{1-x}Fe_xO_2$ ($x$ = 0.02, 0.04, 0.06, 0.08 and 0.10) NPs are due to the result of interfacial polaron effect arising from electron-phonon interaction [262]. The optical band gap ($E_g$) for all samples has been calculated using Tauc's equation [263]:

$$\boldsymbol{\alpha h\upsilon = A(h\upsilon - E_g)^n} \qquad (\mathbf{5.9})$$

Where, $\alpha$ is the absorption coefficient, $h\nu$ is the energy of the incident photon, $E_g$ is the optical band gap energy, A is a constant relative to material and n is an index that depends on the nature of transition ($n$ = 1/2 for direct allowed transition). For direct allowed transition, $(\alpha h\nu)^2$ versus $h\nu$ extrapolate the linear part of the curve to x-axis gives the absorption band gap energy. Figure 5.5(b) shows the Tauc's plots of the pure $CeO_2$ and $Ce_{1-x}Fe_xO_2$ ($x$ = 0.02, 0.04, 0.06, 0.08 and 0.10) NPs. From the Tauc' plot the band gap of pure $CeO_2$, and $Ce_{1-x}Fe_xO_2$ ($x$ = 0.02, 0.04, 0.06, 0.08 and 0.10) NPs has been calculated as 3.06, 2.79, 2.78, 2.74, 2.73 and 2.58 eV, respectively. The band gap of pure $CeO_2$ NPs (3.06 eV) is smaller than that of reported bulk $CeO_2$ (3.2 eV) [167]. This reduction can be attributed to the

modulation of 4f electronic states from $Ce^{4+}$ ($4f^0$) to $Ce^{3+}$ ($4f^1$) implies the entrance of an extra electron into the 4f orbital, and this occupation of an extra electron in the orbital reduces the band gap energy of pure $CeO_2$ NPs [66].

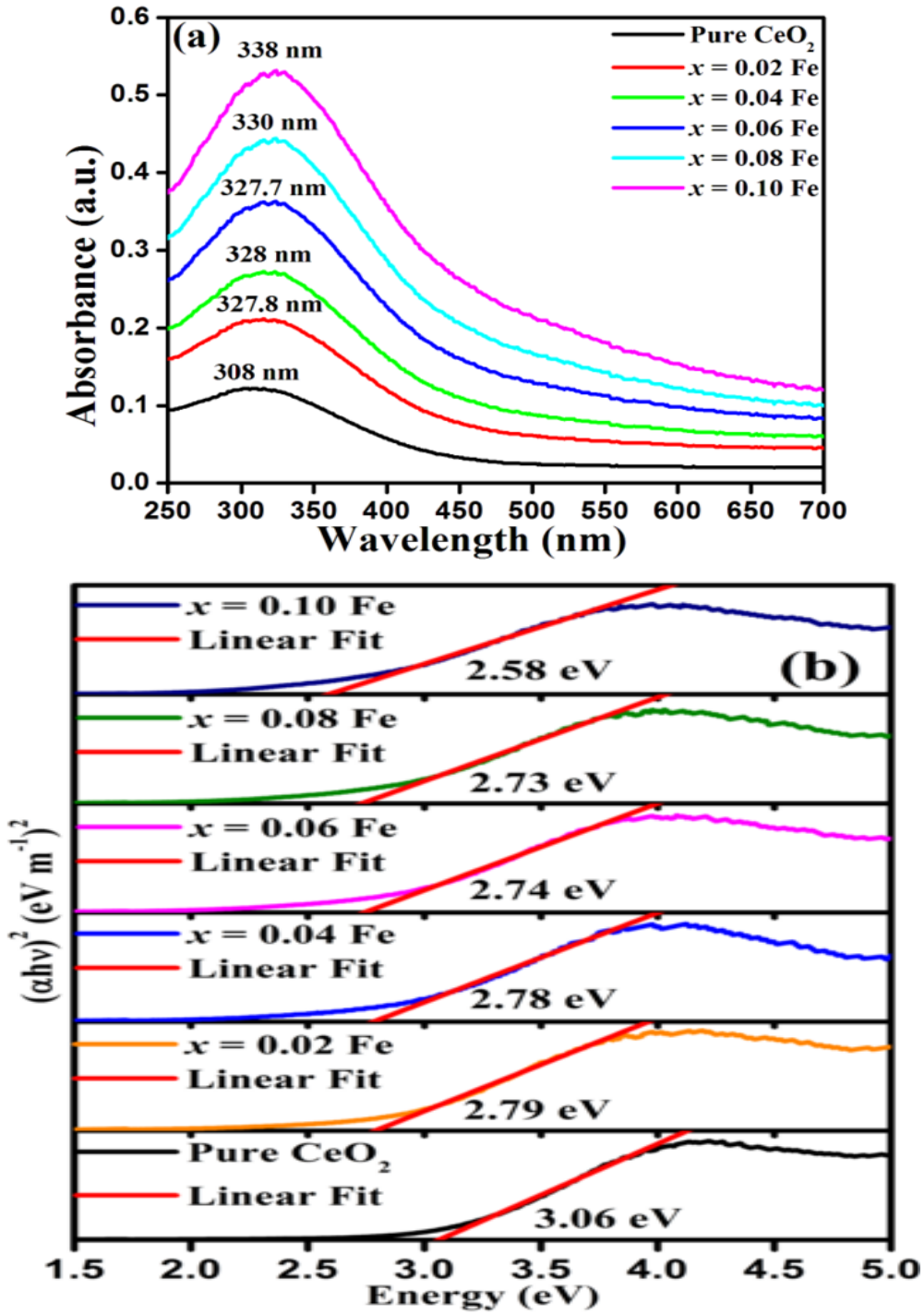


**Figure 5.5: (a) Room temperature optical absorbance spectra taken in the UV-visible range and (b) Tauc's plot of $(\alpha h\upsilon)^2$ versus Energy (eV) for the pure $CeO_2$ and $Ce_{1-x}Fe_xO_2$ (for $x$ = 0.02, 0.04, 0.06, 0.08 and 0.10) samples.**

The variation of $E_g$ with the fluency of Fe-doping concentration is shown in Figure 5.6, from which the band gap energy is observed to reduce with the fluency of $Fe^{3+}$-ions concentration.

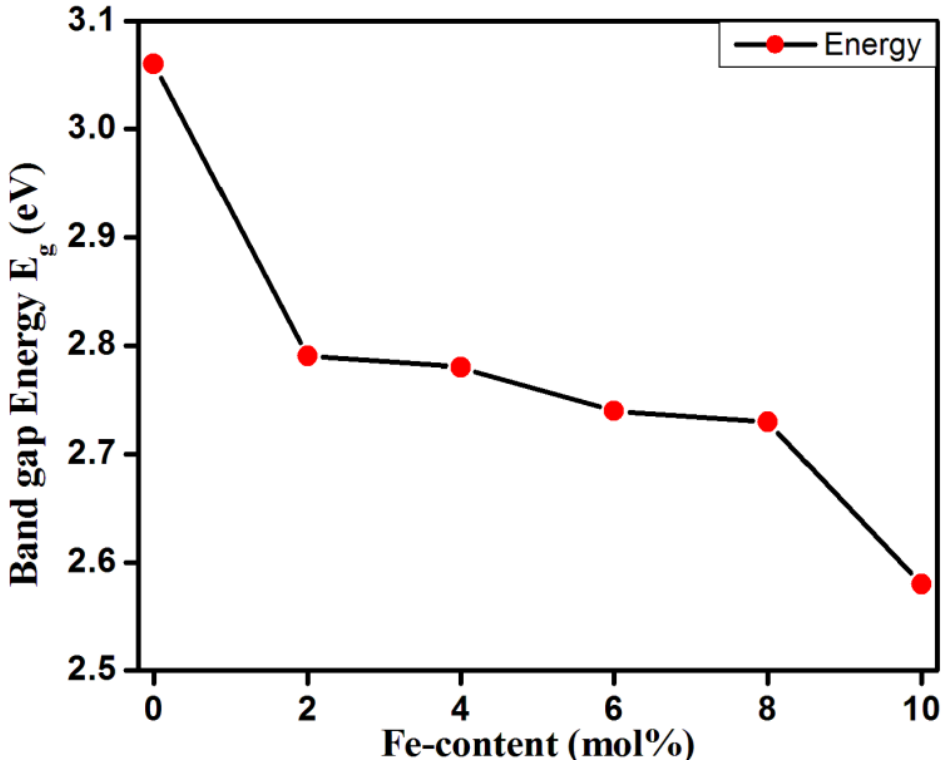


**Figure 5.6: Variation of band gap energy with Fe-doping concentration.**

Reduction of band gap may be due to creation of defect levels due to incorporation of Fe-doping [264]. The band gap energy of the material may also be influenced by either quantum size effect or electronegativity of the oxygen and metallic element [66]. But these factors may not be significant here since the quantum size effect apply only when the nanoparticles are in the narrow range of ~2-3 nm, results increase in band gap, whereas, the large difference in the electronegativity of oxygen and metallic element should also increase the band gap energy. Since, the electronegativity of Fe (1.81) is higher than Ce (1.12), therefore, the band gap of the Fe-doped $CeO_2$ samples should be larger than that of pure $CeO_2$. However, the observed difference in the band gap doesn't explain by the above mention factors. Hence, in the Fe-doped system, the reduction in the band gap may be due to appearance of localized impurity defect level created by the fluency of $Fe^{3+}$ ions doping, which may cause the oxygen vacancies and $Ce^{3+}$ defects [265].

The refractive index ($n$) of pure $CeO_2$ and $Ce_{1-x}Fe_xO_2$ NPs for optical band gap energy ($E_g$) has been calculated using following equation:

$$\frac{n^2-1}{n^2+2} = 1 - \sqrt{\frac{E_g}{20}} \qquad (5.10)$$

The calculated values of refractive index of pure $CeO_2$, $Ce_{1-x}Fe_xO_2$ (for $x$ = 0.02, 0.04, 0.06, 0.08 and 0.10) samples are 2.38, 2.45, 2.46, 2.47, 2.50 and 2.52, respectively. The value of $n$ is increasing with the increase in the Fe-dopant ions in $CeO_2$ NPs, which revel that structure becomes denser with the fluency of Fe-ions concentration indicating a closely packed structure due to incorporation of smaller radie Fe cation [119].

### 5.3.2.2. Raman Analysis

For investigating the effect of Fe-ions doping on phase, change in the local structure and defects such as oxygen vacancies, Raman spectroscopic measurements have been taken on our well characterized pure $CeO_2$ and Fe-doped $CeO_2$ NPs. Figure 5.7 shows the Raman spectra of pure $CeO_2$ and $Ce_{1-x}Fe_xO_2$ ($x$ = 0.02, 0.04, 0.06, 0.08 and 0.10) NPs, measured in the range of 220-1320 $cm^{-1}$.

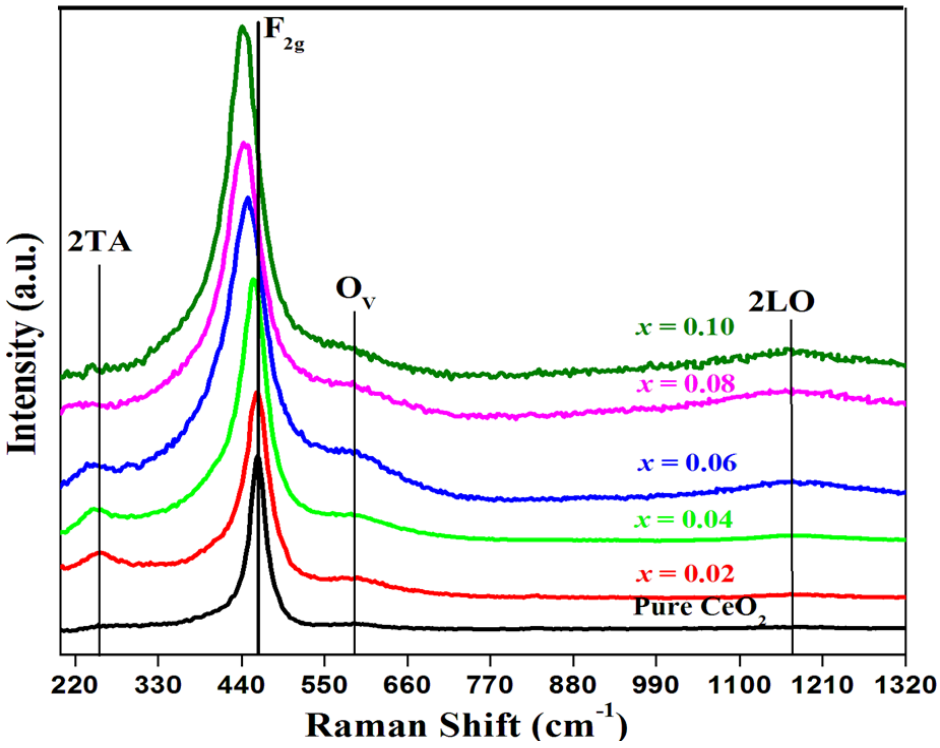


**Figure 5.7: Raman spectra of pure $CeO_2$ and $Ce_{1-x}Fe_xO_2$ (for $x$ = 0.02, 0.04, 0.06, 0.08 and 0.10) samples.**

The Raman peak observed at ~440-460 $cm^{-1}$ is attributed to the Raman active vibrational mode ($F_{2g}$) of pure $CeO_2$ and $Ce_{1-x}Fe_xO_2$ ($x$ = 0.02, 0.04, 0.06, 0.08 and 0.10) NPs, which is corresponding to the symmetrical breathing mode of the oxygen ions around $Ce^{4+}$ ions (O-Ce-O) [253, 266]. The $F_{2g}$ mode is assigned to the cubic fluorite metal dioxide, related to the first-order symmetrical stretching mode of Ce-$O_8$ vibrational unit. This mode is sensitive to any disorder in the oxygen sublattice resulting from thermal, doping and particle size induced effects [267]. The Raman active mode ($F_{2g}$) is shifted about 3.5 $cm^{-1}$ compared with the bulk $CeO_2$ (464 $cm^{-1}$) with the $Fe^{+3}$ ion doping, due to the change in the bond length or lattice spacing [179]. Now, for pure $CeO_2$ NPs, the shifting in the $F_{2g}$ peak is related with the increased value of lattice spacing due to the smaller size of $CeO_2$ (5.87 nm) NPs [268]. Moreover, the frequency shift in Raman active mode can also be calculated by the following equation [269]:

$$\Delta\omega = -3\gamma\omega_o\left(\frac{\Delta a}{a_o}\right) \qquad (5.11)$$

Where, $\Delta\omega$ is the Raman frequency shift, $\gamma$ is the Grüneisen constant (for $CeO_2$ $\gamma$ =1.24), $\omega_o$ is the Raman frequency of bulk $CeO_2$ (464 $cm^{-1}$), $\Delta a$ is the change in the lattice parameter, and $a_o$ is the lattice parameter of bulk $CeO_2$ (0.541 nm). The calculated Raman frequency shift is about 3.19 $cm^{-1}$ which is approximately close to the above experimental value. However, it has been observed that $F_{2g}$ mode is shifted to the lower frequencies (red shift) after incorporation of $Fe^{3+}$ ions, the values are tabulated in Table 5.2. This shift may be ascribed due to symptomatic increase in the tensile stress and related defects such as oxygen vacancies generated when $Fe^{3+}$ ions substitutes the $Ce^{4+}$ ions in the lattice of $CeO_2$ NPs [270]. The fractional change in lattice parameter of pure $CeO_{2-\delta}$ NPs is due to the consequences of the formation of oxygen vacancies that leads to the oxygen deficit ($\delta$) material. The oxygen deficit constant ($\delta$) can be calculated by using the following equation [271]:

$$\delta = 2.66\left(\frac{\Delta\omega}{\omega_o}\right) \qquad (5.12)$$

The δ value of $CeO_{2-\delta}$ NPs is 0.018, which indicates the replacement of $Ce^{4+}$ ions by $Ce^{3+}$ ions, which is partially compensated by the loss of large $O_2$ (1.380 Å) and hence indicate the formation of oxygen vacancies (1.164 Å) [272]. In addition, the broadening of Raman active mode ($F_{2g}$) has been observed after incorporation of $Fe^{3+}$ ions and is found to increase with dopant $Fe^{+3}$ ions concentration, which may be ascribed due to the reduction in the phonon lifetime in the nanocrystalline samples [200, 147]. However, the red shift and the broadening of $F_{2g}$ peak for $Ce_{1-x}Fe_xO_2$ samples may be due to the decrease in the crystallite size, which has been evidenced from our XRD results [273]. Besides of Raman active mode ($F_{2g}$), two second-order Raman modes are also appeared in the range of ~246-275 $cm^{-1}$ and ~548-577 $cm^{-1}$, which are assigned to the second-order transverse acoustic mode (2TA) and non-degenerated longitudinal optical mode (LO), respectively [274]. The latter Raman peak ~548-577 $cm^{-1}$ is related to the defects which results from the formation of oxygen vacancies ($O_v$). This Raman peak for pure $CeO_2$ NPs is appeared due to the replacement of $Ce^{4+}$ ions by $Ce^{3+}$ ions, results in formation of oxygen vacancies at $Ce^{3+}$ site. While, for Fe-doped $CeO_2$ samples this Raman peak originates due to $Fe^{3+}$ ion replaces $Ce^{4+}$ ion and oxygen vacancies are generated to balance the charge compensation [275]. The Raman peak appeared in the range of ~1165-1181 $cm^{-1}$ is another second overtone of the longitudinal optical mode (2LO) [173, 276]. Absence of any Raman peak corresponding to the impurity phase related to Fe-ion such as $Fe_2O_3$ exhibits at 222, 288, 407 and 605 $cm^{-1}$, which are not observed in the $Ce_{1-x}Fe_xO_2$ ($x$ = 0.02, 0.04, 0.06, 0.08 and 0.10) NPs Raman spectra, which confirms the well incorporation of $Fe^{3+}$ ions in the $CeO_2$ matrix [277], also support the observations made from XRD results. The peak intensity of $F_{2g}$ and oxygen vacancy bands has been calculated by Gaussian fitting and indicated as $I_{F_{2g}}$ and $I_{O_v}$, respectively, and their relative intensity ratio is tabulated in Table 5.3.

**Table 5.3: The Position of Raman active modes from Raman spectra, grain size, defect concentration and relative peak intensity ratio**

| Samples | Grain Size ($d_g$) | Defect Concentration N ($cm^{-3}$) | Position of Raman active mode ($cm^{-1}$) and Vibrational Mode | | | | $I_{O_v}/I_{F_{2g}}$ |
|---|---|---|---|---|---|---|---|
| | | | $2TA$ | First-order Scattering | Second-order Scattering | | |
| | | | | $F_{2g}$ | $A_{1g} + F_{2g}$ $(O_v)$ | $2LO$ | |
| **Pure $CeO_2$** | 7.0 | $1.2\times10^{21}$ | 275.8 | 460.5 | 577.9 | 1172.7 | 0.032 |
| $Ce_{0.98}Fe_{0.02}O_2$ | 4.0 | $2.2\times10^{21}$ | 255.8 | 457.7 | 576.9 | 1181.0 | 0.074 |
| $Ce_{0.96}Fe_{0.04}O_2$ | 3.7 | $2.4\times10^{21}$ | 258.6 | 453.1 | 565.5 | 1182.3 | 0.090 |
| $Ce_{0.94}Fe_{0.06}O_2$ | 2.3 | $3.8\times10^{21}$ | 255.1 | 444.5 | 565.9 | 1177.5 | 0.095 |
| $Ce_{0.92}Fe_{0.08}O_2$ | 2.5 | $3.5\times10^{21}$ | 245.8 | 440.9 | 561.1 | 1174.1 | 0.062 |
| $Ce_{0.90}Fe_{0.10}O_2$ | 2.7 | $3.3\times10^{21}$ | 270.1 | 440.6 | 548.2 | 1165.7 | 0.067 |

The $I_{O_v}/I_{F_{2g}}$ ratio reveals the relative concentration of oxygen vacancies present in the respective pure and Fe-doped $CeO_2$ samples. From Table 5.3, it can be observed that Fe-doping gradually increases the amount of oxygen vacancy up to 6% doping concentration of Fe-ions, after that it decrease at 8% and further increase at 10% doping concentration. It can be observed that the larger amount of oxygen vacancy present in the 6% Fe-doped $CeO_2$ sample as compared to the other samples. Moreover, Raman line broadening of $F_{2g}$ mode can be described by the dependence with its half-width at half-maxima (HWHM) on the inverse of grain size, which follows the linear behaviour [278]:

$$\boldsymbol{\Gamma\ (cm^{-1}) = 10 + \left(\frac{124.7}{d_g(nm)}\right)} \qquad \textbf{(5.12)}$$

Where, Γ ($cm^{-1}$) is full width at half maxima (FWHM) of $F_{2g}$ mode and $d_g$ is the grain size. The above mentioned relation can be used for determining the grain size of the samples, we have shown the calculated grain size in Table 5.3. Figure 5.8 displays the dependence of the HWHM of the Raman line of $F_{2g}$ mode on the inverse of the grain size, which is in good correlation with the reports for the $CeO_2$ nanocrystalline samples [147]. HWHM values of $Ce_{1-x}Fe_xO_2$ ($x$ = 0.00, 0.02, 0.04, 0.06, 0.08 and 0.10) samples are 13.8, 20.4, 21.4, 31.2, 29.8 and 27.6 $cm^{-1}$, respectively, shows that HWHM increases with decreasing the grain size.

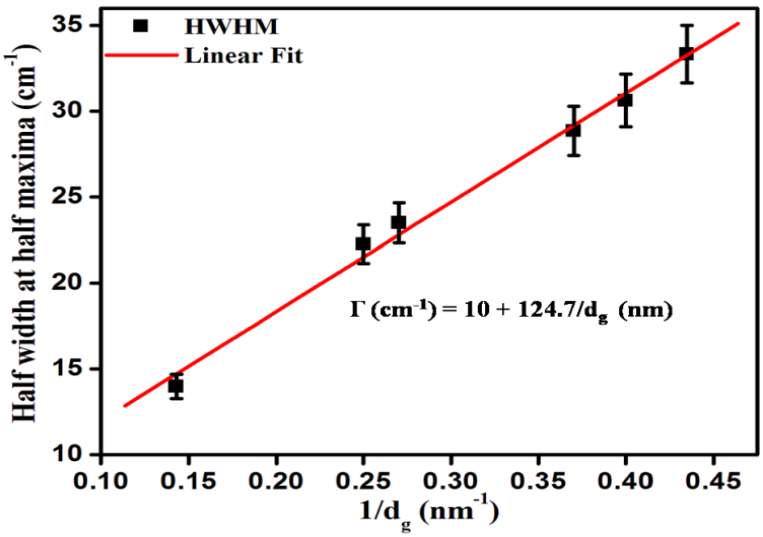


**Figure 5.8: The relationship between the half-width at half-maxima (HWHM) of the Raman line broadening of $F_{2g}$ and the inverse of the grain size ($d_g$) obtained for pure $CeO_2$ and Fe-doped $CeO_2$ NPs.**

The concentration of oxygen vacancies has been calculated using spatial correlation model from the relationship between correlation length (L) and grain size ($d_g$) [279]:

$$\boldsymbol{L\ (nm) = \sqrt[3]{\left(\frac{\alpha}{2d_g}\right)^2 \left[(d_g - 2\alpha)^3 + 4d_g^2\alpha\right]}} \qquad (\mathbf{5.13})$$

Where, L is the average distance between two lattice defects and α is the radius of $CeO_2$ units (0.34 nm) determined from universal constants. The oxygen defect concentration (N) can also be calculated from the correlation length (L) as a function of grain size [279]:

$$\boldsymbol{N\ (cm^{-3}) = \frac{3}{4\pi L^3}} \qquad (\mathbf{5.14})$$

The calculated values of N for all samples are shown in Table 5.3. Figure 5.9 shows the concentration of oxygen vacancy of pure $CeO_2$ and Fe-doped $CeO_2$ samples as a function of their grain size ($d_g$). This shows that $Ce_{0.94}Fe_{0.06}O_2$ sample has highest concentration of oxygen vacancies on their surface ($3.8\times10^{21}$ $cm^{-3}$) as well as lowest grain size, which is confirming that for small grain size the defect concentration become higher for our samples.

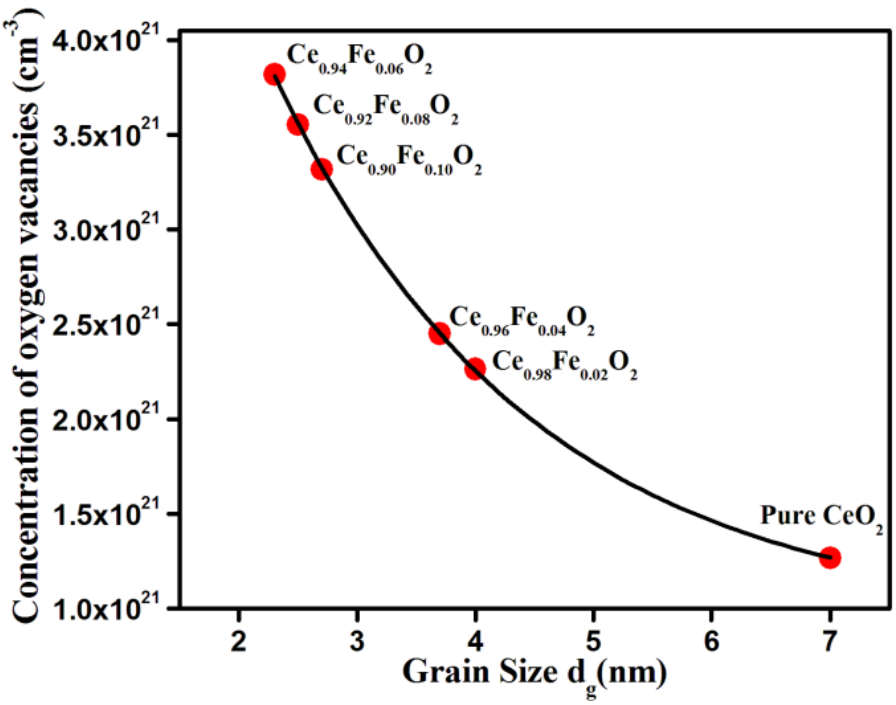


**Figure 5.9: Concentration of oxygen vacancies as a function of grain size of pure $CeO_2$ and Fe-doped $CeO_2$ samples**

### 5.3.3. Electronic Structure Properties

#### 5.3.3.1. XPS analysis

##### 5.3.3.1.1. Ce 3d XPS Spectra

The chemical state of the elements present in the pure $CeO_2$ and $Ce_{1-x}Fe_xO_2$ ($x$ = 0.02, 0.04, 0.06, 0.08 and 0.10) NPs has been investigated by XPS techinque. The core level spectra of Ce 3d, O 1s and Fe 2p has been recorded and depicted in the Figure 5.10, 5.11 and 5.12, respectively. All the peaks has been calibrated with the C 1s peak at 284.6 eV. A Guassian fit has been carried out for all the core level XPS spectra of Ce 3d, O 1s and Fe 2p. Figure 5.10 depicts the Ce 3d core level XPS spectra for pure $CeO_2$ and $Ce_{1-x}Fe_xO_2$ ($x$ = 0.02, 0.04, 0.06, 0.08 and 0.10) NPs. Ce 3d peaks for pure and Fe-doped $CeO_2$ NPs display a complex spectra due to co-existence of multiple oxidation states of Ce-ion. The peaks labelled as '*u*' and '*v*' is due to the $3d_{3/2}$ and $3d_{5/2}$ spin-orbit coupling states, repsectively. The peaks denoted by *v*, *v''*, *v'''*, *u*, *u''* and *u'''* are characteristics peaks of $Ce^{4+}$ ions and remaining other peaks marked as $v_o$, *v'*, $u_o$ and *u'* are of $Ce^{3+}$ ions. It has been reported that the two spin-orbit doubling states for $Ce^{3+}$ ions i.e. $u_o$ ($v_o$) and *u'* (*v'*) are arising due to overlapping of the Ce 4f levels with the O 2p states that contain Ce ($3d^9$ $4f^2$) O $2p^5$ and Ce ($3d^9$ $4f^1$) O $2p^6$ electronic confugration, respectively. Whereas, the three doublet states for $Ce^{4+}$ ions i.e. *u* (*v*), *u''* (*v"*) and *u'"* (*v'"*) are containing Ce ($3d^9$ $4f^2$) O $2p^4$, Ce ($3d^9$ $4f^1$) O $2p^5$, Ce ($3d^9$ $4f^0$) O $2p^6$ electronic confugration, respectively [119].

The spin-orbit splitting energy for the peaks *u* and *v* for pure $CeO_2$ and $Ce_{1-x}Fe_xO_2$ ($x$ = 0.02, 0.04, 0.06, 0.08 and 0.10) NPs is about 18.7, 18.5, 18.9, 18.4, 18.6 and 18.1, respectively. The positions of deconvoluted peaks of all samples are presented in Table 5.3. Form the above mentioned details of Ce 3d XPS spectra of all samples indicate coexistance of both $Ce^{4+}$ and $Ce^{3+}$ oxidation sates for Ce-ions. The surface concentration of $Ce^{3+}$ and $Ce^{4+}$ for all the samples has been calculated using the following equations [206],

$$[Ce^{3+}] = \frac{A_{Ce^{3+}}}{A_{Ce^{3+}} + A_{Ce^{4+}}} \times 100\% \qquad (5.15)$$

$$[Ce^{4+}] = \frac{A_{Ce^{4+}}}{A_{Ce^{3+}} + A_{Ce^{4+}}} \times 100\% \qquad (5.16)$$

Where, $A_{Ce^{3+}} = v_o + v' + u_o + u'$ and $A_{Ce^{4+}} = v + v'' + v''' + u + u'' + u'''$ are the sum of the area of Gaussian peaks of various final states.

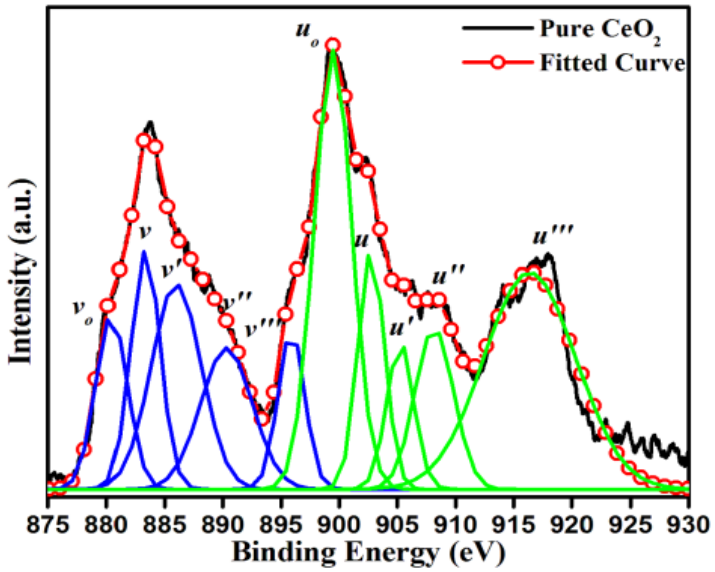
Pure CeO2
Fitted Curve
Intensity (a.u.)
Binding Energy (eV)
875 880 885 890 895 900 905 910 915 920 925 930
uo
u'''
u''
u'
u
v
v'
v''
v'''
vo

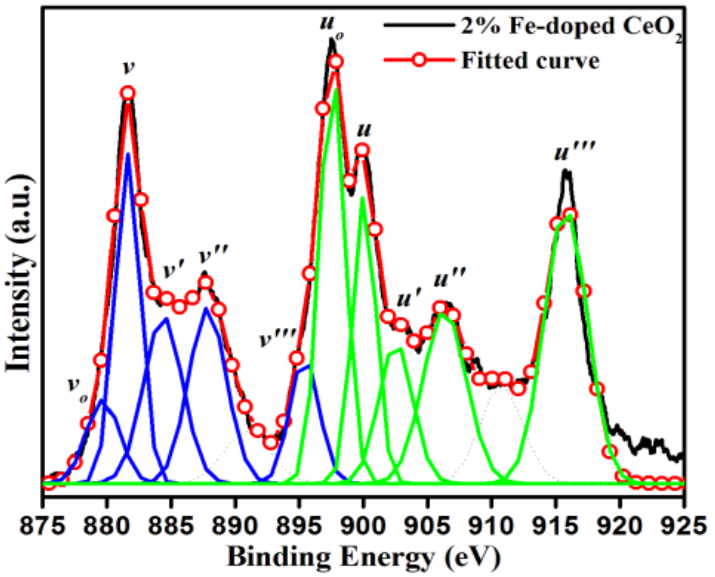
2% Fe-doped CeO2
Fitted curve
Intensity (a.u.)
Binding Energy (eV)
875 880 885 890 895 900 905 910 915 920 925
uo
u'''
u''
u'
u
v
v'
v''
v'''
vo

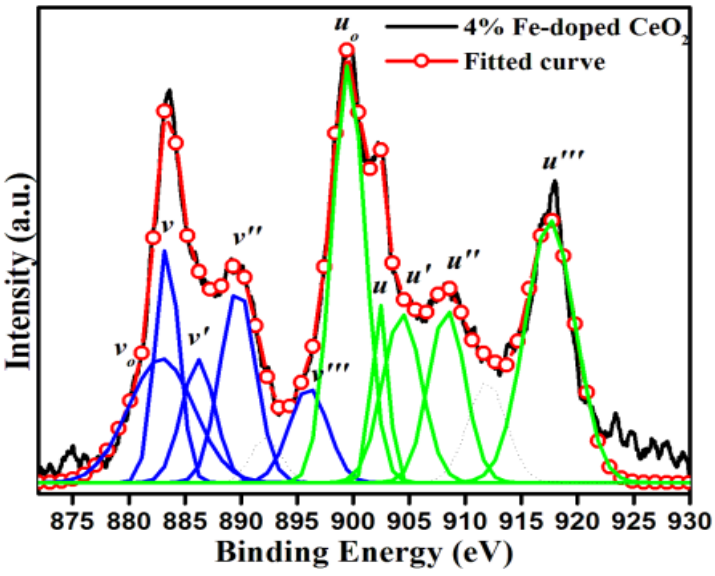
4% Fe-doped CeO2
Fitted curve
Intensity (a.u.)
Binding Energy (eV)
875 880 885 890 895 900 905 910 915 920 925 930
uo
u'''
u''
u'
u
v
v'
v''
v'''
vo

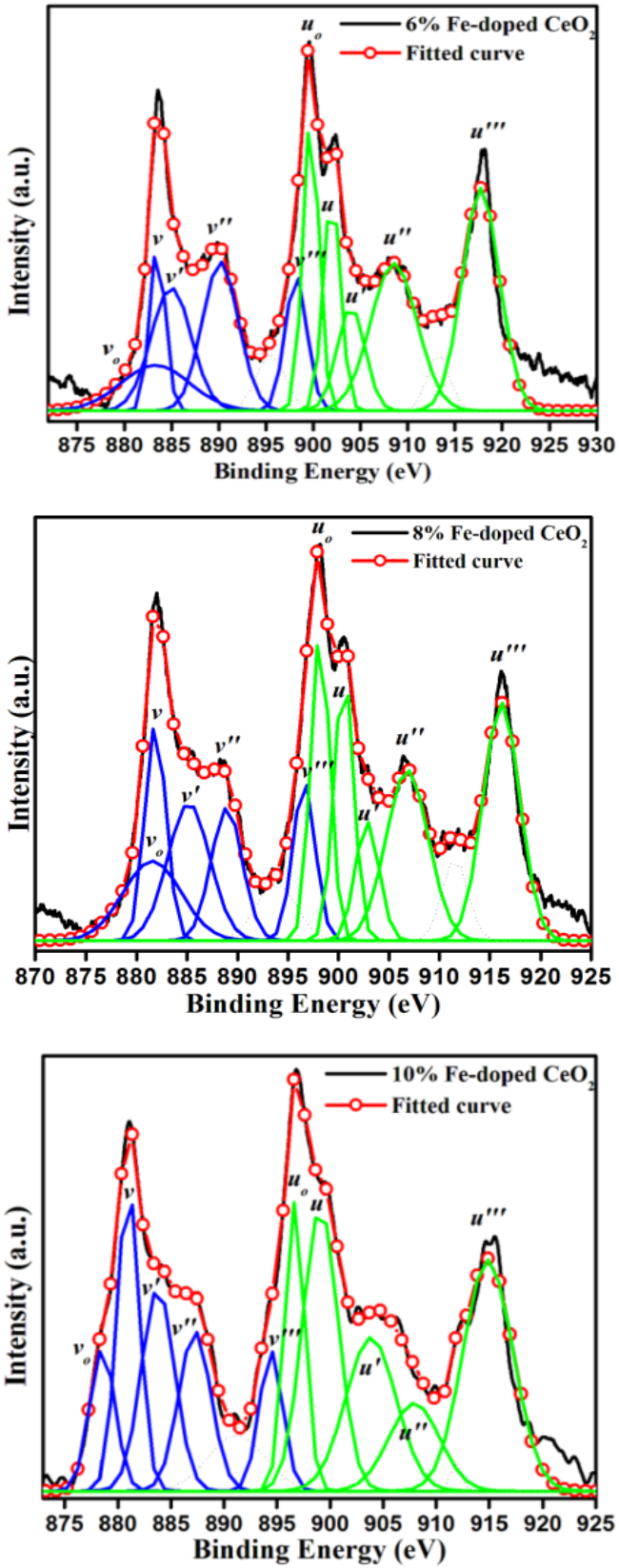


**Figure 5.10: Ce 3d XPS spectra of pure $CeO_2$ and $Ce_{1-x}Fe_xO_2$ ($x$ = 0.02, 0.04, 0.06, 0.08 and 0.10) NPs at 300K**

**Table 5.4: Ce 3d XPS peak assignments for pure $CeO_2$ and $Ce_{1-x}Fe_xO_2$ ($x$ = 0.02, 0.04, 0.06, 0.08 and 0.10) samples**

| Sample | Peak assignments and Binding Energy (eV) | | | | | | | | | | $[Ce^{3+}]$ | $[Ce^{4+}]$ | $[Ce^{3+}]/[Ce^{4+}]$ |
|---|---|---|---|---|---|---|---|---|---|---|---|---|---|
| | $Ce\ 3d_{5/2}$ | | | | | $Ce\ 3d_{3/2}$ | | | | | | | |
| | $v_o$ $Ce^{3+}$ | $v$ $Ce^{4+}$ | $v'$ $Ce^{3+}$ | $v''$ $Ce^{4+}$ | $v'''$ $Ce^{4+}$ | $u_o$ $Ce^{3+}$ | $u$ $Ce^{4+}$ | $u'$ $Ce^{3+}$ | $u''$ $Ce^{4+}$ | $u'''$ $Ce^{4+}$ | | | |
| Pure $CeO_2$ | 880.4 | 883.3 | 885.9 | 890.3 | 895.8 | 899.4 | 902 | 905.2 | 908.1 | 916.3 | 41.51 | 58.48 | 0.71 |
| $Ce_{0.98}Fe_{0.02}O_2$ | 879.6 | 881.5 | 884.3 | 887.8 | 895.4 | 897.5 | 900.0 | 902.5 | 906.3 | 915.7 | 35.72 | 64.27 | 0.56 |
| $Ce_{0.96}Fe_{0.04}O_2$ | 882.8 | 883.4 | 886.2 | 889.7 | 896.0 | 899.5 | 902.3 | 904.3 | 908.3 | 917.5 | 45.93 | 54.06 | 0.85 |
| $Ce_{0.94}Fe_{0.06}O_2$ | 883.2 | 883.5 | 884.9 | 890.2 | 898.2 | 899.7 | 901.9 | 904.0 | 908.5 | 917.7 | 34.50 | 65.49 | 0.53 |
| $Ce_{0.92}Fe_{0.08}O_2$ | 881.5 | 881.9 | 885.2 | 888.9 | 896.6 | 898.2 | 900.5 | 902.8 | 906.8 | 916.1 | 36.37 | 63.62 | 0.57 |
| $Ce_{0.90}Fe_{0.10}O_2$ | 878.5 | 880.9 | 883.7 | 887.2 | 894.4 | 896.6 | 899.0 | 903.8 | 907.9 | 914.8 | 36.69 | 63.30 | 0.58 |

The relative concentration of $Ce^{3+}$ ions has been calculated by $[Ce^{3+}]/[Ce^{4+}]$ ratio, indicates larger $Ce^{3+}$ concentration for $Ce_{0.96}Fe_{0.04}O_2$ sample than that of other samples (as shown in Table 5.4). However, the variation in the fluency of Fe-ions affects the concentration of $Ce^{3+}$ ions of $Ce_{1-x}Fe_xO_2$ ($x$ = 0.02, 0.04, 0.06, 0.08 and 0.10) samples, which may be due to the introduction of $Fe^{3+}$ ions into $CeO_2$ NPs causes the partial reduction of $Ce^{4+}$ ions [280]. Furthermore, increase in the $[Ce^{3+}]/[Ce^{4+}]$ ratio also indicates the formation of oxygen vacancies at the lattice side for maintaining the charge neutrality when the oxidation state $Ce^{4+}$ change to $Ce^{3+}$ state of Fe-doped $CeO_2$ samples.

#### 5.3.3.1.2. Fe 2p XPS Spectra

The Fe 2p XPS spectra of $Ce_{1-x}Fe_xO_2$ ($x$ = 0.02, 0.04, 0.06, 0.08 and 0.10) samples are shown in Figure 5.11. The Fe 2p XPS spectra shows the characteristic peaks Fe $2p_{3/2}$ and Fe $2p_{1/2}$ at binding energies around 714.30 and 728.26 eV (for $Ce_{0.98}Fe_{0.02}O_2$), 715.13 and 728.99 eV (for $Ce_{0.96}Fe_{0.04}O_2$), 715 and 728.46 eV (for $Ce_{0.94}Fe_{0.06}O_2$), 714.98 and 728.83 eV (for $Ce_{0.92}Fe_{0.08}O_2$) and 716.59 and 730.57 eV (for $Ce_{0.90}Fe_{0.10}O_2$), respectively. The observed peak positions at these binding energy positions are corresponding to the $Fe^{3+}$ oxidation state of Fe-ion [281]. The binding energy difference between Fe $2p_{3/2}$ and Fe $2p_{1/2}$ for $Ce_{1-x}Fe_xO_2$ ($x$ = 0.02, 0.04, 0.06, 0.08 and 0.10) samples is about 13.96, 13.01, 13.86, 13.46, 13.85, and 13.98 eV, respectively.

With the change in the concentration of Fe-ions in the $CeO_2$ NP samples, the core level Fe 2p XPS spectra shows variation in the binding energies, which may be due to the incorporation of $Fe^{2+}$ in place of $Fe^{3+}$ ions. The increase in the values of difference in the binding energy suggested presence of $Fe^{3+}$ states and decrement suggested the change in the oxidation state of Fe-ion from $Fe^{3+}$ to $Fe^{2+}$, which may be due to the change in the electro-negativity of the ligands. Since, the elecro-negativity of Fe-ion (1.83) is higher than Ce-ion (1.12) on pauling scale, due to this the electron density near Fe-ions increases. Therefore, with the smaller amount of energy, Fe 3d electrons easily promote to unfilled Fe 4s orbital, due to this reason $Fe^{3+}$ changes to $Fe^{2+}$ state [282].

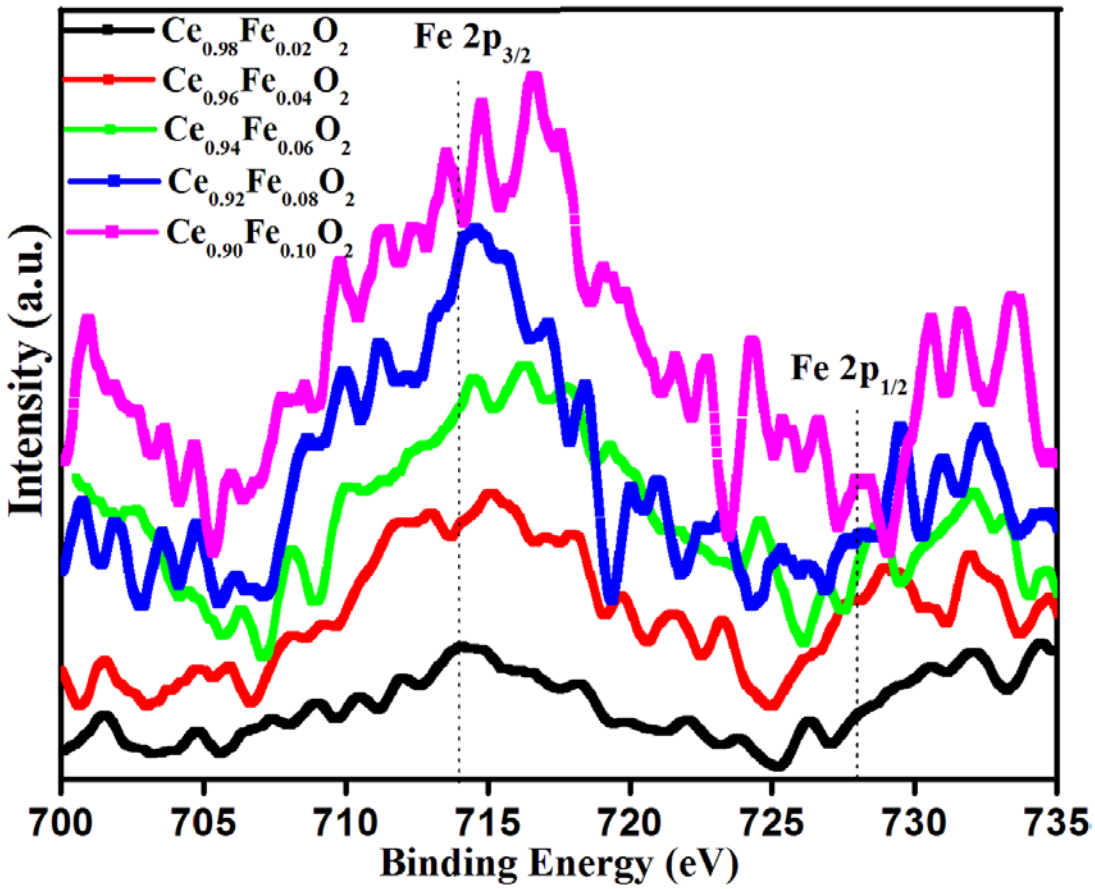


**Figure 5.11: Fe 2p XPS spectra of pure $CeO_2$ and $Ce_{1-x}Fe_xO_2$ ($x$ = 0.02, 0.04, 0.06, 0.08 and 0.10) NPs**

#### 5.3.3.1.3. O 1s XPS Spectra

Figure 5.12 displays the O 1s XPS spectra of pure $CeO_2$ and $Ce_{1-x}Fe_xO_2$ ($x$ = 0.02, 0.04, 0.06, 0.08 and 0.10) NP samples. The O 1s XPS spectra of all samples are fitted with three Gaussians centred at ~525.2-528 eV, ~528.1-529.3 eV and 530.3-531.7 eV is attributed to lattice oxygen $O^{2-}$ ($O_L$), oxygen vacancies ($O_V$) related to the oxygen bound to $Ce^{3+}$ states and surface hydroxyl group and various carbonate species, respectively [281, 283, 284]. The positions of deconvoluted O 1s peaks of all samples are shown in Table 5.5. It can be clearly observed that after incorporation of Fe-ions into the $CeO_2$ lattice site, position of peaks have been found to shift towards the higher binding enegy side, which may be due to higher electro-negativity of Fe-ion (1.83) than that of Ce-ion (1.12). The quantitative estimation of lattice oxygen ($O_L$) and oxygen vacancies ($O_V$) has also been shown in Table 5.5.

**Table 5.5: XPS binding energies of individual peaks of O 1s spectra for pure $CeO_2$ and $Ce_{1-x}Fe_xO_2$ ($x$ = 0.02, 0.04, 0.06, 0.08 and 0.10) samples**

| Sample | O 1s Peak position | | | | |
|---|---|---|---|---|---|
| | Lattice oxygen species ($O_L$) | | Oxygen vacancy species ($O_V$) | | $OH^-$ group species BE (eV) |
| | BE (eV) | $\%O_L = \frac{A_{O_L}}{A_{O_L} + A_{O_V}} \times 100$ | BE (eV) | $\%O_V = \frac{A_{O_V}}{A_{O_L} + A_{O_V}} \times 100$ | ($O_\alpha$) |
| **Pure $CeO_2$** | 525.25 | 34.51 | 528.24 | 65.48 | 531.05 |
| $Ce_{0.98}Fe_{0.02}O_2$ | 527.29 | 47.25 | 528.11 | 52.74 | 530.45 |
| $Ce_{0.96}Fe_{0.04}O_2$ | 527.03 | 53.15 | 528.18 | 46.84 | 531.06 |
| $Ce_{0.94}Fe_{0.06}O_2$ | 528.95 | 58.44 | 529.39 | 41.55 | 531.87 |
| $Ce_{0.92}Fe_{0.08}O_2$ | 526.95 | 38.47 | 528.84 | 61.52 | 531.71 |
| $Ce_{0.90}Fe_{0.10}O_2$ | 525.87 | 40.74 | 528.23 | 59.25 | 530.35 |

The relative area ratio of $O_L$ and $O_V$ indicates that with the incorporation of Fe-ions, the lattice oxygen is increased while oxygen vacancies is found to decrease. From our analysis of Ce 3d XPS core level spectra, we have detected the presence of $Ce^{3+}$ cations in all the samples, which show the production of oxygen vacancy.

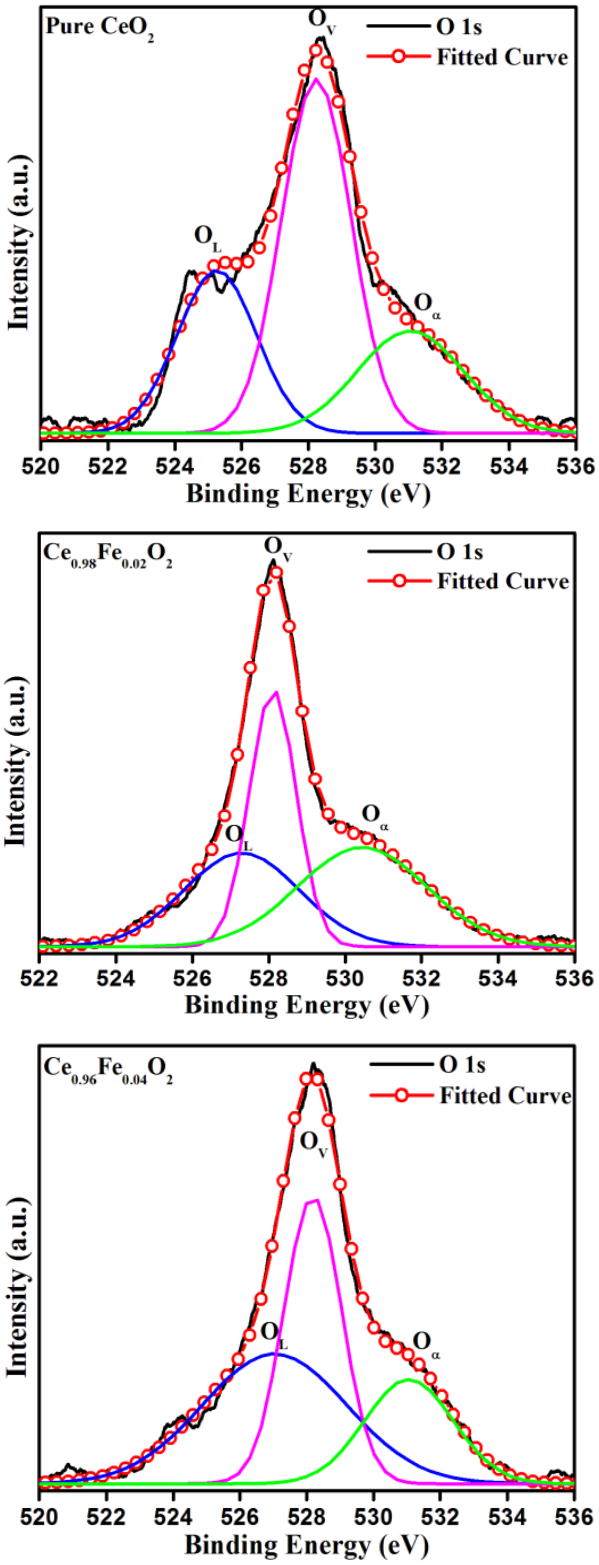

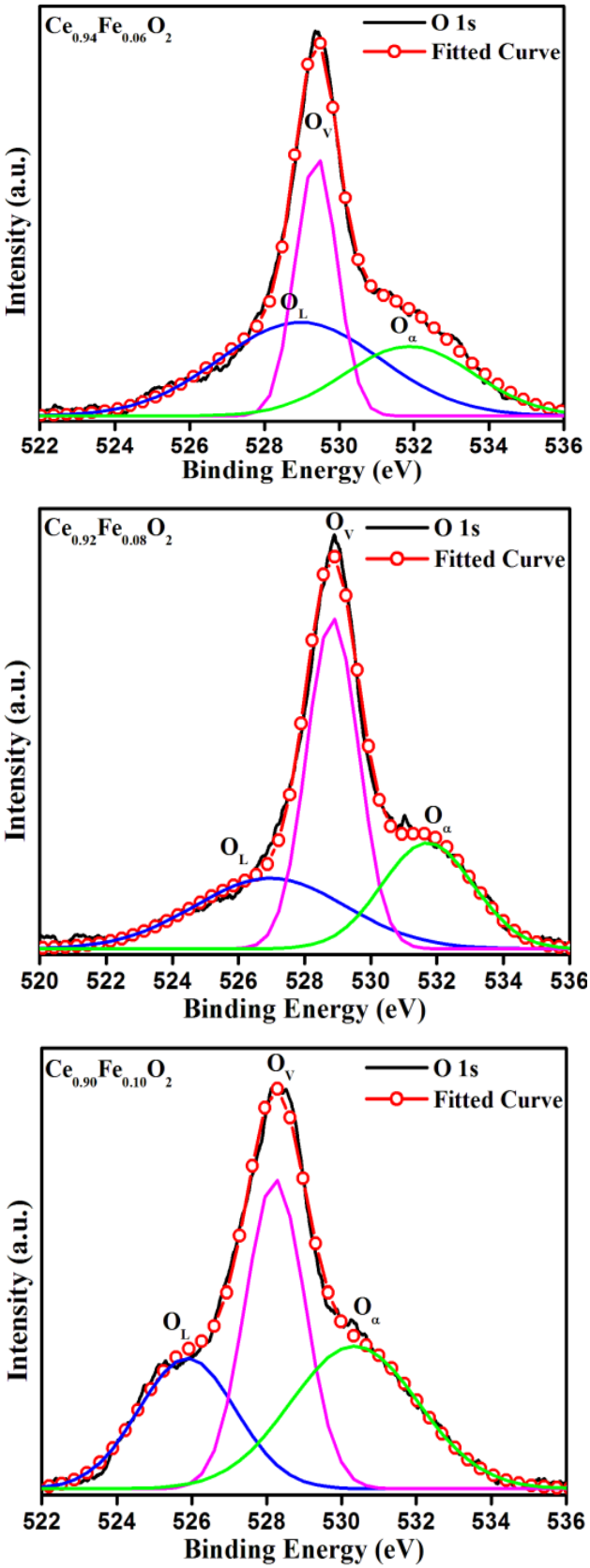


**Figure 5.12: O 1s XPS spectra of pure $CeO_2$ and $Ce_{1-x}Fe_xO_2$ ($x$ = 0.02, 0.04, 0.06, 0.08 and 0.10) NPs**

With the long time aging of the $CeO_2$ samples, $Ce^{3+}$ contents has been reported to decrease [281], similarly we can say that in our samples the $Ce^{+3}$ contents may be changing along with the relative area ratio of $O_L$ and $O_V$. From this observation we can conclude that oxygen vacancy concentration is deceasing with the different doping concnetration of Fe-ions, which may be due to the incorporation of Fe-ions on oxygen vacancy sites, thereby reducing $Ce^{3+}$ concentration in the samples [285].

### 5.3.4. Magnetic Properties

Figure 5.13 shows the room temperature magnetization of the pure $CeO_2$ and $Ce_{1-x}Fe_xO_2$ ($x$ = 0.02, 0.04, 0.06, 0.08 and 0.10) NPs samples measured as a function of magnetic field and calculated saturation magnetization ($M_S$), coercivity ($H_C$) and remanent magnetization ($M_r$) values, which are given in the Table 5.6. It has been found that pure $CeO_2$ NPs shows a systematic hysteresis loop with saturation magnetization $M_s$ = 0.103 emu/g. Furthermore, coercivity and remanent magnetization for pure $CeO_2$ NPs is about $H_C$ = 30.02 Oe and $M_r = 1.28\times10^{-4}$ emu/g, respectively, which shows the weak ferromagnetic behaviour of pure $CeO_2$ NPs at room temperature. Although, it has been reported that the stoichiometric bulk $CeO_2$ is a diamagnetic, but when size of the $CeO_2$ particles dropdown to the nano-meter range it shows RTFM. Same behaviour has been found in our present work i.e. a weak RTFM in pure $CeO_2$ NPs sample, which has reported in some other work also [15, 65].

The origin of RTFM in pure $CeO_2$ NPs is attributed to the formation of oxygen vacancies due to conversion of $Ce^{4+}$ to $Ce^{3+}$ oxidation state of cerium ions. At the nanoscale, $Ce^{4+}$ states get partially reduce to $Ce^{3+}$, which is leading to the existence of Ce cation in the mixed valency, due to it $CeO_2$ deviates from perfect stoichiometry. Our XPS and Raman results support the presence of mixed valency of Ce-ions and oxygen vacancy in $CeO_2$ NPs, respectively. The formation of oxygen vacancy defect leads to induce the magnetic moment in the nearby $Ce^{3+}$ atoms. The $Ce^{3+}$ atom has partially filled 4f orbital with one unpaired electron which is contributing the RTFM in the $CeO_2$ system, whereas $Ce^{4+}$ with empty 4f orbital do not contribute to RTFM.

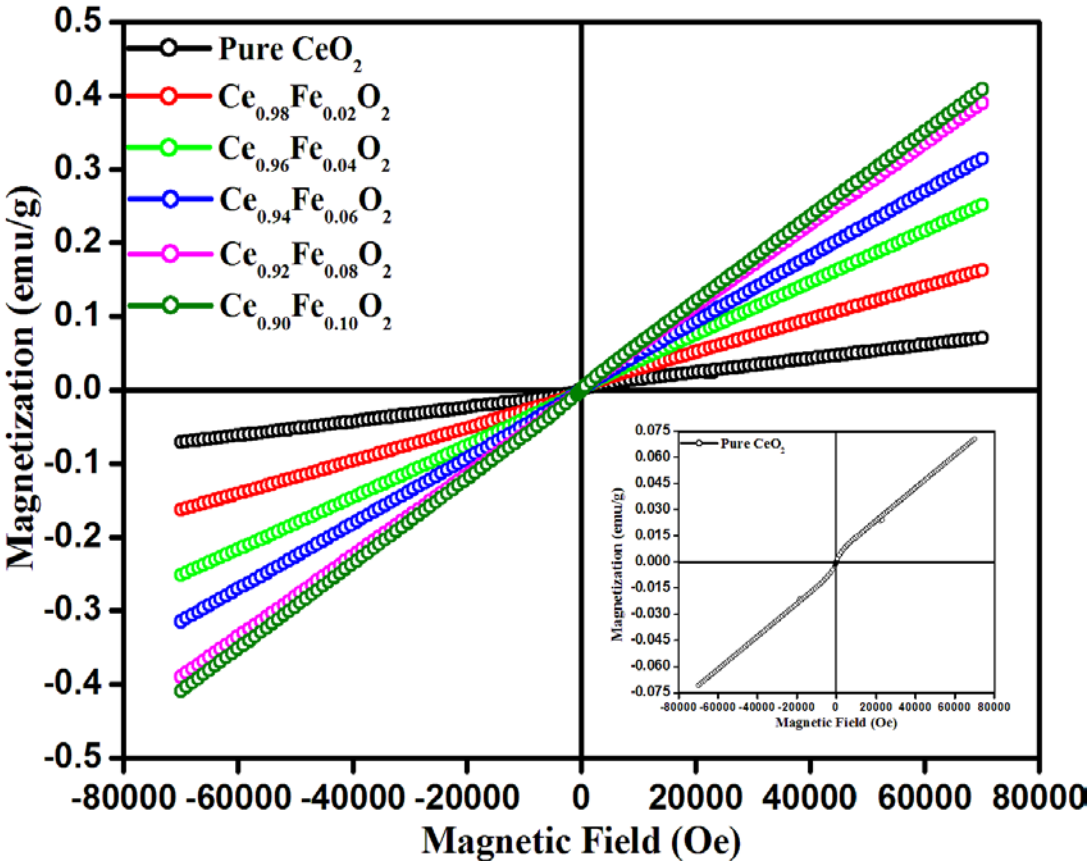


**Figure 5.13: Magnetization versus magnetic field plot for pure $CeO_2$ and $Ce_{1-x}Fe_xO_2$ ($x$ = 0.02, 0.04, 0.06, 0.08 and 0.10) NPs samples at room temperature (300K)**

The spin interaction between $Ce^{3+}$ and oxygen vacancy arises in accordance with FCE mechanism, which leads ferromagnetism in the $CeO_2$ NPs. According to FCE mechanism, it is possible that oxygen vacancy ($V_O$) create magnetic moment on the neighbouring Ce ions such as $Ce^{3+}$-$V_O$-$Ce^{3+}$. Moreover, $Ce_{1-x}Fe_xO_2$ ($x$ = 0.02, 0.04, 0.06, 0.08 and 0.10) NPs samples show a systematic loop of a typical paramagnetic component and this component became prominent with increasing the dopant concentration (as shown in Figure 5.13). The saturation magnetization ($M_s$) value for $Ce_{1-x}Fe_xO_2$ ($x$ = 0.02, 0.04, 0.06, 0.08 and 0.10) NPs samples has been calculated using law of approach and it is about 0.238, 0.371, 0.467, 0.578, and 0.609 emu/g, respectively. The magnetic moment per formula unit for pure and $Ce_{1-x}Fe_xO_2$ ($x$ = 0.02, 0.04, 0.06, 0.08 and 0.10) NPs samples is tabulated in Table 5.6, which shows gradual increment with Fe-dopant in $CeO_2$ NPs.

The influence of Fe-doping causes a decrease in the remanent magnetization from $2.08\times10^{-4}$ emu/g to $8.82\times10^{-5}$ emu/g and increase in the saturation magnetization (Table 5.6).

**Table 5.6: Summary of saturation magnetization ($M_s$), remanent magnetization ($M_r$), coercivity ($H_c$) and magnetic moment per formula unit ($\mu_{f.u.}$) for pure $CeO_2$ and $Ce_{1-x}Fe_xO_2$ ($x$ = 0.02, 0.04, 0.06, 0.08 and 0.10) NPs**

| Sample | $M_s$ (emu/g) | $M_r$ (emu/g) $\times10^{-4}$ | $H_c$ (Oe) | $\mu_{f.u.}$ ($\mu_B/atom$) | $\chi \times 10^{-5}$ (emu/(g-Oe)) |
|---|---|---|---|---|---|
| Pure $CeO_2$ | 0.1029 | 1.28 | 30.02 | 0.0031 | 2.07 |
| $Ce_{0.98}Fe_{0.02}O_2$ | 0.2384 | 2.08 | 25.18 | 0.0072 | 4.57 |
| $Ce_{0.96}Fe_{0.04}O_2$ | 0.3718 | 0.625 | 6.61 | 0.0112 | 4.18 |
| $Ce_{0.94}Fe_{0.06}O_2$ | 0.4672 | - | - | 0.0139 | 4.55 |
| $Ce_{0.92}Fe_{0.08}O_2$ | 0.5789 | 0.782 | 10.23 | 0.0171 | 5.56 |
| $Ce_{0.90}Fe_{0.10}O_2$ | 0.6098 | 0.882 | 7.10 | 0.0178 | 5.96 |

The observed change in the magnetic properties of $CeO_2$ NPs with the increase in the Fe concentration can be correlated with the decrease in the lattice constant (as shown in Table 5.2) due to incorporation of Fe ions in $CeO_2$ [224]. The RTFM in pure $CeO_2$ is due to reduction of $Ce^{4+}$ ion into $Ce^{3+}$, which introduces a non-stoichiometric defect into $CeO_2$ lattice in order to compensate the charges, as discussed previously. While in case of doping, it is reported by many researchers that magnetic properties are related to the formation of metallic clusters, secondary phases or development of defects induced by the doping. In our present work, the formation of magnetic cluster and secondary phases are ruled out by the XRD, TEM, Raman and XPS analysis in $Ce_{1-x}Fe_xO_2$ ($x$ = 0.02, 0.04, 0.06, 0.08 and 0.10) NPs samples. Thus, the magnetic properties of $Ce_{1-x}Fe_xO_2$ ($x$ = 0.02, 0.04, 0.06, 0.08 and 0.10) NPs samples are arise due to owing of doping effect only. In addition of that, the variation of the particle size also affects the magnetic properties of the nanomaterials. Since, the XRD and TEM analyses confirm the gradual decrements in the particle size of all the samples (Table 5.1).

However, it has been seen that $M_s$ is continuously enhanced when particle size decreases with increase in the Fe content in $CeO_2$ NPs. Furthermore, increase of

defects such as oxygen vacancies may also be responsible for enhancing the magnetic properties in nanomaterials. Although, the Raman analysis gave the evidence about increase of defect concentration as well as oxygen vacancies concentration with increasing doping concentration up to an optimal doping (6% Fe) and afterword it is going to decrease. However, $M_s$ values are found to increase continuously with increasing Fe-doping concentration in the present study. This shows that the trivalent Fe-ion doping in $CeO_2$ is inducing additional oxygen vacancies which contribute towards enhancing the magnetization in the material. Generally, $Ce^{3+}$ ($4f^1$) and $Fe^{3+}$ ($3d^5$) ions are paramagnetic, therefore, it is expected that with the fluency of $Fe^{3+}$-ions in the crystalline lattice of $CeO_2$ NPs, reduces the ferromagnetic ordering and increases the linear paramagnetic component in Fe-doped $CeO_2$ samples [286]. Since, every $Fe^{3+}$-ion has one unpaired electron in low spin state ($3d^5$) that can influence ferromagnetic ordering at low doping concentration (2%) of $Fe^{3+}$ ions and the magnetism has been observed in this sample. This behaviour can be associated with the presence of FCE coupling, in which both oxygen vacancies and Fe-ions are involved. According to the FCE, the coupling between the oxygen vacancy and $Fe^{3+}$ ions formed complex structure $Fe^{3+}(\uparrow) - V_O(\downarrow) - Fe^{3+}(\uparrow)$ or $Ce^{3+}(\uparrow) - V_O(\downarrow) - Fe^{3+}(\uparrow)$. This FCE forms bound magnetic polarons (BMP) at low doping concentration of Fe-ions in the structure, which can overlap with the neighbouring BMP. This results in the long range Fe-Fe ferromagnetic coupling in the $CeO_2$ NPs. Our XPS spectra also shows evidence of $Fe^{3+}$ substitution in the $CeO_2$ sample, and presence of $Ce^{3+}$ ions, which can be attributed to the oxygen vacancies in the Fe-doped $CeO_2$ samples. But, the observed paramagnetic effect with the fluency of Fe-ions may be due to the presence of $Fe^{3+}$ ions at interstitial site that are not magnetically ordered irons. Therefore, as Fe-content increases gradually, the Fe-ions comes close together and increases the superexchange interaction between the neighbouring Fe-ions in a complex form $Fe^{3+}$-$O^{2-}$-$Fe^{3+}$, which gives rise to an antiferromagnetic interaction [65].

The temperature dependent magnetization M-T curve of $Ce_{1-x}Fe_xO_2$ ($x$ = 0.02, 0.04, 0.06, 0.08 and 0.10) samples samples are measured under the applied field (H) of 100 Oe in the ZFC and FC modes (Figure 5.14). The ZFC and

FC curves show the similar behaviour of all samples and no evidence of secondary phase has been existed down to 10 K. The Curie temperature ($T_C$) or Neel temperature ($T_N$) in the Fe-doped $CeO_2$ samples do not match to the reported values for FeO ($T_N$ ~200 K), $Fe_2O_3$ ($T_C$ ~240 K) or $Fe_3O_4$ ($T_C$ ~858 K) [287]. The paramagnetic contribution in Fe-doped $CeO_2$ samples is identified by using Curie-Weiss equation, i.e. $\chi = C/(T-\theta)$, where, $\chi$ is the magnetic susceptibility, C is the Curie constant, T is the experimental temperature and $\theta$ is the Curie-Weiss temperature (tabulate in Table 5.6) [286].

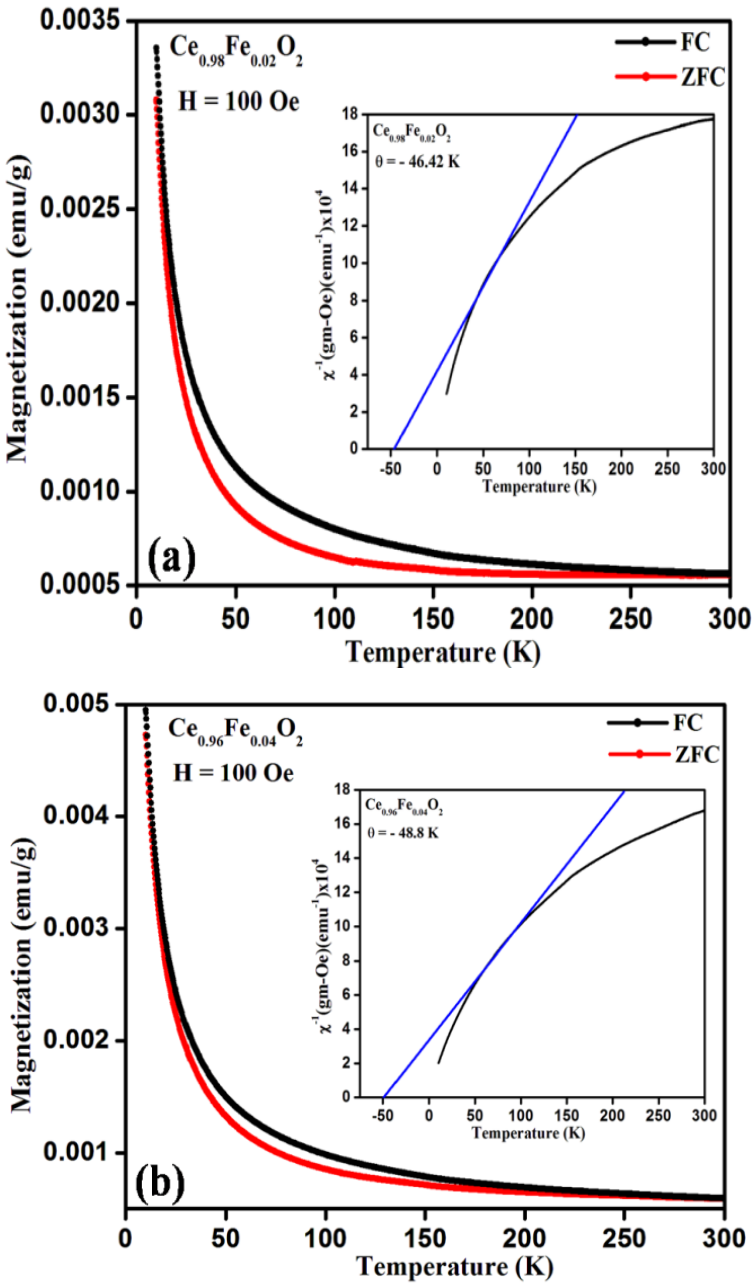

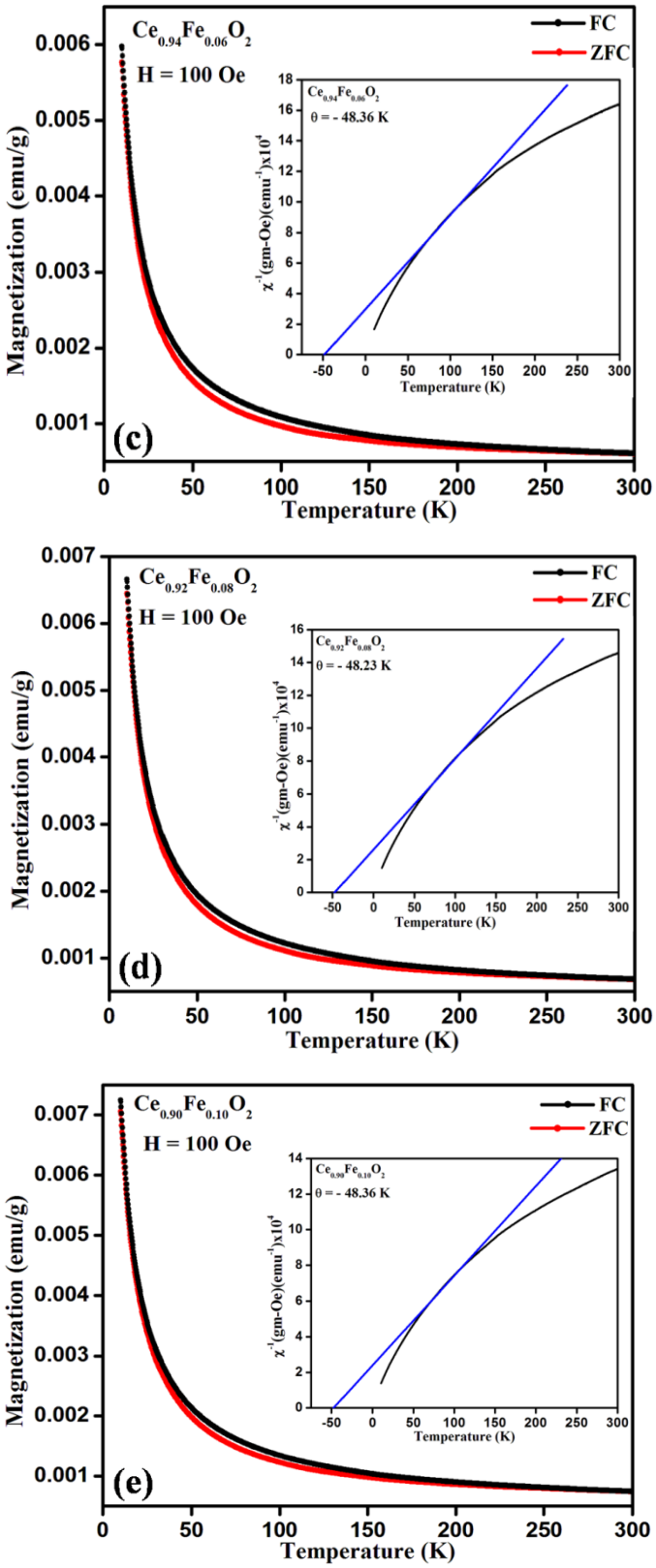


**Figure 5.14 (a-e): M-T curve (ZFC and FC) at 100 Oe of $Ce_{1-x}Fe_xO_2$ ($x$ = 0.02, 0.04, 0.06, 0.08 and 0.10) NPs samples and inset exhibits the Curie-Weiss behaviour of the inverse susceptibility for all samples**

The inset of Figure 5.14 shows a graph plot between the inverse χ and temperature exhibits a good linear fit for $Ce_{1-x}Fe_xO_2$ ($x$ = 0.00, 0.02, 0.04, 0.06, 0.08 and 0.10) NPs samples. This sample had a negative value of θ (~46 K for 2% Fe and ~48 K for 4, 6, 8, 10% Fe as shown in the inset of Figure 5.14), which indicates antiferromagnetic interaction between the Fe-ions. As a result of this, the ferromagnetic behaviour decreases in the average magnetic moment per Fe-ions and shows a paramagnetic effect with the fluency of Fe-contents in our Fe-doped $CeO_2$ samples. However, our XPS and Raman analyse the presence of oxygen vacancies but the existence of both $Ce^{3+}$-oxygen vacancies complexes and $Fe^{3+}$ ions in the low spin state contribute to the paramagnetic dominated weak ferromagnetism in the Fe-doped $CeO_2$ NPs and not only oxygen vacancies.

## 5.4. Conclusions

Pure $CeO_2$ and $Ce_{1-x}Fe_xO_2$ ($x$ = 0.02, 0.04, 0.06, 0.08 and 0.10) NPs are successfully synthesized using co-precipitation method. The XRD and SERS results indicate that all the samples has a cubic fluorite structure with no seconday impurity phase formation, which indicates the incorporation of $Fe^{3+}$ ions at the $Ce^{4+}$ ions lattice positions. The crystallite size, estimated by the Scherrer formula are in good aggrement with the TEM measurments and is found to decrease with the fluency of Fe-ions. A red shift of the absorption spectra is observed for pure $CeO_2$ and $Ce_{1-x}Fe_xO_2$ ($x$ = 0.02, 0.04, 0.06, 0.08 and 0.10) NPs, which can be linked with the decrease in the crystallite size caused by doping. The presence of oxygen vacancies was confirmed by Raman and XPS measurments and the XPS study is revealing the mixed valance state of Fe-ions ($Fe^{3+}$ and $Fe^{2+}$) and Ce-ions ($Ce^{3+}$ and $Ce^{4+}$). The magnetisation recorded at room temperature on the pure $CeO_2$ and $Ce_{1-x}Fe_xO_2$ ($x$ = 0.02, 0.04, 0.06, 0.08 and 0.10) NPs samples shows increase in saturation magnetisation with the increasing concentration of Fe-ion due to presence of mixed valency of Ce-ions and oxygen vacancy, it also represents the arising spin interaction due to FCE mechanism. As the Fe-content increases gradually, the super-exchange interaction increases between the neighbouring Fe-ions in a complex form $Fe^{3+}$-$O^{2-}$-$Fe^{3+}$, to give raise an antiferromagnetic interaction in the lattice. This interaction can be clearly seen in a graph plot between the inverse χ and temperature,

which exhibits a good linear fit for all the samples to obtain a negative value of θ, indicating a weak antiferromagnetic coupling. Due to antiferromagnetic interaction between Fe-ions, inferred from both ZFC and FC curve, the ferromagnetism for Fe-doped samples is found to suppress but this effect is found to increase with fluency of Fe-ion, therefore, Fe-doped $CeO_2$ samples exhibited super paramagnetic dominated weak ferromagnetic behaviour at room temperature. Finally, it has been observed that with Fe-implantation, the optical, electronic structure and magnetic properties of $CeO_2$ NPs can be modified and this kind of implantation can yield better samples for the potential use in the technological applications like spintronics.

# Chapter 6

# Future Scope

# CHAPTER 6
# FUTURE SCOPE

In the present work we have successfully investigated the growth of single phase pure and doped $CeO_2$ based DMS NPs with different dopant concentrations by controlling growth parameters and synthesis method for obtaining smaller particle sized (≥ 8 nm) NPs. Also, we have studied in detail the structural, optical, electronic structure, magnetic and electrical properties of the pure and doped $CeO_2$ samples by various characterization techniques. We are able to achieve ferromagnetic characteristics at room temperature for pure and doped $CeO_2$ based DMS NPs. Still, there is plenty of scope for further research work in this area. The present work can be extended as follows for future scope of work:

- In the Present research thesis, the work has reported RTFM in pure and TM-/RE-doped $CeO_2$ NPs samples which is supplemented due to the presence and generation of oxygen vacancies and other defects/imperfections, reported due to intrinsic reasons however, another opinion on this induced ferromagnetism is due to extrinsic reasons. Hence, as a future work, we would like to undertake this task with the help of other characterization techniques and confirm that the behaviour is intrinsic or extrinsic. However, up to some extent we are quite ascertain that this RTFM is induced due to intrinsic reasons.
- Simultaneous, we will try to explore the theoretical dimensions of various properties and induced ferromagnetism and to explain our results in the direction of FCE, BMP and other supporting theories for the magnetism in these DMS materials.
- For further studies on electronic structure properties of these materials, we also want to take-up the task of XAS analysis to further ascertain more about their properties. For this we will try to submit the beam time proposal for these measurements at Elletra Italy, ESRF and Indus-2 etc. to have this data for our samples to study these properties in more details.
- The recent research work has been limited only on the various properties of 3d-TM (Fe) and 4f -RE (Sm, Gd)-doped $CeO_2$ NPs with different dopant

concentration that are being studied due to their potential application for spintronics devices. On the other hand, there are very few reports on the electronic structure and magnetic properties with the various doping of 4d and 5d elements in $CeO_2$ NPs. It will be very interesting to apply various methods for synthesis of oxide NPs with different dopant concentration of 4d and 5d elements and we will try to investigate their size dependent properties. Therefore, we will synthesize and study the 4d and 5d-doped $CeO_2$ based DMS compounds for further investigation on their technological uses in spintronics devices.

- As in the present thesis work, we have developed the nanomaterials for TM and RE doped $CeO_2$ based DMS materials. So, in near future we will undertake the entire task performed in this thesis by developing thin films on different substrates to compare the results with the nanomaterials of these samples. Further, the binary and ternary dopants of $CeO_2$, $TiO_2$, ZnO and other DMS materials may be tried for significant ferromagnetic ordering.

# Conclusion

# CONCLUSION

The major outcomes of the present research work have been described in terms of the following important conclusions:

- TM (Fe) and RE (Sm, Gd)-doped $CeO_2$ nanocrystalline samples with different dopant concentration (2, 4, 6, 8 and 10%) were successfully synthesized by a simple, facile and cost effective chemical co-precipitation method.
- XRD analysis exhibited face centered cubic fluorite (*fcc*) structure with space group *Fm-3m*, without any secondary phases for the pure $CeO_2$, TM (Fe) and RE (Sm, Gd)-doped $CeO_2$ nanocrystalline samples. The average crystalline size estimated from XRD, TEM and SERS measurements were in good agreement with each other. Due to the incorporation of the dopants ions (Fe, Sm and Gd) in the lattice of $CeO_2$ NPs, variation in the position of XRD peaks and average crystalline size of the samples were detected. Moreover, the lattice strain, dislocation density and specific surface area were also calculated to observe the variation in the lattice of $CeO_2$ sample after the incorporation of smaller radii $Fe^{3+}$ (0.065 nm), larger radii $Sm^{3+}$ (0.1079 nm) and $Gd^{3+}$ (0.1053 nm) ions, which substituted smaller ionic radii $Ce^{4+}$ (0.097 nm) ions and created the larger radii $Ce^{3+}$ ions (0.114 nm).
- The TEM, HRTEM and SAED patterns confirmed the spherical morphology with agglomeration for all pure, TM (Fe) and RE (Sm, Gd)-doped $CeO_2$ samples. However, HRTEM images showed the dislocations in the (111) lattice plane of RE (Sm, Gd)-doped $CeO_2$ samples, due to doping of larger radii RE (Sm, Gd) dopant ions in $CeO_2$ sample. The average crystalline size measured from TEM images were in the range of 4-5 nm, 5-8 nm and 5-7 nm for Fe, Sm and Gd-doped $CeO_2$ NPs, respectively. HRTEM and SAED images showed highly ordered crystalline nature of particles with the incorporation of dopant ions (Fe, Sm and Gd) in the lattice of $CeO_2$ NPs.
- UV-Vis-NIR spectra of all the samples exhibited alteration in the band gap energy and refractive index attesting the incorporation of TM (Fe) and RE (Sm, Gd)-ions into $CeO_2$ NPs. It was observed that band gap energy

decreased (2.80-2.73 eV) with the fluency of Fe-ions in $CeO_2$ NPs, whereas variation in the band gap of Sm and Gd-doped $CeO_2$ samples were explained with the help of Burstein-Moss (BM) effect. Finally, it was concluded that the optical band gap energy could be tuned by the effect of different dopant ions concentrations in the host $CeO_2$ based DMS compound which have good optical behaviour.

- ❖ SERS spectra reported the absence of any impurity phases, formation of clusters and confirmed the face centered cubic fluorite (*fcc*) structure of pure, TM (Fe) and RE (Sm, Gd)-doped $CeO_2$ nanocrystalline samples. Some physical parameters such oxygen deficit ($\delta$) confirmed the formation of oxygen vacancies and using spatial correlation model, correlation length (L) and oxygen defect concentration (N) were also calculated to estimate the concentration of oxygen vacancies as a function of grain size for Fe-doped $CeO_2$ NPs.
- ❖ The XPS analysis provided the information about chemical composition and oxidation states of the elements (Ce, Fe and Gd) for pure, TM (Fe) and RE (Gd)-doped $CeO_2$ nanocrystalline samples. The analysis of core level Ce 3d XPS spectra exhibited the presence of both oxidation state of Ce-ions ($Ce^{4+}$ and $Ce^{3+}$) for both TM (Fe) and RE (Gd)-doped $CeO_2$ samples. The relative concentration ratio ($Ce^{3+}/Ce^{4+}$) for $Ce^{3+}$ ions showed variation in the concentration of $Ce^{3+}$ ions with the incorporation of $Fe^{3+}$-ions (range from 0.53-0.85) and $Gd^{3+}$-ions (range from 0.51-0.70) as well as formation of oxygen vacancies in the Fe and Gd-doped $CeO_2$ samples. However, Ce 3d XPS spectra not only revealed the significant increase in the concentration of $Ce^{3+}$ ions but also increase in the formation of oxygen vacancies due to formation of $Ce_2O_3$ phase in Gd-doped $CeO_2$ samples that was not visible in the XRD patterns, while such kind of phase was not observed in the Ce 3d spectra of Fe-doped $CeO_2$ samples. The O 1s XPS spectra provided the detail information about contribution of lattice oxygen, oxygen vacancies, presence of surface hydroxyl groups and various carbonate species with variation in the concentration of dopants Fe and Gd-ions into $CeO_2$ sample. The core level Fe 2p and Gd 4d spectra provided the information about the presence of

oxidation states of Fe ($Fe^{3+}$ and $Fe^{2+}$) and Gd ($Gd^{3+}$) ions for Fe and Gd-doped $CeO_2$ samples, respectively.

- The magnetic measurements of pure, Fe and Gd-doped $CeO_2$ nanocrystalline samples were carried out at room temperature as a function of applied magnetic field in the range of -7 T to +7 T and -1.5 T to +1.5 T, respectively using MPMS-3 SQUID-VSM system. The pure $CeO_2$ nanocrystalline samples exhibited room temperature ferromagnetism whereas incorporation of Fe and Gd-ions in the lattice of $CeO_2$ suppressed the ferromagnetic behaviour. After incorporation of Gd-ions, the Gd-doped $CeO_2$ samples exhibited paramagnetism dominated weak ferromagnetism behaviour whereas due to antiferromagnetic interaction between Fe-ions the ferromagnetism for Fe-doped samples is suppressed and increases with fluency of Fe-dopant, therefore Fe-doped $CeO_2$ samples exhibited super paramagnetic dominated weak ferromagnetic behaviour at room temperature. The FC and ZFC curves also depicted the antiferromagnetic interaction between the Fe-ions for Fe-doped $CeO_2$ samples. It was clearly noticeable that the saturation magnetization enhanced with doping and thereafter increased with increasing the fluency of dopant (Fe and Gd) ions into $CeO_2$ NPs samples, which could be ascribed due to smaller particle size and oxygen vacancy formation during synthesis process. The magnetic behaviour of pure, Fe and Gd-doped $CeO_2$ samples were explained using F-centered exchange (FCE) mechanism and bound magnetic polaron (BMP) theory. These observations showed that RTFM in both samples was not extrinsic in nature because no oxide phases were found due to doping of Fe and Gd-ions into $CeO_2$ NPs.
- The enhanced DC electrical conductivity at room temperature was observed in pure $CeO_2$ and Sm-doped $CeO_2$ nanocrystalline sample and increased from $0.78\times 10^{-2}$ to $3.84\times 10^{-2}$ S/cm with the fluency of Sm-ion into $CeO_2$ samples. Resistivity of the Sm-doped $CeO_2$ samples decreased with the fluency of Sm-content indicating the n-type behaviour of conduction mechanism.

# Summary

# SUMMARY

This section deals with the summary of the research work that has been reported in this thesis along with the future technological exploration of the work. Earlier conventional electronic devices solely relied on the transportation of the electrical charge of electrons. Addition of spin property in the conventional electronic devices provided an additional degree of freedom, more capabilities and advancement of functionalities. Generally, magnetism of metals serves as the basis for processing and storing the information in magnetic devices. Further advancement in these devices can be done by manipulating both the spin and the charge of the electron. Therefore, "Spintronics" devices may lead to more exotic information devices, which are capable of enhanced functionality, higher processing speed and lesser power consumption. The revolution in this area begun with the discovery of GMR effect, which occurs when a magnetic field is used to align the spin of the electron in the material inducing a large change in the resistance of the material. The practical implementation of spintronics devices requires efficient high spin polarized carrier injection and transport, which is not often fulfilled by conventional ferromagnetic metals because they do to not have 100% spin polarization and their efficiency of spin polarization is often very low due to resistivity mismatch and formation of Schottky barriers. DMS can offer a solution to this problem. DMS are semiconducting materials which have attracted the interest of the researchers due to their potential technological applications such as optoelectronics, magneto-electronics and spintronics devices etc. In DMS, appropriate fractional amount of atoms of the host semiconductors are substituted by the atoms (transition metals or non-metals) which are capable to add localized magnetic moment. Due to this substitution, DMS not only retain the semiconducting properties but also possess well-defined magnetic properties such as paramagnetic, ferromagnetic or antiferromagnetic which are not present in conventional semiconductors. For obtaining DMS compounds, TM (having partially filled d-state such as Ti, V, Cr, Mn, Fe, Co, Ni) and RE (having partially filled f-state such as Ce, Pr, Nd, Sm, Eu, Gd, etc.) have been used as magnetic dopants in the host semiconductor.

The electronic states of host semiconductor and magnetic dopants have a strong spin coupling between them which results in metallic behaviour for one spin channel and semiconducting behaviour for the other in the resultant DMS compound. In other words, DMS compounds shows 100% spin polarization at Fermi level ($E_F$), which makes them promising candidates for spintronics devices. Another challenge to spintronics and magneto-electronics devices is to maintain magnetic properties at room temperature, because most of the semiconductors lose their magnetic properties at room temperature. Large band gap $CeO_2$ is a suitable DMS material for spintronics and other industrial applications due to its multi-functionality and narrower band gap after doping with TM and RE metals at nano-regime, which makes it appropriate DMS compound for Spintronic applications.

In the present research work, we have systematically investigated the structural, optical, magnetic, electronic structure and electrical properties of TM (Fe) and RE (Sm and Gd)-doped $CeO_2$ NPs in different dopant concentrations (2, 4, 6, 8 and 10%). A sound understanding of the origin of magnetism at room temperature has been correlated with the other properties in pure and doped $CeO_2$ NPs which is required to utilize for technological applications.

**OBJECTIVES**

The main objectives of the present study are:

1. To check whether the induced room temperature ferromagnetism (RTFM) is intrinsic property of the sample.
2. To check the defect induced RTFM in Ceria.
3. To check the oxygen vacancies effect in doped $CeO_2$ with various dopant concentration in explaining the nature of RTFM.
4. To study the structural, optical and electrical properties of RE (Sm)-doped $CeO_2$ nanoparticles.
5. To study the structural, optical, electronic structural and magnetic properties of TM (Fe) and RE (Gd)-doped $CeO_2$ nanoparticles.

In order to achieve the above mentioned objectives, the whole research work carried out in the present thesis has been divided into six chapters as per the details given below:

**Chapter 1**

In this chapter, we have briefly described the general introduction of spintronics and spintronic materials based on magnetic properties. DMS emerging as widely used materials in spintronics devices has been introduced briefly in this section. Different theoretical models and mechanisms have been proposed for explaining the origin of room temperature ferromagnetism in DMS materials. The fundamental development of nanomaterials as metal oxide semiconductor and different synthesis routes such as top-down and bottom-up methods have been described for synthesizing metal oxide NPs that can be used for getting high quality NPs. Also, introduction of $CeO_2$, its structure, different physical properties and defects associated with ceria has been described. In the last section of this chapter, review of literature is given describing different physical properties such as structural, morphological, optical, electronic structural, magnetic and electrical properties of pure $CeO_2$ and effect of doping on physical properties of doped $CeO_2$.

**Chapter 2**

In the second chapter, we have presented a brief discussion about various synthesis methods and characterization techniques utilized here in this present work to study various properties of pure and doped $CeO_2$ in nanocrystalline materials. The co-precipitation method used for synthesis of pure and doped $CeO_2$ nanocrystalline powder has been discussed in detail. The various experimental techniques used for characterization like X-ray diffraction (XRD) along with Rietveld Refinement analysis, Transmission Electron Microscopy (TEM), High-Resolution Transmission Electron Microscopy (HRTEM), Selected Area (Electron) Diffraction (SAED), Energy Dispersive X-ray Spectroscopy (EDX), Ultraviolet-Visible-Near Infrared (UV-Vis-NIR) Spectroscopy, Surface-Enhanced Raman Spectroscopy (SERS), X-ray Photoelectron Spectroscopy (XPS), Superconducting Quantum Interference Device-Vibrating Sample Magnetometer (SQUID-VSM) and Keithley 2400 Electrometer have been described in detail with their general principles, working and data analysis.

**Chapter 3**

In this chapter, we have studied the structural, optical and electrical properties of pure $CeO_2$ and $Ce_{1-x}Sm_xO_2$ nanocrystaline samples with different

dopant concentrations $x$ = 0.02, 0.04, 0.06, 0.08 and 0.10 and systematically established a correlation between the concentration of dopant ions and oxygen vacancy defect using XRD, UV-Vis-NIR and SERS measurement techniques. The broadening of XRD pattern confirmed the incorporation of $Sm^{3+}$ ions successfully at the $Ce^{4+}$ ion sites in the face centered cubic (*fcc*) lattice of $CeO_2$ NPs without any impurity phases. TEM, HRTEM and SAED images have confirmed the spherical morphology of particles with crystallite particle size in the range of 5-8 nm for pure and Sm-doped $CeO_2$ samples. EDX spectra have confirmed the presence of Ce, Sm and oxygen element nearly in stoichiometric ratios for Sm-doped $CeO_2$ samples as prepared. The UV-Vis-NIR analysis has revealed that due to particle size variation and aggregation of particles, the optical band gap energy has varied with the dopant concentration in Sm-doped $CeO_2$ samples. Peak asymmetry and broadening of Raman active mode further has been ascribed to the presence of oxygen vacancies (whether extrinsic or intrinsic) and its variation with the fluencies of $Sm^{3+}$ ions in $CeO_2$ NPs. I-V characteristics has been shown the semiconducting nature of all the samples and the conductivity measurements show that the conductivity of the $CeO_2$ increases with increasing the Sm-content. Finally, in this chapter we are able to show the controlled band gap, size, grain morphology, higher conductivity, controlled extrinsic and intrinsic oxygen vacancies with the rare earth cation Sm-doping in the $CeO_2$ lattice.

**Chapter 4**

In the fourth chapter, we have reported the synthesis and characterization of pure $CeO_2$ and $Ce_{1-x}Gd_xO_2$ ($x$ = 0.02, 0.04, 0.06, 0.08 and 0.10) nanocrystalline samples prepared using co-precipitation method. The visible light photocatalytic activity has been experimentally demonstrated and gradual increase in hydrogen production has been observed with increasing the concentration of Gd-content in $CeO_2$ NPs. However, many factors such as particle size of photo catalyst, binding energy, oxygen vacancy concentration and band gap energy have been responsible for the increase in hydrogen generation activity with increasing dopant concentration in ceria. The lattice parameter, volume and particle size of pure and Gd-doped $CeO_2$ NPs has been calculated by XRD pattern. The particle sizes of these samples has been further verified with TEM and SERS analysis and found to be approximately similar to the results obtained with XRD analysis. The particles are spherical in

shape and getting agglomerated with fluencies of $Gd^{3+}$ ions in $CeO_2$ sample having the particle size in the range of 5-7 nm, confirmed from the TEM images. From the analysis of the UV-Vis-NIR absorption spectra we have observed the variation in the refractive index and band gap energy (2.5-2.7 eV) with different concentration of Gd-ions in $CeO_2$ NPs. From the SERS spectral studies on pure and Gd-doped $CeO_2$ NPs, the particle size, oxygen vacancy concentrations etc have been made to understand the mechanism of other properties of these samples. Further, for electronic structural studies of these NPs, core level Ce 3d, O1s and Gd 4d XPS spectra have been recorded and analyzed in details. From this analysis the change of oxidation state of $Ce^{+4}$ to $Ce^{+3}$ ions, incorporation of the $Gd^{+3}$ ions in the lattice and formation of oxygen vacancies has been reported. The magnetic measurements are used to show the paramagnetic dominated weak ferromagnetic behaviour for pure and Gd-doped $CeO_2$ samples, which is reported to be triggered by the change of oxidation state of $Ce^{+4}$ to $Ce^{+3}$ ions, incorporation of the $Gd^{+3}$ ions in the lattice and formation of oxygen vacancies. Finally, a sound knowledge of the particle size, optical band gap, efficiency for storing/releasing oxygen ions via conversion of $Ce^{4+}$ to $Ce^{3+}$ cation that are responsible for the generation of oxygen vacancy defects and magnetic properties position these nanomaterials for potential applications in the field of phtocatalysis, spintronics, antibacterial activity, solar cells etc.

**Chapter 5**

In this chapter, we have presented correlation between RTFM, oxygen vacancy defect, chemical and electronic state of pure $CeO_2$ and $Ce_{1-x}Fe_xO_2$ ($x$ = 0.02, 0.04, 0.06, 0.08 and 0.10) nanocrystalline samples, synthesized using co-precipitation method. The XRD and SERS analysis has confirmed the formation of single phase cubic fluorite-type structure without any secondary phase with incorporation of Fe-ions in the lattice of $CeO_2$ NPs, indicates incorporation of $Fe^{3+}$ ions at the lattice sites of $Ce^{4+}$ ions. TEM, HRTEM and SAED patterns has confirmed that all particles have spherical morphology with agglomeration and the particle size in the range of 4-5 nm, which gradually decreased with the fluency of Fe-ions in $CeO_2$ NPs. From UV-Vis-NIR and SERS analysis the inhomogeneous distribution of the dopant has been significantly discussed in the light of optical band gap energy and surface information such as peak intensity and shape at ~460 and ~577 $cm^{-1}$, as well as observed formation of oxygen vacancies concentration via

ratio $I_{O_v}/I_{F_{2g}}$. A red shift of the absorption spectra has been observed for pure $CeO_2$ and $Ce_{1-x}Fe_xO_2$ ($x$ = 0.02, 0.04, 0.06, 0.08 and 0.10) NPs, which has been linked with the decrease in the crystallite size and formation of oxygen vacancies caused by Fe-doping. The presence of oxygen vacancies and mixed valance states of both Ce ($Ce^{3+}$ and $Ce^{4+}$) and Fe-ions ($Fe^{3+}$ and $Fe^{2+}$) have been discussed using core XPS spectra of Ce 3d, O 1s and Fe 2p. The magnetic measurement are showing a weak RTFM for pure $CeO_2$ NPs whereas $Ce_{1-x}Fe_xO_2$ ($x$ = 0.02, 0.04, 0.06, 0.08 and 0.10) nanocrystalline samples exhibits paramagnetism dominated weak ferromagnetism that has been explained in the correlation with FCE mechanism. Due to antiferromagnetic interaction between Fe-ions, inferred from both ZFC and FC curve the ferromagnetism for Fe-doped samples is found to suppress but this effect is found to increase with fluency of Fe-ion, therefore, Fe-doped $CeO_2$ samples exhibited super paramagnetic dominated weak ferromagnetic behaviour at room temperature. Finally, it has been observed that with Fe-implantation, the optical, electronic structural and magnetic properties of $CeO_2$ NPs can be modified and this kind of implantation can yield better samples for the potential use in the technological applications like spintronics.

**Chapter 6**

In the sixth chapter, the entire work has been summarized chapter wise along with important conclusions of the present thesis work to highlight the new findings on the structural, optical, electronic structure, magnetic and electrical properties of the TM (Fe) and RE (Sm, Gd)-doped $CeO_2$ NPs for their potential use in technological application for spintronics devices. Finally, scope for further work and their future possibilities related to the thesis work has been presented at the end of the chapter.

# Bibliography

# BIBLIOGRAPHY


[1] N. Zheng; ***Solid Sate II, Instructor***, (**2008**)

[2] Z. Wilamowski and A. Werpachowska; *arXiv preprint arXiv:1111.1032*, ***Materials Science Poland***, 24 (3), (**2011**)

[3] I. Žutić, J. Fabian and S. D. Sarma; ***Reviews of modern physics***, *76*(2), 323, (**2004**)

[4] R. Janisch, P. Gopal and N. A. Spaldin; ***Journal of Physics: Condensed Matter***, *17*(27), R657–R689, (**2005**)

[5] A. Mauger and C. Godart; ***Physics Reports***, *141*(2-3), 51-176, (**1986**)

[6] H. Ohno; **Science**, *281*(5379), 951-956, (**1998**)

[7] H. Ohno, A. Shen, F. Matsukura, A. Oiwa, A. Endo, S. Katsumoto and Y. Iye; ***Applied Physics Letters***, *69*(3), 363-365, (**1996**)

[8] T. Dietl; ***Journal of Applied Physics***, *103*(7), 07D111, (**2008**)

[9] T. Jungwirth, J. Sinova, J. Mašek, J. Kučera and A. H. MacDonald; ***Reviews of Modern Physics***, *78*(3), 809, (**2006**)

[10] M. Venkatesan, C. B. Fitzgerald and J. M. D. Coey; ***Nature***, *430*(7000), 630, (**2004**)

[11] J. M. D. Coey, M. Venkatesan and C. B. Fitzgerald; ***Nature materials***, *4*(2), 173, (**2005**)

[12] S. Kumar, Y. J. Kim, B. H. Koo, S. K. Sharma, J. M. Vargas, M. Knobel, S. Gautam, K. H. Chae, D. K. Kim, Y. K. Kim and C. G. Lee; ***Journal of Applied Physics***, *105*(7), 07C520, (**2009**)

[13] S. Kumar, Y. J. Kim, B. H. Koo, S. Gautam, K. H. Chae, R. Kumar and C. G. Lee; ***Materials Letters***, *63*(2), 194-196, (**2009**)

[14] S. Kumar, Y. J. Kim, B. H. Koo and C. G. Lee; ***Journal of nanoscience and nanotechnology***, *10*(11), 7204-7207, (**2010**)

[15] A. Sundaresan, R. Bhargavi, N. Rangarajan, U. Siddesh and C. N. R. Rao; ***Physical Review B***, *74*(16), 161306, (**2006**)

[16] J. M. D. Coey, A. P. Douvalis, C. B. Fitzgerald and M. Venkatesan; ***Applied Physics Letters***, *84*(8), 1332-1334, (**2004**)

[17] J. Y. Kim, J. H. Park, B. G. Park, H. J. Noh, S. J. Oh, J. S. Yang, D. H. Kim, S. D. Bu, T. W. Noh, H. J. Lin and H. H. Hsieh; ***Physical review letters***, *90*(1), 017401, (**2003**)

[18] W. D. Kingery, H. K. Bowen and D. R. Uhlmann; "Introduction to Ceramics", 2nd edition, John Wiley & Sons, New York, (**1976**)

[19] O. H. Wyatt, D. D. Hughes; "Metals, Ceramics and Polymers", Cambridge University Press, London, (**1974**)

[20] R. M. White, R. M. White and B. Bayne; *Quantum theory of magnetism* (Vol. 1). Berlin: Springer-Verlag, (**1983**)

[21] C. Zener; ***Physical Review***, *82*(3), 403, (**1951**)

[22] A. Werpachowska and Z. Wilamowski; *arXiv preprint arXiv:1111.1030*, ***Materials Science-Poland***, *24(3)*, 2006, (**2011**)

[23] A. C. Durst, R. N. Bhatt and P. A. Wolff; ***Physical Review B***, *65*(23), 235205, (**2002**)

[24] T. Dietl and J. Spałek; ***Physical Review B***, *28*(3), 1548, (**1983**)

[25] L. R. Shah, B. Ali, H. Zhu, W. G. Wang, Y. Q. Song, H. W. Zhang, S. I. Shah and J. Q. Xiao; ***Journal of Physics: Condensed Matter***, *21*(48), 486004, (**2009**)

[26] C. B. Fitzgerald, M. Venkatesan, L. S. Dorneles, R. Gunning, P. Stamenov, J. M. D. Coey, P. A. Stampe, R. J. Kennedy, E. C. Moreira and U. S. Sias; ***Physical Review B***, *74*(11), 115307, (**2006**)

[27] J. M. D. Coey, M. Venkatesan, C. B. Fitzgerald; ***Nature materials***, *4*(2), 173, (**2005**)

[28] C. Liu, F. Yun, H. Morkoc; *Journal of Materials Science:* ***Materials in Electronics***, *16*(9), 555, (**2005**)

[29] R. P. Feynman; There's plenty of room at the bottom: An invitation to enter a new field of physics. In ***Handbook of Nanoscience, Engineering, and Technology, Third Edition*** (26-35), CRC Press. (**2012**)

[30] H. Bönnemann and R. M. Richards; ***European Journal of Inorganic Chemistry***, *2001*(10), 2455-2480, (**2001**)

[31] J. Blackman; ***Metallic nanoparticles***, (Vol. 5), Elsevier, (**2008**)

[32] J. N. Tiwari, R. N. Tiwari and K. S. Kim; ***Progress in Materials Science***, *57*(4), 724-803, (**2012**)

[33] P. Christian, F. Von der Kammer, M. Baalousha and T. Hofmann; ***Ecotoxicology***, *17*(5), 326-343, (**2008**)

[34] W. K. Shin, J. Cho, A. G. Kannan, Y. S. Lee and D. W. Kim; ***Scientific reports***, *6*, 26332, (**2016**)

[35] D. Williams, M. Amman, H. Autrup, J. Bridges, F. Cassee, K. Donaldson, E. Fattal, C. Janssen, W. De Jong, T. Jung, and J. P. Marty; The appropriateness of existing methodologies to assess the potential risks associated with engineered and adventitious products of nanotechnologies. *Report for the European Commission Health and Consumer Protection Directorate General by the Scientific Committee on Emerging and Newly Identified Health Risks. Brussels*, (**2005**)

[36] M. Radovic, Z. D. Dohcevic-Mitrovic, A. Golubovic, B. Matovic, M. Ščepanovic and Z. V. Popovic; ***Acta Physica Polonica A***, *116* (4), 614-617, (**2009**)

[37] P. Bera and M. S. Hegde; ***Catalysis letters***, *79*(1-4), 75-81, (**2002**)

[38] Lj. S. Živkovic, V. Lair, O. Lupan, M. Cassir and A. Ringuedé; ***Acta Physica Polonica A***, *120* (2), 298-302, (**2011**)

[39] N. N. Dao, M. Dai Luu, Q. K. Nguyen and B. S. Kim; ***Advances in Natural Sciences: Nanoscience and Nanotechnology***, *2*(4), 045013, (**2011**)

[40] L. S. Živković, V. Lair, O. Lupan and A. Ringuedé; ***Russian Journal of Physical Chemistry A***, *85*(13), 2358-2362, (**2011**)

[41] T. Somekawa, Y. Matsuzaki, Y. Tachikawa, S. Taniguchi and K. Sasaki; ***Ionics***, *23*(1), 95-103, (**2017**)

[42] Y. Dong, S. Hampshire, J. E. Zhou and G. Meng; ***International journal of hydrogen energy***, *36*(8), 5054-5066, (**2011**)

[43] Y. Dong, D. Li, X. Feng, X. Dong and S. Hampshire; ***RSC Advances***, *3*(38), 17395-17401. (**2013**).

[44] W. Zhang, C. Hu, W. Zhai, Z. Wang, Y. Sun, F. Chi, S. Ran, X. Liu and Y. Lv; ***Materials Research***, *19*(3), 673-679, (**2016**)

[45] D. Yin, F. Zhao, L. Zhang, X. Zhang, Y. Liu, T. Zhang, C. Wu, D. Chen and Z. Chen; ***RSC Advances***, *6*(105), 103795-103802, (**2016**)

[46] T. Montini, M. Melchionna, M. Monai and P. Fornasiero; ***Chemical reviews***, *116*(10), 5987-6041, (**2016**)

[47] G. Zhang, Z. Shen, M. Liu, C. Guo, P. Sun, Z. Yuan, B. Li, D. Ding and T. Chen; ***The Journal of Physical Chemistry B***, *110*(51), 25782-25790, (**2006**)

[48] M. Yashima, D. Ishimura, Y. Yamaguchi, K. Ohoyama and K. Kawachi; ***Chemical physics letters***, *372*(5-6), 784-787, (**2003**)

[49] P. K. Slusser; *Transition metal doped cerium oxide for spintronics applications* (Doctoral dissertation, Department of Materials Science and Engineering, University of Utah), (**2009**)

[50] S. Kumar, G. W. Kim, B. H. Koo, S. K. Sharma, M. Knobel, H. Chung and C. G. Lee; ***Journal of nanoscience and nanotechnology***, *11*(1), 555-559, (**2011**)

[51] Q. Y. Wen, H. W. Zhang, Q. H. Yang, S. Li, J. Zha, D. G. Xu, and J. Q. Yao; Characteristics of pure and Fe doped polycrystalline $CeO_2$ using terahertz spectroscopy. In ***Photonics and Optoelectronics Meetings (POEM) 2008: Terahertz Science and Technology***. International Society for Optics and Photonics. 7277, 72770C, (**2009**)

[52] J. Wang, Q. Liu and Q. Liu; ***Journal of the American Ceramic Society***, *91*(8), 2706-2708, (**2008**)

[53] R. K. Hailstone, A. G. DiFrancesco, J. G. Leong, T. D. Allston and K. J. Reed; ***The Journal of Physical Chemistry C***, *113*(34), 15155-15159, (**2009**)

[54] S. Yuan-Qiang, Z. Huai-Wu, W. Qi-Ye, L. Yuan-Xun and J. Q. Xiao; ***Chinese Physics Letters***, *24*(1), 218, (**2007**)

[55] M. C. Dimri, H. Khanduri, H. Kooskora, J. Subbi, I. Heinmaa, A. Mere, J. Krustok and R. Stern; ***physica status solidi (a)***, *209*(2), 353-358, (**2012**)

[56] E. Swatsitang, S. Phokha, S. Hunpratub and S. Maensiri; ***Physica B: Condensed Matter***, *485*, 14-20, (**2016**)

[57] A. A. Aboud, H. Al-Kelesh, W. M. El Rouby, A. A. Farghali, A. Hamdedein and M. H. Khedr; ***Journal of materials research and technology***, *7*(1), 14-20, (**2018**)

[58] Z. P. Li, T. Mori, F. Ye, D. R. Ou, J. Zou and J. Drennan; ***Physical Review B***, *84*(18), 180201, (**2011**)

[59] F. Abbas, T. Jan, J. Iqbal, I. Ahmad, M. S. H. Naqvi and M. Malik; ***Applied Surface Science***, *357*, 931-936, (**2015**)

[60] S. Debnath, M. R. Islam, M. S. R. Khan; ***Bulletin of Materials Science***, *30*(4), 315-319, (**2007**)

[61] T. V. Semikina; ***Semiconductor Physics Quantum Electronics & Optoelectronics***, 7(3), 291-296, (**2004**)

[62] F. Abbas, T. Jan, J. Iqbal, M. S. H. Naqvi and I. Ahmad; ***Materials Chemistry and Physics***, *173*, 146-151, (**2016**)

[63] F. Abbas, T. Jan, J. Iqbal and M. S. H. Naqvi; ***Current Applied Physics***, *15*(11), 1428-1434. (**2015**).

[64] Y. Wu, X. Liu, K. Ur-Rehman, S. Jiang, C. Zhang, C. Liu, X. Meng and H. Li; ***Materials Letters***, *183*, 161-164, (**2016**)

[65] S. Phokha, S. Pinitsoontorn and S. Maensiri; ***Nano-Micro Letters***, *5*(4), 223-233, (**2013**)

[66] W. C. Wang, S. Y. Chen, P. A. Glans, J. Guo, R. J. Chen, K. W. Fong, C. L. Chen, A. Gloter, C. L. Chang, T. S. Chan and J. M. Chen; ***Physical Chemistry Chemical Physics***, *15*(35), 14701-14707, (**2013**)

[67] S. Y. Chen, R. J. Chen, W. Lee, C. L. Dong and A. Gloter; ***Physical Chemistry Chemical Physics***, *16*(7), 3274-3281, (**2014**)

[68] B. Šmíd, M. Škoda, I. Matolínová, L. Sedláček and V. Matolín; ***WDS'05 Proceedings of Contributed Papers***, Part III, 574–579, (**2005**), ISBN 80-86732-59-2

[69] J. Fang, H. Bao, B. He, F. Wang, D. Si, Z. Jiang, Z. Pan, S. Wei and W. Huang; ***The Journal of Physical Chemistry C***, *111*(51), 19078-19085, (**2007**)

[70] J. F. Lee, M. T. Tang, W. C. Shih and R. S. Liu; ***Materials research bulletin***, *37*(3), 555-562, (**2002**)

[71] M. Baron, O. Bondarchuk, D. Stacchiola, S. Shaikhutdinov and H. J. Freund; ***The Journal of Physical Chemistry C***, *113*(15), 6042-6049, (**2009**)

[72] M. S. P. Francisco, V. R. Mastelaro, P. A. Nascente and A. O. Florentino; ***The Journal of Physical Chemistry B***, *105*(43), 10515-10522, (**2001**)

[73] A. Bouaine, R. J. Green, S. Colis, P. Bazylewski, G. S. Chang, A. Moewes, E. Z. Kurmaev and A. Dinia; ***The Journal of Physical Chemistry C***, *115*(5), 1556-1560, (**2010**)

[74] J. P. Rueff, J. P. Itié, M. Taguchi, C. F. Hague, J. M. Mariot, R. Delaunay, J. P. Kappler and N. Jaouen; ***Physical review letters***, *96*(23), 237403, (**2006**)

[75] C. H. Hu, C. H. Xia, F. Wang, M. Zhou, P. F. Yin and X. Y. Han; ***Bulletin of Materials Science***, *34*(5), 1033-1037, (**2011**)

[76] S. Kumar, Y. J. Kim, B. H. Koo, H. Choi and C. G. Lee; ***IEEE Transactions on Magnetics***, *45*(6), 2439-2441, (**2009**)

[77] A. Thurber, K. M. Reddy, V. Shutthanandan, M. H. Engelhard, C. Wang, J. Hays and A. Punnoose; ***Physical Review B***, *76*(16), 165206, (**2007**)

[78] A. Arabac and M. F. Öksüzömer; ***Ceramics International***, *38*(8), 6509-6515, (**2012**)

[79] T. Li and Q. Shi; ***Journal of Materials Science: Materials in Electronics***, 1-6, (**2018**)

[80] R.V. Mangalaraja, S. Ananthakumar, M. Paulraj, H. Pesenti, M. López, C. P. Camurri, L. A. Barcos and R. E. Avila; ***Journal of Alloys and Compounds***, *510*(1), 134-140, (**2012**)

[81] M. P. Lobera, M. Balaguer, J. Garcia-Fayos and J. M. Serra; ***ChemCatChem***, *4*(12), 2102-2111, (**2012**)

[82] B. C. H. Steele; In ***Solid State Ionics***, 17-28, (**1992**)

[83] N Rajput; ***International Journal of Advances in Engineering & Technology***, *7*(6), 1806, (**2015**)

[84] Y. Leng; Materials characterization: introduction to microscopic and spectroscopic methods. ***John Wiley & Sons***, (**2009**)

[85] S. Biz and M. L. Occelli; ***Catalysis Reviews***, *40*(3), 329-407, (**1998**)

[86] A. B. Ravalia; Swift heavy ion induced modifications in the properties of multifunctional oxides, (**2013**)

[87] C. Levy, C. Guizard and A. Julbe; ***Journal of the American Ceramic Society***, *90*(3), 942-949, (**2007**)

[88] M. Jamshidijam, R. V. Mangalaraja, A. Akbari-Fakhrabadi, S. Ananthakumar and S. H. Chan; ***Powder Technology***, *253*, 304–310, (**2014**)

[89] H. Rietveld; ***Journal of applied Crystallography***, *2*(2), 65-71, (**1969**).

[90] L. B. McCusker, R. B. Von Dreele, D. E. Cox, D. Louër and P. Scardi; ***Journal of Applied Crystallography***, *32*(1), 36-50, (**1999**)

[91] R. A. Young; The Rietveld method, ***International union of crystallography***, 5, 1-38, (**1993**).

[92] A. Kumar; Co existense of superconductivity and magnetism in Rutheno cuprates, non oxide perovskite MgCNi3 and FeSe Te systems. (**2012**)

[93] R. J. Hill and H. D. Flack; ***Journal of Applied Crystallography***, *20*(5), 356-361, (**1987**)

[94] W. J. McHardy; ***Chemical Geology***, *30*, 172-173, (**1980**)

[95] A. P. Bhatt; Chiral Metal Complexes As Catalysts In The Synthesis Of Chiral Pharmaceuticals Under Homogeneous And Heterogeneous Conditions, (**2008**)

[96] S. Ahmad; Studies of Cr and Co doped $TiO_2$ based Diluted Magnetic Semiconductor Nanomaterials, (**2015**)

[97] S. Kumar; Spin dynamics of $CoFe_2O_4$ based ferrofluids and matrix assisted film, (**2017**)

[98] M. Sathiya; Synthetic routes for the preparation of rechargeable Li-ion battery electrode materials, (**2012**)

[99] J. P. Sibilia; A guide to materials characterization and chemical analysis. ***John Wiley & Sons***, (**1996**)

[100] G. R. Chatwal and S. K. Anand; ***Instrumental methods of chemical analysis***, Mumbai: Himalaya publishing house, 180-192, (**1979**).

[101] C. V. Raman; A new radiation. In ***Proceedings of the Indian Academy of Sciences-Section A***. Springer India, *37*(3), 333-341, March **(1953**)

[102] D. C. Harris and M. D. Bertolucci; Symmetry and Spectroscopy: an introduction to vibrational and electronic spectroscopy. *Mineola, NY:* ***Dover Publications***, (**1989**)

[103] A. Kitai; (Ed.), ***Luminescent materials and applications***. *John Wiley & Sons*, *25*, (**2008**)

[104] E. C. Le Ru and P. G. Etchegoin; SERS enhancement factors and related topics. *Chapter 4*, 185-264, (**2009**)

[105] W. Leng and P. J. Vikesland; ***Analytical chemistry***, *85*(3), 1342-1349, (**2013**)

[106] Quantum Design, USA. Magnetic Property Measurement System: SQUID VSM User's Manual. (**2009**)

[107] B. D. Josephson; ***Physics letters***, *1*(7), 251-253, (**1962**)

[108] User manual of Keithley 2400 source-meter, A Tektronix Company

[109] M. Balestrieri, S. Colis, M. Gallart, G. Schmerber, M. Ziegler, P. Gilliot and A. Dinia; ***Journal of Materials Chemistry C***, *3*(27), 7014-7021, (**2015**)

[110] T. S. Zhang, J. Ma, L. B. Kong, P. Hing and J. A. Kilner; ***Solid State Ionics***, *167*(1), 191-196, (**2004**)

[111] A. Akbari-Fakhrabadi, R. V. Mangalaraja, F. A. Sanhueza, R. E. Avila, S. Ananthakumar and S. H. Chan; ***Journal of Power Sources***, *218*, 307-312, (**2012**)

[112] T. Mori, J. Drennan, J. H. Lee, J. G. Li and T. Ikegami; ***Solid State Ionics***, *154*, 461-466, (**2002**)

[113] T. Mori and J. Drennan; ***Journal of electroceramics***, *17*(2-4), 749-757, (**2006**)

[114] W. Huang, P. Shuk and M. Greenblatt; ***Chemistry of materials***, *9*(10), 2240-2245, (**1997**)

[115] V. V. Ursaki, V. Lair, L. Živković, M. Cassir, A. Ringuede and O. Lupan; ***Optical Materials***, *34*(11), 1897-1901, (**2012**)

[116] W. Lee, S. Y. Chen, Y. S. Chen, C. L. Dong, H. J. Lin, C. T. Chen and A. Gloter; ***The Journal of Physical Chemistry C***, *118*(45), 26359-26367, (**2014**)

[117] K. Kaviyarasu, P. P. Murmu, J. Kennedy, F. T. Thema, D. Letsholathebe, L. Kotsedi and M. Maaza; *Nuclear Instruments and Methods in Physics Research Section B: Beam Interactions with Materials and Atoms*, (**2017**). https://doi.org/10.1016/j.nimb.2017.02.055

[118] V. Butler, C. R. A. Catlow, B. E. F. Fender and J. H. Harding; ***Solid State Ionics***, *8*(2), 109-113, (**1983**)

[119] S. Soni, V. S. Vats, S. Kumar, B. Dalela, M. Mishra, R. S. Meena, G. Gupta, P. A. Alvi, S. Dalela; ***Journal of Materials Science: Materials in Electronics***, *29*(12), 10141-10153, (**2018**)

[120] W. Lee, S. Y. Chen, E. Tseng, A. Gloter and C. L. Chen; ***The Journal of Physical Chemistry C***, *120*(27), 14874-14882, (**2016**)

[121] L. J. Swartzendruber; Calculations for comparing two-point and four-point probe resistivity measurements on rectangular bar-shaped semiconductor samples (Fortran programs for calculation of four-point probe resistivity measurements on bar-shaped semiconductor samples), (**1964**)

[122] L. Sun, S. S. Park, D. Sheberla and M . Dincă ; ***Journal of the American Chemical Society***, *138*(44), 14772-14782, (**2016**)

[123] S. Soni, S. Kumar, R. S. Meena, V. S. Vats and S. Dalela; ***AIP Conference Proceedings***, *1665*, 130029, (**2015**)

[124] D. R. Ou, T. Mori, F. Ye, T. Kobayashi, J. Zou, G. Auchterlonie and J. Drennan; ***Applied physics letters***, *89*(17), 171911, (**2006**)

[125] P. Kumar, P. Kumar, A. Kumar, I. Sulania, F. Chand and K. Asokan; ***RSC Advances***, *7*(15), 9160-9168, (**2017**)

[126] B. Mandal, A. Mondal, S. S. Ray and A. Kundu; ***Dalton Transactions***, *45*(4), 1679-1692, (**2016**)

[127] L. Truffault, M. T. Ta, T. Devers, K. Konstantinov, V. Harel, C. Simmonard, C. Andreazza, I. P. Nevirkovets, A. Pineau, O. Veron and J.P. Blondeau; ***Materials Research Bulletin***, *45*(5), 527-535, (**2010**)

[128] W. M. A. El Rouby, A. A. Farghali and A. Hamdedein; ***Water Science and Technology***, *74*(10), 2325-2336, (**2016**)

[129] V. N. Morris, R. A. Farrell, A. M. Sexton and M. A. Morris; ***Journal of Physics: Conference Series***, 26(1), 119–122, (**2006**)

[130] P. Bindu and S. Thomas; ***Journal of Theoretical and Applied Physics***, *8*(4), 123-134, (**2014**)

[131] R. Murugan, G. Vijayaprasath, T. Mahalingam and G. Ravi; ***Applied Surface Science,*** *390*, 583-590, (**2016**)

[132] D. Ma, Z. Lu, Y. Tang, T. Li, Z. Tang and Z. Yang; ***Physics Letters A,*** *378* (34), 2570-2575, (**2014**)

[133] M. Nolan, V. S. Verdugo and H. Metiu; ***Surface Science***, *602(16)*, 2734-2742, (**2008**)

[134] İ. Uslu, A. Aytimur, M. K. Öztürk and S. Koçyiğit; ***Ceramics International,*** *38*(6), 4943-4951, (**2012**)

[135] N. S. Arul, D. Mangalaraj, P. C. Chen, N. Ponpandian and C. Viswanathan; ***Materials Letters***, *65*(17), 2635-2638, (**2011**)

[136] Z. Wang, Z. Quan and J. Lin; ***Inorganic chemistry***, *46*(13), 5237-5242, (**2007**)

[137] B. Choudhury and A. Choudhury; ***Current Applied Physics***, *13*(1), 217-223, (**2013**)

[138] M. S. Hosseini and F. Belador; ***Synthesis and Reactivity in Inorganic, Metal-Organic, and Nano-Metal Chemistry***, *46*(6), 950-957, (**2016**)

[139] R. C. Deus, J. A. Cortés, M. A. Ramirez, M. A. Ponce, Juan Andres, L. S. R. Rocha, Elson Longo and A. Z. Simoes; ***Materials Research Bulletin***, *70*, 416-423, (**2015**)

[140] P. Nagaraju, Y. V. Kumar, M. R. Reddy, C. V. Reddy, V. R. Reddy and D. M. Phase; ***International Journal of Scientific & Engineering Research***, *5*(3), 185-190, (**2014**), ISSN 2229-5518

[141] X. Niu and F. Tu; ***Journal of Materials Science: Materials in Electronics***, *28*(2), 2141-2146, (**2017**)

[142] A. C. Cabral, L. S. Cavalcante, R. C. Deus, E. Longo, A. Z. Simoes and F. Moura; ***Ceramics International***, *40*(3), 4445-4453, (**2014**)

[143] R. Zamiri, H. A. Ahangar, A. Kaushal, A. Zakaria, G. Zamiri, D. Tobaldi and J. M. F. Ferreira; ***PloS one***, *10*(7), e0131851, (**2015**)

[144] C. Zhang, F. Meng and L. Wang; ***Materials Letters***, *119*, 1-3, (**2014**)

[145] S. Aškrabić, Z. D. Dohčević-Mitrović, M. Radović, M. Šćepanović and Z. V. Popović; ***Journal of Raman Spectroscopy***, *40*(6), 650-655, (**2009**)

[146] S. A. Acharya, V. M. Gaikwad, V. Sathe and S. K. Kulkarni; ***Applied Physics Letters***, *104*(11), 113508, (**2014**)

[147] W. H. Weber, K. C. Hass and J. R. McBride; ***Physical Review B***, *48*(1), 178, (**1993**)

[148] F. Meng, J. Gong, Z. Fan, H. Li and J. Yuan; ***Ceramics International***, *42*(4), 4700-4708, (**2016**)

[149] S. F. Wang, C. T. Yeh, Y. R. Wang and Y. C. Wu; ***Journal of Material Research and Technology***, *2*(2), 141–148, (**2013**)

[150] Y. U. Jinqiu, C. U. I. Lei, H. E. Huaqiang, Y. A. N. Shihong, H. U. Yunsheng and W. U. Hao; ***Journal of rare earths***, *32*(1), 1-4, (**2014**)

[151] P. Sathishkumar, R. V. Mangalaraja, T. Pandiyarajan, M. A. Gracia-Pinilla, N. Escalona, C. Herrera and R. Garcia; ***RSC Advances***, *5*(29), 22578-22586, (**2015**)

[152] A. G. M. D. Silva, T. S. Rodrigues, A. Dias, H. V. Fajardo, R. F. Gonçalves, M. Godinho Júnior and P. A. R. Dutenhefner; ***Catal. Sci. Technol.***, 4, 814–821, (**2014**)

[153] C. Thiabdokmai, A. Tangtrakarn, S. Promsuy, P. Ngiewlay and C. Mongkolkachit; ***Advances in Materials Science and Engineering***, *2014* (**2014**), Article ID 127531, 10 pages, doi:10.1155/2014/127531

[154] L. D. Jadhava, M. G. Chourashiya, A. P. Jamale, A. U. Chavan and S. P. Patil; ***Journal of Alloys and Compounds***, *506*(2), 739-744, (**2010**)

[155] R. Kostić, S. Aškrabić, Z. Dohčević-Mitrović and Z. V. Popović; ***Applied Physics A: Materials Science & Processing***, *90*(4), 679-683, (**2008**)

[156] M. Kamiya, E. Shimada, Y. Ikuma, M. Komatsu and H. Haneda; ***Journal of the Electrochemical Society***, *147*(3), 1222-1227, (**2000**)

[157] T. Taniguchi, T. Watanabe, N. Sugiyama, A. K. Subramani, H. Wagata, N. Matsushita and M. Yoshimura; ***The Journal of Physical Chemistry C***, *113*(46), 19789-19793, (**2009**)

[158] B. Choudhury and A. Choudhury; ***Materials Chemistry and Physics***, *131*(3), 666-671, (**2012**)

[159] S. Phoka, P. Laokul, E. Swatsitang, V. Promarak, S. Seraphin and S. Maensiri; ***Materials Chemistry and Physics***, *115*(1), 423-428, (**2009**)

[160] R. Suresh, V. Ponnuswamy and R. Mariappan; ***Applied Surface Science***, *273*, 457-464, (**2013**)

[161] W. Duan, A. Xie, Y. Shen, X. Wang, F. Wang, Y. Zhang and J. Li; ***Industrial & Engineering Chemistry Research***, *50*(8), 4441-4445, (**2011**)

[162] Z. Lu, C. Mao, M. Meng, S. Liu, Y. Tian, L. Yu, B. Sun and C.M. Li; ***Journal of colloid and interface science***, *435*, 8-14, (**2014**)

[163] N. Izu, W. Shin, N. Murayama and S. Kanzaki; ***Sensors and Actuators B: Chemical***, *87*(1), 95-98, (**2002**)

[164] Z. Zhan and S. A. Barnett; ***Science***, *308*(5723), 844-847, (**2005**)

[165] S. Kuharuangrong; ***Journal of Power Sources***, *171*(2), 506-510, (**2007)**

[166] C. Artini, M. Pani, M. M. Carnasciali, J. R. Plaisier and Lu-G. A. Costa; ***Inorganic Chemistry***, *55*(20), 10567-10579, (**2016**)

[167] G. Magesh, B. Viswanathan, R. P. Viswanath and T. K. Varadarajan; ***Indian J. Chem.***, *48A*, 480−488, (**2009**)

[168] S. Tsunekawa, J. T. Wang, Y. Kawazoe and J. Kasuya; ***J. Appl. Phys.***, *94*, 3654–3656, (**2003**)

[169] S. Wang, T. Kobayashi, M. Dokiya and T. Hashimoto; ***Journal of the Electrochemical Society***, *147*(10), 3606-3609, (**2000**)

[170] A. K. Lucid, P. R. Keating, J. P. Allen and G. W. Watson; ***The Journal of Physical Chemistry C***, *120*(41), 23430-23440, (**2016**)

[171] X. Xu, C. Xia, G. Xiao and D. Peng; ***Solid State Ionics***, *176*(17), 1513-1520, (**2005**)

[172] T. S. Zhang, J. Ma, H. Cheng and S. H. Chan; ***Materials research bulletin***, *41*(3), 563-568. (**2006**)

[173] S. Soni, S. Kumar, B. Dalela, S. Kumar, P. A. Alvi and S. Dalela; *Journal of Alloys and* ***Compounds***, *752*, 520-531, (**2018**)

[174] J. Kim and D. Lee; ***Korean Journal of Chemical Engineering***, *19*(3), 421-424, (**2002**)

[175] H. Wang, A. Chroneos and U. Schwingenschlögl; ***The Journal of chemical physics***, *138*(22), 224705, (**2013**)

[176] N. Singh, N. K. Singh, D. Kumar and O. Parkash; ***Journal of Alloys and Compounds***, *519*, 129-135, (**2012**)

[177] N. Jaiswal, N. K. Singh, D. Kumar and O. Parkash; ***Journal of Power Sources***, *202*, 78-84. (**2012**)

[178] I. Kosacki, T. Suzuki, V. Petrovsky and H. U. Anderson, ***Solid State Ionics***, *136*, 1225-1233, (**2000**)

[179] G. R. Li, D. L. Qu, L. Arurault and Y. X. Tong; ***The Journal of Physical Chemistry C***, *113*(4), 1235-1241, (**2009**)

[180] B. Matović, M. Stojmenović, J. Pantić, A. Varela, M. Žunić, N. Jiraborvornpongsa and T. Yano; ***Journal of Asian Ceramic Societies***, *2*(2), 117-122, (**2014**)

[181] C. Artini, M. Pani, M. M. Carnasciali, M. T. Buscaglia, J. R. Plaisier and G. A. Costa; ***Inorganic chemistry***, *54*(8), 4126-4137, (**2015**)

[182] W. J. Bowman, J. Zhu, R. Sharma and P. A. Crozier; ***Solid State Ionics***, *272*, 9-17, (**2015**)

[183] M. Li, R. Zhang, H. Zhang, W. Feng and X, Liu; ***IET Micro Nano Letters***, *5*, 95–99, (**2010**)

[184] A. L. Gal and S. Abanades; ***J. Phys. Chem. C***, *116*, 13516−13523, (**2012**)

[185] R J Wu, Y C Hsieh, H C Hung, C Ie and M Chavali; ***J Chin Chem Soc***, *61*, 495-500, (**2014**)

[186] Z. Zhu, J Y Chen, K Y Su and R J Wu; ***J Taiwan Inst Chem E***, *60*, 222-8, (**2016**)

[187] M. Guo, J. Lu, Y. Wu, Y. Wang and M. Luo; ***Langmuir***, *27*(7), 3872-3877, (**2011**)

[188] I. Singh, K. Landfester, R. Muñoz-Espí and A. Chandra; ***Nanotechnology***, *28*(7), 075601. (**2017**)

[189] J. Malleshappa, H. Nagabhushana, B. D. Prasad, S. C. Shad gap rma, Y. S. Vidya and K. S. Anantharaju; ***Optik-International Journal for Light and Electron Optics***, *127*(2), 855-861. (**2016**)

[190] S. Kundu, N. Sutradhar, R. Thangamuthu, B. Subramanian, A. B. Panda and M. Jayachandran; ***Journal of Nanoparticle Research***, *14*(8), 1040, (**2012**)

[191] C. Hu, Z. Zhang, H. Liu, P. Gao and Z. L. Wang; ***Nanotechnology***, *17*(24), 5983, (**2006**)

[192] S. Tsunekawa, R. Sahara, Y. Kawazoe and A. Kasuya; ***Materials Transactions, JIM***, *41*(8), 1104-1107, (**2000**)

[193] M. Karl Chinnu, K. Vijai Anand, R. Mohan Kumar, T. Alagesan and R. Jayavel; ***Journal of Experimental Nanoscience***, *10*(7), 520-531, (**2015**)

[194] A. V. Thorat, T. Ghoshal, P. Carolan, J. D. Holmes and M. A. Morris; ***The Journal of Physical Chemistry C***, *118*(20), 10700-10710, (**2014**)

[195] M. Y. Chen, X. T. Zu, X. Xiang and H. L. Zhang; ***Physica B: Condensed Matter***, *389*(2), 263-268, (**2007**)

[196] I. Hamberg, C. G. Granqvist, K. F. Berggren, B. E. Sernelius and L. Engström; ***Physical Review B***, *30*(6), 3240, (**1984**)

[197] P. Patsalas, S. Logothetidis, L. Sygellou and S. Kennou; ***Physical Review B***, *68*(3), 035104. (**2003**)

[198] B. Sharma, R. R. Frontiera, A. I. Henry, E. Ringe and R. P. Van Duyne; ***Materials today***, *15*(1), 16-25, (**2012**)

[199] J. Cui and G. A. Hope; ***Journal of Spectroscopy***, *2015*, Article ID 940172, 8 pages, (**2015**)

[200] I. Kosacki, T. Suzuki, H. U. Anderson and P. Colomban; ***Solid State Ionics***, *149*(1), 99-105, (**2002**)

[201] X. Ma, P. Lu and P. Wu; ***Journal of Alloys and Compounds***, *734*, 22-28, (**2017**)

[202] A. K. Sinha and K. Suzuki; ***The Journal of Physical Chemistry B***, *109*(5), 1708-1714, (**2005**)

[203] P. Venkataswamy, K. N. Rao, D. Jampaiah and B. M. Reddy; ***Applied Catalysis B: Environmental***, *162*, 122-132, (**2015**)

[204] Y. L. Kuo, C. Lee, Y. S. Chen and H. Liang; ***Solid State Ionics***, *180*(26), 1421-1428, (**2009**)

[205] M. R. Rao and T. Shripathi; ***Journal of electron spectroscopy and related phenomena***, *87*(2), 121-126, (**1997**)

[206] J. Zhang, H. Wong, D. Yu, K. Kakushima and H. Iwai; ***AIP Advances***, *4*(11), 117117, (**2014**)

[207] F. Meng, L. Wang and J. Cui; ***Journal of Alloys and Compounds***, *556*, 102-108, (**2013**)

[208] M. M. Khan, S. A. Ansari, D. Pradhan, D. H. Han, J. Lee and M. H. Cho; ***Industrial & Engineering Chemistry Research***, *53*(23), 9754-9763, (**2014**)

[209] F. Pagliuca, P. Luches and S. Valeri; ***Interfacial Surface Science***, *607*, 164-169, (**2013**)

[210] P. Bera, H. Seenivasan, K. S. Rajam, C. Shivakumara and S. K. Parida; ***Surface and Interface Analysis***, *45*(6), 1026-1036, (**2013**)

[211] A. Galtayries, R. Sporken, J. Riga, G. Blanchard and R. Caudano; ***Journal of electron spectroscopy and related phenomena***, *88*, 951-956, (**1998**)

[212] S. A. Ansari, M. M. Khan, M. O. Ansari, S. Kalathil, J. Lee and M. H. Cho; ***RSC Advances***, *4*(32), 16782-16791, (**2014**)

[213] S. A. Acharya, V. M. Gaikwad, S. W. D'Souza and S. R. Barman; ***Solid State Ionics***, *260*, 21-29, (**2014**)

[214] D. N. Durgasri, T. Vinodkumar, P. Sudarsanam and B. M. Reddy; ***Catalysis letters***, *144*(6), 971-979, (**2014**)

[215] J. L. Rupp, T. Drobek, A. Rossi and L. J. Gauckler; ***Chemistry of materials***, *19*(5), 1134-1142, (**2007**)

[216] M. Pramanik, F. K. Shieh, S. M. Alshehri, Z. A. Alothman, K. C. W. Wu and Y. Yamauchi; ***RSC Advances***, *5*(53), 42762-42767, (**2015**)

[217] A. Sundaresan and C. N. R. Rao; ***Nano Today***, *4*(1), 96-106, (**2009**)

[218] Y. Liu, Z. Lockman, A. Aziz and J. MacManus-Driscoll; ***Journal of Physics: Condensed Matter***, *20*(16), 165201, (**2008**)

[219] M. Y. Ge, H. Wang, E. Z. Liu, J. F. Liu, J. Z. Jiang, Y. K. Li, Z. A. Xu and H. Y. Li; ***Applied Physics Letters***, *93*(6), 062505, (**2008**)

[220] X. Chen, G. Li, Y. Su, X. Qiu, L. Li and Z. Zou; ***Nanotechnology***, *20*(11), 115606, (**2009**)

[221] S. Y. Chen, Y. H. Lu, T. W. Huang, D. C. Yan and C. L. Dong; ***The Journal of Physical Chemistry C***, *114*(46), 19576-19581, (**2010**)

[222] K. Ackland, L. M. Monzon, M. Venkatesan and J. M. D. Coey; ***IEEE transactions on magnetic***, *47*(10), 3509-3512, (**2011**)

[223] S. Phokha, S. Pinitsoontorn, P. Chirawatkul, Y. Poo-arporn and S. Maensiri; ***Nanoscale research letters***, *7*(1), 425, (**2012**)

[224] K. S. Ranjith, P. Saravanan, S. H. Chen, C. L. Dong, C. L. Chen, S. Y. Chen, K. Asokan and R. T. R. Kumar; ***J. Phys. Chem.***, *118*, 27039-27047, (**2014**)

[225] N. Paunović, Z. Dohčević-Mitrović, R. Scurtu, S. Aškrabić, M. Prekajski, B. Matović and Z. V. Popović; ***Nanoscale***, *4*(17), 5469-5476, (**2012**)

[226] M. Akyol, A. Ekicibil and K. Kiymaç; ***Journal of superconductivity and novel magnetism***, *26*(11), 3257-3262, (**2013**)

[227] M. Petersen, J. Hafner and M. Marsman; ***Journal of Physics: Condensed Matter***, *18*(30), 7021, (**2006**)

[228] H. T. Wong, H. L. Chan and J. H. Hao; ***Applied physics letters***, *95*(2), 022512, (**2009**)

[229] S. Ghosh, G. G. Khan and K. Mandal; ***ACS applied materials & interfaces***, *4*(4), 2048-2056, (**2012**)

[230] N. Nithyaa and N. V. Jaya; ***Journal of Superconductivity and Novel Magnetism***, *31*(12), 4117-4126, (**2018**)

[231] V. Ney, S. Ye, T. Kammermeier, K. Ollefs, F. Wilhelm, A. Rogalev, S. Lebegue, A.L. da Rosa and A. Ney; ***Phys. Rev. B: Condens. Matter***, *85*, 235203, (**2012**)

[232] G. Vijayaprasath, R. Murugan, Y. Hayakawa and G. Ravi; ***Journal of Luminescence***, *178*, 375-383, (**2016**)

[233] A. Jr. Franco and H. V. S. Pessoni; ***Physica B***, *506*, 145–151, (**2017**)

[234] S. Y. Chen, C. H. Tsai, M. Z. Huang, D. C. Yan, T. W. Huang, A. Gloter, C. L. Chen, H. J. Lin, C. T. Chen and C. L. Dong; ***The Journal of Physical Chemistry C***, *116*(15), 8707-8713, (**2012**)

[235] G. Niu, E. Hildebrandt, M. A. Schubert, F. Boscherini, M. H. Zoellner, L. Alff, D. Walczyk, P. Zaumseil, I. Costina, H. Wilkens and T. Schroeder; ***ACS applied materials & interfaces***, *6*(20), 17496-17505, (**2014**)

[236] G. Lindbergh and D. Simonsson; ***J. Electrochem. Soc.***, *36*, 1985-1994, (**1991**)

[237] H. A. Schwarz; ***J. Phys. Chem.***, *96* (22), 8937–8941,(**1992**)

[238] J. A. Seetula, I. R. Slagle and D. Gutman; ***Chemical Physics Letters***, *224*(5–6), 533-538, (**1994**)

[239] N. Chouhan, R. S. Liu and S. F. Hu; ***Journal of Materials Chemistry A***, *1*(25), 7422-7432, (**2013**)

[240] H. Li, G. Wang, F. Zhang, Y. Cai, Y. Wang and I. Djerdj; ***RSC Advances***, *2*(32), 12413-12423, (**2012**)

[241] A. Trovarelli, M. Boaro, E. Rocchini, C. de Leitenburg and G. Dolcetti; ***Journal of Alloys and Compounds***, *323*, 584-591, (**2001**)

[242] T. S. Zhang, J. Ma, L. B. Kong, S. H. Chan and J. A. Kilner; ***Solid State Ionics***, *170*(3-4), 209-217, (**2004**)

[243] K. L. Duncan, Y. Wang, S. R. Bishop, F. Ebrahimi and E. D. Wachsman; ***Journal of applied physics***, *101*(4), 044906, (**2007**)

[244] S. Aškrabić, Z. Dohčević-Mitrović, A. Kremenović, N. Lazarević, V. Kahlenberg and Z. V. Popović; ***Journal of Raman Spectroscopy***, *43*(1), 76-81, (**2012**)

[245] A. Khare, R. J. Choudhary, D. M. Phase and S. P. Sanyal; ***Journal of Applied Physics***, *109*(12), 123706, (**2011**)

[246] A. Tiwari, V. M. Bhosle, S. Ramachandran, N. Sudhakar, J. Narayan, S. Budak and A. Gupta; ***Applied physics letters***, *88*(14), 142511, (**2006**)

[247] S. Phokha, D. Prabhakaran, A. Boothroyd, S. Pinitsoontorn and S. Maensiri; ***Microelectronic Engineering***, *126*, 93-98, (**2014**)

[248] S. Kumar, F. Ahmed, M. S. Anwar, H. K. Choi, H. Chung and B. H. Koo; ***Materials Research Bulletin***, *47*(10), 2980-2983, (**2012**)

[249] S. Maensiri, S. Phokha, P. Laokul and S. Seraphin; ***Journal of nanoscience and nanotechnology***, *9*(11), 6415-6420, (**2009**)

[250] Z. Zhang, D. Han, S. Wei and Y. Zhang; ***Journal of Catalysis***, *276*(1), 16-23, (**2010**)

[251] H. Bao, K. Qian, J. Fang and W. Huang; ***Applied Surface Science***, *414*, 131-139, (**2017**)

[252] R. N. Bharathi and S. Sankar; ***Journal of Materials Science: Materials in Electronics***, *29*(8), 6679-6691, (**2018**)

[253] P. Kumar, B. Ahmad, F. Chand and K. Asokan; ***Applied Surface Science***, *452*, 217-222, (**2018**)

[254] F. A. Mir, K. M. Batoo, I. Chatterjee and G. M. Bhat; ***J. Mater. Sci***, *25*, 1564–1570, (**2014**)

[255] R. Tholkappiyan and K. Vishista; ***Mater. Sci. Semicond. Process***, *40*, 631–642, (**2015**)

[256] A. A. Akl, S. A. Mahmoud, S. M. AL-Shomar and A. S. Hassanien; ***Materials Science in Semiconductor Processing***, *74*, 183-192, (**2018**)

[257] A. K. Tripathi, M. C. Mathpal, P. Kumar, M. K. Singh, M. A. G. Soler and A. Agarwal; ***Journal of Alloys and Compounds***, *622*, 37-47, (**2015**)

[258] T. Jarlborg, B. Barbiellini, C. Lane, Y. J. Wang, R. S. Markiewicz, Z. Liu, Z. Hussain and A. Bansil; ***Physical Review B***, *89*(16), 165101, (**2014**)

[259] R. Tholkappiyan and K. Vishista; ***Physica B: Condensed Matter***, *448*, 177-183, (**2014**)

[260] J. Pal and P. Chauhan; ***Materials characterization***, *61*(5), 575-579, (**2010**)

[261] A. Maurya, P. Chauhan, S. K. Mishra and R. K. Srivastava; ***Journal of Alloys and Compounds***, *509*(33), 8433-8440, (**2011**)

[262] R. N. Bharathi and S. Sankar; ***Superlattices and Microstructures***, *123*, 37-51, (**2018**)

[263] A. M. Salem and M. S. Selim; ***Journal of Physics D: Applied Physics***, *34*(1), 12, (**2001**)

[264] B. Tatar, E. D. Sam, K. Kutlu and M. Ürgen; ***Journal of materials science***, *43*(15), 5102, (**2008**)

[265] K. S. Ranjith, C. L. Dong, Y. R. Lu, Y. C. Huang, C. L. Chen, P. Saravanan, K. Asokan and R. T. Rajendra Kumar; ***ACS Sustainable Chemistry & Engineering***, *6*(7), 8536-8546, (**2018**)

[266] P. Kumar, F. Chand, and K. Asokan; ***Materials Research Express***, *4*(3), 036403, (**2017**)

[267] I. Kosacki, V. Petrovsky, H. U. Anderson and P. Colomban; ***Journal of the American Ceramic Society***, *85*(11), 2646-2650, (**2002**)

[268] J. E. Spanier, R. D. Robinson, F. Zhang, S. W. Chan and I. P. Herman, ***Physical Review B***, *64*(24), 245407, (**2001**)

[269] J. R. McBride, K. C. Hass, B. D. Poindexter and W. H. Weber; ***Journal of Applied Physics***, *76*(4), 2435-2441, (**1994**)

[270] S. H. Yang and Y. L. Zhang; ***Materials Science Forum (Trans Tech Publications Ltd.)***, *848*, 682, (**2016**)

[271] Y. Lee, G. He, A. J. Akey, R. Si, M. Flytzani-Stephanopoulos and I. P. Herman; ***Journal of the American Chemical Society***, *133*(33), 12952-12955, (**2011**)

[272] Z. Zhang, J. Yu, J. Zhang, Q. Ge, H. Xu, F. Dallmann, R. Dittmeyer and J. Sun; ***Chemical science***, *9*(13), 3386-3394, (**2018**)

[273] L. Truffault, Q. W. Yao, D. Wexler, I. P. Nevirkovets, K. Konstantinov, T. Devers and S. Nightingale; ***Journal of nanoscience and nanotechnology***, *11*(5), 4019-4028, (**2011**)

[274] Z. X. Li, L. L. Li, Q. Yuan, W. Feng, J. Xu, L. D. Sun, W. G. Song and C. H. Yan; ***The Journal of Physical Chemistry C***, *112*(47), 18405-18411, (**2008**)

[275] P. C. Brito, D. A. Santos, J. G. S. Duque and M. A. Macêdo; ***Physica B: Condensed Matter***, *405*(7), 1821-1825, (**2010**)

[276] M. Piumetti, S. Bensaid, T. Andana, M. Dosa, C. Novara, F. Giorgis, N. Russo and D. Fino; ***Catalysts***, *7*(6), 174, (**2017**)

[277] H. Bao, X. Chen, J. Fang, Z. Jiang and W. Huang; ***Catalysis letters***, *125*(1-2), 160-167, (**2008**)

[278] T. Suzuki, I. Kosacki and H. U. Anderson; ***J. Am. Ceram. Soc.***, *84* (9), 2007–14, (**2001**)

[279] P. Trogadas, J. Parrondo and V. Ramani; ***ACS applied materials & interfaces***, *4*(10), 5098-5102, (**2012**)

[280] Y. Wang, F. Wang, Y. Chen, D. Zhang, B. Li, S. Kang, X. Li and L. Cui; ***Applied Catalysis B: Environmental***, *147*, 602-609, (**2014**)

[281] H. Li, K. Li, H. Wang, X. Zhu, Y. Wei, D. Yan, X. Cheng and K. Zhai; ***Applied Surface Science***, *390*, 513-525, (**2016**)

[282] A. P. Grosvenor, B. A. Kobe, M. C. Biesinger and N. S. McIntyre; *Surface and Interface Analysis: An International Journal devoted to the development and application of techniques for the analysis of surfaces, interfaces and thin films*, *36*(12), 1564-1574, (**2004**)

[283] D. Mukherjee, B. G. Rao and B. M. Reddy; ***Topics in Catalysis***, *60*(19-20), 1673-1681, (**2017**)

[284] T. Baidya, T. Murayama, P. Bera, O. V. Safonova, P. Steiger, N. K. Katiyar, K. Biswas and M. Haruta; ***The Journal of Physical Chemistry C***, *121*(28), 15256-15265, (**2017**)

[285] V. K. Paidi, N. S. Ferreira, D. Goltz and J. van Lierop; ***Journal of Physics: Condensed Matter***, *27*(33), 336001, (**2015**)

[286] R. Brackmann, F. S. Toniolo, E. dos Santos Filho, O. C. Alves, Â. M. de Souza Gomes, C. B. Woyames and M. Schmal; ***Topics in Catalysis***, *61*(15-17), 1694-1706, (**2018**)

[287] V. Fernandes, P. Schio, A. J. A. De Oliveira, W. H. Schreiner, J. Varalda and D. H. Mosca; ***Journal of Applied Physics***, *110*(11), 113902, (**2011**)

# List of Publications

# LIST OF PUBLICATIONS

## Published in International Journals:

**1.** Electronic Structure and Room Temperature Ferromagnetism in Gd-doped Cerium Oxide nanoparticles for Hydrogen Generation via Photocatalytic Water Splitting

S. Soni, N. Chouhan, R. K. Meena, S. Kumar, B. Dalela, M. Mishra, R. S. Meena, G. Gupta, S. Kumar, P. A. Alvi and S. Dalela,

***Global Challenges***, 1800090, **2019 https://doi.org/10.1002/gch2.201800090**

**2.** Defects and oxygen vacancies tailored structural and optical properties in $CeO_2$ nanoparticles doped with $Sm^{3+}$ cation

S. Soni, S. Kumar, B. Dalela, S. Kumar, P. A. Alvi and S. Dalela

***Journal of Alloys and Compounds***, *752*, 520-531, **2018**

**3.** Structural, optical and magnetic properties of Fe-doped $CeO_2$ samples probed using X-ray photoelectron spectroscopy

S. Soni, V. S. Vats, S. Kumar, B. Dalela, M. Mishra, R. S. Meena, G. Gupta, P. A. Alvi and S. Dalela

***Journal of Materials Science: Materials in Electronics***, *29*(12), 10141-10153, **2018**

**4.** Study of electronic structure and magnetic properties of epitaxial $CO_2FeAl$ Heusler Alloy Thin Films.

S. Soni, S. Dalela, S. S. Sharma, E. K. Liu, W. H. Wang, G. H. Wu, M. Kumar and K. B. Garg

***Journal of Alloys and Compounds***, *674*, 295-299, **2016**

**5.** Interplay of structural, optical and magnetic properties in Gd doped $CeO_2$
S. Soni, S. Kumar, R. S. Meena, V. S. Vats and S. Dalela

***American Institute of Physics Conference Proceedings***, *1665*(1), 130029, **June 2015**.

## Published in Conferences:

**1.** Study of the oxygen vacancies and other defects with doping of $Gd^{3+}$ cation in Cerium Oxide

Swati Soni, Sudhish Kumar, B. Dalela, Monu Mishra, R. S. Meena, Govind Gupta, P. A. Alvi and S. Dalela

**5th Nano Today Conference**, 6th-10th December **2017**, Hawaii, **United States (USA)**

**2.** Interplay of structural, optical and magnetic properties in Gd doped $CeO_2$

S. Soni, S. Kumar, R. S. Meena, V. S. Vats and S. Dalela

***American Institute of Physics Conference Proceedings***, *1665*(1), 130029, **June 2015**.

**3.** Band structure properties of Ceramic Composite superconductor $Bi_{1.7}Pb_{0.3}Sr_2Ca_1Cu_2O_{8+\delta}$ using XPS

S. Soni, Neena D, B. Dalela and S. Dalela

***ISBN***: 978-81-7233-976-0, pp. 20-24, **AFMA-2015**

## Communicated in International Journals:

1. Defect induced room temperature Ferromagnetism in Fe-doped $CeO_2$ nano-materials probed through X-Ray Photoemission Spectroscopy

Swati Soni, S. Dalela

***RSC advances*** (Communicated), **2018**

# Electronic Structure and Room Temperature Ferromagnetism in Gd-doped Cerium Oxide Nanoparticles for Hydrogen Generation via Photocatalytic Water Splitting

*Swati Soni, Neelu Chouhan, Rajesh Kumar Meena, Sudhish Kumar, Bhavna Dalela, Monu Mishra, Rajendra Singh Meena, Govind Gupta, Shalendra Kumar, Parvez Ahmad Alvi, and Saurabh Dalela**

**Enhanced visible light photocatalytic activity of Gd-doped $CeO_2$ nanoparticles (NPs) is experimentally demonstrated, whereas there are very few reports on this mechanism with rare earth doping. All-pure and Gd-doped $CeO_2$ NPs are synthesized using a coprecipitation method and characterized using X-ray diffraction (XRD), absorption spectroscopy, surface-enhanced Raman Spectroscopy (SERS), X-ray photoelectron spectroscopy (XPS), and superconducting quantum interference device (SQUID). The effect of Gd-doping on properties of $CeO_2$ is discussed along with defects and oxygen vacancies generation. The XRD confirms the incorporation of $Gd^{3+}$ at the $Ce^{3+}/Ce^{4+}$ site by keeping the crystal structure same. The average particle size from transmission electron microscopy (TEM) images is in the range of 5–7 nm. The XPS spectra of Ce 3d, O 1s, and Gd 4d exhibits the formation of oxygen vacancies to maintain the charge neutrality when $Ce^{4+}$ changes to $Ce^{3+}$. The gradual increase in hydrogen production is observed with increasing Gd concentration. The observed results are in good correlation with the characterization results and a mechanism of water splitting is proposed on the basis of analyses. The absorption spectra reveal optical band gap (2.5–2.7 eV) of samples, showing band gap narrowing leads to desired optical absorbance and photoactivity of NPs.**

## 1. Introduction

Rare earth (RE) oxide-$CeO_2$ has attracted great interest of research due to their unique properties, including high oxygen storage capacity and ability to uptake and release oxygen ($O^{2-}$) ions via conversion of oxidation state of cerium ion from $Ce^{4+}$ to $Ce^{3+}$, due to formation of defect space such as oxygen vacancies in the lattice of $CeO_2$.[1] On account of this uniqueness, $CeO_2$ has been widely used as three-way catalysts for eliminating vehicle exhaust gases,[2] UV blocker materials in sunscreens, UV-shielding used in cotton fabrics,[3] functionalize silk fiber for antibacterial activity,[4] oxygen sensors,[5] and oxygen ion conductors in solid oxide fuel cells (SOFCs).[6] Generally, it has been reported that type of dopant strongly influenced the electrical properties of ceria and high conductivity at low temperature is an essential requirement for SOFCs, therefore, rare earth (RE)-doped cerium oxide, $Ce_{1-x}RE_xO_{2-\delta}$ (RE = Sm,

S. Soni, Dr. S. Dalela
Department of Pure and Applied Physics
University of Kota
Kota 324005, Rajasthan, India
E-mail: sdphysics@rediffmail.com

Dr. N. Chouhan, R. K. Meena
Department of Pure and Applied Chemistry
University of Kota
Kota 324005, Rajasthan, India

Prof. S. Kumar
Department of Physics
Mohan Lal Sukhadia University
Udaipur, Rajasthan, India

The ORCID identification number(s) for the author(s) of this article can be found under https://doi.org/10.1002/gch2.201800090.



**DOI: 10.1002/gch2.201800090**

Dr. B. Dalela
Department of Physics
Govt. Khetan Polytechnic College
Jhalana Dungri, Jaipur, Rajasthan, India

M. Mishra, Dr. R. S. Meena, G. Gupta
CSIR-National Physical Laboratory
Dr. K. S. Krishnan Road, New Delhi 110012, India

Dr. S. Kumar
Electronic Materials and Nanomagnetism Lab
Department of Applied Physics
Amity School of Applied Sciences
Amity University Haryana
Gurgaon 122413, Haryana, India

Dr. P. A. Alvi
Department of Physics
Banasthali University
Newai 304022, Rajasthan, India

Gd, Dy, Er, Lu) are preferable dopants used as electrolytes for intermediate-temperature SOFCs.[7,8] Alike $TiO_2$, bulk cerium dioxide ($CeO_2$) is a wide band gap (3.2 eV) cubic fluorite semiconductor,[9] which possesses the interesting properties such as a high dielectric constant ($\varepsilon = 26$), good transparency in the visible range, nontoxic, and capacity to exhibit the high photocatalytic activity under UV light irradiation. Therefore, $CeO_2$ seems to be a promising inorganic material that can be used for the UV filtration in sunscreen/cosmetic products and as a potential material for UV filtration.[10] Therefore, to enhance the workability of this compound in visible light some kind of structural engineering and doping of heavy metal might be done for reducing the band gap of $CeO_2$.

Among all RE-doped $CeO_2$, Sm and Gd-stabilized ceria has been extensively studied for utilization as electrolyte and anode material.[11,12] It has been reported that addition of $Sm^{3+}$ and $Gd^{3+}$ cations in $CeO_2$ system produced highest conductivity with least distortion of parent lattice, which is attributed to the smallest association enthalpy between the dopant cation and the oxygen vacancies in the $CeO_2$ lattice.[13–15] Besides of dopant type, theoretical and experimental observations have also suggested that the ionic conduction can be altered by the concentration of dopant.[16–19] Moreover, it is well known that material properties changes when particle size reduces to nanoscale, as reported by Kosacki et al.[20] in their nanocrystalline $CeO_2$ thin film, electrical conductivity has found to be enhanced due to reduced enthalpy of oxygen vacancy formation. Li et al.[21] have reported increase in catalytic activity as well as in optical and magnetic properties of porous $Gd^{3+}$-doped $CeO_2$ (10 at% Gd) nanostructure due to $Gd^{3+}$ ions or formation of oxygen vacancies. In most of these studies, the local ordering of oxygen vacancies on grain boundaries in heavily RE-doped $CeO_2$ samples has been reported.[22–24] Chen et al.[25] have reported dopant-induced structural differences and defects in Sm-doped $CeO_2$ nanoparticles (NPs) with doping concentration 3%, 5%, 7%, 9%, and 11%. On the basis of their results based on X-ray absorption spectroscopy, extended X-ray absorption fine structure, Raman, and scanning transmission electron microscope-electron energy loss spectroscopy measurements they have discussed that below 7% and above 7% distribution of defects strongly depend on the concentration of $Sm^{3+}$ ions in $CeO_2$ NPs. Since, there is a lack of literature available on the evidence of the distribution of defect study with small doping concentration of RE-doped $CeO_2$ NPs.

Metal oxide photocatalyst have attracted increasing attention due to their potential applications in the environmental protection and energy utilization, such as water splitting for hydrogen production. In the Zn-, Mg-, and Ca-doped $CeO_2$ materials the impurities tend to shift the band position and can tune the band gap because of their effects on electronic transition.[26] Gd-doped $CeO_2$ is used for thermolysis of water that can produce 101.6 $H_2$ ($\mu mol\ g^{-1}$) hydrogen.[27] It has been demonstrated experimentally that the rare earth dopants and oxygen vacancies greatly influenced the photocatalytic properties of $CeO_2$; however, the effect of interaction between the rare earth dopant and oxygen vacancy defects on enhanced visible light photocatalytic activity of $CeO_2$ is still not investigated so far.

Hence in this study, we systematically explore to develop the correlation between the rare earth dopants, its concentration and oxygen vacancy defects to enhance the photocatalytic activity of doped $CeO_2$. To undertake this study we have investigated the structural properties, dopant distribution, and their association with oxygen vacancies in Gd-doped $CeO_2$ NPs. The $CeO_2$ NPs have been doped with different concentrations of $Gd^{3+}$ ions (2%, 4%, 6%, 8%, and 10%) to discuss the presence of defect induced oxygen vacancies (either intrinsic or extrinsic) and their association with doped cation with surface-enhanced Raman spectroscopy (SERS) measurements. Transmission electron microscopy (TEM) has been used to observe changes in the surface morphology and particle size with increased fluencies of $Gd^{3+}$ ions in $CeO_2$ lattice. The optical absorption spectra have been measured using ultraviolet–visible–near infrared (UV–Vis–NIR) spectrometer to find out the band gap energy. Finally, we have attempted to investigate how doping concentration affect the oxygen vacancies and cation ($Ce^{3+}$) defects, present in pure and Gd-doped $CeO_2$ NPs. These results offer a physical understanding for the available experimental results to explain the enhanced photocatalytic activities of Gd-doped $CeO_2$ NPs, which can be useful for designing and understanding the novel doped $CeO_2$ photocatalyst.

## 2. Result and Discussion

### 2.1. X-Ray Diffraction (XRD) Analysis

X-ray diffraction measurements have been made on $Ce_{1-x}Gd_xO_2$ nanoparticles for $x = 0.0$, 0.02, 0.04, 0.06, 0.08, and 0.10 at room temperature are shown in **Figure 1**a. Nanocrystalline Gd-doped $CeO_2$ samples exhibit fundamental Bragg reflections corresponding to the fluorite type face centered cubic structure in the space group of *Fm-3m*, in which Ce and Gd atoms are located at 4a position, surrounded by eight O (located at 8b) positions.[28] Absence of any secondary phase corresponding to $Gd_2O_3$ or other impurity peaks indicates well incorporation of $Gd^{3+}$ ions on $CeO_2$ lattice site, which confirms the single phase formation of all the $Ce_{1-x}Gd_xO_2$ nanoparticles. The intensity of XRD diffraction peaks is found to vary with incorporation of $Gd^{3+}$ ions in $CeO_2$ NPs (as shown in Figure 1a).

The rising intensity signifies an improvement in the crystalline nature while falling intensity signifies low crystallinity of $Ce_{1-x}Gd_xO_2$ samples.[29] Moreover, with fluency of $Gd^{3+}$ ions, no peak shifting is observed for $x = 0.02$ doping concentration, whereas with increasing concentration ($x \leq 0.06$) diffraction peak (111) is shifted toward higher angle side (as shown inset of Figure 1a). For higher doping concentrations ($x = 0.08$ and 0.10) peak is again shifted toward lower angle side. This shifting of (111) peak toward lower and higher angle side is attributed to the lattice expansion and reduction, respectively, which is induced by incorporation of $Gd^{3+}$ ions in $CeO_2$ NPs.[30] Furthermore, it can be seen in Figure 1a, diffraction peaks become broader after doping and broadness of peaks are also observed to change with fluency of $Gd^{3+}$ ions in $CeO_2$ NPs, indicating that crystal size and crystallinity of the samples are affected with the fluencies of $Gd^{3+}$ ions. The average nanocrystalline particle size ($D$) of Gd-doped $CeO_2$ samples has been calculated with XRD diffraction spectra using the Debye–Scherrer's formula[31]

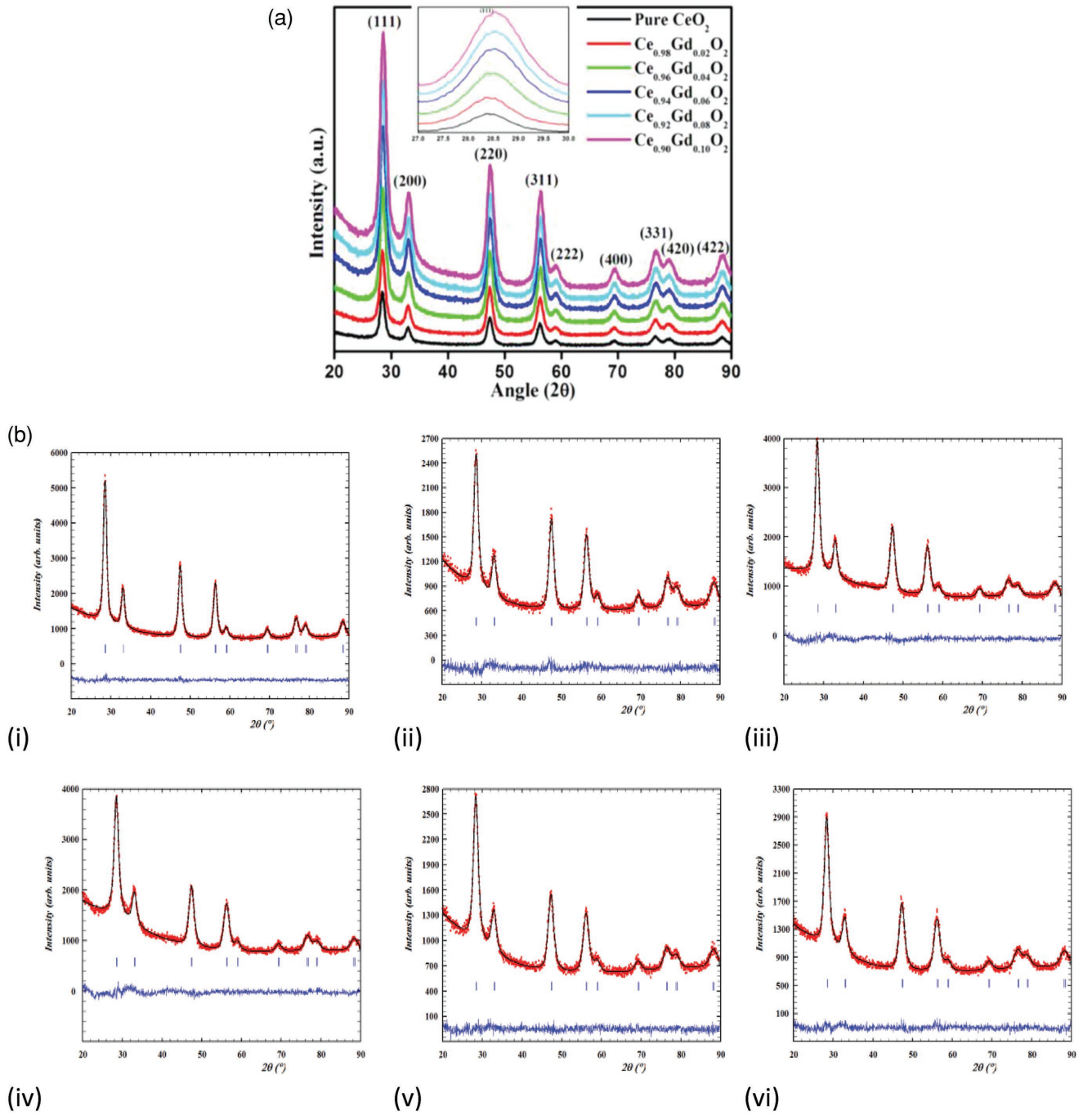


**Figure 1.** a) XRD pattern of pure $CeO_2$ and $Ce_{1-x}Gd_xO_2$ (for $x = 0.02$, 0.04, 0.06, 0.08, and 0.10) samples. b) Refined and fitted X-ray diffraction patterns of $Ce_{1-x}Gd_xO_2$ at 300 K (i) $x = 0.00$ (ii) $x = 0.02$, (iii) $x = 0.04$, (iv) $x = 0.06$, (v) $x = 0.08$, and (vi) $x = 0.10$. Observed (calculated) profiles are shown by dotted (solid) lines. The short vertical marks represent Bragg reflections. The lower curve is the difference plot.

$$D = \frac{k\,\lambda}{\beta \cos\theta} \quad (1)$$

where, all the parameters are as per the details given in ref. [15]. The lattice parameters of all the samples corresponding to (111) diffraction peak have been calculated by the following formula[32]

$$a = d\,(h^2 + k^2 + l^2)^{1/2} \quad (2)$$

where "$a$" refers to the lattice parameter, $d$ is the crystalline lattice spacing, and $h$, $k$, $l$, are the miller indices of crystal. The calculated value of lattice parameter with fluency of $Gd^{3+}$ ions in $CeO_2$ NPs is tabulated in **Table 1**.

**Table 1.** Calculated values of lattice parameter ($a$), lattice spacing ($d$) for (111) plane, average crystalline size ($D$) measured from TEM, XRD line broadening, and Raman line broadening, dislocation density ($\delta$), lattice strain ($\varepsilon$), absorbance wavelength ($\lambda$), optical band gap energy ($E_g$), and refractive index ($n$) are summarized in this table.

| Sample | Parameters | | | | | | | | | |
|---|---|---|---|---|---|---|---|---|---|---|
| | $a$ [Å] | $d$ [nm] | $D$ [nm] | | | $\delta = \frac{1}{D^2}$ [nm$^{-2}$] [33] | $\varepsilon = \frac{\beta \cos\theta}{4} \times 10^{-2}$[34,35] | $\lambda$ [nm] | $E_g$ [eV] | $n$ |
| | | | TEM | XRD | Raman spectra | | | | | |
| Pure $CeO_2$ | 5.436 | 0.318 | 5.55 | 9.21 | 10.9 | 0.0324 | 3.88 | 367 | 2.60 | 2.51 |
| $Ce_{0.98}Gd_{0.02}O_2$ | 5.433 | 0.307 | 5.27 | 6.95 | 7.52 | 0.0360 | 8.60 | 363 | 2.66 | 2.49 |
| $Ce_{0.96}Gd_{0.04}O_2$ | 5.392 | 0.318 | 6.44 | 7.10 | 6.45 | 0.0241 | 8.89 | 359 | 2.71 | 2.48 |
| $Ce_{0.94}Gd_{0.06}O_2$ | 5.394 | 0.316 | 7.47 | 6.51 | 6.07 | 0.0179 | 7.82 | 365 | 2.67 | 2.49 |
| $Ce_{0.92}Gd_{0.08}O_2$ | 5.393 | 0.324 | 5.55 | 6.22 | 5.66 | 0.0324 | 14.18 | 368 | 2.64 | 2.50 |
| $Ce_{0.90}Gd_{0.10}O_2$ | 5.398 | 0.312 | 6.34 | 6.26 | 5.06 | 0.0248 | 9.11 | 371 | 2.52 | 2.54 |

The variation in the calculated values of lattice parameter can be directly related to the ionic radii of the dopant ion. Since, the larger ionic radii $Gd^{3+}$ (0.1053 nm) ions are substituted for the smaller ionic radii $Ce^{4+}$ (0.097 nm) ions and created the larger radii $Ce^{3+}$ ions (0.114 nm).[36] Furthermore, for maintaining charge neutrality in $CeO_2$ lattice, $Gd^{3+}$ and $Ce^{3+}$ ions are collectively creating oxygen vacancies in the $CeO_2$ lattice, which causes further lattice expansion.[30]

Rietveld profile refinements (shown in Figure 1b(i–vi)) of all the samples are carried out and the results are listed in Table 1. The XRD patterns indicate that Gd-doping in $CeO_2$ does not affect the cubic fluorite structure of the $CeO_2$, as no additional diffraction peaks related to possible impurity phases of Gd and oxides of Gd are observed in these Gd-doped $CeO_2$ samples. It is further confirmed the formation of a single phase of $Ce_{1-x}Gd_xO_2$. The refinement results clearly indicate that Gd ions are well incorporated in the $CeO_2$ matrix and Gd-doping in $CeO_2$ leads to small enhancement in the unit-cell volume.

It is clear from Table 1, the dislocation density is found to increase for $x = 0.02$ doping concentration but decreases for $x = 0.04$ and 0.06, which is again increased for $x = 0.08$ and decreased for $x = 0.10$ doping concentrations of $Gd^{+3}$ cation. This variation in dislocation density is related to the promotion and reduction of disorder in the crystal structure.[29]

Looking to Table 1, the values of strain indicates tensile strain for Gd-doped $CeO_2$ NPs. Due to incorporation of $Gd^{3+}$ (0.1053 nm) cations in $CeO_2$ NPs, the maximum value of strain is for $x = 0.08$ doping concentration. Some theoretical investigation revealed that tensile strain promotes the formation of oxygen vacancies rather than compressive strain.[37] Therefore, in Gd-doped $CeO_2$ samples, increased value of tensile strain can be directly related to the endorsement of oxygen vacancies in doped $CeO_2$ samples, which may be associated to the bonding length and the strength between the surface O and Ce atoms.[38] Since, for tensile strain, the bandwidth of the O 2p orbital decreases and overlapping between O 2p and Ce 5d as well as 4f orbital also decreases, which leads a weaker Ce—O bond and responsible for the formation of oxygen vacancies in doped $CeO_2$ system.[37] The crystallinity, morphology, and particle size of the Gd-doped $CeO_2$ samples are discussed in the next segment by TEM, high-resolution transmission electron microscopy (HRTEM), and selected area (electron) diffraction (SEAD) images.

### 2.2. Surface Morphology

The average crystallite particle size of all the samples is confirmed by electron microscopy investigations. TEM measurement is used to manifest the information about the shape, size, and the presence of any secondary phase in pure and Gd-doped $CeO_2$ NPs. The particle size and morphology of pure and Gd-doped $CeO_2$ NPs are analyzed by TEM as shown in Figure 3. From TEM analysis, it is observed that the particles are crystallized nanoparticles and agglomerated with spherical morphology. The average particle size calculated from TEM images are ranging from 5 to 7 nm for pure and Gd-doped $CeO_2$ NPs, which are in good agreement with the results obtained from Debye–Scherrer formula (listed in Table 1). It can be observed from TEM images that crystal growth is promoted with doping concentration of Gd-ions. However, the morphology of all samples is not changing but the agglomeration of particles is increased with the doping concentration of Gd-ions (as shown in **Figure 2**).

The particle-size distribution histogram (shown in the inset of Figure 2) shows that the distribution is quite narrow in the size range of 5–7 nm for Gd-doped $CeO_2$ NPs. This agglomeration of particles with smaller particle-size (<7 nm) indicates that the obtained particles are nanocrystalline. Furthermore, HRTEM and SAED analysis are also used to decipher the information about the nanocrystallinity and impurity phases, if any present in Gd-doped $CeO_2$ NPs. HRTEM images (shown in **Figure 3**) indicate that the lattice fringes are well developed and randomly oriented with respect to each other. Most of the lattice fringes of Gd-doped $CeO_2$ samples are about at a distance of 0.31 nm (values are tabulated in Table 1) that corresponding to the (111) lattice plane of the fluorite like cubic structure.

As shown in Table 1, no significant change is observed in the interplanar distance ($d$) for Gd-doped $CeO_2$ samples but for 8% Gd-doped $CeO_2$ sample, the interplanar distance ($d = 0.32$ nm for (111) plane) is slightly increased, which again promotes the crystal growth and indicates the low crystallinity. Some defects, such as dislocations (shown in Figure 3c,d, marked with a red ring) are also observed in the HRTEM image of 4% and 6% Gd-doped $CeO_2$ samples. Moreover, SAED patterns are also taken (shown in the insets of Figure 3) for Gd-doped $CeO_2$ samples. SAED pattern exhibits four broad rings, which could be attributed to (111), (200), (220), and (311) planes. These rings

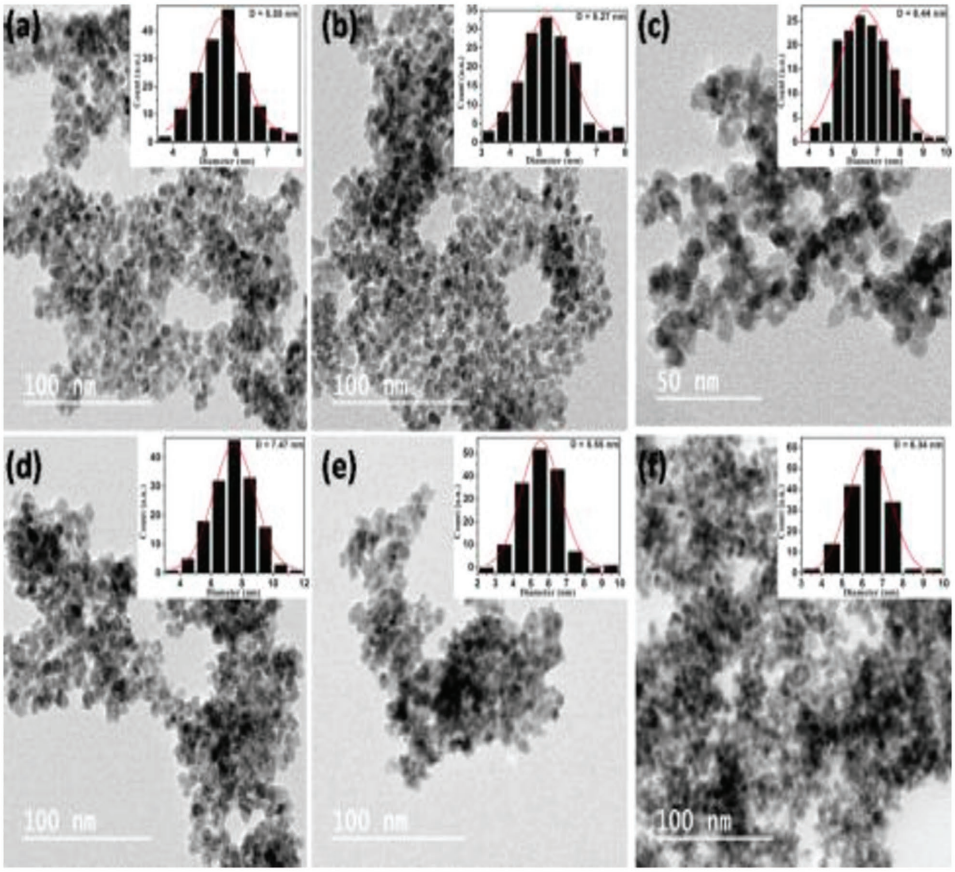


**Figure 2.** TEM image for Gd-doped $CeO_2$. a) Pure $CeO_2$, b) 2% Gd-doped $CeO_2$, c) 4% Gd-doped $CeO_2$, d) 6% Gd-doped $CeO_2$, e) 8% Gd-doped $CeO_2$, f) 10% Gd-doped $CeO_2$ and inset histogram graphs show the particle size of the corresponding sample.

indicate that the particles are crystallized and diffraction rings are very well matched with the XRD measurement results. The fluency of $Gd^{3+}$ ions in $CeO_2$ NPs also affect the optical band gap energy, which is further discussed in the next segment by UV–Vis–NIR spectroscopy.

### 2.3. Optical Absorption

**Figure 4**a shows the UV–Vis–NIR absorption spectra of $Ce_{1-x}Gd_xO_2$ samples ($x = 0.00$, 0.02, 0.04, 0.06, 0.08, and 0.10). These samples exhibit a strong absorption below 400 nm with an absorption peak in UV-range corresponding to the different doping concentration of $Gd^{3+}$ ions in $CeO_2$ NPs as tabulated in Table 1. These peaks are originated due to direct charge transfer transition from 2p valance band of $O^{2-}$ to 4f conduction band of $Ce^{4+}$ ions.[39] It is well known that $CeO_2$ have wide band gap semiconductor with a forbidden gap of 5.5 eV.[40] The valance band consists of O 2p level with a width of 4 eV and conduction band consist of Ce 5d level. Ce 4f level is present in between these two states, just above the Fermi level, that lies about 3 eV higher than the valance band (O 2p).[41] Hence there is direct recombination of the electrons in $Ce^{4+}$ (4f) conduction band with the holes in the $O^{2-}$ (2p) valance band. It can be seen from Figure 4a, the absorbance peak is obtained at 367 nm for pure $CeO_2$ but after incorporation of $Gd^{3+}$ ions peak is shifted toward lower wavelength (blue shift) up to optimal doping concentration $x = 0.04$, while for further fluencies $x = 0.06$ to 0.10 peak is shifted toward higher wavelength (red shift) side. It has been reported that when metal NPs are forming smaller size particles, the $\lambda_{max}$ shifts toward shorter wavelength (blue shift) side, whereas, when the smaller particles aggregate to form bigger/larger size particles, the $\lambda_{max}$ value shifts toward longer wavelength (red shift) side.[42] This may indicate that smaller-sized particles have been formed up to doping concentration ($x = 0.04$), while with increasing fluencies of Gd-ions (for $x = 0.06$ to 0.10) in $CeO_2$ NPs, these smaller sized particles are agglomerated (as shown in Figure 2). As Hu et al. reported that the agglomeration of nanoparticles occurs because nanoparticles have a tendency to decrease the exposed surface in order to lower the surface energy, which results decreases in particle size with strong agglomeration.[43] Furthermore, blue shifting in the absorption spectra with the fluency of $Gd^{3+}$ ions in $CeO_2$ NPs can be due to change of $Ce^{4+}$ to $Ce^{3+}$ state, that increases the direct charge-transfer transition gap between O 2p and Ce 4f bands and reduces the particle size.[21,44] In addition of that the average particle size obtained from TEM images for Gd-doped $CeO_2$ NPs is in the range of 5–6 nm at lower doping concentration ($x = 0.02$ and 0.04), which is smaller than the predictable Bohr exciton radius for $CeO_2$ (7–8 nm).[21,45]

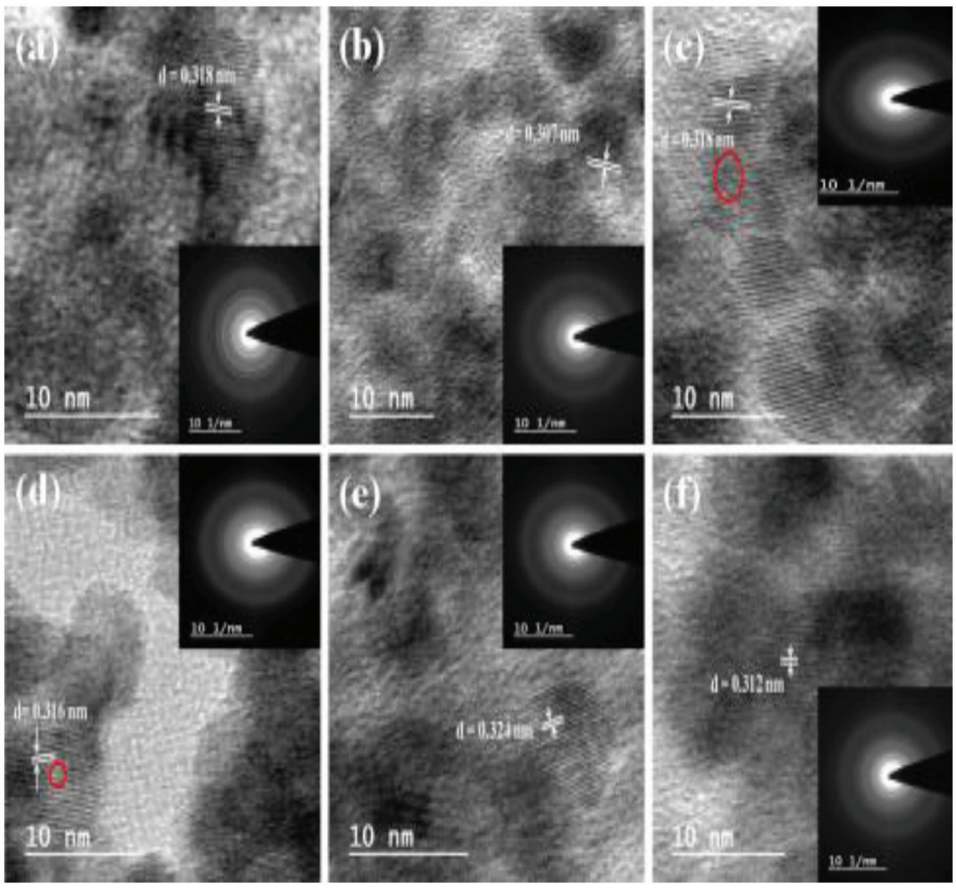


**Figure 3.** HRTEM images of Gd-doped $CeO_2$ with *d*-spacing for (111) plane. a) Pure $CeO_2$, b) 2% Gd-doped $CeO_2$, c) 4% Gd-doped $CeO_2$, d) 6% Gd-doped $CeO_2$, e) 8% Gd-doped $CeO_2$, f) 10% Gd-doped $CeO_2$ and inset graphs show the SAED pattern of corresponding sample.

Therefore, the quantum confinement effect may also be taken place that contributes to the blue shift of the absorption spectra with small fluencies of Gd-ions in $CeO_2$ NPs. Generally, quantum confinement effect results when the Bohr radius of an exciton approaches the grain or particle size, spatially confining the electron–hole pair. When this happens, the energy of the lowest excited state increases and the increased band gap produces a blue shift in the absorption spectra. Now at the higher fluencies (for $x = 0.06$ to 0.10) of $Gd^{3+}$ ions, the contribution of blue shifting from $Ce^{4+}$ to $Ce^{3+}$ valance state change will become small. Therefore, red shifting is occurred in the absorption spectra of Gd-doped $CeO_2$ (for 6%, 8%, and 10%)

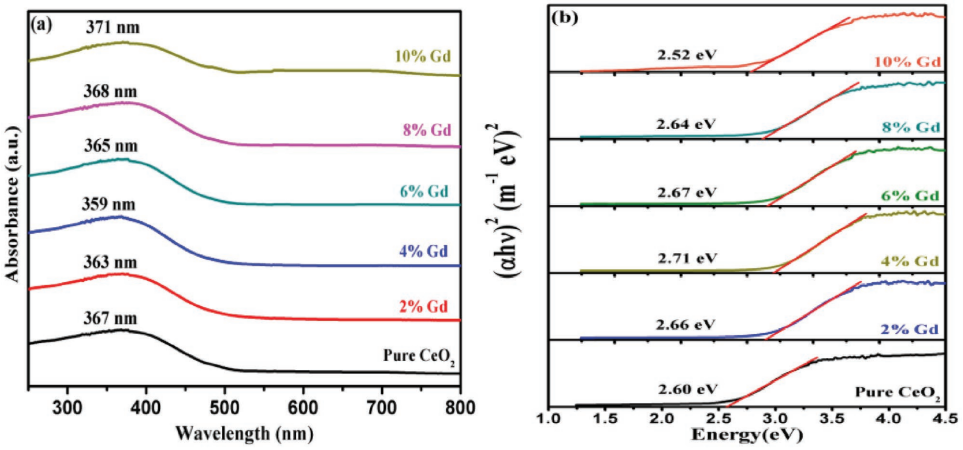


**Figure 4.** a) Room temperature optical absorbance spectra of pure $CeO_2$ and $Ce_{1-x}Gd_xO_2$ ($x = 0.02$, 0.04, 0.06, 0.08, and 0.10) samples taken in the UV–vis range. b) Tauc's plot of $(\alpha h\nu)^2$ versus energy (eV) for the pure $CeO_2$ and Gd-doped $CeO_2$ nanocrystalline samples.

samples. This red shifting may be the outcome of an interfacial polaron effect arising from electron–phonon coupling phenomenon.[46,47] Form all above absorption data, the band gap energy ($E_g$) of pure $CeO_2$ and $Ce_{1-x}Gd_xO_2$ ($x$ = 0.02, 0.04, 0.06, 0.08, and 0.10) NPs has been calculated using Tauc's equation

$$\alpha h\nu = A\left(h\nu - E_g\right)^n \tag{3}$$

where all the parameters have their usual meaning. For direct transition $n$ = 1/2 and for $n$ = 2 for indirect transition.[48] Figure 4b displays the measured values of $(\alpha h\nu)^2$ as a function of the incident photon energy ($h\nu$). Table 1 contains the calculated value of band gap energy ($E_g$) of all samples. Pure $CeO_2$ NPs shows band gap energy of 2.60 eV that is smaller than the band gap energy reported for bulk ceria, i.e., 3.15 eV.[49] This decrease in band gap energy may be attributed due to increase in the concentration of $Ce^{3+}$ states on grain boundaries. Moreover, the optical band gap energy is found to increase for low fluency of $Gd^{3+}$ ions (for $x$ = 0.02 and 0.04) in $CeO_2$ NPs while it decreases subsequently with increasing fluencies of $Gd^{3+}$ ions (for $x$ = 0.06 to 0.10) in $CeO_2$ NPs (as shown in Table 1). This blue shift in the band gap energy at lower doping concentration (for $x$ = 0.02 and 0.04) of $Gd^{3+}$ ions may be correlated with the decrease of $Ce^{3+}$ concentration as well as oxygen vacancies during annealing process. This may eliminate some localized defect energy states within the band gap due to the corresponding decrease of vacancies content, which results increase in the band gap energy.[50] Another reason for explaining the increase in band gap energy may be correlated with the Burstein–Moss (BM) shift[49]

$$\Delta E_g^{BM} = \frac{h^2}{2m_{vc}^*}\left(3\pi^2 n_e\right)^{2/3} \tag{4}$$

Here, $m_{vc}^*$ is effective mass of electrons, $n_e$ is the electron concentration, and $h$ is the Plank constant. Now, according to BM effect, above the Mott critical density, the increased number of free electron concentration is leading to fill 4f level partially, which in turn blocks the lowest states and leads to band gap widening.[49,51] With incorporation of $Gd^{3+}$ ions into $CeO_2$ sample, the crystalline size is reduced (as shown in Table 1). Therefore, the charge carriers are more confined in the small sized particles, which in turn increasing the band gap energy at lower doping concentration of Gd-doped $CeO_2$ NPs. This implies that, both particle size and BM effect results in the increase in band gap energy. Besides that, the red shift in band gap energy with higher fluencies of $Gd^{3+}$ ions ($x$ = 0.06, 0.08, and 0.10) is caused with the existence of $Ce^{3+}$ contents at the grain boundaries, which increases with decreasing particle size.[52] The refractive index of Gd-doped $CeO_2$ NPs has been calculated by using the following formula[53]

$$\frac{n^2-1}{n^2+2} = 1 - \sqrt{\frac{E_g}{20}} \tag{5}$$

The obtained values for the refractive index of pure and Gd-doped $CeO_2$ NPs are tabulated in Table 1. These values indicates that the refractive index is found to decrease with fluency of Gd ions up to optimal doping concentration $x$ = 0.04, whereas it is increased for further fluencies ($x$ = 0.06, 0.08, and 0.10) of $Gd^{3+}$ ions in $CeO_2$ NPs. The variation in the refractive index and band gap energy has been shown in **Figure 5** with different concentration of Gd-ions in $CeO_2$ NPs. Therefore, absorption of UV light at low concentration of Gd-ions ($x$ = 0.02 and 0.04) in $CeO_2$ NPs has been increased due to reduction of particle size as well as refractive index, whereas, due to increasing doping concentration the transparency and UV protection qualities are decreased.[54]

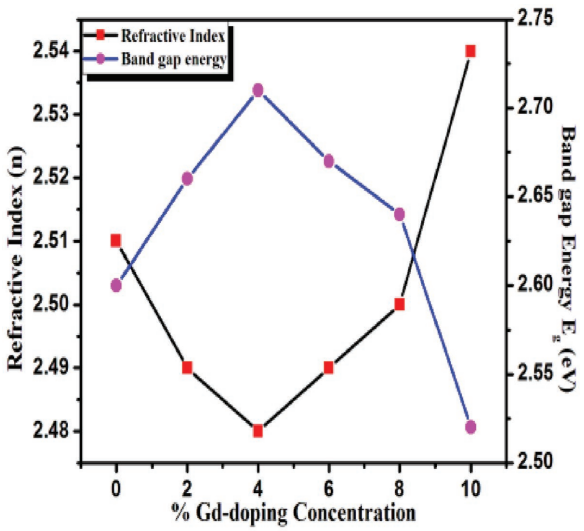


**Figure 5.** Variation of refractive index and bang gap energy with Gd-doping concentration in nanocrystalline $CeO_2$ samples.

### 2.4. Raman Spectra

Surface enhanced Raman spectroscopy is a powerful vibrational technique, which allows for highly sensitivity structural detection of low concentration analyses through the amplification of electromagnetic fields generated by the excitation of localized surface plasmons.[55] SERS provides the same information as traditional Raman spectroscopy does, but with enhanced signals. It can easily detect additional modes that cannot be observed in the traditional Raman spectrum. Therefore, SERS has been used for getting information of different modes presented in Gd-doped $CeO_2$ NPs.

**Figure 6** shows Raman active ($F_{2g}$) mode for pure $CeO_2$ and $Ce_{1-x}Gd_xO_2$ ($x$ = 0.02, 0.04, 0.06, 0.08, and 0.10) samples, at 463.3 $cm^{-1}$ and in the range of 461.4–459.5 $cm^{-1}$, assigned for first-order scattering.[56] This Raman active mode is attributed to a symmetrical stretching mode of Ce-O8 vibration unit. Therefore, this mode is very sensitive for any disorder in the oxygen sublattice results from nonstoichiometry of ceria.[57] We can see from Figure 6 the absence of characteristic band for $Gd_2O_3$ (360 $cm^{-1}$) clearly indicating the incorporation of $Gd^{3+}$ ions into $CeO_2$ lattice, confirms the absence of any impurity phase in the lattice, in agreement with XRD results.[58,59] $F_{2g}$ mode corresponding to pure $CeO_2$ and $Ce_{1-x}Gd_xO_2$ is slightly shifted toward lower wavenumber side (or lower energy side) and broadening in its FWHM can also be observed with doping fluencies of $Gd^{3+}$ ions in $CeO_2$ sample. These structural changes in Raman spectra with Gd-doping are attributed to the inhomogeneous strain and defects caused by substitution at the smaller radii $Ce^{4+}$ (0.97 Å) site by larger ionic radii $Gd^{3+}$ (1.08 Å) ions.[60] In addition of

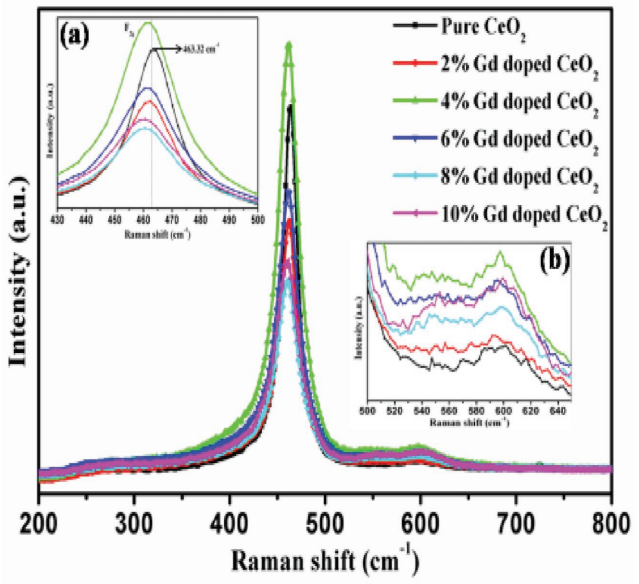


**Figure 6.** Raman spectra of pure $CeO_2$ and $Ce_{1-x}Gd_xO_2$ ($x$ = 0.02, 0.04, 0.06, 0.08, and 0.10) nanoparticles. a,b) Inset of figure contains the enlarge views of their corresponding Raman spectra in the 430–500 $cm^{-1}$ energy range related to $F_{2g}$ mode and 500–650 $cm^{-1}$ range related to oxygen defects, respectively.

$F_{2g}$ mode, weak intensity second-order Raman peaks are also obtained at 598.5 and 595.6 $cm^{-1}$ for pure $CeO_2$ and 2% Gd-doped $CeO_2$, respectively, generated due to nondegenerated longitudinal optical (LO) mode.[61] These peaks are assigned to defect space that include intrinsic oxygen vacancies due to nonstoichiometry of $CeO_2$. The three possible defect induced mechanism for oxygen vacancies in pure $CeO_2$ sample can be given as[62]

$$Ce_{Ce} + 2O_O \rightarrow V''''_{Ce} + 2V_O^{\bullet\bullet} + CeO_2 \quad (6)$$

$$Ce_{Ce} \rightarrow V''''_{Ce} + Ce_i^{\bullet\bullet\bullet\bullet} \quad (7)$$

$$O_O \rightarrow V_O^{\bullet\bullet} + O_i'' \quad (8)$$

Since, these peaks are generated for maintaining the electrically neutrality in the system, therefore all Ce-ions not only shows $Ce^{4+}$ state but also $Ce^{3+}$ state. For doing so, oxygen ($O^{2-}$) ions are released from the structure and finally oxygen vacancies are formed in the system. The intensity of this peak is increased with incorporation of Gd-ions indicates the rise of oxygen vacancies in ceria lattice. With increasing the fluency of Gd-ions, two weak second-order Raman modes in the range of 554.3–558 and 598–600.1 $cm^{-1}$ are also obtained (as shown in the inset of Figure 6b). The Raman mode in the range of 554.3–558 $cm^{-1}$ is related to the extrinsic oxygen vacancies, which are generated due to charge compensating defects due to substitution of $Ce^{4+}$ ions by $Gd^{3+}$ ions. The possible disorder mechanism for extrinsic oxygen vacancies in $Ce_{1-x}Gd_xO_2$ ($x$ = 0.02, 0.04, 0.06, 0.08, and 0.10) NPs can be given as[63]

$$Gd_2O_3 + 2Ce_{Ce}^{x} + O_O^{x} \rightarrow 2Gd'_{Ce} + V_O^{\bullet\bullet} + 2CeO_2 \quad (9)$$

where symbols have the following meaning as: $Ce_{ce}^{x}$ and $Gd'_{Ce}$ are $Ce^{4+}$ and $Gd^{3+}$ ions on the $CeO_2$ lattice site, respectively, $O_O^{x}$ is $O^{-2}$ ions on an oxygen lattice site, and $V_O^{\bullet\bullet}$ is neutral oxygen vacancy site. In addition, another vacancy peak can also be observed in the range of 598–600.1 $cm^{-1}$, which is assigned to the defect space including intrinsic oxygen vacancies due to reduction of $Ce^{4+}$ to $Ce^{3+}$, i.e., nonstoichiometry of ceria.[62] The possible disorder reaction for intrinsic oxygen vacancies in the sample can be given as[64]

$$2Ce_{Ce}^{x} + O_O^{x} \rightarrow 2Ce'_{Ce} + V_O^{\bullet\bullet} + 1/2O_2(g) \quad (10)$$

where symbols have the following meaning as: $Ce_{ce}^{x}$ and $Ce'_{Ce}$ are $Ce^{4+}$ and $Ce^{3+}$ ions on the Ce lattice site, respectively, $O_O^{x}$ is $O^{-2}$ ions on an oxygen lattice site, and $V_O^{\bullet\bullet}$ is neutral oxygen vacancy site.[65] As shown in the inset of Figure 6b, the intensity of intrinsic and extrinsic oxygen vacancies mode increases with doping fluency up to $x$ = 0.04. With further increase in fluency, the intensity of this mode decreases and then again increases at $x$ = 0.10 concentration. The variation of intensity of vacancy mode is related to the concentration of oxygen vacancies. The quantitative estimation of oxygen vacancies of pure $CeO_2$ and Gd-doped $CeO_2$ samples is made from the relative peak area of vacancy modes (intrinsic and extrinsic) with area of $F_{2g}$ mode. For doing so, Lorentzian fitting is done for measuring the peak area of the respected peaks. All calculated values are tabulated in **Table 2**, which indicates an

**Table 2.** The position of Raman active modes ($cm^{-1}$) from Raman spectra and relative peak area ratio.

| Sample | Position of Raman active mode ($cm^{-1}$) and vibrational mode | | | | | $A_{O_v}/A_{F_{2g}}$ | $\left(A_{(O_v)_1}+A_{(O_v)_2}\right)/A_{F_{2g}}$ |
|---|---|---|---|---|---|---|---|
| | First-order scattering | Second-order scattering[66,67] | | | | | |
| | $F_{2g}$ | $A_{1g}$ ($O_v$) | $A_{1g}+F_{2g}$ $(O_v)_1$ | $A_{1g}+E_g+F_{2g}$ $(O_v)_2$ | 2LO | | |
| Pure $CeO_2$ | 463.3 | 598.5 | – | – | 1064.9 | 0.036 | – |
| $Ce_{0.98}Gd_{0.02}O_2$ | 461.4 | 595.6 | – | – | 1173.9 | 0.076 | – |
| $Ce_{0.96}Gd_{0.04}O_2$ | 460.9 | – | 554.3 | 598 | 1175.6 | – | 0.084 |
| $Ce_{0.94}Gd_{0.06}O_2$ | 460.5 | – | 554.9 | 597 | 1176 | – | 0.114 |
| $Ce_{0.92}Gd_{0.08}O_2$ | 459.8 | – | 555.6 | 598.3 | 1175.7 | – | 0.121 |
| $Ce_{0.90}Gd_{0.10}O_2$ | 459.5 | – | 558 | 600.1 | 1175.3 | – | 0.119 |

Note: Vibrational modes corresponding to second-order scattering were given based on refs. [66] and [67].

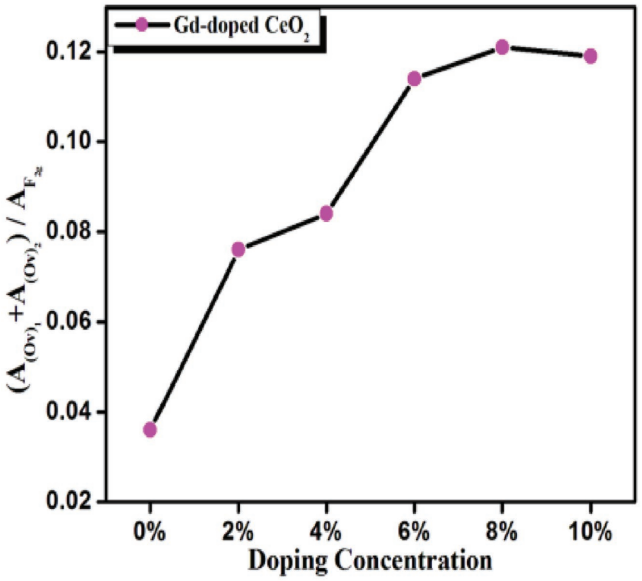


**Figure 7.** Relative peak area ratio for bands of oxygen vacancies and $F_{2g}$ mode for $Ce_{1-x}Gd_xO_2$ ($x$ = 0.00, 0.02, 0.04, 0.06, 0.08, and 0.10) samples.

increment in the concentration of oxygen vacancies with fluency of Gd-ions up to $x = 0.08$ (i.e., maximum in this range) and then slightly decreased at $x = 0.10$ concentration. The increment in the concentration of oxygen vacancies can be explained by considering, with incorporation and rising fluency of large radii $Gd^{3+}$ ions (0.105 nm), the dislocation density as well as strain has been increased up to $x = 0.08$ doping concentration in ceria. Due to this reason every two $Gd^{3+}$ ions substituted the smaller radii $Ce^{4+}$ (0.097 nm) ions increases the probability of oxygen ion ($O^{2-}$) to leave the ceria lattice to maintain electrical neutrality in the lattice and creates more oxygen vacancies (as shown in **Figure 7**).[68] In addition to that, pure $CeO_2$ and Gd-doped $CeO_2$ samples also exhibit one more extra weak second-order Raman mode at 1064.9 $cm^{-1}$ and in the range of 1173.9–1175.3 $cm^{-1}$, (as shown in Table 2), which are assigned to 2LO mode that emanate from the second-order scattering of the surface superoxide species ($O_2^-$) , and has small additional contribution from $F_{2g}$ symmetry (which is not mentioned in Figure 6).[56,65]

The particle size of all the $Ce_{1-x}Gd_xO_2$ samples has been calculated from Raman spectra using the equation

$$\Gamma\left(\mathrm{cm}^{-1}\right) = 10 + \left(\frac{124.7}{D}\right)\mathrm{nm} \tag{11}$$

where $\Gamma$ ($cm^{-1}$) is full width at half maximum (FWHM) of Raman active ($F_{2g}$) mode and $D$ is particle size of pure $CeO_2$ and $Ce_{1-x}Gd_xO_2$ ($x$ = 0.02, 0.04, 0.06, 0.08, and 0.10) samples.[61,69] The calculated particle size from Raman spectra is in good agreement with the particle size calculated from XRD and TEM images (as shown in Table 1). The quantitative estimation of the overall concentration of oxygen vacancies has been made by the peak area of the oxygen vacancies $A_{O_v}$ corresponding to 598.5 and 595.6 $cm^{-1}$ for pure $CeO_2$ and 2% Gd-doped $CeO_2$. The relative ratios of $A_{(OV)_1}$, $A_{(OV)_2}$ and $A_{F_{2g}}$ bands, which are corresponding to 554.3–558, 598–600.1, and for $F_{2g}$ band is also calculated to estimate the oxygen vacancies concentration for further doping concentrations of Gd for 4% onward. The calculated values are shown in Figure 7.

This relative peak area ratio of oxygen vacancies and $F_{2g}$ mode is calculated by fitting the Lorentzian function for the corresponding modes. Ratio $A_{O_v}/A_{F_{2g}}$ for pure $CeO_2$ and 2% Gd-doped $CeO_2$, whereas, $(A_{(OV)_1} + A_{(OV)_2})/A_{F_{2g}}$ ratios are calculated for $Ce_{1-x}Gd_xO_2$ (for $x$ = 0.04, 0.06, 0.08, and 0.10) samples. From these calculated values one can infer that the relative oxygen vacancy concentration is found to gradually increase with fluencies of $Gd^{3+}$ ions in $CeO_2$ NPs.

### 2.5. X-Ray Photoelectron Spectroscopy (XPS) Measurements

#### *2.5.1. XPS Spectra in Ce 3d Region*

The chemical composition and the valence state of the pure $CeO_2$ and Gd-doped $CeO_2$ NPs have been further characterized using XPS measurements of Ce 3d, Gd 4d, and O 1s core levels. **Figure 8** illustrates the Ce 3d core level XP spectra of $Ce_{1-x}Gd_xO_2$ ($x$ = 0.02, 0.04, 0.06, 0.08, and 0.10) samples. All binding energies have been corrected for the charge shift using the C 1s peak (binding energy = 284.6 eV) as reference.[70] The high-resolution Ce 3d core level spectra in the energy range of 880–930 eV have been deconvoluted by mean of Gaussian shape fitting as shown in Figure 8. These deconvoluted Ce 3d core-level spectra are generally characterized by distinct features which are related to the final-state occupation of Ce 4f level.[71] On Account of spin–orbit coupling, these deconvoluted Ce 3d core-level spectra are resolved into ten peaks, which include six and four structures arise from $Ce^{4+}$ and $Ce^{3+}$ ions, respectively. These series of peaks are labeled as "$u$" and "$v$," which are due to $3d_{3/2}$ and $3d_{5/2}$ spin–orbit states, respectively.[30] The four peaks labeled with $v_o$, $v'$, $u_o$, and $u'$ are characteristic peaks of $Ce^{3+}$, whereas, the peaks labeled with $v$, $v''$, $v'''$, $u$, $u''$, and $u'''$ are characteristic peaks of $Ce^{4+}$ (shown in Figure 8).[72] The separation in binding energy between $v$ and $u$ spin–orbit doublets is found around ≈18.4 eV for pure $CeO_2$, and for $Ce_{1-x}Gd_xO_2$ ($x$ = 0.02, 0.04, 0.06, 0.08, and 0.10) samples, which are in good agreement with the reported papers.[73,74]

We can see from the Ce 3d core level spectra that Ce ions are present in mixed valance state of both $Ce^{3+}$ and $Ce^{4+}$ for pure $CeO_2$ and $Ce_{1-x}Gd_xO_2$ ($x$ = 0.02, 0.04, 0.06, 0.08, and 0.10) samples. All peak positions for "$u$" and "$v$" of pure $CeO_2$ and $Ce_{1-x}Gd_xO_2$ ($x$ = 0.02, 0.04, 0.06, 0.08, and 0.10) samples have been tabulated in **Table 3**. The total concentration of $Ce^{3+}$ and $Ce^{4+}$ in the samples has been calculated using the following formula[75]

$$\%\,Ce^{3+} = \frac{A_{Ce^{3+}}}{A_{Ce^{3+}} + A_{Ce^{4+}}} \times 100\% \tag{12}$$

$$\%\,Ce^{4+} = \frac{A_{Ce^{4+}}}{A_{Ce^{3+}} + A_{Ce^{4+}}} \times 100\% \tag{13}$$

Here, $A_{Ce^{3+}} = v_o + v' + u_o + u'$ and $A_{Ce^{4+}} = v + v'' + v''' + u + u'' + u'''$ are the sum of the integrated area of all characteristics peaks of

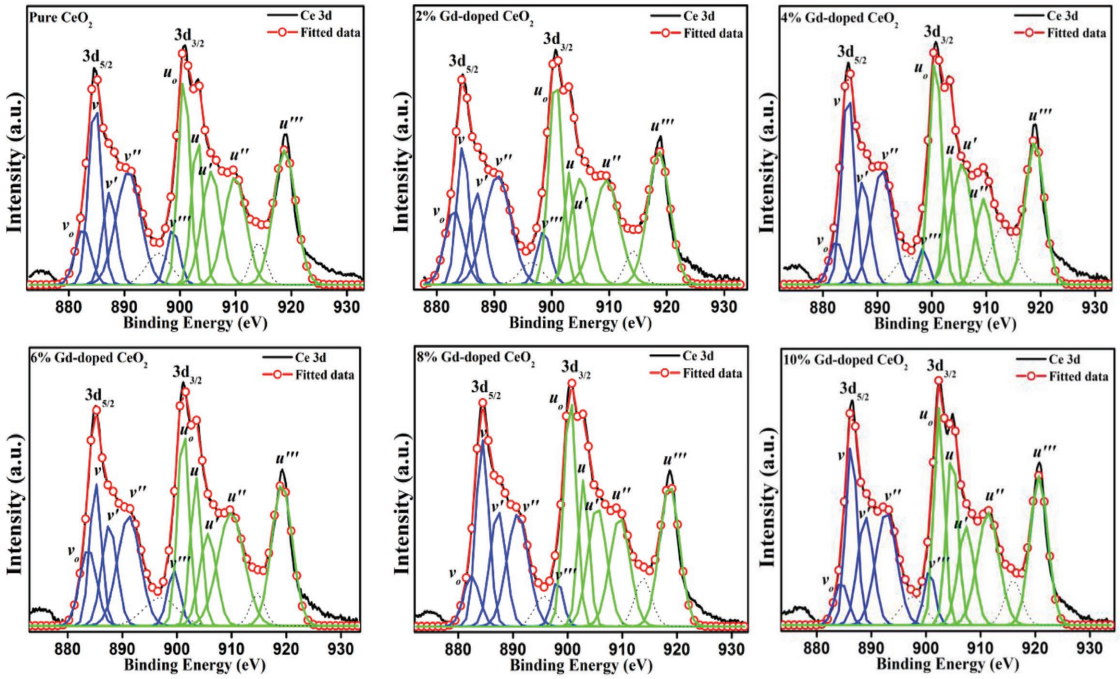


**Figure 8.** Deconvoluted XP spectra of Ce 3d profile of pure $CeO_2$ and $Ce_{1-x}Gd_xO_2$ ($x$ = 0.02, 0.04, 0.06, 0.08, and 0.10) samples.

$Ce^{3+}$ and $Ce^{4+}$, respectively. These calculated values are tabulated in Table 3. The quantitative ratio of $Ce^{3+}/Ce^{4+}$ shows that the concentration of $Ce^{3+}$ ions over $Ce^{4+}$ ions is gradually increasing for $Ce_{1-x}Gd_xO_2$ ($x$ = 0.00, 0.02, and 0.04) samples. While, at 6% Gd-doping concentration $Ce^{3+}/Ce^{4+}$ value is deceased, which is again increased and then decreased at 8% and 10% doping.

This shows that due to incorporation of larger radii $Gd^{3+}$ ions (0.105 nm) in $CeO_2$ NPs, replacing the smaller radii $Ce^{4+}$ ions (0.97 Å) and for maintaining the charge neutrality, the concentration of $Ce^{3+}$ ions (0.114 nm) is gradually increased for $x$ = 0.02 and 0.04 doping concentrations. The presence of $Ce^{3+}$ may be due to either the formation of $Ce_2O_3$ or the creation of oxygen vacancies in $CeO_2$ lattice. This can be verified by calculating the stoichiometry ratios $x$ = [O]/[Ce] and $x'$ = $[O_{1s}]/[Ce_{3d}]$, which can be estimated from their integrated peak area while considering their sensitivity factor. In order to calculate oxygen content in the samples, we assume that the total oxygen content is the sum of the required oxygen to fully oxidize $Ce^{3+}$ and $Ce^{4+}$ to form $Ce_2O_3$ and $CeO_2$. Then, considering the stoichiometry $x$ = [O]/[Ce], which is equal to 1.5 for $Ce_2O_3$ and 2 for $CeO_2$. Now, the stoichiometric ratio of the oxygen to the total Ce ions ($Ce^{3+}$ + $Ce^{4+}$) can be determined using the concentration of $[Ce^{3+}]$ and $[Ce^{4+}]$ as given in **Table 4** according to the following equation[52]

$$x = \frac{[O]}{[Ce]} = \frac{3}{2} \times \left[Ce^{3+}\right] + 2 \times \left[Ce^{4+}\right] \tag{14}$$

The stoichiometry calculated from Equation (14) has been compared with the actual stoichiometry determined from the XPS integrated area $A_O$ and $A_{Ce}$ of the O 1s and Ce 3d peaks, respectively, which has been calculated according to the following equation[76]

$$x' = \frac{O_{1s}}{Ce_{3d}} = \frac{A_O}{A_{Ce}} \times \frac{S_{Ce}}{S_O} \tag{15}$$

where $S_{Ce}$ = 7.399 and $S_O$ = 0.711 are the sensitivity factors of the Ce and O atoms, respectively.[77] **Figure 9** shows the stoichiometry variation with the concentration of Gd-dopant determined by both methods, $x$ and $x'$, which is provided the concentration of $Ce^{3+}$ and $Ce^{4+}$ ions in pure $CeO_2$ and $Ce_{1-x}Gd_xO_2$ ($x$ = 0.02, 0.04, 0.06, 0.08 and 0.10) samples (as listed in Table 4).

**Table 3.** Ce 3d XPS peak assignments for pure $CeO_2$ and $Ce_{1-x}Gd_xO_2$ ($x$ = 0.02, 0.04, 0.06, 0.08, and 0.10) samples.

| Sample | Peak assignment | Ce $3d_{5/2}$ | | | | | Ce $3d_{3/2}$ | | | | | $Ce^{3+}$ [%] | $Ce^{4+}$ [%] | $Ce^{3+}/Ce^{4+}$ |
|---|---|---|---|---|---|---|---|---|---|---|---|---|---|---|
| | | $\nu_o$ $Ce^{3+}$ | $\nu$ $Ce^{4+}$ | $\nu'$ $Ce^{3+}$ | $\nu''$ $Ce^{4+}$ | $\nu'''$ $Ce^{4+}$ | $u_o$ $Ce^{3+}$ | $u$ $Ce^{4+}$ | $u'$ $Ce^{3+}$ | $u''$ $Ce^{4+}$ | $u'''$ $Ce^{4+}$ | | | |
| Pure $CeO_2$ | Binding energy [eV] | 882.5 | 884.7 | 887.7 | 890.7 | 898.7 | 900.7 | 903.1 | 905.6 | 909.8 | 918.8 | 34.23 | 65.76 | 0.52 |
| $Ce_{0.98}Gd_{0.02}O_2$ | | 883 | 884.5 | 887 | 890.5 | 898.5 | 900.6 | 903 | 904.9 | 909.5 | 918.6 | 38.86 | 61.13 | 0.63 |
| $Ce_{0.96}Gd_{0.04}O_2$ | | 882.4 | 884.6 | 887.3 | 890.8 | 898.3 | 900.6 | 903.1 | 905.5 | 909.5 | 918.9 | 41.36 | 58.63 | 0.70 |
| $Ce_{0.94}Gd_{0.06}O_2$ | | 883.7 | 885.1 | 887.6 | 891.2 | 899.3 | 901.1 | 903.4 | 905.6 | 909.9 | 919.2 | 35.04 | 64.95 | 0.54 |
| $Ce_{0.92}Gd_{0.08}O_2$ | | 882.4 | 884.4 | 887.2 | 890.8 | 898.1 | 900.4 | 902.9 | 905.4 | 909.5 | 918.6 | 39.50 | 60.49 | 0.65 |
| $Ce_{0.90}Gd_{0.10}O_2$ | | 884.4 | 886.3 | 888.9 | 892.7 | 900.6 | 902.4 | 904.7 | 907.3 | 911.3 | 920.6 | 33.61 | 66.38 | 0.51 |

**Table 4.** Concentration of $Ce^{3+}$ and $Ce^{4+}$ ions and stoichiometry $x = [O]/[Ce]$ and $x' = [O_{1s}]/[Ce_{3d}]$ of the pure $CeO_2$ and $Ce_{1-x}Gd_xO_2$ ($x$ = 0.02, 0.04, 0.06, 0.08, and 0.10) samples.

| Sample | $[Ce^{3+}]$ | $[Ce^{4+}]$ | $x = [O]/[Ce]$[a)] | $x' = [O_{1s}]/[Ce_{3d}]$[b)] |
|---|---|---|---|---|
| Pure $CeO_2$ | 0.342 | 0.657 | 1.83 | 2.73 |
| $Ce_{0.98}Gd_{0.02}O_2$ | 0.388 | 0.611 | 1.80 | 1.84 |
| $Ce_{0.96}Gd_{0.04}O_2$ | 0.413 | 0.586 | 1.79 | 1.60 |
| $Ce_{0.94}Gd_{0.06}O_2$ | 0.350 | 0.649 | 1.82 | 1.71 |
| $Ce_{0.92}Gd_{0.08}O_2$ | 0.395 | 0.604 | 1.80 | 1.51 |
| $Ce_{0.90}Gd_{0.10}O_2$ | 0.336 | 0.663 | 1.83 | 1.61 |

[a)]Using Equation (14); [b)]Using Equation (15).

Although, the calculated values of actual stoichiometry ($x'$) are higher than that ($x$) calculated by Equation (5) for pure $CeO_2$ and $Ce_{0.98}Gd_{0.02}O_2$ sample, which exhibits low concentration of $Ce^{3+}$ ions for pure $CeO_2$ NPs in comparison with $Ce_{0.98}Gd_{0.02}O_2$ sample. This means that due to incorporation of $Gd^{3+}$ ions in $CeO_2$ NPs, $Gd^{3+}$ ions replaces the $Ce^{4+}$ ions with formation of oxygen vacancies in the $Ce_{0.98}Gd_{0.02}O_2$ sample. On the other hand, the value of ($x'$) is smaller than ($x$) for $x$ = 0.04, 0.06, 0.08, and 0.10 doping concentrations, which suggested that the entire $Ce^{3+}$ ions are consumed in the formation of $Ce_2O_3$. Simultaneously, the oxygen deficiency with increasing $Ce^{3+}$ ions suggests that $Ce^{3+}$ ions are associated with $Ce_2O_3$ as well as oxygen vacancies in $CeO_2$ and both kinds may coexist in Gd-doped $CeO_2$ ($x$ = 0.04, 0.06, 0.08, and 0.10) samples.

This means that core level Ce 3d spectra prove the existence of $Ce_2O_3$ in the $Ce_{1-x}Gd_xO_2$ ($x$ = 0.02, 0.04, 0.06, 0.08, and 0.10) samples, while from XRD analysis only $CeO_2$ is identified. This $Ce_2O_3$ phase has amorphous character and indicates that this phase is located at the grain surface and at the grain boundaries. Patsalas et al.[52] have reported a dimensional analysis, which determined that $Ce_2O_3$ and $CeO_2$ are located at grain surface and volume, respectively. A linear correlation can be established between third power of $[Ce^{4+}]$ (grain volume distribution) as well as third power of $D$ (which is proportional to the grain volume $V_g$) with square of $[Ce^{3+}]$ (surface distribution).

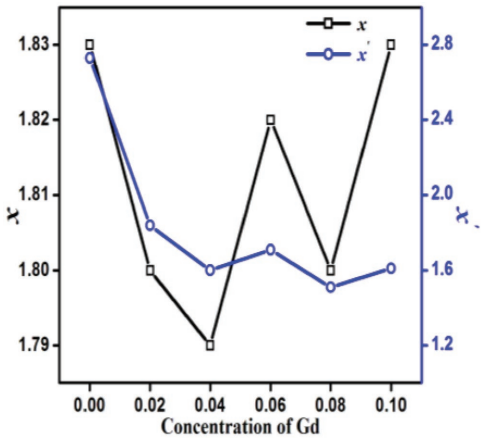


**Figure 9.** The $CeO_x$ stoichiometry for pure $CeO_2$ and Gd-doped $CeO_2$ samples calculated from stoichiometry ratio $x = [O]/[Ce]$ and $x' = [O_{1s}]/[Ce_{3d}]$.

**Figure 10** shows a linear relation between $[Ce^{3+}]^2$ and $[Ce^{4+}]^3$ that confirms the distribution of $Ce_2O_3$ and $CeO_2$ at the grain surface and volume. While, the experimental points of $D^3$ versus $[Ce^{3+}]^2$ are more scattered around straight line of the dimensional analysis, which is attributed to the strain in the grain that affects the broadening of the XRD peaks with Gd-doping in $CeO_2$ samples. From Table 4, it can also be seen that the difference between $x$ and $x'$ increases and decreases with increase and decrease of $Ce^{3+}$ ions for $Ce_{1-x}Gd_xO_2$ ($x$ = 0.04, 0.06, 0.08, and 0.10) samples, which show an up and down in the formation of oxygen vacancies in these samples.

### 2.5.2. O 1s XPS Spectra

The O 1s spectra for pure $CeO_2$ and $Ce_{1-x}Gd_xO_2$ ($x$ = 0.02, 0.04, 0.06, 0.08, and 0.10) samples are shown in **Figure 11**. The asymmetrical O 1s core level spectra in the binding energy range 526–540 eV are deconvoluted into four peaks to determine the surface concentration of oxygen ions for all samples. The deconvoluted binding energy peaks of O 1s core level spectra at ≈528.6–529.9 eV can be assigned to the lattice oxygen $O^{2-}$ (denoted as $O_L$) in pure $CeO_2$ and $Ce_{1-x}Gd_xO_2$ ($x$ = 0.02, 0.04, 0.06, 0.08, and 0.10) samples, while peak at higher binding energy side ≈530.3–533.3 eV and ≈533.5–536.4 eV are possibly assigned to oxygen vacancies (denoted as $O_V$) corresponds to $Ce^{3+}$ species originated from $Ce_2O_3$[78] and formation of hydroxyl or absorbed $H_2O$ species[79] (denoted as $O_\alpha$ and $O_\beta$) on the surface of the samples, respectively (as shown in **Table 5**).[80,81]

As shown in Figure 11, all the samples are showing the similar O 1s core level spectra, which are also used as another source of information about Ce oxidation state. Since, it is well known that the electronegativity of Gd ion (1.21) is higher than Ce ion (1.12) on Pauling scale, therefore, O 1s peak from $Gd_2O_3$ should be at higher binding energy than that from metal oxide $CeO_2$.[82] Thus, due to incorporation of $Gd^{3+}$ ions in the lattice of $CeO_2$, not only the intensity of the lattice oxygen peak ($O_L$) but also oxygen vacancies peak ($O_V$) are found to increase for 2% Gd-doped $CeO_2$ NPs. The quantitative estimation of $O_L$ and $O_V$ peaks shows that due to incorporation of $Gd^{3+}$ ions the oxygen vacancies are formed on the surface of the Gd-doped $CeO_2$ samples. These vacancies are found to show variation with change in the concentration of Gd-ions in the $CeO_2$ NPs. Furthermore, as 1s electron of oxygen atom attached more tightly bound to $Ce^{3+}$ rather than $Ce^{4+}$ oxidation state. Thus, change in the oxidation state of Ce-ions (+4 to +3) due to incorporation of $Gd^{3+}$ ions in the $CeO_2$ NPs, may also be responsible for the change in the formation of oxygen vacancies. The quantitative percentage of $Ce^{3+}$ oxidation state from core level spectra of Ce 3d for pure $CeO_2$ and $Ce_{1-x}Gd_xO_2$ ($x$ = 0.02, 0.04, 0.06, 0.08, and 0.10) samples, if compared with quantitative percentage of $O_V$ from O 1s core level spectra, one can infer that the increasing $Ce^{3+}$ concentration is also helpful in increasing the oxygen vacancies on the surface of samples (as shown in Tables 3 and 5) along with the percentage increase in the concentration of the $Gd^{3+}$ ions.

### 2.5.3. Gd 4d XPS Spectra

The deconvoluted Gd 4d core level XPS spectra are split into doublet (Gd $4d_{5/2}$ and Gd $4d_{3/2}$) due to spin–orbit coupling for

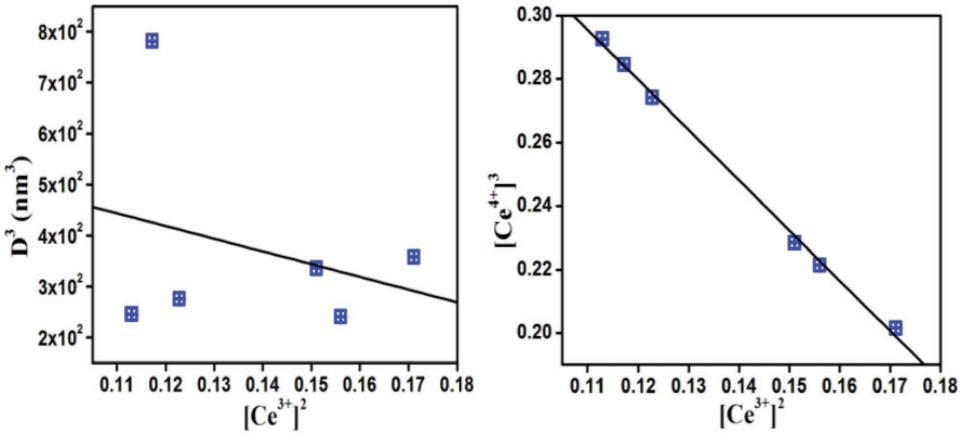


**Figure 10.** The correlation of the $[Ce^{3+}]^2$ with $[Ce^{4+}]^3$ and grain volume ($V_g \propto D^3$), showing that $Ce^{3+}$ and $Ce^{4+}$ ions are located at the grain surface and volume, respectively.

$Ce_{1-x}Gd_xO_2$ ($x$ = 0.02, 0.04, 0.06, 0.08, and 0.10) samples, as shown in **Figure 12**. These two peaks existed in the range of ≈143.7–145.8 eV and ≈148.7–151.7 eV can be attributed to Gd $4d_{5/2}$ and Gd $4d_{3/2}$ states, respectively, which are indicating the presence of $Gd^{3+}$ ions in $Ce_{1-x}Gd_xO_2$ ($x$ = 0.02, 0.04, 0.06, 0.08, and 0.10) doped lattice.[83–85]

### 2.6. Magnetic Measurements

**Figure 13**a,b shows the room temperature magnetization ($M$) versus magnetic field ($H$) curves for pure $CeO_2$ and $Ce_{1-x}Gd_xO_2$ ($x$ = 0.02, 0.04, 0.06, 0.08, and 0.10) NPs. It is observed that pure $CeO_2$ nanoparticles are found to exhibit weak ferromagnetic (FM) behavior at room temperature with saturation magnetization $M_s$ = 0.049 emu $g^{-1}$. Although, it has been reported that bulk $CeO_2$ exhibit diamagnetic behavior where it is reported that at nanoregime the undoped $CeO_2$ NPs exhibit weak ferromagnetism with small value of saturation magnetization by few reports.[86–92] Since, a significant amount of coercivity $H_c$ = 77.95 Oe has been observed for pure $CeO_2$ NPs, which ensures the ferromagnetic nature in our pure $CeO_2$ sample. The weak ferromagnetic behavior in pure $CeO_2$ NPs at room temperature is associated with oxygen vacancies that have been originated by the conversion of $Ce^{4+}$ to $Ce^{3+}$ oxidation state of cerium.[93]

Although, after incorporation of $Gd^{3+}$ ions in $CeO_2$ NPs, $Ce_{0.98}Gd_{0.02}O_2$ sample still exhibit weak ferromagnetic (FM) behavior with increasing $M_s$ = 0.140 emu $g^{-1}$ while $H_c$ has been

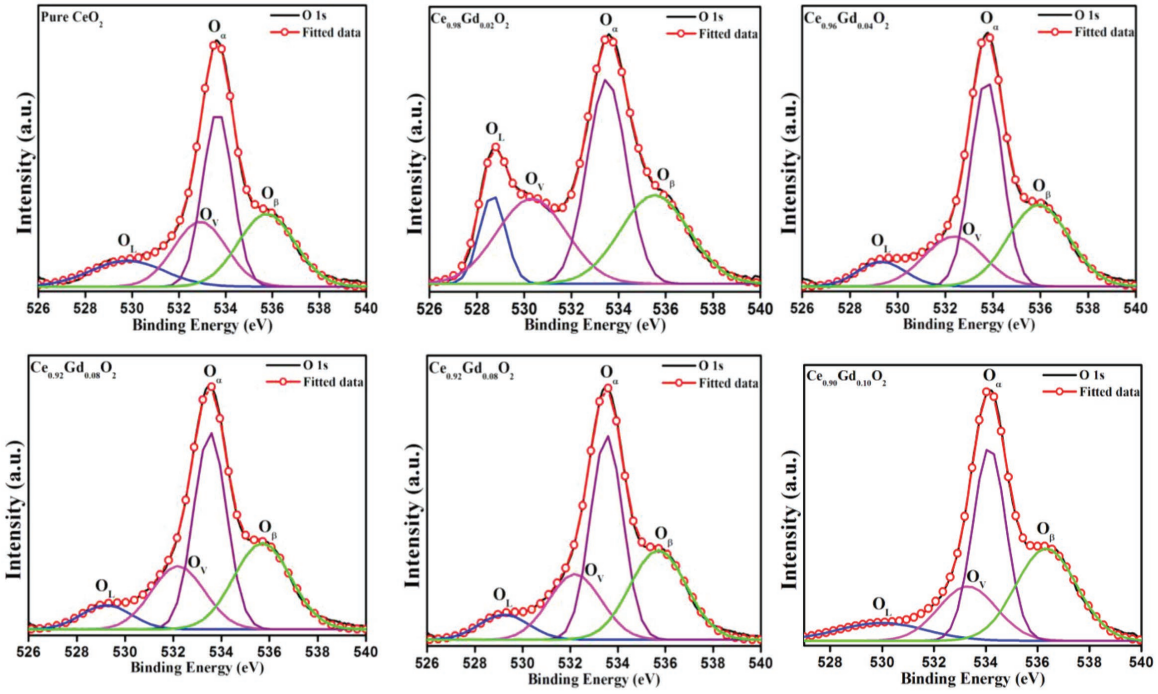


**Figure 11.** Deconvoluted core level spectra of O 1s profile for pure $CeO_2$ and $Ce_{1-x}Gd_xO_2$ ($x$ = 0.02, 0.04, 0.06, 0.08, and 0.10) samples.

**Table 5.** XPS binding energies of individual peaks of O 1s spectra for pure $CeO_2$ and $Ce_{1-x}Gd_xO_2$ ($x = 0.02$, 0.04, 0.06, 0.08, and 0.10) samples.

| Sample | O 1s peak position | | | | | |
|---|---|---|---|---|---|---|
| | Lattice oxygen species ($O_L$) | | Oxygen vacancy species ($O_V$) | | $OH^-$ group species BE [eV] | |
| | BE [eV] | $\%\,O_L = \frac{A_{O_L}}{A_{O_L}+A_{O_V}} \times 100$ | BE [eV] | $\%\,O_V = \frac{A_{O_V}}{A_{O_L}+A_{O_V}} \times 100$ | ($O_\alpha$) | ($O_\beta$) |
| Pure $CeO_2$ | 529.8 | 35.94 | 532.9 | 64.05 | 533.6 | 535.7 |
| $Ce_{0.98}Gd_{0.02}O_2$ | 528.6 | 28.16 | 530.3 | 71.84 | 533.5 | 535.5 |
| $Ce_{0.96}Gd_{0.04}O_2$ | 529.3 | 28.41 | 532.4 | 71.58 | 533.7 | 535.9 |
| $Ce_{0.94}Gd_{0.06}O_2$ | 529.8 | 35.79 | 532.6 | 64.20 | 533.9 | 536.1 |
| $Ce_{0.92}Gd_{0.08}O_2$ | 529.2 | 26.60 | 532.2 | 73.40 | 533.5 | 535.7 |
| $Ce_{0.90}Gd_{0.10}O_2$ | 529.9 | 33.32 | 533.3 | 66.70 | 534.1 | 536.3 |

decreased 22.48 Oe as compared to pure $CeO_2$ NPs. While, further increase in $Gd^{3+}$ ions concentration are not able to maintain this FM behavior, that can be clearly seen from the hysteresis curves (in Figure 13b) for $Ce_{1-x}Gd_xO_2$ ($x = 0.04$, 0.06, 0.08, and 0.10) samples. The magnetization of the Gd-doped $CeO_2$ samples is increased with increasing dopant concentration (as shown in **Table 6** and Figure 13b). Since, the electronic configuration of $Gd^{3+}$ is [Xe] $6s^25d^14f^7$ with 7 unpaired electrons in the 4f shell. These unpaired 4f electrons polarize the 6s and 5d valence electrons, results high effective magnetic moment $\mu_{eff} = 7.94\ \mu_B$ (calculated by the formula $\mu_{eff} = g_J\sqrt{J(J+1)}\ \mu_B$, where $g_J$ is the Lande *g*-factor and for $Gd^{3+}$ ion ground state $^8S_{7/2}$, $S = 7/2$, $L = 0$, $J = 7/2$, $g_J = 2$).[94,95] With increasing dopant concentration, the interaction of these unpaired spins of 4f electrons with the outermost ligands or other $Gd^{3+}$ is anticipated to get weaker. These noninteracting and localized magnetic spins of $Gd^{3+}$ ions have induced the paramagnetism with increase in magnetization.[96,97] The paramagnetic moment from the $Gd^{3+}$ ions incorporated into the $CeO_2$ lattice increases with increasing the dopant concentration, which results in reduction of ferromagnetic ordering in Gd-doped samples. Therefore, 4%, 6%, 8%, and 10% Gd-doped samples have small ferromagnetic behavior in addition to linear paramagnetic signals, which is gradually increasing with the fluency of $Gd^{3+}$ ions in $CeO_2$ NPs. Though Raman and XPS analyses are showing an increase in the oxygen vacancies but this increase in oxygen vacancy concentration may not enhance the ferromagnetic ordering in Gd-doped samples.[98] Nithyaa and Jaya reported the ferromagnetic behavior of pure $TiO_2$ NPs but incorporation of Gd-ions enhanced the paramagnetic nature, which has been reported due to oxygen defects.[99] In other reports on Gd doping in ZnO, the paramagnetism in these samples is reported due to high magnetic moment of Gd-ions ($\mu = 7.1\ \mu_B$) and due to presence of secondary phases of $Gd_2O_3$.[100–102]

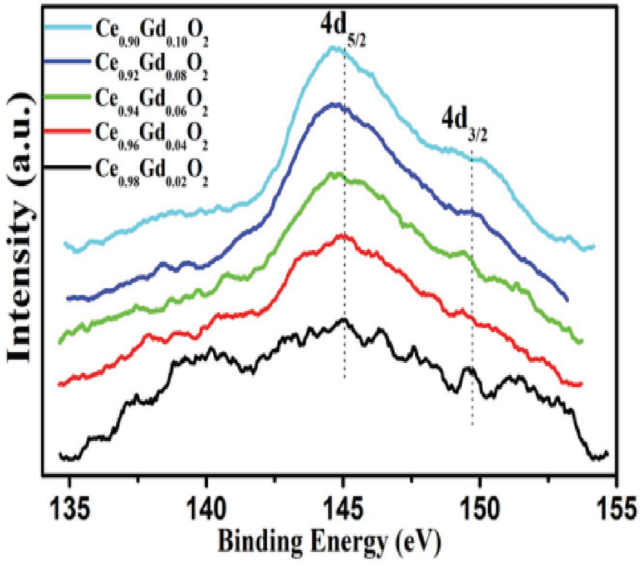


**Figure 12.** Gd 4d core level XP spectra of $Ce_{1-x}Gd_xO_2$ ($x = 0.02$, 0.04, 0.06, 0.08, and 0.10) samples.

Now, the main issue herein is to understand the possible origin of ferromagnetic dominated paramagnetic behavior in pure $CeO_2$ and Gd-doped $CeO_2$ NPs, respectively. The origin of FM behavior has been discussed in this paper accounting the F-center exchange (FCE) mechanism as a subcategory of bound magnetic polaron (BMP) model.[103] The conception of FCE coupling is based on BMP model that has been interpreted with the presence of oxygen vacancies ($V_O$). These oxygen vacancies and magnetic ions constitute a BMP that produces the ferromagnetism in these systems. In pure $CeO_2$ NPs, the origin of ferromagnetism is supposed to the reduction of the oxidation state of Ce ions, i.e., $Ce^{4+}$ to $Ce^{3+}$. The formations of oxygen vacancies give rise to the reduction of $Ce^{4+}$ to $Ce^{3+}$ state. The formation of oxygen vacancy left two electrons which may be transferred to a $Ce^{4+}$ ion converting $Ce^{4+}$ into $Ce^{3+}$. Due to this process, mixed $Ce^{3+}$ and $Ce^{4+}$ states yield in the pure $CeO_2$ NPs, which has already been confirmed by Ce 3d core level spectra analysis. The ferromagnetism in pure $CeO_2$ NPs may be arise from the nearest-neighbor interaction, i.e., either double exchange ($Ce^{3+}$–$V_O$–$Ce^{4+}$) or superexchange ($Ce^{3+}$–$V_O$–$Ce^{3+}$), which is mediated by oxygen ions.[104] The double exchange interaction forms an $F^+$ center because the two electrons left by $V_O$ are trapped on $Ce^{4+}$ ion and $V_O$ (hydrogenic orbital), while superexchange interaction forms an $F^{2+}$ center due to the both electrons are trapped on $Ce^{4+}$ ions.[105] When Gd ion is incorporated into $CeO_2$, it has suppressed the ferromagnetism of $CeO_2$ NPs (as shown in Figure 13b). Now, for $Ce_{0.98}Gd_{0.02}O_2$ sample, the $F^+$ center may be coupled with

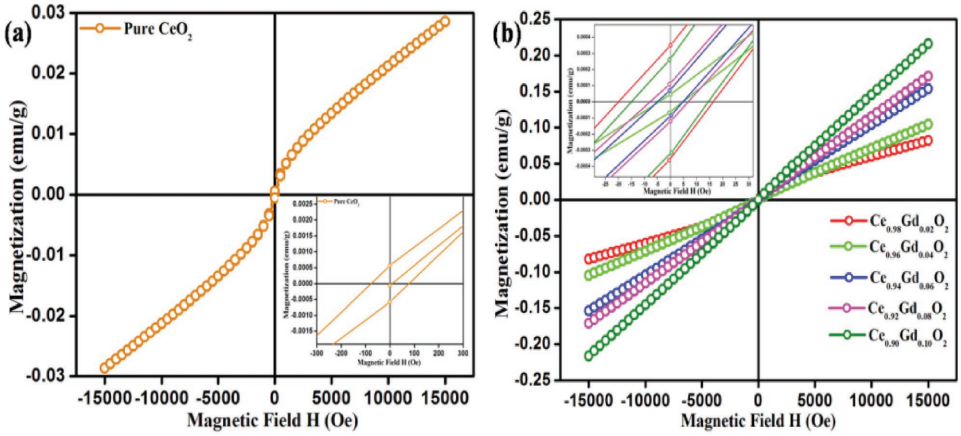


**Figure 13.** Magnetization versus magnetic field plot for a) pure $CeO_2$ and b) $Ce_{1-x}Gd_xO_2$ ($x$ = 0.02, 0.04, 0.06, 0.08, and 0.10) samples at room temperature (300 K).

the nearest $Ce^{3+}$ or Gd 4f orbital and form $Ce^{3+}$–$V_O$–$Gd^{3+}$ complex (BMP), which is dominated in this sample. When the size of this BMP is large enough to percolate through the lattice, long-range (weak) room temperature ferromagnetism can be realized with higher saturation magnetization. However, it is clearly observed that ferromagnetism has been suppressed with the increase in Gd-doping concentration up to $x$ = 0.10. Due to increase in Gd-ion doping concentration, the number of Gd-ions in the interior of $CeO_2$ lattice is less than that on its surface or on the grain boundaries. Only those Gd-ions are allowed to enter the lattice that is permitted by the host ions and rest is expelled. Due to higher doping concentration the separation among $Gd^{3+}$ ions is decreased. These largely separated $Gd^{3+}$ ions suppress the ferromagnetism and undergo superexchange interaction with each other via $O^{2-}$ ions and results in antiparallel alignment of the magnetic spins of Gd 4f shell present in the nearest-neighbor ions that do not negotiate in ferromagnetic ordering. Thus higher doping concentration of $Gd^{3+}$ ions tends to destroy the observed ferromagnetism in Gd-doped $CeO_2$ NPs. Hence in our case the increase in paramagnetic signals may be attributed to increase in oxygen vacancy concentrations without enhancing the ferromagnetic ordering of the samples. This ferromagnetic ordering is further suppressed due to the increased concentrations of $Gd^{3+}$-cation as the separation between these $Gd^{3+}$ -ions is decreased results in anti-parallel alignment of the spins of Gd 4f state due to superexchange interaction.

**Table 6.** Summary of saturation magnetization ($M_s$), retentivity ($M_r$), and coercivity ($H_c$) for pure $CeO_2$ and $Ce_{1-x}Gd_xO_2$ ($x$ = 0.02, 0.04, 0.06, 0.08, and 0.10) NPs.

| Sample | $M_s$ [emu $g^{-1}$] | $M_r$ [emu $g^{-1}$] [$\times 10^{-4}$] | $H_c$ [Oe] |
|---|---|---|---|
| Pure $CeO_2$ | 0.049 | 5.77 | 77.95 |
| $Ce_{0.98}Gd_{0.02}O_2$ | 0.140 | 3.56 | 22.48 |
| $Ce_{0.96}Gd_{0.04}O_2$ | 0.194 | 0.46 | 1.30 |
| $Ce_{0.94}Gd_{0.06}O_2$ | 0.296 | 0.87 | 1.38 |
| $Ce_{0.92}Gd_{0.08}O_2$ | 0.333 | 1.16 | 6.18 |
| $Ce_{0.90}Gd_{0.10}O_2$ | 0.421 | 3.15 | 12.96 |

### 2.7. Water Splitting Analysis

The amount of photocatalytic $H_2$ evolved from the samples has been hourly monitored (**Table 7** and **Figure 14**a) and after 4 h exposure to light the respective release of hydrogen is observed as 1.47406, 1.4847, 1.4923, 1.4984, 1.51367, and 1.5243 mmol $h^{-1}$ $g^{-1}$ for pristine $Pt/CeO_2$, $Pt/Gd_{0.02}Ce_{0.98}O_2$, $Pt/Gd_{0.04}Ce_{0.96}O_2$, $Pt/Gd_{0.06}Ce_{0.94}O_2$, $Pt/Gd_{0.08}Ce_{0.092}O_2$, $Pt/Gd_{0.10}Ce_{0.90}O_2$ samples, respectively (Figure 14a). According to the mechanism, when the surface of the molecular device $Pt/GdCeO_2$ exposed to the light, an electron of the valance band (VB) gets energized after receiving that energy of light and jumped from VB to conduction band (CB), which generates a pair of photohole (at VB) and photoelectron (at CB) at $Gd/CeO_2$ surface. Nascent photoelectrons of CB are arrived at the junction of Pt/electrolyte interface by passing through the electron-pool of the metallic Pt (that can segregate the photoelectrons from photoholes). These photoelectrons interact with $H^+$ ions[106] of the water at the interface and liberate the nascent H that combined with another nascent H atom to generate $H_2$ gas. Hole amassed at VB of the doped semiconductor is responsible for the breakdown of $CH_3OH$ in formaldehyde or formic acid or both as mentioned in Equations (16)–(26),[107,108] which can be used to depict the proposed electron transfer mechanism of the water splitting, as illustrated by Figure 14b.

$$\mathrm{Gd-CeO_2} \xrightarrow{\text{light}} (\text{CV of Gd}-\mathrm{CeO_2})e^- + (\text{VB of Gd}-\mathrm{CeO_2})h^+ \ (\text{photocarriers generation}) \quad (16)$$

$$(\text{CV of Gd}-\mathrm{CeO_2})e^- \rightarrow \mathrm{Pt}\ e^- \ (\text{transfer of photoelectron}) \quad (17)$$

$$(\text{CV of Gd}-\mathrm{CeO_2})e^- + \mathrm{H_2O} \rightarrow \mathrm{H^*} + \mathrm{OH^-} \ (\text{generation of free radical } \mathrm{H^*}) \quad (18)$$

$$\mathrm{H^* + H^* \rightarrow H_2}(0.00\ \mathrm{eV}) \ (\text{generation of } \mathrm{H_2}) \quad (19)$$

$$\mathrm{H^* + h^+ \rightarrow H^+} \ (\text{generation of } \mathrm{H^+}) \quad (20)$$

**Table 7.** Comparative band gaps with their CB and VB positions, hydrogen production with and without Pt loading, with respect to the pure $CeO_2$ and 2%, 4%, 6%, 8%, and 10% Gd-doped $CeO_2$ compound.

| Compound | Oxygen vacancy [%] | ⟨D⟩ [nm] | $Ce^{3\pm}/Ce^{4+}$ | Band gap [eV] | CB [eV] | VB [eV] | $H_2$ generation without Pt loading [mol $g^{-1}$ $h^{-1}$] | $H_2$ generation with Pt loading [mol $g^{-1}$ $h^{-1}$] |
|---|---|---|---|---|---|---|---|---|
| Pure $CeO_2$ | 64.05 | 8.50 | 0.52 | 2.60 | −0.240 | 2.360 | (1.4695) | 1.47406 |
| $Ce_{0.98}Gd_{0.02}O_2$ | 71.84 | 6.58 | 0.63 | 2.66 | −0.270 | 2.390 | (1.4771) | 1.4847 |
| $Ce_{0.96}Gd_{0.04}O_2$ | 71.58 | 6.66 | 0.70 | 2.71 | −0.295 | 2.415 | (1.4832) | 1.4923 |
| $Ce_{0.94}Gd_{0.06}O_2$ | 64.20 | 6.68 | 0.54 | 2.67 | −0.275 | 2.395 | (1.4923) | 1.4984 |
| $Ce_{0.92}Gd_{0.08}O_2$ | 73.40 | 5.81 | 0.65 | 2.64 | −0.260 | 2.380 | (1.5030) | 1.51367 |
| $Ce_{0.90}Gd_{0.10}O_2$ | 66.70 | 5.88 | 0.51 | 2.52 | −0.200 | 2.320 | (1.5167) | 1.5243 |

$$H^+ + H^+ \rightarrow H_2(0.00\ \text{eV})\ (\text{generation of } H_2) \quad (21)$$

$$(\text{VB of } Gd-CeO_2)\, h^+ + CH_3OH \rightarrow CH_2OH^* + H^+\ (-0.1264\ \text{eV}) \quad (22)$$

$$h^+ + CH_2OH^* + OH^- \rightarrow HOCH_2OH^* \rightarrow HCHO + H_2O\ (-3.848\ \text{eV})\ (\text{formation of HCHO}) \quad (23)$$

$$CH_2OH^* + O \rightarrow OCH_2OH^* \rightarrow HCHO + OH^*(-3.18\ \text{eV})\ (\text{formation of HCHO}) \quad (24)$$

$$CH_2OH^* + O \rightarrow OCH_2OH^* \rightarrow HCOOH + H^*\ (-4.125\ \text{eV})\ (\text{formation of HCOOH}) \quad (25)$$

$$HCOOH + 2h^+ \rightarrow CO_2 + 2H^+(-0.19\ \text{eV})\ (\text{formation of } CO_2 \text{ from HCHO}) \quad (26)$$

There are many factors which can dominate the water splitting activity such as particle size of photocatalyst, binding energy, dopant concentration and position (either $Gd^{3+}$ ion is taking position of $Ce^{3+}$ or $Ce^{4+}$ ion), oxygen vacancies, band gap and band positions, and many more. All of the above factors collectively responsible for increase in hydrogen generation activity on increasing the dopant concentration in ceria. Usually the steady decrease in particle size increases water splitting activity with increase in Gd proportion due to the large. Introduction of dopant Gd into the $CeO_2$ lattice, also gradually increases the oxygen vacancy in the lattice arrangement of $CeO_2$ because $Gd^{3+}$(radius of $Gd^{3+}$ = 0.105 nm and charge density = 91) replaced the high charged but small $Ce^{4+}$ ion(radius of $Ce^{4+}$ = 0.097 nm and charge density = 148) in 2%, 4%, and 8% doped samples but also replaced low charged but bigger sized $Ce^{3+}$ (radius of $Ce^{3+}$ cation = 0.114 nm and charge density = 75) in 6% and 10% Gd samples.[109]

All of the above changes due to Gd-doping in ceria lattice maintained the phase purity (checked with XRD) with minor but favorable changes in lattice parameters and suggested the lattice arrangement of atoms with expanded electron clouds between high charge M($Ce^{4+}/Ce^{3+}$) and low charge M($Gd^{3+}$) bonds through bridging O and O as shown in **Figure 15**a. That results into creating active side to generate more carriers that bring about the enhanced photocatalytic activity of the doped ceria.

Usually the steady decrease in particle size increases water splitting activity with increase in Gd proportion due to the large. Introduction of dopant Gd into the $CeO_2$ lattice also gradually increases the oxygen vacancy in the lattice arrangement of $CeO_2$ because $Gd^{3+}$ (radius of $Gd^{3+}$ = 0.105 nm and charge density = 91) replaced the high charged but small $Ce^{4+}$ ion (radius of $Ce^{4+}$ = 0.097 nm and charge density = 148) in 2%, 4%, and 8% doped samples but also replaced low charged but bigger sized $Ce^{3+}$ (radius of $Ce^{3+}$ cation = 0.114 nm and charge density = 75) in 6% and 10% Gd samples.[109]

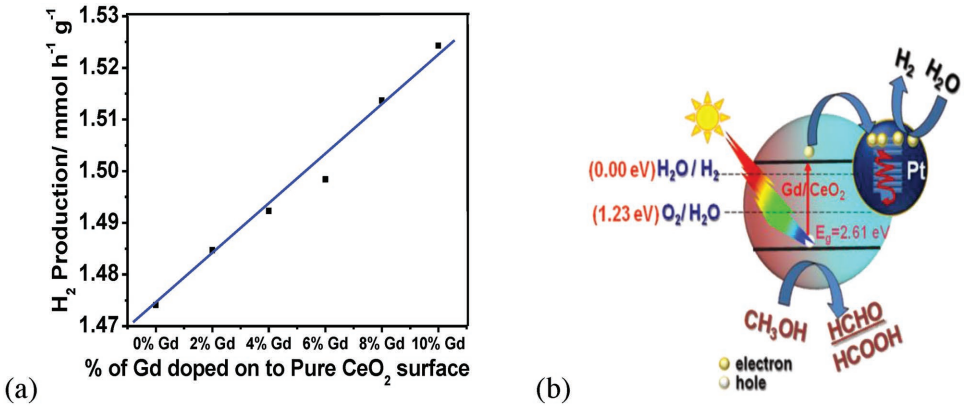


**Figure 14.** a) Hydrogen production rate for pristine $CeO_2$ and 2%, 4%, 6%, 8%, and 10% Gd-doped $CeO_2$ compounds in 10% $CH_3OH$ under visible light exposure of 300 W Xe light source and b) charge transfer reaction at oxidative and reductive sites.

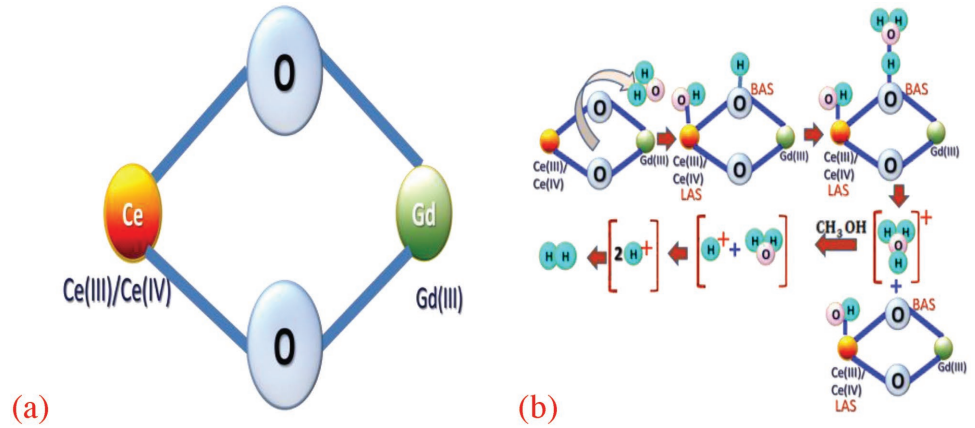


**Figure 15.** a) M–M bond through bridging O atoms and b) water splitting phenomena at atomic lattice level through Lewis acid site (LAS) and Brønsted acid site (BAS).

Local cluster framework of the tetrahedral coordinated groups of multivalent metal cations ($Ce^{4+}/Ce^{3+}$and $Gd^{3+}$) and anions ($O_2^{2-}$) generates a strong local electrostatic field inside the tetrahedra, as confirmed by the XRD, XPS, and Raman results. Residual water molecules are captured by the strong local electrostatic field of the molecular device $Ce_{1-x}Gd_xO_2$ ($x$ = 0.02, 0.04, 0.06, 0.08, and 0.10). These water molecules attract the bridging oxygen through the protonic side and the metallic cation, i.e., Ce through the hydroxyl side (Figure 15b).

Finally, we get bridging oxygen impregnated with a hydroxyl proton and the Ce metallic side with a hydroxyl group that function as Lewis acid sites, which create strong electron withdrawing centers neighboring bridging O–H groups[110] as shown by Figure 15b. These withdrawing centers can act as superacidic Brnsted acid sites (BAS) with a highly negative cluster framework. $H_3O^+$ that detached from BAS to release the tension of the bulky species and generate $H^+$. These $H^+$ reacts with the photoelectrons of the solid solutions and produce nascent H that couples with another H. Thus, hydrogen gas is generated.

## 3. Conclusion

In summary, Gd-doped $CeO_2$ nanoparticles have been successfully synthesized by the coprecipitation method. The structural and morphological studies have been made by XRD, TEM, HRTEM, and SEAD analysis. From the XRD analysis all the lattice parameters, volume, particle size of pure and Gd-doped $CeO_2$ NPs have been calculated, the particle size of these nanoparticles is further verified with TEM and SERS analysis and observed approximately similar to the results obtained with XRD analysis. The particles are spherical in shape and getting agglomerated with fluencies of $Gd^{3+}$ ions in $CeO_2$ sample and the particle size is in the range of 5–7 nm, which is confirmed from the TEM images. From the TEM results and analysis we have observed the broadening of diffraction rings, which indicates that the particles are small in size and crystallinity becomes low with increasing doping concentration of $Gd^{3+}$ ions in $CeO_2$ NPs.

From the analysis of the UV-Vis-NIR absorption spectra we have observed the variation in the refractive index and band gap energy with different concentration of Gd-ions in $CeO_2$ NPs. The reduction of refractive index with incorporation of $Gd^{3+}$ ions in $CeO_2$ NPs is beneficial to UV protection. Normally, UV protection ability is strongly depending on the particle size and at nanoregime UV absorption ability is stronger than that of microsized ones. From the SERS spectra on pure and Gd-doped $CeO_2$ NPs, the particle size, oxygen vacancy concentrations, etc. have been made to understand the mechanism of other properties of these samples. From the SERS spectra we can say that no other impurity phases are present in our samples and hence the nature of ferromagnetism in these NPs is intrinsic in nature and derived from the defects and intrinsic and extrinsic oxygen vacancy concentrations, which is found to gradually increase with fluencies of $Gd^{3+}$ ions in $CeO_2$ NPs.

Further for electronic structure of these NPs the core level Ce 3d, O1s, and Gd 4d XPS spectra have been recorded and analyzed in detail. From this analysis the change of oxidation state of $Ce^{+4}$ to $Ce^{+3}$ ions, incorporation of the $Gd^{+3}$ ions in the lattice and formation of oxygen vacancies are reported. From the core level Ce 3d spectra the presence of both $Ce^{3+}$ and $Ce^{4+}$ ions in all the samples and an increase in the $Ce^{3+}$ concentration can be seen with the fluencies of $Gd^{3+}$ dopant ions in $CeO_2$ NPs, due to the formation of defects or an amorphous phase of $Ce_2O_3$. From the O 1s core level spectra analysis we are able to demonstrate that doping of $Gd^{3+}$ ions in $CeO_2$ NPs can modify the rate of reduction of $Ce^{4+}$ to $Ce^{3+}$ oxidation state as well as affects the formation of oxygen vacancies in $Ce_{1-x}Gd_xO_2$ ($x$ = 0.02, 0.04, 0.06, 0.08, and 0.10) doped samples. However, the Gd 4d core level spectra cannot be recorded with good statistics due to very small concentrations but reports the presence of Gd ion in our NPs. In our magnetic measurements we can see that all the samples pure $CeO_2$ and $Ce_{1-x}Gd_xO_2$ ($x$ = 0.02, 0.04, 0.06, 0.08, and 0.10) are showing the weak ferromagnetism dominated paramagnetic behavior, which is assumed to be triggered due to change of oxidation state of $Ce^{+4}$ to $Ce^{+3}$ ions, incorporation of the $Gd^{+3}$ ions in the lattice and formation of oxygen vacancies. From Raman and XPS analyses, the presence of oxygen vacancy related defects is apparent. From Ce 3d XPS spectra one can reveal that a significant increase in $Ce^{3+}$ ions is not only able to increase the oxygen vacancies due to formation of $Ce_2O_3$ phase in $Ce_{1-x}Gd_xO_2$ ($x$ = 0.02, 0.04,

0.06, 0.08, and 0.10), which is not traceable with the XRD analysis but also may be due to the substitution of $Ce^{4+}$ ions by $Gd^{3+}$ ions and this substitution actually creates the oxygen vacancies and owe the presence of ferromagnetic ordering in $Ce_{0.98}Gd_{0.02}O_2$ sample.

In the water splitting results, the amount of photocatalytic $H_2$ evolved from the samples is monitored, and the respective release of hydrogen is found to increase for pristine Pt/$CeO_2$, Pt/Gd-doped $CeO_2$ samples with the increased doping concentrations of the Gd-ion. The particle size of photocatalyst, binding energies, oxygen vacancy concentrations, band gap, and many other factors are collectively responsible for increase in hydrogen generation activity with increasing dopant concentration in ceria. The observed release of hydrogen is found in good correlation with the characterization results and the proposed mechanism of water splitting is reported on the basis of analyses.

## 4. Experimental Section

*Materials*: Ammonium cerium (IV) nitrate $(NH_4)_2Ce(NO_3)_6$ (Alpha Aesar 99.99%), gadolinium (III) nitrate hexahydrate $Gd(NO_3)_3{\cdot}6H_2O$ (Alpha Aesar 99.9%), and sodium hydroxide (NaOH) were used.

*Material Preparation*: Nanocrystalline pure $CeO_2$ and $Ce_{1-x}Gd_xO_2$ ($x$ = 0.02, 0.04, 0.06, 0.08, and 0.10) samples were synthesized using coprecipitation method. The appropriate stoichiometric amount of $(NH_4)_2Ce(NO_3)_6$ and $Gd(NO_3)_3{\cdot}6H_2O$ were used for synthesizing $Ce_{1-x}Gd_xO_2$ NPs. Initially, $(NH_4)_2Ce(NO_3)_6$ and $Gd(NO_3)_3{\cdot}6H_2O$ precursor solution was prepared in distilled water with magnetic stirring at the rate of 600 rpm. Then NaOH solution was added drop by drop to this solution until the pH level reached about 11. This solution was stirred about 4 h and then the synthesized pale-yellow precipitate was collected. The precipitate was dried at room temperature and annealed in the furnace about 500 °C for 8 h. A set of samples, i.e., pure $CeO_2$ and $Ce_{1-x}Gd_xO_2$ ($x$ = 0.02, 0.04, 0.06, 0.08, and 0.10) were prepared. The main chemical reactions during the experimental process are as follows

$$6NaOH_{(S)} \rightarrow 6Na^{+}_{(aq)} + 6OH^{-}_{(aq)} \tag{27}$$

$$(NH_4)_2Ce(NO_3)_6 \rightarrow Ce^{3+}_{(aq)} + 6NO^{-}_{3(aq)} + 2NH^{+}_{4(aq)} \tag{28}$$

$$6Na^{+}_{(aq)} + 6NO^{-}_{3(aq)} \rightarrow 6NaNO_{3(aq)} \tag{29}$$

$$2NH^{+}_{4(aq)} + 2OH^{-}_{(aq)} \rightarrow 2NH_{3(g)}\uparrow + 2H_2O_{(aq)} \tag{30}$$

$$Ce^{3+}_{(aq)} + 4OH^{-}_{(aq)} + xH_2O_{(aq)} \rightarrow Ce(OH)_4 \cdot xH_2O_{(s)}\downarrow \tag{31}$$

$$Ce(OH)_4 \cdot xH_2O_{(S)} \overset{\text{at RT}}{\rightarrow} Ce(OH)_{4(s)} + xH_2O_{(g)}\uparrow \tag{32}$$

$$Ce(OH)_{4(s)} \overset{500\ ^{\circ}C}{\rightarrow} CeO_{2(s)} + 2H_2O_{(g)} \tag{33}$$

The complete chemical reaction can be combined as

$$(NH_4)_2Ce(NO_3)_6 + 6NaOH \rightarrow Ce(OH)_4 + 6NaNO_3 + 2NH_3 + 2H_2O \tag{34}$$

$$Ce(OH)_4 \rightarrow CeO_2 + 2H_2O \tag{35}$$

The final chemical reaction for the growth of various concentrations 2%, 4%, 6%, 8% and 10% of dopant Gd-ions in $CeO_2$ lattice are as follows

$$(1-x)\left[(NH_4)_2Ce(NO_3)_6\right] + x[Gd(NO_3)_3 \cdot 6H_2O] + 6NaOH \rightarrow Ce_{1-x}Gd_xO + \text{molecular gases}\uparrow \tag{36}$$

*Nanomaterial's Characterization*: The structural properties of all the samples were characterized using XRD measurements on a Brucker D8 Advance diffractometer with Cu K$\alpha$ radiation ($\lambda$ = 1.5406 Å). The diffraction patterns were recorded at room temperature in the 2$\theta$ range from 10° to 90°. The surface morphology, particle size, and crystallinity of the samples were studied using TEM with Technai G2 20 S-TWIN (FEI Netherlands) instrument operating at an accelerating voltage of 200 kV. Samples for the TEM investigation were prepared by dispersing the nanopowder in ethanol using an ultrasonicator to produce a dilute suspension. Then a standard holey carbon film supported on Cu grid was immersed in the suspension to produce the TEM sample. The particle size distribution was calculated for a total 150 number of particles using imagej software for TEM images. The optical characterizations were carried out by using SERS. For collecting Raman spectra, SERS of make Thermo Scientific DXRxi Raman Imaging Microscope with charge injection device detector using green laser with 532 nm excitation light source with its power kept at 10 mW were used. The UV–vis–NIR absorbance spectra on the samples in the wavelength range of 200–1000 nm with $BaSO_4$ as standard were recorded employing a Shimadzu UV-3600 Plus spectrophotometer with an integrating sphere. XPS spectra were recorded on a ultrahigh vacuum based Omicron Multiprobe Surface analysis System (Germany, Gmbh) operating at a base pressure of $5 \times 10^{-11}$ Torr. Mg K$\alpha$ radiation source (with energy of 1253.6 eV) was used for data acquisition. An OMICRON EA125 hemispherical analyzer equipped with a 7 channeltron parallel detection unit was used to collect the XPS spectra. The calibration of binding energy in photoemission spectra was done referring to standard Au $4f_{7/2}$ emission line with energy resolution of ≈0.9 eV FWHM on Au $4f_{7/2}$ with pass energy of 20 eV during the measurement. The XPS core level data were analyzed after necessary carbon corrections for the Fermi energy referencing. The magnetic properties of the samples were investigated at room temperature using a Quantum Design MPMS-3 SQUID system. The magnetization measurements were conducted by varying the applied field from –1.5 T to +1.5 T.

Photocatalytic cleavage of the water for hydrogen generation was carried out using the powder of photocatalytic molecular device (0.3 g powder of Pt/$CeO_2$ or Pt/$Gd_xCe_{1-x}O_2$ or $CeO_2$ or $Gd_xCe_{1-x}O_2$) that was suspended in 120 mL of aqueous hole-scavenger electrolyte (20% $CH_3OH$; pH = 7.0) in a reaction cell, under the irradiation of 1 sun (100 mW $cm^{-2}$, AM1.5 G) visible light. The powder of the photocatalyst (0.2 g with and without Pt loading) was suspended in 120 mL of aqueous electrolyte (20% $CH_3OH$ pH = 7.0) in a double walled-Pyrex glass reaction cell (volume ≈150 mL, with water jacket) that was sealed with a rubber septum and plastic wire lock.[111,112] Prior to start the photochemical reaction, the suspension was continuously purged with Ar for 1 h by maintaining the 1 atm pressure of the inner jacket solution for expelling the air content from the solution. Circulating water bath is used to maintain the temperature of the outer jacket at 25 °C. Afterward, the suspension was irradiated with a 300 W Xe lamp (>420 nm, light intensity $1 \times 10^{22}$ photons per hour Xe lamp-HX1, Model PE300UV, ISS). All the experiments were carried out under ambient conditions. Photocatalytic responses were hourly monitored in terms of the amount of hydrogen generated at 1–4 h time intervals. Hydrogen gas has very small density and not soluble in water. Therefore, the evolved hydrogen was collected into the inverted gas collection graduated bottle by displacement of water from a container. The collected gas was checked with the gas chromatograph (Shimazdu, Japan, thermal conductivity detector and molecular sieve with 5 A columns) throughout the course of the reaction.

## Acknowledgements

S.S. acknowledges Department of Science & Technology, Government of India for financial support vide Reference No. SR/WOS-A/PM-1021/2015, under Women Scientist Scheme-A (WOS-A) to carry out this work. N.C. thanks to Department of Science and Technology (SERB), India (SB/S1/PC-31/2012) for financial support. The authors are also grateful to UGC-DAE CSR, Indore Centre vide Project No. CSR-IC-BL-69/CSR-186/2016-17/850, and CSR-IC-MSRSR-25/CRS-233/2017-18/1314 for providing the support. The authors are also grateful to the "Banasthali Centre for Research and Education in Basic Sciences" under CURIE programme supported by the Department of Science & Technology, Government of India, New Delhi for providing the experimental measurements. This work was also supported by the Ministry of Science and Technology of Taiwan under Contract No. MOST-104-2113-M-002-012-MY3.

## Conflict of Interest

The authors declare no conflict of interest.

## Keywords

hydrogen generation, SERS, water splitting, XPS

Received: September 12, 2018
Revised: November 29, 2018
Published online:

[1] X. Niu, F. Tu, *J Mater Sci: Mater Electron* **2017**, *28*, 2141.
[2] T. Montini, M. Melchionna, M. Monai, P. Fornasiero, *Chem. Rev.* **2016**, *116*, 5987.
[3] W. Duan, A. Xie, Y. Shen, X. Wang, F. Wang, Y. Zhang, J. Li, *Ind. Eng. Chem. Res.* **2011**, *50*, 4441.
[4] Z. Lu, C. Mao, M. Meng, S. Liu, Y. Tian, L. Yu, B. Sun, C. M. Li, *J. Colloid Interface Sci.* **2014**, *435*, 8.
[5] N. Izu, W. Shin, N. Murayama, S. Kanzaki, *Sens. Actuators, B* **2002**, *87*, 95.
[6] Z. Zhan, S. A. Barnett, *Science* **2005**, *308*, 844.
[7] S. Kuharuangrong, *J. Power Sources* **2007**, *171*, 506.
[8] C. Artini, M. Pani, M. M. Carnasciali, J. R. Plaisier, L.-G. A. Costa, *Inorg. Chem.* **2016**, *55*, 10567.
[9] G. Magesh, B. Viswanathan, R. P. Viswanath, T. K. Varadarajan, *Indian J. Chem.* **2009**, *48A*, 480.
[10] S. Tsunekawa, J.-T. Wang, Y. Kawazoe, J. Kasuya, *J. Appl. Phys.* **2003**, *94*, 3654.
[11] S. Wang, T. Kobayashi, M. Dokiya, T. Hashimoto, *J. Electrochem. Soc.* **2000**, *147*, 3606.
[12] A. K. Lucid, P. R. Keating, J. P. Allen, G. W. Watson, *J. Phys. Chem. C* **2016**, *120*, 23430.
[13] X. Xu, C. Xia, G. Xiao, D. Peng, *Solid State Ionics* **2005**, *176*, 1513.
[14] T. S. Zhang, J. Ma, H. Cheng, S. H. Chan, *Mater. Res. Bull.* **2006**, *41*, 563.
[15] S. Soni, S. Kumar, B. Dalela, S. Kumar, P. A. Alvi, S. Dalela, *J. Alloys Compd.* **2018**, *752*, 520.
[16] J. Kim, D. Lee, *Korean J. Chem. Eng.* **2002**, *19*, 421.
[17] H. Wang, A. Chroneos, U. Schwingenschlögl, *J. Chem. Phys.* **2013**, *138*, 224705.
[18] N. Singh, N. K. Singh, D. Kumar, O. Parkash, *J. Alloys Compd.* **2012**, *519*, 129.
[19] N. Jaiswal, N. K. Singh, D. Kumar, O. Parkash, *J. Power Sources* **2012**, *202*, 78.
[20] I. Kosacki, T. Suzuki, V. Petrovsky, H. U. Anderson, *Solid State Ionics* **2000**, *136–137*, 1225.
[21] G. R. Li, D. L. Qu, L. Arurault, Y. X. Tong, *J. Phys. Chem. C* **2009**, *113*, 1235.
[22] B. Matović, M. Stojmenović, J. Pantić, A. Varela, M. Žunić, N. Jiraborvornpongsa, T. Yano, *J. Asian Ceram. Soc.* **2014**, *2*, 117.
[23] C. Artini, M. Pani, M. M. Carnasciali, M. T. Buscaglia, J. R. Plaisier, G. A. Costa, *Inorg. Chem.* **2015**, *54*, 4126.
[24] W. J. Bowman, J. Zhu, R. Sharma, P. A. Crozier, *Solid State Ionics* **2015**, *272*, 9.
[25] S. Y. Chen, R. J. Chen, W. Lee, C. L. Dong, A. Gloter, *Phys. Chem. Chem. Phys.* **2014**, *16*, 3274.
[26] M. Li, R. Zhang, H. Zhang, W. Feng, X. Liu, *Micro Nano Lett.* **2010**, *5*, 95.
[27] A. L. Gal, S. Abanades, *J. Phys. Chem. C* **2012**, *116*, 13516.
[28] S. Soni, S. Kumar, R. S. Meena, V. S. Vats, S. Dalela, *AIP Conf. Proc.* **2015**, *1665*, 130029.
[29] P. Kumar, P. Kumar, A. Kumar, I. Sulania, F. Chand, K. Asokan, *RSC Adv.* **2017**, *7*, 9160.
[30] B. Mandal, A. Mondal, S. S. Ray, A. Kundu, *Dalton Trans.* **2016**, *45*, 1679.
[31] C. Levy, C. Guizard, A. Julbe, *J. Am. Ceram. Soc.* **2007**, *90*, 942.
[32] M. Jamshidijam, R. V. Mangalaraja, A. Akbari-Fakhrabadi, S. Ananthakumar, S. H. Chan, *Powder Technol.* **2014**, *253*, 304.
[33] İ. Uslu, A. Aytimur, M. K. Öztürk, S. Koçyiğit, *Ceram. Int.* **2012**, *38*, 4943.
[34] P. Bindu, S. Thomas, *J. Theor. Appl. Phys.* **2014**, *8*, 123.
[35] R. Murugan, G. Vijayaprasath, T. Mahalingam, G. Ravi, *Appl. Surf. Sci.* **2016**, *390*, 583.
[36] W. M. A. El Rouby, A. A. Farghali, A. Hamdedein, *Water Sci. Technol.* **2016**, *74*, 2325.
[37] D. Ma, Z. Lu, Y. Tang, T. Li, Z. Tang, Z. Yang, *Phys. Lett. A* **2014**, *378*, 2570.
[38] M. Nolan, V. S. Verdugo, H. Metiu, *Surf. Sci.* **2008**, *602*, 2734.
[39] M. Guo, J. Lu, Y. Wu, Y. Wang, M. Luo, *Langmuir* **2011**, *27*, 3872.
[40] I. Singh, K. Landfester, R. Muñoz-Espí, A. Chandra, *Nanotechnology* **2017**, *28*, 075601.
[41] J. Malleshappa, H. Nagabhushana, B. D. Prasad, S. C. Shad gap rma, Y. S. Vidya, K. S. Anantharaju, *Optik* **2016**, *127*, 855.
[42] S. Kundu, N. Sutradhar, R. Thangamuthu, B. Subramanian, A. B. Panda, M. Jayachandran, *J. Nanoparticle Res.* **2012**, *14*, 1040.
[43] C. Hu, Z. Zhang, H. Liu, P. Gao, Z. L. Wang, *Nanotechnology* **2006**, *17*, 5983.
[44] S. Tsunekawa, R. Sahara, Y. Kawazoe, A. Kasuya, *Mater. Trans., JIM* **2000**, *41*, 1104.
[45] Z. Wang, Z. Quan, J. Lin, *Inorg. Chem.* **2007**, *46*, 5237.
[46] M. Karl Chinnu, K. Vijai Anand, R. Mohan Kumar, T. Alagesan, R. Jayavel, *J. Exp. Nanosci.* **2015**, *10*, 520.
[47] A. V. Thorat, T. Ghoshal, P. Carolan, J. D. Holmes, M. A. Morris, *J. Phys. Chem. C* **2014**, *118*, 10700.
[48] N. S. Arul, D. Mangalaraj, P. C. Chen, N. Ponpandian, C. Viswanathan, *Mater. Lett.* **2011**, *65*, 2635.
[49] B. Choudhury, A. Choudhury, *Curr. Appl. Phys.* **2013**, *13*, 217.
[50] M. Y. Chen, X. T. Zu, X. Xiang, H. L. Zhang, *Phys. B* **2007**, *389*, 263.
[51] I. Hamberg, C. G. Granqvist, K. F. Berggren, B. E. Sernelius, L. Engström, *Phys. Rev. B* **1984**, *30*, 3240.
[52] P. Patsalas, S. Logothetidis, L. Sygellou, , S. Kennou, *Phys. Rev. B* **2003**, *68*, 035104.
[53] P. Nagaraju, Y. Vijaya Kumar, M. V. Ramana Reddy, C. Vishnuvardhan Reddy, V. Raghavendra Reddy, D. M. Phase, *Int. J. Sci. Eng. Res.* **2014**, *5*, 185.
[54] N. N. Dao, M. Dai Luu, Q. K. Nguyen, B. S. Kim, *Adv. Nat. Sci. Nanosci. Nanotechnol.* **2011**, *2*, 045013.

[55] B. Sharma, R. R. Frontiera, A. I. Henry, E. Ringe, R. P. Van Duyne, *Mater. Today* **2012**, *15*, 16.
[56] J. Cui, G. A. Hope, *J. Spectrosc.* **2015**, *2015*, 1.
[57] I. Kosacki, T. Suzuki, H. U. Anderson, P. Colomban, *Solid State Ionics* **2002**, *149*, 99.
[58] Y. U. Jinqiu, C. U. I. Lei, H. E. Huaqiang, Y. A. N. Shihong, H. U. Yunsheng, W. U. Hao, *J. Rare Earths* **2014**, *32*, 1.
[59] P. Sathishkumar, R. V. Mangalaraja, T. Pandiyarajan, M. A. Gracia-Pinilla, N. Escalona, C. Herrera, R. Garcia, *RSC Adv.* **2015**, *5*, 22578.
[60] T. Taniguchi, T. Watanabe, N. Sugiyama, A. K. Subramani, H. Wagata, N. Matsushita, M. Yoshimura, *J. Phys. Chem. C* **2009**, *113*, 19789.
[61] B. Choudhury, A. Choudhury, *Mater. Chem. Phys.* **2012**, *131*, 666.
[62] S. A. Acharya, V. M. Gaikwad, V. Sathe, S. K. Kulkarni, *Appl. Phys. Lett.* **2014**, *104*, 113508.
[63] C. Thiabdokmai, A. Tangtrakarn, S. Promsuy, P. Ngiewlay, C. Mongkolkachit, *Adv. Mater. Sci. Eng.* **2014**, *2014*, 1.
[64] M. Kamiya, E. Shimada, Y. Ikuma, M. Komatsu, H. Haneda, *J. Electrochem. Soc.* **2000**, *147*, 1222.
[65] X. Niu, F. Tu, *J. Mater. Sci.: Mater. Electron.* **2017**, *28*, 2141.
[66] W. H. Weber, K. C. Hass, J. R. McBride, *Phys. Rev. B* **1993**, *48*, 178.
[67] A. C. Cabral, L. S. Cavalcante, R. C. Deus, E. Longo, A. Z. Simões, F. Moura, *Ceram. Int.* **2014**, *40*, 4445.
[68] L. D. Jadhav, M. G. Chourashiya, A. P. Jamale, A. U. Chavan, S. P. Patil, *J. Alloys Compd.* **2010**, *506*, 739.
[69] S. Phoka, P. Laokul, E. Swatsitang, V. Promarak, S. Seraphin, S. Maensiri, *Mater. Chem. Phys.* **2009**, *115*, 423.
[70] X. Ma, P. Lu, P. Wu, *J. Alloys Compd.* **2018**. *734*, 22.
[71] A. K. Sinha, K. Suzuki, *J. Phys. Chem. B* **2005**, *109*, 1708.
[72] P. Venkataswamy, K. N. Rao, D. Jampaiah, B. M. Reddy, *Appl. Catal., B* **2015**, *162*, 122.
[73] Y. L. Kuo, C. Lee, Y. S. Chen, H. Liang, *Solid State Ionics* **2009**, *180*, 1421.
[74] M. R. Rao, T. Shripathi, *J. Electron Spectrosc. Relat. Phenom.* **1997**, *87*, 121.
[75] J. Zhang, H. Wong, D. Yu, K. Kakushima, H. Iwai, *AIP Adv.* **2014**, *4*, 117117.
[76] F. Meng, L. Wang, J. Cui, *J. Alloys Compd.* **2013**, *556*, 102.
[77] M. M. Khan, S. A. Ansari, D. Pradhan, D. H. Han, J. Lee, M. H. Cho, *Ind. Eng. Chem. Res.* **2014**, *53*, 9754.
[78] F. Pagliuca, P. Luches, S. Valeri, *Surf. Sci.* **2013**, *607*, 164.
[79] P. Bera, H. Seenivasan, K. S. Rajam, C. Shivakumara, S. K. Parida, *Surf. Interface Anal.* **2013**, *45*, 1026.
[80] A. Galtayries, R. Sporken, J. Riga, G. Blanchard, R. Caudano, *J. Electron Spectrosc. Relat. Phenom.* **1998**, *88-91*, 951.
[81] S. A. Ansari, M. M. Khan, M. O. Ansari, S. Kalathil, J. Lee, M. H. Cho, *RSC Adv.* **2014**, *4*, 16782.
[82] S. A. Acharya, V. M. Gaikwad, S. W. D'Souza, S. R. Barman, *Solid State Ionics* **2014**, *260*, 21.
[83] D. N. Durgasri, T. Vinodkumar, P. Sudarsanam, B. M. Reddy, *Catal. Lett.* **2014**, *144*, 971.
[84] J. L. Rupp, T. Drobek, A. Rossi, L. J. Gauckler, *Chem. Mater.* **2007**, *19*, 1134.
[85] M. Pramanik, F. K. Shieh, S. M. Alshehri, Z. A. Alothman, K. C. W. Wu, Y. Yamauchi, *RSC Adv.* **2015**, *5*, 42762.
[86] A. Sundaresan, C. N. R. Rao, *Nano Today* **2009**, *4*, 96.
[87] Y. Liu, Z. Lockman, A. Aziz, J. MacManus-Driscoll, *J. Phys.: Condens. Matter* **2008**, *20*, 165201.
[88] M. Y. Ge, H. Wang, E. Z. Liu, J. F. Liu, J. Z. Jiang, Y. K. Li, Z. A. Xu, H. Y. Li, *Appl. Phys. Lett.* **2008**, *93*, 062505.
[89] X. Chen, G. Li, Y. Su, X. Qiu, L. Li, Z. Zou, *Nanotechnology* **2009**, *20*, 115606.
[90] S. Y. Chen, Y. H. Lu, T. W. Huang, D. C. Yan, C. L. Dong, *J. Phys. Chem. C* **2010**, *114*, 19576.
[91] K. Ackland, L. M. Monzon, M. Venkatesan, J. M. D. Coey, *IEEE Trans. Magn.* **2011**, *47*, 3509.
[92] S. Phokha, S. Pinitsoontorn, P. Chirawatkul, Y. Poo-arporn, S. Maensiri, *Nanoscale Res. Lett.* **2012**, *7*, 425.
[93] K. S. Ranjith, P. Saravanan, S. H. Chen, C. L. Dong, C. L. Chen, S. Y. Chen, K. Asokan, R. T. R. Kumar, *J. Phys. Chem.* **2014**, *118*, 27039.
[94] N. Paunović, Z. Dohčević-Mitrović, R. Scurtu, S. Aškrabić, M. Prekajski, B. Matović, Z. V. Popović, *Nanoscale* **2012**, *4*, 5469.
[95] M. Akyol, A. Ekicibil, K. Kiymaç, *J. Supercond. Novel Magn.* **2013**, *26*, 3257.
[96] M. Petersen, J. Hafner, M. Marsman, *J. Phys.: Condens. Matter* **2006**, *18*, 7021.
[97] H. T. Wong, H. L. Chan, J. H. Hao, *Appl. Phys. Lett.* **2009**, *95*, 022512.
[98] S. Ghosh, G. G. Khan, K. Mandal, *ACS Appl. Mater. Interfaces* **2012**, *4*, 2048.
[99] N. Nithyaa, N. V. Jaya, *J. Supercond. Novel Magn.* **2018**, *31*, 4117.
[100] V. Ney, S. Ye, T. Kammermeier, K. Ollefs, F. Wilhelm, A. Rogalev, S. Lebegue, A. L. da Rosa, A. Ney, *Phys. Rev. B* **2012**, *85*, 235203.
[101] G. Vijayaprasath, R. Murugan, Y. Hayakawa, G. Ravi, *J. Lumin.* **2016**, *178*, 375.
[102] A. Franco Jr., H. V. S. Pessoni, *Phys. B* **2017**, *506*, 145.
[103] L. R. Shah, B. Ali, H. Zhu, W. G. Wang, Y. Q. Song, H. W. Zhang, S. I. Shah, J. Q. Xiao, *J. Phys.: Condens. Matter* **2009**, *21*, 486004.
[104] S. Y. Chen, C. H. Tsai, M. Z. Huang, D. C. Yan, T. W. Huang, A. Gloter, C. L. Chen, H. J. Lin, C. T. Chen, C. L. Dong, *J. Phys. Chem. C* **2012**, *116*, 8707.
[105] G. Niu, E. Hildebrandt, M. A. Schubert, F. Boscherini, M. H. Zoellner, L. Alff, D. Walczyk, P. Zaumseil, I. Costina, H. Wilkens, T. Schroeder, *ACS Appl. Mater. Interfaces* **2014**, *6*, 17496.
[106] G. Lindbergh, D. Simonsson, *J. Electrochem. Soc.* **1991**, *36*, 1985.
[107] H. A. Schwarz, *J. Phys. Chem.* **1992**, *96*, 8937.
[108] J. A. Seetula, I. R. Slagle, D. Gutman, *Chem. Phys. Lett.* **1994**, *224*, 533.
[109] A. L. Gal, S. Abanades, *J. Phys. Chem. C* **2012**, *116*, 13516.
[110] N. Chouhan, R. S. Liu, S. F. Hu, *J. Mater. Chem. A* **2013**, *1*, 7422.
[111] R. J. Wu, Y. C. Hsieh, H. C. Hung, C. Ie, M. Chavali, *J. Chin. Chem. Soc.* **2014**, *61*, 495.
[112] Z. Zhu, J. Y. Chen, K. Y. Su, R. J. Wu, *J. Taiwan Inst. Chem. Eng.* **2016**, *60*, 222.

Journal of Alloys and Compounds 752 (2018) 520–531

Contents lists available at ScienceDirect

Journal of Alloys and Compounds

journal homepage: http://www.elsevier.com/locate/jalcom

# Defects and oxygen vacancies tailored structural and optical properties in $CeO_2$ nanoparticles doped with $Sm^{3+}$ cation

Swati Soni [a], Sudhish Kumar [b], B. Dalela [c], Shalendra Kumar [d], P.A. Alvi [e], S. Dalela [a, *]

[a] Department of Pure & Applied Physics, University of Kota, Kota, 324005, India
[b] Department of Physics, Mohanlal Sukhadia University, Udaipur, 313002, India
[c] Department of Physics, Govt. Khetan Polytechnic College, Jhalana Dungri, Jaipur, India
[d] Electronic Materials & Nanomagnetism Lab, Department of Applied Physics, Amity School of Applied Sciences, Amity University Haryana, Gurgaon, 122413, India
[e] Department of Physics, Banasthali Vidyapith, Banasthali, 304022, Rajasthan, India

ARTICLE INFO

*Article history:*
Received 12 January 2018
Received in revised form
9 April 2018
Accepted 12 April 2018
Available online 17 April 2018

*Keywords:*
Surface-enhanced Raman spectroscopy
Sm-doped $CeO_2$
Extrinsic and intrinsic
Oxygen vacancies

ABSTRACT

In this study, the correlation between the concentration of dopant ions and oxygen vacancy defect of Sm-doped $CeO_2$ Nano-particles (NPs) were investigated systematically by X-ray diffraction (XRD), Ultraviolet −visible-Near Infrared spectroscopy (UV−Vis−NIR) and Surface-enhanced Raman spectroscopy (SERS). The nano-crystalline $Ce_{1-x}Sm_xO_2$ ($x = 0.00$, 0.02, 0.04, 0.06, 0.08 and 0.10) samples were synthesized using co-precipitation chemical route. The XRD measurements revealed that $Sm^{3+}$ ions are successfully incorporated at the $Ce^{4+}$ ion sites in the face centered cubic (*fcc*) lattice of $CeO_2$ NPs. The high-resolution transmission electron microscopy (HRTEM) and Selected area electron diffraction (SEAD) patterns were analyzed to study the surface morphology, crystallinity, atomic structure of the samples. The average particle size calculated with TEM images was obtained in the range of 5−8 nm for $Ce_{1-x}Sm_xO_2$ samples for all the doping concentrations. The UV−Vis−NIR spectroscopy and Surface-enhanced Raman Spectroscopy were analyzed to investigate the optical properties and defect structure in these NPs. The UV −Vis−NIR spectroscopy measurements revealed that due to aggregation of particles the optical band gap energy was varied with fluencies of $Sm^{3+}$ ions as well as due to particle size variations of NPs. Peak asymmetry and broadening of Raman active mode further ascribed the presence of oxygen vacancy (whether extrinsic or intrinsic), which were varied with the fluencies of $Sm^{3+}$ ions in $CeO_2$ NPs. This paper presented a systematic study on the fluencies of Sm doping in $CeO_2$ nano-particle lattice to understand the role of vacancies, intrinsic and extrinsic oxygen vacancies and their effect on tailoring the structural and optical properties of doped $CeO_2$ nano-particles for various applications like luminescent materials, oxygen transportation, catalysts, ultraviolet fuel cells, corrosion prevention etc.



## 1. Introduction

In recent years dilute magnetic semiconductors (DMS) have been extensively studies due to their enormous spintronic properties for various spintronic applications, among them Cerium oxide is considered as a promising candidate, which has evoked a great deal of interest among the researchers for its wide range of applications such as solid electrolyte in solid oxide fuel cells (SOFC's) [1], three way catalysts for automobile exhaust systems, oxygen gas sensors, having wide band gap energy of 3.2 eV used as sunscreen for UV absorbent [2], blocking material in UV-shielding [3], and $CeO_2$ films can also be used as protective coating of SOFC's interconnector [4] Most of the chemical, mechanical and magnetic properties of $CeO_2$ directly depend on the presence of related point defects, such as oxygen vacancies, which are believed to be generated due to reduction of $Ce^{4+}$ to $Ce^{3+}$ oxidation states of cerium ions and further change in material properties may be attributed due its particle size change from micro to nano-scale. It is also reported by researchers that $CeO_2$ nanoparticles (NPs) have a tendency to liberate more oxygen ions and create more oxygen vacancies than bulk $CeO_2$, due to increased surface-to-volume ratio [5], which may result into increase in oxygen storage

* Corresponding author.
*E-mail addresses:* skmlsu@gmail.com (S. Kumar), parveznihal@gmail.com (P.A. Alvi), sdphysics@rediffmail.com (S. Dalela).

https://doi.org/10.1016/j.jallcom.2018.04.157
0925-8388/

capacity as well as oxygen ion conductivity in these materials [6,7]. Further, it is also reported that the type of dopant also alters the ion conductivity of $CeO_2$ NPs i.e. rare earth ions as dopant significantly increases the oxygen vacancies, which is responsible for enhancement in the oxygen ion conductivity and in mechanical properties in RE-doped $CeO_2$ nanomaterials [8–10]. V. V. Ursaki et al., reported that substitution of $Ce^{4+}$ ions by $Sm^{3+}$ ions could be formed the oxygen vacancies which are responsible for enhancement of the ionic conductivity of Sm-doped $CeO_2$ film synthesized by using electrochemical deposition method [11]. The room temperature ferromagnetic properties are also reported to be enhanced due to RE doping into $CeO_2$ nanomaterials [12] i.e. recently enhanced room temperature ferromagnetic properties were reported by *K. Kaviyaras* et al. for Gd-doped $CeO_2$ nanocrystal prepared using hydrothermal method, attributed due to the formation of the oxygen vacancies due to Gd ion incorporation and increased annealing temperature [13]. *Chen* et al., have observed that the concentration of dopant ions also affect the localized environment of the $CeO_2$ NPs, for their Sm-doped $CeO_2$ nanoparticles (for 3, 5, 7, 9, 11 and 15% doping concentrations) prepared using precipitation method [14]. E. Swatsitang et al., have been observed stable room temperature ferromagnetism induced by oxygen vacancies in accordance with BMP model, for pure and Sm-doped $CeO_2$ (5, 10, 15 and 20%) nanoparticles synthesized by polymer pyrolysis method [15]. However, a correlation between dopant and oxygen vacancies also affects the conductivity and ferromagnetism in doped ceria that not only depends on the size of the dopants but also on the optimum value of doping concentration [12,16]. Recently, the electronic structure of the pure $CeO_2$ and Fe-doped $CeO_2$ polycrystalline samples have been investigated by X-ray photoemission spectroscopy (XPS) and it is revealed that the $Ce^{4+}$ states are reduced to $Ce^{3+}$ states for Fe-doped $CeO_2$ samples, which may be explained by the formation of the oxygen vacancies in the samples [17]. Further, *Lee* et al. [18], reported that the trapping effect of the oxygen vacancies between dopant and cerium ions can be varied with small and large size RE-dopant ions in ceria, which finally affects the local structure in the lattice by generating strain due to strain caused by dopant ion radius. Although there are few experimental reports have been seen to study the oxygen vacancy defect variation with small doping concentrations in Sm-doped $CeO_2$ NPs. The origin of ferromagnetism in these compounds is still controversial; there are doubts whether the ferromagnetism is intrinsic or extrinsic in these compounds. Generally, it is acceptable that the Sm-ions are substituting the Ce-site in the lattice and hence the ferromagnetism in these compounds is intrinsic in nature. Hence, the main motive behind this study is to explore the formation of defects, oxygen vacancy defect arises due to the small doping concentration of $Sm^{3+}$ ions in $CeO_2$ NPs.

It is requisite that the microstructure of the $Sm^{3+}$ ions doped $CeO_2$ NPs have to be studied using some appropriate method and hence in the present work, pure and Sm-doped $CeO_2$ NPs with different doping concentration (2, 4, 6, 8 and 10%) synthesized by co-precipitation method is studied using Surface-enhanced Raman Spectroscopy (SERS) as this technique can be used to identify the information on direct defects and oxygen vacancies as the other techniques like X-ray Diffraction (XRD), electron microscopies are not suitable for probing the atomic scale defect structures in the lattice. The effect of Sm doping on the structural, surface morphological, optical properties of Sm-doped $CeO_2$ NPs with different doping concentration (2, 4, 6, 8 and 10%) has been investigated using various techniques such as XRD, Transmission electron microscopy (TEM), Energy-dispersive X-ray spectroscopy (EDX), UV–Vis–NIR spectroscopy and SERS. Specifically, we have also discussed the relationship between doping concentration and oxygen vacancies defects with a view to explain the microstructure of Sm-doped $CeO_2$ NPs.

## 2. Experimental details

### 2.1. Materials

Cerium (III) Choride heptahydrate ($CeCl_3.7H_2O$) (Alpha Aesar 99.9%), Samarium (III) Choride hexahydrate ($SmCl_3.6H_2O$) (Alpha Aesar 99.9%) and Ammonium hydroxide ($NH_4OH$) 30% solution.

### 2.2. Material preparation

Nanocrystalline $Ce_{1-x}Sm_xO_2$ ($x = 0.00$, 0.02, 0.04, 0.06, 0.08, and 0.10) samples were synthesized using co-precipitation method. The appropriate stoichiometric amount of $CeCl_3.7H_2O$ and $SmCl_3.6H_2O$ were used for synthesizing $Ce_{1-x}Sm_xO_2$ NPs. Initially, $CeCl_3.7H_2O$ and $SmCl_3.6H_2O$ precursor solution was prepared in distilled water with magnetic stirring at the rate of 600 rpm. Then 30% $NH_4OH$ solution was added drop wise to this solution until the pH level was reached about 10. This solution was stirred about 4 h with the stirring rate of 1600 rpm at room temperature. After that, the synthesized pale-yellow precipitate were collected and washed with distilled water. The samples were dried at room temperature and annealed in the furnace about 500 °C for 8 h. A set of samples, i.e. pure $CeO_2$, 2%, 4%, 6%, 8% and 10% of Sm-doped $CeO_2$ nanoparticles were formed. The chemical reaction occurring during the experimental process can be written as follows:

$$\boldsymbol{CeCl_3 \cdot 7H_2O_{(aq)} + 3NH_4OH_{(aq)} \rightarrow Ce(OH)_{3(s)} + 3NH_4Cl_{(aq)} + 7H_2O_{(aq)}} \quad (1)$$

$$\boldsymbol{2Ce(OH)_{3(s)} \xrightarrow{500^{\circ}C} 2CeO_{2(s)} + 2H_2O_{(g)} + H_{2(g)}\uparrow} \quad (2)$$

Assumed chemical reactions for the growth on various ratios ($x = 0.00$, 0.02, 0.04, 0.06, 0.08, and 0.10) of dopant Sm-ion in $CeO_2$ NPs can be occurred as follows:

$$\boldsymbol{(1-x)[CeCl_3 \cdot 7H_2O] + x[SmCl_3 \cdot 6H_2O] + 3NH_4OH \rightarrow Ce_{1-x}Sm_xO_2 + \text{Molecular gases}\uparrow} \quad (3)$$

### 2.3. Nano-materials characterization

The structural properties of the samples were studied using x-ray diffraction (XRD) method on Brucker D8 Advance diffractometer utilizing Cu $K_\alpha$ radiation ($\lambda = 1.5406$ Å). The diffraction patterns were recorded at room temperature in the $2\theta$ range from 10 to 90° with 0.05° $min^{-1}$ scanning speed and the counting time of 5 s per step. The surface morphology, particle size and crystalline nature of the samples was studied using Transmission electron microscopy (TEM) with Technai G2 20 S-TWIN (FEI Netherlands) instrument operated at an accelerating voltage of 200 kV. Samples for the TEM investigation were prepared by dispersing the nanopowder in ethanol using an ultrasonicator to produce a dilute suspension for correct particle size measurements. A standard carbon film mesh supported on Cu grid was immersed in the suspension to produce the sample for TEM measurements. The particle size distribution was measured for a total 150 particles using the Image-j software. Energy-dispersive X-ray (EDX) spectra were recorded from TESCAN MIRA 3 FESEM equipped with EDX (OXFORD detector with AZtec software) operating at an accelerating voltage of 15 kV. EDX

analysis was used to confirm the presence of the elements. The optical and defect characterizations were carried out by Surface-enhanced Raman spectroscopy (SERS) on a Thermo Scientific DXRxi Raman Imaging Microscope with Charge Injection device (CID) detector having a green laser with 532 nm excitation light source with its power was kept at 10 mW. The Ultra-violet–visible–Near infrared (UV-VIS-NIR) spectroscopy was performed for the optical absorbance spectra of the samples in the range of 200–1000 nm with $BaSO_4$ as an internal standard, were recorded employing a Shimadzu UV-3600 Plus spectrophotometer with an integrating sphere.

## 3. Result and discussion

### 3.1. Structural analysis

Fig. 1(a) displays the indexed powder XRD patterns for $Ce_{1-x}Sm_xO_2$ ($x = 0.00, 0.02, 0.04, 0.06, 0.08$, and 0.10) nanoparticles (NPs). All major Bragg peaks (111), (200), (220), (311), (222), (400), (331), (420) and (422) corresponding to the crystallographic plane having face-centered cubic fluorite (*fcc*) structure with the space group *Fm3m* in which Ce is located at *4a* position and surrounded by eight oxygen located at *8b* position [19] are marked on the XRD pattern. Further, in order to rule out the presence of any peak

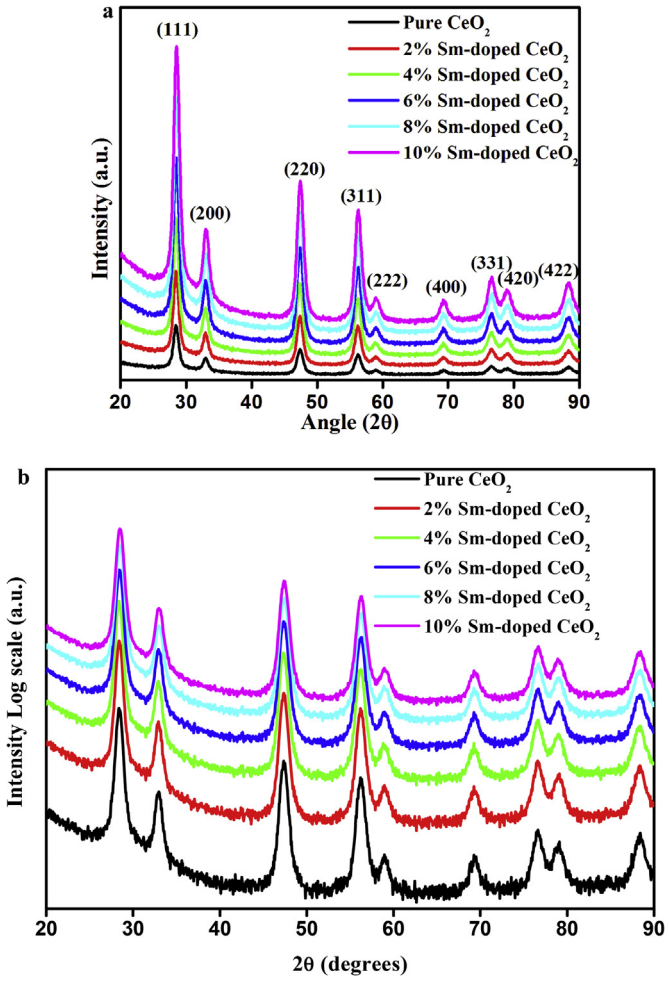


**Fig. 1.** **a**: XRD patterns of pure $CeO_2$ and $Ce_{1-x}Sm_xO_2$ (for $x = 0.02, 0.04, 0.06, 0.08$, and 0.10) nanoparticles. **b**: XRD patterns of pure $CeO_2$ and $Ce_{1-x}Sm_xO_2$ (for $x = 0.02, 0.04, 0.06, 0.08$, and 0.10) NPs plotted on Log scale.

corresponding to secondary impurity phase such as $Sm_2O_3$ the XRD patterns are plotted on Log scale (see Fig. 1(b)). Fig. 1(b) depicts only the allowed Bragg reflections and no impurity peak can be detected in the XRD patterns of all the samples. These observations clearly indicate well incorporation of $Sm^{3+}$ ions on $CeO_2$ lattice site and indeed confirming the single phase formation of doped $Ce_{1-x}Sm_xO_2$ samples.

Fig. 2(a–f) shows the Rietveld refined and fitted X-ray diffraction spectra for all the pure and doped $Ce_{1-x}Sm_xO_2$ samples, which has been carried out on a series of $x = 0.02, 0.04, 0.06, 0.08$ and 0.10 doping concentration at room temperature and the results of the Rietveld refinement are tabulated in Table 1. It indicates that all peaks are in good agreement with the standard data for $CeO_2$ (with peak intensity according to JCPDS Card No. 43–1002) [20].

As shown in Fig. 3, the intensity of most intense Bragg diffraction peak (111) is not changed much with the incorporation of $Sm^{3+}$ ions for $x = 0.02$ and 0.04 fluencies, but with further increase in concentration of Sm (for $x = 0.06, 0.08$ and 0.10) the peak intensity is changed drastically. It is reported that the increasing intensity in the diffraction peak signifies an improvement in the crystalline nature while decreasing intensity signifies low crystalline nature of the $CeO_2$ NPs samples [21]. Simultaneously, Fig. 3 indicates that incorporation of $Sm^{3+}$ ions for $x = 0.02$ and 0.04 the diffraction peak (111) is shifted towards lower angle side and for $x = 0.06, 0.08$ and 0.10 concentration peak is shifted towards higher angle side. It is also reported that the shifting of (111) peak to the lower and higher angle side is attributed to the lattice expansion and contraction, respectively, with the doping of $Sm^{3+}$ ions in $CeO_2$ NPs [22].

As clearly seen in Fig. 1, the XRD diffraction peaks become broader after doping and broadness of peaks are changed with the fluency of $Sm^{3+}$ ions in $CeO_2$ NPs, indicating that crystal size and crystalline nature of the samples are affected due to change in the concentration of dopant ions in $CeO_2$ NPs. The average nano-crystalline particle size (D) of pure $CeO_2$ and $Ce_{1-x}Sm_xO_2$ samples is calculated using the Debye Scherrer's formula [23,24]:

$$D = \frac{k\,\lambda}{\beta\,\cos\theta} \tag{4}$$

where $k$ is the particle shape factor (0.9), $\lambda$ is the X-ray wavelength of Cu $K_\alpha$ radiation (1.5406 Å), $\beta$ is the full width at half maxima (FWHM) of XRD (111) diffraction peak, which was calculated by $\beta = (\beta_m^2 - \beta_i^2)^{1/2}$, here $\beta_m$ and $\beta_i$ are the measured and instrumental broadening (in radian) respectively and $\theta$ is the Bragg's diffraction angle of the peak in degree. Table 1 incorporates the calculated lattice parameter of $Ce_{1-x}Sm_xO_2$ samples. The increase in the lattice parameter corresponding to pure $CeO_2$ indicates that the volume of the $CeO_2$ cell has been increased with Sm-doping, which is related with the effective ionic radius of the dopant ion [25], as the ionic radius of $Sm^{3+}$ (0.1079 nm) is larger than the ionic radius of $Ce^{4+}$ (0.097 nm) ions [26]. This incorporation of $Sm^{3+}$ ions in $CeO_2$ sample possibly will create the larger radius of $Ce^{3+}$ ions (0.114 nm) rather than smaller radii $Ce^{4+}$ ions. Furthermore, in order to maintain charge equilibrium, $Sm^{3+}$ and $Ce^{3+}$ ions are collectively creating oxygen vacancies in the $CeO_2$ lattice, which is also reported for further lattice expansion [22]. These variations in lattice parameter clearly indicate the effect of $Sm^{3+}$ ions doping concentration in $CeO_2$ NPs. It has been reported that lattice parameter and particle size are directly related to each other, as particle size increases this causes a decrease in the lattice parameter [27]. This can be explained by the increased rigidity, which may be caused by increasing lattice strain results from the substitution of $Ce^{4+}$ ions by $Sm^{3+}$ ions. Now, lattice strain ($\varepsilon$) is calculated using formula [28,29]:

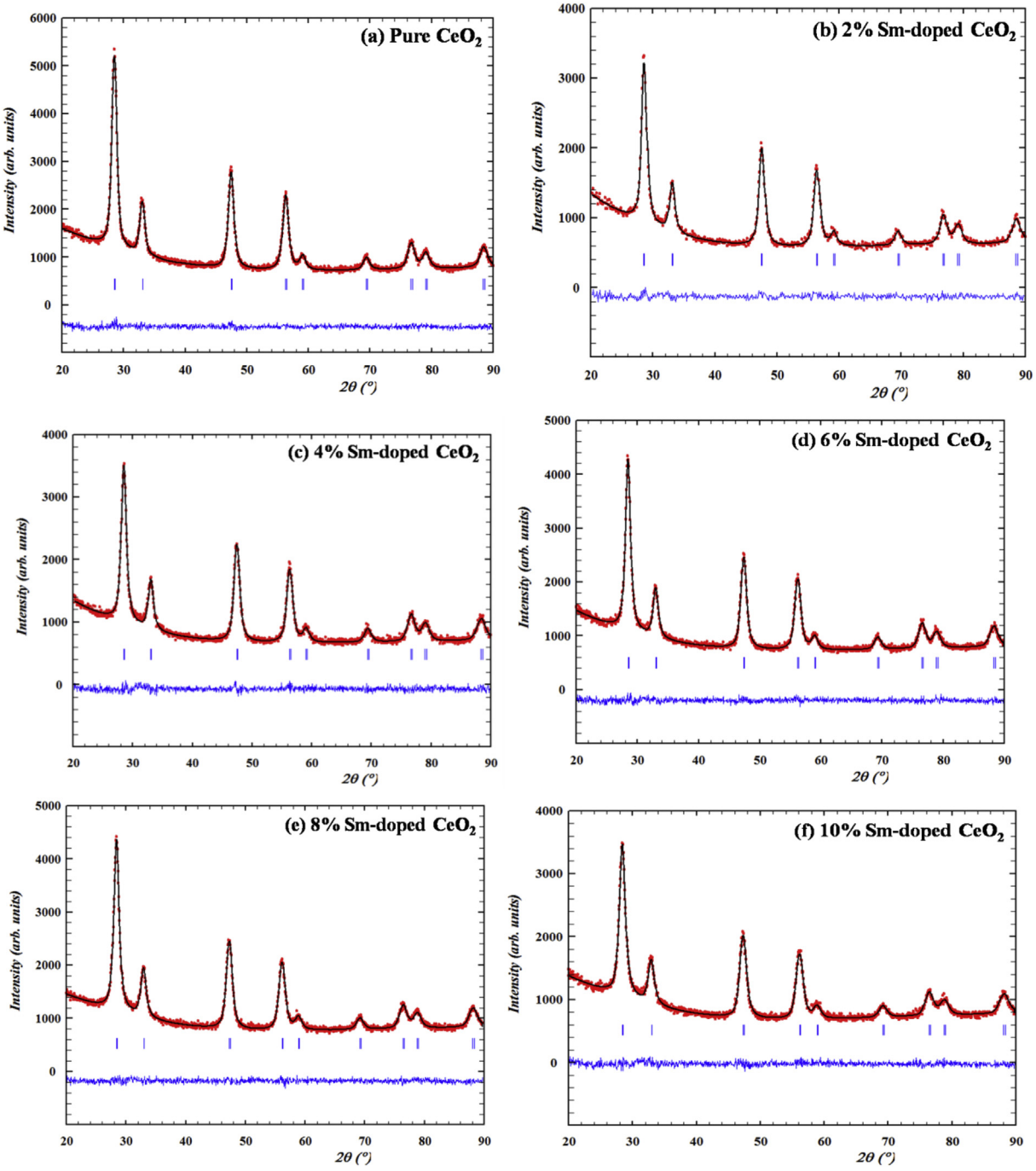


**Fig. 2.** (a–f): Rietveld refined and fitted X-ray diffraction patterns of Pure $CeO_2$ and $Ce_{1-x}Sm_xO_2$ ($x = 0.02$, 0.04, 0.06, 0.08 and 0.10) samples NPs at 300 K. Observed (calculated) profiles are shown by dotted (solid) lines. The short vertical marks represent Bragg reflections. The lower curve is the difference plot.

**Table 1**
Obtained values of lattice parameter ($a$), unit cell volume and other fine details from Rietveld refinement analysis of the X-ray Diffraction data.

| Samples $Ce_{1-x}Sm_xO_2$ | $x = 0.00$ | $x = 0.02$ | $x = 0.04$ | $x = 0.06$ | $x = 0.08$ | $x = 0.10$ |
|---|---|---|---|---|---|---|
| Lattice Parameter a (Å) | 5.4146 (2) | 5.4105 (25) | 5.4167(18) | 5.4195(18) | 5.4209 (30) | 5.4294(22) |
| Unit Cell Volume V($Å^3$) | 158.74(8) | 158.38(13) | 158.93(9) | 159.41(9) | 160.01 (9) | 160.05 (12) |
| $R_p$ | 2.50 | 2.83 | 2.71 | 2.56 | 2.44 | 2.70 |
| $R_{wp}$ | 3.17 | 3.57 | 3.47 | 3.26 | 3.10 | 3.39 |
| $R_{exp}$ | 3.01 | 3.39 | 3.25 | 3.08 | 3.01 | 3.19 |
| $\chi^2$ | 1.11 | 1.11 | 1.14 | 1.12 | 1.06 | 1.13 |
| $R_{Bragg}$ | 1.28 | 1.30 | 1.76 | 1.96 | 1.42 | 2.84 |

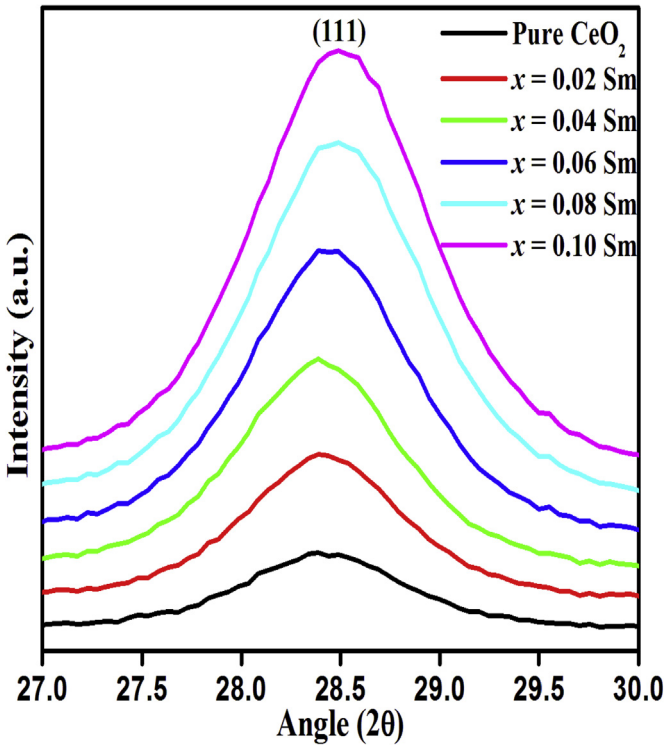


**Fig. 3.** Limited range XRD diffraction pattern plotted in the vicinity of the (111) Bragg peak for Sm-doped $CeO_2$ nanoparticles.

$$\varepsilon = \frac{\beta \cos\theta}{4} \tag{5}$$

As tabulated in Table 2, all positive values of strain are related to the tensile strain in Sm-doped $Ce_{1-x}Sm_xO_2$ samples. The results revealed that due to incorporation of $Sm^{3+}$ ions, strain is decreased for initial doping concentration $x = 0.02$, which increases for $x = 0.04$ concentration, decreases for $x = 0.06$ and increase can be seen for further doping concentrations. This indicates that due to incorporation of larger radii $Sm^{3+}$ (0.1079 nm) ion, lattice is relaxed for $x = 0.02$ and 0.06 concentrations, while strain expands the lattice for other doping concentrations (as shown in Table 2). It is also reported in some theoretical investigation that the tensile strain promotes the formation of oxygen vacancies more than the compressive strain [30]. Hence, the increment in tensile strain in our samples can be directly related to the endorsement of oxygen vacancies, which is related to the bonding length and the strength between the surface oxygen and Ce atom [31]. Since, for tensile strain, the bandwidth of the O 2p orbital decreases and overlapping between O 2p and Ce 5 d as well as Ce 4f orbital also decreases, which leads a weaker Ce–O bond and responsible for the formation of oxygen vacancies [30].

Furthermore, the dislocation density is another crystallographic defect, or irregularity, which is also found within a crystal structure. The dislocation density (δ) is defined as the total length of dislocation lines per unit volume, which is calculated using formula [32]:

$$\delta = \frac{1}{D^2} \tag{6}$$

Here, D is average particle size measured from TEM images.

The dislocation density is found to increase after incorporation of $Sm^{3+}$ ions for all the doping concentrations of Sm in $CeO_2$ NPs (except for $x = 0.06$), δ found to be decreased (as shown in Table 2). This increase in dislocation density corresponds to the promotion of disorder for Sm-doped $CeO_2$ samples [21].

### 3.2. Surface morphology

The average crystallite particle size of all the samples was further confirmed by Transmission electron microscopy (TEM), which is used to get the information about the shape, size and the presence of any secondary phase in doped $Ce_{1-x}Sm_xO_2$ NPs samples. The particle size and morphology of $Ce_{1-x}Sm_xO_2$ samples analyzed by TEM are shown in Fig. 4.

It can be clearly seen from the TEM images that the particles are crystallized nanoparticles and agglomerated with spherical geometry. The particle-size distribution (histogram is shown in the inset of Fig. 4) shows that the distribution is quite narrow in the size range of 5–8 nm for all the $Ce_{1-x}Sm_xO_2$ NPs samples, which are in good agreement with the results obtained from XRD data (listed in Table 2). This agglomeration of particles with smaller particle-size (<8 nm) indicates that the obtained particles are nanocrystallites. The particle size measured directly from TEM images promotes crystal growth with the doping concentration of $Sm^{3+}$ ions. However, the morphology of all samples is not changing but the agglomeration of particles is increased with increasing doping concentration of $Sm^{3+}$ ions (as shown in Fig. 4). Since, agglomeration of nanoparticles is more stable configuration according to the energy point of view, which allows nanoparticles for crystallite growth [33]. Furthermore, high-resolution transmission electron microscopy (HRTEM) and selected area diffraction analysis (SAED) are also used to get the information about the nanocrystallinity and the impurity phase present in the $Ce_{1-x}Sm_xO_2$ samples.

HRTEM images (as shown in Fig. 5) indicate that the lattice fringes are well developed and randomly oriented with respect to each other. Most of the lattice fringes of $Ce_{1-x}Sm_xO_2$ samples are about at a distance of 0.31 nm (values are tabulated in Table 2) that corresponding to the (111) lattice plane of the fluorite like cubic structure. However, interplanar distance ($d$) has been changed with $Sm^{3+}$ ions doping in $CeO_2$ NPs. As shown in Table 2, there is no significant change has been observed in the interplanar distance ($d$)

**Table 2**
Calculated values of lattice spacing ($d$) for (111) plane, average crystalline size (D) measured from TEM, XRD and Raman line broadening, dislocation density (δ), lattice strain ($\varepsilon$), absorbance wavelength (λ), optical band gap energy ($E_g$) and refractive index ($n$) are summarized in the table.

| Sample | $d$ (nm) | D (nm) | | | δ ($nm^{-2}$) | $\varepsilon \times 10^{-2}$ | λ (nm) | $E_g$ (eV) | $n$ |
|---|---|---|---|---|---|---|---|---|---|
| | | TEM | XRD | Raman spectra | | | | | |
| Pure $CeO_2$ | 0.317 | 7.24 | 9.16 | 8.07 | 0.019 | 3.88 | 313 | 2.87 | 2.43 |
| $Ce_{0.98}Sm_{0.02}O_2$ | 0.308 | 5.94 | 9.49 | 9.28 | 0.028 | 3.75 | 329 | 2.69 | 2.48 |
| $Ce_{0.96}Sm_{0.04}O_2$ | 0.317 | 6.45 | 9.12 | 8.04 | 0.024 | 3.83 | 320 | 2.86 | 2.43 |
| $Ce_{0.94}Sm_{0.06}O_2$ | 0.316 | 8.13 | 9.62 | 7.40 | 0.015 | 3.78 | 324 | 2.83 | 2.44 |
| $Ce_{0.92}Sm_{0.08}O_2$ | 0.317 | 6.62 | 7.72 | 6.34 | 0.022 | 4.68 | 323 | 2.87 | 2.43 |
| $Ce_{0.90}Sm_{0.10}O_2$ | 0.322 | 6.76 | 6.91 | 5.03 | 0.021 | 6.98 | 316 | 2.64 | 2.50 |

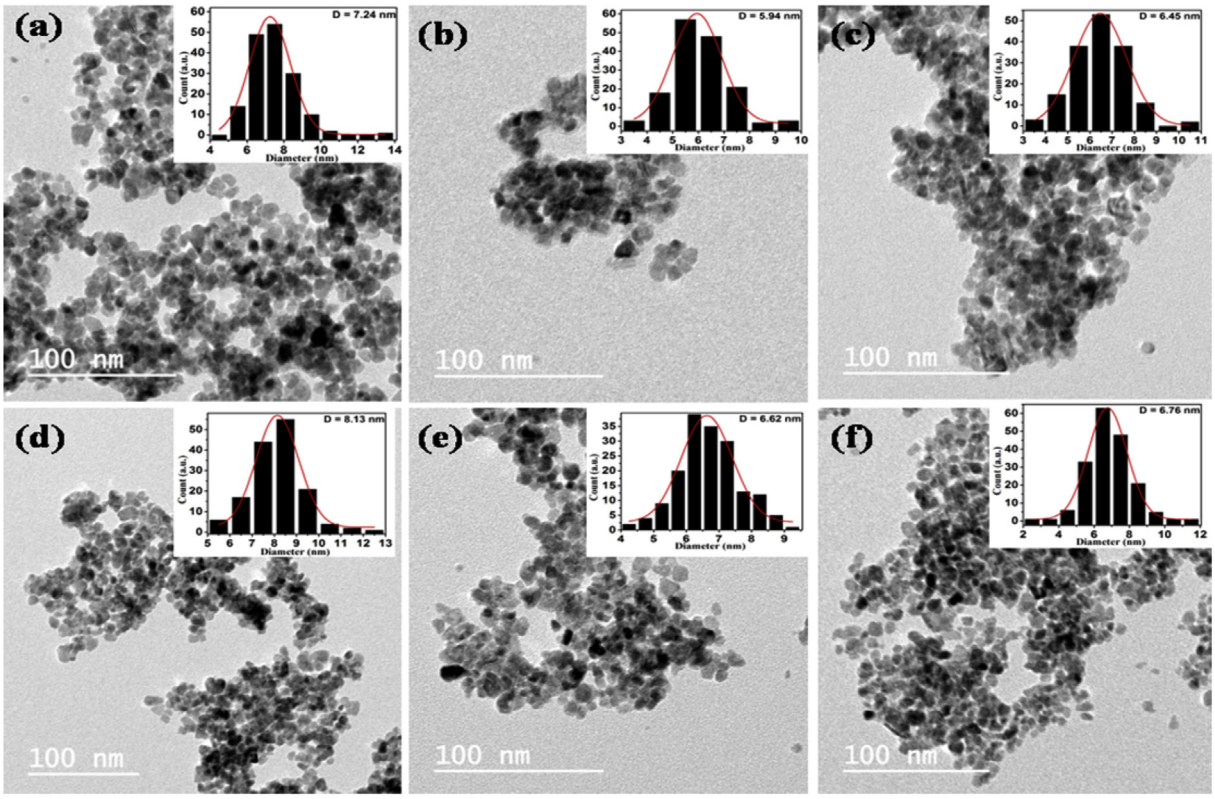


**Fig. 4.** TEM image for Sm-doped (a) Pure $CeO_2$, (b) 2% Sm-doped $CeO_2$, (c) 4% Sm-doped $CeO_2$, (d) 6% Sm-doped $CeO_2$, (e) 8% Sm-doped $CeO_2$, (f) 10% Sm-doped $CeO_2$ NPs and inset histogram show the particle-size distribution of the corresponding samples.

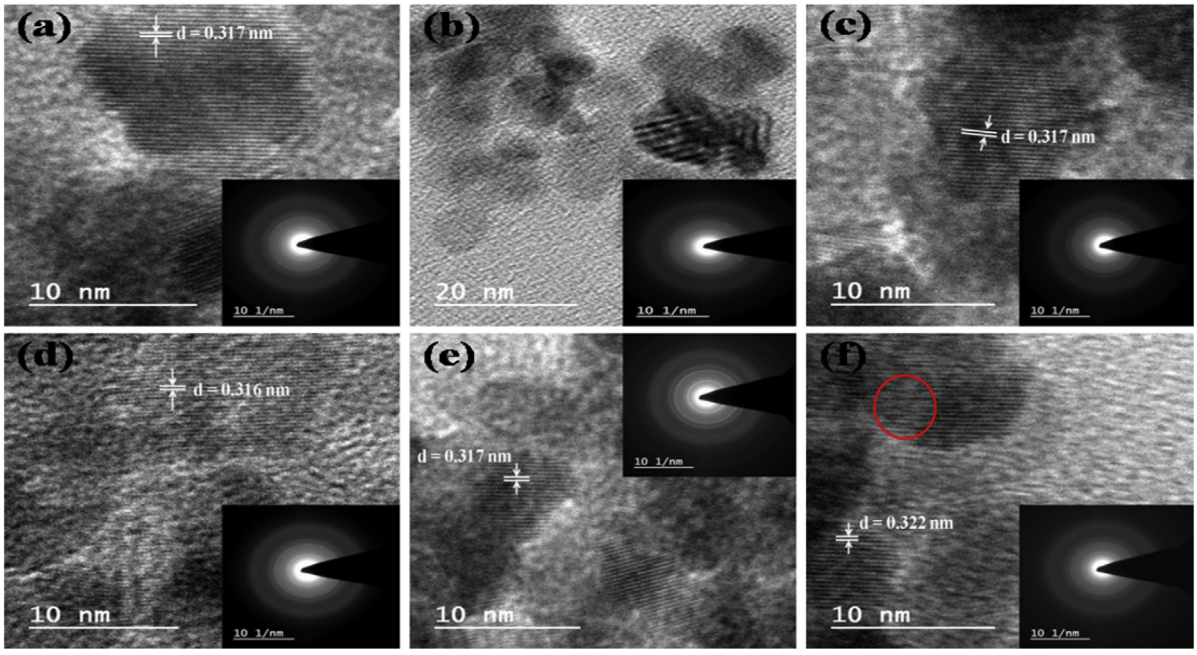


**Fig. 5.** HRTEM images of Sm-doped with interplanar distance (d)-spacing for (111) plane for (a) Pure $CeO_2$ (b) 2% Sm-doped $CeO_2$ (c) 4% Sm-doped $CeO_2$ (d) 6% Sm-doped $CeO_2$ (e) 8% Sm-doped $CeO_2$ (f) 10% Sm-doped $CeO_2$ NPs and inset shows the SAED pattern of corresponding sample.

for $x = 0.00$, 0.04, 0.06 and 0.08 Sm-doped $CeO_2$ samples but for $x = 0.02$ and 0.10 Sm-doped $CeO_2$ samples, the interplanar distance $d = 0.308$ and 0.322 nm for (111) plane, respectively, has been changed. The increased value of interplanar distance ($d$) indicates the crystal growth and the low crystallinity. Some defects, such as dislocations (shown in Fig. 5(f) marked with a red ring) are also observed in the HRTEM micrograph of 10% Sm-doped $CeO_2$ NPs. Moreover, The SAED patterns are also taken (shown in the insets of

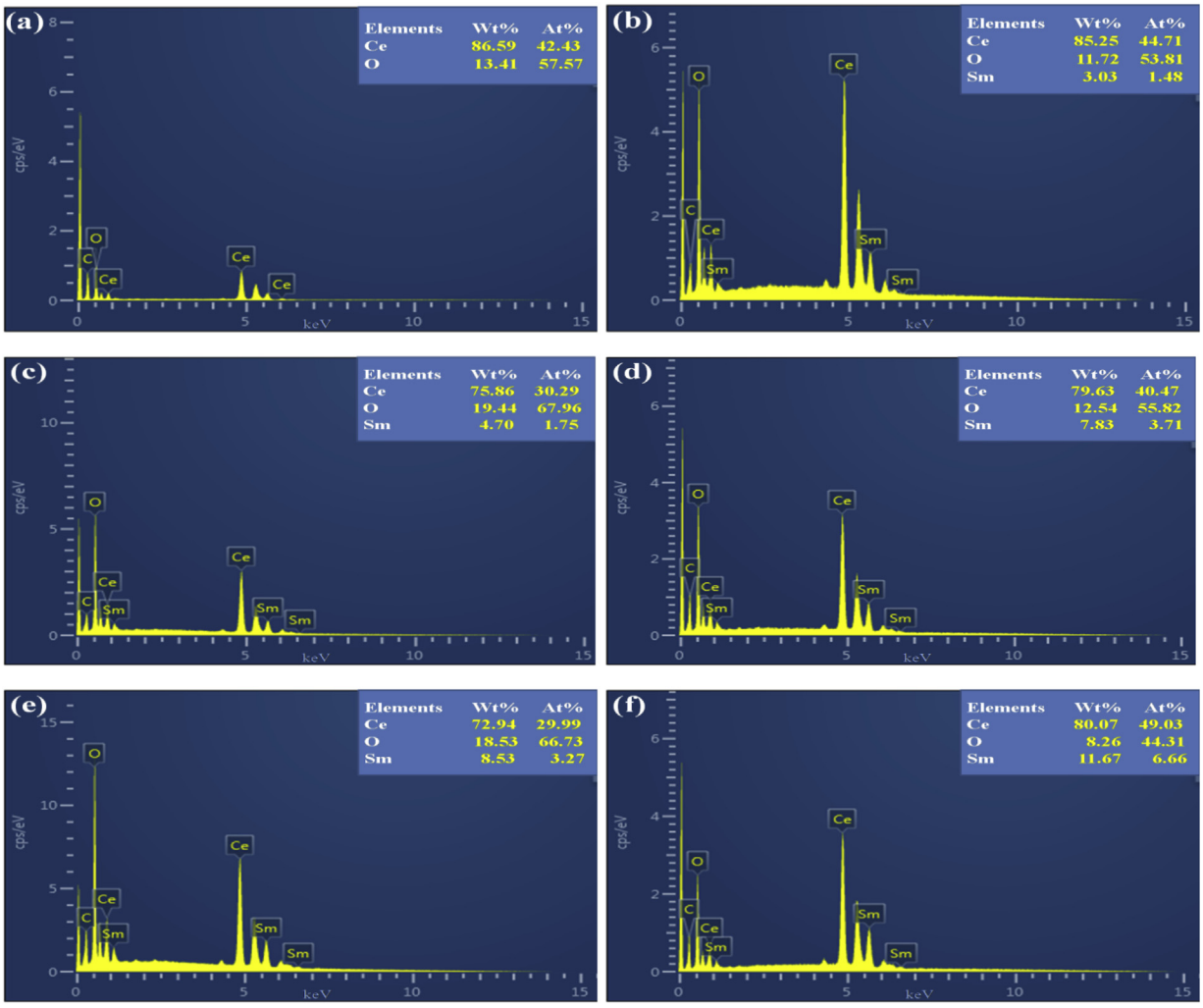


**Fig. 6.** EDX spectrum of the (a) pure $CeO_2$, (b) 2% Sm-doped $CeO_2$, (c) 4% Sm-doped $CeO_2$, (d) 6% Sm-doped $CeO_2$, (e) 8% Sm-doped $CeO_2$, and (f) 10% Sm-doped $CeO_2$ nanoparticles.

Fig. 5) for all the pure and doped $Ce_{1-x}Sm_xO_2$ NPs samples. The SAED pattern exhibits four broad rings, which could be attributed to (111), (200), (220) and (311) planes. These rings indicate that the particles are crystallized and diffraction rings are very well agreeing to the XRD pattern of all the samples. The broadening of diffraction rings indicates the sizes of the particles are small and crystalline nature of all the samples getting low with increasing doping concentration of $Sm^{3+}$ ions.

Fig. 6(a–f) gives the Energy-dispersive X-ray (EDX) spectra for the pure $CeO_2$ and $Ce_{1-x}Sm_xO_2$ ($x = 0.02$, 0.04, 0.06, 0.08, and 0.10) nanoparticles. It is observed that the cerium (Ce), samarium (Sm) and oxygen (O) elements are present in the spectra nearly in the stoichiometric ratio. No other elements were found in the spectra reflecting the high purity of the synthesized samples. Note that the Carbon signals were from the carbon conducting adhesive double side tape on which the powder sample were loaded for measurements. The EDX data on the oxygen is not reliable to have an estimation of oxygen in these samples; it also reflects the surface oxygen contamination.

### 3.3. UV–Vis–NIR analysis

Fig. 7(a) shows the UV–visible absorption optical spectra for all the pure and Sm-doped $Ce_{1-x}Sm_xO_2$ NPs samples. It can be seen that these samples exhibit strong absorption below 400 nm with an absorption peak in UV-range corresponding to the different doping concentration of $Sm^{3+}$ ions in $CeO_2$ NPs, which are tabulated in Table 2. These peaks are originated due to charge transfer from $O^{2-}$ (2p) valance band to $Ce^{4+}$ (4f) conduction band, which is a direct recombination of the electrons in $Ce^{4+}$ (4f) conduction band with the holes in the $O^{2-}$ (2p) valance band. As shown in Fig. 7(a), due to formation of the smaller size nanocrystals with the incorporation of $Sm^{3+}$ ions in $CeO_2$ NPs lattice, the wavelength is shifted towards longer wavelength (red shift) side i.e. 329 nm (for $x = 0.02$). Whereas, aggregation of NPs is expected to increase with increasing doping concentration of $Sm^{3+}$ ions (for $x = 0.04$) in $CeO_2$ NPs, due to this reason wavelength is shifted towards lower wavelength side (i.e. blue shift). Again, it increases towards the higher wavelength side for $x = 0.06$ and 0.08 doping concentrations and for $x = 0.10$, the wavelength is again decreased which shows a decrement in the aggregation of NPs.

Form all the absorption data, the optical band gap energies ($E_g$) of the $Ce_{1-x}Sm_xO_2$ samples were calculated using Tauc's equation:

$$\alpha h\nu = A(h\nu - E_g)^n \quad (7)$$

where, all the symbols have their usual meaning.

Fig. 7(b) shows the graphical variation of $(\alpha h\nu)^2$ vs Energy ($h\nu$)

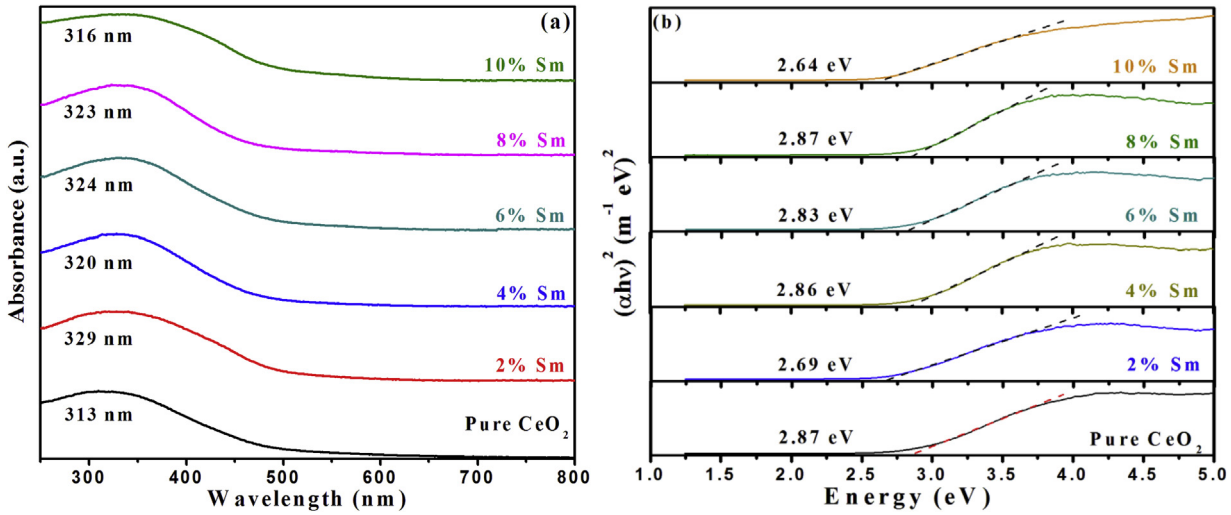


**Fig. 7.** (a) Room temperature optical absorbance spectra of all the $Ce_{1-x}Sm_xO_2$ NPs samples taken in the UV–visible range, (b) Tauc's plot of $(\alpha h\upsilon)^2$ versus Energy (eV) for the $Ce_{1-x}Sm_xO_2$ samples nanoparticles.

curve shown as per the direct transition n = 1/2 in equation (7) as per reference [34]. The calculated values of band gap energies are tabulated in Table 2 (generally reported band gap energy of bulk $CeO_2$ is 3.15 eV [35]). Since, nanoparticles show much different UV-absorption behavior than their corresponding bulk structure, the direct band gap energy ($E_g$) of pure $CeO_2$ NPs were found to be 2.87 eV, which is attributed to owe this position due to increase in the concentration of $Ce^{3+}$ level on grain boundaries, confirms the increase in concentration of $Ce^{3+}$ ions in pure $CeO_2$ lattice.

While incorporation of $Sm^{3+}$ ion in $CeO_2$ sample, further reduction in the band gap energy can be seen as ~2.69 eV for 2% Sm doping, this may be attributed to the creation of oxygen defect or local bond distortions in the $CeO_2$ lattice. The incorporation of $Sm^{3+}$ ions may increase the concentration of $Ce^{3+}$ ions in $CeO_2$ sample due to the creation of oxygen defects or vacancies in the $CeO_2$ lattice. These oxygen defects create impurity levels, which are present in between O 2p and Ce 4f states and capture the excited electrons to decrease the band gap energy of Sm-doped $CeO_2$ sample [36]. This red shifting implies successful incorporation of $Sm^{3+}$ ions in $CeO_2$ lattice [37]. For other doping of $Sm^{3+}$ ions in $CeO_2$ NPs, band gap energy is found to increase and decrease irregularly from $x = 0.04$ to 0.10 doping concentration (as shown in Table 2). These irregularities in the band gap values with increasing $Sm^{3+}$ ions may be related to the formation of new impurity energy levels in-between the band gap of the doped samples [38]. However, the UV-absorption ability of $Ce_{1-x}Sm_xO_2$ samples also depends on its particle size. The variation of the band gap energy with particle size measured from TEM images has been shown in Fig. 8, which shows a decrease in the particle size at 4% Sm doping may be attributed to the confinement of the carriers, finally increasing the band gap energy of the 4% Sm-doped $CeO_2$ NPs. Again the band gap energy is decreased for $x = 0.06$ concentration, which can be explained with Burstein-Moss (BM) effect [36].

$$\Delta E_g^{BM} = \frac{h^2}{2m_{vc}^*}\left(3\pi^2 n_e\right)^{2/3} \tag{8}$$

Here, $m_{vc}^*$ is an effective mass of electrons, $n_e$ is the electron concentration, $h$ is the Plank constant. BM effect suggested that, above the Mott critical density, the increased number of free electron concentration lead to fill 4f level partially, which in turn blocks the lowest states and led to increase the band gap. Here we can say that

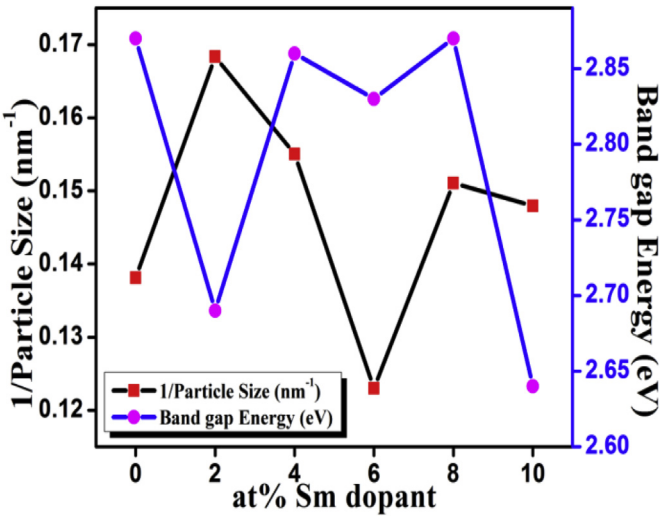


**Fig. 8.** Variation of particle size and band gap energy with Sm-doping concentration ($x = 0\%$, 2%, 4%, 6%, 8% and 10%) in $Ce_{1-x}Sm_xO_2$ sample nanoparticles.

the 6% Sm doping is not sufficiently enough to cross the Mott critical density concentration for BM effect, lead to a decrement in band gap energy. The increment in band gap energy at 8% and then decrement for 10%, Sm doping can be attributed from the fact that the ground and excited f-energy states are created in the mid-band gap of $CeO_2$. At 8%, these energy states of Sm take up few excited electrons coming from O 2p level but at 10%, many of excited electrons already have taken up these energy states and hence could not occupy the states, which finally lead to increase and decrease the band gap energy respectively for 8% and 10%, Sm doping concentrations.

The refractive indices of Sm-doped nanocrystalline $CeO_2$ have also been calculated by using the following formula [39]:

$$\frac{n^2 - 1}{n^2 + 2} = 1 - \sqrt{\frac{E_g}{20}} \tag{9}$$

where $n$ is the refractive index of the material and $E_g$ is the optical band gap energy. Table 2 shows the calculated value of refractive

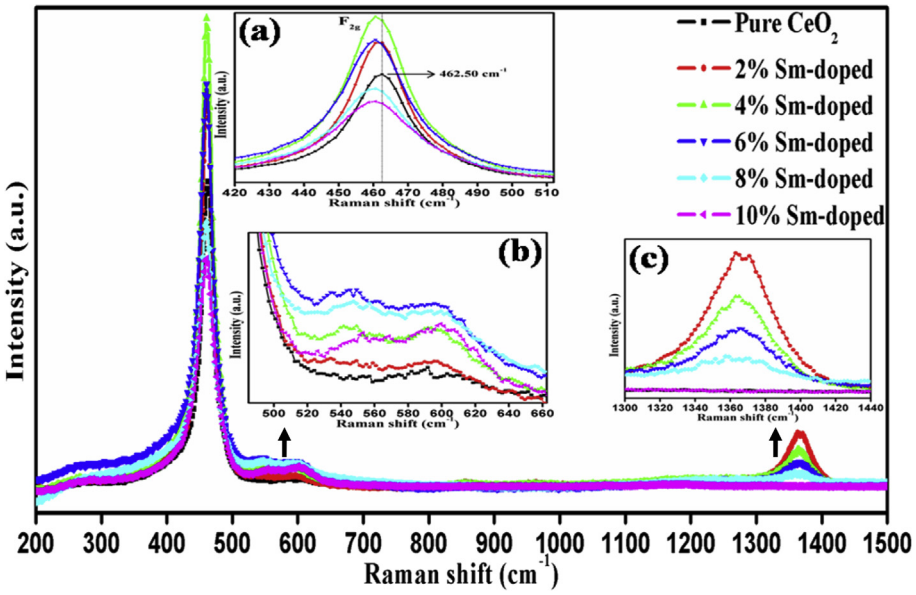


**Fig. 9.** Raman spectra of Sm-doped $CeO_2$ nanoparticles. Inset (a), (b) and (c) of the figure contains the enlarged views of their corresponding Raman spectra in the 420-510 $cm^{-1}$ energy range related to $F_{2g}$ mode, 500-660 $cm^{-1}$ range related to oxygen defects and 1300-1440 $cm^{-1}$ range related to 3LO, respectively.

index of $Ce_{1-x}Sm_xO_2$ samples as a function of the doping concentration of Sm-ions. Compare to pure $CeO_2$, value of $n$ is increased with incorporation of $Sm^{3+}$ ions ($x = 0.02$) in $CeO_2$ NPs lattice, whereas for $x = 0.04$, 0.06 and 0.08 concentrations a minute variation can be seen and finally at $x = 0.10$, the value of $n$ is found to increase. These results show that the refractive index is depending on the concentration of $Sm^{3+}$ ions in $CeO_2$ NPs.

### 3.4. Raman spectra

Surface-enhanced Raman spectroscopy (SERS) is an important characterization technique for investigating the structural symmetry and defects in nanocrystalline samples due to doping of few percentages of dopant ions. Fig. 9 shows the Raman spectra of $Ce_{1-x}Sm_xO_2$ NPs sample with various doping concentrations ($x = 0.00$, 0.02, 0.04, 0.06, 0.08 and 0.10) of Sm-ion. As shown in Fig. 9, pure $CeO_2$ nanoparticles exhibit a Raman peak at 462.50 $cm^{-1}$, which can be associated to the triply degenerate $F_{2g}$ mode of the cubic fluorite crystal structure of $CeO_2$. This mode can be considered as the symmetrical stretching mode of eight oxygen atoms around $Ce^{4+}$ ions (O–Ce–O) and the molecule maintain its tetrahedral symmetry throughout [40]. This vibrational mode is nearly independent of the cation mass due to the movement of oxygen atoms, therefore, this peak is very sensitive to any disorder in the oxygen sub-lattice resulting from thermal, doping or grain size induced non-stoichiometric disorders [41]. Besides of $F_{2g}$ mode, some other weak intensity Raman peaks are also observed in the Raman spectra of pure $CeO_2$ samples (as shown in the inset of Fig. 9 b–c). The peak located at 598.5 $cm^{-1}$ (in Fig. 9(b)) for pure $CeO_2$ is attributed to the second order Raman spectrum, with phonon mode ωTO(X) + LA(X), ascribed its presence due to $Ce^{3+}$ ions and oxygen vacancies [42,43]. In the $CeO_2$ lattice, oxygen vacancies are reported to be formed when the average particle size decreased down to dimensions of the order of nano-size [44]. In our results, we can see that the particle size measured from TEM images (as shown in Table 2) are decreased down to nano-size.

According to this, there can be three possible defect induction mechanisms for generation of oxygen vacancy in the pure $CeO_2$ lattice, which can be given as [45]:

$$Ce_{Ce} + 2O_O \rightarrow V''' + 2V_O^{\cdot\cdot} + CeO_2 \quad (10)$$

$$Ce_{Ce} \rightarrow V_{Ce}'''' + Ce_i^{\cdot\cdot\cdot\cdot} \quad (11)$$

$$O_O \rightarrow V_O^{\cdot\cdot} + O_i'' \quad (12)$$

In the SERS spectra, another second-order Raman peak can be seen at 1175.8 $cm^{-1}$ for pure $CeO_2$, which is associated with 2LO (second overtone band of longitudinal optical mode) Raman mode. The Raman active mode ($F_{2g}$) for $Ce_{1-x}Sm_xO_2$ samples (for $x = 0.02$, 0.04, 0.06, 0.08 and 0.10) is also obtained in the range of ~461-459 $cm^{-1}$ (as shown in Table 3). We can see from the SERS spectra

**Table 3**
The Position of Raman active modes ($cm^{-1}$) from Raman spectra and relative peak area ratio.

| Sample | Position of Raman active mode ($cm^{-1}$) and Vibrational Mode[a] | | | | | | $A_{O_V}/A_{F2g}$ | $\frac{(A_{(O_V)1}+A_{(O_V)2})}{A_{F2g}}$ |
|---|---|---|---|---|---|---|---|---|
| | First-order Scattering | Second-order Scattering [46,47] | | | | Third-order Scattering | | |
| | $F_{2g}$ | $A_{1g}$ $(O_V)$ | $A_{1g} + F_{2g}$ $(O_V)_1$ | $A_{1g} + E_g + F_{2g}$ $(O_V)_2$ | 2LO | 3LO | | |
| Pure $CeO_2$ | 462.5 | 598.5 | – | – | 1175.8 | – | 0.044 | – |
| $Ce_{0.98}Sm_{0.02}O_2$ | 461.1 | – | 537.1 | 591.3 | – | 1364.6 | – | 0.062 |
| $Ce_{0.96}Sm_{0.04}O_2$ | 460.5 | – | 548.6 | 593.5 | – | 1361.5 | – | 0.091 |
| $Ce_{0.94}Sm_{0.06}O_2$ | 459.6 | – | 546.5 | 589.5 | – | 1360.2 | – | 0.185 |
| $Ce_{0.92}Sm_{0.08}O_2$ | 459.1 | – | 546.9 | 590.7 | – | 1349.9 | – | 0.271 |
| $Ce_{0.90}Sm_{0.10}O_2$ | 459.5 | – | 558.5 | 600.1 | 1175.2 | – | – | 0.123 |

[a] Vibrational modes corresponding to Second-order Scattering are given as per Ref. [46,47].

that with increasing doping fluency of $Sm^{3+}$ ions, $F_{2g}$ mode is shifted towards the lower wave-number side with the asymmetrical broadening of the mode. This may be attributed due to the cell expansion, inhomogeneous strain, phonon confinement and variation in phonon relaxation with the substitution of $Sm^{3+}$ ions in the $CeO_2$ lattice [48,49]. In Fig. 9 the characteristic band for $Sm_2O_3$ i.e. 345 $cm^{-1}$ is absent in the Raman spectra [50,51], clearly indicates the successful incorporation of $Sm^{3+}$ ions into the $CeO_2$ lattice, which is in agreement with XRD results. As incorporation of $Sm^{3+}$ ions in $CeO_2$ (for $x = 0.02$), 3 s-order Raman modes are detected at 537.1, 591.3 and 1364.6 $cm^{-1}$, where first two are assigned to the presence of oxygen vacancies generated into $CeO_2$ lattice due to incorporation of $Sm^{3+}$ ions and third mode is 3LO (third overtone band of longitudinal optic mode) mode.

Moreover, with increasing fluencies of $Sm^{3+}$ ions (for $x = 0.04$, 0.06, 0.08 and 0.10 doping concentrations) into $CeO_2$ lattice, the second-order Raman features near the value of ~548–558 $cm^{-1}$, associated with extrinsic oxygen vacancies induced by replacing $Ce^{4+}$ ions by $Sm^{3+}$ ions in order to maintain charge neutrality into $CeO_2$ NPs [52,53]. The possible disorder mechanism for extrinsic oxygen vacancies in Sm-doped $CeO_2$ NPs can be given as:

$$Sm_2O_3 + 2Ce_{Ce}^{x} + O_O^{x} \rightarrow 2Sm_{Ce}^{'} + V_O^{\cdot\cdot} + 2CeO_2 \quad (13)$$

where, symbols has the following meaning as; $Ce_{ce}^{x}$ and $Sm_{Ce}^{'}$ are $Ce^{4+}$ and $Sm^{3+}$ ions on the $CeO_2$ lattice site, respectively, $O_O^{x}$ is $O^{-2}$ ions on an oxygen lattice site, and $V_O^{\cdot\cdot}$ is neutral oxygen vacancy site.

Another oxygen vacancy peak can also be seen in the range of ~593–600 $cm^{-1}$ attributed to the defect space including intrinsic oxygen vacancies due to the presence of $Ce^{3+}$ ions as reported [54,55]. The possible disorder mechanism for the creation of intrinsic oxygen vacancies in the sample can be given as per the reaction [56]:

$$2Ce_{Ce}^{x} + O_O^{x} \rightarrow 2Ce_{Ce}^{'} + V_O^{\cdot\cdot} + 1/2O_2(g) \quad (14)$$

where, symbols has the following meaning as; $Ce_{ce}^{x}$ and $Ce_{Ce}^{'}$ are $Ce^{4+}$ and $Ce^{3+}$ ions on the Ce lattice site, respectively, $O_O^{x}$ is $O^{-2}$ ions on an oxygen lattice site, and $V_O^{\cdot\cdot}$ is neutral oxygen vacancy site [40]. Moreover, a band near ~1364-1349 $cm^{-1}$ is assigned to 3LO Raman mode, which is activated due to multiphonon relaxation by resonance Raman Effect [57]. The intensity of 3LO Raman mode is decreasing with fluencies of $Sm^{3+}$ ions in $CeO_2$ NPs from $x = 0.02$ to 0.08 and its peak is shifted near at ~1175 $cm^{-1}$ for $x = 0.10$ doping concentration, which is assigned for 2LO mode. The intensity of Raman peaks near ~548-558 $cm^{-1}$ and ~593-600 $cm^{-1}$ is increasing with $Sm^{3+}$ ions concentration from $x = 0.02$ to 0.06, which indicates that both extrinsic and intrinsic oxygen vacancies are increased with fluency of $Sm^{3+}$ ions, while for further doping fluencies ($x = 0.08$ and 0.10) the intensity of these peaks is decreased (shown in Fig. 9(b)). This behavior can be explained as, due to the incorporation of $Sm^{3+}$ ions, which substitutes $Ce^{4+}$ ions by creating $Ce^{3+}$ ions in the $CeO_2$ lattice, release the oxygen ions for maintaining the electroneutrality of the lattice system.

The particle size of $Ce_{1-x}Sm_xO_2$ NPs samples can also be calculated from Raman spectra using following equation:

$$\Gamma\left(cm^{-1}\right) = 10 + \left(\frac{124.7}{D}\right)nm \quad (15)$$

where $\Gamma$ ($cm^{-1}$) is FWHM of Raman active ($F_{2g}$) mode and D is particle size of $Ce_{1-x}Sm_xO_2$ NPs samples measured from TEM images [58,59]. The calculated particle size from Raman spectra is in good agreement with the particle size calculated by XRD spectra

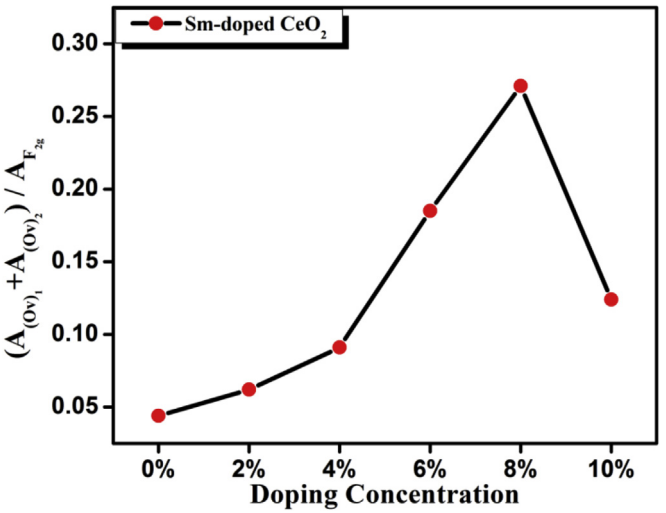


**Fig. 10.** Relative peak area ratio for bands of oxygen vacancies and $F_{2g}$ mode for $Ce_{1-x}Sm_xO_2$ ($x = 0.00$, 0.02, 0.04, 0.06, 0.08 and 0.10) nanoparticles.

and TEM images (as shown in Table 2). The quantitative estimation of the overall concentration of oxygen vacancies (intrinsic and extrinsic) is also calculated by the peak area of the oxygen vacancies $A_{O_v}$, $A_{(O_v)_1}$, $A_{(O_v)_2}$and $A_{F_{2g}}$ bands, which are corresponding to 598.5 $cm^{-1}$, ~548-558 $cm^{-1}$, ~593-600 $cm^{-1}$ and for the $F_{2g}$ band, respectively. The calculated values of $Ce_{1-x}Sm_xO_2$ NPs samples are tabulated in Table 3 and shown in Fig. 10. The relative peak area ratios are calculated by fitting the Lorentzian function for the corresponding oxygen vacancies mode and $F_{2g}$ mode [$A_{O_v}/A_{F2g}$ and $(A_{(O_v)_1} + A_{(O_v)_2})/A_{F2g}$ for pure $CeO_2$ and $Ce_{1-x}Sm_xO_2$ NPs samples for all doping ($x = 0.02$, 0.04, 0.06, 0.08 and 0.10), respectively], which reflect the relative oxygen vacancy concentration. It can be seen from Table 3 the relative peak area ratio is increased for $Ce_{1-x}Sm_xO_2$ samples from $x = 0.00$ to 0.08 and then decrease at $x = 0.10$ doping concentration, hence we can conclude that with increasing $Sm^{3+}$ ions fluency in the $CeO_2$, oxygen vacancies are gradually increased but at higher fluency ($x = 0.10$) they are found to decrease.

## 4. Conclusion

$CeO_2$ nanocrystalline samples of size 5–8 nm with different doping concentration ($x = 0.00$, 0.02, 0.04, 0.06, 0.08 and 0.10) of $Sm^{3+}$ ions are successfully synthesized by co-precipitation route of chemical synthesis, having *fcc* structure without having any impurity phases present in the lattice as confirmed by X-ray diffraction results. The crystallinity of $Ce_{1-x}Sm_xO_2$ samples is found to be increased after incorporation of $Sm^{3+}$ ions in the lattice up to a certain doping level after that it is found to be decreased. Further, it is also observed that the value of tensile strain is increasing, which is related to the promotion of oxygen vacancies due to incorporation of larger ionic radii $Sm^{3+}$ ions, which leads to increase in the lattice parameter and expansion of the $CeO_2$ lattice, which also promoted the $Ce^{3+}$ ions as well as oxygen vacancies with lattice expansion. We have also calculated the dislocation density, which also reveal the disordering in the $CeO_2$ lattice system after doping of $Sm^{3+}$ ions. As per our analysis of TEM images of $Ce_{1-x}Sm_xO_2$ samples the spherical-size crystalline nanoparticles in the size range of 5–8 nm are obtained, it is also confirmed that nanoparticles get agglomerated as the concentration of $Sm^{3+}$ ions is increased in $CeO_2$ NPs, finally leads to the crystal growth in $Ce_{1-x}Sm_xO_2$ samples. HRTEM images are also revealed that there is

no significance change in the interplanar distance (d) for (111) plane of $x = 0.00$, 0.04, 0.06 and 0.08 doping concentrations while for $x = 0.02$ and 0.10, it was changed and some dislocation can also be seen for $x = 0.10$ Sm-doped $CeO_2$ sample. SAED patterns indicated that nanosized particles are formed with low crystallinity, which is confirmed by the broadness of diffraction rings. Further from our UV–Vis–NIR spectrum, mainly originated from defect state existing extensively between the Ce 4f band and O 2p band, we can say that with the Sm doping in the $CeO_2$ NPs lattice, above the Mott critical density, the increased number of free electron concentration lead to fill Ce 4f level partially, which in turn blocks the lowest states available for occupancy and led to increase the band gap. Hence up to the Mott critical density, the band gap is found to decrease and above this, it starts to increase. Raman spectra are also shown to the formation of cubic fluorite structure of pure $CeO_2$ and Sm-doped $CeO_2$ samples without any impurity phases. Raman results are also further clarifying the presence of oxygen vacancies for pure $CeO_2$ NPs, which is found to increase with increasing doping of $Sm^{3+}$ ions (both intrinsic and extrinsic oxygen vacancies) but for further higher doping concentrations, it is found to decrease. Finally, in this manuscript we are able to show controlled band gap, size, grain morphology, controlled extrinsic and intrinsic oxygen vacancies with the rare earth cation Sm-doping in the $CeO_2$ lattice. The size and Sm-doping controlled morphologies, microstructure, and optical properties of $CeO_2$ nanoparticles can make these nanoparticles suitable alternatives for various applications like luminescent materials, oxygen transportation, catalysts, ultraviolet fuel cells, corrosion prevention etc. Further control on the density and nature of the oxygen vacancies can be used to provide a means to tailor the reactivity of ceria catalyst.

## Acknowledgement

One of the Author [Swati Soni] acknowledge Department of Science & Technology, Government of India for financial support vide Reference No. SR/WOS-A/PM-1021/2015, under Women Scientist Scheme-A (WOS-A), to carry out this work. Authors are also grateful to UGC-DAE CSR, Indore Centre vide project no. CSR-IC-BL-69/CSR-186/2016–17/850 for providing the support. Authors are also to the "Banasthali Centre for Research and Education in Basic Sciences" under CURIE programme supported by the Department of Science & Technology, Government of India, New-Delhi for providing the experimental measurements.

## References

[1] M. Radovic, Z.D. Dohcevic-Mitrovic, A. Golubovic, B. Matovic, M. Ščepanovic, Z.V. Popovic, Hydrothermal synthesis of $CeO_2$ and $Ce_{0.9}Fe_{0.1}O_2$; nanocrystals, Acta Phys. Pol. A 116 (4) (2009) 614–617.
[2] Lj S. Živkovic, V. Lair, O. Lupan, M. Cassir, A. Ringuedé, Samarium-doped ceria nanostructured thin films grown on FTO Glass by electrodeposition, Acta Phys. Pol. A 120 (2) (2011) 298–302.
[3] N.N. Dao, M. Dai Luu, Q.K. Nguyen, B.S. Kim, UV absorption by cerium oxide nanoparticles/epoxy composite thin films, Adv. Nat. Sci. Nanosci. Nanotechnol. 2 (4) (2011), 045013 (4pp).
[4] L.S. Živković, V. Lair, O. Lupan, A. Ringuedé, Electrochemical synthesis and properties of ceria films grown on stainless steel, Russ. J. Phys. Chem. 85 (13) (2011) 2358–2362.
[5] M. Balestrieri, S. Colis, M. Gallart, G. Schmerber, M. Ziegler, P. Gilliot, A. Dinia, Photoluminescence properties of rare earth (Nd, Yb, Sm, Pr)-doped $CeO_2$ pellets prepared by solid-state reaction, J. Mater. Chem. C 3 (27) (2015) 7014–7021.
[6] T.S. Zhang, J. Ma, L.B. Kong, P. Hing, J.A. Kilner, Preparation and mechanical properties of dense $Ce_{0.8}Gd_{0.2}O_{2-\delta}$, ceramics, Solid State Ionics 167 (1) (2004) 191–196.
[7] A. Akbari-Fakhrabadi, R.V. Mangalaraja, F.A. Sanhueza, R.E. Avila, S. Ananthakumar, S.H. Chan, Nanostructured Gd–$CeO_2$ electrolyte for solid oxide fuel cell by aqueous tape casting, J. Power Sources 218 (2012) 307–312.
[8] T. Mori, J. Drennan, J.H. Lee, J.G. Li, T. Ikegami, Oxide ionic conductivity and microstructures of Sm-or La-doped $CeO_2$-based systems, Solid State Ionics 154 (2002) 461–466.
[9] T. Mori, J. Drennan, Influence of microstructure on oxide ionic conductivity in doped $CeO_2$ electrolytes, J. Electroceram. 17 (2–4) (2006) 749–757.
[10] W. Huang, P. Shuk, M. Greenblatt, Hydrothermal synthesis and properties of $Ce_{1-x}Sm_xO_{2-x/2}$ and $Ce_{1-x}Ca_xO_{2-x}$ solid solutions, Chem. Mater. 9 (10) (1997) 2240–2245.
[11] V.V. Ursaki, V. Lair, L. Živković, M. Cassir, A. Ringuede, O. Lupan, Optical properties of Sm-doped ceria nanostructured films grown by electrodeposition at low temperature, Opt. Mater. 34 (11) (2012) 1897–1901.
[12] W. Lee, S.Y. Chen, Y.S. Chen, C.L. Dong, H.J. Lin, C.T. Chen, A. Gloter, Defect structure guided room temperature ferromagnetism of Y-Doped $CeO_2$ Nanoparticles, J. Phys. Chem. C 118 (45) (2014) 26359–26367.
[13] K. Kaviyarasu, P.P. Murmu, J. Kennedy, F.T. Thema, D. Letsholathebe, L. Kotsedi, M. Maaza, Structural, optical and magnetic investigation of Gd implanted $CeO_2$ nanocrystals, Nucl. Instrum. Methods Phys. Res. Sect. B Beam Interact. Mater. Atoms (2017). https://doi.org/10.1016/j.nimb.2017.02.055.
[14] S.Y. Chen, R.J. Chen, W. Lee, C.L. Dong, A. Gloter, Spectromicroscopic evidence of interstitial and substitutional dopants in association with oxygen vacancies in Sm-doped ceria nanoparticles, Phys. Chem. Chem. Phys. 16 (7) (2014) 3274–3281.
[15] E. Swatsitang, S. Phokha, S. Hunpratub, S. Maensiri, Characterization of Sm-doped $CeO_2$ nanoparticles and their magnetic properties, Phys. B Condens. Matter 485 (2016) 14–20.
[16] V. Butler, C.R.A. Catlow, B.E.F. Fender, J.H. Harding, Dopant ion radius and ionic conductivity in cerium dioxide, Solid State Ionics 8 (2) (1983) 109–113.
[17] S. Soni, V.S. Vats, Sudhish Kumar, B. Dalela, M. Mishra, R.S. Meena, G. Gupta, P.A. Alvi, S. Dalela, Structural, optical and magnetic properties of Fe-doped $CeO_2$ samples probed using x-ray photoelectron spectroscopy, J. Mater. Sci. Mater. Electron. (2018) 1–13, https://doi.org/10.1007/s10854-018-9060-x.
[18] W. Lee, S.Y. Chen, E. Tseng, A. Gloter, C.L. Chen, Study of defect structure in ferromagnetic nanocrystalline $CeO_2$: effect of ionic radius, J. Phys. Chem. C 120 (27) (2016) 14874–14882.
[19] S. Soni, S. Kumar, R.S. Meena, V.S. Vats, S. Dalela, Interplay of structural, optical and magnetic properties in Gd doped $CeO_2$, in: AIP Conference Proceedings, 1665, 2015, 130029.
[20] D.R. Ou, T. Mori, F. Ye, T. Kobayashi, J. Zou, G. Auchterlonie, J. Drennan, Oxygen vacancy ordering in heavily rare-earth-doped ceria, Appl. Phys. Lett. 89 (17) (2006), 171911.
[21] P. Kumar, P. Kumar, A. Kumar, I. Sulania, F. Chand, K. Asokan, Structural, optical and magnetic properties of N ion implanted $CeO_2$ thin films, RSC Adv. 7 (15) (2017) 9160–9168.
[22] B. Mandal, A. Mondal, S.S. Ray, A. Kundu, Sm doped mesoporous $CeO_2$ nanocrystals: aqueous solution-based surfactant assisted low temperature synthesis, characterization and their improved autocatalytic activity, Dalton Trans. 45 (4) (2016) 1679–1692.
[23] C. Levy, C. Guizard, A. Julbe, Soft-chemistry synthesis, characterization, and stabilization of CGO/$Al_2O_3$/Pt nanostructured composite powders, J. Am. Ceram. Soc. 90 (3) (2007) 942–949.
[24] M. Jamshidijam, R.V. Mangalaraja, A. Akbari-Fakhrabadi, S. Ananthakumar, S.H. Chan, Effect of rare earth dopants on structural characteristics of nano-ceria synthesized by combustion method, Powder Technol. 253 (2014) 304–310.
[25] L. Truffault, M.T. Ta, T. Devers, K. Konstantinov, V. Harel, C. Simmonard, C. Andreazza, I.P. Nevirkovets, A. Pineau, O. Veron, J.P. Blondeau, Application of nanostructured Ca doped $CeO_2$ for ultraviolet filtration, Mater. Res. Bull. 45 (5) (2010) 527–535.
[26] W.M.A. El Rouby, A.A. Farghali, A. Hamdedein, Microwave synthesis of pure and doped cerium (IV) oxide ($CeO_2$) nanoparticles for methylene blue degradation, Water Sci. Technol. 74 (10) (2016) 2325–2336.
[27] V.N. Morris, R.A. Farrell, A.M. Sexton, M.A. Morris, Lattice constant dependence on particle size for ceria prepared from a citrate sol-gel, J. Phys. Conf. 26 (1) (2006) 119–122.
[28] P. Bindu, S. Thomas, Estimation of lattice strain in ZnO nanoparticles: X-ray peak profile analysis, J. Theor. Appl. Phy. 8 (4) (2014) 123–134.
[29] R. Murugan, G. Vijayaprasath, T. Mahalingam, G. Ravi, Enhancement of room temperature ferromagnetic behavior of rf sputtered Ni-$CeO_2$ thin films, Appl. Surf. Sci. 390 (2016) 583–590.
[30] D. Ma, Z. Lu, Y. Tang, T. Li, Z. Tang, Z. Yang, Effect of lattice strain on the oxygen vacancy formation and hydrogen adsorption at $CeO_2$(111) surface, Phys. Lett. 378 (34) (2014) 2570–2575.
[31] M. Nolan, V.S. Verdugo, H. Metiu, Vacancy formation and CO adsorption on gold-doped ceria surfaces, Surf. Sci. 602 (16) (2008) 2734–2742.
[32] İ. Uslu, A. Aytimur, M.K. Öztürk, S. Koçyiğit, Synthesis and characterization of neodymium doped ceria nanocrystalline ceramic structures, Ceram. Int. 38 (6) (2012) 4943–4951.
[33] L. Truffault, M.T. Ta, T. Devers, K. Konstantinov, V. Harel, C. Simmonard, C. Andreazza, I.P. Nevirkovets, A. Pineau, O. Veron, J.P. Blondeau, Application of nanostructured Ca doped $CeO_2$ for ultraviolet filtration, Mater. Res. Bull. 45 (5) (2010) 527–535.
[34] N.S. Arul, D. Mangalaraj, P.C. Chen, N. Ponpandian, C. Viswanathan, Strong quantum confinement effect in nanocrystalline cerium oxide, Mater. Lett. 65 (17) (2011) 2635–2638.
[35] Z. Wang, Z. Quan, J. Lin, Remarkable changes in the optical properties of $CeO_2$ nanocrystals induced by lanthanide ions doping, Inorg. Chem. 46 (13) (2007)

5237–5242.
[36] B. Choudhury, A. Choudhury, Lattice distortion and corresponding changes in optical properties of $CeO_2$ nanoparticles on Nd doping, Curr. Appl. Phys. 13 (1) (2013) 217–223.
[37] M.S. Hosseini, F. Belador, Investigation on structural, optical, and magnetic properties of Dy-Doped-$CeO_2$ nanoparticles synthesized by microwave-induced combustion method, Synth. React. Inorg. Metal-Org. Nano-Metal Chem. 46 (6) (2016) 950–957.
[38] R.C. Deus, J.A. Cortés, M.A. Ramirez, M.A. Ponce, Juan Andres, L.S.R. Rocha, Elson Longo, A.Z. Simoes, Photoluminescence properties of cerium oxide nanoparticles as a function of lanthanum content, Mater. Res. Bull. 70 (2015) 416–423.
[39] P. Nagaraju, Y.V. Kumar, M.R. Reddy, C.V. Reddy, V.R. Reddy, D.M. Phase, Indore-India UGC-DAE-CSR. Preparation, Micro structural characterization and Optical characterization of pure and Gd-doped ceria thin films, Int. J. Sci. Eng. Res. 5 (3) (2014) 185–190. ISSN 2229–5518.
[40] X. Niu, F. Tu, Hydrothermal synthesis, optical and magnetic properties of $CeO_2$ nanosheets with some cracks in their wafery centre, J. Mater. Sci. Mater. Electron. 28 (2) (2017) 2141–2146.
[41] A.C. Cabral, L.S. Cavalcante, R.C. Deus, E. Longo, A.Z. Simoes, F. Moura, Photoluminescence properties of praseodymium doped cerium oxide nanocrystals, Ceram. Int. 40 (3) (2014) 4445–4453.
[42] R. Zamiri, H.A. Ahangar, A. Kaushal, A. Zakaria, G. Zamiri, D. Tobaldi, J.M.F. Ferreira, Correction: dielectrical properties of $CeO_2$ nanoparticles at different temperatures, PLoS One 10 (7) (2015) e0131851.
[43] C. Zhang, F. Meng, L. Wang, Controlled synthesis and magnetic properties of bowknot-like $CeO_2$ microstructures by a CTAB-assisted hydrothermal method, Mater. Lett. 119 (2014) 1–3.
[44] S. Aškrabić, Z.D. Dohčević-Mitrović, M. Radović, M. Šćepanović, Z.V. Popović, Phonon–phonon interactions in $Ce_{0.85}Gd_{0.15}O_{2-\delta}$ nanocrystals studied by Raman spectroscopy, J. Raman Spectrosc. 40 (6) (2009) 650–655.
[45] S.A. Acharya, V.M. Gaikwad, V. Sathe, S.K. Kulkarni, Influence of gadolinium doping on the structure and defects of ceria under fuel cell operating temperature, Appl. Phys. Lett. 104 (11) (2014), 113508.
[46] W.H. Weber, K.C. Hass, J.R. McBride, Raman study of $CeO_2$: second-order scattering, lattice dynamics, and particle-size effects, Phys. Rev. B 48 (1) (1993) 178.
[47] A.C. Cabral, L.S. Cavalcante, R.C. Deus, E. Longo, A.Z. Simões, F. Moura, Photoluminescence properties of praseodymium doped cerium oxide nanocrystals, Ceram. Int. 40 (3) (2014) 4445–4453.
[48] F. Meng, J. Gong, Z. Fan, H. Li, J. Yuan, Hydrothermal synthesis and mechanism of triangular prism-like monocrystalline $CeO_2$ nanotubes via a facile template-free hydrothermal route, Ceram. Int. 42 (4) (2016) 4700–4708.
[49] S.F. Wang, C.T. Yeh, Y.R. Wang, Y.C. Wu, Characterization of samarium-doped ceria powders prepared by hydrothermal synthesis for use in solid state oxide fuel cells, J. Mater. Res. Technol. 2 (2) (2013) 141–148.
[50] Y.U. Jinqiu, C.U.I. Lei, H.E. Huaqiang, Y.A.N. Shihong, H.U. Yunsheng, W.U. Hao, Raman spectra of $RE_2O_3$ (RE = Eu, Gd, Dy, Ho, Er, Tm, Yb, Lu, Sc and Y): laser-excited luminescence and trace impurity analysis, J. Rare Earths 32 (1) (2014) 1–4.
[51] P. Sathishkumar, R.V. Mangalaraja, T. Pandiyarajan, M.A. Gracia-Pinilla, N. Escalona, C. Herrera, R. Garcia, Low frequency ultrasound assisted sequential and co-precipitation syntheses of nanoporous RE (Gd and Sm) doped cerium oxide, RSC Adv. 5 (29) (2015) 22578–22586.
[52] A.G.M.D. Silva, T.S. Rodrigues, A. Dias, H.V. Fajardo, R.F. Gonçalves, M. Godinho Júnior, P.A.R. Dutenhefner, $Ce_{1-x}Sm_xO_{1.9-\delta}$ nanoparticles obtained by microwave-assisted hydrothermal processing: an efficient application for catalytic oxidation of α-bisabolol, Catal. Sci. Technol. 4 (2014) 814–821.
[53] C. Thiabdokmai, A. Tangtrakarn, S. Promsuy, P. Ngiewlay, C. Mongkolkachit, Templateless synthesis and characterization of hollow gadolinium doped cerium oxide nanofibers by electrospinning, Adv. Mate. Sci. Eng. 2014 (2014), 127531, https://doi.org/10.1155/2014/127531, 10 pages.
[54] L.D. Jadhava, M.G. Chourashiya, A.P. Jamale, A.U. Chavan, S.P. Patil, Synthesis and characterization of nano-crystalline $Ce_{1-x}Gd_xO_{2-x/2}$ ($x = 0–0.30$) solid solutions, J. Alloy. Comp. 506 (2) (2010) 739–744.
[55] R. Kostić, S. Aškrabić, Z. Dohčević-Mitrović, Z.V. Popović, Low-frequency Raman scattering from $CeO_2$ nanoparticles, Appl. Phys. Mater. Sci. Process 90 (4) (2008) 679–683.
[56] M. Kamiya, E. Shimada, Y. Ikuma, M. Komatsu, H. Haneda, Intrinsic and extrinsic oxygen diffusion and surface exchange reaction in cerium oxide, J. Electrochem. Soc. 147 (3) (2000) 1222–1227.
[57] T. Taniguchi, T. Watanabe, N. Sugiyama, A.K. Subramani, H. Wagata, N. Matsushita, M. Yoshimura, Identifying defects in ceria-based nanocrystals by UV resonance Raman spectroscopy, J. Phys. Chem. C 113 (46) (2009) 19789–19793.
[58] B. Choudhury, A. Choudhury, $Ce^{3+}$ and oxygen vacancy mediated tuning of structural and optical properties of $CeO_2$ nanoparticles, Mater. Chem. Phys. 131 (3) (2012) 666–671.
[59] S. Phoka, P. Laokul, E. Swatsitang, V. Promarak, S. Seraphin, S. Maensiri, Synthesis, structural and optical properties of $CeO_2$ nanoparticles synthesized by a simple polyvinyl pyrrolidone (PVP) solution route, Mater. Chem. Phys. 115 (1) (2009) 423–428.

# *Structural, optical and magnetic properties of Fe-doped $CeO_2$ samples probed using X-ray photoelectron spectroscopy*

**Swati Soni, V. S. Vats, Sudhish Kumar, B. Dalela, Monu Mishra, R. S. Meena, Govind Gupta, P. A. Alvi & S. Dalela**

**Journal of Materials Science: Materials in Electronics**

ISSN 0957-4522

J Mater Sci: Mater Electron
DOI 10.1007/s10854-018-9060-x

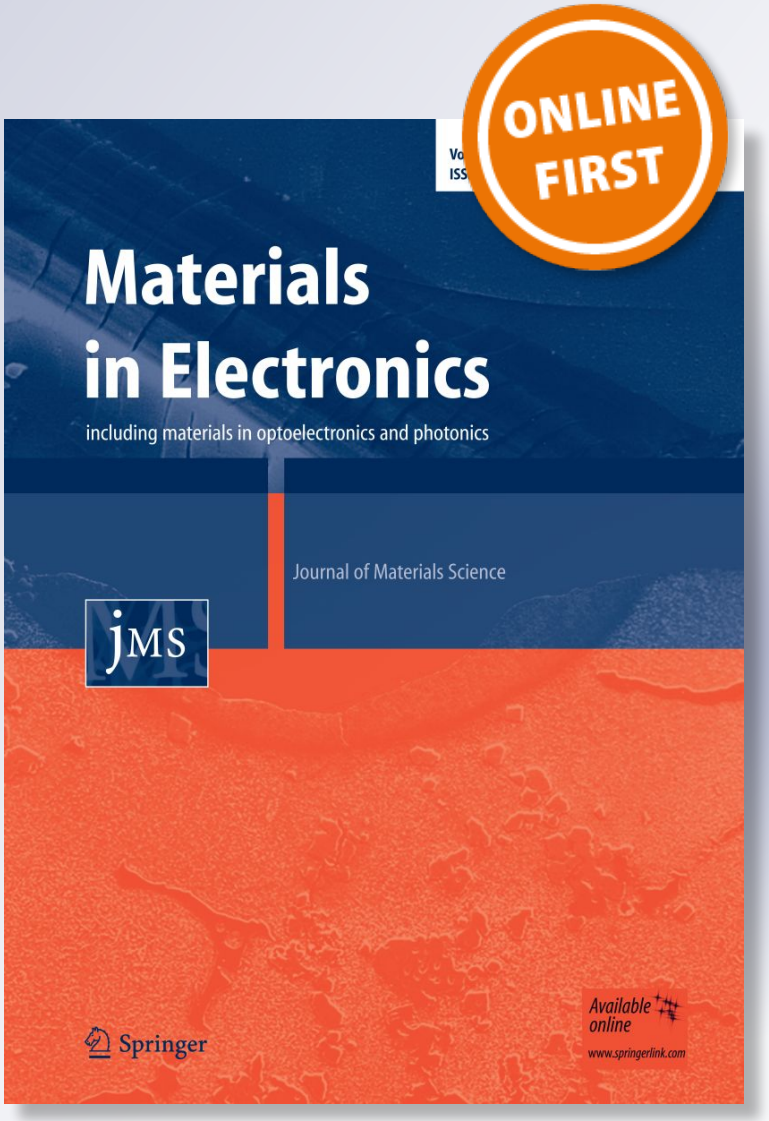


Springer

Journal of Materials Science: Materials in Electronics
https://doi.org/10.1007/s10854-018-9060-x

# Structural, optical and magnetic properties of Fe-doped $CeO_2$ samples probed using X-ray photoelectron spectroscopy

Swati Soni[1] · V. S. Vats[2] · Sudhish Kumar[3] · B. Dalela[4] · Monu Mishra[5] · R. S. Meena[5] · Govind Gupta[5] · P. A. Alvi[2] · S. Dalela[1]

Received: 5 January 2018 / Accepted: 5 April 2018


**Abstract**
The present study reports the effect of Fe-doping on the structural, optical, magnetic and electronic properties of polycrystalline $CeO_2$ (for 5 and 10% doping concentration of Fe-cation) samples synthesized by low-temperature solid-state reaction method. Rietveld refinement of the X-ray diffraction patterns establishes fluorite-type face-centred cubic structure of the Fe-doped $CeO_2$ samples and also confirms successful incorporation of Fe ions in the $CeO_2$ lattice. The UV–Vis–NIR absorption spectra displays reduce band gap energy with rising fluency of Fe-ions, which confirm red shifts in the Fe-doped $CeO_2$ samples. The electronic structure of the pure $CeO_2$ and Fe-doped $CeO_2$ polycrystalline samples have been investigated by X-ray photoemission spectroscopy (XPS). The XPS spectra of Ce 3d reveals the reduction of $Ce^{4+}$ to $Ce^{3+}$ states Fe-doped $CeO_2$ samples, which are well supported by the Fe 2p and O 1s spectra. Pure polycrystalline $CeO_2$ displays diamagnetic behaviour at room temperature. Interestingly, 5% Fe-doped $CeO_2$ sample displays S-shape hysteresis loop and establishes room temperature ferromagnetism, whereas, 10% Fe-doped $CeO_2$ sample shows weak ferromagnetic behaviour. A decrement is observed in the magnetization on increasing the doping concentration. The possible reason for ferromagnetism in the Fe-doped $CeO_2$ samples may be incorporation of oxygen vacancies, which are further discussed using F-centre exchange mechanism and double exchange interaction. These experimental findings offer potential opportunities for spintronics and optoelectronics applications by integrating them into device structures and evaluating their performance as a function of their material properties.

## 1 Introduction

Intense research investigations on the ferromagnetism in dilute magnetic semiconductors (DMS) are being pursued due to their potential applications in the field of spintronics, magneto-optoelectronic devices and magnetic sensors [1, 2]. Basically, DMS are non-magnetic semiconductors but can display room temperature ferromagnetism (RTFM) when doped with small percentages of magnetic elements such as transition metals (TM). These metals can be easily integrated with existing semiconductors, making semiconducting materials highly spin polarised. Therefore, TM doped DMS materials are considered as promising materials for spintronics applications due to theoretically predicated high Curie temperature ($T_c$) [3]. Some studies have been focused on RTFM in thin film and nanocrystalline samples of DMS materials, such as ZnO [4–7], $TiO_2$ [8, 9], $SnO_2$ [2], $In_2O_3$ [10], CuO [11] and $CeO_2$ [12] doped with TM. In these studies, it was reported that ferromagnetism arises due to the presence of oxygen vacancies on the surface or on the interface of the samples which is generated by surface defects or cluster formation. Among these systems, $CeO_2$ has received special attention due to its applications in various industrial fields such as solid oxide fuel cells, catalysis, ceramic materials and oxygen sensors [13, 14].

The nature of magnetism shown by $CeO_2$ is quite different for different forms of material synthesis. Such as, $CeO_2$

✉ S. Dalela
sdphysics@rediffmail.com

[1] Department of Pure & Applied Physics, University of Kota, Kota 324005, India

[2] Department of Physics, Banasthali University, Newai, India

[3] Department of Physics, Mohanlal Sukhadia University, Udaipur 313002, India

[4] Department of Physics, Govt. Khetan Polytechnic College, Jhalana Dungri, Jaipur, India

[5] CSIR-National Physical Laboratory, Dr. K.S. Krishnan Road, New Delhi 110012, India

Published online: 10 April 2018

nanoparticles show paramagnetism at ambient temperatures [15], but bulk $CeO_2$ exhibits diamagnetic behaviour [16]. Besides this, TM and rare earth (RE) doped $CeO_2$ shows ferromagnetic behaviour at room temperature. Dimri et al [15] have reported RTFM in the RE (Nd, Sm, Gd, Tb, Er and Dy) doped $CeO_2$ bulk samples, which is associated to the oxygen vacancies created by the RE dopants. Brito et al. [17] have reported weak ferromagnetism caused by the formation of oxygen vacancies, in 0.5 and 1% Fe-doped $CeO_2$ nanoparticles. However, the origin of RTFM for thin film and $CeO_2$ nanoparticles is explained on the basis of F-centre exchange mechanism (FCE) but it is still a matter of controversy. Almeida et al. [18] have reported that $Ce_{1-x}Fe_xO_2$ nanocrystals ($0 < x < 0.05$) samples showed weak RTFM with increasing Fe-content, which can be associated with the formation of the magnetic cluster. As recently, Rakhmatullin et al. [19] have reported RTFM in nanocrystalline $CeO_2$, which may be caused by the defects on the surface of the nanoparticles, is explained by the charge-transfer mechanism supported by electron paramagnetic resonance study, rather than FCE mechanism. Since, the cause of magnetism in pure and doped $CeO_2$ samples is either from magnetically ordered spin of 3d dopants or the defects at the surface [20]. However, limited reports are available so far, which are supported the FCE mechanism and double exchange interaction for explaining the origin of RTFM in Fe-doped polycrystalline $CeO_2$ sample [21–23]. Therefore, in this present scenario, a systematic study is required to be undertaken on the $CeO_2$ samples doped with Fe-ions to better understand the reason behind RTFM in these samples.

In this article, we have synthesized $Ce_{1-x}Fe_xO_2$ (for $x = 0.00$, 0.05 and 0.10) samples using low-temperature solid-state reaction method. Investigations on the structural, optical, magnetic and electronic structure properties have been carried out using X-ray diffraction (XRD), UV–Vis–NIR optical absorption spectroscopy, DC magnetization using vibrating sample magnetometer (VSM) and X-ray photoelectron spectroscopy (XPS) measurements.

## 2 Experimental details

Polycrystalline $Ce_{1-x}Fe_xO_2$ (for $x = 0.00$, 0.05 and 0.10) samples were prepared using the conventional low-temperature solid-state reaction route. In the solid-state diffusion process, the stoichiometric proportions of cerium oxide and iron powders (purity better than 4N, purchased from Sigma Aldrich) were mixed thoroughly using an agate pestle and mortar and then calcinated for 15 h at 500 °C in a microprocessor controlled furnace. The obtained polycrystalline precursors were crushed to a fine powder form and then were pressed into Pellets using a hydraulic pressure of nearly 6 tons and then sintered at 500 °C in Ar atmosphere. The phase purity and crystalline structure of the samples were determined using XRD and for data analysis, the Rietveld profile refinements of the XRD patterns were carried out using the FULLPROF Program. The XPS spectra were recorded on an ultrahigh vacuum based Omicron Multiprobe Surface analysis System (Germany, Gmbh) operating at a base pressure of $5 \times 10^{-11}$ Torr. Mg Kα radiation source (with the energy of 1253.6 eV) was used for data acquisition of various core levels. An OMICRON EA125 hemispherical analyzer equipped with a 7 channeltron parallel detection unit was used to collect the XPS spectra. The calibration of binding energy in photoemission spectra was done referring to standard Au $4f_{7/2}$ emission line with the energy resolution of ~0.9 eV FWHM on Au $4f_{7/2}$ with the pass energy of 20 eV during the measurement. Magnetization measurements were carried out on Lake Shore make VSM. Optical absorption spectra were recorded on a Perkin-Elmer Lambda make (Model: 750) UV–Vis–NIR spectrophotometer with pre-aligned Tungsten, Halogen, and Deuterium sources.

## 3 Results and discussion

### 3.1 XRD analysis

Figure 1 presents the indexed powder XRD patterns of $Ce_{1-x}Fe_xO_2$ (for $x = 0.00$, 0.05 and 0.10) polycrystalline samples. All the observed nine Bragg peaks in the XRD patterns corresponding to the fluorite-type face-centred cubic structure of $CeO_2$ are assigned to the Miller indices (111), (200), (220), (311), (222), (400), (331), (420) and (422). Absence of any un-indexed peaks corresponding to secondary phase related to Fe-based impurities such as FeO, $Fe_2O_3$, or $Fe_3O_4$ in Fe-doped $CeO_2$ samples confirms the single phase formation of $Ce_{1-x}Fe_xO_2$ (for $x = 0.05$ and 0.10) samples [24]. However, the changes in the intensity peaks of $CeO_2$ have been clearly observed with Fe-doping. The larger intensity peak has been observed for 5% Fe-doped $CeO_2$, while the intensity peak decreases for 10% Fe-doped $CeO_2$ sample. The decreasing intensity peak indicates that Ce ions are transferred to the interstitial sites due to the substitution of $Fe^{2+}$ or $Fe^{3+}$ ions at $Ce^{4+}$ sites and which are also responsible for decreasing the atomic concentration in these planes. To get a clear enhanced view and shifting of peaks, we have plotted the diffraction pattern in a limited 2θ range in the vicinity of the most intense Bragg reflection (111) (see Fig. 1). This plot establishes that increase in Fe-doping (from 5 to 10%) leads to shifting the Bragg peaks towards the higher angle side. These observations further confirm the good incorporation of Fe ions in the $CeO_2$ matrix and decrease in the unit cell volume as shown in Table 1.

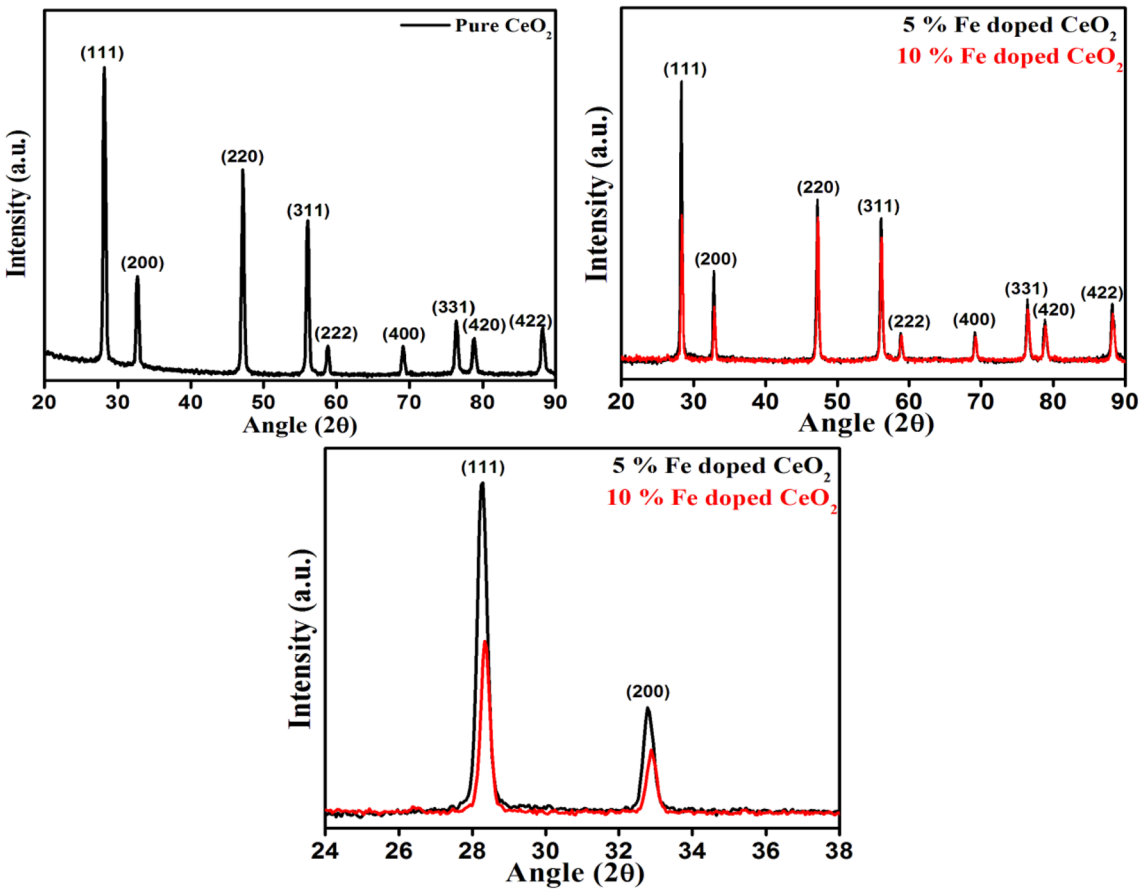


**Fig. 1** XRD spectra for pure $CeO_2$, 5 and 10% Fe-doped polycrystalline $CeO_2$ samples

**Table 1** Rietveld profile refinement results $Ce_{1-x}Fe_xO_2$ (for $x = 0.00$, 0.05 and 0.10) polycrystalline samples in the space group of *Fm3m*

| Sample $Ce_{1-x}Fe_xO_2$ | Lattice parameter $a$ (Å) | Unit cell volume $V$ (Å$^3$) | $R_p$ | $R_{wp}$ | $R_{exp}$ | $\chi^2$ | $R_{Bragg}$ |
|---|---|---|---|---|---|---|---|
| Pure $CeO_2$ | 5.4025(7) | 157.66(3) | 2.78 | 3.56 | 2.98 | 1.43 | 4.35 |
| $Ce_{0.95}Fe_{0.05}O_2$ | 5.4053(7) | 157.92(3) | 4.15 | 5.40 | 3.56 | 2.30 | 6.32 |
| $Ce_{0.90}Fe_{0.1}O_2$ | 5.4044(6) | 157.85 (3) | 3.80 | 4.91 | 3.36 | 2.13 | 6.38 |

### 3.1.1 Rietveld profile refinement

The Rietveld refinement of the of the XRD patterns of polycrystalline samples of $Ce_{1-x}Fe_xO_2$ (for $x = 0.00$, 0.05 and 0.10) are carried out in the space group of *Fm3m*, in which Ce atoms are located at 4*a* position, surrounded by eight oxygen (located at 8b) positions. The best fitted XRD patterns shows good agreement between the experimental relative intensities and simulated intensities for all the samples, as presented in Fig. 2.

The data analysis further confirms that the observed Bragg reflections are consistent with the fluorite-type face-centered cubic structure of $CeO_2$ and rules out the presence of any impurity crystalline or amorphous phases. The analysis reveals that Fe doping in $CeO_2$ does not affect the cubic fluorite structure of the $CeO_2$, which further confirms the formation of a single phase in $Ce_{1-x}Fe_xO_2$ (for $x = 0.05$ and 0.10) lattice. The best fitted values of the lattice parameter, unit cell volume and agreement factors like: $R_p$, $R_{wp}$, $R_{exp}$, $R_{Bragg}$, and $\chi^2$ are given in Table 1. The results show that the lattice parameter of the powder samples changes with Fe concentration ($x$). The reported cubic lattice parameter ($a$) for bulk $CeO_2$ is 5.411 Å [25] and, the obtained lattice parameters for our Fe-doped $CeO_2$ samples are found to be slightly smaller than the reported value for pure bulk $CeO_2$ (see Table 1).

It can be observed that the value of lattice parameter is slightly decreasing with increasing Fe-content in $CeO_2$. These

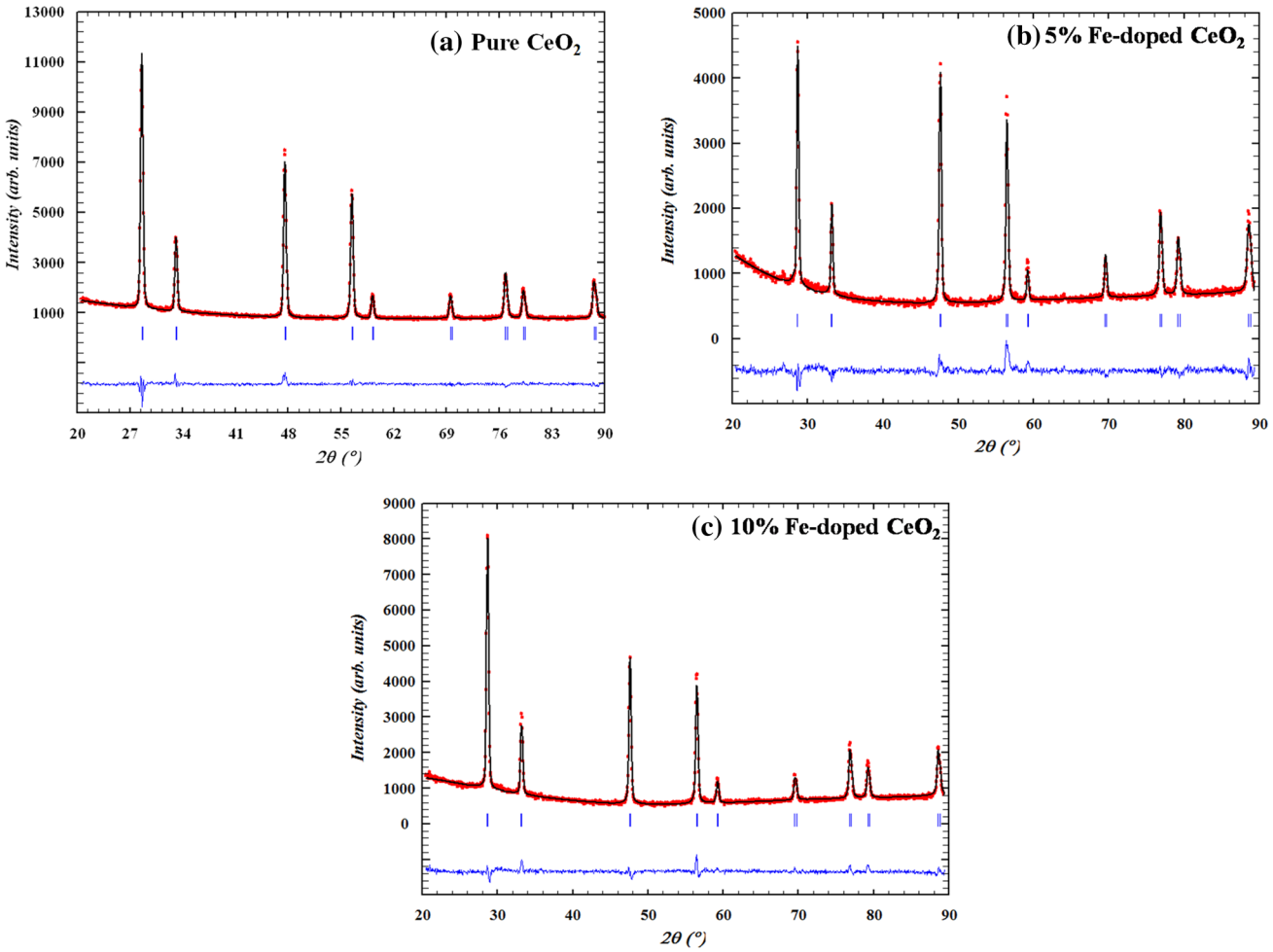


**Fig. 2** Rietveld refined and fitted XRD patterns of **a** pure $CeO_2$, **b** 5% Fe-doped $CeO_2$ and **c** 10% Fe-doped $CeO_2$ polycrystalline samples at 300 K. Observed (calculated) profiles are shown by dotted (solid) lines. The short vertical marks represent Bragg reflections. The lower curve is the difference plot

slight changes are possible due to the replacement of the larger radii $Ce^{4+}$ ions (0.92 Å) by a smaller radii $Fe^{2+}$ ions (0.78 Å) or $Fe^{3+}$ (0.65 Å) ions in the crystal lattice [1]. Moreover, it is also observed that fluency of Fe-ions in $CeO_2$ leads to decrease in the unit cell volume. However, the change in the lattice parameter with the fluency of Fe content can also be related to the formation of defects such as oxygen vacancies on lattice sites, which are being further discussed in details with our XPS analysis.

## 3.2 X-ray photoemission spectroscopy (XPS)

### 3.2.1 XPS spectra in Ce 3d region

XPS measurements are used to analyze the chemical composition and valence state of Ce 3d, Fe 2p and O 1s in the $Ce_{1-x}Fe_xO_2$ (for $x = 0.00$, 0.05 and 0.10) polycrystalline samples. Ce 3d region in XPS spectra is used to determine the core level electronic nature of the samples as well as the chemical state of the Ce element. The Ce 3d XPS spectra for pure $CeO_2$ and $Ce_{1-x}Fe_xO_2$ (for $x = 0.05$ and 0.10) polycrystalline samples with six distinct peaks are shown in Fig. 3.

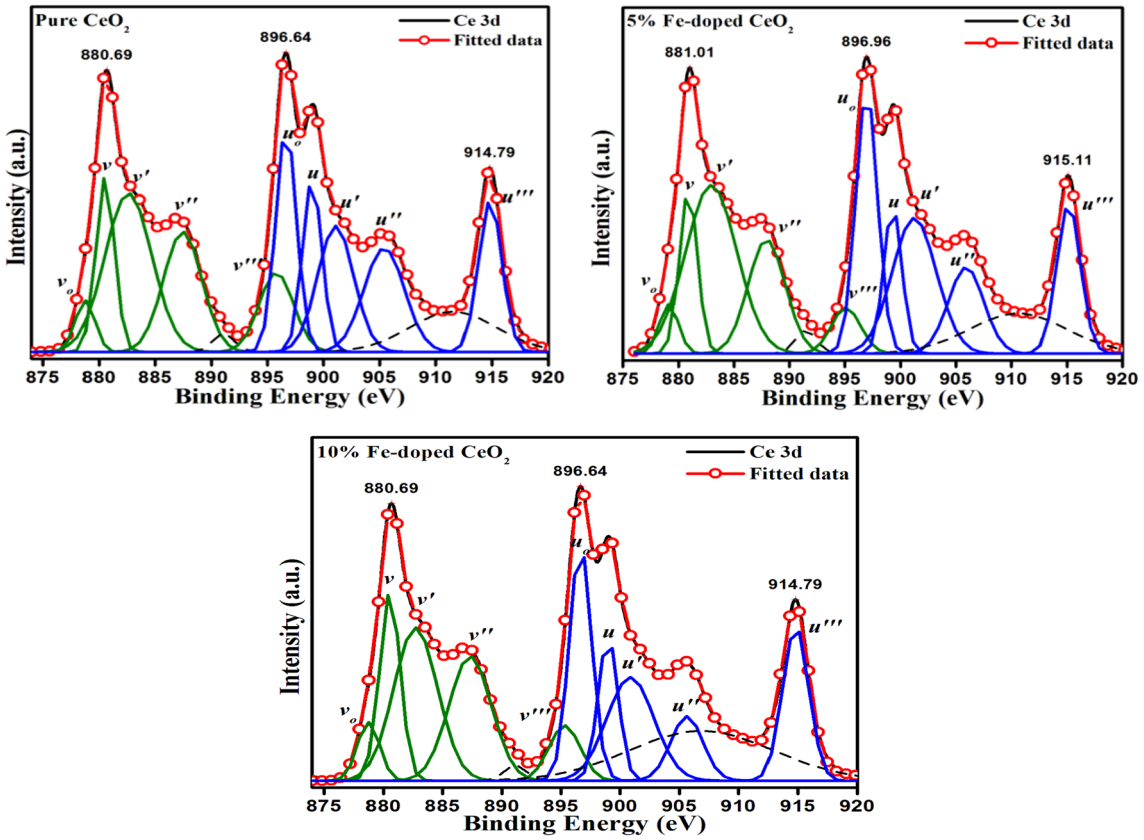


**Fig. 3** Ce 3d XPS spectra for pure $CeO_2$, 5 and 10% Fe-doped $CeO_2$ polycrystalline samples

In pure $CeO_2$ total ten Gaussian peaks fittings have been reported by the researchers [26] and hence we have also fitted ten distinct Gaussian peaks in Ce 3d XPS spectra for our pure $CeO_2$, $Ce_{0.95}Fe_{0.05}O_2$ and $Ce_{0.90}Fe_{0.10}O_2$ polycrystalline samples. These multiple peaks are reported to be arisen from the occupancy of Ce 4f levels in final states [27].

The sets of peaks are labelled as $u$ and $v$ corresponding to the spin–orbit doublets of Ce $3d_{3/2}$ and Ce $3d_{5/2}$ core holes energy to 898.9 and 880.5 eV (for pure $CeO_2$), 899.3 and 880.8 eV (for $Ce_{0.95}Fe_{0.05}O_2$), 898.9 and 880.5 eV (for $Ce_{0.90}Fe_{0.10}O_2$), respectively. In case of Ce(IV) oxide, the spin–orbit splitting energy for peaks $u$ and $v$ for pure $CeO_2$, $Ce_{0.95}Fe_{0.05}O_2$ and $Ce_{0.90}Fe_{0.10}O_2$ samples is about 18.4, 18.5 and 18.4 eV [28], respectively. Whereas, in case of Ce(III) oxide, Ce 3d spectra have been reported to consist of two pairs of doublets, labeled as $u_o$, $v_o$, $u'$ and $v'$ [29]. The binding energies of all peaks are shown in Table 2 as obtained from XPS spectra. The concentrations of both oxidation states $Ce^{3+}$ and $Ce^{4+}$ in $Ce_{1-x}Fe_xO_2$ (for $x = 0.00$, 0.05 and 0.10) polycrystalline samples are obtained using the following expression as reported in Ref. [30],

$$\%\ Ce^{3+} = \frac{A_{Ce^{3+}}}{A_{Ce^{3+}} + A_{Ce^{4+}}} \times 100\% \quad (1)$$

$$\%Ce^{4+} = \frac{A_{Ce^{4+}}}{A_{Ce^{3+}} + A_{Ce^{4+}}} \times 100\% \quad (2)$$

where $A_{Ce^{3+}} = v_o + v' + u_o + u'$ and $A_{Ce^{4+}} = v + v'' + v''' + u + u'' + u'''$ are the sum of the integrated intensity of the Gaussian peaks of various final states.

The characteristics peak denoted by $u_o$ ($v_o$) and $u'$ ($v'$) are reported as the two final states of $Ce^{3+}$ ions containing Ce ($3d^9\ 4f^2$) O $2p^5$ and Ce ($3d^9\ 4f^1$) O $2p^6$ respectively, whereas those marked by $u$ ($v$), $u''$ ($v''$) and $u'''$ ($v'''$) are also reported as the three final states of $Ce^{4+}$ ions containing Ce ($3d^9\ 4f^2$) O $2p^4$, Ce ($3d^9\ 4f^1$) O $2p^5$, and Ce ($3d^9\ 4f^0$) O $2p^6$ respectively [31]. The peak denoted by $u'''$ associated to the Ce $3d_{3/2}$ is the fingerprint of $Ce^{4+}$ state in all samples [28]. So from the details mentioned above, we can say that all the samples have both $Ce^{3+}$ and $Ce^{4+}$ oxidation states for Ce-ions. The calculated $Ce^{3+}/Ce^{4+}$ ratios of the samples are shown in Table 2, which shows that concentration of $Ce^{3+}$ states are gradually increasing whereas $Ce^{4+}$ states are decreasing for $Ce_{0.95}Fe_{0.05}O_2$ sample. However, the results so obtained for $Ce_{0.90}Fe_{0.10}O_2$ sample are not following the same fashion. These results indicate that both $Ce^{3+}$ and $Ce^{4+}$

**Table 2** The binding energies of all components of Ce 3d and $Ce^{3+}/Ce^{4+}$ ratios calculated from of Ce 3d XPS spectra for $Ce_{1-x}Fe_xO_2$ (for $x = 0.00$, 0.05 and 0.10) polycrystalline samples

| Sample $Ce_{1-x}Fe_xO_2$ | Peak assignment Binding energy (eV) | | | | | | | | | | $Ce^{3+}$ (%) | $Ce^{4+}$ (%) | $Ce^{3+}/Ce^{4+}$ |
|---|---|---|---|---|---|---|---|---|---|---|---|---|---|
| | Ce $3d_{5/2}$ | | | | | Ce $3d_{3/2}$ | | | | | | | |
| | $v_o\ Ce^{3+}$ | $v\ Ce^{4+}$ | $v'\ Ce^{3+}$ | $v''\ Ce^{4+}$ | $v'''\ Ce^{4+}$ | $u_o\ Ce^{3+}$ | $u\ Ce^{4+}$ | $u'\ Ce^{3+}$ | $u''\ Ce^{4+}$ | $u'''\ Ce^{4+}$ | | | |
| Pure $CeO_2$ | 878.7 | 880.7 | 882.5 | 887.4 | 895.7 | 896.6 | 898.9 | 901.1 | 905.3 | 914.8 | 44.88 | 55.11 | 0.81 |
| $Ce_{0.95}Fe_{0.05}O_2$ | 879.1 | 881.0 | 882.9 | 887.9 | 895.1 | 896.9 | 899.3 | 901.2 | 905.9 | 915.1 | 54.53 | 45.46 | 1.91 |
| $Ce_{0.90}Fe_{0.10}O_2$ | 878.7 | 880.7 | 882.7 | 887.3 | 895.3 | 896.6 | 898.9 | 900.8 | 905.6 | 914.8 | 47.68 | 52.31 | 0.91 |

states are present in the samples but the percentage of 3+ and 4+ states are being altered with the fluency of Fe-ions in the Fe-doped $CeO_2$ samples. This variation indicates that there is a transition between $Ce^{4+}$ to $Ce^{3+}$ states, which may be due to the substitution of $Ce^{4+}$ ions by $Fe^{3+}$ ions.

In addition, the integrated ratio $Ce^{3+}/Ce^{4+}$ increased for $Ce_{0.95}Fe_{0.05}O_2$, which may indicate the formation of oxygen vacancies at the lattice site to maintain the charge neutrality when $Ce^{4+}$ states changes to $Ce^{3+}$ states [32]. The formation of oxygen vacancies plays an important role in the development of RTFM in the $Ce_{0.95}Fe_{0.05}O_2$ sample. Moreover, the integrated ratio $Ce^{3+}/Ce^{4+}$ for $Ce_{0.90}Fe_{0.10}O_2$ is found to decrease, which may indicate that $Ce^{3+}$ states change to $Ce^{4+}$ states in the sample, which further represents the decrease in oxygen vacancies on the lattice site of the $Ce_{0.90}Fe_{0.10}O_2$ sample. Therefore, the RTFM is found to decrease in the $Ce_{0.90}Fe_{0.10}O_2$ samples, as discussed in the magnetic properties section. The effect of oxygen vacancies on the $Ce_{1-x}Fe_xO_2$ (for $x = 0.00$, 0.05 and 0.10) polycrystalline samples is further discussed in O 1s XPS spectra in the next section.

### 3.2.2 O 1s XPS spectra

The O 1s spectra for $Ce_{1-x}Fe_xO_2$ (for $x = 0.00$, 0.05 and 0.10) polycrystalline samples are shown in Fig. 4. The XPS spectra of O 1s region are used to reveal the information about the absorbed oxygen, lattice oxygen, oxygen vacancies and surface hydroxyl group ($OH^-$) [33, 34].

In Fig. 4, all the O 1s spectra show asymmetric peaks, which are further fitted with two Gaussian peaks, labelled as $I_1$ and $I_2$ for pure $CeO_2$, $Ce_{0.95}Fe_{0.05}O_2$ and $Ce_{0.90}Fe_{0.10}O_2$ samples. The peak ($I_1$) at lower binding energy ~528.6–528.8 eV may be assigned to $O^{2-}$ ions in the cubic structure associated with the lattice oxygen, whereas the peak ($I_2$) at higher binding energy ~530.9 eV may be attributed to the $O^{2-}$ ions in the oxygen-deficient region [31, 35]. It can be seen from Fig. 4, peak ($I_1$) shift slightly towards higher binding energy (up to ~0.2 eV) for $Ce_{0.95}Fe_{0.05}O_2$ sample, whereas no peak shifting is observed for $Ce_{0.90}Fe_{0.10}O_2$ sample. The contribution of peak $I_1$ and $I_2$ in O 1s spectra is shown in Table 3, which indicates that due to the incorporation of Fe-ions on the Ce site, the lattice oxygen is decreased while oxygen vacancies are increased in $Ce_{0.95}Fe_{0.05}O_2$sample as concluded from Ce 3d spectra analysis. This indicates that smaller size $Fe^{3+}$ ion replaces the bigger size $Ce^{4+}$ ion and for maintaining the charge neutrality $Ce^{4+}$ ions are reduced to $Ce^{3+}$ ions, which may be accompanied by the formation of the oxygen vacancies in $Ce_{0.95}Fe_{0.05}O_2$ sample. This could also be attributed from the spectra that the peak $v'$ shows an increase in the concentration of $Ce^{3+}$ ions while peak $u'''$ highlight decrement in the concentration of $Ce^{4+}$ ions in the Ce 3d spectra

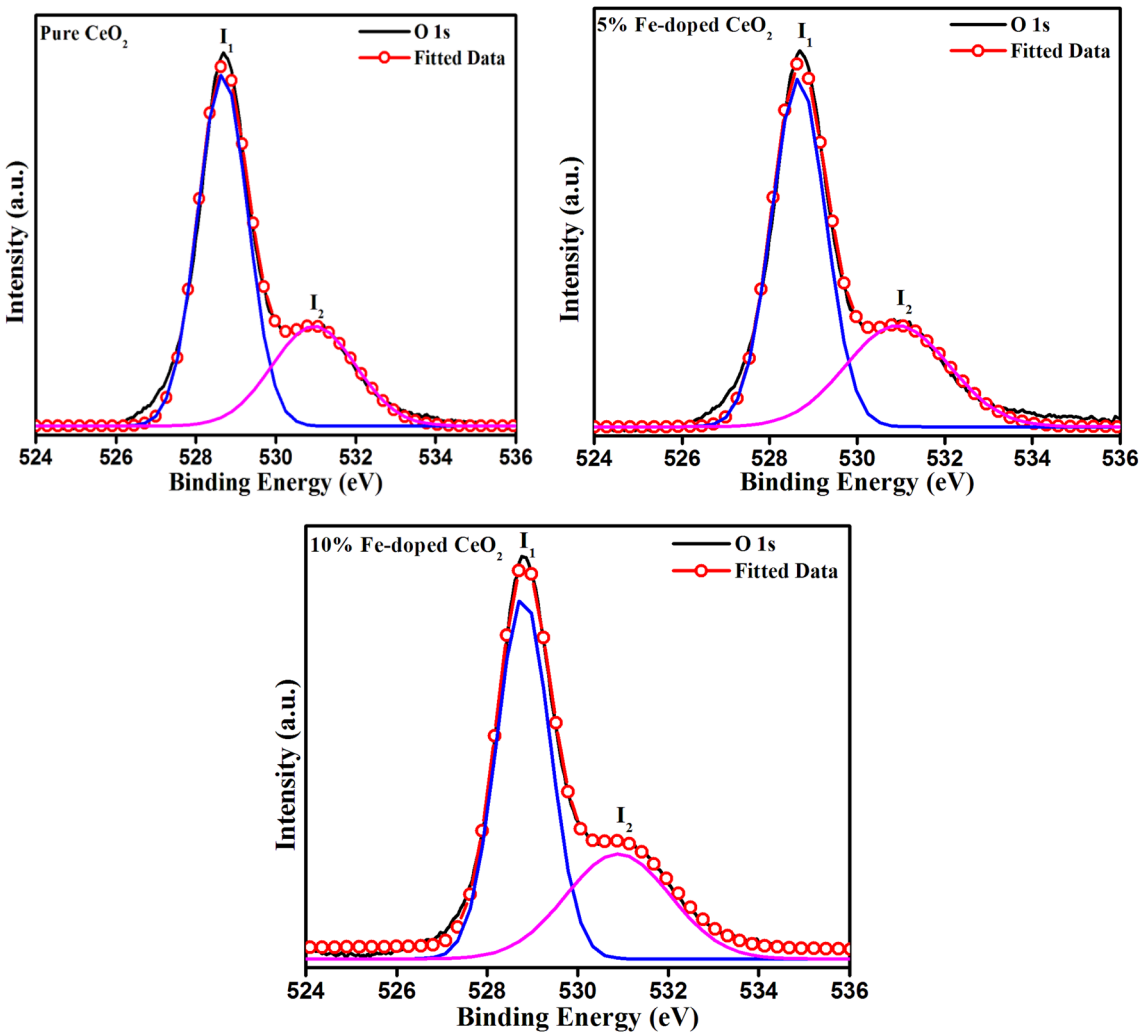


**Fig. 4** O 1s XPS spectra for pure $CeO_2$, 5% Fe-doped $CeO_2$ and 10% Fe-doped $CeO_2$ samples

**Table 3** The area ratio of the peak $A_{I_2}/A_{I_1}$ of O 1s XPS spectra for the entire samples

| Sample | Peak position Binding energy (eV) | | $A_{I_2}/A_{I_1}$ |
|---|---|---|---|
| | $I_1$ | $I_2$ | |
| Pure $CeO_2$ | 528.6 | 530.9 | 0.47 |
| $Ce_{0.95}Fe_{0.05}O_2$ | 528.6 | 530.9 | 0.55 |
| $Ce_{0.90}Fe_{0.1}O_2$ | 528.8 | 530.9 | 0.39 |

[32]. However, for $Ce_{0.90}Fe_{0.10}O_2$ sample the lattice oxygen is increasing, while the oxygen vacancies are decreasing, which indicates the reduction of $Ce^{3+}$ ions to $Ce^{4+}$ ions.

Apart from this, while increasing the doping concentration the electrostatic repulsion between Fe–Fe ions increases which in turn increases the interaction between Fe and ligand oxygen. Due to this, $O^{2-}$ ions again occupy their position and oxygen vacancy gets suppressed. Moreover, the area ratio of the peak $A_{I_2}/A_{I_1}$ is also representing the formation of oxygen vacancies in $Ce_{0.95}Fe_{0.05}O_2$ sample and decrement of oxygen vacancies in $Ce_{0.90}Fe_{0.10}O_2$ sample. The calculated values are shown in Table 3.

Besides this, the existence of $Fe^{3+}$ or $Fe^{2+}$ state in $Ce_{0.90}Fe_{0.10}O_2$ sample may also affect the suppression of oxygen vacancies, which is further discussed in Fe 2p XPS spectra.

### 3.2.3 Fe 2p XPS spectra

The Fe 2p XPS spectra for Fe-doped polycrystalline $CeO_2$ samples are shown in Fig. 5.

Fe 2p XPS spectra shows Fe $2p_{3/2,1/2}$core levels at binding energies 709.5 and 723.1 eV for $Ce_{0.95}Fe_{0.05}O_2$ sample. The position of binding energies is showing a clear evidence of $Fe^{3+}$ oxidation states for $Ce_{0.95}Fe_{0.05}O_2$ sample

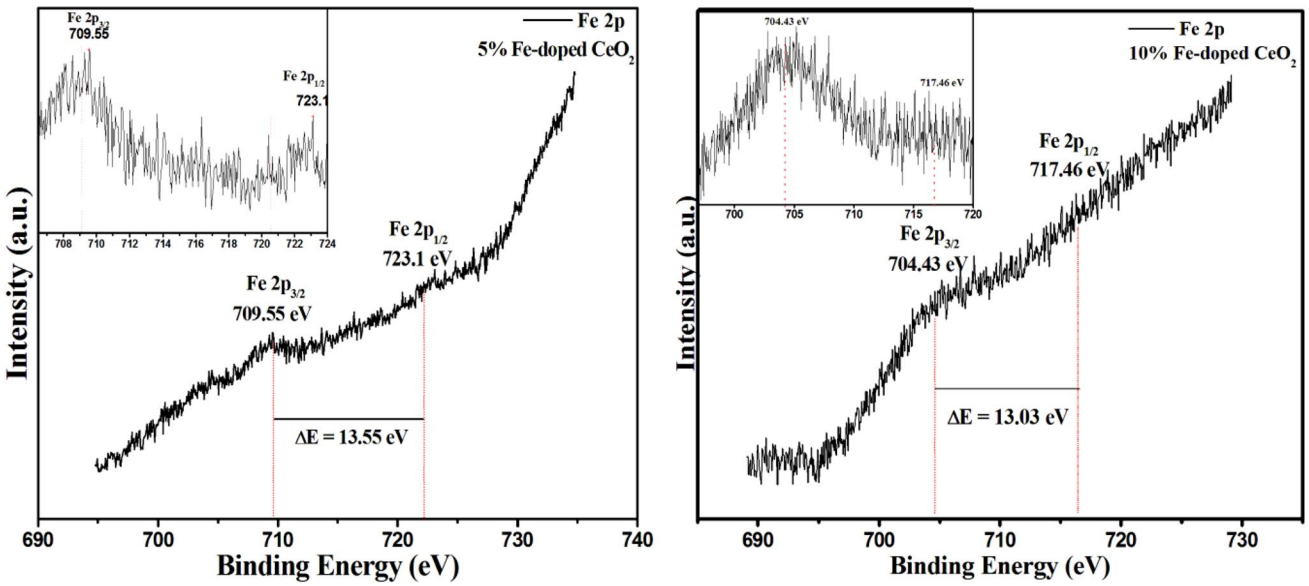


**Fig. 5** Fe 2p XPS spectra for 5% Fe-doped $CeO_2$ and 10% Fe-doped $CeO_2$ samples

[31, 36, 37]. While as the Fe contents are further increased in $Ce_{0.90}Fe_{0.10}O_2$ sample, core level Fe $2p_{3/2,1/2}$ spectra are shifted towards the lower binding energy side at 704.4 and 717.4 eV, respectively, which may be due to decrement in $Fe^{3+}$ states. This decrease in $Fe^{3+}$ states may be related to the difference in the energy separation of Fe $2p_{3/2}$ and Fe $2p_{1/2}$ peaks, which are 13.55 and 13.05 eV, for $Ce_{0.95}Fe_{0.05}O_2$ and$Ce_{0.90}Fe_{0.10}O_2$ samples, respectively. This difference in the binding energy of the core level peaks is attributed to the changing electro-negativity of the ligands. As the electro-negativity of the ligand decreases, the electron density surrounding the Fe ion increases, which establishes that nucleus is more shielded. Therefore, less energy is required to promote Fe 3d electron to the unfilled Fe 4s orbital [38]. Due to this reason, $Fe^{3+}$ states change in $Fe^{2+}$ states. The existence of $Fe^{3+}$ states plays an important role in the ferromagnetic interaction of our $Ce_{0.95}Fe_{0.05}O_2$and $Ce_{0.90}Fe_{0.10}O_2$ samples.

## 3.3 Magnetic behaviour

### 3.3.1 Field dependent dc magnetization measurements

Figure 6, shows the field dependence of magnetization (M–H curve) for pure $CeO_2$ and $Ce_{1-x}Fe_xO_2$ (for $x = 0.05$ and 0.10) polycrystalline samples. It can be seen that pure polycrystalline $CeO_2$ sample exhibit a diamagnetic behaviour with $4f^0$ electronic configuration of $Ce^{4+}$ ions, which has been previously reported for the bulk samples of $CeO_2$, $Al_2O_3$, ZnO, $In_2O_3$, and $SnO_2$ [16]. However, 5% Fe-doping in $CeO_2$ results in an appreciable enhancement in the magnetization. The observed S-shaped hysteresis loop in this sample clearly, indicating towards dominated ferromagnetic states in this 5% Fe-doped sample. Thus the magnetic behaviour of the pure bulk $CeO_2$ to 5% Fe-doped $CeO_2$ samples has changed from diamagnetic to ferromagnetic. Surprisingly, when Fe concentration is increased from 5 to 10% the ferromagnetic ordering seems to be suppressed.

However, M-H curves in these two Fe doped samples do not get saturated up to the maximum applied magnetic field, which is an indication of high magnetocrystalline anisotropy in these samples. These observations are suggestive of weak ferromagnetic ordering in these two Fe doped samples and also in case of 10% Fe-doped $CeO_2$ paramagnetic behaviour can be seen to be dominating over the ferromagnetic ordering. Previously it has been reported by Sharma et al. [22], that the magnetization of the Fe-doped bulk $CeO_2$ samples (at 300 K) is changed with different concentration (1, 3 and 5%) of Fe contents.

## 3.4 Optical behaviour

### 3.4.1 UV–Vis–NIR absorption measurements

Figure 7a shows the UV–Vis–NIR absorption spectra for pure $CeO_2$ and $Ce_{1-x}Fe_xO_2$ (for $x = 0.05$ and 0.10) polycrystalline samples. Below 400 nm the maximum absorption can be observed for pure $CeO_2$, 5 and 10% Fe-doped polycrystalline $CeO_2$, which may arise due to charge-transfer transition from $O^{2-}$ (2p) (valence band) and 4f, 5d states of $Ce^{4+}$ (4f) energy levels in $CeO_2$, indicating that $Ce^{4+}$ overlaps with $4f^15d^1$ states of $Ce^{3+}$ ion, which is popularly known as f–f spin–orbit splitting of Ce 4f states [39, 40].

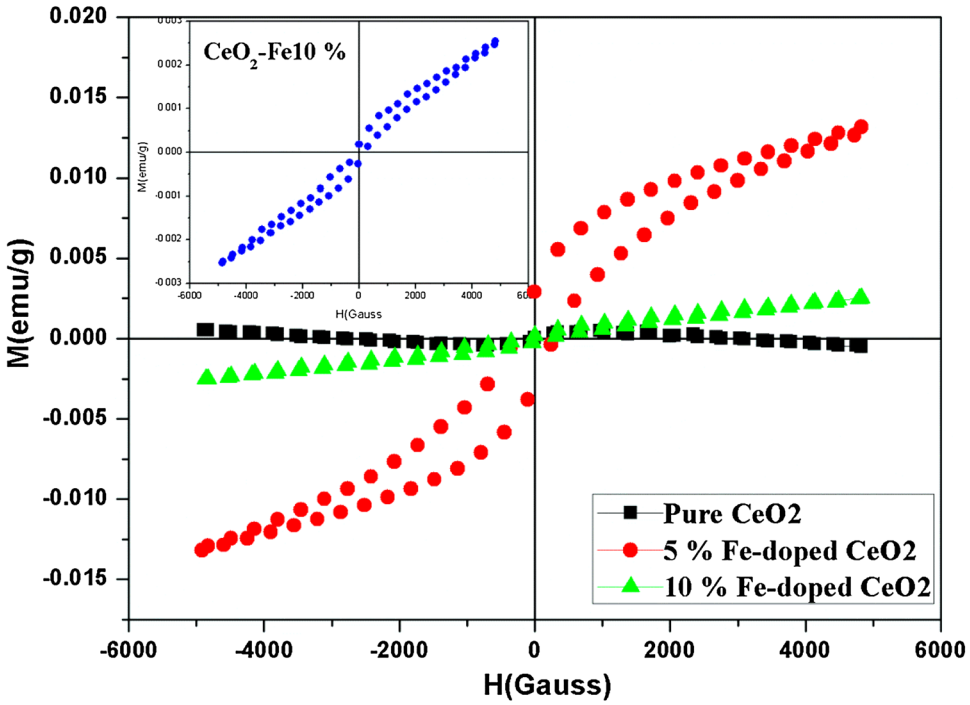


**Fig. 6** Magnetization (M) versus magnetic field (H) hysteresis curve for a pure $CeO_2$, 5 and 10% Fe-doped $CeO_2$ samples

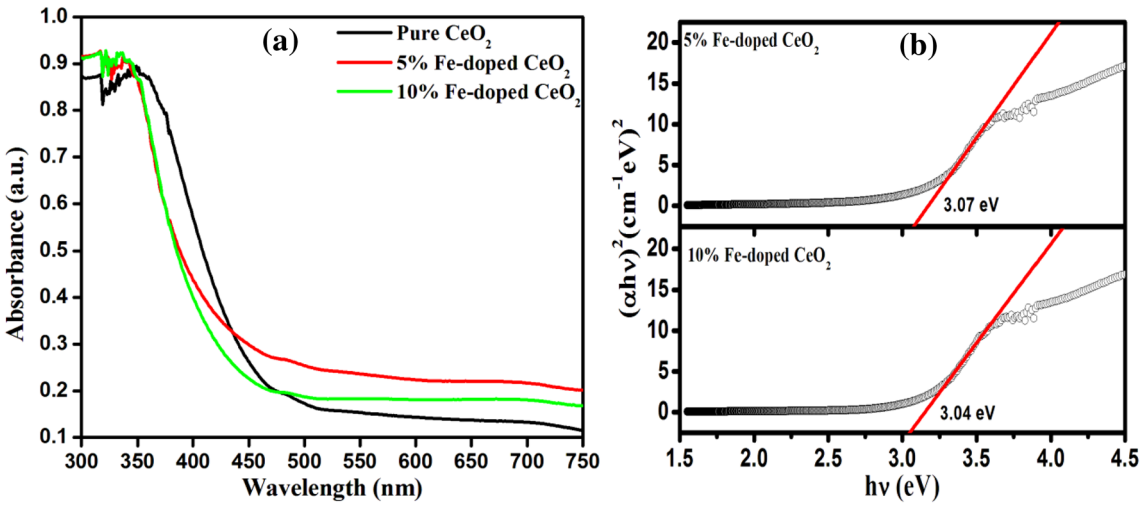


**Fig. 7** UV–Vis–NIR absorption spectra of **a** 5 and 10% Fe-doped $CeO_2$ and **b** Tauc's Plot of $(\alpha h\nu)^2$ versus photon energy ($h\nu$)

The direct band gap ($E_g$) is determined by extrapolating the curve $(\alpha h\nu)^2$ versus $h\nu$ to zero absorption (Tauc's plot), which has been shown in Fig. 6b, which is given as [41],

$$\alpha h\nu = A\,(h\nu - E_g)^m \tag{3}$$

where $\alpha$ = Absorption coefficient (which can be calculated by $\alpha = 2.303A/d$ and $\alpha$ is replaced by k/s.), h = Planck's constant, $\nu$ = frequency of incidence light, $E_g$ = optical band gap of material and m = factor affecting the direct or indirect transition of electrons from the valance band to conduction band (m can have values 1/2, 3/2, 2 and 3 depending up on the mode of inter band transition i.e. direct allowed, direct forbidden, indirect allowed and indirect forbidden transition, respectively).

The refractive index of Fe-doped $CeO_2$ samples is calculated using the following formula [42] and shown in Table 4:

$$\frac{n^2-1}{n^2+2} = 1 - \sqrt{\frac{E_g}{20}} \tag{4}$$

**Table 4** Values of the estimated band-gap energy and refractive index from absorption spectra

| Sample | Band gap energy $E_g$ (eV) | Refractive index (n) |
|---|---|---|
| $CeO_2$ | 3.10 | 2.20 |
| $Ce_{0.95}Fe_{0.05}O_2$ | 3.07 | 2.37 |
| $Ce_{0.90}Fe_{0.10}O_2$ | 3.04 | 2.38 |

where n is the refractive index of the material and $E_g$ is the optical band gap energy. From the calculations, it is clear that the refractive index increases with increasing Fe contents in $CeO_2$ samples, which indicates that structure of the Fe-doped samples becomes denser as appears from the volume reduction with Fe doping from our XRD analysis also.

The calculated value of band gap energy ($E_g$) by Tauc's plot for pure $CeO_2$ and $Ce_{1-x}Fe_xO_2$ (for $x=0.05$ and 0.10) polycrystalline samples shows a shifting towards the lower energy side i.e. red shift, which is shifted about ~0.03 eV for 10% Fe-doped sample in comparison to 5% Fe-doped $CeO_2$ sample. This red shift in the band gap energy ($E_g$) of pure $CeO_2$ and $Ce_{1-x}Fe_xO_2$ (for $x=0.05$ and 0.10) polycrystalline samples may be attributed to the surface and interface effects. Due to the incorporation of the Fe-ions, $Fe^{2+}$ or $Fe^{3+}$ ions occupy the Ce-sites. For maintaining the charge neutrality, some lattice defects such as oxygen vacancies are introduced on the Ce site in the Fe-doped samples. These defects are considered to play an important role in establishing the ferromagnetism in the Fe-doped $CeO_2$ samples. From Fig. 7a an observable increase in the absorbance with increasing Fe contents can be easily seen. This increase in absorbance is attributed to the lattice disorder and defect induced structure in the sample lattice. However, further increases in doping of Fe ions for 10% Fe-doped $CeO_2$ sample decreases the band gap energy ($E_g$) as shown in Table 4, which may be attributed to the formation of trap levels between the conduction and valence band of $CeO_2$. These levels are originated from the oxygen vacancy defect states and electronic states of $Fe^{3+}$ ions [43].

## 3.5 Discussion

Generally, the ferromagnetic behaviour in the TM doped $CeO_2$ samples can be attributed to the formation of oxygen vacancies as observed in $CeO_2$ doped with Co [44], Ni [45], Cr [46] and Zn [47]. In these studies, the ferromagnetic behaviour is reported to be associated with the FCE mechanism, in which the oxygen vacancies traps an electron to form F-centre between the TM dopant ions. Since, bulk $CeO_2$ is an insulator oxide with $Ce^{4+}$ in the $4f^0$ configuration, which induces anti-ferromagnetic ordering due to super-exchange coupling [23]. But when $CeO_2$ is doped with divalent or trivalent ions ($Fe^{2+}$ or $Fe^{3+}$), oxygen vacancies are formed to maintain the charge neutrality to support the magnetic behaviour.

In the present study, XRD and XPS results are in support to confirm the formation of oxygen vacancy due to the incorporation of $Fe^{3+}$ ions on the Ce site. It is well known that $CeO_2$ can be used as the storage medium and oxygen vacancies can easily be formed in Fe-doped bulk $CeO_2$ during the grinding or annealing process as reported experimentally [22]. Now, during the incorporation of Fe ions in the bulk $CeO_2$ sample, oxygen vacancies are formed near the Fe ions, which may contribute to the ferromagnetic ordering in $Ce_{0.95}Fe_{0.05}O_2$ sample. This ferromagnetic behaviour in $Ce_{0.95}Fe_{0.05}O_2$ sample may be explained on account of FCE coupling between oxygen vacancy and Fe ions.

Our XRD and XPS results clearly show the evidence of substitution of $Fe^{3+}$ ions on Ce sites and Ce ions in 3+ oxidation states (with $4f^1$ configuration) may be attributed to the oxygen vacancy formation. This $4f^1$ configuration produces exchange interaction between the spin of $Ce^{3+}$ ion and oxygen vacancy at the surface, forming a direct ferromagnetic coupling between Ce ions like $Ce^{3+} - \nabla - Ce^{3+}$, where $\nabla$ denotes oxygen vacancy. Due to incorporation of $Fe^{3+}$ (with $3d^5$ configuration) ions with low-spin states, which have only unoccupied minority spin orbitals with spin-up (↑) state, are trapped with electrons in oxygen vacancy with spin down (↓) state. According to the Pauli Exclusion Principle and Hund's rule, the oxygen vacancy may be coupled between the two neighbouring $Fe^{3+}$ ions like $Fe^{3+} - \nabla - Fe^{3+}$. This FCE coupling forms bound magnetic polarons (BMP's), which are reported to overlap neighbouring BMP's and produce a long-range ferromagnetic coupling in $Ce_{0.95}Fe_{0.05}O_2$ sample [23], as shown in Fig. 8.

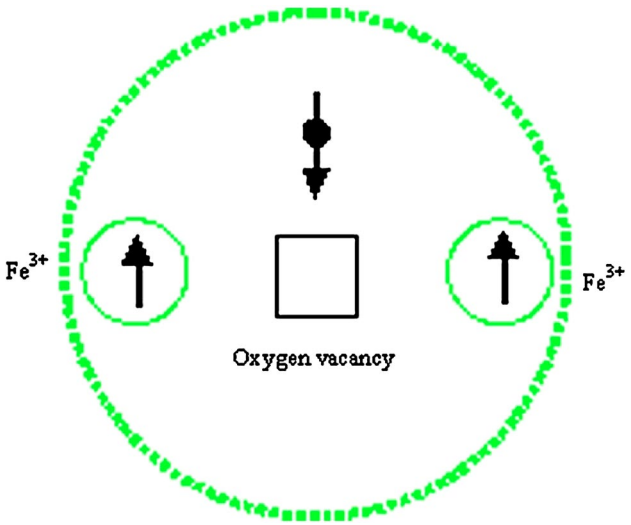


**Fig. 8** F-centre exchange interaction for $Ce_{0.95}Fe_{0.05}O_2$ sample [48]

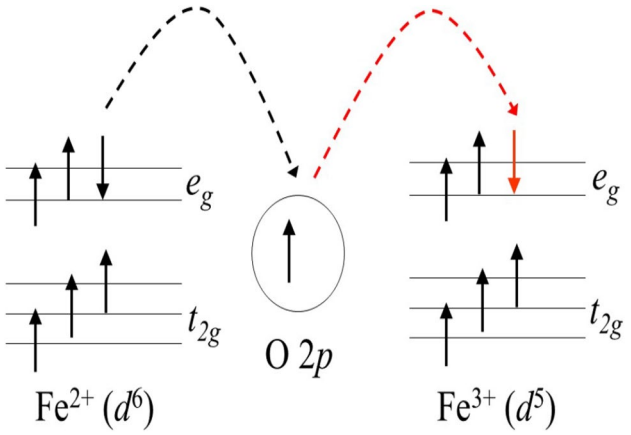


**Fig. 9** Illustration of double exchange interaction in $Ce_{0.90}Fe_{0.10}O_2$ sample [48]

This ferromagnetic coupling between $Fe^{3+}$ ions and oxygen vacancy may be attributed to originate the ferromagnetism in the $Ce_{0.95}Fe_{0.05}O_2$ sample. But this ferromagnetic ordering may get destroyed with further increase in the doping of Fe ions and decreases in $Ce_{0.90}Fe_{0.10}O_2$ sample, which can be clearly seen from the M–H curve.

Now, the double exchange interaction may be proposed for explaining the decrement of the ferromagnetic contribution in $Ce_{0.90}Fe_{0.10}O_2$ sample [23, 49, 50]. It has been already confirmed by Fe 2p XPS spectra that $Fe^{3+}$ states are converted into the $Fe^{2+}$ state with increasing the doping concentration of Fe-ions in $Ce_{0.90}Fe_{0.10}O_2$ sample. Since, $Fe^{3+}$ ion has five electrons in d-subshell, whose spins are parallel to one another as dictated by Hund's rule, whereas, $Fe^{2+}$ ion has an additional spin down electron occupying d-subshell. The electron transport between $Fe^{2+}$ and $Fe^{3+}$ ions occur via oxygen ion (such as $Fe^{2+} - O^{2-} - Fe^{3+}$) is known as the double exchange interaction. In this interaction the extra electron at the $Fe^{2+}$ site can hop into the $Fe^{3+}$ site only those spins are parallel to each other. This process cause delocalization of this extra electron hence increases its bandwidth and minimizes the kinetic energy [49]. Thus, this interaction tends to couple the ions ferromagnetically but cannot produce long-range magnetic order because of the less concentration of $Fe^{3+}$ ions in the structure, which may cause the suppression of the magnetic properties of $Ce_{0.90}Fe_{0.10}O_2$ sample. The mechanism is shown in Fig. 9.

Therefore, to some extent, the presences of $Fe^{2+}$ on $Ce^{4+}$ sites obviate the formation of oxygen vacancies and its associated ferromagnetism. Due to this reason, the ferromagnetism in the system decreases with further doping of Fe ion in the lattice. This similar behaviour is also reported for Co [51] and Ni-doped $CeO_2$ [52] samples, in which the ferromagnetic behaviour occurs up to certain concentration and the further increase in doping concentration gradually decreases the ferromagnetism in the $CeO_2$ sample.

## 4 Conclusions

Single phase polycrystalline samples of pure $CeO_2$, 5 and 10% Fe doped $CeO_2$ have been successfully synthesized using low-temperature solid-state reaction route and well characterized using XRD and XPS measurements. From the Rietveld refinement of the XRD patterns, we have established a fluorite-type face-centred cubic structure for pure $CeO_2$ and both Fe-doped $CeO_2$ samples, which further confirm successful incorporation of Fe ions in the $CeO_2$ matrix. The unit cell volume and other parameters obtained through the Rietveld refinement also show a decrement in the value of cubic lattice parameter, which further supports the incorporation of smaller size Fe ions for larger Ce ions in the host lattice of $CeO_2$. Our UV–Vis–NIR optical absorption studies on Fe doped $CeO_2$ samples displays a red shift in the UV–Vis–NIR absorption spectra, which is accounted for a decrease in the band gap energy and the corresponding increase in the refractive index. The pure $CeO_2$ sample displays diamagnetic behaviour at room temperature, whereas, 10% Fe-doped sample shows weak ferromagnetic behaviour coupled with paramagnetic behaviour. Interestingly the 5% Fe sample display RTFM. The XPS measurements have confirmed presence and transformation of $Fe^{3+}$ to $Fe^{2+}$ and $Ce^{4+}$ to $Ce^{3+}$ chemical states. Therefore, to some extent, the presences of $Fe^{3+}$ at $Ce^{4+}$ sites may be attributed to the formation of oxygen vacancies and trigger ferromagnetism. The FCE coupling forms BMP's to produce a long-range ferromagnetic coupling between $Fe^{3+}$ ions and oxygen vacancy may also be attributed for the observed ferromagnetism in the $Ce_{0.95}Fe_{0.05}O_2$ and $Ce_{0.90}Fe_{0.10}O_2$ sample.

**Acknowledgements** One of the authors (Swati Soni) is thankful to Department of Science and Technology (DST), New Delhi for financial assistance vide grant no. F.No.SR/WOS-A/PM-1021/2015. Authors are also thankful to Banasthali Vidyapith, Niwai, Rajasthan, for extending the experimental facilities of ''Banasthali Centre for Education and Research in Basic Sciences" sanctioned under CURIE programme of the Department of Science and Technology, New Delhi.

## References

1. S. Kumar, G.W. Kim, B.H. Koo, S.K. Sharma, M. Knobel, C.G. Lee, Structural and magnetic study of a diluted magnetic semiconductor: Fe-doped $CeO_2$ nanoparticles. J. Nanosci. Nanotechnol. **11**, 555–559 (2011)
2. K. Srinivas, M. Vithal, B. Sreedhar, M. Manivel Raja, P. Venugopal Reddy, Structural, optical, and magnetic properties of nanocrystalline Co doped $SnO_2$ based diluted magnetic semiconductors. J. Phys. Chem. C **113**, 3543–3552 (2009)

3. T. Dietl, H. Ohno, F. Matsukura, J. Cibert, E.D. Ferrand, Zener model description of ferromagnetism in zinc-blende magnetic semiconductors. Science **287**(5455), 1019–1022 (2000)
4. K. Ueda, H. Tabata, T. Kawai, Magnetic and electric properties of transition-metal-doped ZnO films. Appl. Phys. Lett. **79**, 988 (2001)
5. K.C. Verma, R.K. Kotnala, Oxygen vacancy induced by La and Fe into ZnO nanoparticles to modify ferromagnetic ordering. J. Solid State Chem. **237**, 211–218 (2016)
6. K.C. Verma, R.K. Kotnala, Realizing ferromagnetic ordering in $SnO_2$ and ZnO nanostructures with Fe, Co, Ce ions. Phys. Chem. Chem. Phys. **18**(26), 17565–17574 (2016)
7. A. Kaushik, B. Dalela, R. Rathore, V.S. Vats, B.L. Choudhary, P.A. Alvi, S. Kumar, S. Dalela, Influence of Co doping on the structural, optical and magnetic properties of ZnO nanocrystals. J. Alloys Compd. **578**, 328–335 (2013)
8. B. Santara, P.K. Giri, S. Dhara, K. Imakita, M. Fujii, Oxygen vacancy-mediated enhanced ferromagnetism in undoped and Fe-doped $TiO_2$ nanoribbons. J. Phys. D **47**, 235304 (2014)
9. B. Kaushik, S. Dalela, P.A. Kumar, S. Alvi, Dalela, Role of Co doping on structural, optical and magnetic properties of $TiO_2$. J. Alloys Compd. **552**, 274–278 (2013)
10. S. Yan, S. Ge, W. Qiao, Y. Zuo, F. Xu, Li, Xi, Control of ferromagnetism in Fe-doped $In_2O_3$ by carbothermal annealing. J. Magn. Magn. Mater. **323**, 264–267 (2011)
11. Z. Jing, X. Qinglin, L. Jinmin, Ferromagnetism in Fe-doped CuO nanopowder. J. Semicond. **33**, 013001 (2012)
12. S.K. Sharma, P. Thakur, S. Kumar, D.K. Shukla, N.B. Brookes, C.G. Lee, K.R. Pirota, B.H. Koo, M. Knobel, Room temperature ferromagnetism in Fe-doped $CeO_2$ thin films grown on $LaAlO_3$ (001). Thin Solid Films **519**, 410–413 (2010)
13. F. Vaja Dumitru, O. Oprea, D. Ficai, A. Ficai, C. Guran, Synthesis of $CeO_2$ nanoparticles on the mesoporous Silica support via nanocasting. Dig. J. Nanomater. Biostruct. **9**, 187–195 (2014)
14. M. Dudek, Ceramic electrolytes in the $CeO_2$-$Gd_2O_3$-SrO system—preparation, properties and application for solid oxide fuel cells. Int. J. Electrochem. Sci. **7**, 2874–2889 (2012)
15. M.C. Dimri, H. Khanduri, H. Kooskora, J. Subbi, I. Heinmaa, A. Mere, J. Krustok, R. Stern, Ferromagnetism in rare earth doped cerium oxide bulk samples. Phys. Status Solidi A **209**, 1–6 (2011)
16. A. Sundaresan, R. Bhargavi, N. Rangarajan, U. Siddesh, C.N.R. Rao, Ferromagnetism as a universal feature of nanoparticles of the otherwise nonmagnetic oxides. Physical Review B **74**, 161306 (R) (2006)
17. P.C.A. Brito, D.A.A. Santos, J.G.S. Duque, M.A. Macedo, Structural and magnetic study of Fe-doped $CeO_2$. Physica B **405**, 1821–1825 (2010)
18. J.M.A. Almeida, P.E.C. Santos, L.P. Cardoso, C.T. Meneses, A simple method to obtain Fe-doped $CeO_2$ nanocrystals at room temperature. J. Magn. Magn. Mater. **327**, 185–188 (2013)
19. R.M. Rakhmatullin, V.V. Pavlov, V.V. Semashko, EPR study of nanocrystalline $CeO_2$ exhibiting ferromagnetism at room temperature. Phys. Status Solidi B **253**, 1–5 (2015)
20. S. Phokha, D. Prabhakaran, A. Boothroyd, S. Pinitsoontorn, S. Maensiri, Ferromagnetic induced in Cr-doped $CeO_2$ particles. Microelectron. Eng. **126**, 93–98 (2014)
21. W. Qi-Ye, Z. Huai-Wu, Y. Qing-Hui, L. Sheng, X. De-Gang, Y. Jian-Quan, Fe-doped polycrystalline $ceo_2$ as terahertz optical material. Chin. Phys. Lett. **26**(4), 047803 (2009)
22. S.K. Sharma, M. Knobel, C.T. Meneses, S. Kumar, Y.J. Kim, B.H. Koo, C.G. Lee, D.K. Shukla, R. Kumar, Ferromagnetic properties of bulk Fe-doped $CeO_2$ dilute magnetic semiconductors. J. Korean Phys. Soc. **55**(3), 1018–1021 (2009)
23. S. Phokha, S. Pinitsoontorn, S. Maensiri, Structure and magnetic properties of monodisperse $Fe^{3+}$-doped $CeO_2$ nanospheres. Nano-Micro Lett. **5**(4), 223–233 (2013)
24. A. Lassoued, M.S. Lassoued, B. Dkhil, S. Ammar, A. Gadri, Synthesis, structural, morphological, optical and magnetic characterization of iron oxide ($\alpha$-$Fe_2O_3$) nanoparticles by precipitation method: effect of varying the nature of precursor. Physica E **97**, 328–334 (2018)
25. R.K. Hailstone, A.G. DiFrancesco, J.G. Leong, T.D. Allston, K.J. Reed, A study of lattice expansion in $CeO_2$ nanoparticles by transmission electron microscopy. J. Phys. Chem. C **113**, 15155–15159 (2009)
26. F. Zhang, P. Wang, J. Koberstein, S. Khalid, S.-W. Chan, Cerium oxidation state in ceria nanoparticles studied with X-ray photoelectron spectroscopy and absorption near edge spectroscopy. Surf. Sci. **563**, 74–82 (2004)
27. R.K. Singhal, S. Kumar, A. Samariya, M. Dhawan, S.C. Sharma, Y.T. Xing, Investigating the mechanism of ferromagnetic exchange interaction in non-doped $CeO_2$ with regard to defects and electronic structure. Mater. Chem. Phys. **132**, 534–539 (2012)
28. E. Beche, P. Charvin, D. Perarnau, S. Abanades, G. Flamant, Ce 3d XPS investigation of cerium oxides and mixed cerium oxide ($Ce_xTi_yOz$). Surf. Interface Anal. **40**, 264–267 (2008)
29. A.Q. Wang, T.D. Golden, Anodic electrodeposition of cerium oxide thin films, I. formation of crystalline thin films. J. Electrochem. Soc. **150**, C616-C620 (2003)
30. R. Suresh, V. Ponnuswamy, R. Mariappan, Effect of annealing temperature on the microstructural, optical and electrical properties of $CeO_2$ nanoparticles by chemical precipitation method. Appl. Surf. Sci. **273**, 457–464 (2013)
31. S. Sonsupap, P. Kidkhunthod, N. Chanlek, S. Pinitsoontorn, S. Maensiria, Fabrication, structure, and magnetic properties of electrospun $Ce_{0.96}Fe_{0.04}O_2$ nanofibers. Appl. Surf. Sci. **380**, 16–22 (2016)
32. R. Lubna, B. Shah, H. Ali, W.G. Zhu, Y.Q. Wang, H.W. Song, S.I. Zhang, J.Q. Shah, Xiao, Detailed study on the role of oxygen vacancies in structural, magnetic and transport behavior of magnetic insulator: Co–$CeO_2$. J. Phys.: Condens. Matter. **21**, 486004 (2009)
33. S.A. Ansari, M.M. Khan, M.O. Ansari, S. Kalathil, J. Leea, M.H. Cho, Band gap engineering of $CeO_2$ nanostructure using an electrochemically active biofilm for visible light applications. RSC Adv. **4**, 16782 (2014)
34. X. Zhang, J. Qin, Y. Xue, P. Yu, B. Zhang, L. Wang, R. Liu, Effect of aspect ratio and surface defects on the photocatalytic activity of ZnO nanorods. Sci. Rep. **4**, 4596 (2014)
35. M. Caglar, F. Yakuphanoglu, Structural and optical properties of copper doped ZnO films derived by sol–gel. Appl. Surf. Sci. **258**, 3039–3044 (2012)
36. T.C. Lin, G. Seshadri, J.A. Kelber, A consistent method for quantitative XPS peak analysis of thin oxide films on clean polycrystalline iron surfaces. Appl. Surf. Sci. **119**, 83–92 (1997)
37. T. Yamashita, P. Hayes, Analysis of XPS spectra of $Fe^{2+}$ and $Fe^{3+}$ ions in oxide materials. Appl. Surf. Sci. **254**, 2441–2449 (2008)
38. A.P. Grosvenor, B.A. Kobe, M.C. Biesinger, N.S. McIntyre, Investigation of multiplet splitting of Fe 2p XPS spectra and bonding in iron compounds. Surf. Interface Anal. **36**, 1564–1574 (2004)
39. E.K. Goharshadi, S. Samiee, P. Nancarrow, Fabrication of cerium oxide nanoparticles: Characterization and optical properties. J. Colloid Interface Sci. **356**, 473–480 (2011)
40. A.A. Ansari, Optical and structural properties of sol–gel derived nanostructured $CeO_2$ film. J. Semicond. **31**(5), 053001 (2010)
41. A. Lassoued, M.S. Lassoued, B. Dkhil, A. Gadri, S. Ammar, Structural, optical and morphological characterization of Cu-doped $\alpha$-$Fe_2O_3$ nanoparticles synthesized through co-precipitation technique. J. Mol. Struct. **1148**, 276–281 (2017)
42. P. Nagaraju, Y. Vijaya Kumar, M.V. Ramana Reddy, C. Vishnuvardhan Reddy, V. Raghavendra Reddy, D.M. Phase, Indore-India UGC-DAE-CSR, Preparation, Micro structural characterization

and Optical characterization of pure and Gd-doped ceria thin films. Int. J. Sci. Eng. Res. **5**(3), 185–190 (2014)
43. M. Radovic, Z.D. Dohcevic-Mitrovic, A. Golubovic, B. Matovic, M. Ščepanovic, Z.V. Popovic, Hydrothermal synthesis of $CeO_2$ and $Ce_{0.9}Fe_{0.1}O_2$ nanocrystals. Acta Phys. Pol. A **116**, 614–617 (2009)
44. A. Tiwari, V.M. Bhosle, S. Ramachandran, N. Sudhakar, J. Narayan, S. Budak, A. Gupta, Ferromagnetism in Co doped $CeO_2$: observation of a giant magnetic moment with a high Curie temperature. Appl. Phys. Lett. **88**, 142511 (2006)
45. J.C. Bear, P.D. McNaughter, P. Southern, P. O'Brien, C.W. Dunnill, Nickel-doped ceria nanoparticles: the effect of annealing on room temperature ferromagnetism. Crystals **5**, 312–326 (2015)
46. N.S. Ferreira, L.G. Abracado, M.A. Macedo, The effects of Cr-doping on the room temperature ferromagnetism of chemically synthesized $CeO_{2-\delta}$ nanoparticles. Physica B **407**, 3218–3221 (2012)
47. T.S. Santos, W.S.D. Folly, M.A. Macedo, Ferromagnetism in diluted magnetic Zn-Co-doped $CeO_{2-\delta}$. Physica B **407**, 3233–3235 (2012)
48. Z. Ren, G. Xu, X. Wei, Y. Liu, X. Hou, P. Du, W. Weng, G. Shen, G. Han, Room-temperature ferromagnetism in Fe-doped $PbTiO_3$ nanocrystals. Appl. Phys. Lett. **91**(6), 063106 (2007)
49. A.D. Fauzi, Theoretical study of the effect of oxygen vacancies on magnetism and charge transport of $Fe_3O_4$, March 2017
50. M. Radovica, Z. Dohcevic-Mitrovica, N. Paunovica, M. Ščepanovica, B. Matovicb, Z.V. Popovica, Effect of $Fe^{2+}(Fe^{3+})$ doping on structural properties of $CeO_2$ nanocrystals. Acta Phys. Pol. A **116**(1), 84–87 (2009)
51. Q.-Y. Wen, H.-W. Zhang, Y.-Q. Song, Q.-H. Yang, H. Zhu, J.Q. Xiao, Room-temperature ferromagnetism in pure and Co doped $CeO_2$ powders. J. Phys.: Condens. Matter. **19**, 246205 (2007)
52. A. Thurber, K.M. Reddy, V. Shutthanandan, M.H. Engelhard, C. Wang, J. Hays, A. Punnoose, Ferromagnetism in chemically synthesized $CeO_2$ nanoparticles by Ni doping. Phys. Rev. B **76**, 165206 (2007)

# Study of Electronic structure and Magnetic Properties of Epitaxial Co 2 FeAl Heusler Alloy Thin Films

**ARTICLE** *in* JOURNAL OF ALLOYS AND COMPOUNDS · MARCH 2016

Impact Factor: 3 · DOI: 10.1016/j.jallcom.2016.03.052



**8 AUTHORS**, INCLUDING:

S. Dalela

University of Kota

**53** PUBLICATIONS **138** CITATIONS

SEE PROFILE

Swati Soni

University of Kota

**2** PUBLICATIONS **0** CITATIONS

SEE PROFILE

Krishna Garg

University of Rajasthan

**190** PUBLICATIONS **782** CITATIONS

SEE PROFILE

Journal of Alloys and Compounds 674 (2016) 295–299

Contents lists available at ScienceDirect

Journal of Alloys and Compounds

journal homepage: http://www.elsevier.com/locate/jalcom

# Study of electronic structure and magnetic properties of epitaxial $Co_2FeAl$ Heusler Alloy Thin Films

S. Soni [a], S. Dalela [a, *], S.S. Sharma [b], E.K. Liu [c], W.H. Wang [c], G.H. Wu [c], M. Kumar [d], K.B. Garg [e]

[a] Department of Pure & Applied Physics, University of Kota, Kota 324007, India
[b] Department of Physics, Govt. Women Engineering College, Ajmer, India
[c] State Key Laboratory for Magnetism, Beijing National Laboratory for Condensed Matter Physics, Institute of Physics, Chinese Academy of Sciences, Beijing 100190, China
[d] Department of Physics, Malviya National Institute of Technology, Jaipur-302017, India
[e] Department of Physics, University of Rajasthan, Jaipur-302004, India

ARTICLE INFO

*Article history:*
Received 24 January 2016
Accepted 9 March 2016
Available online 12 March 2016

*Keywords:*
Heusler compound
Dichroism
X-ray absorption spectroscopy (XAS)
X-ray magnetic circular dichroism (XMCD)
Electronic and magnetic properties

ABSTRACT

This work reports the magnetic and electronic characterization of plane magnetized buried Heusler $Co_2FeAl$ nano thin films of different thickness by X-ray absorption spectroscopy (XAS) and X-ray magnetic circular dichroism (XMCD) measurements. . The spectra on both Fe- and Co $L_{2,3}$ edges show a pronounced magnetic dichroic signal in remanence, corresponding to a ferromagnetically-aligned moments on Fe and Co atoms conditioning the peculiar characteristics of the $Co_2FeAl$ Heusler compound (a half-metallic ferromagnet). The detailed knowledge of the related magnetic and electronic properties of these samples over a wide range of thickness of films are indispensable for achieving a higher tunnel magnetoresistance ratio, and thus for spintronics device applications.



## 1. Introduction

New magnetic materials, magnetic semiconductor and half metallic (HM) ferromagnets have been developed by researchers throughout the world so the spintronics devices can exhibit full potential. Out of them, the HM ferromagnets attract the interest of research community as these are the ideal candidates for spintronics due to their exceptional electronic structure [1]. The versatile magnetism of Heusler compounds have been attracted interest for more than 100 years with the invention of the ternary metallic compound $Cu_2MnAl$ by A. Heusler in 1903 [2]. Recently Co-based Heusler alloy thin films have been achieved a great interest as electrodes for magnetic tunnel junctions (MTJ's) [3,4] and as low damping magnetic materials for RF applications [5].

Half-metallic ferromagnetism (HMF) was given by de Groot et al. [6] on the basis of band structure calculation in NiMnSb and PtMnSb, which are termed as half-metals i.e. semi Heusler alloy. Due to ferromagnetic decoupling, these materials have unequal density of states (DOS) of spin up and spin down states at Fermi level ($E_F$) and behave like metals for one electron spin direction and like semiconductor for other spin direction. The spin polarization at $E_F$ for half metallic ferromagnets is 100% which maximizes the efficiency of spintronic devices [7].

Heusler alloys are ternary intermetallic compounds, which are classified as full Heusler alloys $X_2YZ$ and half Heusler alloys XYZ. At the stoichiometric composition, $X_2YZ$ and XYZ have $L2_1$ and $C1_b$ structure, where X and Y are transition 3d-elements like Co, Fe, Ni, Mn, Cr, Ti, V etc and Z is an element of group III, IV or V like Al, Si, Ge, Sb, Ga, As, Sn etc. [8]. The X and Y elements are magnetic but Z is a non-magnetic element. The unit cell have four interpenetrating fcc sub lattices with atoms at A(0,0,0) and C(1/2.1/2.1/2) for X, B(1/4.1/4.1/4) for Y and D(3/4.3/4.3/4) for Z atom, which gives $L2_1$ crystal structure for full compounds, in which $X_1$ and $X_2$ sub lattices are fully occupied, but in half compounds the (1/2.1/2.1/2) site is empty. In full Heusler alloys, the four sub lattices A, B, C, and D are occupied by X, Y, X, and Z atoms, respectively [9]. But in reality, this fully ordered state is difficult to be attained, so different degree of sites get disordered for atoms on X, Y and Z sites. $C1_b$ structure presents vacancies in lattice site, while in $L2_1$ structure these vacancies are occupied by X atoms. The B2 structure presents (Y, Z) site disorder,

* Corresponding author.
*E-mail address:* sdphysics@rediffmail.com (S. Dalela).

http://dx.doi.org/10.1016/j.jallcom.2016.03.052
0925-8388/

while A2 structure presents totally (X, Y, Z) site disorder comparatively to the perfectly ordered $L2_1$ structure [8]. The cobalt-based Heusler compounds, crystallizing in the $L2_1$ structure, show some of the highest Curie temperature (1100 K), high magnetic moment (5–6 $\mu_B$ /f.u.) and complete spin polarization (100% at Fermi level) described as half-metallic ferromagnetism (HMF's). Shan et al. have found that Co-based quaternary full-Heusler compound $Co_2FeAl_{0.5}Si_{0.5}$ behaves like a half metal at room temperature (RT) [10] with 100% spin polarized at Fermi level, and, recently, it has been shown that this material is a magnetic tunnel junctions (MTJ's) with 832% tunnelling magnetoresistance (TMR) at 2 K and 386% at RT [11]. Among Co-based full-Heusler alloys, $Co_2FeAl$ (CFA) is a good material because it shows giant tunnelling magnetoresistance up to 330% [12] and it has low damping [13] which is an important parameter because it is related to the material's dynamic time of response, and thereby, fundamental for high speed device applications [14]. Heusler alloys have attractive magnetic properties due to diverse magnetic phenomena like itinerant and localized magnetism, antiferromagnetism, heavy-fermions behaviour, helimagnetism and Pauli paramagnetism [15–18].

Recent investigations have been revealed that most of the Heusler alloys (not Co based) have either small magnetic moment or even no magnetic moment at all, even though both X and Y elements are ferromagnetic [19,20]. On the other hand, a number of antiferromagnetic compounds also exist, like $Ni_2MnAl$ or $Pd_2MnAl$ [21,22]. Some Heusler compounds with large magnetic moment on both X and Y-sites also exist. For such compounds the ferromagnetic Curie temperature ($T_C$) becomes high, and the ferromagnetic states are very stable. For example, the highest $T_C$ values have been found for $Co_2MnSi$ and $Co_2FeSi$ are 958 K [23] and 1100 K [24] respectively, which show a magnetic moment of Co about 1 $\mu_B$. Experimental results show that for $Cu_2MnAl$ the total magnetic moment of 3.58 $\mu_B$/f.u. is distributed at Cu (0.07 $\mu_B$), Mn (3.49 $\mu_B$), Al (− 0.05 $\mu_B$) [25]. But if the X-constituent is Co, its magnetic moment is larger, e.g. in $Co_2MnSi$ the total magnetic moment per f.u. is distributed at Co (1.02 $\mu_B$), Mn (2.92 $\mu_B$), Si (− 0.07 $\mu_B$), for $Co_2FeAl$, it is distributed at Co (1.12 $\mu_B$), Fe (2.71 $\mu_B$), and Al (− 0.10 $\mu_B$) [26]. If a non-magnetic element is at X-site, the exchange interaction between the Y spins becomes weaker super-exchange type due to hybridization, which is mediated by the electrons of the non-magnetic Z atoms. Depending on the valence of Z, the magnetic interaction can have either sign [27].

X-ray magnetic circular dichroism (XMCD) is the difference between the absorption of light due to a reversal of the light polarization or magnetisation. XMCD spectroscopy is used to investigate the magnetic properties such as orbital and spin contributions to the magnetic moment on specific shell and element. In the case of 3*d* systems, $2p_{1/2,3/2} \rightarrow 3d$ transitions ($L_{2,3}$-edges) give direct information on the 3*d* band responsible for magnetism. The application of the sum rules allows the determination of spin, orbital moments and their anisotropies. Very schematically, if $I_{L_2}$ and $I_{L_3}$ are the dichroic intensities involving electronic excitation from the $2p_{1/2}$ and $2p_{3/2}$ sub-levels, respectively, the combination of $(I_{L_2} + I_{L_3})$ will account for orbital polarization only, and $(I_{L_2} - I_{L_3})$ will give a direct measure of spin polarization [28].

In this paper, we focus on the electrical and magnetic transport properties of $Co_2FeAl$ nano thin film on MgO (001) substrates of different thickness of 5 nm, 10 nm, 20 nm, and 30 nm at room temperature (RT).

## 2. Experimental

The Heusler $Co_2FeAl$ nano-thin films of different thickness of 5 nm, 10 nm, 20 nm, and 30 nm were deposited on MgO (001) single crystal substrates at room temperature (RT) using the ultra-high vacuum magnetron sputtering system with base pressure of below $8 \times 10^{-8}$ Pa. The as-deposited CFA film was composited with stoichiometric $Co_{2.20}Fe_{1.00}Al_{0.91}$ through inductively coupled plasma analysis (ICP). After CFA film deposition, an in-suit post-deposition annealing at 480 °C were carried out for getting highly B2-ordered structure [29]. Finally, to prevent oxidation of the film, the capping of 2 nm thick MgO was deposited. The structural characterization of all CFA film has been performed by *ex-situ* XRD-spectra with *Cu* $K_\alpha$ radiation, and measurements has been performed with out-of-plane ($2\theta/\theta$ scan) and in-plane ($2\theta\chi/\phi$ scan) diffraction. The magnetic properties have been investigated using VSM at room temperature (RT). The magnetic field has been applied in-plane along the [100] and [110] crystallographic orientation of 30 nm thickness of CFA film. The magnetic hysteresis loop of all CFA film showed thickness dependant behaviour. For further details regarding XRD and magnetic hysteresis loop of all CFA film please refer to the paper by *X.Wang* et al. [29].

XAS and XMCD measurements were performed on these films at the BACH beamline of the IOM-CNR at Elettra Synchrotron in Trieste, Italy, on Fe-$L_{2,3}$ and Co-$L_{2,3}$ edges in total electron yield mode (TEY), collecting the drain current on the samples with an energy resolution of 0.3 eV. The samples were magnetized at RT, prior to the XAS/XMCD measurements, along the [001] direction by means of a permanent magnet (~0.5 T) brought in close proximity to the sample. The measurements were then acquired in remanence with the light propagation direction along the [001] direction.

## 3. Result & discussion

### 3.1. XAS results

#### 3.1.1. Co $L_{2,3}$ edge

Fig. 1 shows the XAS and XMCD spectra on Co-$L_{2,3}$ edge for 5, 10, 20 and 30 nm thick $Co_2FeAl$ thin films with right and left incident x-ray circular polarization. The right-polarized XAS spectra ($\mu^+$) are shown with the $L_3$ maximum normalized to 1 and the left-polarized ($\mu^-$) spectra rescaled accordingly. XMCD spectra were normalized to the corresponding isotropic XAS spectra. These absorption peaks, corresponding to the Co-$L_2$ and $L_3$ edges show the transition from $2p_{1/2} \rightarrow 3d$ and $2p_{3/2} \rightarrow 3d$ with the main peaks at 794.2 eV and 778.8 eV respectively. The dichroic spectrum has same feature on $L_2$ and $L_3$ edge at 794.2 eV and 778.7 eV respectively. In particular, XAS-spectra at $L_3$-edge, shows a small feature at 778.8 eV [30]. This small feature is better visible in the XAS spectra acquired with right light polarization at thicknesses $\leq$20 nm, but it is no longer visible for thickness above 30 nm, which is larger than the XAS probe depth at this energy [31]. It is likely associated to oxidization of Co at the interface region with MgO, but surface oxidation cannot be excluded. The oxidized interface presents an isotropic signal of XAS spectrum in the form of $CoO_x$, and in the remanence XMCD signal any ferromagnetic contribution of $CoO_x$ is excluded and multiple structures are no longer visible [32,33]. Inspite of that, another shoulder at higher energy side (~4 eV) from the main Co-$L_3$ peak at 782.7 eV is likely associated with magnetic and atomic ordering of $Co_2FeAl$ thin film at MgO barrier interface [34,35], which has been previously reported by Saito et al. for $Co_2MnSi$ (50 nm) [36]. This shoulder gradually becomes prominent with increasing the thickness of the film, which may be attributed to the characteristic peak of full-Heusler alloy, refers as “Heusler Peak” with $L2_1$ structure [37], and it has been commonly observed for both bulk and thin films [38–40].

#### 3.1.2. Fe $L_{2,3}$ edge

XAS and XMCD signals for thicknesses 5, 10, 20 and 30 nm

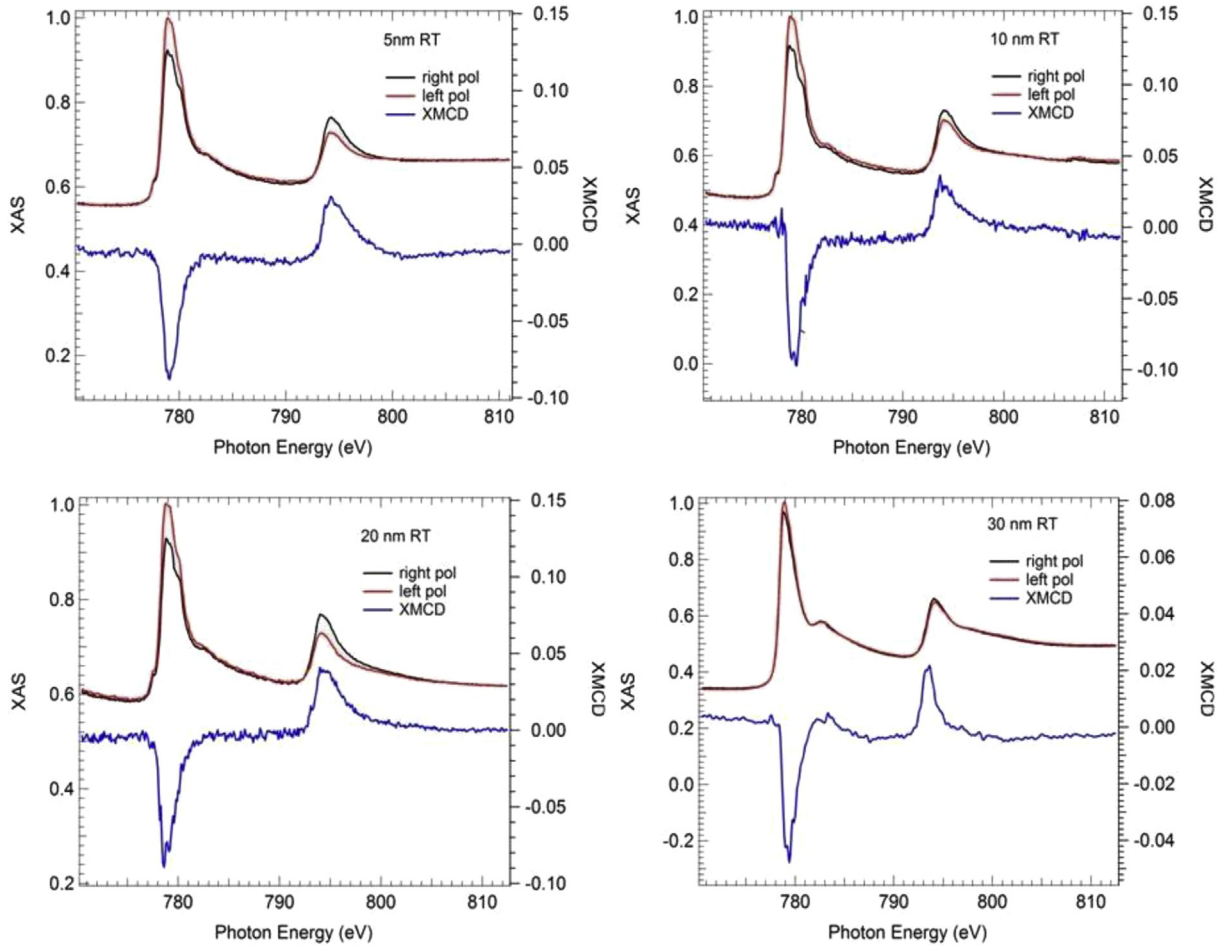


**Fig. 1.** X-ray absorption spectra (XAS) and dichroic spectra (XMCD) on Co-$L_{2,3}$ edges for 5, 10, 20 and 30 nm thick $Co_2FeAl$ thin film.

$Co_2FeAl$ thin films are reported in Fig. 2, showing different Fe-$L_{2,3}$ edge profiles. As in the case of Co, the $L_3$ maximum of right-polarized XAS spectra were normalized to 1 and the left-polarized ones were rescaled accordingly. The XMCD signals were normalized to the corresponding isotropic XAS spectra.

Fig. 2 shows that there is a clear contribution of two components at the $L_3$ edge around 708 and 709 eV for 5 nm, 10 nm, and 20 nm thin films, while a single peak is observed for 30 nm thick sample. The isotropic peak at $L_3$ edge around 709.5 eV is associated to a partial Fe oxidation at the interface with MgO or at the surface [31]. The remanence XMCD signal does not show multiple features in any of these samples due to the absence of ferromagnetic contribution of $FeO_x$. Thus, the 30 nm shows a good crystallographic order of $Co_2FeAl$ thin film and no traces of surface oxidation.

### 3.2. XMCD results

From XMCD we also found a clear ferromagnetic signal at Co-$L_{2,3}$ edge and the data clearly show that Fe and Co are ferromagnetically aligned in all samples. It has been reported that $Co_2FeAl$ films grown on MgO display a soft ferromagnetic behaviour. The magnetic properties are affected by the different film structure, and it is has been found that annealing temperature and thickness of the film strongly change the Curie temperature and magnetic moment of the film [41]. The spin and orbital magnetic moments of both Fe and Co-$L_{2,3}$ edges have been calculated for the 30 nm-thick $Co_2FeAl$ film from XMCD data by applying the sum rules. The numbers of 3d holes for Fe and Co have been considered as $n_d = 3.29$ and 7.51 respectively, which are directly taken from the SPR-KKR density of band calculation, reported elsewhere [42] and neglecting the magnetic dipole term. Calculated values of orbital ($m_L$), spin ($m_S$) and total magnetic moment ($m_L + m_S$) of Fe and Co at $L_{2,3}$ edges for 30 nm thick film of the sample at room temperature are reported in Table 1.

The orbital moment ($m_L$) of Fe-atom (0.070 $\mu_B$/atom) is large in comparison to Co-atom (0.042 $\mu_B$/atom). Our XMCD spectra show a clear dichroic signal at Fe-$L_{2,3}$ edge and the corresponding magnetic moment is 2.77 $\mu_B$/atom. In particular, the value calculated for 30 nm thick film is very well consistent with the theoretically calculated value for Fe-atom in $Co_2FeAl$ thin film of 2.71 $\mu_B$/atom [43]. Magnetic moment of Co and Fe are directly related to the spin polarization at Fermi level. Since spin polarization is reduced due to atomic disordering, this can reduce the magnetic moment of Co and Fe-atom. A recent study of epitaxial $Co_2FeAl$ (CFA) films on MgO (001) with different thickness 5, 10, 20, 30, 50 and 80 nm shows a high ordered B2 structure with an in-plane uniaxial magnetic anisotropy [29]. This type of disordered phase was also observed in $Co_2MnAl$ film [44]. Our XMCD data indicate a parallel alignment of Fe spins, which means that no atomic disorder has been observed in our 30 nm sample. Both the present XMCD data and theoretical analysis of density of state (DOS) shows that there is also substantial magnetic moment located on the Co-site. This moment arises from the two unoccupied bands in the minority conduction band, i.e. the double degenerated Co-states. The presence of Al decreases the localized magnetic moment on both Co and Fe-sites, which are due to the empty majority bands. The important fact is

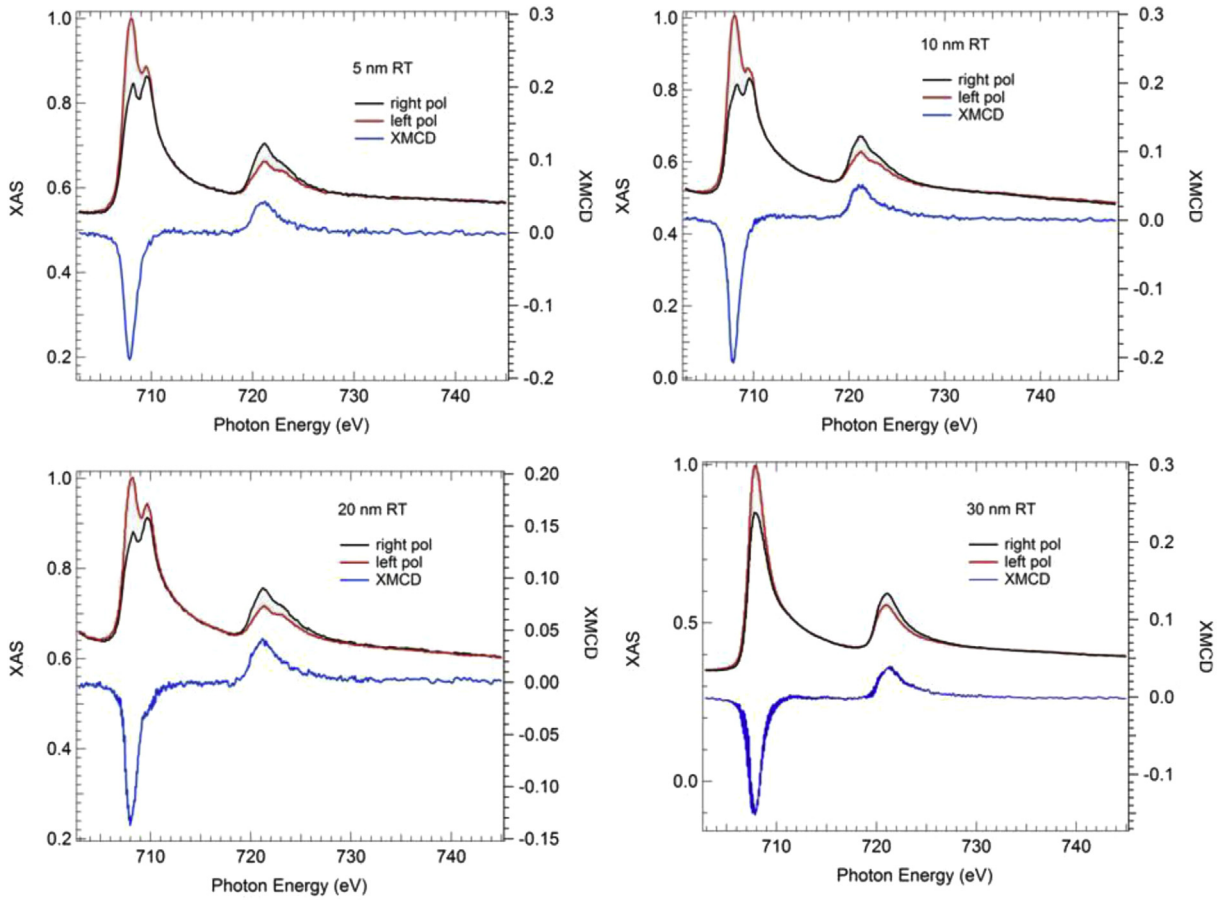


**Fig. 2.** X-ray absorption spectra (XAS) and dichroic spectra (XMCD) on Fe-$L_{2,3}$ edge for 5, 10 and 30 nm thick $Co_2FeAl$ thin film.

**Table 1**
Orbital, Spin and total magnetic moments of Fe and Co atom for 30 nm thick $Co_2FeAl$ thin film at room temperature (RT).

| Thickness of film | Sum rules on Fe $L_{2,3}$ edges | | | |
|---|---|---|---|---|
| | Orbital moment ($m_L$) ($\mu_B$/atom) | Spin moment ($m_S$) ($\mu_B$/atom) | ($m_L/m_S$) | ($m_L+m_S$) ($\mu_B$/atom) |
| Fe 30 nm | 0.070 | 2.70 | 0.03 | 2.77 |
| Co 30 nm | 0.042 | 0.75 | 0.056 | 0.792 |

that Fe atom does not contribute much to the magnetic moment of Al-atom because there is a weak bonding interaction between Fe and Al, due to small electro-negativity of Al. The magnetic moment of Al is negative and it is not large as −0.10 $\mu_B$/f.u [45]. XMCD also show a clear ferromagnetically aligned moment at the Co site. The clear dichroic signals on both Fe and Co-sites indicate a parallel spin alignment. Generally, it is found that $m_L/m_S$ are quite large in these compounds [46,47], but in our 30 nm sample $m_L/m_S$ ratio for Fe-atom is small.

Magnetic moment of Co and Fe is directly related to the spin polarization at Fermi level. Since spin polarization is reduced due to atomic disordering, the magnetic moment on both Co and Fe-sites can be also reduced. Our XMCD spectra shows parallel alignment of Co and Fe-moments, but also parallel alignment of Fe spins which increases the spin moment on Fe-site. The theoretically predicted magnetic moment for Co-based $Co_2FeAl$ thin film with $L2_1$ structure is 3.8 $\mu_B$/f.u., but some other calculation has been reported different values for the magnetic moment as 4.89 $\mu_B$/f.u. [45], 4.9 $\mu_B$/f.u. [48] and 5.0 $\mu_B$/f.u [49]. On the other hand, the bulk samples have smaller magnetic moment than the calculated value [50,51]. In our 30 nm sample, considering the calculated value for the moment at the Al site (−0.10 $\mu_B$/f.u.), the total magnetic moment of the $Co_2FeAl$ film has been experimentally evaluated to be 4.254 $\mu_B$/f.u.

## 4. Conclusion

The electronic and magnetic properties of epitaxial Heuslar $Co_2FeAl$ alloy thin films of different thickness have been investigated using XAS and XMCD measurements. In the Fe and Co-$L_{2,3}$ XAS spectra contributions from $FeO_x$ and $CoO_x$ are present in thinner films. These signals are likely coming from the interfaces with MgO, but they should not contribute to the ferromagnetic signal which is probed by the present XMCD in remanence. On the XAS signal of Fe, the presence of a shoulder at 709.9 eV shows hybridization in the bond between Fe and Al. Our XMCD spectra show that there is a parallel alignment of Fe spins, which means that no atomic disordering exists in our sample. Due to this reason the total magnetic moment of Fe at $L_{2,3}$ edges increases with the thickness of the $Co_2FeAl$ thin film. From XMCD we also found a clear ferromagnetic signal at Co site and the data clearly show that Fe and Co are ferromagnetically aligned for all films.

## Acknowledgement

The authors are thankful to Elettra Synchrotron Trieste and CNR, Italy for the beamtime at the BACH beam line. The authors are also thankful to DST, New Delhi for providing the financial support to carry out the experiment at Elettra under Indo-Italic research programme.

## References

[1] P.J. Webster, Contemp. Phys. 10 (1969) 559.
[2] I. Zutic, J. Fabian, S. Das Sarma, Rev. Mod. Phys. 76 (2004) 323.
[3] S. Kammerer, A. Thomas, A. Hutten, G. Reiss, Appl. Phys. Lett. 85 (2004) 79.
[4] S. Tsunegi, Y. Sakuraba, M. Oogane, K. Takanashi, Y. Ando, Appl. Phys. Lett. 93 (2008) 112506.
[5] B. Rejaei, M. Vroubel, J. Appl. Phys. 96 (2004) 6863.
[6] R.A. de Groot, F.M. Mueller, P.G. van Engen, K.H.J. Buschow, New class of materials: half-metallic ferromagnets, Phys. Rev. Lett. 50 (1983) 2024.
[7] J. De Boeck, W. van Roy, J. Das, V. Motsnyi, Z. Liu, L. Lagae, H. Boeve, K. Dessein, G. Borghs, Semicond. Sci. Tech. 17 (2002) 342. Thin Solid Films 412, 3(2002).
[8] G. Ortiz, M.S. Gabor, T. Petrisor Jr., F. Boust, F. Issac, C. Tiusan, M. Hehn, J.F. Bobo, J. Appl. Phys. 109 (07D324) (2011).
[9] J. Dubowik, I. Goscianska, A. Szlaferek, Y.V. Kudryavtsev, Mater. Pol. 25 (2) (2007).
[10] R. Shan, H. Sukegawa, W.H. Wang, M. Kodzuka, T. Furubayashi, T. Ohkubo, S. Mitani, K. Inomata, K. Hono, Phys. Rev. Lett. 102 (2009) 246601.
[11] N. Tezuka, N. Ikeda, F. Mitsuhashi, S. Sugimoto, Appl. Phys. Lett. 94 (2009) 162504.
[12] W. Wang, H. Sukegawa, R. Shan, S. Mitani, K. Inomata, Appl. Phys. Lett. 95 (2009) 182502.
[13] S. Mizukami, D. Watanabe, M. Oogane, Y. Ando, Y. Miura, M. Shirai, T. Miyazaki, J. Appl. Phys. 105 (2009) 07D306.
[14] R.L. Yilgin, Y. Sakuraba, M. Oogane, S. Mizukami, Y. Ando, T. Miyazaki, Jpn. J. Appl. Phys. 46 (2007) L205.
[15] P.J. Webster, K.R.A. Ziebeck, Alloys and Compounds of D-Elements with Main Group Elements - Part 2. H. P. J. Wijn, Landolt-bornstein, New Series, Group III, 19/c (Springer, Berlin), 1988.
[16] P.J. Webster, K.R.A. Ziebeck, K.-U. Neumann, Magnetic Properties of Metals., New Series, Group III, 32/c (Springer, Berlin), 2001.
[17] J. Pierre, R.V. Skolozdra, J. Alloys Comp. 101 (1997) 262.
[18] J. Tobola, J. Pierre, S. Kaprzyk, R. Skolozdra, M. Kouacou, J. Phys. Condens. Matter 10 (1998) 1013.
[19] J. Kubler, A. Williams, C. Sommers, Phys. Rev. B 28 (1983) 1745, 73.
[20] A. Bergmann, Ladungstransporteigenschaften von Schichtsystemen aus Heusler- verbindungen, Diploma thesis, Ruhr-Universitat Bochum, 2001.
[21] K.R.A. Ziebeck, P.J. Webster, J. Phys. F. 5 (1975) 1756.
[22] P.J. Eewster, R.S. Tebbel, J. Appl. Phys. 39 (1968) 471.
[23] P.J. Eewster, J. Phys. Chem. Sol. 32 (1971) 1221.
[24] K.H.J. Buschow, P.G. Van Engen, J. Magn. Mag. Mat. 25 (1983) 90.
[25] S. Ishida, Y. Kubo, J. Ishida, S. Asan, J. Phys. Soc. Jpn. 48 (1980) 814.
[26] S.E. Kulkova, S.V. Eremeev, T. Kakeshita, S.S. Kulkov, G.E. Rudenski, Mater. Trans. 47 (3) (2006) 599–606.
[27] J. Kuebler, A.R. Williams, C.B. Sommers, Phys. Rev. B 28 (1983) 4.
[28] Cinthia Piamonteze, Piter Miedema, Frank.M. F. de Groot, Phys. Rev. B 80 (2009) 184410.
[29] Xiaotian Wang, Yueqing Li, Yin Du, Xuefang Dai, Guodong Liu, Enke Liu, Zhongyuan Liu, Wenhong Wang, Guangheng Wu, J. Magnetism Magnetic Mater. 362 (2014) 52–57.
[30] Daniel Ebke, Zoe Kugler, Patrick Thomas, Oliver Schebaum, Markus Schafers, Dennis Nissen, Jan Schmalhorst, Andreas Hutten, Elke Arenholz, Andy Thomas, IEEE Trans. Magnetics 46 (6) (June 2010) 1925–1928.
[31] G. Akgul, F. Aksoy, A. Bozduman, O.M. Ozkendir, Y. Ufuktepe, J. Luning, Thin Solid Films 517 (2008) 1000–1004.
[32] T.J. Regan, H. Ohldag, C. Stamm, F. Nolting, J. Lüning, J. Stohr, R.L. White, Phys. Rev. B 64 (2001) 214422.
[33] T. Katayama, S. Yuasa, S. Saito, Y. Kurosaki, T. Saito, T. Kamino, K. Kobayashi, Y. Suzuki, H. Manaka, T. Koide, J. Appl. Phys. 100 (2006) 023912.
[34] J. Schmalhorst, S. Kammerer, M. Sacher, G. Reiss, A. Hutten, Phys. Rev. B 70 (2) (2004) 024426.
[35] W. Regan, Phys. Rev. B 64 (21) (2001) 214422.
[36] Toshiaki Saito, Toshikazu Katayama, Ai Emura, Noa Sumida, Nanae Matsuoka, Takayuki Ishikawa, Tetsuya Uemura, Masafumi Yamamoto, Daisuke Asakura, Tsuneharu Koide, J. Appl. Phys. 103 (2008) 07D712.
[37] Benjamin Balke, Sabine Wurmehl, Gerhard.H. Fecher, Claudia Felser, Jurgen Kubler, Sci. Technol. Adv. Mater 9 (2008) 014102.
[38] J. Schmalhorst, S. Kammerer, M. Sacher, G. Reiss, A. Hutten, A. Scholl, Phys. Rev. B 70 (2004) 024426.
[39] N.D. Telling, P.S. Keatley, G. Van der Laan, R.J. Hicken, E. Arenholz, Y. Sakuraba, M. Oogane, Y. Ando, T. Miyazaki, Phys. Rev. B 74 (2006) 224439.
[40] S. Wurmehl, G.H. Fecher, H.C. Kandpal, V. Ksenofontov, C. Felser, H.J. Lin, Appl. Phys. Lett. 88 (2006) 032503.
[41] A. D. Rata, H. Braak, D. E. Burgler, S. Cramm, And C. M. Schneider, Eur. Phys. J. B Condens. Matter Phys.; 52, 4; 445–451.
[42] H. Ebert, Electronic Structure and Physical Properties of Solids, in: H. Dreyssè (Ed.), Lecture Notes in Physics, 535, Springer, Berlin (, 2000, p. 191. The Munich SPR-KKR package, Version 3.6, http://olymp.cup.uni-muenchen.de/ak/ebert/SPRKKR. H. Ebert.
[43] S.E. Kulkova, S.V. Eremeev, T. Kakeshita, S.S. Kulkov, G.E. Rudenski, Mater. Trans. 47 (3) (2006) 599.
[44] A. Hirohata, M. Kikuchi, N. Tezuka, K. Inomata, J.S. Claydon, Y.B. Xu, G. van der Laan, Curr. Opin. Solid State Mater. Sci. 10 (2006) 93–107.
[45] I. Galanakis, P.H. Dederichs, N. Papanikolaou, Phys. Rev. B 66 (2002) 174429.
[46] H.J. Elmers, S. Wurmehl, G.H. Fecher, Field dependence of orbital magnetic moments in the Heusler compounds $Co_2FeAl$ and $Co_2Cr_{0.6}Fe_{0.4}Al$, Appl. Phys. A 79 (3) (2004), 557–56.
[47] A. Yamasaki, S. Imada, R. Arai, Orbital angular momentum and interpretation of core-absorption magnetic circular dichroism on the band picture in Co-based Heusler alloys $Co_2YSn$ (Y=Ti, Zr, and Nb), Phys. Rev. B 65 (10) (2002) 104410l.
[48] I. Galanakis, J. Phys. Condens. Matter 16 (2004), 3089. 50.
[49] S.H. Nie, Y.Y. Chin, W.Q. Liu, J.C. Tung, J. Lu, H.J. Lin, G.Y. Guo, K.K. Meng, L. Chen, L.J. Zhu, D. Pan, C.T. Chen, Y.B. Xu, W.S. Yan, J.H. Zhao, Phys. Rev. Lett. 111 (2013) 027203.
[50] H.J. Elmers, G.H. Fecher, D. Valdaitsev, S.A. Nepijko, A. Gloskovskii, G. Jakob, G. Schonhense, S. Wurmehl, T. Block, C. Felser, P.-C. Hsu, W.-L. Tsai, S. Cramm, Phys. Rev. B 67 (2003) 104412.
[51] H.J. Elmers, S. Wurmehl, G.H. Fecher, G. Jakob, Appl. Phys. A 79 (2004) 557.

# Interplay of structural, optical and magnetic properties in Gd doped CeO2

S. Soni, Sudish Kumar, R. S. Meena, V. S. Vats, and S. Dalela

Citation: AIP Conference Proceedings **1665**, 130029 (2015); doi: 10.1063/1.4918177
View online: http://dx.doi.org/10.1063/1.4918177
View Table of Contents: http://scitation.aip.org/content/aip/proceeding/aipcp/1665?ver=pdfcov
Published by the AIP Publishing

# Interplay of Structural, Optical and Magnetic properties in Gd doped $CeO_2$

S. Soni[1], Sudish Kumar[2], R.S. Meena[3], V. S. Vats[4] and S. Dalela[1,*]

[1]*Department of Pure & Applied Physics, University of Kota, Kota-324007, Rajasthan, INDIA*
[2]*Department of Physics, Mohan Lal Sukhadia University, Udaipur, Rajasthan, INDIA*
[3]*National Physical Laboratory, Pusa, New-Delhi, INDIA*
[4]*Department of Physics, Govt. College, Dhaliara, India*
**Email:sdphysics@rediffmail.com*

**Abstract.** In this research wok systematic investigation on the synthesis, characterization, optical and magnetic properties of $Ce_{1-x}Gd_xO_2$ (where x=0.02, 0.04, 0.06, and 0.10) synthesized using the Solid-state method. Structural, Optical and Magnetic properties of the samples were investigated by X-ray diffraction (XRD), UV-VIS-NIR spectroscopy and VSM. Fluorite structure is confirmed from the XRD measurement on Gd doped $CeO_2$ samples. Magnetic studies showed that the Gd doped polycrystalline samples display room temperature ferromagnetism and the ferromagnetic ordering strengthens with the Gd concentration.
Keywords: Gd-$CeO_2$ polycrystalline, RTFM, SQUID, Structural and Optical properties..
**PACS:** 85.75.-d, 75.50.Pp, 61.43.Dq, 78.20.-e

## INTRODUCTION

Dilute magnetic semiconductors (DMSs) have attracted wide research attention due to their potential application in Spintronics and microelectronics [1]. Research interests were triggered by reports of robust enhancement in their magnetization at 300K upon their hydrogenation [2]. Defects, especially, the oxygen vacancies and their link to ferromagnetism, have been focus of recent research in magnetic semiconductors. It is proposed that oxygen vacancies form donor impurity band that assist in establishing exchange coupling in ZnO, $TiO_2$, $SnO_2$ etc[3]. Besides these semiconductors, some dielectrics/insulators like $CeO_2$ are also found to show the room temperature ferromagnetism (RTFM) [4]. However, the exchange mechanism in them is expected to be different than that in the magnetic semiconductors. Many studies on transition metal doped $CeO_2$ have been reported. Tiwari *et al.* [5] showed that the Co-doped $CeO_2$ displays room temperature ferromagnetism with high magnetic moment ($8.2\mu_B$/Co) and Curie temperature (725 K).

In this research paper, we have carried out a systematic study of the Gd doped $CeO_2$ polycrystalline samples prepared by solid-state reaction method with the help of XRD, UV-VIS-NIR Spectroscopy, and VSM techniques.

## EXPERIMENTAL DETAILS

Polycrystalline samples in the series $Ce_{1-x}Gd_xO_2$ (where x = 0.02, 0.04, 0.06 and 0.10) were prepared using the solid-state reaction route. In solid-state reaction route of preparation, the powders were calcinated for 15 hours at 500 $^oC$ in a microprocessor controlled furnace to obtain the polycrystalline precursors. Then the powder were pressed into Pellets (12 mm diameter and 1 mm thickness) using a hydraulic pressure of nearly 5 tons and then sintered at 900 $^oC$ in Ar atmosphere.

The phase purity and crystalline structure of the samples were determined by powder X-ray diffraction. Rietveld profile refinements of the XRD patterns were carried out using the FULLPROF Program. Optical absorption spectra were studied using a Perkin-Elmer Lambda 750 UV-VIS-NIR spectrophotometer with pre-aligned Tungsten, Halogen and Deuterium sources. The magnetic properties were studied on a VSM.

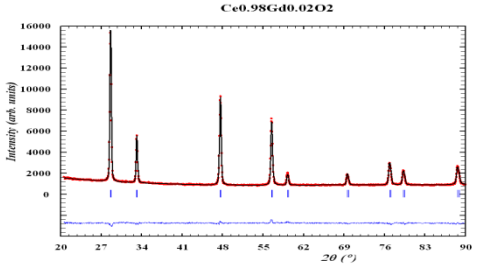


**FIGURE 1.** XRD Pattern of $Ce_{1-x}Gd_{0.02}O_2$ sample.

## RESULTS AND DISCUSSION

*Solid State Physics*
AIP Conf. Proc. 1665, 130029-1–130029-3; doi: 10.1063/1.4918177

### *XRD Spectra of Gd doped $CeO_2$ samples*

Figure 1 shows the XRD pattern of $Ce_{1-x}Gd_xO_2$ (where x=0.02, 0.04, 0.06, and 0.10) samples, all diffraction peaks corresponds to $CeO_2$ fluorite structure. No secondary phase was detected within the sensitivity of XRD. It is clear from the XRD spectra that all the exhibited peaks are consistent with the face centered cubic fluorite structure of $CeO_2$ in the space group of *Fm*-3*m*, in which Ce is located at 4*a* position, surrounded by eight O (located at 8*b)* positions. The XRD patterns indicate that the cubic fluorite structure of the $CeO_2$ samples is not altered by Gd substitution as none of the diffraction peaks corresponding to cluster formation of Gd and $Gd_2O_3$ type related impurity phases have been observed in the Gd-doped $CeO_2$ samples, which further confirmed the formation of a single phase of $Ce_{1-x}Gd_xO_2$ and also confirmed the substitution of Gd at Ce sites. Rietveld profile refinements of all the samples have been carried out and the results are listed in Table 1. Gd doping at Ce-site in $CeO_2$ leads to monotonic enhancement in the lattice parameter in comparison to undoped $CeO_2$. This change is possibly due to the replacement of the smaller $Ce^{+4}$ ions (0.97 **Å**) by the larger $Gd^{+3}$ ions (1.053 **Å**) into the crystal lattice

### *Optical properties of Gd doped $CeO_2$ samples*

Figure 2 shows the UV-visible optical absorption spectra of 2, 4, 6 and 10% Gd doped bulk $CeO_2$. The samples show a strong absorption below 400 nm with an absorbance peak in the UV range, due to charge-transfer transition from $O^{2-}$ (2p) to $Ce^{4+}$ (4f) orbital's in $CeO_2$, which indicate that the charge transfer transition of $Ce^{4+}$ overlaps with the $4f^1$-$5d^1$ transition of $Ce^{3+}$ [6], it is also known as f-f spin orbit splitting of the Ce 4f state [7]. The band gap energies of Gd doped $CeO_2$ have been calculated from their absorption curves, using Tauc's relation. The refractive index of bulk $CeO_2$ has been calculated by using the equation (1). Where n is the refractive index of the material and $E_{Opt.}$ is the optical band gap. We can see that the calculated values of refractive index for Gd doped bulk Ceria is found to decrease with increasing doping concentration of Gd ion in Ceria.

Form the calculated values of optical band gap it is clear that as the doping concentration of Gd increased in bulk $CeO_2$ band gap energy is also increased. This indicates blue shift due to increasing the doping concentration. At the outermost $CeO_2$ surface, $Ce^{4+}$ ion coexist with $Ce^{3+}$ ions.

**Table 1: Details of XRD data Analysis**

| ***Samples $Ce_{1-x}Gd_xO_2$*** | ***x=0.00*** | ***x=0.02*** | ***x=0.04*** | ***x=0.06*** | ***x=0.10*** |
|---|---|---|---|---|---|
| ***Lattice Parameter - a (Å)*** | *5.4025(7)* | *5.4038(5)* | *5.4088(4)* | *5.4127(6)* | *5.4135(6)* |
| ***Unit Cell Volume - V($Å^3$)*** | *157.66(3)* | *157.80 (2)* | *158.23(2)* | *158.58(3)* | *158.65(2)* |
| $R_p$ | *2.78* | *2.61* | *3.42* | *2.86* | *3.01* |
| $R_{wp}$ | *3.56* | *3.32* | *4.56* | *3.70* | *3.85* |
| $R_{exp}$ | *2.98* | *2.86* | *3.08* | *3.58* | *3.55* |
| $\chi^2$ | *1.43* | *1.34* | *2.19* | *1.07* | *1.18* |
| $R_{Bragg}$ | *4.35* | *5.51* | *8.18* | *3.89* | *3.38* |

**Table 2: The calculated optical band gap values and refractive index**

| *S.No.* | *Name of the sample* | *Optical band gap in eV* | *Refractive index (n)* |
|---|---|---|---|
| *1* | ***$Ce_{1-x}Gd_xO_2$(x=0.02)*** | *3.09* | *2.37* |
| *2* | ***$Ce_{1-x}Gd_xO_2$(x=0.04)*** | *3.11* | *2.368* |
| *3* | ***$Ce_{1-x}Gd_xO_2$(x=0.06)*** | *3.14* | *2.360* |
| *4* | ***$Ce_{1-x}Gd_xO_2$(x=0.10)*** | *3.17* | *2.352* |

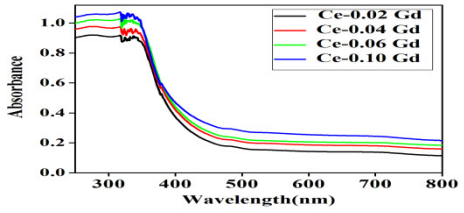


**FIGURE 2.** Absorption spectra of 2%, 4%, 6% and 10% Gd doped bulk $CeO_2$

### *Magnetic Measurements*

The magnetization (M) of $Ce_{1-x}Gd_xO_2$ (where x=0.02, 0.04, 0.06, and 0.10) polycrystalline samples as a function of magnetic field (H) measured at room temperature using VSM. The well defined exhibited hysteresis loops, readily reveal an unmistakable RTFM ordering in the samples. We can see that the magnetization of $Ce_{1-x}Gd_xO_2$ samples increases with Gd content. As seen from the figure 3 the doped

sample is the superposition of two components; one is paramagnetic and second is ferromagnetic.

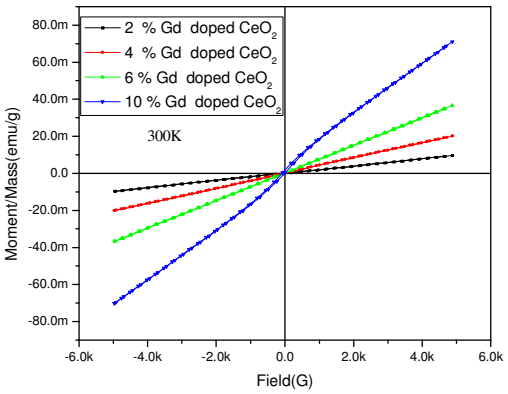


**FIGURE 3.** Field dependent magnetization M (H) measurements of Gd doped $CeO_2$ sample.

In nature, 2% Gd doped sample shows a approximate linear M-H behavior, which indicates that a dominant paramagnetic ordering is present in the sample, which is superimposed with ferromagnetic ordering but in the case of 10% Gd-doped sample, a curvature is observed near the origin, which indicates that a ferromagnetic component is superimpose over the strong paramagnetic background at room temperature. Bulk Gd is ferromagnetic with Curie temperature ~300K, but in our sample it has been observed that for the low concentration of Gd-ions could not able to enhance the ferromagnetism in the sample at room temperature but for 10% Gd-doped sample a small change in the strong paramagnetic to ferromagnetic behavior at RT is seen. Similarly Dimri et al. reported ferromagnetic behavior with some linear paramagnetic behavior at room temperature for 20% Nd and Sm doped $CeO_2$ and ferromagnetism originated due to phase purity and oxygen vacancies which may be created due to rare earth doping, but 10% Gd doped $CeO_2$ bulk sample could not exhibit room temperature ferromagnetism in their sample [8]. In our sample the RT-FM has been achieved as trivalent Gd ion concentration increased in $CeO_2$ sample, which may be due to oxygen vacancies and the defect formation on cluster sites. The direct ferromagnetic coupling is called F-centre exchange (FCE) mechanism. In FCE mechanism, the magnetic ions and oxygen vacancy gives the ferromagnetic ordering. As the $CeO_2$ can have variable valance states like $Ce^{+3}$ or $Ce^{+4}$, so it is possible that oxygen vacancy can create magnetic moment on neighboring Ce-ions of $Ce^{+3}Ce^{+3}$, where  denotes the oxygen vacancy. When trivalent Gd ion is doped in $CeO_2$ sample, according to the FCE mechanism F centre consists of an electron trapped in oxygen vacancy with two Gd ions (i.e. $Gd^{+3}Gd^{+3}$). The electron trapped in oxygen vacancy occupies an orbital which overlaps the d-shell of neighboring Gd ions. According to the Hund's rule and Pauli principle the trapped electrons spin should have direction parallel to two neighboring Gd ions, which results ferromagnetic ordering. The ferromagnetic ordering in our sample is associated with FCE coupling between Gd ions and oxygen vacancy. The XRD spectra of the sample shows that $Gd^{+3}$ ion is substituted in $CeO_2$ and Ce ion in +3 state (with $4f^1$ configuration), which can be ascribed the oxygen vacancy in Gd doped $CeO_2$ sample. Therefore, FCE mechanism in complex structure of $Gd^{+3}Gd^{+3}$ shows RT-FM in the sample. This F-centre exchange coupling between oxygen defect and Gd ions form BMP's (bound magnetic ploarons), these neighboring BMP's can overlap and give result in the long range Gd-Gd ferromagnetic coupling in doped $CeO_2$ sample.

The effect of Gd doping on the crystal structure, optical and magnetic properties of $CeO_2$ have been investigated systematically. As the concentration of Gd ion is increased in the sample, therefore this long range magnetic ordering exist in between the different states of Gd ions and oxygen ion. Therefore, RTFM in the sample may be arising due to F-centre exchange coupling between oxygen defect and the overlapping of BMP's formed by Gd ions.

## REFERENCES


1. K. E., Goharshadi, S. Samiee, and P. Nancarrow, *J. of Colloid and Interface Sc.* **356**, 473–480 (2011).
2. D. Zhang, X Ni, H. Zheng, X Zhang, and J Song, *Solid State Sci.* **8**,1290 (2006).
3. S. Burinskas, V. Adomonis, V. Žalnierukynas, J. Dudonis, and D. Milčius *Mater. Sc.* **16,** ISSN 1392–1320( 2010).
4. A Hartridg,, *J. of Phys. and Chem. of Solids* **59**, 859 – 866 (1998).
5. V. E. Gaffet, and C. Meunier, *Mat. Sc. and Engineering A* **366,** 229 – 238 (2004).
6. M. Radovic, Z. Dohcevic-Mitrovic A. Golubovic, V. Fruthb, S. Predab, M. Sc epanovic, and Z. V. Popovic, *Cearmics International* **39**, 4929–4936(2013).
7. D. E. Zhang, X. M. Ni, H. G. Zheng, X. J. Zhang, and J. M. Song, *Solid State Sciences* **8**, 1290–1293(2006).
8. M. C. Dimri, H. Khanduri, H. Kooskora, J. Subbi, I. Heinmaa, A. Mere, J. Krustok, and R. Stern, *Phys. Status Solidi A* **209**, 353-358 (2012).